V.F. Modeling Advanced Electrode Materials

V.F.1. Electrode Materials Design and Failure Prediction (LBNL)

Venkat Srinivasan, Principal Investigator
Lawrence Berkeley National Laboratory
1 Cyclotron Road
Berkeley, CA 94720
Phone: 510-495-2679
E-mail: vsrinivasan@lbl.gov

Tien Q. Duong, DOE Program Manager
U.S. Department of Energy
Advanced Battery Materials Research (BMR)
Vehicle Technologies Office
1000 Independence Avenue, SW
Washington, DC 20585
Phone: 202-586-7836
E-mail: Tien.Duong@ee.doe.gov

Start Date: October 1, 2015
End Date: September 30, 2016

Abstract

Lithium-sulfur (Li-S) cells promise to increase the energy density and decrease the cost of batteries compared to the state-of-the-art. If the performance and cycling challenges can be alleviated, these systems hold the promise for meeting the required EV targets. The main aim of this project is to develop mathematical models that can describe the power and cycling performance of next-generation battery systems. The present focuses are on microscale modeling of conventional electrodes and on Li-S cells. The models will serve as a guide for better design of materials, such as in the kinetics and solubility needed to decrease the morphological changes in sulfur cells and increase power performance.

Objectives

- Use continuum-level mathematical models along with controlled experiments on model cells to:
  - Understand the performance and failure modes associated with next-generation battery materials.
  - Design battery materials and electrodes to alleviate these challenges.
- For Li-S systems, develop a mathematical model for the chemistry along with obtaining the necessary experimental data.
- Develop a modified macro-homogenous porous electrode model that incorporates microscale data in order to improve predictive accuracy under demanding conditions.

Accomplishments

- A correlation between film growth inside the cathode and electrochemical response has been established.
- Concentration dependent transport properties (conductivity and diffusivity) of electrolyte and polysulfide solutions have been measured.
- The measured transport parameters have been incorporated within the porous-electrode-theory model developed for Li-S batteries, and the cell performance predicted by the model has been compared with the experimental results.

- Porosity gradient and tortuosity were obtained from tomography data of NMC porous electrodes and have been incorporated into a macroscale electrochemical model.

Future Achievements

- Produce a mathematical model that can describe the power and cycling performance of next-generation lithium-ion battery systems.
- Use this model to guide the design of materials and morphology to increase energy and power performance.

Technical Discussion

Background

High energy and power density combined with long cycle life and safety are critical for reducing the cost of rechargeable batteries and, in turn, electric vehicles. Proper optimization of design parameters in such systems can be challenging; for example, thick porous electrodes result in large energy densities, but their power density can become a concern. Mathematical modeling is useful for understanding physical, chemical and transport phenomena inside electrodes, and in this way can assist in design optimization. The main goal of this project is to develop such mathematical models for candidate battery chemistries.

The lithium-sulfur chemistry could potentially lead to a new generation of highly cost-effective batteries. Since one mole of sulfur (S_8) reacts with sixteen moles of electrons, sulfur-based cathodes have the potential to produce very high energy density. Also, abundance of sulfur in earth's crust can make Li-sulfur batteries a cheaper alternative to present lithium-ion batteries with metal-oxide cathodes. However, due to the heterophase multistep chemical and electrochemical reactions associated with reduction of sulfur, the power density and cycle life of Li-S cells is very poor. Also, even at extremely low rates of operation, the Li-S systems are unable to deliver full theoretical capacity. From these observations, it can be concluded that the Li-S system is not well-understood. The goal of the Srinivasan group's work in this project is to supply insight into the operation of these systems.

In a range of battery chemistries, porous electrode microstructure is known to influence battery performance. However, traditional macro-homogeneous porous electrode models average out spatial information in order to reduce computational costs. In addition, it is well-known that such macroscale models tend to diverge from experimental results at higher rates. Work by the Srinivasan group on comparing macroscale and microscale models, and modifying macroscale models with non-traditional microscale information, is meant to determine the extent to which spatial averaging harms predictive accuracy of the macroscale models.

Introduction

Complementary modeling and experimental approaches have been adopted by the Srinivasan group in order to better understand next-generation Li-S systems, specifically in the limitations in power density and cycle life of Li-S cells and in the transport of electrolytes and polysulfide ions within the cathode microstructure and separator. Electrochemical measurements were performed and transport properties of electrolyte solutions were measured in order to inform the development of a new model that captures the qualitative discharge behavior of a Li-S cell.

In FY15, X-ray microtomography of NMC porous electrodes was used to generate interlocking surface meshes containing active material and solution-soaked regions, for use as the basis of spatial domains for microscale electrochemical simulations. A macroscale model based on this material was previously developed by the Srinivasan group. The goal of the microstructure-related work in FY16 was to introduce modifications into this macroscale model based on microscale information, in order to determine if this additional information leads to a significant improvement in predictive capabilities.

Approach

Fabrication of Li-S cells

Sulfur cathode laminates were prepared from slurries of conductive carbon, sulfur and PVDF binder, with a dried coating thickness of 75μm. These were incorporated into coin cells with lithium metal anodes and 1M LiTFSI salt dissolved in 1:1 (by volume) DOL/DME solvent as electrolyte solution. The cells were cycled at different C-rates at room temperature.

Measurement of transport properties

Sulfur (S_8) and lithium sulfide (Li_2S) were dissolved in stoichiometric amounts in a 1:1 DOL/DME solvent mixture. The resulting polysulfide solutions were expected to contain primarily Li_2S_6 or Li_2S_8, depending on the stoichiometry. Additionally, electrolyte solutions with a range of concentrations of LiTFSI in 1:1 DOL/DME solvent were prepared. Concentration-dependent conductivity values of both the polysulfide and electrolyte solutions were measured using a conductivity meter. Additional experiments were performed to explore the dependence of LiTFSI salt solution conductivity with polysulfide (Li_2S_6 and Li_2S_8) concentration. Transference number values were obtained using the Bruce-Vincent method. A methodology based on the restricted diffusion technique was developed to measure concentration-dependent diffusion coefficients of Li^+ and polysulfide species (S_8^{2-} and S_6^{2-}). This analysis used the slope of the log (potential) vs. time curve obtained during relaxation of a cell. Lithium metal electrodes were used for measuring the diffusion coefficient of Li^+ in LiTFSI salts, and glassy carbon electrodes were used for measuring diffusivity of the polysulfide species (S_8^{2-} and S_6^{2-}).

Modification of macroscale model with microscale information

Tortuosity for an NMC porous electrode was obtained by constructing a new simulation in which the spatial domain, obtained by processing X-ray microtomography data obtained in FY15, was placed between two virtual electrodes maintained at different potentials, with the phase previously representing active and conductive material now taken as an insulator, and the phase previously representing the pore space now taken as a conductor. Laplace's equation, describing electrical potential, was then solved over the combined domain. The average current density through a plane parallel to the electrodes was then used to determine the ratio of effective conductivity of the microporous structure to intrinsic conductivity of the pore "material". This ratio is equal to the ratio of porosity and tortuosity.

Custom programs were written and applied to the raw tomography data in order to determine the spatially-averaged porosity of each voxel "slice" through the electrode parallel to the current collector and to then compute a least-squares straight-line fit to the results. This line provides a simple position-dependent description of porosity, with the slope describing an approximate porosity gradient.

Results

Film growth and impact on electrochemical performance

We have investigated physical processes by observing the relaxation behavior of Li-S batteries. The concentration gradient will build up within a cell when current is applied and vanish after interrupting the applied current. Figure V-164a shows the relaxation behavior of Li-S cells at different C-rates, recorded after the cells reached end of discharge. The relaxation kinetics clearly depend on rate of discharge. The slow approach of the potentials toward asymptotes at long times might be attributed to a combination of electrochemical reactions and double-layer capacitance effects; the different C-rates might lead to different amount of discharge product and different capacitance, resulting in different relaxation kinetics. Alternatively, transport phenomena, including those within the film formed on the reaction surface during discharge, suggest another possible explanation for the relaxation behavior.

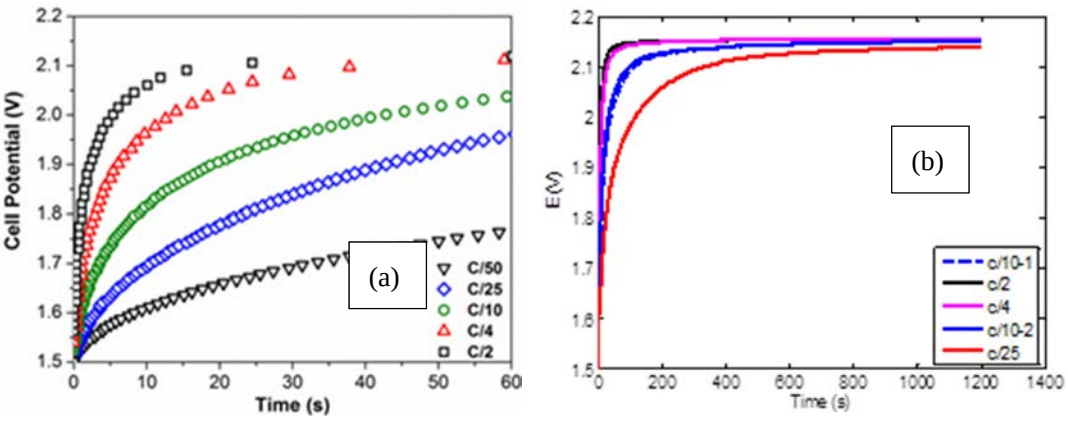

Figure V-164: (a) Relaxation behavior of Li-S cells previous discharged at different C-rates, which were recorded after the cells reached end of discharge. (b) Relaxation behavior at different C-rates of a Li-S cell which has been previously discharged to 1.5 V at a C/10 rate

In order to explore these possible explanations, we examined relaxation behavior at different C-rates of a Li-S cell, discharged initially to 1.5 V at a C/10 rate in order to set a reference film thickness. After the initial discharge step, the cell underwent a sequence of rest and discharge steps at different C-rates. Relatively small amounts of current were passed during the discharge steps. In Figure V-164b the curve labeled "C/10-1" shows the relaxation after the initial C/10 discharge step, and "C/10-2" is from the subsequent C/10 discharge. The relaxation behavior is rate-dependent despite the fixed film thickness, indicating that relaxation is more like a transport-limited process than a double-layer capacitance effect. Figure V-165a shows a plot of $\ln(E_{oc}-E_{ss})$ vs. time. A linear region at the later stage of relaxation (Figure V-165b) confirms the transport-limited process. The extracted slopes of linear lines (Figure V-165c) are quite similar at different C-rates due to the essentially fixed film thickness. The calculated characteristic transport time (L^2/D) is around 1.23×10^4 s, which is large and may limit cell performance.

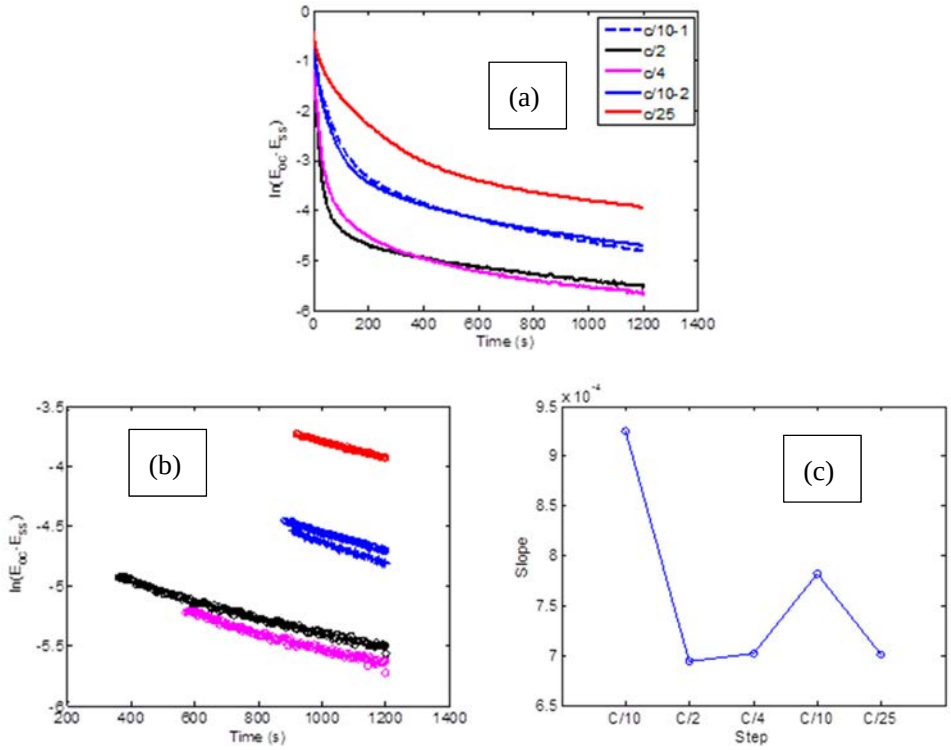

Figure V-165: (a) ln (Eoc-Ess) vs. Time (s); (b) plot of linear region of curves in (b) with fitting line; (c) extracted slopes of fitting lines at different C-rates

Measurement of Transport Properties

Since the electrolyte used in Li-S cells consist of a binary salt and a neutral solvent, three different parameters should be sufficient to accurately characterize the transport of ions through the liquid. In the present context, we measure the conductivity, transference number and diffusivity of the electrolyte solution. Concentration-dependent conductivities of S_6^{2-} and S_8^{2-} (by stoichiometric ratios) polysulfide solutions (see Figure V-166a) and LiTFSI electrolyte salts (see Figure V-166b) were measured using a conductivity meter. Figure V-166a indicates that with increasing concentration of sulfur within the polysulfide solution, conductivity increases and eventually saturates. Higher concentrations of sulfur were not studied because at sufficiently high concentrations, saturation and precipitation of polysulfides occurs at room temperature. As demonstrated in Figure V-166b, the decrease in conductivity of LiTFSI is attributed to the high concentration of salt and subsequent increase in viscosity of the electrolyte.

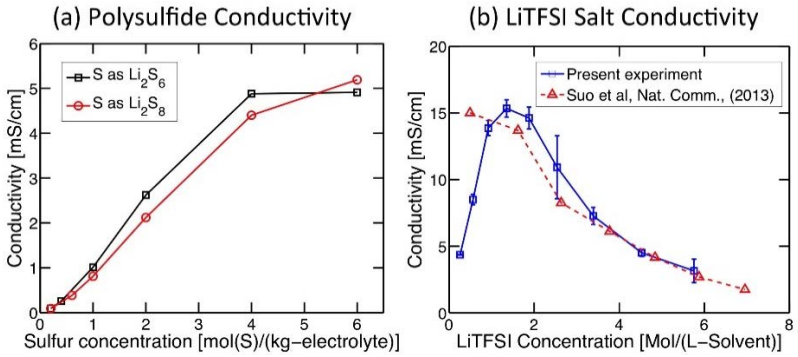

Figure V-166: (a) Concentration dependent conductivity of two different polysulfide solutions, Li_2S_6 and Li_2S_8. (b) Concentration dependent conductivity of LiTFSI salt in 1:1 DOL/DME solvent compared with published results

In a real Li-S cell, the electrolyte solution contains not only LiTFSI salt dissolved into DOL/DME, but also significant amount of polysulfides (Li_2S_8 and Li_2S_6). Hence, it is important to investigate how the conductivity of the electrolyte salt changes with increasing amount of polysulfide concentration. It was observed that the conductivity variation is very similar for both of these polysulfide species. Figure V-167 demonstrates that increased presence of polysulfides does not impact the conductivity significantly at low concentration of LiTFSI salt. However, the maximum conductivity and conductivity at high concentration both experience rapid decay with increasing polysulfide concentration.

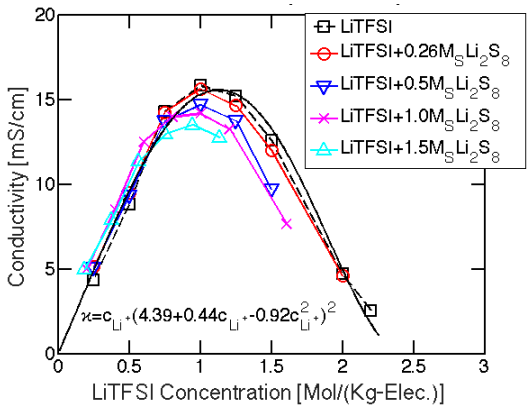

Figure V-167: Conductivity of the LiTFSI salt dissolved in 1:1 DOL/DME solvent combined with different amounts of polysulfide (Li_2S_8) solution

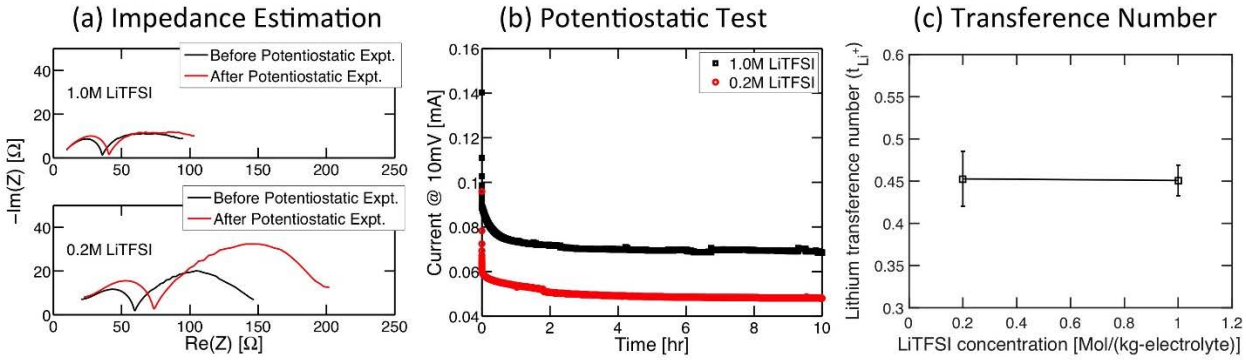

Figure V-168: (a) Nyquist plot to estimate the impedance before and after potentiostatic polarization for two different concentrations of LiTFSI salt. (b) Current profile during potentiostatic polarization at 10 mV for 0.2 M and 1.0 M LiTFSI salt concentrations. (c) Transference number of lithium ions extracted using the Bruce-Vincent method

The Bruce-Vincent method has been adopted to measure the concentration-dependent transference number values for LiTFSI salt dissolved in DOL/DME solvent. Figure V-168a shows the Nyquist plot used to estimate interfacial resistance. Evolution of current during potentiostatic polarization is shown in Figure V-168b. Figure V-168c indicates that in the low concentration regime, the transference number of LiTFSI salt is around 0.45 and independent of lithium concentration.

The only transport property remaining is the diffusion coefficient. Initially, dilute solutions of the polysulfides were prepared, and fixed diffusion coefficients were measured using the choronoamperometry methodology. The Cottrell equation was adopted to extract the value of diffusivity from the current decay under potentiostatic polarization. The slope of "current" vs. "reciprocal of square root of time" plot (not shown here) is correlated with diffusivity. Based on this, the magnitude of diffusion coefficient for Li_2S_6 and Li_2S_8 was obtained as 1.84×10^{-10} m^2/s and 2.68×10^{-10} m^2/s, respectively.

Based on the restricted diffusion technique, the concentration-dependent diffusivity of Li^+ in LiTFSI solution was measured using Li metal electrodes in a symmetric cell (see Figure V-169a). Similarly, using glassy carbon as the electrodes, concentration-dependent diffusivities of S_8^{2-} and S_6^{2-} were measured for different concentrations of Li_2S_8 and Li_2S_6 (see Figure V-169b). High diffusivity was observed at low concentration in all cases and was inversely proportional to concentration for both lithium cations and polysulfide anions.

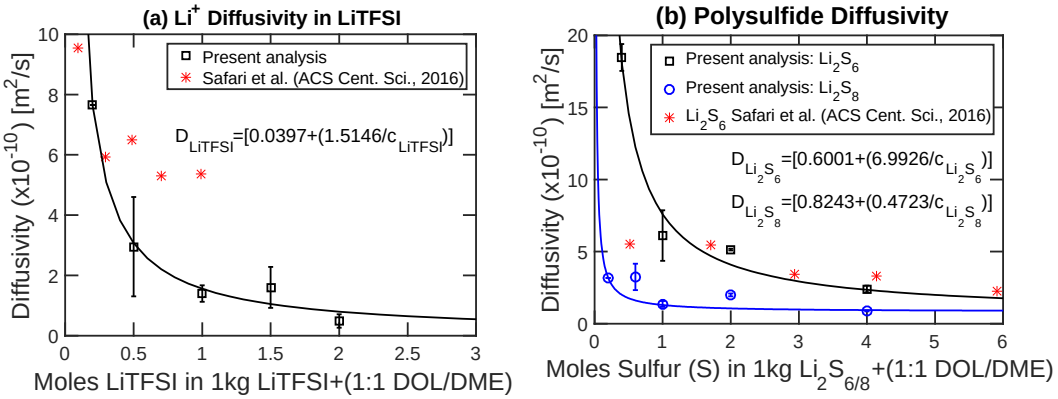

Figure V-169: (a) Concentration-dependent diffusivity of Li^+ from LiTFSI salt dissolved in 1:1 DOL/DME solvent. (b) Concentration-dependent diffusivity of polysulfide anions in two different types of polysulfide salts (Li_2S_6 and Li_2S_8) dissolved in 1:1 DOL/DME solvent

Performance of thick Li-S cells

Thick Li-S coin cells were constructed and cycled at different C-rates at room temperature. Discharge curves are shown in Figure V-170a, where significant decay in capacity can be observed with increasing rate of operation. The rising over-potential at higher rates shifts the voltage plateau downward. A computational methodology has been developed based on porous electrode theory to predict the performance of thick Li-S cells. Concentrated solution assumptions were incorporated within the mathematical model, along with the variation in transport properties with species concentration. The theoretical predictions are plotted in Figure V-170b for two different C-rates, along with the corresponding experimental results. The mismatch in performance curve might be attributed to several causes, such as unknown electrochemically active surface area, unknown porosity and tortuosity, lack of information about sulfur distribution within the cathode, isolation of sulfur, limited information about side reaction and the polysulfide shuttling mechanism. Optimization and refinement of different model parameters can lead to more accurate prediction of experimental results; the development of this model, based on concentrated solution theory, which can capture the overall performance curve, was the key accomplishment for this phase of the project.

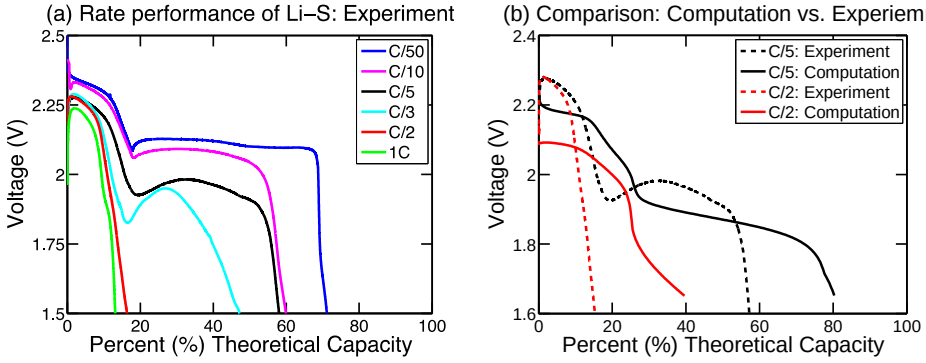

Figure V-170: (a) Experimentally-obtained performance curves for lithium-sulfur cells discharged at different C-rates. (b) Comparison between experimental results and computational predictions at two different C-rates

Determination of porosity and tortuosity

The ratio of effective to intrinsic conductivity was obtained as describe in the earlier “approach” section. A porosity of 0.43 was used for consistency with the macroscale model developed earlier in our group. The tortuosity value extracted from the conduction simulation results was then approximately 1.2, which is within the range of values measured by M. Ebner, D.-W. Chung, R. E. Garcia, and V. Wood in Adv. Energy. Mater. 2013 in NMC electrodes with larger NMC particles, but which is substantially different from the value of approximately 22 used with the original macroscale simulations, determined through a fitting procedure over a range of C-rates. This might suggest that the intrinsic diffusivity in electrolyte solution, obtained from the literature and used in the macroscale model, is too high.

The average value of the porosity gradient computed over the electrode is approximately 0.48, somewhat larger than the porosity obtained from electrode composition. Some discrepancy was expected from these very different approaches. A modified porosity function was constructed, using the average porosity obtained from the composition and the derivative of the linear fit. This spatially-varying description of porosity was then incorporated into the macroscale simulation, as was the newly determined tortuosity value. The resulting discharge curve is shown along with those from the original macroscale model and microscale model in Figure V-171. Primarily as a consequence of using very different tortuosity values, the original and modified macroscale simulations show very different results; capacity in the former case is limited by solution-phase transport, and in the latter case, solid-phase transport; again, this may be the result of using an intrinsic diffusivity that might be too large. The introduction of microscale information into the porous electrode model moves the discharge curve in the direction of the microscale simulation results, but to even higher capacities.

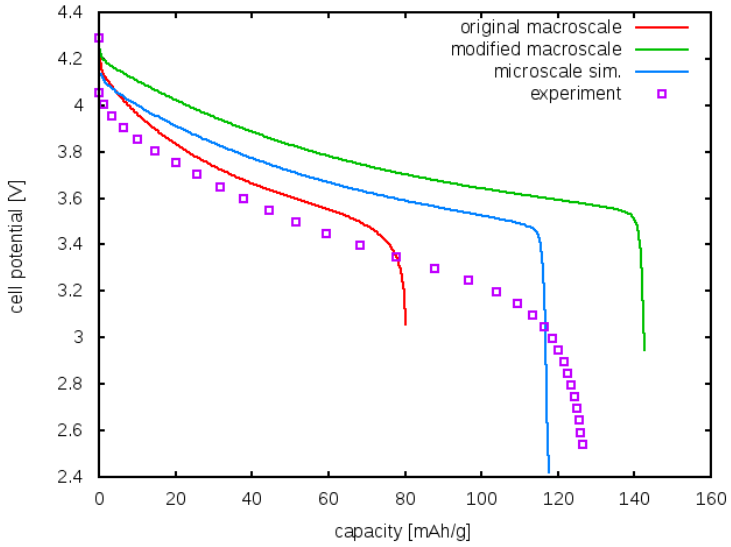

Figure V-171: Comparison of results for a 3C discharge using original porous electrode model, modified model with porosity gradient, and tortuosity extracted from micro-tomography data and conductivity simulations, microscale model, and experimental data

Conclusions

In FY16, the Srinivasan group has focused on two areas: understanding Li-S battery performance and exploring microscale-informed modifications to traditional macroscale battery models. To summarize, insulating lithium-sulfide film formation on the carbon substrate has been identified as a major limiting factor that not only limits the power density of Li-S cells, but also reduces the overall energy density at low rates of operation. Impact of lithium-sulfide film growth on the electrochemical performance has been characterized, and diffusivity of lithium cations through the insulating layer has also been estimated. Variation in the three major transport properties (conductivity, diffusivity and transference number) with increasing species concentration has been successfully measured. A mathematical framework based on concentrated solution theory has been developed that can successfully capture the qualitative discharge behavior of thick Li-S cells. Finally, microscale information in the form of porosity distribution and tortuosity has been incorporated into a corresponding macroscale model, from which it was determined that the intrinsic diffusivity in electrolyte solution as used in the original macroscale model is likely to be too large, and that the porosity gradient is too small to account for discrepancies between macroscale model and experimental results at high rates.

Products

Presentations/Publications/Patents

1. K. Takahashi*, K. Higa*, S. Mair, M. Chintapalli, N. Balsara, and V. Srinivasan, “Mechanical Degradation of Graphite/PVDF Composite Electrodes: A Model-Experimental Study”, *J. Electrochem. Soc.* 2016 volume 163, issue 3, A385-A395. *These authors share equal credit for this work.
2. Open source software release: K. Higa and V. Srinivasan, PyGDH: the Python-based Grid Discretization Helper, available from https://sites.google.com/a/lbl.gov/pygdh/.
3. K. Higa*, S.-L. Wu*, D. Y. Parkinson, Y. Fu, V. Battaglia, and V. Srinivasan, “Macroscale vs. Microscale Simulation of Porous Battery Electrodes,” 229th Meeting of the ECS, #209, San Diego, CA, June 2016. *These authors share equal credit for this work. Part of this work was funded through the CAEBAT program.
4. Y. Dai, J. Y. Wang, G. Ai, G. Liu and V. Srinivasan, “Mechanistic Understanding of Physical Processes in Lithium-Sulfur Batteries through Experiments and Modeling,” 229th Meeting of the ECS, San Diego, CA, June 2016.

V.F.2. Predicting and Understanding Novel Electrode Materials from First-Principles (LBNL)

Kristin Persson, Principal Investigator
Lawrence Berkeley National Laboratory
Energy and Environmental Technologies Division
1 Cyclotron Road
Berkeley, CA 94563
Phone: 510-486-7218
E-mail: kapersson@lbl.gov

Tien Q. Duong, DOE Program Manager
U.S. Department of Energy
Advanced Battery Materials Research (BMR)
Vehicle Technologies Office
1000 Independence Avenue, SW
Washington, DC 20585
Phone: 202-586-7836
E-mail: Tien.Duong@ee.doe.gov

Start Date: October 2012
End Date: October 2017

Abstract

Objectives

- Model and predict the behavior of electrode materials from first-principles.
- Understand the atomistic interactions underlying the behavior and performance of the high-capacity lithium excess and related composite cathode materials.
- Predict new materials using the recently developed Materials Project high-throughput computational capabilities at LBNL.

Technical Barriers

Investigating electrode materials with atomistic modeling require rigorous bench marking as well as insight into the materials chemistry and its effect on electrode performance. In the case of the Li-excess materials, it is challenging, as there are an increased number of variables associated with the unknowns regarding possible composite or solid solution structure of the material, the amounts of each phase, synthesis procedure etc.

Technical Targets

- Identify stable crystal facets of Li_2MnO_3 as an end-member of Li-excess Mn-rich layered materials.
- Evaluate the spontaneous oxygen evolutions on low Miller index crystal for all stable surfaces as a function of Li-concentration.
- Predict favorable particle morphologies to enhance the electrochemical performance of layered Li-excess Mn-rich materials.

Accomplishments

- The stable facets of pristine Li_2MnO_3 as well as their chemical composition have been calculated and organized according to their composition.
- The thermodynamic favorable shape of the material (the Wulff shape) is found to exhibit 5 low-index surfaces.

- All surface facets are found to spontaneously evolve oxygen when the bulk Li concentration x < 1.7 in Li_xMnO_3 which compares excellently with experimental results.
- Combined with earlier year results within the BMR program, we conclude that Li_2MnO_3 is inherently a fast Li diffusing material; however first cycle surface oxygen loss causes severe surface reconstruction which deteriorates the material and inhibits good rate behavior.

Technical Discussion

Introduction

There is increasing evidence that many of the performance limiting processes present in electrode materials are highly complex reactions occurring on the atomic level. The Persson BATT effort at LBNL is studying these processes using first-principles density-functional theory modeling tools. By understanding the underlying reasons for the electrode materials working performance, improvements or design schemes can be directed at the root cause of the process.

The Li excess cathode materials show great promise for high voltage and high capacity; however, they also present voltage fade, structural degradation and safety concerns. In this work we have systematically elucidated the charging mechanism, the Li diffusion and lastly the surface stability of Li2MnO3, which presents the archetype Li-excess, Mn-rich material. In the first year, we conclusively elucidated oxygen-oxidation as the charging mechanism of Li_2MnO_3 (see Lee and Persson, Adv Energy Materials 2013). This result, together with rampant Mn migration into the Li layer, effectively reproduces the first cycle voltage profile of the material and explains its structural and chemical evolution. In the second and third year, we found that Li diffusion – contrary to expectation- is excellent in the pristine Li2MnO3, however, subsequent Mn re-distribution effectively locks out the Li in the transition layer which causes capacity degradation. Finally, in this year, we have addressed the surface stability of the material, which is identified as the main culprit for the observed inferior rate behavior of Li_2MnO_3.

Approach

The Persson group uses atomistic modeling to study the relevant thermodynamic and kinetic processes. The calculations are performed at NERSC and on the Lawrencium cluster at LBNL. To elucidate the atomistic interactions, first-principles zero-temperature calculations are employed and coupled with the cluster expansion technique to examine the structural and chemical space, establish ground states, and resulting electrochemical signature of the materials. To examine temperature-induced properies, statistical mechanics and kinetic Monte Carlo methologies are utilized.

Results

The pristine Li_2MnO_3 surfaces: The crystal structure of pristine Li_2MnO_3 belongs to the monoclinic C2/m space group (Figure V-172-a), which consists of laminating layers exhibiting alternating Li-layer and Mn (transition metal)-layers. Both Li and Mn ions reside on octahedral sites in both layers. Intuitively, it is evident that an arbitrary facet of this system, excluding the (001) and (010) surfaces, inevitably contains both exposed Li and Mn ions (Figure V-172-b).

The particle shape of Li_2MnO_3 can be anticipated by calculating the Wulff structure, which is constructed using the final surface energies. The low Miller index surfaces of pristine Li_2MnO_3 have 7 distinguishable facets, which can be classified into 3 groups with respect to their relationship between a given surface and the Li layer percolation direction. As illustrated in Figure V-172(c-e), the surface normal direction and the Li layer percolation direction can be parallel (∥-(001) surface; Figure V-172-c), perpendicular (⊥-(001) surfaces; Figure V-172-d), or slanted angle (∠-(001) surfaces; Figure V-172-e).

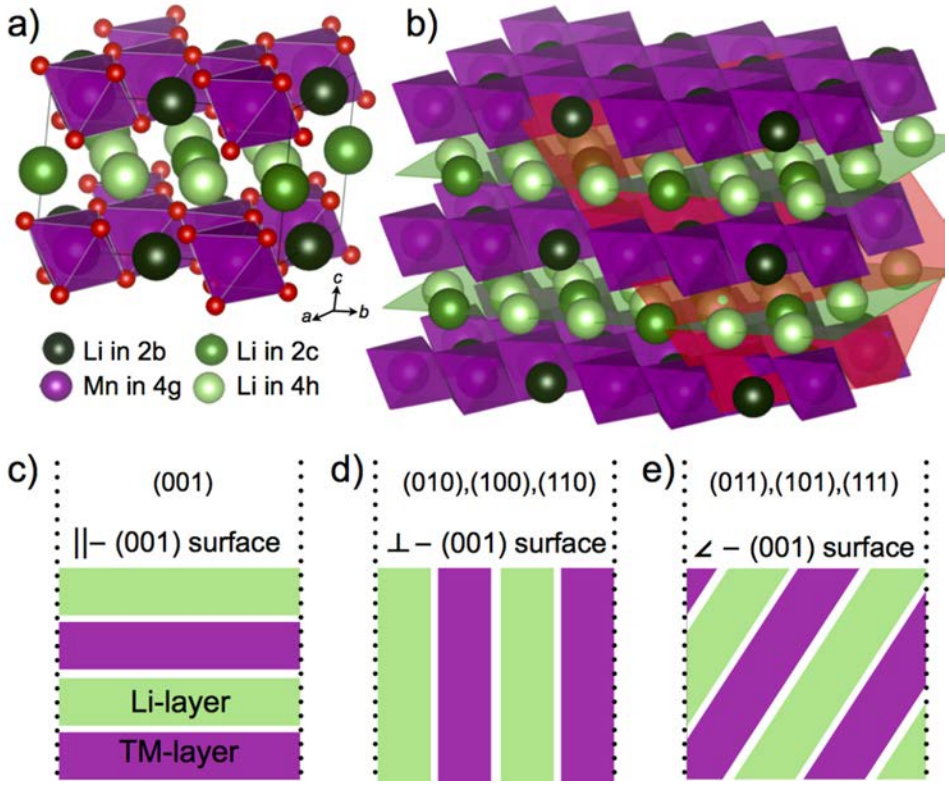

Figure V-172: Illustration of Li_2MnO_3 crystal structure and low Miller index surfaces

To mimic the behavior of a real surface, we employ surface reconstructions that allow the exposed cations to reorganize and find their most stable site on the surface and sub-surface layers. The final arrangement strongly depends on the cation specie as well as their local surface environment. Therefore, surface reconstruction rules of each cation (here Li and Mn) are investigated separately. First, the preferred position of the lithium ions on the surface was investigated. The lithium ions can be located on top of a i) a sub-surface lithium ion contained octahedral site, ii) on top of a sub-surface Mn-ion contained octahedral site, or iii) tetrahedral site. Our calculations indicate that the Li-containing octahedral site is the preferred location of lithium ion on the surface, and the Mn-containing octahedral site is the worst location. Furthermore, we find that Mn-ions are favorably reconstructed to a sub-surface layer, by swapping sites with a sub-surface octahedral lithium ion.

In Figure V-173, we systematically investigated the Mn-ion reconstruction as a function of the defect depth. Figure V-173-(d) shows the surface formation energy at the (100) surface as a function of site and the depth of the Mn defect from the surface to bulk. Our computations clearly show that the surface formation energy by swapping the Mn defect is significantly decreased when Mn defect located at the 1st sub-surface layer. However, this energy dramatically increases by increasing the swapping depth. Therefore, we conclude that the surface Mn are favorably swapped with a 1st sub-surface Li as a deeper defect reconstruction carries an penalty energy that outweighs the surface reconstruction energy.

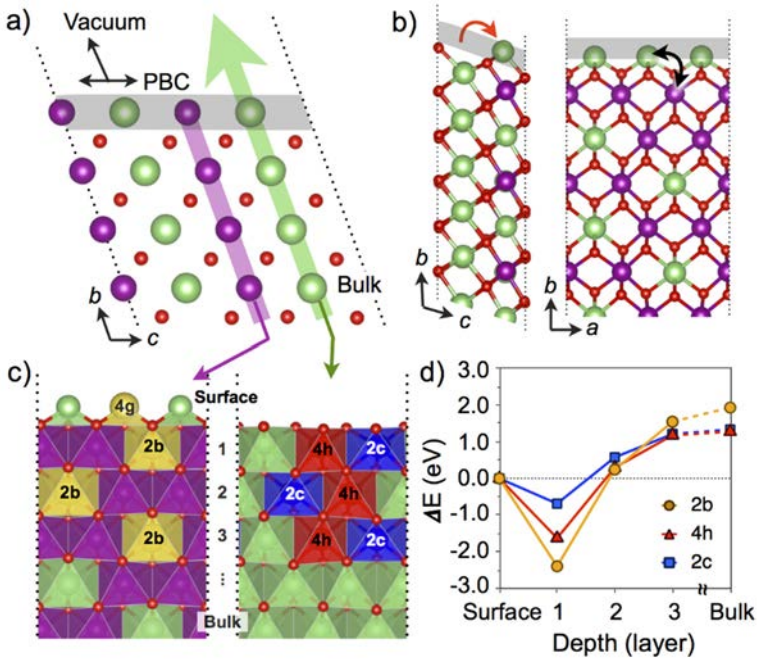

Figure V-173: Energetics illustrating the general rules for surface and ion topology

Li_2MnO_3 surface oxygen evolution: From our previous work on Li_2MnO_3, we know that the oxygen evolution in the bulk is energetically unfavorable until 50% lithiation ($1 < x < 2$), and kinetically hindered for all compositions. However, surface oxygen is not energetically impeded, and hence is likely to be lost from the material during charging.

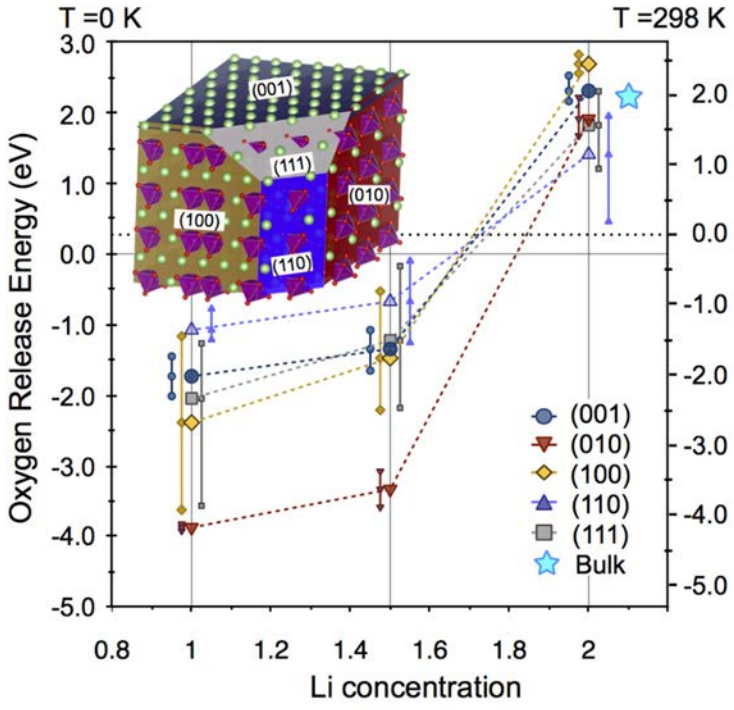

Figure V-174: A schematic of a migrated Mn ion, impacting the Li site preference in the Li layer

Figure V-174 shows the systematic investigation of the oxygen evolution from all 5 surfaces as a function of Li-concentration. Here, a positive oxygen release energy represents unfavorable oxygen loss, and a negative oxygen release energy presents spontaneous oxygen evolution. Our evaluation shows that oxygen is released spontaneously on all facets for Li extractions larger than $x < 1.7$ (charging beyond 0.3 Li per formula unit). This result agrees well with experimental observations of oxygen evolution at 19% Li extraction ($Li_{1.63}MnO_3$).

Our results in Figure V-174 indicates that no facet is stable against spontaneous oxygen evolution, for the most stable particle shape of Li_2MnO_3. However, some facets are relatively more stable than others against oxygen release. For instance, the (110) surface is more stable than others in all Li-concentration regions, and the (010) surface is more unstable than others. Therefore, we would expect a Li_2MnO_3particle with minimized (010) facets and maximized (110) areas to exhibit improved oxygen retention, less surface reorganization and hence improved rate behavior and stability.

Conclusions

During the last year of the current BMR program we have elucidated the surface stability and vulnerability against surface oxygen loss of the end member, Li_2MnO_3,as a Li-excess, Mn-rich representative of this class of materials. We systematically elucidate all possible stoichiometric low Miller index surfaces with various cation ordering on each surface. We apply surface cation reconstruction rules that depend on the local environment, including target Mn− Li site exchanges, and optimize the resulting surface Li confi gurations using metadynamics. The equilibrium Wulff shape shows dominant (001), (010) surface facets, and almost all facets exhibit favorable Mn reconstruction. Most importantly, we find that while all equilibrium Li_xMnO_3 surfaces become unstable toward oxygen release for $x < 1.7$, some facets are consistently more resistant than others which may provide a design metric for more stable particle morphologies and enhanced surface oxygen retention.

Products

Presentations/Publications/Patents

1. Shin, Y.; Persson, K. (2015) “Elucidating the Delithiation Mechanism of Lithium-Excess Materials” Presented at 2015 MRS fall meeting, Boston, MA.
2. Shin, Y.; Ding, H.; Persson, K. (2016) “Revealing the Intrinsic Li Mobility in the Li_2MnO_3 Lithium-excess Material.” Chemistry of Materials, 28 (2016), 2081−2088.
3. Shin, Y.; Persson, K. (2016) “Surface Morphology and Surface Stability against Oxygen Loss of the Li-excess Li_2MnO_3 Cathode Material as a function of Li concentration.” Applied Materials & Interfaces, 8 (2016), 25595–25602.
4. Shin, Y.; Persson, K. (2016) “Delithiation Mechanisms and the Surface Morphology of Lithium-Excess Li_2MnO_3 Material” Presented at PRiME 2016, Honolulu, HI.

V.F.3. First Principles Calculations of Existing and Novel Electrode Materials (LBNL)

Gerbrand Ceder
Lawrence Berkeley National Laboratory
1 Cyclotron Road
Berkeley, CA 94607
Phone: 510-486-7913; Fax: 510-486-6279
E-mail: gceder@lbl.gov

Tien Q. Duong, DOE Program Manager
U.S. Department of Energy
Advanced Battery Materials Research (BMR)
Vehicle Technologies Office
1000 Independence Avenue, SW
Washington, DC 20585
Phone: 202-586-7836
E-mail: Tien.Duong@ee.doe.gov

Start Date: January 1, 2013
End Date: December 31, 2016

Abstract

Objectives

Identify layered cathode structures leading to high capacity. Clarify the role of the initial structure as well as that of structural changes upon first charge and discharge. Gain insight into the role of Li-excess and develop methodologies to predict ion migration in layered cathodes upon cycling and during overcharge. Develop computational tools to accurately model and predict oxygen charge transfer and oxygen loss in Li-excess and cation-disordered materials. Design and synthesize very high capacity layered cathodes with high structural stability (> 250 mAh/g).

Accomplishments

- Developed model to predict compositions that will disorder as synthesized.
- Carried out a comprehensive computational search for new cation-disordered cathode materials for binary combinations of transition metal. Successfully synthesized a novel $LiCo_{0.5}Zr_{0.5}O_2$ material with a disordered rocksalt structure, consistent with our predictions.
- Devised a predictive model for the voltage curve (slope) of cation-disordered materials.
- Using a recently-developed computational methodology, carried out an in-depth computational study of oxygen redox mechanisms in Li-excess materials.

Future Achievements

- Identify higher capacity lithium-ion cathode materials and novel chemistries for higher energy density storage devices. Guide the field in the search for higher energy density lithium-ion materials.
- Design high capacity cathode materials that are tolerant to transition metal migration.

Technical Discussion

Background

Layered Li-excess cathode materials can deliver very high capacities from 250 up to 300 mAh g^{-1}, which has been attributed to the additional charge compensation mechanism activated by Li-excess through either the oxidation of O^{2-} to O^{-} or the release of O_2 followed by cation densification. Recently, the design space for Li-excess materials was expanded to rocksalts with partial or complete cation disorder following the realization that more than 10% Li-excess creates a percolation network of 0-TM channels through which Li can diffuse. This opens the possibility to explore and find more candidate cathode materials with very high energy density.

Introduction

It was recently demonstrated that cathode materials based on cation-disordered Li transition metal (TM) oxides can deliver high capacities and sustain efficient Li transport provided Li is in an excess of at least 10% with respect to the transition metal concentration [1,2]. In addition, cation disorder was found to improve the structural stability of $Li_{1.211}Mo_{0.467}Cr_{0.3}O_2$, which undergoes only negligible volume changes during cycling [1]. Similarly, cation-disordered $Li_{1.25}Nb_{0.25}Mn_{0.5}O_2$ was reported, exhibiting a large capacity of 287 mAh/g from TM and O^{2-}/O^{-} redox activity and no evidence for structural decay through oxygen release [3].

The discovery of novel Li-excess cation-disordered cathode materials has so far either been by chance or through the modification of known disordered materials. This motivated us to develop computational methodologies to aid the systematic design of new Li-excess cation-disordered cathode materials with a high performance. In some cases, we tested our theoretical predictions through experimental synthesis and characterization of novel compounds.

First, we developed a methodology for the theoretical prediction of materials that will disorder as synthesized. This new method was subsequently applied to search for new cation-disordered materials for binary combinations of transition metals. Following on our predictions, a novel cation-disordered $LiCo_{0.5}Zr_{0.5}O_2$ compound was successfully synthesized, confirming the validity of our computational methodology. Since the energy density is the product of capacity and voltage, an understanding of the effect of cation disorder on the voltage is crucial for the design of novel high-energy-density cathodes. In this respect, we developed a methodology to predict the effect of cation disorder on the voltage slope. Finally, using a recently-developed computational methodology [4], we thoroughly investigated the chemical and structural origins of oxygen redox processes in Li-excess cathodes.

Approach

A combination of first-principles computations and experimental synthesis/characterization are used to evaluate existing and novel materials. Voltages and intercalation curves are calculated with GGA+U, and if highly accurate results are required hybrid functionals (HSE) are used. Phase diagrams are calculated with the Materials Project infrastructure based on high-throughput computations. Configurational disorder for elevated temperature and off-stoichiometry is modeled with either point defect models (when off-stoichiometry is small) or with the cluster expansion for larger disorder. Ion mobility is evaluated with the Nudged Elastic Band Method or with direct Molecular Dynamics Simulations. Thermal stability is investigated with the approach developed previously under this program. Some of the computational work is performed in collaboration with Persson and with the Materials Project. Work on Li-excess layered materials is done in coordination with Persson (computational) and with the experimental efforts in the BATT Program (e.g. Grey).

Results

Theoretical prediction of compositions with cation-disorder as synthesized

To aid the systematic design of new cation-disordered cathode materials, we devised a methodology for the theoretical prediction of materials that will disorder as synthesized. Our approach is based on estimating the

temperature of the configurational order-disorder phase transition from first principles calculations. As an example, Figure V-175 shows the result of Monte-Carlo heat-up simulations of $LiCrO_2$ and $LiNiO_2$ using lattice-model Hamiltonians based on first-principles calculations, and the temperatures of the order-disorder transitions are indicated by vertical dashed lines. Note that the energies after the order-disorder transitions are still significantly lower than the energy of fully random cation arrangements (E - E_0 = 0 in Figure V-175), which is due to short-range interactions present in the cation-disordered phases. While these MC simulations did not consider melting or decomposition of the materials, they nevertheless allow us to rank different compositions by their likeliness to disorder. However, the construction of lattice models is time consuming, especially for compositions with multiple TM species.

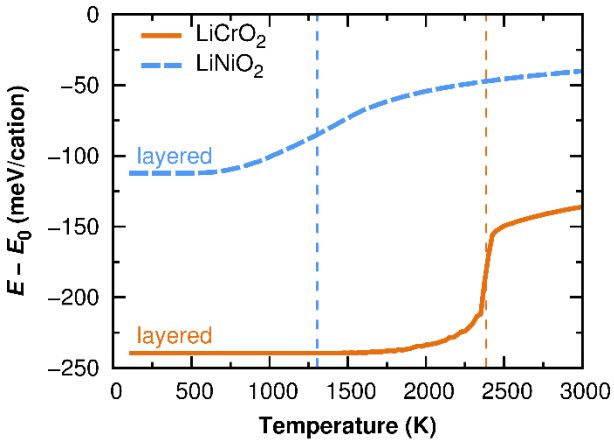

Figure V-175: Internal energy of $LiCrO_2$ (solid orange line) and $LiNiO_2$ (blue dashed line) during heat-up simulations of their layered ground state configurations from 100 K to 3000 K. The vertical dashed lines indicate the temperatures of their respective order-disorder phase transitions. The zero-point of the *y* axis corresponds to the energy of a fully random cation arrangement

Despite material-dependent short-range interactions, we found that the temperature of the order-disorder transition correlates strongly with the energy difference between the completely random state and the ordered ground state (Figure V-176). The energy of the random state can be well approximated based on *special quasi-random structures* (SQS), so that only two first principles calculations, the ground state structure and the SQS, are required to estimate the likeliness of cation disorder in any given composition. This approach has proved successful for compositions with multiple TM species (see next section) and is, hence, suitable for an automated computational search for new cation-disordered cathode materials.

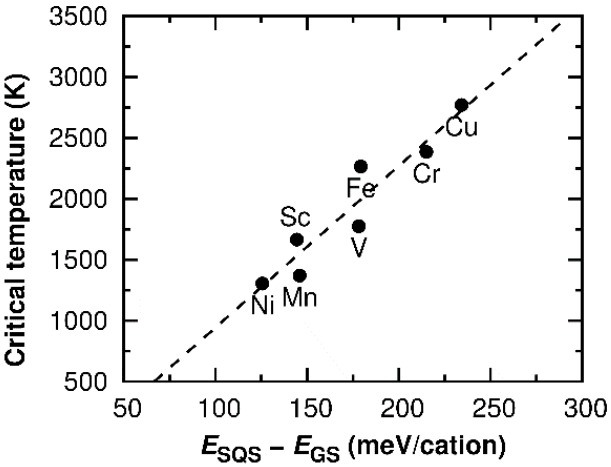

Figure V-176: Correlation of the temperature of the order-disorder transition of different $LiTMO_2$ (TM = Sc, V, Cr, Mn, Fe, Ni, Cu) with the energy difference of the random cation arrangement (E_{SQS}) and the ordered ground state (E_{GS})

Computational search for new cation-disordered cathode materials for binary combinations of transition metals

Using the methodology discussed in the first section, an automated computational search for new cation-disordered cathode materials was conducted for binary combinations of transition metals, with results presented in Figure V-177. In the figure below, every TM combination is represented by a circle, and the radius of the circle indicates the cation ordering strength. In addition the color of each circle in Figure V-177 encodes the mixing enthalpy with respect to oxides with transition-metal oxidation states between 2 and 4.

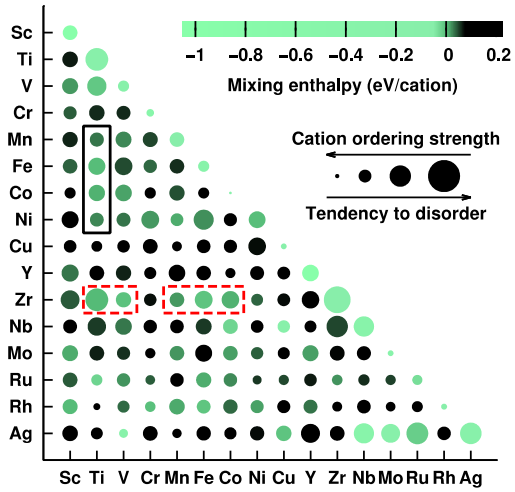

Figure V-177: Screening results for the $LiA_{0.5}B_{0.5}O_2$ composition space. A circle represents each combination AB of transition metals. The color of the circle visualizes the predicted stability in terms of the estimated mixing enthalpy (bright green: more stable; dark: less stable), and the size of the circle indicates the tendency to disorder (small circle: strongly ordered; large circle: likely disordered)

To confirm the accuracy of the computational predictions, $LiCo_{0.5}Zr_{0.5}O_2$ was selected for experimental investigation. While the $LiCo_{0.5}Zr_{0.5}O_2$ material is predicted to form as a disordered rocksalt structure, as shown in Figure V-177, it has so far never been reported in the literature. Solid-state synthesis methods yielded samples of cation-disordered $LiCo_{0.5}Zr_{0.5}O_2$ with a ~95% purity (Figure V-178), confirming the validity of our computational model.

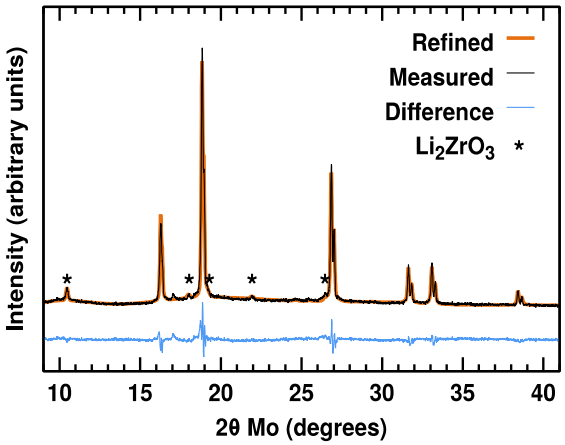

Figure V-178: Unprocessed x-ray diffraction spectrum of as-synthesized $LiCo_{0.5}Zr_{0.5}O_2$ (thin black line) and refined spectrum based on the disordered rocksalt structure and the Li_2ZrO_3 impurity phase (thin orange line). Li_2ZrO_3 peaks are indicated with stars. The double-peak intensities are due to signals from Mo $K_{\alpha1}$ and $K_{\alpha2}$ radiation

Theoretical prediction of the voltage curve of cation-disordered materials

The energy density of a cathode material is the product of its capacity and average voltage, hence, an understanding of the effect of cation disorder on the voltage is crucial for the design of novel high energy density cathodes. The effects of cation disorder on the average Li intercalation voltage in $LiTMO_2$ were investigated, and our results show that Li-TM disorder can either increase or reduce the TM redox voltage depending on the TM species [5]. However, cation disorder not only modulates the average voltage but also the slope of the voltage profiles. Large voltage slopes are generally undesirable, as they can lead to inaccessible capacity at the end of charge.

In the layered (α-$NaFeO_2$) structure, all Li sites are equivalent and the cations are arranged in such a way that every Li site is surrounded by exactly 6 TM sites and 6 Li sites. In contrast, in cation-disordered structures a distribution of local environments around Li sites exists, so that the energies of the Li sites vary. This effect necessarily leads to an additional slope in the voltage profile. Figure V-179 shows the distribution of Li site environments in a disordered structure with ideal random cation arrangement.

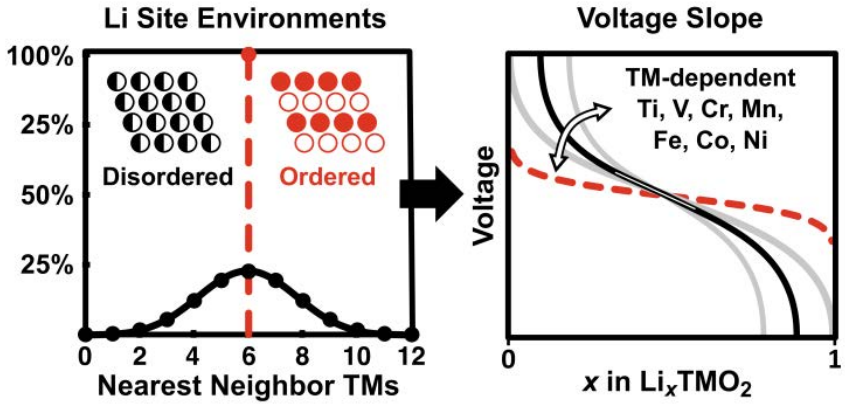

Figure V-179: Unlike in the layered structure, Li sites in cation-disordered structures are not equivalent. The spread of Li site energies manifests itself as additional slope in the voltage profile
Diagram reproduced from Abdellahi et al.[5]

Apart from the slope due to non-equivalent Li sites, cation disorder may also result in the stabilization of tetrahedral Li sites at the top of charge, which gives rise to an additional step in the voltage profile. Tetrahedral sites that are not coordinated by TM ions (0-TM sites) become stable for Li when 3 of the surrounding 4 Li atoms are extracted. Such 0-TM sites are not present in the layered structure, but may be created by cation disorder. To investigate to which extent the voltage slope and the stabilization of tetrahedral Li depends on the TM species, we employed Monte-Carlo simulations using first-principles based lattice model Hamiltonians. The results from our calculations are shown in Figure V-180.

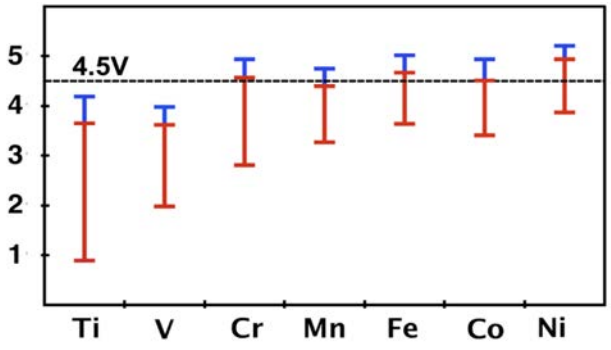

Figure V-180: Calculated voltage range owing to non-equivalent Li sites (red) and tetrahedral Li (blue) for the Li transition-metal oxides of the first-row transition metals. The dashed line indicates a voltage of 4.5 V as a guideline for the stability limit of conventional liquid electrolytes
Diagram reproduced from Abdellahi et al.[5]

As shown in the above figure, the voltage slope resulting from non-equivalent Li sites leads to a voltage spread between 1 V ($LiFeO_2$) and 3.5 V ($LiTiO_2$) depending on the TM species (red bars in Figure V-180). The voltage slope for the early TMs Ti, V, and Cr is significantly larger than the slope predicted for the later TMs, as the strong TM-O hybridization in the $LiTMO_2$ of the later TMs effectively shields the Li-TM interaction in these structures, so that the energy of the Li sites becomes less sensitive with respect to their local TM environment. In comparison to the Li-site energy contribution, the voltage spread owing to tetrahedral Li (blue bars) is with 0.2-0.4 V much smaller.

Theoretical understanding and prediction of oxygen redox activity in Li-excess cation-disordered materials

The reversible oxygen redox in Li-excess materials can substantially enlarge the composition space of potential high-capacity and high-energy-density cathodes because it can deliver excess capacity beyond the theoretical transition metal (TM) redox capacity, eliminating the need for heavy and expensive TM ions. Nevertheless, the origin of the oxygen redox process is not well understood, preventing the rational design of better Li-excess cathodes with oxygen redox. Using first-principles calculations, we demonstrated that specific chemical and structural features in layered and cation-disordered Li-excess cathode materials lead to labile oxygen electrons that can be easily extracted and participate in the practical capacity of these materials.

Our first-principles calculations on the cation-mixed layered $LiNiO_2$ and Li_2MnO_3 showed that some electronic states of oxygen ions that are linearly coordinated by two Li ions (Li–O–Li configuration) are less stable than those of other oxygen ions. O 2*p* orbitals along the Li–O–Li configurations do not have an M (metal ion) *d* orbital with which to hybridize and do not hybridize with the Li 2*s* orbital either because of the large energy difference between the O 2*p* and Li 2*s* orbitals. Consequently, their energy levels are close to that of the unhybridized O 2*p* orbital, which has higher energy than the hybridized O bonding states (t_{1u}^b, a_{1g}^b, and e_g^b states), as shown in Figure V-181.

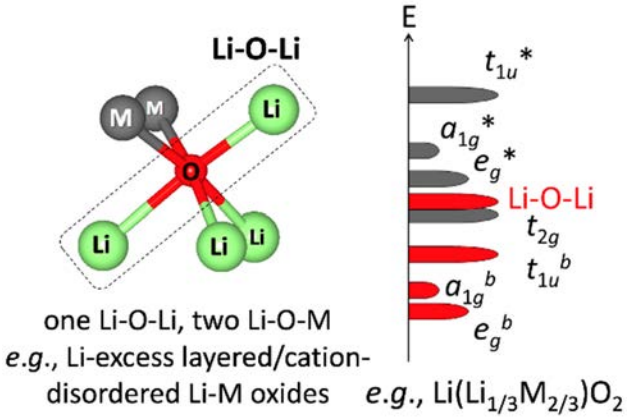

Figure V-181: Local atomic coordination around oxygen in Li-excess materials and schematic of the band structure for Li-excess layered Li-M oxides

Diagram adapted from Seo et al.[6].

We applied this understanding to practical Li-excess materials to reveal the origin of oxygen oxidation and the excess capacity. Our first-principles calculations showed that the hole is localized around oxygen ions along the Li–O–Li configuration, as illustrated in Figure V-182, indicating that these states are oxidized and the extraction of electrons from such unstable oxygen states is the origin of the oxygen redox activity and the extra capacity beyond theoretical TM redox capacity in Li-excess TM oxides.

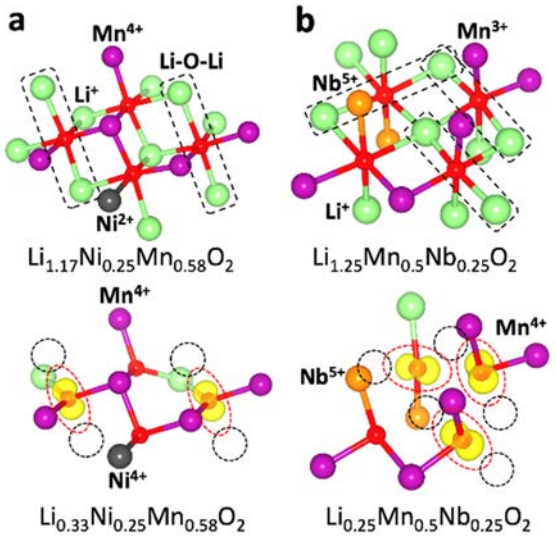

Figure V-182: Atomic configurations and the iso-surface of spin density (yellow) around oxygen (red spheres) in (a) $Li_{1.17-x}Ni_{0.25}Mn_{0.58}O_2$ and (b) $Li_{1.25-x}Mn_{0.5}Nb_{0.25}O_2$

Diagram adapted from Seo et al.[6].

Our findings are in stark contrast with the prevailing argument whereby the covalency of TM-O bonding leads to excess capacity beyond TM redox capacity. We demonstrated that, in fact, only oxygen oxidation through the extraction of labile electrons from unhybridized O 2*p* states sitting in Li–O–Li configurations can create excess capacity. This distinction is important, because the number of electrons, and thus the capacity, from the hybridized TM *d* states (*e.g.* e_g^* states) remains the same regardless of covalency and is already accounted for in the TM redox capacity.

Conclusions

The work carried out over the past year resulted in the development of powerful tools for the theoretical prediction of the synthesizability and electrochemical properties of Li-excess cation-disordered cathodes. The propensity for cation disorder in binary transition metal oxides was successfully predicted using a simple computational method based on the comparison of the energy of the ordered ground state structure with that of *special quasi-random structures* (SQS) mimicking a fully disordered arrangement of the cations. The accuracy of the computational results was corroborated by experimental data, and a novel cation-disordered $LiCo_{0.5}Zr_{0.5}O_2$ cathode material was successfully synthesized. In parallel, we devised a model to evaluate the effect of cation disorder on the voltage slope, which is of tremendous importance for the design of high energy density cathodes with a practical voltage window within the stable potential range of common liquid electrolytes. Finally, we gained insight into the structural and chemical requirements for oxygen redox activity in transition metal oxides, demonstrating that both Li-excess and cation disorder increase the oxygen redox capability of Li transition metal oxide cathodes.

Products

Presentations/Publications/Patents

Publications

1. J.C. Kim, D.-H. Seo, G. Ceder, Theoretical Capacity Achieved in a $LiMn_{0.5}Fe_{0.4}Mg_{0.1}BO_3$ Cathode by Using Topological Disorder, Energy and Environmental Science, 8, 1790-1798 (2015).
2. J.C. Kim, X. Li, B. Kang, G. Ceder, High-Rate Performance of a Mixed Olivine Cathode with Off-Stoichiometric Composition, Chemical Communications, 51, 13279-13282 (2015).
3. D.-H. Seo, A. Urban and G. Ceder, Calibrating Transition Metal Energy Levels and Oxygen Bands in First Principles Calculations: Accurate Prediction of Redox Potentials and Charge Transfer in Lithium Transition Metal Oxides, Physical Review B, 92, 115118 (2015).

4. J.C. Kim, D.-H. Seo, H. Chen, G. Ceder, The Effect of Antisite Disorder and Particle Size on Li Intercalation Kinetics in Monoclinic $LiMnBO_3$, Advanced Energy Materials, 5, 1401916 (2015).
5. Jain, G. Hautier, S.P. Ong, S. Dacek, G. Ceder, Relating Voltage and Thermal Safety in Lithium-ion Battery Cathodes: A High-Throughput Computational Study, Physical Chemistry Chemical Physics, 17, 5942-5953 (2015).
6. A. Urban, D.-H. Seo, G. Ceder, Computational understanding of Lithium-ion batteries, npj Computational Materials, 2, 16002 (2016).
7. D.-H. Seo, J. Lee, A. Urban, R. Malik, S. Kang, G. Ceder, The structural and chemical origin of the oxygen redox activity in layered and cation-disordered Li-excess cathode materials, Nature Chemistry, 8, 692 (2016).
8. A. Abdellahi, A. Urban, S. Dacek, G. Ceder, Understanding the Effect of Cation Disorder on the Voltage Profile of Lithium Transition-Metal Oxides, Chemistry of Materials, 28, 5373−5383 (2016).

Presentations

1. Engineering High and Constant Cation Diffusivity in Oxides through Percolation Theory, TMS meeting, Nashville, TN, February 15th, 2016.
2. Three-dimensional Li migration facilitated by antisite disorder in Li storage materials with a one-dimensional diffusion channel, Gordon Research Conferences: Batteries, Ventura, CA, February 21st-26th, 2016.
3. New directions for cathode and solid state electrolytes in Lithium-ion batteries, Jao Tong University, Shanghai, China, March 14th, 2016.
4. Cation-Disordered Cathode Materials, BMR Cathode Workshop at Oak Ridge National Laboratory, Oak Ridge, TN, March 15th, 2016.
5. Cation-disordered cathode materials for Lithium-ion batteries, BMR Electrochemistry seminar at LBNL, Berkeley, CA, March 28th, 2016.
6. New directions for cathode and solid state electrolytes in Lithium-ion batteries, Stanford Departmental Colloquium, Stanford, CA, April 29th, 2016.
7. From 1-D to 3-D Li intercalation: channel-to-channel Li migration facilitated by antisite disorder, 229th ECS Meeting, San Diego, CA, May 29th-June 2nd, 2016.
8. Combining Reversible Oxygen Charge Transfer and Li-excess to achieve High Capacity Cathodes, International Meeting on Lithium Batteries, Chicago, IL, June 22nd, 2016.
9. The Origin of the Oxygen Redox Activity in Layered and Cation-Disordered Li-Excess Cathode Materials, 230th ECS Prime Meeting, Hawaii, HI, October 3rd, 2016.
10. Understanding Cation-Disordered Cathode Materials Based on Percolation Theory and Ligand Field Theory, 230th ECS Prime Meeting, Hawaii, HI, October 5th, 2016.

References

1. J. Lee, A. Urban, X. Li, D. Su, G. Hautier, G.Ceder, Unlocking the potential of cation-disordered oxides for rechargeable lithium batteries, Science, 343, 519-522 (2014).
2. A. Urban, J. Lee, G. Ceder, The Configurational Space of Rocksalt-Type Oxides for High-Capacity Lithium Battery Electrodes, Advanced Energy Materials, 4, 1400478 (2014).
3. R. Wang, X. Li, L. Liu, J. Lee, D.-H. Seo, S.-H. Bo, A. Urban, G. Ceder, A disordered rock-salt Li-excess cathode material with high capacity and substantial oxygen redox activity: $Li_{1.25}Nb_{0.25}Mn_{0.5}O_2$, Electrochemistry Communications, 60, 70–73 (2015).
4. D.-H. Seo, A. Urban and G. Ceder, *Calibrating Transition Metal Energy Levels and Oxygen Bands in First Principles Calculations: Accurate Prediction of Redox Potentials and Charge Transfer in Lithium Transition Metal Oxides*, Physical Review B, 92, 115118 (2015).

5. A. Abdellahi, A. Urban, S. Dacek, G. Ceder, Understanding the Effect of Cation Disorder on the Voltage Profile of Lithium Transition-Metal Oxides, Chemistry of Materials, 28, 5373−5383 (2016).
6. D.-H. Seo, J. Lee, A. Urban, R. Malik, S. Kang, G. Ceder, The structural and chemical origin of the oxygen redox activity in layered and cation-disordered Li-excess cathode materials, Nature Chemistry, 8, 692 (2016).

V.F.4. First Principles Modeling of SEI Formation on Bare and Surface/Additive Modified Silicon Anode (TAMU)

Perla B. Balbuena, Principal Investigator
Texas A&M University
3122 TAMU
College Station, TX 77843
Phone: 979-845-3375; Fax: 979-845-6446
E-mail: balbuena@tamu.edu

Tien Q. Duong, DOE Program Manager
U.S. Department of Energy
Advanced Battery Materials Research (BMR)
Vehicle Technologies Office
1000 Independence Avenue, SW
Washington, DC 20585
Phone: 202-586-7836
E-mail: Tien.Duong@ee.doe.gov

Start Date: April 1, 2013
End Date: March 31, 2017

Abstract

Objectives

- Develop fundamental understanding of the molecular processes that lead to the formation of a solid electrolyte interphase (SEI) layer due to electrolyte decomposition on Si anodes.
- Develop a rational selection of additives and/or coatings.

Accomplishments

- Stability of SEI products tested for the main SEI components was identified as one of the main properties required for a passivating layer. A paper was published in the Journal of Physical Chemistry C.
- SEI nucleation and growth characterized for oligomers derived from ethylene carbonate (EC) and vinyl carbonate (VC) on bare lithiated Si surfaces and on Si surfaces partially covered with LiF showed the effects of the nature and structure of the surface on the adhesion and growth properties of the films. A paper was published in Electrochimica Acta.
- Structure, dynamics, and Li transport characterized in electrolyte solutions using classical molecular dynamics simulations yielding good agreement with experimental values including drift ionic velocities, solvent dielectric responses, and ion transference numbers. Significant force field development and test was a key ingredient to the success of this aspect of the project. Three papers were published in J. Phys. Chem. C, J. of Phys. Chem. B, and J. of Chemical Theory and Computation respectively.
- A coarse-grained Kinetic Monte Carlo (KMC) model was developed to represent the long time SEI growth. Reaction rates of microscopic events were obtained from ab initio simulations and fed to the coarse-grained KMC model. As a first approximation, only EC decomposition reactions were included, leading to oligomer dilithium ethylene dicarbonate (Li_2EDC) nucleation on the surface.
- Leakage of electrons through SEI blocks was assessed for various SEI components including lithium carbonate, silicon oxide, and Li silicates. The rates of leakage were assessed as a function of the applied potential, yielding information regarding the build-up of SEI resistances. A paper was published in the Journal of Physical Chemistry C.

- Preliminary models were developed and tested for the electron transfer through model grain boundaries defined between SEI blocks.
- Alternative electrolyte formulations were tested computationally using the SEI products stability as the selectivity criterion.
- Swelling effects of Si nanoparticles were assessed via MD simulations of the first battery charge. A full nanobattery model was developed and initial results were obtained and compared with experimental rates of volume expansion during lithiation. A paper is under review in the Journal of Physical Chemistry C.
- Alternative coatings synthesized by NREL collaborators were computationally tested to determine their reactivity. It was found that the artificial SEI layer given by an alucone coating may be modified during cycling because of solvent penetration into the film and reactions with the AlO_x groups in the film.

Future Achievements

- LiF deposition and nucleation on lithiated Si surfaces are currently investigated to determine SEI structural details and reactivity in contact with an electrolyte solution.
- Chemical, electrochemical, and stability effects of Mn cation migration from the cathode on the SEI layer formed on lithiated Si anode surfaces are currently being studied.
- Further collaborations with experimental groups are being carried out to characterize possible changes into the chemical nature of the alucone coating as predicted by the AIMD simulations.

Technical Discussion

Background

Many aspects of SEI formation on silicon are unique to this material. As-synthesized silicon surfaces are typically covered with a nanometer-thick SiO_2 layer. The surface contains silanol (SiOH) groups and siloxane (Si-O-Si) linkages. There is no analogous C_xO_y coating on graphitic carbon except on graphene edges. The SiO_2 layer remains after cycling power. A mixed oxide component, apparently Li_4SiO_4, has also been discovered. Chemically etching away the oxide leads to Si-H terminated anodes and diminishes the lifetime of the anode.

The above experimental results have been reported for electrolytes in the absence of additives. Additives that replace SiOH groups with siloxane and/or Si-CH3 terminations yield much better Coulomb efficiency. Another important issue is the role of fluorine atoms, since they may be incorporated into the SEI as LiF and $LiPF_x$, just like on graphitic carbon. Unlike on graphite, PF_xO_y compounds are also found. In addition, some F atoms are covalently bonded to Si, which suggests that at some point (e.g., on cracked surfaces) bare Si not covered with oxide or SEI, becomes directly exposed to the $LiPF_6$-containing electrolyte. At the same time, although adding fluorinated ethylene carbonate (FEC) has been found to improve cycling, FEC decomposition products needed to be elucidated, and the breakdown mechanism was not well understood. The structure and Li^+ conductivity of Si-F containing structures, and how it apparently improves silicon anode lifetime, is therefore of significant fundamental and technological interest. Finally, additives like vinylene carbonate (VC), succinic anhydride, other organic compounds, metal nanoparticles, and ether-based electrolytes have been demonstrated to improve cycling for silicon anodes. VC is also used as additive in graphitic carbon anode-based batteries. But the specific interactions between VC and Si are of interest because of their potential role in self-healing and sealing of cracks in Si. This work focused on VC as a prototype of organic additive that may have these favorable properties.

Coating the Si anode with conductive materials such as carbon, aluminum, copper, or gold, have shown to dramatically improve the anode performance by imparting stability and enhancing electronic conductivity. In all these cases, very little is known about the specific interfacial structure and its effect on electron and ion transfer, and much less about the reactivity of the composite material towards electrolyte reduction. These have been key foci of these studies.

Introduction

Investigation of formation/growth mechanisms of the SEI layer on bare surfaces requires incorporation of effects from surface structure and chemical state: presence of functional groups, surface oxidation, nature of exposed facets, and electrolyte composition including additive species. Finding the correspondence between additive molecular properties and SEI formation mechanism, structure, and properties in additive-induced SEI layers will allow identification of new/improved additives. Including the state of lithiation of the surface is also a key factor to determine possible changes in the electrolyte reduction mechanism and/or nature of the products. Finally, it is crucial to understand how the electron transfer from the electrode to the electrolyte is modified by deposition of the initial SEI intermediates or products of the SEI formation reaction.

Approach

A comprehensive first-principles computational approach employed in this work includes density functional theory (DFT), ab initio molecular dynamics (AIMD), classical molecular dynamics (CMD), and ab initio-Green's function theory. Static DFT is utilized within two approaches: cluster models are used to investigate bond dissociation energies, activation barriers for reduction of individual molecules, and polymerization pathways, whereas periodic surfaces representing both quasi-amorphous low lithiated surfaces and well-characterized crystalline Si_xLi_y alloys are used to follow the dynamics of electrolyte decomposition reactions. For CMD simulations, the team has invested significant efforts in force field development and test. Nucleation and growth of SEI components have been studied by using a sequential adsorption mechanism of oligomers on lithiated Si surfaces, and a similar approach is currently used to determine nucleation of LiF molecules over the anode surfaces. These models of periodic surfaces in contact with liquid electrolyte mixtures are utilized to investigate mechanisms of SEI nucleation and growth using ab initio molecular dynamics (AIMD). Electron transport through the composite material (electrode/ SEI layer/electrolyte molecule) is also characterized using ab initio Green's functions calculations (J. Seminario, Co-PI, TAMU). Co-PI Seminario has also developed simulation shecmes to investigate the first battery charge, including the effect of applied potential, and the lithiation and swelling of the Si matrix. In addition, a multiscale modeling approach is utilized to develop a mesoscopic model able to predict SEI layer nucleation and growth at realistic length/time scales (in collaboration with P. Mukherjee, TAMU). Sandia's collaborator Leung developed ab initio procedures to characterize instantaneous electronic voltage of the half-cell including anode in contact with electrolyte; this new method allowed identifying voltage effects on SEI reactions. Sandia's collaborator's Rempe focused on the development of accurate classical force fields for ionic solvation in typical non-aqueous solvents. NREL collaborator Chunmei Ban provided detailed experimental information on MLD-deposited alucone-coated Si electrodes.

Results

Stability of SEI products: One of the main findings of this project[1] was that the quality of the SEI layer is determined not only by the electrochemical stability of the electrolyte components but also by that of the products formed after their decomposition. DFT and AIMD analyses of organic species such as lithium ethylene dicarbonate (Li_2EDC) and lithium vinylene dicarbonate (Li_2VDC) demonstrated that they are thermodynamically unstable. Thus, when these species decompose, they generate radical species that are also highly reactive and are able to continue the reactions and therefore lead to SEI growth. Besides these organic products other common SEI constituents are Li_2O, LiF, and $LiCO_3$. Recent work in collaboration with Kevin Leung (Sandia National Labs) addressed the chemical and electrochemical stability of Li_2CO_3, Li2EDC and Li_2O on Li metal and lithiated Si surfaces.[2] It was found that both Li_2CO_3 and Li_2EDC are electrochemically stable but thermodynamically unstable near the equilibrium Li/Li+ potential and interfacial reactions may trigger their decomposition. Exothermic reactions were predicted on Li metal surfaces with barriers sufficiently low to be overcome in time scales of battery operation. For example, on Li metal Li_2EDC is predicted to decompose with barriers of the order of 1 hour, whereas the reactions are slightly slower on lithiated Si surfaces. The decomposition of the organic species was proved not only on Li metal and lithiated amorphous Si (Figure V-183 a-d), but also on LiF-partially covered $Li_{13}Si_4$ surfaces, as a model of a highly lithiated surface (Figure V-183e and f). The presence of radical species such as Li atoms during plating is identified as one of the most typical drivers for these reactions. Among all the species considered, only Li_2O was found stable at least in the tested environments.

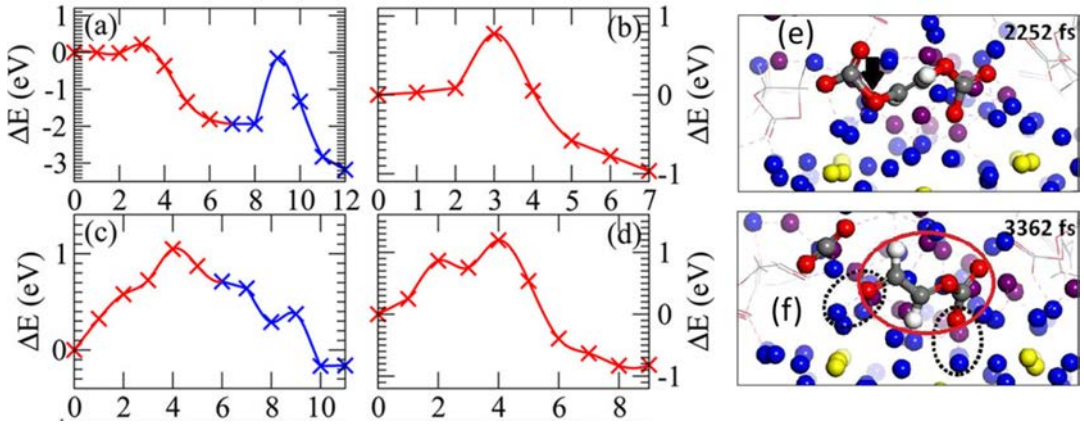

Figure V-183: Nudged elastic band reaction energy profiles, illustrating reaction barriers and exothermicities. (a) Li_2EDC on Li(100), red and blue denote the detachment of first a CO_2^{2-} and then a O_2^-; (b) CO_2^{2-} reaction on Li(100); (c) Li_2EDC on a-Si, red and blue denote formation of C–Si bond and then breaking of C–O bond; (d) Li_2CO_3 decomposition on Li(100). (e) Zoomed-in snapshots showing the time evolution of the LiF cluster -covered $Li_{13}Si_4$ (010) surface in contact with a 1.0 M $LiPF_6$/FEC electrolyte solution and 5 Li_2VDC oligomers adsorbed on the surface at 2.25 ps; (f) at 3.36 ps. Only the dissociating Li_2VDC oligomer is shown. FEC molecules are shown in a line display style. From J. Phys. Chem. C, 2016, 120, 6302−6313

SEI nucleation and growth: Li_2EDC and Li_2VDC molecules were added sequentially to surfaces to evaluate their potential nucleation and growth on lithiated Si surfaces both bare and partially covered with LiF clusters. Strong adsorption energies (in the order of 3-4 eV) are found between the oligomers and the surfaces. Surface-oligomer interactions dominate up to coverages of 1 oligomer per nm2, and for higher coverages oligomer-oligomer interactions become dominant. Li_2EDC associates with the $Li_{13}Si_4$ surface forming Li..O..Li bridges between surface Li and O of the carbonate groups, but Li(oligomer)-Si (surface) interactions are also important, and LiF bonds between the oligomer Li and the F atoms of the LiF cluster partially covering the surface (Figure V-184). On the other hand, Li_2VDC grows closer to the surface forming a more flexible structure. On Si anodes, this SEI structural flexibility would be an important property to facilitate volume changes. Although the charge transfer from the surface to the adsorbate is smaller for the case where the LiF is present, the corresponding adsorption energies are stronger. This is because there is a difference in the nature of the bonding that changes from a more ionic (LiO bonds) in the bare surface to a more covalent (LiF bonds) on the partially covered surface. Thus the role of the LiF layer goes beyond the surface passivation and helps stabilizing the organic SEI. Finally, this study also confirms the previous finding related to the stability of the SEI products. Some of the adsorbed oligomers are found to decompose forming CO_2 anions that are the precursors of Li_2CO_3, and other radical anion organic fragments which may consume more Li ions thus increasing the irreversible capacity and/or trigger further reactions involving fresh solvent or SEI components. A paper has been published in Electrochimica Acta.[3]

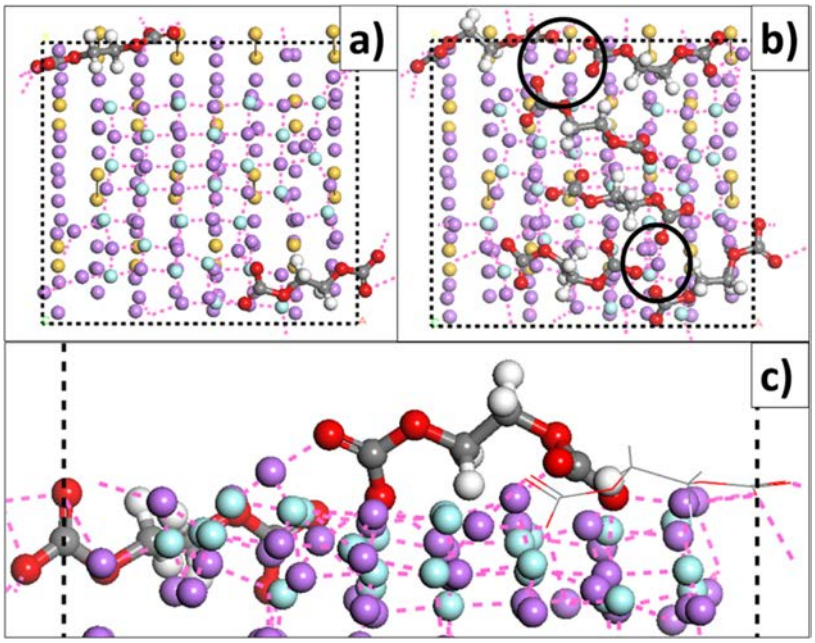

Figure V-184: Snapshots show the sequential association of Li_2EDC oligomers on top of a Li-F partially covered lithiated Si surface. Panel a) shows an extended periodic image for the case where two Li_2EDC oligomers are adsorbed at the surface. Panel b) shows a side view snapshot of a Li2EDC adsorbed on top of the LiF layer. For clarity one oligomer is shown in a line display style. The pink dashed lines show the closest connections between atoms. Panel c) displays the relaxed structure when six Li_2EDC oligomers are attached to the surface. Dark black circles highlight the O-Li-O bridges between oligomers. Blue sphere represents Fluorine atoms. Li atoms associated with the oligomer are shown in purple. From Electrochimica Acta, 2016, 220, 312-321

Structure, dynamics, and Li transport in electrolyte solutions: Understanding the solvation behavior of currently used electrolyte solutions is critical for future electrolyte development. Initially, solvation properties of anions and Li cations were examined in 1M $LiPF_6$/EC solutions. In this work, special efforts by the Seminario group at TAMU were dedicated to force field development including effective charges of the atomic sites.[4] Coordination numbers of the solvated anion and cation species were found to be in good agreement with experimental reports. Li diffusion coefficients were calculated without and with the presence of an electric field. Under an electric field, the so-called drift velocities were evaluated and the influence of the neighboring species (anions, other solvent molecules) was carefully investigated. The drift velocity increases almost linearly with the magnitude of the electric field until a threshold value where the influence of the neighboring molecules including ion-pairs and solvent-separated ions is overcame (Figure V-185a). The calculated lithium ion mobilities were in the same order of magnitude as those reported for Li ions in a liquid-gel electrolyte under similar electric fields. In addition, the Rempe group (Sandia collaborator) focused on ion dissolution and diffusion and their correlation to solvent dielectric response.[5] Dielectric constants, relaxation times, and molecular mobilities of the EC and PC solvents were evaluated with classical molecular dynamics simulations. Dielectric relaxation assesses the lag of the material polarization in relation to a change in an applied electric field, and depends on the frequency of the applied field. At high frequencies, the dipole reorientation lags behind the field, whereas at low frequencies dipoles can successfully reorient following the changes in the field. These properties were evaluated from CMD simulations from the dipole moment autocorrelation function, and relaxation times were obtaining from fitting to an exponential function. The calculated relaxation times were found in good agreement with the experiments. The values of the relaxation times of the organic solvents are significantly larger than those of water, indicating that their dynamic is much sluggish compared to that of water. Further analyses were carried out with CMD simulations of EC and PC solvents to investigate whether the atomic charges could be scaled to correctly describe solvation and transport properties. Such scaling of charges was led by Susan Rempe from Sandia National Labs. The force field parameters were assessed by comparing solvation structures from AIMD and CMD simulations.[6] Solvation free energies computed by CMD and quasi-chemical theory were then compared to experimental values. The anion and cation calculated transference numbers showed good agreement with experimental values (Figure V-185 b and c). It was concluded that the adjustment of partial charges is a good approach for reliable force fields needed in large-scale CMD simulations.

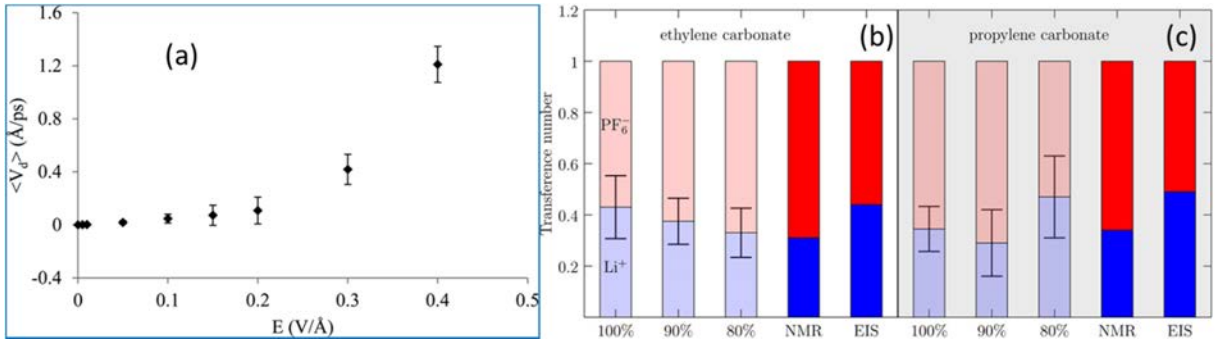

Figure V-185: (a) Drift velocity of Li+ ions in EC under an external electric field. The deviations in drift velocity are due to the presence of different neighboring molecules around the cations, which can be present in both coupled ion pairs and solvent-separated ions. There is threshold electric field where solvent effects are overcome. From J. Phys. Chem. C, 2016, 120, 16322-16332. (b) and (c) Transference numbers for Li+ and PF_6^- in EC (b) and PC (c) calculated using CMD simulations. The percentages reflect full and reduced charges on the atoms of EC and PC. The NMR diffusion constants at 1 M salt concentration were used to calculate experimental transference numbers (NMR), and the combined AC impedance and DC polarization results apply to 0.1 M salt concentration (EIS). The experimental results show little dependence on salt concentration, and the calculated results agree with the experimental numbers. From J. Chem. Theory Comput. , 2016, in press

Coarse-grained model of SEI layer: In collaboration with Prof. Mukherjee from TAMU, a Kinetic Monte Carlo (KMC) model was developed on the basis of ab initio rates obtained for microscopic events. The KMC model involves multiple-step reactions; but it was based on the simplification of a single-component SEI layer. Thus, the adsorption, reduction, configurational change, ring opening, and desorption and diffusion of products were all included based on our previous results of activation energies for elementary steps. It was found that the reduction of EC limits the film growth rate. A simple approach was used to incorporate the effect of the SEI thickness which shows the reduction of the growth rate as the film thickness increases. The evolution of the surface pattern was detected as a function of SEI thickness.

Quantification of electron leakage from the surface to the electrolyte: Electron transport characteristics were studied by Seminario's group (TAMU) in selected finite models of materials formed at the SEI located between the anode silicon surface and the electrolyte solvent.[7] The SEI products examined were lithium carbonate ($LiCO_3$) silicon oxide (SiO_2) and lithium disilicate ($Li_2Si_2O_5$). Results showed that the leakage of electrons from the Si anode to the solvent was greatly reduced (up to 4 orders of magnitude) with the addition and growth of the SEI components as compared with the solvent-anode sample where no SEI is present (Figure V-186). Moreover, it was found that at a charging voltage of 2 V, the electron leakage current decays exponentially with the length, decaying up to 3 orders of magnitude at about 30 Å in Li_2CO_3, 2 orders of magnitude at about 16 Å in SiO_2, and up to 3 orders of magnitude at about 47 Å in $Li_2Si_2O_5$. An estimate of the change in current associated with energy changes using the Heisenberg uncertainty principle yielded currents in the range of 10−4 A. Electron transport results provided particular details on the SEI layer formation and growth. A 100% Si cluster yielded the largest resistance to electron transport, when compared to the lithiated electrodes modeled by $Li_{13}Si_4$ and LiSi clusters. These analyses are useful as input to the KMC model discussed above. More work is planned in the future along these directions.

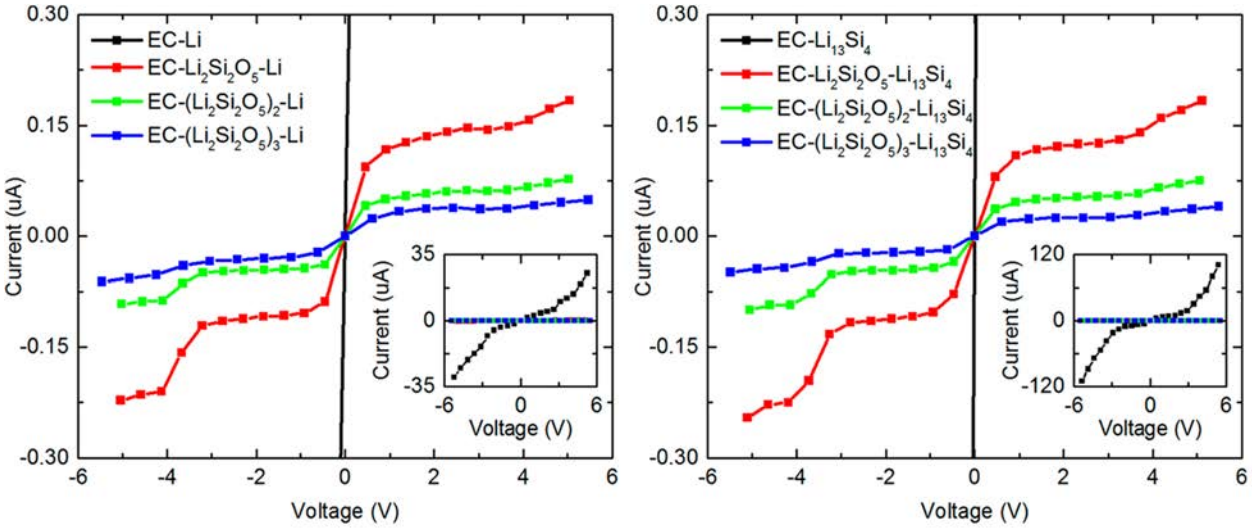

Figure V-186: Current–voltage curves for electron transport through $Li_2Si_2O_5$ for all Li_xSi_y clusters. Inset shows results (black) of EC–Li_xSi_y systems without the SEI layer. From J. Phys. Chem. C, 2016, 120, 17978−17988

Reactivity at grain boundaries: In collaboration with Kevin Leung at Sandia National Lab, we have been investigating simple models representing grain boundaries in the SEI layer. This work explored the effect of SEI structural heterogeneity at the atomic length-scale. Figure X displays a LiF/Li_2O "grain boundary" model. Blue, purple, and red represent Li, F, and O atoms, respectively. The upper panel is the local electrostatic potential, in volts, normalized to the Li^+/Li(s) reference. Note that the voltage of the entire metallic lithium anode should be constant; the local variations are however pertinent to electron tunneling barriers and should affect further SEI formation electrochemical reactions. The Li-contents at the grain boundaries are adjusted to match the lithium chemical potential by attempting to introduce Li vacancies and interstitials. The overall Fermi level of the Li_2O/LiF-coated Li metal anode model is roughly 0.1 V vs. the Li^+/Li(s) reference. However, the local electrostatic potential (V(x)) far from the coated Li surface, averaged along the grain boundary direction and referenced to $Li^{+/}$Li(s), reveals more interesting physics. V(x) can be thought of as a "local voltage," has a variation of ~0.6 V, with its lowest value at one of the two "grain boundaries." Electrolyte and even SEI decomposition are expected to be enhanced at such low V(x) regions where the electron tunneling barrier from the anode surface should be the lowest. Previous findings of this team suggested that LiF and Li_2O are key SEI inorganic components on the immediate surfaces of reactive anode materials. The described LiF/Li_2O "grain boundary" model exhibits substantial spatial variation in its effective "local potential" V(x). Therefore, Leung's group at Sandia focused on the reactivity of FEC molecules at Li_2O surfaces and grain boundaries. It was found that an FEC molecule initially placed on a V(x) ~ -0.3 V region, is rapidly electrochemically decomposed. This qualitatively illustrates that the spatial heterogeneities ("hot spots") can accelerate electrolyte decomposition. Here V(x) represents local voltage variation due to the effects of the local electrostatics added to the constant voltage.

Alternative electrolytes: A systematic procedure was implemented to determine potential solvent, salt, and additive candidates that may favor a stable SEI on lithiated Si anodes. Based on the demonstrated good properties of fluorinated ethylene carbonate (FEC) on Si anodes, the work was focused on the effect of fluorinated additives resulting from modifications of FEC, such as trifluoropropylene carbonate (TFPC) and trifluoroethyl ethyl carbonate (TFEEC). AIMD simulations were carried out on a lithiated silicon slab model surface in contact with an electrolyte phase containing the tested additive (solvent) + salt ($LiPF_6$). The following aspects were examined: a) salt solvation by candidate additive, and its effect on salt dissociation/ decomposition; b) initial SEI reactions and subsequent SEI products; c) effect of additive concentration on the previous issues; d) electrochemical stability of the SEI products. The main preliminary conclusions are: i) solvation properties and steric constraints determine a very different pattern of SEI reactions for each molecule: TFPC results in intermediate products that lead to Li_2O and has a faster decomposition than the salt, whereas TFEEC favors salt anion decomposition first (leading to LiF) and later solvent decomposition yielding Li_2O. ii) In both cases the formation of fluorinated polymers is expected since the CF_3 group remains intact in one of the radical anion products. Current efforts focus on refining these conclusions and examining the product stabilities. This systematic analysis is expected to lead to guidelines for electrolyte selection.

Swelling effects of the Si lithiation: CMD simulations of a complete nanobattery were carried out by Seminario's group (TAMU) to investigate the first charge and the volume expansion effects on a Si nanoanode particle. Although all the battery components (cathode, current collectors, electrolyte, anode) were included at the atomistic level, the study was focused on the interface between the electrolyte and the anode, and inside the anode. A detailed report has been submitted for publication. External electric fields were applied to emulate the charging, causing the migration of the lithium ions from the cathode to the anode, by drifting through the electrolyte solution, thus converting pristine Si gradually into $Li_{14}Si_5$ when fully lithiated. When the electric field is applied to the nanobattery, the temperature never exceeds 360 K due to a temperature control imposed resembling a cooling mechanism. The volume of the anode increases with the amorphization of the silicon as the external field is applied by creating a layer of LiSi alloy between the electrolyte and the silicon nanocrystal and then, at the arrival of more lithium ions changing to an alloy, where the drift velocity of lithium ions is greater than the velocity in the initial nanocrystal structure. Charge neutrality is maintained by concerted complementary reduction-oxidation reactions at the anode and cathode, respectively. At 524 ps the anode expanded covering all the initial empty spaces, reaching a volume 2.6 times the initial one. The volume once the anode converts to a $Li_{3.5}Si$ alloy follows a linear relationship $V/Vo = 0.65X + 0.89$, where X is the number of Li in the Li_xSi alloy. This yields a volume 316% larger when the full anode reaches the $Li_{3.5}Si$ structure. The results were also compared with experimental values. The experimental volume increases faster than in the simulation due to the different initial anode structure and cell geometry. The experiment was done on amorphous silicon as an initial structure rather than a crystallographic one used in the simulations. The other difference between simulation and experiment is the geometry of the anode. In the experiment, the silicon can only expand in one direction whereas expansion along two directions is allowed. A paper has been submitted for publication.

Reactivity of artificial coatings: Together with collaborator Chunmei Ban from NREL, the team has modeled coating effects on Si particles. In particular, the NREL group deposited a thin Al_2O_3 layer over a Si anode using molecular layer deposition methods, and the TAMU team carried out DFT and AIMD simulations to elucidate the effects of such layer on the reactivity of a lithiated Si anode. In summary, it was found that the Al_xO_y groups in the film may play a significant role in the formation of an SEI layer with a larger inorganic component. New chemistry was discovered that takes place at the alucone/lithiated Si anode and the alucone/electrolyte interfaces due to electrolyte decomposition. The AlO_x and OH groups in the film play a very important role in the SEI formation as was revealed by AIMD simulations. EC is able to migrate through the porous film and get reduced at the anode surface and sometimes at the alucone/electrolyte interface. Most of the EC decomposition products may be found bonded to AlO_x. H product of OH decomposition may act as a reduction agent. Thus, besides the usual LiF, Li_2CO_3 and Li_2O products, the SEI film is predicted to have a mixed organic/inorganic nature due to the presence of numerous AlO_x groups participating of the SEI film. Currently these findings are being tested with NMR and XPS techniques in collaborative work with NREL.

Conclusions

Further confirmation of low thermodynamic stability of the SEI products was obtained on various surfaces including Li metal and lithiated amorphous Si. The role of the interfacial mismatch and formation of microscopic cracks on such reactions was investigated and it was found that interfacial instability can give rise to significant reactivity within the SEI layer. The formation of interfaces between the various nucleation products (for example LiF and organic oligomers) was characterized by sequential addition of adsorbates and the differences between adhesion of organic oligomers on the inorganic surfaces was identified. Strong adhesion results from Li..O..Li, Li..Si, and Li..F interactions. Oligomer-oligomer interactions determine the degree of compactness of the surface films. Again, some degree of instability of the adsorbed species was verified. Electronic conductivity through various silicate film thicknesses was assessed. Solvation effects were studied in the bulk electrolyte including the effects of electric field on the drift velocities and the characterization of the evaluation of cation and anion transference numbers using classical force fields. Classical MD simulations have been also done including all the battery components to emulate the first charge of a Si nanoparticle addressing volume expansion and the formation of a Si alloy. Alternative fluorinated electrolytes were tested computationally based on the criteria of product stability, salt solvation and effects of the solvents/additives on salt decomposition. It was found that solvation and steric effects play an important role to define the type of SEI layer compounds that nucleate first. Additional work is currently carried out to determine the role of interfacial mismatching on the evolution of the multicomponent SEI layer. Although the problem is very complex we expect some guidelines to be established. Finally, significant efforts have been

invested in the characterization of the reactivity of an alucone film deposited on Si anodes. Interestingly, it was found that the Al atoms of the film participate in the SEI reactions and the film may act as a passivation layer formed by additional products derived from electrolyte decomposition bonded to AlOx groups of the film.

Products

Presentations/Publications/Patents

1. S. Perez-Beltrán, G. E. Ramirez-Caballero, and P. B. Balbuena, "First Principles Calculations of Lithiation of a Hydroxylated Surface of Amorphous Silicon Dioxide," J. Phys. Chem. C, 119, 16424-16431, (2015).
2. Y. Ma, J. M. Martinez de la Hoz, I. Angarita, J. M. Berrio-Sanchez, L. Benitez, J. M. Seminario, S.-B. Son, S.-H. Lee, S. M. George, C. M. Ban, and P. B. Balbuena, "Structure and Reactivity of Alucone-Coated Films on Si and LixSiy Surfaces," ACS Appl. Mater. Inter., 7, 11948-11955, (2015).
3. J. M. Martinez de la Hoz, F. A. Soto, and P. B. Balbuena, "Effect of the electrolyte composition on SEI reactions at Si anodes of Lithium-ion batteries," J. Phys. Chem. C, 119, 7060-7068, (2015)
4. F. A. Soto, Y. Ma, J. M. Martinez de la Hoz, J. M. Seminario, and P. B. Balbuena, "Formation and Growth Mechanisms of Solid-Electrolyte Interphase Layers in Rechargeable Batteries," Chem. Mater., 27 (23) 7990-8000 (2015).
5. X. You, M. I. Chaudhari, S. B. Rempe, and L. R. Pratt "Dielectric Relaxation of Ethylene Carbonate and Propylene Carbonate from Molecular Dynamics Simulations," J. Phys. Chem. B, 120, (8), 1849-1853 (2016).
6. K. Leung, F. A. Soto, K. Hankins, P. B. Balbuena, and K. L. Harrison, "Stability of Solid Electrolyte Interphase Components on Reactive Anode Surfaces," J. Phys. Chem. C, 120, 6302-6313, (2016).
7. N. Kumar and J. M. Seminario, "Lithium-Ion Model Behavior in an Ethylene Carbonate Electrolyte Using Molecular Dynamics," J. Phys. Chem. C, 120, 16322-16332, (2016).
8. M. Chaudhari, J. Nair, L. Pratt, F. A. Soto, P. B. Balbuena, and S. B. Rempe, "Scaling Atomic Partial Charges of Carbonate Solvents for Lithium ion (Li+) Solvation and Diffusion," J. Chem. Theory Comp., (2016), DOI: 10.1021/acs.jctc.6b00824.
9. L. Benitez and J. M. Seminario, " Electron Transport and Electrolyte Reduction in the Solid-Electrolyte Interphase of Rechargeable Lithium Ion Batteries with Silicon Anodes," J. Phys. Chem. C, 120, 17978-17988, (2016).
10. F. A. Soto and P. B. Balbuena, "Elucidating Oligomer-Surface and Oligomer-Oligomer Interactions at a Lithiated Silicon Surface," Electrochimica Acta, 220, 312-321, (2016). Text (1APR_para Numbered Listing).

References

1. Soto, F. A.; Ma, Y.; Martinez-DeLaHoz, J. M.; Seminario, J. M.; Balbuena, P. B. Formation and Growth Mechanisms of Solid-Electrolyte Interphase Layers in Rechargeable Batteries Chem. Mater. 2015, 27, 7990-8000.
2. Leung, K.; Soto, F. A.; Hankins, K.; Balbuena, P. B.; Harrison, K. L. Stability of Solid Electrolyte Interphase Components on Li metal and Reactive Anode Material Surfaces. J. Phys. Chem. C 2016, 120, 6302-6313.
3. Soto, F. A.; Balbuena, P. B. Elucidating Oligomer-Surface and Oligomer-Oligomer Interactions at a Lithiated Silicon Surface. Electrochim. Acta 2016, 220, 312-321.
4. Kumar, N.; Seminario, J. M. Lithium-Ion Model Behavior in an Ethylene Carbonate Electrolyte Using Molecular Dynamics. J. Phys. Chem. C 2016, 120, 16322-16332.
5. You, X. L.; Chaudhari, M. I.; Rempe, S. B.; Pratt, L. R. Dielectric Relaxation of Ethylene Carbonate and Propylene Carbonate from Molecular Dynamics Simulations. J. Phys. Chem. B 2016, 120, 1849-1853.

6. Chaudhari, M.; Nair, J.; Pratt, L.; Soto, F. A.; Balbuena, P. B.; Rempe, S. B. Scaling Atomic Partial Charges of Carbonate Solvents for Lithium ion (Li+) Solvation and Diffusion. J. Chem. Theory Comp. 2016, in press.
7. Benitez, L.; Seminario, J. M. Electron Transport and Electrolyte Reduction in the Solid-Electrolyte Interphase of Rechargeable Lithium Ion Batteries with Silicon Anodes. J. Phys. Chem. C 2016, 120, 17978-17988.

V.F.5. A Combined Experimental and Modeling Approach for the Design of High Current Efficiency Si Electrodes (GM)

Xingcheng Xiao, Principal Investigator
General Motors Global Research and Development Center
30500 Mound Road, MC 480-106-RA1
Warren, MI 48090-2031
Phone: 248-912-8132; Fax: 586-986-9260
E-mail: xingcheng.xiao@gm.com

Yue Qi, Co-Principal Investigator
Michigan State University
3509 Engineering Building,
East Lansing, MI 48824
Phone: 517-432-1243; Fax: 517-432-1105
E-mail: yueqi@egr.msu.edu

Brian W. Sheldon, Co-Principal Investigator (Brown University)
Huajian Gao, Co- Principal Investigator (Brown University)
Yang-Tse Cheng, Co- Principal Investigator (University of Kentucky)

Tien Q. Duong, DOE Program Manager
U.S. Department of Energy
Advanced Battery Materials Research (BMR)
Vehicle Technologies Office
1000 Independence Avenue, SW
Washington, DC 20585
Phone: 202-586-7836
E-mail: Tien.Duong@ee.doe.gov

Start Date: June 2013
End Date: March 2017

Abstract

Objectives

Combine modeling and experimental approaches to understand, design, and fabricate stabilized nano-structured Si anode with high capacity and high coulombic efficiency.

Accomplishments

- Identified critical mechanical and electrochemical properties of the SEI coating which can enable high current efficiency.
- Designed a practically useful Si electrode where degradation of the SEI layer is minimized during lithiation and delithation.
- Constructed an artificial SEI design map for Si electrodes, based on critical mechanical and transport properties of desirable SEI for a given Si architecture.

Future Achievements

Optimize Si structures integrated with desirable SEI layer that can be made at high-volume and achieve high cycle efficiency / long cycle life.

Technical Discussion

Background

The use of high capacity Si based electrode has been hampered by its mechanical degradation due to the large volume expansion/contraction during cycling. Nanostructured Si can effectively avoid Si cracking/fracture. Unfortunately, the high surface to volume ratio in nanostructures leads to unacceptable amount of solid-electrolyte interphase (SEI) formation and growth, thereby low current/coulombic efficiency and short life. Based on mechanics models we demonstrate that the artificial SEI coating can be mechanically stable despite the volume change in Si, if the material properties, thickness of the SEI, and the size/shape of Si are optimized.

Introduction

The real challenges to developing a model that allows us to design high current efficiency Si electrodes with electrochemically and mechanically stable artificial SEI layer are: a) poor understanding of SEI failure mechanisms; b) lack of accurate mechanical properties of the SEI; and c) difficulty in validation of the model. All of these are due to the extreme challenges associated with characterizing the properties of nano-meter thin SEI layer on lithiated Si in real battery systems. Therefore, we will first address these questions based on simpler thin film electrodes.

Approach

- Combine simulation with experiments to obtain critical material properties of SEI layer and lithiated silicon.
- Develop a multi-scale model to establish correlation between coulombic efficiency and mechanical degradation of SEI on Si.
- Use the validated model to guide synergetic design of surface coating with Si size/geometry/architecture.

Results

Part I: Identify SEI mechanical failure mechanisms on Si

The lifetime and performance of rechargeable lithium-ion batteries are closely related to the formation and evolution of the solid electrolyte interphase (SEI). A mechanistic understanding of SEI layers is particularly important for high capacity anode materials such as silicon, which goes through large volume changes (~300%) during cycling. In this study we used *in situ* atomic force microscopy (AFM) to monitor the formation, evolution and failure of SEI on patterned Si island electrodes. The unique PeakForce tapping mode made it possible to image the extremely complex SEI layer, which is very challenging for conventional AFM modes in organic solvents.

Figure V-187 further shows SEI surface topography on a patterned mode a-Si electrode system at the initial, fully lithiated and delithiated states during the first and second cycles. It is the first direct observation that the crack generates and propagates normal to the surface, which is associated with tensile stress during lithiation (but not in the underlying Si). The lateral sliding of patterned island puts SEI layer in tension and compression during lithiation and delithiation respectively. During first cycle lithiation, at 0.1V hold, cracking begins to occur in the edge and corner regions due to tensile stress buildup in the SEI layer. This tensile state is further substantiated when these cracks open further as the Si expansion continues. More surface cracks appear in the edge region and other corners of the island during further insertion of Li at 0.05V.

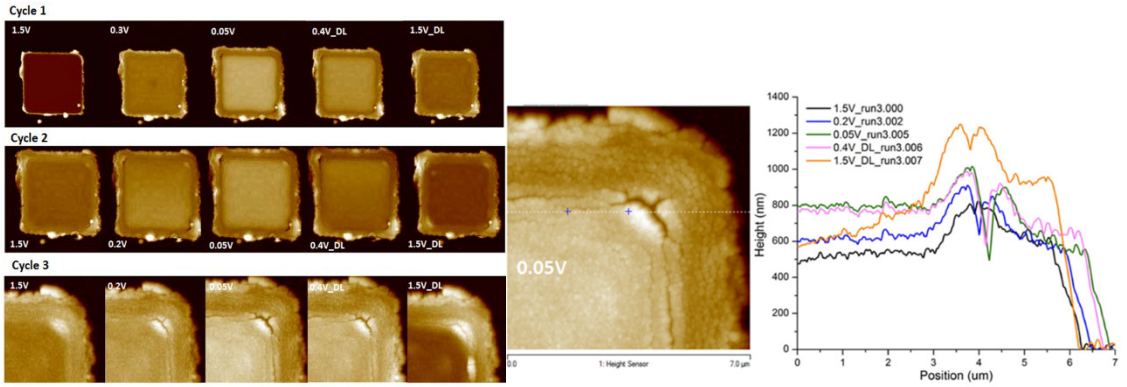

Figure V-187: (a) *In situ* AFM images during cycling of patterned Si electrode (15 um X 15 um X 225 nm) showing failure of SEI in shear lag zone. (b)The evolution of section height with cycling (also showing how the crack is evolving)

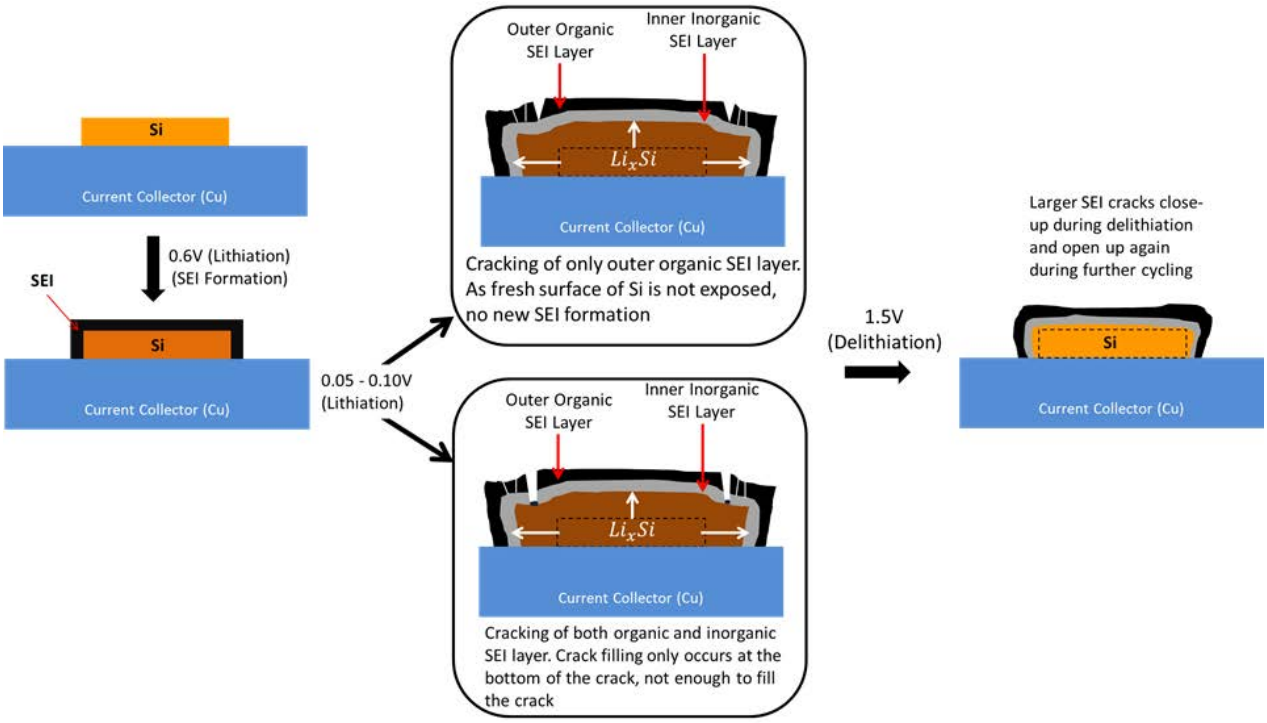

Figure V-188: Schematic showing deformation of patterned Si island during cycling, and the resulting impact of volume changes on SEI formation and failure

Two possible mechanisms are proposed to explain SEI failure based on a bilayer SEI structure, as shown in Figure V-188. One of the possible explanations is that the crack only runs through the top organic layer and doesn't reach the interface of SEI and Si to cause further SEI formation. Another explanation could be that the cracks run all the way to the interface of SEI and Si but crack filling only occurs at the bottom of the crack, not enough to fill up whole crack. During delithiation, there is compressive stress buildup in SEI layer and at first these cracks become narrower at 0.4V. With further removal of Li, it is observed that there is huge buildup of material at the edge crack site. The material buildup at the crack site is a result of compressive stress which causes buckling of the SEI layer.

A continuum modeling is established to explain the growth and crack formation of SEI on lithiated a-Si. As shown in Figure V-189, the model shows that the SEI layer near the edge of the island is under pronounced in-plane tensile stress, which is consistent with the region where surface cracks were observed in experiments. The model predicts that the energy release rate for the growth of the surface crack increases with the length of the crack until it reaches a maximum value as the crack approaches the SEI/Si interface. This result suggests

that a surface crack in the SEI layer would propagate unstably toward the interface, but it will stop or change to a path parallel to the interface in the later stage.

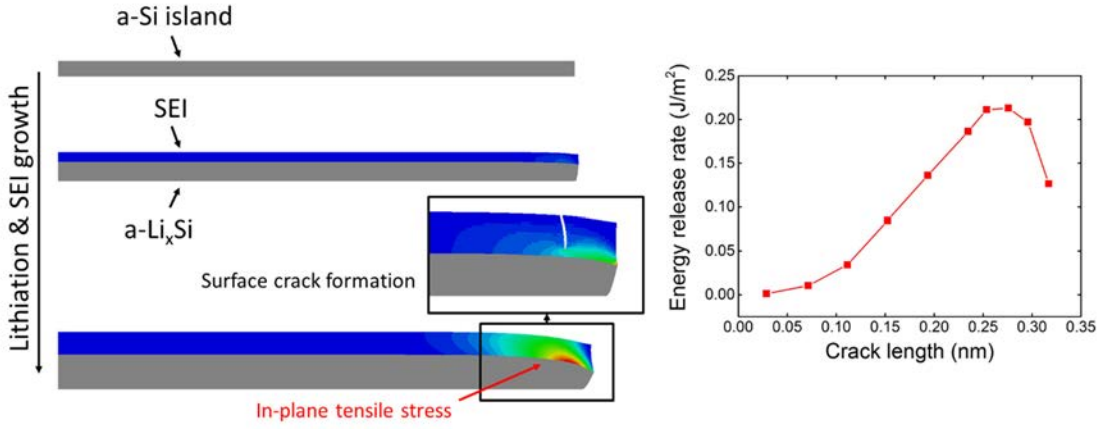

Figure V-189: A continuum model established to describe how crack generates in the SEI layer

Part II: Correlate the SEI transport properties with lithiation and delithiation dynamics of Si

Si based electrode is typically covered with a thin oxide layer, such as SiO_2, which can be lithiated. This is different than some SEI components, such as LiF, which cannot be lithiated. Therefore, we investigated and compared the impact of these two types of SEI materials on the lithiation and delithiation dynamics of Si electrode. In order to simulate these systems, we finished developing ReaxFF parameters for Li-Si-O-Al and Li-Si-O-F systems. Reactive molecular dynamics simulations were performed to compare lithiation dynamics of a-SiO_2 and a-LiF coated a-Si thin film electrode. A new de-lithiation algorithm was developed. A new continuous delithiation algorithm was implemented to investigate the impact of delithiation rates on oxide coated Si thin film electrode.

During lithiation, distinct Li diffusion behavior between SiO_2 and LiF layers on Si electrode were observed. For SiO_2 case, Li diffuses very fast through the SiO_2 layer leading to subsequent lithiation to Si electrode (Figure V-190 (a)). On the contrary, for LiF layer case, instead of passing through the LiF layer, Li plating occurs accompanied by the growth of the mixture of LiF and Li layer (Figure V-190 (b)). This further support our previous DFT conclusion that LiF is a Li transport barrier.

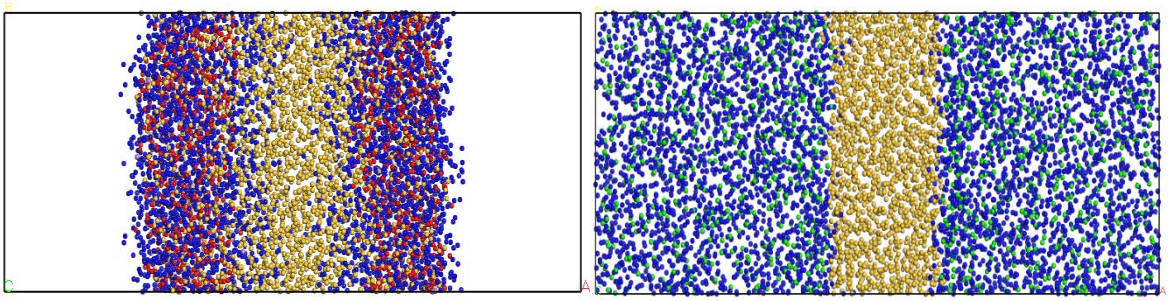

(a) SiO2 layer on Si electode (b) LiF layer on Si electrode

Figure V-190: Final configurations of lithiated SiO_2 layer on Si electrode (a) and lithiated LiF layer on Si electrode (b) (Si:yellow, O:red, F:green, Li: blue)

During delithiation SEI delamination and Li trapping was observed (Figure V-191). Upon fast delithiation, only the Li atoms near the surface can diffuse out in to the oxide coating, while the Li atoms in the center of the film do not have enough time to diffuse to the oxide coating layer. Therefore, a Li concentration gradient, which is characterized by low Li concentration near the surface and high Li concentration near the center as shown in Figure V-191d, is generated. Thus, Figure V-191a shows a dilated Si with trapped lithium at the end

of fast delithiation. In contrast, during slow delithiation, Li atoms have enough time to diffuse out and the lithium concentration remains nearly a constant throughout the delithiation process (Figure V-191d). As shown in Figure V-191b, the delithiated Si thin film has a much smaller volume with no trapped lithium after slow delithiation. In both cases, Si and the oxide coating start to show delamination crack. Since the number of available Li are directly related to the capacity, trapping of significant amount of Li in the delithiated a-LixSi upon fast delithiation results in irreversible capacity loss, as shown in Figure V-191c.

These detailed atomistic simulations revealed that the diffusion properties of SEI can have a dramatic impact on the lithiation and delithiation of Si electrode, causing different failure mechanisms.

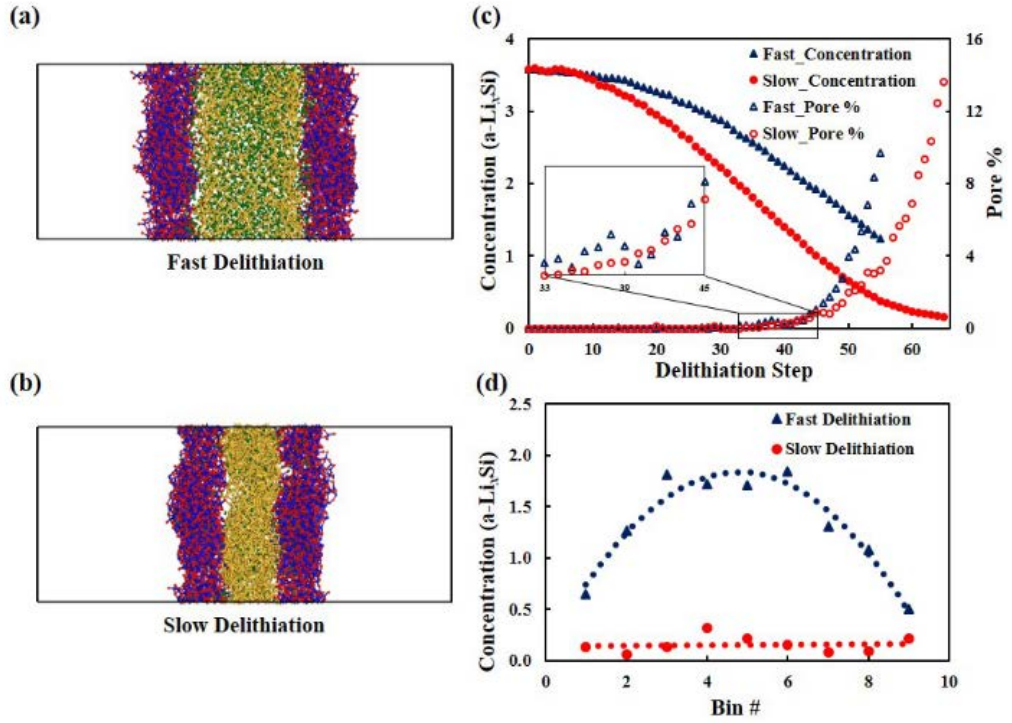

Figure V-191: Structural snapshots at the final delithiation stage of (a) fast and (b) slow rates. (c) Li concentration change upon delithation. (d) The concentration profile of a-LixSi core at the final delithation stage

Part III: Develop practical Si electrode

New lithium-ion battery electrode design concepts are required to meet the increasingly stringent performance of emerging commercial technologies, including electric vehicles. We collaborated with Prof. Zhongwei Chen at University of Waterloo and developed a simple process to make Si/graphene composited electrode, aiming to stabilize SEI layer and mitigate the mechanical degradation of Si nanoparticles. The technique is to create the covalent bonding of Si nanoparticles (SiNP) with sulfur-doped graphene (SG), followed by sealing this covalent hybrid with cyclized polyacrylonitrile (Figure V-192). The strong interactions occurring between SiNP and SG are demonstrated by the density functional theory calculations. This binding led to significantly improved electrode integrity and a stabilized reversible capacity of 1033 mAh g-1 (based on electrode mass) over 2000 cycles at 1C rate. (See Figure V-193.) The areal capacity was 3.5 mAh cm-2, approaching the ambitious performance targets required for electric vehicles. After cycling, the spatial rearrangement of SiNPs was confined within the graphene layers, despite the mechanical fracture caused by large volumetric changes. The excellent performance combined with the simplistic, scalable and non-hazardous synthesis approach render these materials as very promising commercial candidates for lithium-ion battery anodes.

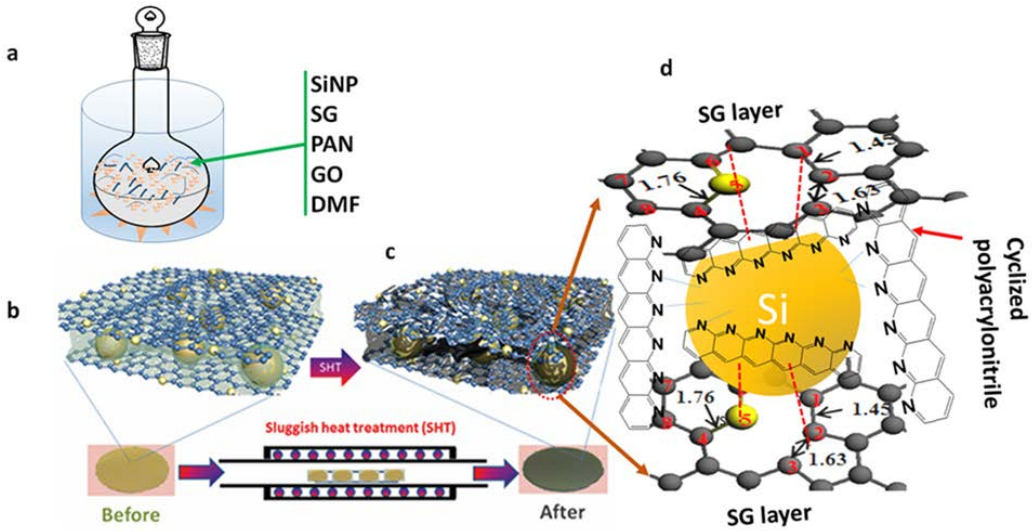

Figure V-192: The process of making Si-S-doped graphene nanocomposite electrodes

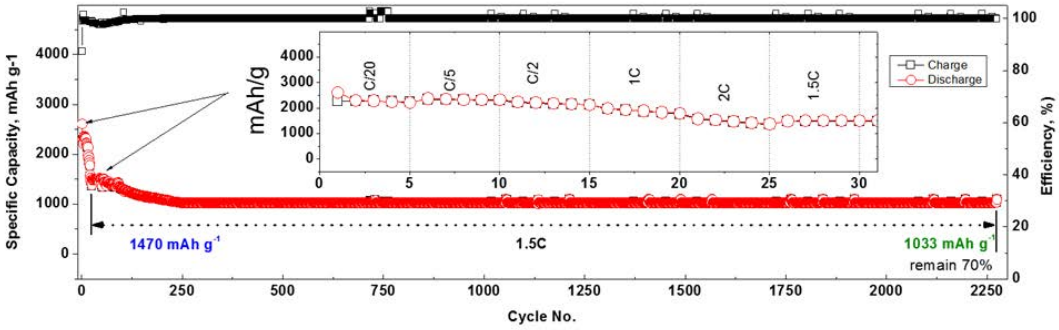

Figure V-193: Electrochemical performance of SG-Si

Conclusions

- It is the first time *in operando* demonstrated that the volume expansion and contraction of Si electrodes leads to significant mechanical damage of the SEI layer. During lithiation Si expansion puts the SEI in tension, which causes through-thickness cracking in the surface layer. Controlling stress level in SEI would be future focus to improve the cycle efficiency.
- Revealed the impact of lithium transport properties in SEI components on the lithiation and delithiation dynamics of coated Si. SEI fracture was observed during lithiation (last year report) and SEI coating delamination was observed during delithiation.
- The mechanical integrity of electrode is critical for maintaining long-term cycle stability. The combination of Si nano particles wrapped by graphene and PAN creates a robust 3D structure and significantly improves the electrode integrity; The covalent interaction between Si and S anchors Si nano particles onto the graphene surface and immobilizes the fractured Si, attributing to the improved capacity retention; The highly electrical conductivity of S doped graphene with the 3D network structure is responsible for the good rate capability of the composite electrode.

Products

Presentations/Publications/Patents

1. X. Wang, G. Li, M. Seo, G. Lui, F. M Hassan, K. Feng, X. Xiao, and Z. Chen, Carbon-Coated Silicon Nanowires on Carbon Fabric as Self-Supported Electrodes for Flexible Lithium-Ion Batteries, ACS Appl. Mater. Interfaces, DOI: 10.1021/acsami.6b12080.
2. R. Kumar, A. Tokranov, B. W. Sheldon, X. Xiao, Z. Huang, C. Li, and T. Mueller, "Direct Observations of Cracking in the Solid Electrolyte Interphase on Silicon Electrodes for Lithium-ion Batteries", ACS Energy Lett., 2016, 1, pp 689–697. (RESEARCH HIGHLIGHTS, Silicon islands under strain, Nature Reviews Materials, doi:10.1038/natrevmats.2016.77).
3. S. Kim, A. Ostadhossein, A. van Duin, X. Xiao, H. Gao, Y. Qi, Self-generated concentration and modulus gradients coating design to protect Si nano-wire electrodes during lithiation, Phys. Chem. Chem. Phys., 2016, DOI: 10.1039/C5CP07219K.
4. J. Pan, Q. Zhang, X. Xiao, Y. Cheng, Y. Qi, Design of Nanostructured Heterogeneous Solid Ionic Coatings through a Multiscale Defect Model, ACS Appl. Mater. Interfaces, 2016, 8 (8), pp 5687–5693.
5. A. Tokranov, R. Kumar, C. Li, S. Minne, X. Xiao, B.W. Sheldon, Control and Optimization of the Electrochemical and Mechanical Properties of the Solid Electrolyte Interphase on Silicon Electrodes in Lithium Ion Batteries, Advanced Energy Materials, DOI: 10.1002/aenm.201502302.
6. Q. Zhang, J. Pan, P. Lu, Z. Liu, M. W. Verbrugge, B. W. Sheldon, Y. Cheng, Y. Qi, X. Xiao, Synergetic Effects of Inorganic Components in Solid Electrolyte Interphase on High Cycle Efficiency of Lithium Ion Batteries, Nano Letters, 2016, 16 (3), pp 2011–2016.
7. A. Ostadhossein, S.Y. Kim, E.D. Cubuk, Y. Qi, A. van Duin, Atomic Insight into the Lithium Storage and Diffusion Mechanism of SiO2/Al2O3 Electrodes of Lithium-ion Batteries: ReaxFF Reactive Force Field Modeling, J. Phys. Chem. A, 2016, 120 (13), pp 2114–2127.
8. J. Li, Q. Zhang, X. Xiao*, Y. Cheng, C. Liang, and N. J. Dudney*, Unravelling the Impact of Reaction Paths on Mechanical Degradation of Intercalation Cathodes for Lithium-Ion Batteries, Journal of American Chemical Society, 2015 DOI: 10.1021/jacs.5b06178.
9. K. Feng, W. Ahn, G. Lui, H. Park, A. Kashkooli, G. Jiang, X. Wang, X. Xiao, Z. Chen, Implementing an *in situ* carbon network in Si/reduced graphene oxide for high performance lithium-ion battery anodes, Nano Energy, Nano Energy 19 (2015)187-197.
10. F. M. Hassan, R. Batmaz, J. Li, X. Wang, X. Xiao*, A. Yu, and Z. Chen*, Evidence of covalent synergy in silicon-sulfur-graphene yielding highly efficient and long-life lithium-ion batteries, Nature Communication, 2015, DOI: 10.1038/ncomms9597.
11. K. J. Kim, Y. Qi, Vacancies in Si Can Improve the Concentration-Dependent Lithiation Rate: Molecular Dynamics Studies of Lithiation Dynamics of Si Electrodes, J. Phys. Chem. C, 2015, 119 (43), pp 24265–24275.
12. X. Xiao, "Towards High Cycle Efficiency of Si Based Negative Electrodes for Next Generation Lithium Ion Batteries", MRS Fall meeting, Boston, MA, USA, Dec 2, 2015.
13. H. Gao, Plenary Lecture, "Brittle vs ductile fracture in amorphous alloys: from metallic glasses to lithiated Si electrodes," International Symposium on Advanced Materials and Structures (ISAMS 2016), Hong Kong University of Science and Technology, January 3, 2016.
14. B. W. Sheldon, "Stress Evolution and Degradation Mechanisms in Energy Materials", Rice University, Houston, Texas, February 11, 2016.
15. Y. Cheng, "Surface Engineering for Electrochemical Energy Storage – Challenges and Opportunities," Society of Vacuum Coaters 59th Annual Technical Conference, May 9-13, 2016, Indianapolis, Indiana.
16. Y. Qi, Computational Design of Coatings, Interfaces, and nano-structures for Si based electrodes, 229th ECS Meeting, May. 2016, San Diego, CA.
17. X. Xiao, Synergetic Effects of Inorganic Components in Solid Electrolyte Interphase on High Cycle Efficiency of Lithium Ion Batteries, IMLB 2016, June 23, Chicago, IL.

18. H. Gao, Investigating Mechanical Degradation Mechanisms in Silicon Electrodes for Lithium Ion Batteries: a Thin Film Approach", Invited Talk, International Workshop on Cutting-edge Problems on Chemomechanics, Xi'an Jiaotong University, Xi'an, China, June 27, 2016.
19. Y. Cheng, Understanding the mechanical behavior of materials for electrochemical energy storage, Symposium E-1: Mechanics and Electrochemistry of Energy Materials, 2016 Society of Engineering Science, October 2-5, 2016 University of Maryland.

V.F.6. Predicting Microstructure and Performance for Optimal Cell Fabrication (Brigham Young University)

Dean Wheeler, Principal Investigator
Brigham Young University
Department of Chemical Engineering
350 Clyde Building
Provo, UT 84602
Phone: 801-422-4126; Fax: 801-422-0151
E-mail: dean_wheeler@byu.edu

Brian Mazzeo, Co-Principal Investigator
Brigham Young University
Department of Electrical and Computer Engineering
459 Clyde Building
Provo, UT 84602
Phone: 801-422-1240; Fax: 801-422-0201
E-mail: bmazzeo@byu.edu

Tien Q. Duong, DOE Program Manager
U.S. Department of Energy
Advanced Battery Materials Research (BMR)
Vehicle Technologies Office
1000 Independence Avenue, SW
Washington, DC 20585
Phone: 202-586-7836
E-mail: Tien.Duong@ee.doe.gov

Start Date: April 2013
End Date: December 2016

Abstract

Objectives

- This work uses microstructural modeling coupled with extensive experimental validation and diagnostics to understand and optimize fabrication processes for composite particle-based electrodes. A main objective is a revolutionary method to assess electronic conductivities of porous electrodes attached to current collectors, including local heterogeneities and anisotropic effects.
- A second main objective is a particle-dynamics model parameterized with fundamental physical properties that can predict electrode morphology and transport pathways resulting from particular fabrication steps.
- A subsidiary objective is to improve measurements of effective ionic conductivity of porous electrodes.

Accomplishments

- Demonstrated that the dynamic particle packing (DPP) model can accurately imitate the manufacturing process, including mechanical calendaring, for a representative electrode film.
- Developed a robust numerical routine for interpreting N-line conductivity measurements.
- Improvements in the N-line probe were achieved to enable greater probe life and enhanced localization abilities for microscopic positioning.
- Measurements of film properties were delivered to both academic and commercial collaborators using the N-line probe apparatus and ionic conductivity measurements.

- Developed a new SPH model to start overcoming hurdles in LAMMPS for properties of interest.
- Preliminary anisotropic conductivities were measured for test materials using N-line conductivity measurements coupled with numerical inversion routine.
- Demonstrated correlation between the DPP modeled conductivities and those determined by FIB/SEM and N-line probe (to be published).

Future Achievements

Demonstrate correlation between the DPP modeled conductivities and those determined by FIB/SEM and N-line probe (in progress).

Technical Discussion

Background

A lack of fundamental understanding about the relationships between fabrication parameters, microstructure, and performance prevents appropriate feedback and hurts the development of next-generation battery materials and process improvement in battery manufacturing. For instance, one problem with large-format batteries is ensuring uniformity in the manufacturing process, so that all components perform equally well and no component contributes unduly to performance limitations and failure. This improvement in manufacturing will not be possible without additional information on the nature of heterogeneities and how they relate to electrode fabrication steps. Even more beneficial is if the information is made available in a timely manner through the use of convenient and reliable experimental and modeling tools.

Introduction

This work addresses a longstanding unmet industry need to be able to conveniently quantify conductivities of thin-film electrodes and current collector contact resistance—solving this problem will accelerate process improvement. Additionally, this work remedies our poor understanding of the influence of fabrication parameters on heterogeneities in microstructure, which affect cell energy, power, and cycle life.

In this project both experimental measurements and predictive models have been used to make processing-to-structure and structure-to-performance connections for battery electrodes. The experimental and modeling approaches are complementary and validate each other. The overarching goals are to generate for composite electrode films: (1) rapid, reliable, and standardized methods for measuring electrochemical performance; (2) a predictive microstructure model that imitates fabrication processes; and (3) an improved understanding of tradeoffs between fabrication parameters and electrode performance. Research performed in FY2016 directly dealt with all 3 goals.

Approach

The first major thrust of FY2016 was to model the calendering process using our predictive 3D particle-scale microstructure model. The first-quarter milestone dealt with validating that the dynamic particle packing (DPP) model we have developed can accurately predict the microstructural changes that happen during the calendaring process. This built on previous work showing that the model accurately predicts the slurry drying process. Calendering serves to compress the composite structure, increasing electronic contact and decreasing porosity, and thus is a key fabrication step. Differing levels of calendering were applied to the model and the evolution of the structure was tracked.

The second major thrust of FY2016 was to create an improved N-line probe and inversion model to allow determination of local conductivity, including anisotropic characteristics. The new probe allowed additional information to be collected on the surface of electrode films. In principle the additional information allows one to determine how conductivity varies in each direction (anisotropic conductivity), but this also requires extensions and modifications to the previous numerical inversion routine. The second-quarter milestone dealt with building and validating the N-line inversion routine. The third-quarter milestone was a Go/No-Go decision as to whether the method is working and should be developed further.

The third and final major thrust of FY2016 was to begin integrating the modeling and diagnostic elements of this project. The fourth quarter milestone was to show that local conductivity properties and microstructure in electrodes can be correlated between the DPP model, FIB/SEM structural determination, and N-line probe measurements. The intention was to map conductivity and microstructure in carefully prepared commercial-grade electrode samples, showing how these properties relate to the fabrication steps used in produce the electrode film. These results in turn can be compared to predictions from the DPP 3D microstructure model. This effort will continue into FY2017, at which point this project is concluded.

Results

The first milestone of FY2016 was to demonstrate that the dynamic particle-packing (DPP) model can accurately imitate the mechanical calendering process for a representative electrode film. In FY2015 it was demonstrated that the DPP model could reproduce experimental viscosities for the slurry, the shrinkage ratio during drying, the elasticity of the dried but uncalendered electrode film, and some additional microstructural properties. This success leads researchers at BYU to continue developing and improving the model. The primary test material was and continues to be Toda NCM 523 cathodes supplied by Argonne National Lab. In addition, tests are done on a material developed at BYU to imitate the carbon black and binder domains of the electrode film.

Initially the DPP model showed correct qualitative agreement with experiment for the calendering process. In particular, the model showed plastic deformation during application of calendering pressure, including a reduction in the larger-size pores. However, the onset of plastic deformation took place at small pressures (around 3 bar). Small adjustments to the solid particle interaction parameters were made in order to improve agreement. The results of this effort are shown in Figure V-194, which is a stress-strain curve for the DPP model and 4 redundant Toda 523 films. The agreement between model and experiment is quite satisfactory, at least at the moderate pressures tested. However, it was found that at higher pressures (not shown), the model begins to depart from known experimental behavior. This was considered a model deficiency that must be remedied in later iterations of the model.

Nevertheless, these results as well as those reported in FY2015 show the agreement between model and experiment for a broad range of properties. For instance, substantial work was done this year to enable the model to predict structures formed during realistic coating operations (see Figure V-195). This suggests that the simulations reasonably reproduce the relevant physics of particle arrangement during fabrication. It is anticipated that it will become a powerful platform for predicting the effects of fabrications steps on the evolution of the particle microstructure and will accelerate efforts to optimize electrodes.

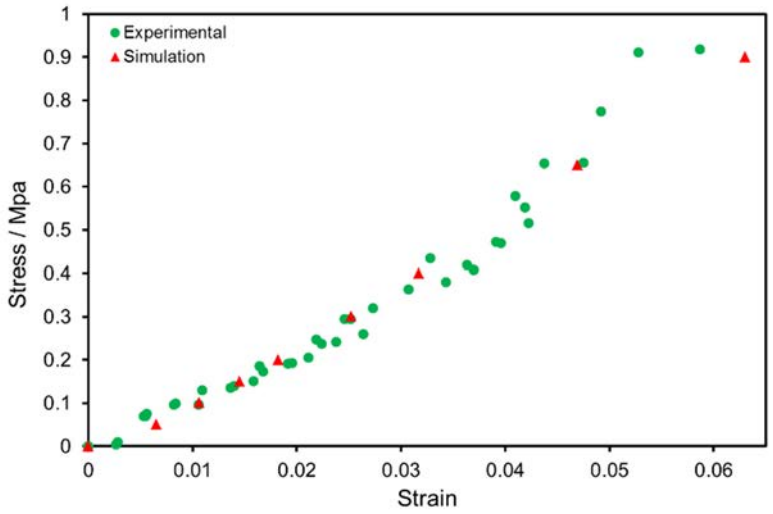

Figure V-194: Stress-strain data for Toda 523 cathode film, compressed in the out-of-plane direction to imitate the effect of calendering. Both experimental and DPP model results are indicated. Experiments were performed on 4 different films by sequentially increasing the stress

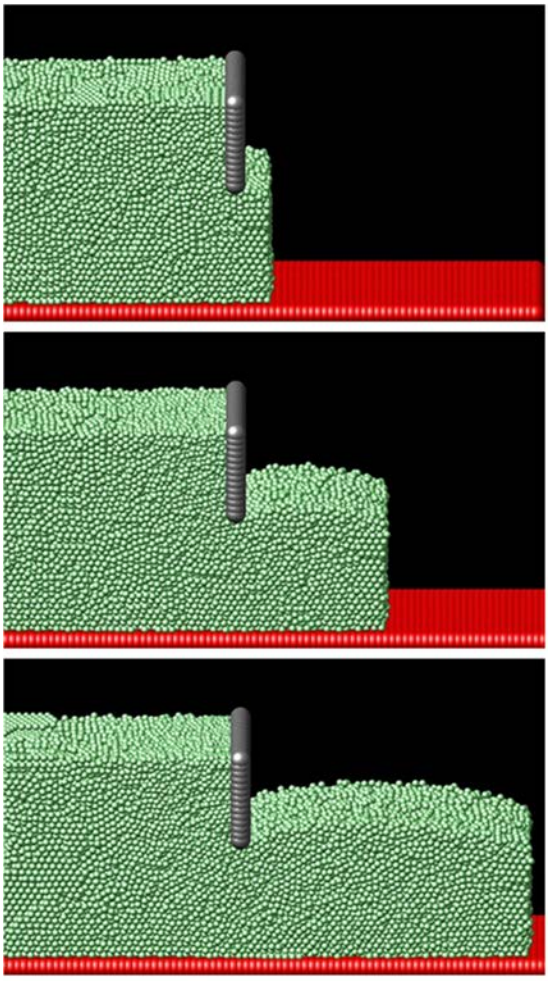

Figure V-195: Time-lapse simulation results (at *t* = 0, 3.5 ms, and 7.6 ms, respectively) for a coating operation using the DPP model

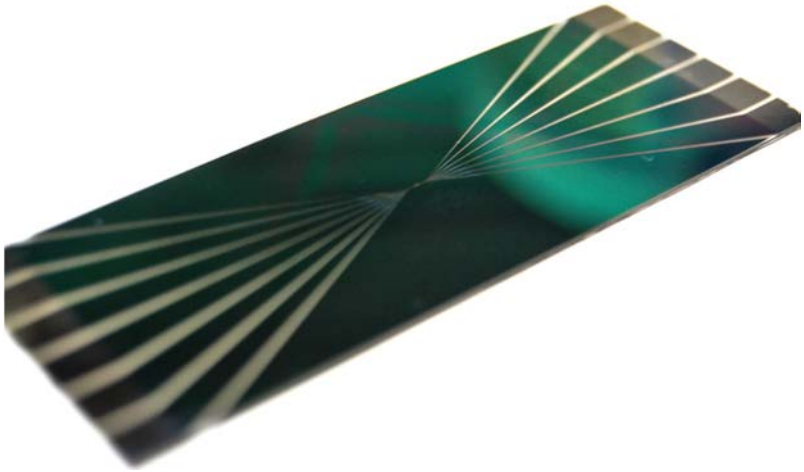

Figure V-196: Photograph of 6-line probe, showing dual sets of external connections on the edges of the probe, converging to a µm-scale sampling region in the center. The probe is mounted in a computer-controlled xyz stage

The second milestone of FY2016 was to develop a robust numerical routine for interpreting N-line conductivity measurements. This model accompanies improvements that were made in the fabrication process of the N-line probe (see Figure V-196).

A model is necessary to invert the conductivity measurements because (1) conductivity measurements are performed by placing electrical probes on the external surface of a sample, (2) the geometry of the probes and sample are complex and include 3D effects, and (3) multiple experiments are being used to regress multiple properties simultaneously. The model is formulated to produce shape factors (see Figure V-197) that account for these complexities and are used to convert the voltage and current measurements into geometry-independent material properties of the battery electrode sample film. At the same time, the model must include a least-squares or optimization routine to produce the simultaneous properties. Previously BYU researchers had developed a numerical routine that worked, but was not robust enough to automate the interpretation of the additional experiments possible with the new 6-line probe produced in FY2015 and improved in FY2016.

The new numerical routine was completed. The new routine uses a specialized quadrature algorithm and Fourier transforms to solve the underlying partial differential equation for the required geometry. The code also includes an implementation of a generalized Newton's method to do the inversion of the multiple experiments. The routine was initially implemented as VBA code inside a spreadsheet. It was found to be at least 100 times faster than the previous code and is considered fast enough for general purpose use. The code can also be implemented in other platforms for additional speed advantages. This means that the inversion model will not be the limiting factor to do real-time interpretation of the conductivity experiments.

One of the final goals of this project was to determine by means of the N-line probe the degree of anisotropy, meaning the difference in electronic conductivity in the in-plane and through-plane directions. This was measured for a baseline Toda 523 cathode (provided by ANL) to show less through-plane conductivity than the in-plane conductivity by a factor of around 2. This anisotropy represents an inefficiency in the structure of typical electrodes, because higher through-plane conductivity is more desirable for battery performance.

The major development that allowed this measurement was an improvement in the N-line probe inversion routine. These results were considered satisfactory to meet the threshold of the Go/No-Go decision. Nevertheless, it was found that results are sensitive to experimental noise. It is believed that improvements in the probe design (FY2017) coupled with the improved model will enable this measurement to be improved in accuracy. Table V-5 contrasts the results on the same electrode film using the old (isotropic) and new (anisotropic) inversion routines. Substantial progress was made toward the final milestone of FY2016, though it was not fully completed; a related milestone will be completed in FY2017 under a new contract. The essence of the milestone is to demonstrate substantial agreement between experiment and the predicted conductivity of the DPP model for realistic battery electrode microstructures. It was determined that while the predicted conductivities were qualitatively correct, this was only for uncalendered electrodes. The model needs additional improvements in order to predict the anisotropic structures of realistically coated and calendered electrodes. Such improvements were begun and will be at a stage in FY2017 that the accuracy of the model can again be assessed. The ultimate goal is to have a quantitatively accurate structure prediction model that will allow process changes to be assessed.

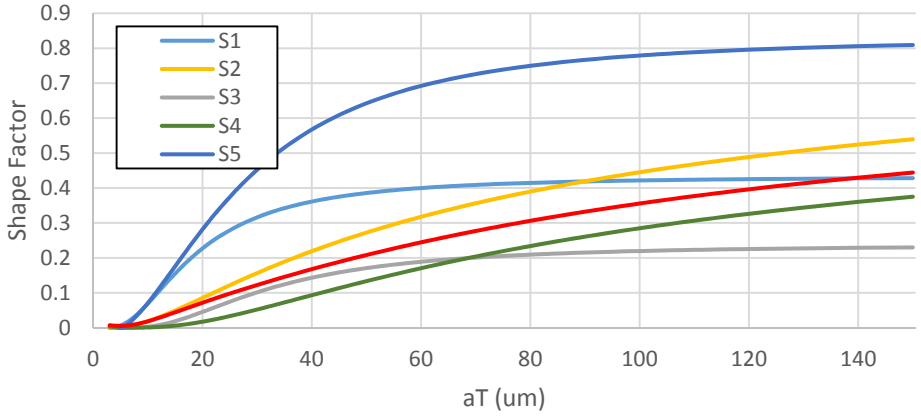

Figure V-197: Example of shape factors produced by the inversion model for different geometries

Table V-5: Comparison of Two Model Inversion Results

	Isotropic Model	Anisotropic Model
Conductivity - out of plane (mS/cm)	474±32	230±31
Conductivity - in plane (mS/cm)	474±32	542±46
Current collector contact resistance (Ω-sq. cm)	0.165±0.013	0.179±0.022

Figure V-198 shows a finite-volume method used to assess the conductivity of an uncalendered electrode. Three phases are shown: active (red), carbon/binder domain (black), and pore (white). The method has a number of novel features, namely a multigrid/coarse-graining technique to speed up computation, causing it to take only a few minutes for a typical set of results.

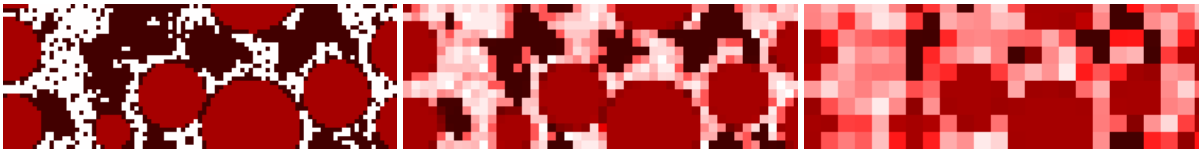

Figure V-198: Sequential coarse-graining procedure (left to right) used to speed up finite-volume conductivity calculation

Though unrelated to the milestones of FY2016, significant progress was achieved toward conveniently measuring ionic conductivity of electrodes. The method was used to measure a series of commercial electrodes provided by a major battery vendor. This improved method will likewise be further developed during the next fiscal year and will be discussed in subsequent reports using non-proprietary materials.

Conclusions

The combination of electronic and ionic conductivity measurements made possible by this work provides a more complete picture of electrode performance. This work has clearly showed that conductivity, even for commercially prepared pristine electrodes, can be highly variable. In general, it has been determined that electronic conductivity is “overdesigned” for typical pristine electrodes, meaning it is much larger than is corresponding effective ionic conductivity. This is believed to be necessary because electronic conductivity is more highly variable, and is more likely to degrade over time. This latter conjecture is currently being tested and will be the subject of future reports.

There has been growing industrial and research interest in the conductivity measurement tool developed under this work. A partnership was negotiated and established this year with Bosch in which BYU will be testing battery materials using these techniques. In addition, battery materials were tested for another (as yet unnamed) battery manufacturer.

Development on the DPP microstructure prediction model continued this year, and will likewise continue in FY2017 under a separate contract. The DPP model is unique in that it directly connects the microstructure prediction to the processing conditions of the electrode, and is specifically designed to operate at the relevant length scales for battery film manufacturing. The model has shown quantitative agreement with a range of physical measures on real electrodes, but has only been validated for one type of active material. Therefore additional work is needed to broaden its applicability. Long-term plans include the integration of the model into comprehensive battery development platforms being developed by other researchers.

Work performed under this contract was presented at the PRiME/Electrochemical Society Meeting in October 2016, as well as at other venues such as the Annual Merit Review. The DPP model and results were published in The Journal of Power Sources. An additional publication is under preparation that directly relates local microstructures to observed conductivity heterogeneity.

Products

Presentations/Publications/Patents

1. J.W. Nichols and D.R. Wheeler, “Fourier correlation method for simulating mutual diffusion coefficients in condensed systems at equilibrium,” Indust. Eng. Chem. Res. 54, 12156 (2015).
2. F. Pouraghajan, R.L. Fitzhugh, M. Wray, B.A. Mazzeo and D.R. Wheeler, “Measurement of ionic conductivity of intact battery electrodes using a four-line probe,” 2015 Annual Meeting of AIChE, Salt Lake City, UT.
3. M.M. Forouzan, C.-W. Chien, D. Bustamante, W. Lange, B.A. Mazzeo, and D.R. Wheeler, “Predicting transport, mechanical, and microstructural properties of porous Lithium-ion battery electrodes by a particle-based simulation,” 2015 Annual Meeting of AIChE, Salt Lake City, UT.
4. D.R. Wheeler, “Battery modeling using porous electrode theory,” 2015 Annual Meeting of AIChE, Salt Lake City, UT.
5. A. Riet, J. Sedgewick, J. Vogel, D. Clement, A. Cutler, B.A. Mazzeo, D.R. Wheeler, “Non-destructive high-resolution conductivity mapping of thin-film battery electrodes,” 228th Meeting of the Electrochemical Society, Phoenix, AZ, 2015.
6. D. Wheeler, “A particle-based model to optimize electrode microstructure and manufacturing,” Workshop on Advanced Battery Research, University of Illinois at Chicago, Department of Mechanical and Industrial Engineering and the Joint Center for Energy Storage Research, 2015.
7. M.M. Forouzan, C.-W. Chao, D. Bustamante, B.A. Mazzeo, and D.R. Wheeler, “Experiment and simulation of the fabrication process of lithium-ion battery cathodes for determining microstructure and mechanical properties,” J. Power Sources 312, 172-183 (2016).
8. M. Mehdi Forouzan, Anthony Gillespie, Nicholas Lewis, Brian A. Mazzeo, and Dean R. Wheeler, “A Predictive Model of Lithium-Ion Electrode Fabrication, including Mixing, Coating, Drying, and Calendering,” ECS/PRiME Meeting, Honolulu, Hawaii, October 2016.
9. John E. Vogel, William Lange, Derek Clement, Brian A. Mazzeo, and Dean R. Wheeler, “Correlation of Local Conductivity to Microstructure for Lithium-ion Battery Electrodes by Use of a Contact Probe and SEM/FIB,” ECS/PRiME Meeting, Honolulu, Hawaii, October 2016.

V.G. Metallic Lithium and Solid Electrolytes

V.G.1. Mechanical Properties at the Protected Lithium Interface (ORNL)

Nancy Dudney, Principal Investigator
Oak Ridge National Laboratory
P.O. Box 2008, MS6124
Oak Ridge, TN 37831
Phone: 865-576-4874
E-mail: dudneynj@ornl.gov

Tien Q. Duong, DOE Program Manager
U.S. Department of Energy
Advanced Battery Materials Research (BMR)
Vehicle Technologies Office
1000 Independence Avenue, SW
Washington, DC 20585
Phone: 202-586-7836
E-mail: Tien.Duong@ee.doe.gov

Start Date: October 2015
End Date: December 2017

Abstract

Objectives

- Provide critical information and insight into the complex coupling between the microstructure, lattice defects and the mechanical behavior of Li metal anodes. Use this to guide future electrolyte and anode designs for robust performance.
- Examine the Li metal / solid electrolyte interface using state-of-the-art mechanical nanoindentation methods coupled with electrochemical cycling.
- Assess how the mechanical properties and homogeneity of both the lithium anode and candidate solid electrolytes affects the uniformity of Li cycled at higher current densities and the potential failure modes including formation of dendritic shorts, Li roughening, and the gradual increase in the interface resistance.

Accomplishments

- The elastic properties of Al- and Ta-doped LLZO ceramic solid electrolyte by nanoindentation maps were found to be homogeneous and in good agreement with other acoustic tests and DFT models.
- Acoustic wave-speeds in LLZO were observed to decrease prior to formation of electronic shorts; this is interpreted as due to formation of micro-cracks in the ceramic.
- The elastic properties and hardness of thin films of lithium were determined for the first time by nano-indentation. Because of the extreme plasticity of the lithium, modification in the normal dynamic indentation measurements were implemented and corrections for a stiff substrate where necessary.
- Surface contamination of the Li is not homogeneous and impacts the mechanical properties, even when the film appears silver and shiny.
- Extended cycling of thin film lithium batteries leads to gradual changes in the lithium morphology that depend on the duty cycle and cathode; such processes may also be expected for lithium batteries with higher energy per active area.

Future Achievements

- *In situ* study of the lithium / solid electrode assembly during electrochemical cycling will capture the formation and annealing of vacancies and other defects in the lithium and correlate this with the interface and current density.
- X-ray tomography will identify changes in the microstructure of the solid electrolytes due to cycling and failures.
- Li adhesion at the solid electrolyte interface will be evaluated by lap shear tests.

Technical Discussion

Background

The use of a metallic lithium anode is required for advanced battery chemistries like Li-air and Li-S to realize dramatic improvements in energy density, vehicle range, cost requirements and safety. However, the use of metallic Li with liquid and polymer electrolytes has been so far limited due to parasitic SEI reactions and dendrite formation. Adding excess lithium to compensate for such losses effectively negates the high-energy density for lithium in the first place. For a long lifetime and safe anode, it is essential that no lithium capacity is lost to either physical isolation from roughening, dendrites or delamination processes, or to chemical isolation from side reactions. The key risk and limitation for this technology is the gradual loss of lithium over the cycle life of the battery.

To date there are no examples of battery materials and architectures that realize such highly efficient cycling of metallic lithium anodes for a lifetime of 1000 cycles due to degradation of the Li-electrolyte interface. A much deeper analysis of the degradation processes is needed, so that materials can be engineered to fulfill the target level of performance for EV, namely 1000 cycles and a 15-year lifetime, with adequate pulse power. Projecting the performance required in terms of just the Li anode, this requires a high rate of lithium deposition and stripping reactions, specifically about 40μm Li per cycle, with pulse rates up to 10 and 20 nm/s (15mA/cm^2) charge and discharge, respectively. This is a conservative estimate, yet daunting in the total mass and rate of material transport. While such cycling has been achieved for state-of-the-art batteries using molten Na in Na-S and zebra cells, solid Na and Li anodes are proving more difficult.

Introduction

This project will develop the understanding of the Li metal-solid electrolyte interface through state of the art nanoindentation and other mechanical testing methods. By coupling the mechanical probes with electrochemical analysis, we hope to probe the defects and processes that may cause premature failures, by shorting, increasing resistance, or lithium redistribution and isolation. Our goal is to provide the critical information that will enable transformative insights into the complex coupling between the microstructure, lattice defects and the mechanical behavior of Li metal anodes. Work will progress from the study of the component materials, the lithium films and various solid electrolytes, toward study of the electrode assembly during electrochemical cycling of the anode. We hope to capture the formation and annealing of defects in the lithium and correlate this with the properties of the solid electrolyte and the interface.

Instability and/or high resistance at the interface of lithium metal with various solid electrolytes limit the use of the metallic anode for batteries with high energy density batteries, such as Li-air and Li-S. The critical impact of this endeavor will be a much deeper analysis of the degradation, so that materials can be engineered to fulfill the target level of performance for EV batteries, namely1000 cycles and15 year lifetime, with adequate pulse power.

Approach

Mechanical properties studies through state of the art nanoindentation techniques are used to characterize the materials and follow the evolution of the Li and solid electrolyte upon transport of the Li across the interface. Typically, for dynamic indentation studies, a small harmonic oscillation is superimposed on the normal

loading/unloading tests to determine the elastic response as a function of the penetration depth. With rapid data acquisition, automated mapping can generate arrays of 100 or more dents and profile large areas of the surface. Because of the extreme plasticity of the Li metal, new approaches for indentation are needed. Additionally, acoustic pulse echo, x-ray imaging and profilometry techniques are employed, along with the standard electrochemical analysis.

All materials and interfaces are formed and/or refined under a protective inert or vacuum atmospheres to reduce the influence of uncontrolled impurity phases. The lithium is formed by vacuum vapor deposition to thicknesses similar to those that will be required to seed the anode and form energy dense lithium batteries. When the lithium is deposited rapidly and directly onto the solid electrolyte, this forms the cleanest interface possible. The Li coverage on the solid electrolyte is determined by line of sight, so for a smooth solid electrolyte surface, the Li forms complete coverage; also, the film is fully dense and with good adhesion. No conditioning of the lithium is required to establish a low contact resistance when the electrolyte surface is cleaned or polished, as needed, just before the Li deposition. While the active Li interface is buried, protecting the exposed Li surface from extensive reaction is also important to our study and to maintain the lithium inventory. This is accomplished with a passivation layer, a protective coating or a small gas tight container.

This project is a collaborative effort of Oak Ridge National Laboratory with Professors Erik Herbert at Michigan Technological University and Jeff Sakamoto at University of Michigan.

Results

Work in FY16 has continued to examine candidate solid electrolytes and thin films (1-20μm) of Li metal independently, as well their interface before and after lithium transport. Fixtures and processes are being developed to extend this to studies during the active Li deposition and dissolution.

Investigation of the solid electrolyte was confined to that of the cubic lithium lanthanum zirconate (LLZO) ceramic as produced and continuously improved by Sakamoto's team. This material is proving to be stable or passivated when contacted by Li metal. When the LLZO pellets are very dense, single phase, and polished to removed surface contamination, the rapid mapping of the surface using nanoindentation reveals uniform properties. No differences in the elastic properties were identified near grain boundaries, or between different grains. The elastic properties determined from the dynamic nanoindentation proved to be in excellent agreement with those from acoustic impulse excitation and DFT modeling for both Al and Ta doped LLZO. (Collaboration with Sakamoto's project, V.G.2.) The nanoindentation examines the properties of single grains, while impulse excitation examined the average bulk property. The most accurate properties for LLZO were determined at penetrations of 140-230 nm from the surface. The LLZO pellets were also examined following Li cycling at increasing current densities until failure. While the gray areas surrounding the sites of dendrite formation are apparent by visual examination when the Li contacts are removed, nanoindentation has not revealed significant changes in the elastic properties. Here *in situ* determinations and bulk determinations, such as by acoustic pulse echo, are more effective.

Pulse echo methods were developed to detect changes in the elastic properties of large LLZO samples during cycling and ultimately to failure due to shorting. As shown in Figure V-199, a change in the wave speed was observed and correlated with a decrease in the elastic stiffness. This occurred just minutes before the electrical short circuit was recorded and is consistent with models for microcrack formation in a material. In future work, this may provide a way to stop the current and arrest the failure mechanism before the short circuit flaw is complete.

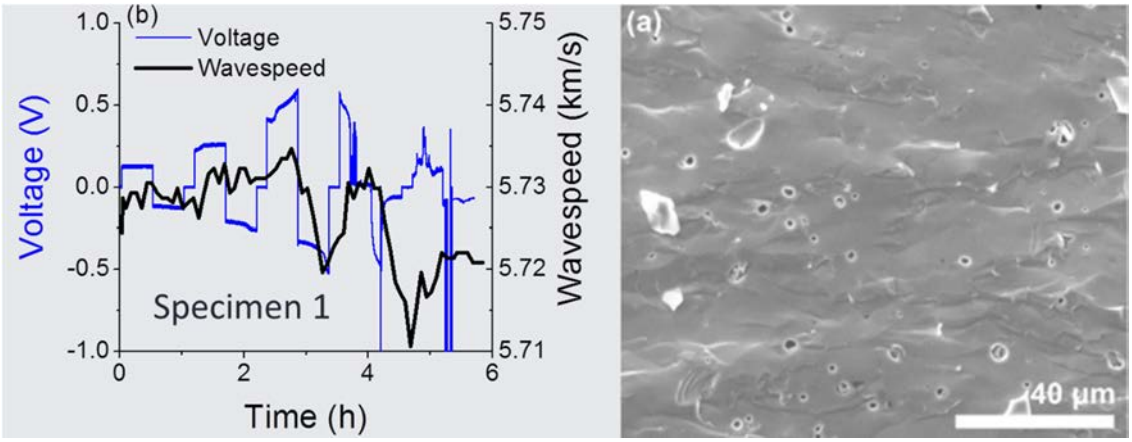

Figure V-199: Wave speed and voltage recorded as the increasing current initiates an electronic short. SEM micrograph of polished surface of the LLZO sample used in the test

A variety of Li films were deposited on glass substrates for examination by nanoindentation, such as for Figure V-200 These varied in thickness, grain size, and controlled gas treatment to passivate the surface. Generally, the formation of passivated reaction layers created by controlled gas exposure have proven to be too thick for good nanoindentation studies, so it is important to protect the cleaner surface. At this time, maps of the Li surface show distinct point to point inhomogeneity due to the surface reaction layer even when the surface appears shiny and smooth. This harder surface "crust" results in a woodpecking or pop-in behavior; an example of the latter is shown in Figure V-200. The consequence of this observation is that interfaces formed by pressing together the solid electrolyte and thin Li foils will likely be greatly affected by variations in the mechanical properties across the lithium surface

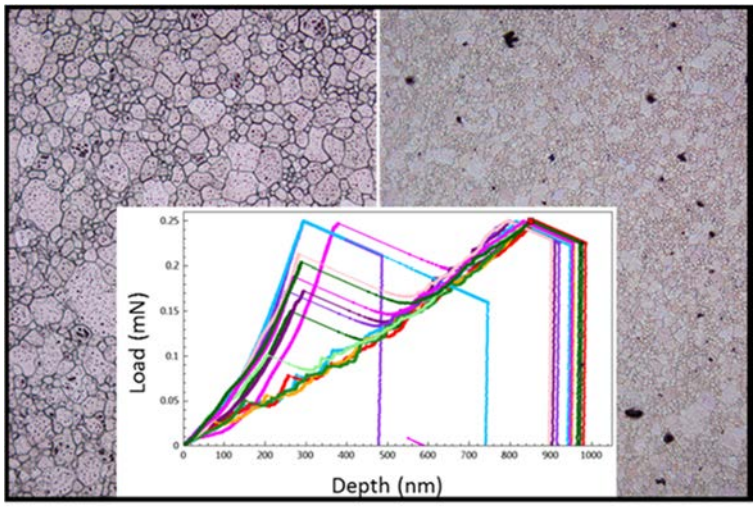

Figure V-200: Lithium films with different grain sizes, photographed at same 10X magnification. The inset shows the pop-in effect that varies from spot to spot on the surface. Full depth scale for the plot is 0 to 1000 nm

Because of the extreme plasticity of the lithium, the normal dynamic indentation procedure was modified. Several procedures were used, one with periodic load-holds to measure the dynamic response when the creep was very slow, and another with a continuous but very small harmonic displacement. Examples are shown in Figure V-201. Displacement must be deeper than about 200nm to assess the bulk properties of the Li grains, which is so far homogeneous across and through the film. Combining these innovations with corrections for the substrate stiffness at large displacement give reliable and consistent values for the elastic properties.

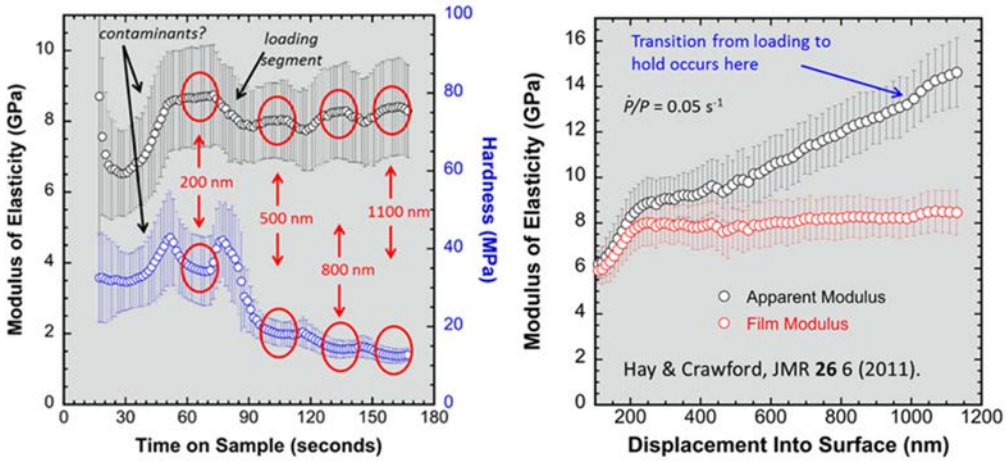

Figure V-201: Elastic modulus determined by different tests described in text. At left, there are periodic load holds at four different displacements. Results at small displacement are distorted by surface contamination. At right, the harmonic oscillation is small and continuous. The red symbols have been corrected for the underlying glass substrate, following Hay and Crawford

Several trials have been conducted to compare the nanoindentation of Li after electrochemical deposition with after dissolution reaction. In one case, an LLZO pellet was coated with 8µm on one side and 3µm Li on opposing sides, being contacted with just a wire or ring. A small DC current was applied to drive Li toward equal ~5µm thicknesses on each side. Unfortunately, the exposed lithium surfaces became too rough for proper analysis by indentation. The two Li films, with Li deposited versus dissolved, were different in appearance and the combined interface resistance had increased substantially. New procedures are now in place to monitor indentation during the Li transport, and alternatively to use protective pressure contacts that can be removed for indentation.

Finally, existing profilometry results for Li films cycled on a thin film battery were analyzed. Here the Li, protected by a hermetic polymer coating, is observed to gradually redistribute over hundreds and thousands of cycles. The features that develop, either a wavy surface (as shown in Figure V-202) or widely distributed rimmed pits, depend on both the cathode used in the battery and the timing of holds for the duty cycle. These results are interpreted following dewetting behavior reported for metastable metallic thin films, although wrinkling processes due to residual stress is also a possibility. In the literature, the dewetting of thin metal films at an interface is initiated by heating, while for these Li films between Lipon and the polymer coating, the dewetting is initiated by the electrochemical cycling. Whether similar processes occur for solid state batteries with larger areal capacity is unknown, but because excess lithium will be minimal, the anode is expected to be very thin and metastable at full discharge.

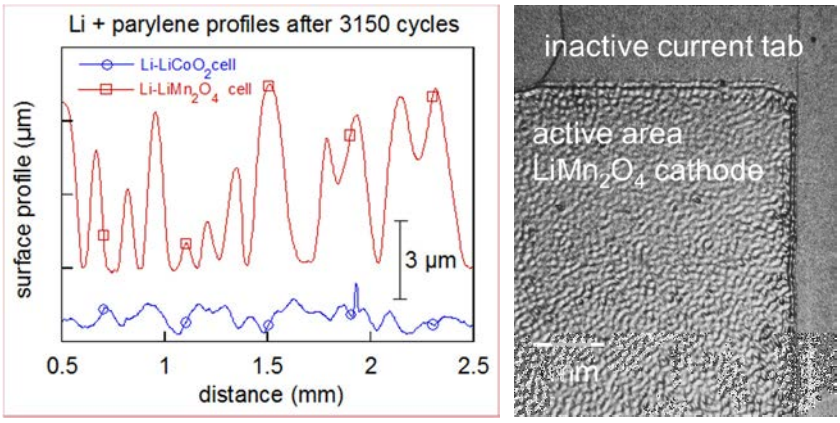

Figure V-202: Changes in the lithium profile after 3150 cycles (left) and 1000 cycles (right). Before cycling the Li is very smooth. The inactive current tab remains smooth, but the active Li area gradually becomes wavy as show by the stylus profile and photograph

Conclusions

The mechanical properties of both lithium metal and the LLZO ceramic solid electrolyte were studied. For the LLZO, nanoindentation indicates that a clean surface has uniform elastic properties and no indication of variation near grain boundaries. Values for the elastic properties by nanoindentation agree well with acoustic tests and DFT models. Pulse echo acoustic tests indicate a decrease in the elastic modulus, which is consistent with formation of microcracks, just prior to failure due to an electrical short. For the lithium thin films, this work determined the elastic properties by indentation for the first time. This was challenging due to the extreme plasticity and influence of surface contamination. Continuing work will evaluate how the elastic behavior and the plasticity depend on the grain structure and extent of cycling of the lithium. For a thin film battery, extensive redistribution of the lithium contacting the Lipon solid electrolyte was observed upon prolonged cycling. Whether or not similar trends are expected for higher energy batteries requires further investigation.

Products

Presentations/Publications/Patents

1. E.G. Herbert, P.S. Phani, N. J. Dudney, G. M. Pharr, R. Schmidt, A. Sharafi, T. Thompson, J. Sakamoto, “The Hardness and Elastic Modulus of Lithium and Solid Electrolytes for Next Generation Battery Applications”, invited presentation at the Fifth International Indentation Workshop, Austin TX, November 2015.
2. Robert D. Schmidt, Jeffrey S. Sakamoto, Travis R. Thompson, Asma Sharafi, Nancy J. Dudney, “Acoustic monitoring of solid state electrolytes to enable next generation Lithium-ion battery development,” MRS presentation, Boston, December 2015.
3. Seungho Yu, Robert D. Schmidt, Regina Garcia-Mendez, Erik Herbert, Nancy J. Dudney, Jeffrey B. Wolfenstine, Jeff Sakamoto, and Donald J. Siegel, “Elastic Properties of the Solid Electrolyte $Li_7La_3Zr_2O_{12}$ (LLZO)”, Chem. Mat. (2016) 28, 197.
4. Nancy Dudney, Erik Herbert, Jeff Sakamoto, P.S. Phani, R. Schmidt, A. Sharafi, T. Thompson, “Mechanical Properties at the Protected Lithium Interface” poster presentation at 2016 DOE AMR Meeting, Robert D. Schmidt and Jeffrey Sakamoto, “*In situ* non-destructive acoustic characterization of solid state electrolyte cells”, J. Power Sources 324 (2016) 126-133. June 6-10, 2016, Washington DC.
5. Robert D. Schmidt and Jeffrey Sakamoto, “*In situ* non-destructive acoustic characterization of solid state electrolyte cells”, J. Power Sources 324 (2016) 126-133.
6. Erik G. Herbert, Nancy J Dudney, Owen Mills and Violet Thole, “Dynamic Nanoindentation: State of the Art Experimental Methods”, presented by Erik Herbert at the Gordon Research Conference on Thin Film and Small Scale Mechanical Behavior July 24, 2016. (Invited presentation)
7. Nancy J. Dudney, “Evolution of the Lithium Morphology from Cycling of Thin Film Solid-State Batteries,” submitted to Journal of Electroceramics. Invited for issue dedicated to Solid State Batteries.

V.G.2. Solid Electrolytes for Solid-State and Lithium-Sulfur Batteries (U of Michigan, ORNL, ARL, Oxford U)

Jeff Sakamoto (Principal Investigator)
University of Michigan
Mechanical Engineering
2350 Hayward Avenue
Ann Arbor, MI, 48109
Phone: 734-769-2213
jeffsaka@umich.edu

Prof. D. Siegel, UM (Co-Investigator)
J. Wolfenstine, ARL (Co-Investigator)
Prof. C. Monroe, Oxford University (Co-Investigator)
J. Nanda, ORNL (Co-Investigator)

Tien Q. Duong, DOE Program Manager
U.S. Department of Energy
Advanced Battery Materials Research (BMR)
Vehicle Technologies Office
1000 Independence Avenue, SW
Washington, DC 20585
Phone: 202-586-7836
E-mail: Tien.Duong@ee.doe.gov

Kimberly Nuhfer, NETL
Phone: 304-285-6544
E-mail: Kimberly.Nuhfer@netl.doe.gov

Start Date: January 1, 2015
End Date: December 31, 2017

Abstract

LLZO garnet ($Li_7La_3Zr_2O_{12}$) is the first bulk-scale ceramic electrolyte to exhibit the combination of superionic conductivity (1mS/cm at 298K), high shear modulus (61 GPa) to suppress Li dendrite penetration, and apparent electrochemical stability (0-6V vs Li/Li^+), thus enabling Li metal anodes. However, to date there are no reports confirming LLZO can tolerate current densities $\geq$ 1mA/cm^2, thus demonstrating relevance to PHEV/EV batteries. Our goal is to investigate the mechanisms that govern the Li-LLZO interfacial stability as a function of current density. We hypothesize that defects in polycrystalline LLZO reduce the critical current density(CCD). Using our experience with synthesis and processing (Sakamoto and Wolfenstine) and sophisticated materials characterization (Nanda), we will precisely control atomistic and microstructural defects and correlate their effects on controlling the critical current density. These data will feed into multi-scale computation models (Siegel and Monroe) to isolate and quantify the roles that each defect plays in controlling the critical current density. Bridging this knowledge gap will allow us to accurately determine if LLZO can withstand $\geq$ 1mA/cm^2. If in the initial stages the critical current density is < 1 mA/cm^2, the fundamental knowledge garnered from this program may allow us to establish a path towards demonstrating relevance to vehicle electrification.

Objectives

Enable advanced Lithium-ion solid-state and lithium-sulfur EV batteries using LLZO solid-electrolyte membrane technology. Owing to its combination of fast ion conductivity, stability, and high elastic modulus, LLZO exhibits promise as an advanced solid-state electrolyte. To demonstrate relevance in EV battery technology, several objectives must be met. First, LLZO membranes must withstand current densities

approaching ~1 mA/cm^2 (commensurate with EV battery charging and discharging rates). Second, low area specific resistance (ASR) between Li and LLZO must be achieved to achieve cell impedance comparable to conventional lithium-ion technology (~10 Ohms/cm^2). Third, low ASR and stability between LLZO and sulfur cathodes must be demonstrated.

Accomplishments

- Characterized the electronic band gap of Al and Ta doped LLZO. Chronoamperometry, electrochemical impedance spectroscopy (EIS), and density functional theory were used to determine electronic conductivity as a function of voltage. The electronic band gap of LLZO was determined to range from ~ 0.20 to 5.8 eV.
- Achieved a Li-LLZO interfacial resistance of < 20 Ohms cm^{-2}.
- Completed an investigation of phosphate polyanion zirconate (NASICON LZP) as an approach to improve stability against moisture thereby reducing interfacial resistance and increasing critical current density.
- Identified the primary microstructural and atomistic defects that govern Li metal filament propagation and Li-LLZO interfacial resistance, respectively.
- Demonstrated the ability to control the primary microstructural feature that governs the maximum current density of the Li-LLZO interface.

Future Achievements

In the final reporting period, the experimental and theoretical collaboration will culminate into a model to describe and correlate Li metal filament propagation through polycrystalline LLZO as function of current density. We believe the fundamental understanding of Li metal filament propagation will enable strategies to engineer the LLZO microstructure and LLZO-Li interface to achieve a CCD of $\geq$ 1mA/cm^2. Furthermore, this knowledge and experience will allow for the fabrication, testing, and independent validation of prototypical cells employing Li anodes protected by LLZO solid electrolyte membrane technology.

Technical Progress

Background

The stringent demands placed on batteries by emerging vehicle technologies such as plug-in and battery electric vehicles suggest that improvements in the safety and performance of electrochemical energy storage devices, as well as concurrent reductions in their cost, are highly desirable. Current strategies for improving performance have largely focused on lithium-ion battery chemistries. In the present study we propose to go beyond the state of the art by pursuing electrolyte chemistries that will enable the use of Li metal anodes and sulfur cathodes, either concurrently in a solid state Li-S battery, or as a means to achieve a Li metal anode which is stable upon cycling. *More specifically, our effort will advance a common technology that underlies these two promising battery concepts: solid-state electrolytes.*

Introduction

Going beyond lithium-ion requires advanced anode, cathode, and electrolyte technology. In theory, the lithium-sulfur (Li-S) system offers over a six-fold increase in specific energy (2567 Wh/kg) compared to state-of-the-art (SOA) lithium-ion (387 Wh/kg). However, the potential of the Li-S system has not been realized due to electrolyte instabilities. First, other than Lipon, no electrolyte has demonstrated stability against metallic Li. Second, dissolution of Li-polysulfides in SOA liquid electrolytes results in passivation of the Li anode. Thus, there is a compelling need to develop novel electrolyte technology to enable beyond lithium-ion battery technologies employing Li metal anodes.

Approach

Our effort will focus on the promising new electrolyte known as LLZO ($Li_7La_3Zr_2O_{12}$). LLZO is the first bulk-scale ceramic electrolyte to simultaneously exhibit the favorable combination of high conductivity (~1 mS/cm at 298K), high shear modulus (61 GPa) to suppress Li dendrite penetration, and apparent electrochemical stability (0-6V vs Li/Li^+). While these attributes are encouraging, additional R&D is needed to demonstrate that LLZO can tolerate current densities in excess of $1mA/cm^2$, thereby establishing its relevance for PHEV/EV applications. We hypothesize that defects and the polycrystalline nature of realistic LLZO membranes can limit the critical current density. However, the relative importance of the many possible defect types (porosity, grain boundaries, interfaces, surface and bulk impurities), and the mechanisms by which they impact current density, have not been identified. Using our experience with the synthesis and processing of LLZO (Sakamoto and Wolfenstine), combined with sophisticated materials characterization (Nanda), we will precisely control atomic and microstructural defects and correlate their concentration with the critical current density. These data will inform multi-scale computation models (Siegel and Monroe) which will isolate and quantify the role(s) that each defect plays in controlling the current density. By bridging the knowledge gap between composition, structure, and performance we will determine if LLZO can achieve the current densities required for vehicle applications.

Results

In FY 2016, the defects we believe are primarily responsible for governing the CCD. First, interaction between metallic Li and LLZO and the defects that may form to govern interface kinetics was investigated. Theory and experimentation were conducted in concert to evaluate the electronic band structure of the Li-LLZO interface. Second, approaches to apply high purity Li metal anodes on contamination free LLZO interfaces were investigated. Electrochemical Impedance Spectroscopy (EIS) along with equivalent circuit modeling were used to evaluate the Li-LLZO interface kinetics. Third, because it is known that LLZO reacts with moisture in ambient air (albeit subtly, but enough to increase interfacial resistance), LZP (NASICON) was investigated based on its known stability against moisture. Materials and electrochemical characterization were conducted to compare the stability of LLZO (garnet) with LZP (NASICON). Though there were activities that involved microstructural defects and the role they play in governing the CCD in FY 2016, for the sake of brevity, the focus of this report is on interface stability.

1) Characterizing the Li metal LLZO interface

Through theory and experiment, the Li-LLZO interface was characterized. DFT was used to study the electrochemical window (EW) of LLZO. The EW determines an electrolyte's resistance to undesirable electronic transport, and by extension, controls phenomena such as short-circuiting and self-discharge. Accurate estimates do not yet exist for basic EW-related properties of LLZO such as its band gap and the positions of its band edges. These properties are now routinely examined in the assessment of liquid electrolytes [1], but have not been thoroughly explored for solid electrolytes.

The present work is concerned with a solid-state electrolyte; in this case the electronic bands of the solid replace the discrete energy levels present in a liquid. Similarly, the solid's band gap (BG) establishes the magnitude of the EW, while the valence band maximum (VBM) and conduction band minimum (CBM) of the solid can be associated, respectively, with the HOMO and LUMO of the liquid electrolyte (i.e., VBM ≈ HOMO and CBM ≈ LUMO). Based on these definitions, the criterion for a suitable EW for a solid electrolyte can be recast as BG > OCV. A solid electrolyte that satisfies this requirement will be stable against hole injection (i.e., electrochemical oxidation) from the positive electrode, and against electron injection (i.e., electrochemical reduction) from the negative electrode.

The preceding discussion suggests that LLZO has a sufficiently large band gap (6.4 eV) to enable its use with high voltage electrodes, in principle allowing for an all solid state cell with OCV > 6 V. However, it is important to recognize that a large band gap represents a *necessary, but not sufficient condition* for a viable electrolyte; the positions of the band edges relative to the electrochemical potentials of the electrodes are also critical. More specifically, a solid electrolyte will be stable against electron injection if the CBM lies at a higher energy (i.e., more negative potential) than the Fermi level of the negative electrode: $E(CBM) > \eta_-$.

Figure V-203A shows the lowest energy (100) surface along with an overlay of the planar-averaged electrostatic potentials, ϕ, evaluated from the slab and bulk cells. These data were used to determine the absolute positions of the CBM and VBM in bulk LLZO, shown in Figure V-203B, for both the lowest energy (100) and (110) slabs. To place the band edges in context, the electrochemical potentials of a Li metal anode, η_-, and a hypothetical 5V cathode, η_+, are also illustrated.

Figure V-203B demonstrates that the calculated band edge positions satisfy the electrochemical stability criteria, E(CBM) > η_- and E(VBM) < η_+, regardless of the slab model used. That is, for the Li/5V couple considered here, LLZO should be susceptible neither to electron injection from the Li negative electrode, nor to the hole-injection from the cathode.

While the positions of the band edges suggest a suitably-wide EW, a few caveats apply. First, as shown by the (100)-oriented slab, the energy difference between the CBM and the Li/Li$^+$ level can be modest, only 0.2 eV in this case. Second, the present band edge model depicts LLZO as a fictitious "isolated" solid: that is, it omits interfacial effects that will be present in a real electrochemical cell and which can potentially narrow [2] or expand the effective EW.[3,4] For example, *chemical* reactions at LLZO/electrode interfaces could yield thin product layers that "kinetically stabilize" LLZO by preventing further redox reactions from occurring.[4,5,6]

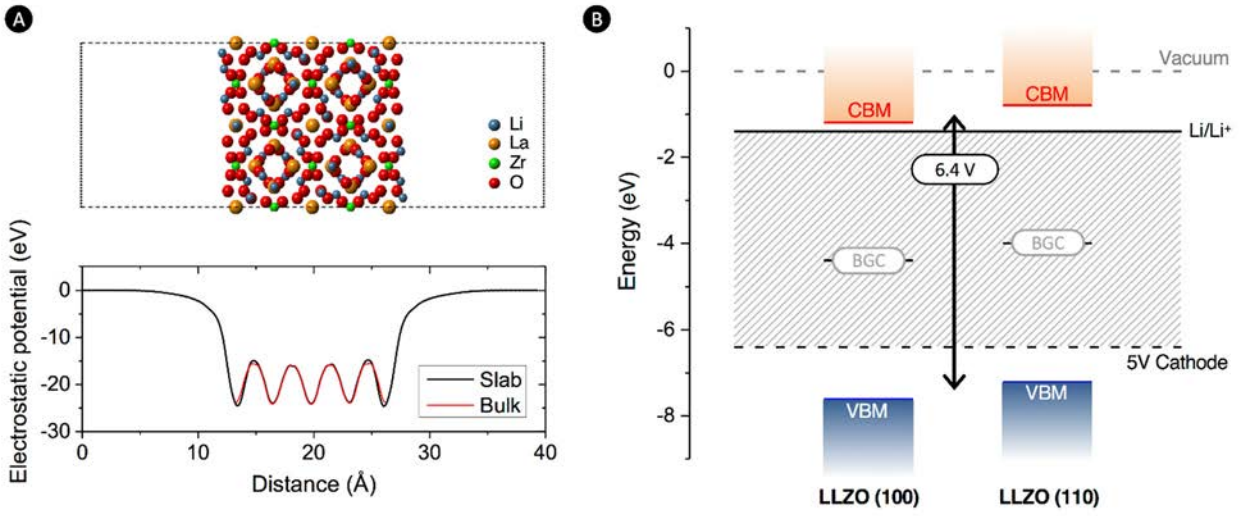

Figure V-203: (A) Ball-and-stick model of the lowest energy (100) slab of LLZO (top) and the associated planar-averaged electrostatic potential (bottom panel, black curve). The electrostatic potential from a bulk supercell is overlaid (red data). The vacuum level in the slab supercell corresponds to an electrostatic potential of zero. (B) Position of the conduction band minimum (CBM) and valence band maximum (VBM) of LLZO for the lowest energy (100) and (110) surface slabs relative to the Li/Li$^+$ level and a hypothetical 5V cathode. The position of the vacuum level is identified with a dotted grey line, while the band gap center appears as a solid black line [7]

To evaluate the stability between Li and LLZO, transmission electron micron (TEM) spectroscopy was conducted.[8] Achieving this is not trivial since handling, preparing, and imaging Li and fast ion conductors such as LLZO presents difficulties. Hi phase purity and dense LLZO from this project was provided to Dr. M. Chi (ORNL) for *in situ* TEM analysis. It was shown through that a ~ 60 nm thick solid electrolyte interphase (SEI) formed when Li metal contacted LLZO. Electron energy loss spectroscopy (EELS) was also conducted during TEM analysis. The EELS analysis indicated that that the Li, La, Zr, and O coordination likely changed in the quasi-SEI layer, which was consistent with the formation of the Li-rich tetragonal garnet polymorph. This observation agrees with the EW DFT calculations that predict electron injection at the Li-LLZO interface, which is necessary to charge balance the spontaneous uptake of lithium ions. The implication of this finding suggests that while an SEI in LLZO forms at the Li metal anode, the garnet structure is still maintained. Though tetragonal, the conductivity of the quasi-SEI is comparable in conductivity to bulk cubic LLZO, thus the increase in Li-LLZO interfacial resistance is negligible. These findings underly the importance of charge carrier injection at the interfaces to predict SEI growth kinetics

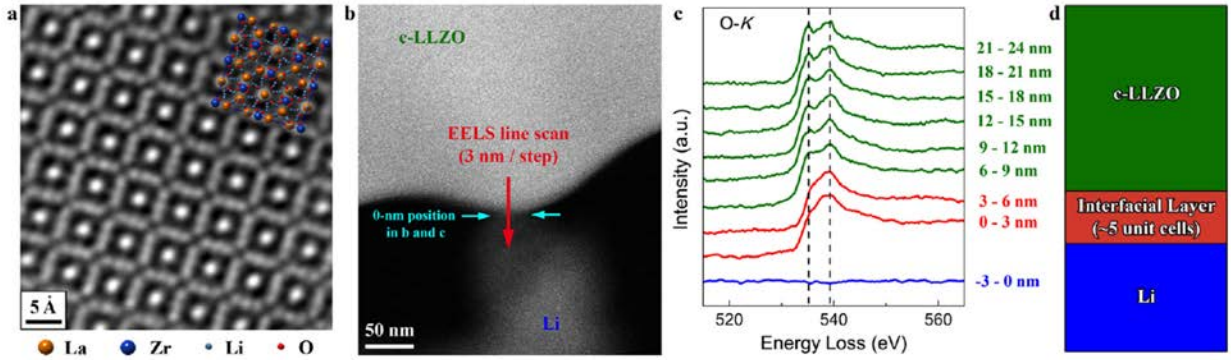

Figure V-204: Formation of the c-LLZO–Li interfacial layer. (a) Atomic-resolution high-angle annular dark-field (HAADF) STEM image of the pristine c-LLZO specimen. When this image was taken, the specimen was mounted on a double-tilt TEM holder instead of the *in situ* TEM holder so that its [001] zone axis can be tilted to the electron beam direction. (b) HAADF-STEM image of c-LLZO *in situ* contacted with Li. For clarity, the contact point is arbitrarily designated as the 0 nm position. The variation of the O K-edge across the c-LLZO–Li interface was examined using an EELS line scan with a 3 nm step size. (c) O K-edges obtained in the EELS line scan described in panel b. The two-peaks characteristic of c-LLZO are indicated with dashed lines. (d) Schematic illustration of the interfacial behavior suggested by the EELS line scan [8]

2) Establishing low Li-LLZO charge transfer kinetics

Building upon the theoretical and TEM work, establishing low Li-LLZO interfacial resistance was achieved in collaboration with Task V.G.1. Materials processing techniques and protocol were developed to achieve unprecedented Li-LLZO interfacial resistance. Li metal anodes were integrated with hot pressed LLZO disks, heated and cooled to room temperature for EIS testing (Figure V-205). Equivalent circuit modeling between 7 MHz and 0.1 Hz allowed deconvolution of the bulk, grain boundary, and Li-LLZO charge transfer resistance. The Li-LLZO charge transfer was determined to be 16 Ohms.cm^2; comparable to state-of-the-art lithium-ion liquid electrolyte cells.

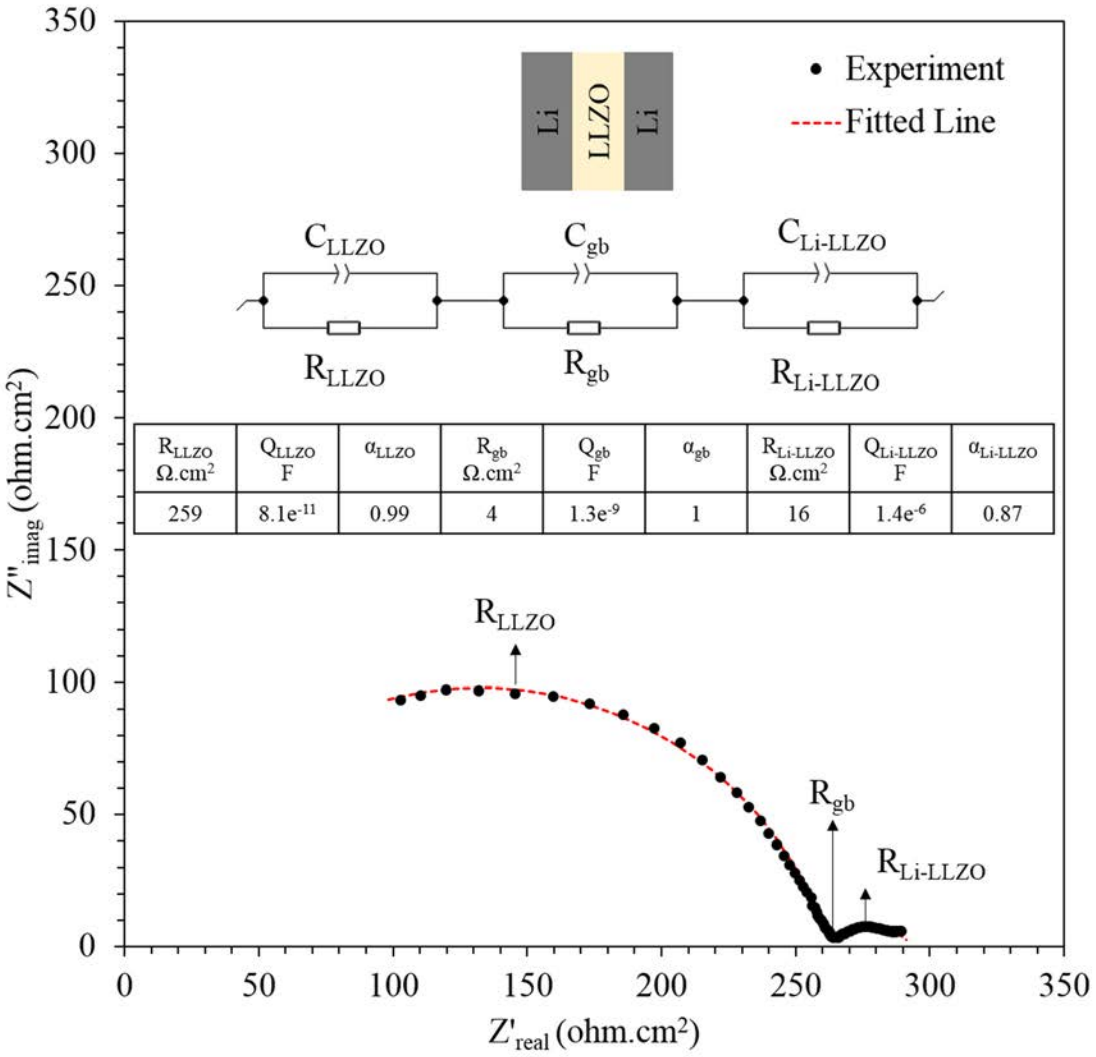

R_{LLZO} Ω.cm²	Q_{LLZO} F	α_{LLZO}	R_{gb} Ω.cm²	Q_{gb} F	α_{gb}	$R_{Li-LLZO}$ Ω.cm²	$Q_{Li-LLZO}$ F	$\alpha_{Li-LLZO}$
259	$8.1e^{-11}$	0.99	4	$1.3e^{-9}$	1	16	$1.4e^{-6}$	0.87

Figure V-205: EIS analysis of Li-LLZO-Li cells. The LLZO disks were 12.7 mm in diameter and 1mm thick. 0.8 mm thick Li anodes were scraped and placed against the LLZO disks compressed at a constant 350 kPa. The equivalent circuit modeling data agree well with the constant phase elements for RLLZO, Rgrain boundary, and RLi-LLZO, respectively. The RLi-LLZO value in the table is calculated by dividing the diameter of the RLi-LLZO resistance by a factor of two since the cell consisted of two Li-LLZO interfaces

3) Characterizing the stability of the Li-$LiZr_2(PO_4)_3$ (LZP) NASICON

In FY2016, the stability of LLZO in air was studied. A correlation between exposure time to air and the Li-LLZO interfacial resistance indicated that LLZO reacts with moisture in air. Though measures can be taken to clean the LLZO interface, ideally, an intrinsic stability against moisture is preferred. To this end, $LiZr_2(PO_4)_3$ (LZP) NASICON, which is known to have improved stability against moisture, was evaluated. Specifically, the stability of the Li-LZP interface was characterized. The stability was evaluated using EIS on Li-LZP-Li cells (Figure V-206). Unlike previous similar studies on Li-LLZO-Li cells that maintained the same cell impedance over time, the Li-LZP-Li cell impedance significantly increased over 230 hours. This suggests that the Li-LZP interface is not stable. After testing, the cell was disassembled and inspected visually. Severe discoloration of the LZP confirms that LZP is not chemically stable against Li. XPS analysis was also conducted confirming the degraded surface. The implications of this study indicate that despite the same Zr-cation framework structure, the oxygen anion in LLZO garnet is more stable against Li compared to the phosphate polyanion in LZP NASICON.

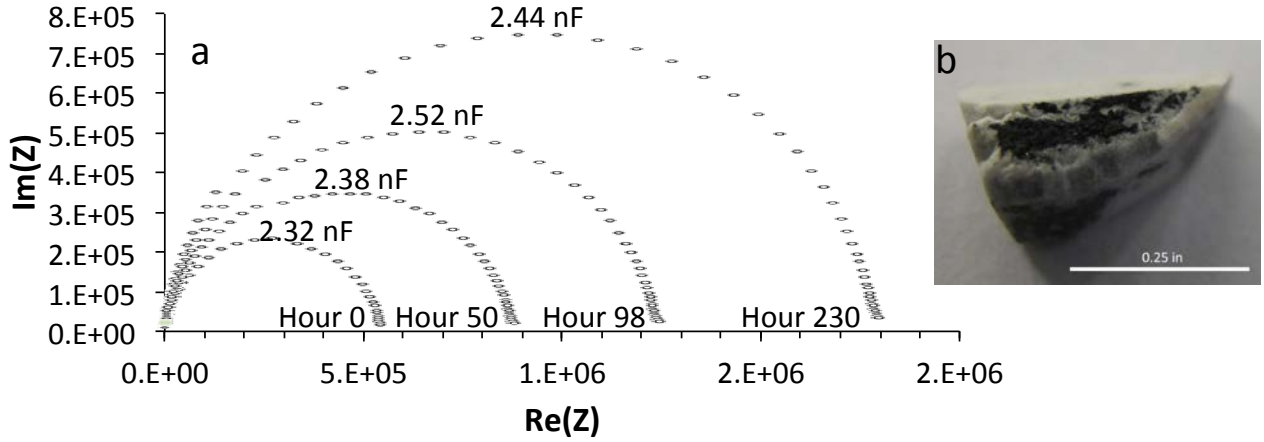

Figure V-206: (a) EIS analysis of Li-LZP-Li cells. The LZP disks were 12.7 mm in diameter and 1mm thick. 0.8 mm thick Li anodes were scraped and placed against the LZP disks compressed at a constant 350 kPa. The EIS data are taken at various time points between 0 and 230 hours at room temperature. The capacitance values in nanoFarads (nF) are indicated for each EIS spectrum at various time points. Capacitances in the nF range indicates that charge transfer is the transport mechanism dominating the cell impedance. (b) A wedge cut from the LZP disk after 230h exposure against Li metal

Conclusions

Enabling Li metal anodes requires approaches to stabilize the Li interface while preventing dendrite formation during cycling. Our approach entails the integration of a solid electrolyte that is chemically, electrochemically, and mechanically stable against Li. Based on its conductivity and stability, LLZO garnet is the focus of this project. In FY 2016, our team identified the primary defects that we believe govern the maximum tolerable lithium-ion current density of the Li-LLZO interface. This report summarizes the key findings in FY 2016 with an emphasis on interfacial stability: 1) Through theory and experiment, it was determined that LLZO is relatively stable against metallic Li, 2) By maintaining contamination free Li and LLZO interfaces, a Li-LLZO charge transfer resistance of 16 Ohms.cm^2 was achieved, and 3) Though reported to be more stable against water, LZP NASICON is not a viable alternative to LLZO garnet, due to its instability against Li metal. These and other findings in FY 2016 establish key fundamental knowledge that we hope will allow us to achieve our goal of demonstrated a Li-LLZO CCD of $\geq$ 1mA/cm^2 in FY 2017.

Products

Presentations/Publications/Patents

1. Publication: Accepted from last reporting period: *Chemistry of Materials*, "Elastic Properties of the Solid Electrolyte $Li_7La_3Zr_2O_{12}$ (LLZO)" Seungho Yu, Robert D. Schmidt, Regina Garcia-Mendez, Erik Herbert, Nancy J. Dudney, Jeffrey B. Wolfenstine, Jeff Sakamoto, and Donald J. Siegel.
2. Publication: Submitted to *Electrochemica Acta in final review:* "Intergranular Li metal propagation through polycrystalline $Li_{6.25}Al_{0.25}La_3Zr_2O_{12}$ ceramic electrolyte.
3. Publication: C. Ma, Y. Cheng, K. Yin, J. Luo, A. Sharafi, J. Sakamoto, J. Li, K. L. More, N. J. Dudney, and M. Chi, Accepted in NanoLett., September 2016.
4. Publication: Submitted to *ACS Energy Letters*: Title: "Electrochemical window of the Lithium-ion solid electrolyte LLZO"Author(s): Thompson, Travis; Yu, Seungho; Williams, Logan ; Schmidt, Robert; Garcia-Mendez, Regina; Wolfenstine, Jeffrey; Allen, Jan; Kioupakis, Emmanouil; Siegel, Donald; Sakamoto, Jeff.
5. Publication: Submitted to *Solid State Ionics in final review*, S. Smith, T. Thompson, J. Allen, J. Sakamoto, and Wolfenstine, Electrical, Mechanical and Chemical Stability of $Li_{1.2}Zr_{1.9}Sr_{0.1}(PO_4)_3$
6. Invited Presentation: Beyond Lithium-ion, PNNL, June 2016, Richland, WA.

7. Invited Presentation: Electrochemical Society, June 2016, San Diego, CA.
8. Invited Presentation: USAABC, June 2016, June 2016, Detroit, MI.
9. Invited Presentation and symposium organizer: The Battery Show, September 2016, Novi, MI.
10. Invited Presentation XXV International Materials Research Congress (IMRC), August 14-19, 2016. Cancun, Mexico.
11. Invited Presentation Danish Battery Society Annual Symposium, April 7th, 2016. Copenhagen, Denmark.
12. Invited Presentation Technical University of Denmark (DTU), Department of Energy Conversion and Storage.
13. Invited Presentation Department Colloquium, February 1st, 2016, Lyngby, Denmark.
14. Invited Presentation University of Florida Material Science/Mechanical & Aerospace Engineering Seminar, December 7th, 2015, Gainesville, FL.
15. Invited Presentation Nordic Battery Conference (NORDBATT2), December 2-3, 2015, Trondheim, Norway.
16. Invited Presentation Lithium Battery Power 2015, November 17-19, 2015, Baltimore, MD.
17. Invited Presentation Electrochemical Society Fall Meeting, October 11-16, 2015, Phoenix, AZ.

References

1. K. Xu, *Chem. Rev.*, **2014**, *114*, 11503.
2. N. Kumar, D. J. Siegel. *J. Phys. Chem. Lett*., **2016**, *7*, 874.
3. T. Thompson, J. Wolfenstine, J.L Allen, M. Johannes, A. Huq, I.N. David, J. Sakamoto, *J. Mater. Chem. A*, **2014**, *33*, 13431. [16] Y. Zhu, X. He, Y. Mo, *ACS Appl. Mater. Inter*., **2015**, *7*, 23685.
4. L. J. Miara, S. P. Ong, Y. Mo, W. D. Richards, Y. Park, J.-M. Lee, H. S. Lee, G. Ceder, *Chem. Mater.*, **2013**, *25*, 3048.
5. F. D. Murnaghan, *Proc. Natl. Acad. Sci.*, **1944**, *30*, 244. [19] S. Yu, R. D. Schmidt, R. Garcia-Mendez, E. Herbert, N. J. Dudney, J. B. Wolfenstine, J. Sakamoto, D. J. Siegel, *Chem. Mater.*, **2016**, *28*, 19.
6. A. C. Luntz, J. Voss, K. Reuter, *J. Phys. Chem. Lett.*, **2015**, *6*, 4599. [21] G, Kresse, J. Furthmüller, *Phys. Rev. B*, **1996**, *54*, 11169.
7. T. Thompson, S. Yu, L. Williams, R. D. Schmidt, R. Garcia-Mendez, J. Wolfenstine, J. L. Allen, E. Kioupakis, D. J. Siegel,* and J. Sakamoto, Submitted to *ACS Energy Lett.*, October **2016**.
8. C. Ma, Y. Cheng, K. Yin, J. Luo, A. Sharafi, J. Sakamoto, J. Li, K. L. More, N. J. Dudney, and M. Chi, Accepted in *NanoLett.*, September **2016**.

V.G.3. Composite Electrolytes to Stabilize Metallic Lithium Anodes (ORNL)

Nancy Dudney, Principal Investigator
Oak Ridge National Laboratory
P.O. Box 2008, MS6124
Oak Ridge, TN 37831
Phone: 865-576-4874
E-mail: dudneynj@ornl.gov

Tien Q. Duong, DOE Program Manager
U.S. Department of Energy
Advanced Battery Materials Research (BMR)
Vehicle Technologies Office
1000 Independence Avenue, SW
Washington, DC 20585
Phone: 202-586-7836
E-mail: Tien.Duong@ee.doe.gov

Start Date: October 2015
End Date: September 2018

Abstract

Objectives

- Prepare composites of representative polymer and ceramic electrolyte materials to achieve thin membranes which have the unique combination of electrochemical and mechanical properties required to stabilize the metallic lithium anode while providing for good power performance and long cycle life.
- Understand the lithium ion transport at the interface between polymer and ceramic solid electrolytes which is critical to the effective conductivity of the composite membrane.
- Identify key features of the composite composition, architecture and fabrication that optimize the performance and develop practical and scalable fabrication methods.

Accomplishments

- Ceramic-polymer composite electrolytes formed by spray coating an aqueous slurry which were thin (20-50 µm), homogeneous and crack-free membranes over large areas. Following drying, the coatings were further compacted, approaching the expected theoretical density.
- Addition of TEGDME, which was necessary for a high quality membrane, forms a passivating reaction layer at the interface with the Li metal as tested in Li//Li and Li//thin-film cathode configurations.
- While TEGDME facilitates Li conduction through the polymer phase, it does not facilitate the ion transfer between ceramic and polymer phases, so the conductivity of this composite is not sufficient for practical use.

Future Achievements

- Improved Li ion conductivity for the spray coated composite through higher salt concentration, alternative and surface treated ceramic powders, or higher ceramic loading by tailoring the particle size distribution.
- Characterize the passivated interface of the composite with lithium metal, its effect on the reversible Li deposition. Reduce the interface reaction by adjusting the electrolyte composition and by addition of a barrier coating to further stabilize the interface and prevent Li dendrites.

- Demonstrate advanced manufacturing processes where the architecture of the composite membrane can be developed and tailored to maximize performance and cost-effective manufacturing.

Technical Discussion

Background

Composite solid electrolytes have been investigated for decades, but have few applications and are not fully understood. Most are based on ceramic electrolytes which show enhanced conductivity with a small addition of very fine powders of an insulator, such as alumina. The enhancement is attributed to enhanced concentration or mobility of the ionic carriers along the interfaces and grain boundaries formed by incorporating the second phase. For polymer electrolytes containing a similar dispersion of fine particles, the results are more ambiguous, and there is evidence that impurity molecules such as water contribute when enhanced conductivity is observed. An obvious extension of these studies is for the dispersed phase to be a good ionic conductor, rather than insulator, but there are only a few reports showing that this further enhances the conductivity. The premise in the current study is that composites of two solid electrolytes may be formed with much greater range of composition and structure without inhibiting the ion transport. This gives the potential for composites to have a much more uniform current distribution across the membrane and toward the interface with the metallic lithium anode. Also such composites may be engineered to optimize the mechanical properties and new approaches to practical and low-cost processing can be proposed. These advantages would make use of a composite electrolyte much more attractive for solid state batteries. This forms the basis for the current work.

Introduction

A stable lithium anode is critical to achieve high energy density with excellent safety, lifetime and cycling efficiency. This study will identify the key design strategies that should be used to prepare composite electrolytes to meet the challenging combination of physical and chemical and manufacturing requirements to protect and stabilize the lithium metal anode for advanced batteries. By utilizing well characterized and controlled component phases, the design rules developed for the composite structures will be generally applicable toward the substitution of alternative and improved solid electrolyte component phases as they become available. Success in this program will enable these specific DOE technical targets: 500-700Wh/kg, 3000-5000 deep discharge cycles, robust operation.

Approach

This program seeks to develop practical solid electrolytes that will provide stable and long-lived protection for the lithium metal anode. Current electrolytes all have serious challenges when used alone: oxide ceramics are brittle, sulfide ceramics are air sensitive, polymers are too resistive and soft, and many electrolytes react with lithium. Composites provide a clear route to address these issues. This program does not seek discovery of new electrolytes, rather the goal is to study combinations of current well-known electrolytes that can provide critical understanding towards the effects of the interfaces and architecture on the ion transport and stability with the Li anode. The program emphasizes the investigation of polymer-ceramic interfaces formed as bilayers and as simple composite mixtures where the effects of the interface properties can be readily isolated. In general, the ceramic phase is several orders of magnitude more conductive than the polymer electrolyte, and interfaces can contribute an additional source of resistance. Using finite element simulations as a guide, composites with promising compositions and architectures are fabricated and evaluated for lithium transport properties using AC impedance and DC cycling with lithium in symmetric or half cells. General design rules will be determined that can be widely applied to other combinations of solid electrolytes.

Over the last year, thin composite membranes were formed by spray coating of aqueous slurries because this is an inexpensive and scalable processing route that can achieve high loadings of the ceramic component to ensure a high shear modulus. The membranes are formed as both free standing sheets supported by a nylon mesh and as coatings adhered to metal foils or dense, thin-film cathodes. These recent results are compared to those obtained during FY15 where composites are formed by dry milling the components followed by melt

pressing samples as small disks, all within a high purity inert atmosphere. This is providing valuable insight to how solvents and impurities effect the ion transport through the composite.

Results

Toward the end of FY15, use of slurries was first adopted as a means to form very thin composite membranes over basically unlimited areas. These were cast by doctor blade and then spray coating which proved to be more efficient. Most effort in FY16 was devoted to furthering the processing for such spray coated electrolytes and establishing the effects of additives on the ionic conductivity and stability with lithium.

Slurry coated membranes targeted a 50 volume percent loading of ceramic powder, using mainly powder obtained from Ohara Corp. The Ohara powder is based on the lithium aluminum titanium phosphate (LATP) electrolytes with submicron and near spherical particles. Slurries were prepared using both water and acetonitrile carriers, both of which were easily dried as the spray coating layers were built up and then further when warmed under vacuum. Results described here are all obtained from spray coating of the aqueous slurries using Ohara powder, polyethylene oxide (PEO, MW=600,000), Li triflate salt (LiTf, $LiCF_3SO_3$) with a 16:1 atomic ratio of PEO ether oxygens per dissolved Li^+ ion. Although other Li salts dissolved in PEO have higher conductivity, this salt was chosen because crystallization, if it occurs, will happen more quickly and because it provides a stronger contrast to conductivity of Ohara.

Because of the large 50% volume fraction of the ceramic phase needed for good mechanical stability, the processing to create a uniform and dense composite requires a slurry that is well dispersed. Agglomerates of the ceramics may cause jamming of the particles and poor packing. Details of the slurry formation, including the drying, milling, sequence of additions, slurry mixing, are all important to establishing a stable slurry and well dispersed ceramic particles coated with the polymer electrolyte. Details of the spray coating are also critical to achieving a smooth clump-free coating. Addition of a plasticizer was found to improve wetting and adhesion of the slurry to Cu, Ni, and C-coated foils. It also helped to eliminate crack formation when the coating was dried. Good results were obtained with addition of tetraethylene glycol dimethyl ether (abbreviated tetraglyme or TEGDME) which is a solvent that is stable to low voltages versus Li metal and has been reported to passivate the Li metal interface. While several concentrations were tested, a typical addition of TEGDME to the slurry is 2:1 moles TEGDME:Li, providing another 10 oxygens per Li^+ ion. The TEGDME content in the dried composite was verified by TGA and FTIR characterization, and also by gravimetric tests upon vacuum evaporation of water from a liquid solution of water and TEGDME. The TGA shown in Figure V-206(a) demonstrates that the TEGDME is stable to about 250°C. The XRD, DSC and activation energy for ionic conduction determined by electrochemical impedance spectroscopy (EIS) shows that TEGDME prevents crystallization of the PEO in the composite. For comparison, Figure V-206(b) shows that DMC loss from a similar Ohara+PEO+LiTf composite begins at lower temperature.

Density of the as-sprayed and dried coatings varied from 1.45 to 1.9 g/cm^3, as determined for punched disks of electrolyte-coated copper foil. The density is increased by cold pressing (2.1g/cm^3) and then further by hot pressing the coating at 100°C (2.4g/cm^3). The hot pressed membranes are estimated to be about 95% of theoretical density, if the PEO swells by ≤10% with the salt plus TEGDME addition. This swelling seems reasonable, but remains to be carefully analyzed. For measurements of the density and EIS, two coated disks are pressed together, face to face, forming a sandwich with Cu blocking electrodes.

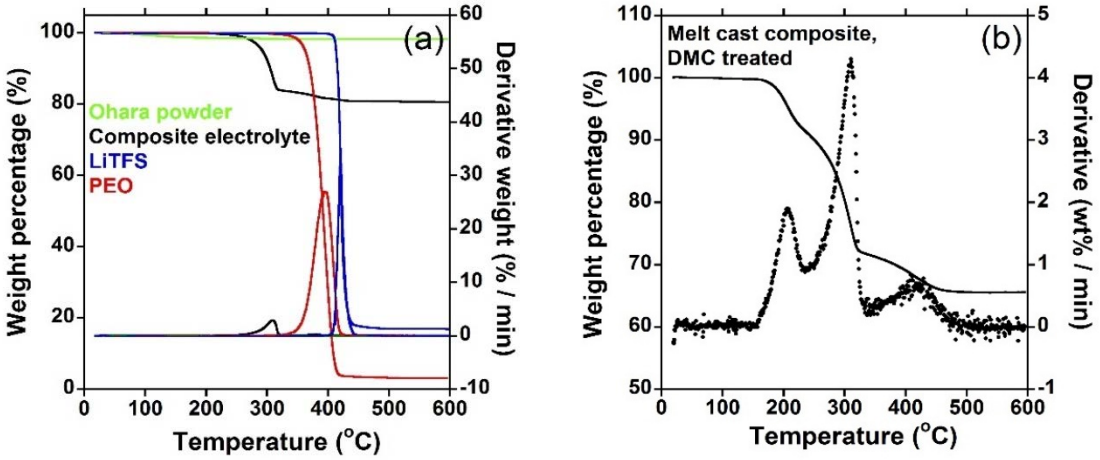

Figure V-207: TGA scans of composites (black curves) and individual component phases. For (a), the composite was spray coated with a slurry containing TEGDME. For (b), the composite was prepared by dry mill and melt cast, then treated in DMC vapor

While the relative change in density of the composite is small, the room temperature conductivity increases 4 orders of magnitude from the unpressed to the hot pressed coatings. Clearly the voids in the composite are distributed so as to greatly limit the ion transport paths. However as shown in Figure V-208a, the conductivity of the hot-pressed composite is still too low and is, in fact, lower than for the polymer phase without addition of the Ohara ceramic powder. This suggests that the Li ions move around the ceramic particles due to a resistive interface. This is contrary to results from FY15, where vapor addition of dimethyl carbonate (DMC) to a melt cast composite greatly enhanced the ionic conductivity well above the matrix phase. This comparison is shown in Figure V-208b, with curved arrows to emphasize the difference of the two plasticizing molecules in Figure V-208a and Figure V-208b. It appears that the DMC can provide a bridge for Li^+ to move between the polymer and ceramic, while TEGDME likely chelates the Li ions. So far, the presence of TEGDME in the composite appears to block adsorption of DMC molecules, but because of the reactivity with lithium, DMC is not an acceptable solution to the interface resistance problem.

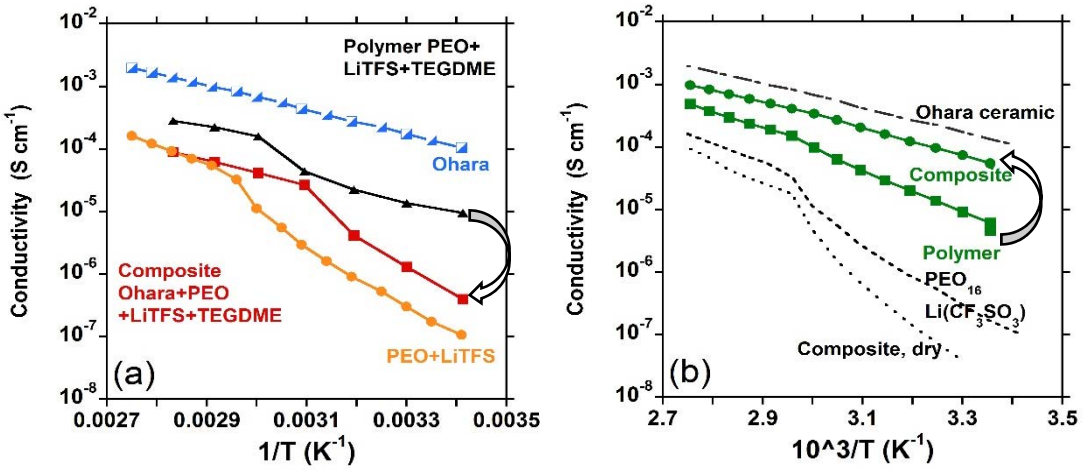

Figure V-208: Conductivity of the plasticized polymer and composite electrolytes, compared to the single phase ceramic and polymer electrolytes. For (a), the polymer (black) and composite (red) are spray coated from aqueous slurry and contain TEGDME. For (b), the polymer and composite (green) are melt cast and treated in DMC vapor. The curved arrows emphasize the relative conductivities of the composites relative to the polymer matrix in both figures

To prepare samples suitable for testing stability with lithium electrodes or in a Li/cathode cell, the slurry was spray coated onto both sides of a thin (78µm) nylon mesh with 47% open area. Upon compression to densify the membrane, the conductivity was comparable to that of the side-by-side coating onto Cu foil. A polarization

test of this composite pressed with Li foil electrodes is shown in Figure V-209a, and Figure V-209b. The current relaxes within minutes following each step in the potential and then more slowly. The conductivity determined from the current-voltage of Figure V-209b is in good agreement with that from EIS analysis. Batteries prepared using the composite electrolyte with a lithium vanadate cathode versus Li anode have so far not cycled well, but do have a stable open circuit potential. Vacuum vapor deposition of Li metal films has so far been unsuccessful. While TGA indicates that the TEGDME is quite stable in flowing nitrogen, treatment under vacuum for Li deposition leads to reaction of the lithium.

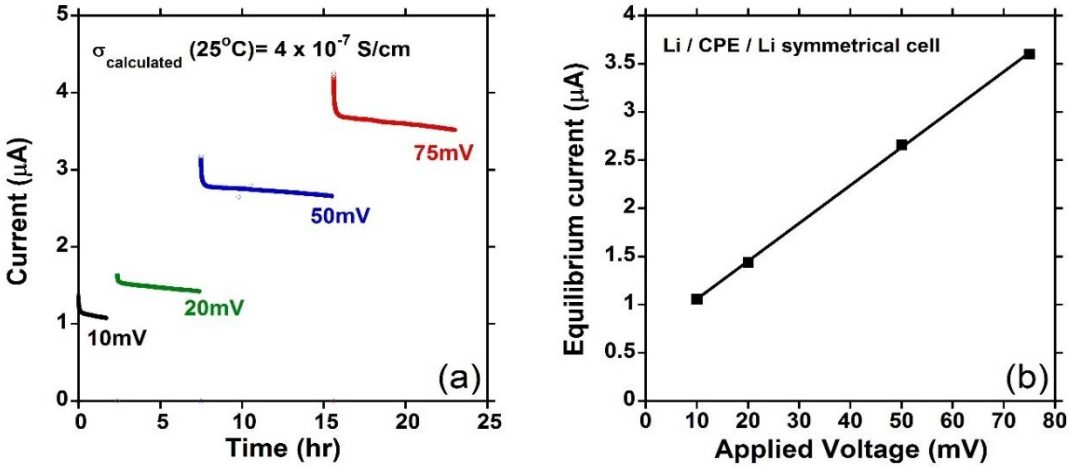

Figure V-209: Potentiostatic polarization curves (a) for a spray coated composite with Li contacts to both faces. At (b), the final current is plotted to obtain the DC conductivity of 0.4 μS/cm

Conclusions

Ceramic-polymer composite electrolytes formed by spray coating an aqueous slurry were demonstrated. The spray coatings which contained a small amount of TEGDME were thin and dried to uniform and crack-free membranes over large areas. Following drying, the coatings were further compacted, approaching the expected density. Unfortunately, the composite had a rather low conductivity at room temperatures. Initial results suggest that the interface with lithium is passivated and the DC conductivity and battery open circuit voltage prove stable. Because the conductivity of the composite was lower than the polymer matrix, it is clear that TEGDME is coordinated with the mobile Li ions, but does not facilitate the ion transfer between ceramic and polymer phases as does the smaller DMC molecule.

Products

Presentations/Publications/Patents

1. Nancy J. Dudney, Sergiy Kalnaus, Cara Herwig, and Frank Delnick, “A composite electrolyte for solid state Lithium batteries,” MRS meeting, December 2015, Boston.
2. Nancy Dudney, Amaresh Samuthira Pandian, and Frank Delnick, “Composite Electrolyte to Stabilize Metallic Lithium Anodes”, poster presentation at 2016 DOE AMR Meeting, June 6-10, 2016, Washington DC.
3. Amaresh Samuthira Pandian, Frank Delnick and Nancy Dudney, “Composite Polymer-Ceramic Electrolyte for High Energy Lithium Secondary Batteries”, presented at PRiME meeting of Electrochemical Society, 2016 Hawaii.

V.G.4. Overcoming Interfacial Impedance in Solid-State Batteries (University of Maryland)

Eric Wachsman, Principal Investigator
University of Maryland
1206 Engineering Laboratory Building
College Park, MD 20742
Phone: 301-405-8193
E-mail: ewach@umd.edu

Tien Q. Duong, DOE Program Manager
U.S. Department of Energy
Advanced Battery Materials Research (BMR)
Vehicle Technologies Office
1000 Independence Avenue, SW
Washington, DC 20585
Phone: 202-586-7836
E-mail: Tien.Duong@ee.doe.gov

Start Date: October 2014
End Date: September 2017

Abstract

Objectives

Develop a multifaceted and integrated experimental and computational approach to solve the key issue in solid-state lithium-ion batteries (SSLiBs), interfacial impedance. The research will focus on garnet-based solid-state electrolytes (SSEs), but the knowledge can be applied to other SSE chemistries. The interfacial impedance in this proposal includes charge transfer, ionic and electronic transport, and interfacial structural/chemical stability over charge-discharge cycling. The developed low interface technique will be tested with solid state Li-NMC cell and Li-S cell testbeds that have 350-450 Wh/kg and 200 cycles.

Accomplishments

- Identified compositions of gel electrolyte to achieve 100 $\Omega*cm^2$. (Q1FY16 Milestone)
- Determined interfacial impedance in layered and 3D controlled solid state structures. (Q2FY16 Milestone)
- Developed computation models to investigate interfacial ion transport with interlayers. (Q3FY16 Milestone)
- Identified compositions of interlayers and processing with electrolyte/electrode interfacial impedance of ~10 $\Omega*cm^2$. (Q4FY16 Milestone and Budget Period Go/NoGo)

Future Achievements

- Fabrication of SSLiBs with Li-NMC Chemistry. (Q1FY17 Milestone)
- Fabrication of SSLiBs with Li-S Chemistry. (Q2FY17 Milestone)
- Develop model to investigate interfacial transport for Li-S and Li-NMC SSLiBs. (Q3FY17 Milestone)
- Achieve full cell (Li-S or Li-NMC) performance of 350-450 Wh/kg and 200 cycles. (Q4FY17 Milestone）

Technical Discussion

Background

Due to their intrinsic safety, SSLiBs could provide low-cost safe energy storage solutions for electrical vehicle applications. However, the interfacial impedance in current state-of-the-art SSLiBs is ~1000 Ohm*cm^2, which is 100-1000 times higher than lithium-ion batteries with organic electrolytes. Such high interfacial impedance not only limits the initial rate performance of SSLiBs, but also increases dramatically over charge-discharge cycling, greatly impacting the battery cycle life. Thus, grand challenges exist at the SSE-electrode interface, specifically: (1) large interfacial impedance for charge transfer and transport; and (2) mechanical degradation of interface with electrochemical charge/discharge cycles.

To overcome critical issues related to organic electrolytes, such as safety and degradation, numerous solid-state inorganic lithium-ion electrolytes, including perovskite $Li_{0.36}La_{0.55}(□)_{0.09}TiO_3$ (□=vacancy), layered Li_3N and Li-β -alumina, $Li_{14}ZnGe_4O_{16}$ (Lithium Super-ionic Conductors, (LISICON)), $Li_{2.88}PO_{3.86}N_{0.14}$(LiPON), Li_9AlSiO_8 and $Li_{10}GeP_2S_{12}$, are being investigated to replace organic LIB electrolytes.[1-4] However, each of these has significant issues, including low ionic conductivity, instability with Li or air, and/or difficulty to produce. Moreover, all the SSLiBs incorporating these state-of-the-art SSEs suffer from high interfacial impedance due to their low surface area, planar electrode/electrolyte interfaces.

Recently Thangadurai (our international collaborator) discovered Li-garnet-type metal oxides, $Li_5La_3M_2O_{12}$ (M = Nb, Ta). [4] The conductivity of these SSEs has continued to improve by judicious doping to increase the Li content ("stuffing") of the garnet structure. These Li-stuffed garnets exhibit the most promising physical and chemical properties for SSEs including: (1) The highest known RT bulk conductivity (~10^{-3} S/cm obtained by Thangadurai with cubic $Li_7La_3Zr_2O_{12}$);[5,6] (2) High electrochemical stability for high voltage cathodes (up to 6 V), about 2 V higher than current organic electrolytes and about 1 V higher than the more popular LiPON; (3) Excellent thermal and chemical stability in contact with elemental and molten Li anodes up to 400°C, unlike NASICON-type $LiTi_2P_3O_{12}$ and perovskite-type $La_{(2/3)-x}$ $Li_{3x}□_{(1/3)-2x}TiO_3$; (4) Li^+ transference number close to the maximum of 1.00, which is critical to battery cycle efficiency, while typical polymer electrolytes are only ~0.35. (5) Wide operating temperature capability, the electrical conductivity increases with increasing temperature reaching 0.1 S/cm at 300°C, and maintains appreciable conductivity below 0°C. In contrast, polymer electrolytes are flammable at high temperature; (6) Synthesizable as simple mixed oxide powders in air, hence easy scale up for bulk synthesis and creation of low-cost supply chain.

However, challenges exist in garnet based electrolytes, which may explain the limited success in SSLiBs based on garnet electrolytes. These challenges include: (1) Large interface resistance in the cells between electrode particle-electrolyte particle, between electrode particles, and between electrolyte particles; (2) Poor structure interface integrity during cycling as garnet SSEs are typically fragile; (3) High temperature processing temperature that is not compatible with most anode and cathode materials.

Introduction

Solid state garnet-electrolyte lithium-ion batteries have tremendous potential due to their inherent safety, high voltage stability, and reasonably high conductivity. However, the interfacial impedance between solid state electrolytes and electrodes is currently too high. This work will focus on reducing the interfacial impedance, by making controlled structures on the garnet electrolyte surface, and introducing conductive and conformal interfacial layers between the garnet and the electrodes. These results will address the primary issue and significantly advance solid-state Li-battery technology.

Approach

The objectives outlined above will be accomplished by optimizing the garnet surface structure and electrode material, and investigating high conductivity conformal interfacial layers.

1. Effect of Interfacial Structure on Impedance

While we and others have made tremendous advances in understanding interfacial resistance in solid oxide fuel cells (SOFCs), to date no one has applied these techniques to SSLiBs. Therefore, we use SOFC techniques to develop a fundamental understanding of interfacial impedance in terms of intrinsic charge transfer rates, ionic and electronic transport, and effect of interfacial structure. Electrochemical impedance spectroscopy (EIS) of solid electrolyte, electrode, and interfacial layer pellets are being performed to identify the mechanistic frequency dependence of the EIS response for each material as well as blocking electrode and DC measurements to separate out ionic vs. electronic conductivity for each material. Then the materials are combined into bilayer electrolyte and electrode/interfacial layer pellets with smooth and controlled interfaces and tested with EIS. This allows for determination of the specific interfacial impedance as an additional EIS frequency response. This interfacial impedance is then being used to calculate the charge transfer reaction rate across the electrolyte/electrode and electrolyte/interfacial layer interfaces. Bilayered pellets with tailored nano/micro-rod interfaces have been fabricated (by templated deposition and additive manufacturing) with different aspect ratios. The EIS data from these cells is deconvoluted and compared with known ionic and electronic transport rates, and charge transfer rates, to create fundamental models of interfacial impedance as a function of 3-dimensional interfacial structure.

2. Investigate Interfacial Modifications and Cell Performance

We are investigating four types of materials as interfacial layers in SSLiBs.

Type 1, we use nonflammable organic electrolytes such as perfluoropolyethers (PFPE) based electrolytes. It has been confirmed that such organic electrolytes cannot catch fire and are intrinsically safe. Although, PFPE-based electrolytes have very low ionic conductivity (~ 10^{-5} S/cm) and cannot meet the power density requirement in the FOA by itself, PFPE based organic electrolyte can greatly increase the interface contact across electrolyte grain boundaries, or electrolyte/electrode interface for enhancing the battery performance.

Type 2, we also use a polymer electrolyte or gel electrolyte, composed of bis(trifluoromethane)sulfonimide lithium salt (LiTFSI) in poly(vinylidene fluoride-co-hexafluoropropylene) (PVDF-HFP). Although the polymer or gel electrolyte has a much lower ionic conductivity, its thickness is low as an interface layer and thus its contribution in overall impedance is negligible. These soft electrolytes can largely improve the contact between the electrodes and electrolyte toward better charge transport and mechanical integrity.

Type 3, we are investigating thin inorganic layers by atomic layer deposition (ALD) and other thin film deposition techniques to form a nano-scale conducting phase between the garnet and the electrode.

Type 4, we are using soft conformable materials such as β-Li_3PS_4 (LPS) or liquids to bridge the gap between the garnet and electrode material.

Results

In budget period 2 we have achieved the following progress:

1. Cathode interface resistance

a. Gel electrolyte interface

Gel electrolyte interfacial layers can significantly reduce interfacial impedance between garnet solid state electrolytes and cathodes. Figure V-210a is the electrochemical impedance spectroscopy (EIS) plot of a cathode/garnet/cathode symmetric cell without any interfacial layer modification. The total resistance of cathode/garnet/cathode symmetric cell without gel interfacial layer is ~10^6 Ohm*cm^2 due to the poor contact between garnet and $LiFePO_4$ cathode material, the difficulty of charge transfer through the interface between two solid materials, the non-conductive binder, and the rough surface of the garnet pellet.

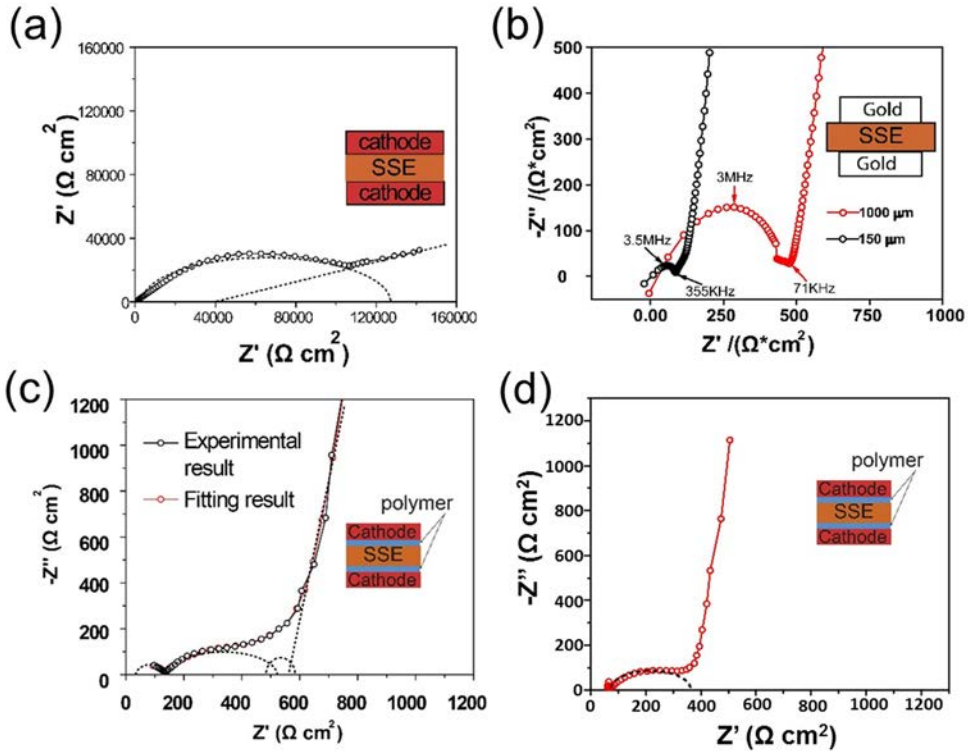

Figure V-210: (a) EIS plot of cathode/garnet/cathode symmetric cell without gel electrolyte. (b) EIS of garnet itself. (c) EIS of cathode/gel/garnet/gel/cathode symmetric cell. (d) EIS figure of symmetric cell with mixed cathode and gel

Figure V-210b is the EIS plot of cathode/garnet/cathode symmetric cell with gel interface. The impedance curve has three components. In the high frequency region (f >9 kHz) is an incomplete semi-circle, corresponding to the bulk and grain boundary impedance of the garnet electrolyte. In the middle frequency region (7 Hz < f < 9 kHz) is a combination of two semi-circles corresponding to interfacial charge transfer impedance between garnet and cathode, including impedance on the gel/garnet and cathode/gel interfaces, as the impedance of the gel layer itself is very small. In the low frequency region (f <7 Hz) is a straight line, corresponding to diffusion impedance of the cathode.

The interfacial resistance is obtained by subtracting the garnet resistance obtained separately by EIS of garnet samples from the total symmetric cell resistance, then dividing by two as there are two interfaces, e.g.:

- Thickness of garnet pellet is 500 μm, and garnet conductivity is $2.1*10^{-4}$ S/cm (Figure V-210b). Therefore, area specific resistance (ASR) of garnet pellet is 239 Ohm*cm^2.
- The total symmetric cell resistance (Figure V-210b) is 600 Ohm*cm^2. Therefore, the ASR of one interface is (600-239)/2 =180 Ohm*cm^2, which is ~4 orders of magnitude less than the same symmetric cell without the interfacial layers.

To further reduce the garnet/cathode interfacial impedance the procedure was improved by making a gel/cathode composite, instead of using separate gel layers, thus reducing the gel thickness and improving the contact between gel and cathode. Figure V-210d shows the impedance of symmetric cell using $LiFePO_4$/gel cathode on both sides of garnet. The corresponding interfacial ASR is now reduced to only 67 Ohm*cm^2 for one interface (using same approach described above).

b. Effect of structure on interface - 3D printed garnet interface

A 3D garnet surface structure can dramatically increase the effective surface area relative to the planar areal surface area. 3D structured garnet line patterns were printed on surface polished garnet pellets and sintered to form structured ionic conductive paths with varying line spacing (Figure V-211). Cathode slurries ($LiFePO_4$, CNT, and gel) were coated on both flat and structured garnet surfaces. EIS of the symmetrical cells was obtained at room temperature.

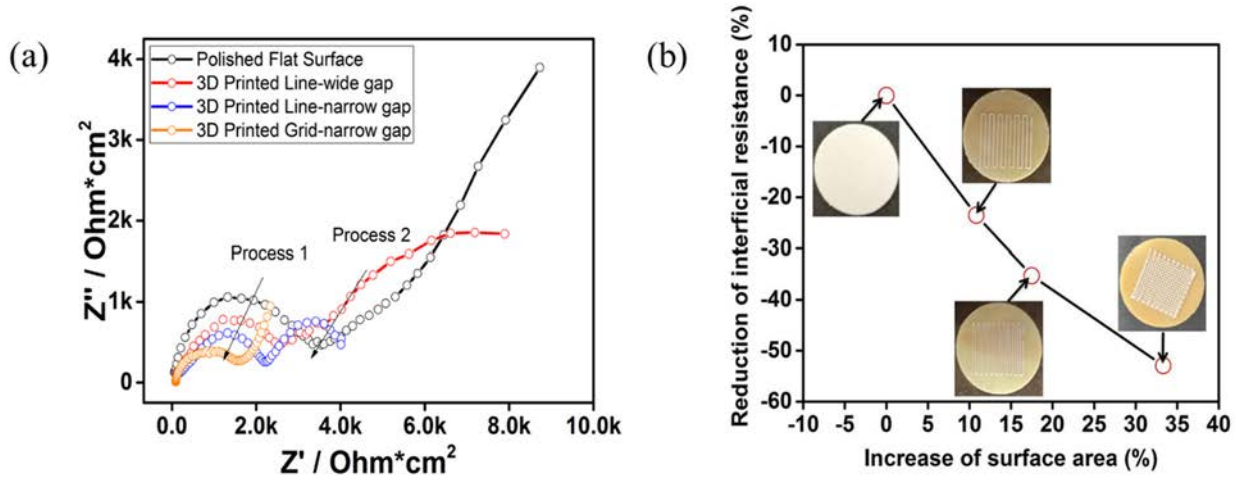

Figure V-211: Comparison of cathode/electrolyte interfacial impedance on flat and 3D-structured garnet pellets. (a) EIS plot of garnet without 3D printing and with different 3D printings. (b) Reduction of interfacial resistance with increase in surface area

The depressed arcs, which can be assigned to Li ion diffusion and charge transfer steps, became much smaller after effective extension of surface area. The 3D printed lines (40 μm height and 70 μm width) increased the effective sample surface areas from 36 mm^2 for polished pellet to 39.9, 42.3 and 48 mm^2 with increasing line density, resulting in 22%, 35% and 52% reduction of interfacial resistance (from the intercept of real axis high frequency arc (Figure V-211a)) proportional to the increase in effective surface area (Figure V-211b). Therefore, as expected the 3D printed structures reduced the cathode-electrolyte interfacial resistance linearly with increasing effective surface area. Further impedance reduction is anticipated with increase in line density (using smaller printing tips and reduced particle size).

c. Aqueous interface

To further reduce the cathode/garnet interfacial resistance we evaluated an aqueous solution interface (e.g., Type 4). We anticipated a lower cathode/garnet interfacial resistance with the aqueous interface compared with the gel interface as the aqueous solution has higher conductivity and fluidity than the organic electrolyte used for the gel interfaces. Figure V-212a shows a schematic of the symmetric cell with the aqueous cathode/garnet interface. The cathode material ($LiFePO_4$, Carbon black and PVDF) was coated on a carbon cloth. Then these electrodes were immersed into aqueous electrolyte to wet them and then the two electrodes and a garnet pellet were pressed together. As shown in Figure V-212b, the EIS semi-circle of the cell yields a resistance of 253 Ohm*cm^2, which after correcting for garnet ASR and dividing by 2 for the dual interfaces results in a single cathode/garnet interfacial resistance of only 7.5 Ohm*cm^2, 5 orders of magnitude lower than the non-interfacial-layer cell, and achieving the Q4FY16 and budget period 2 Go/NoGo milestones.

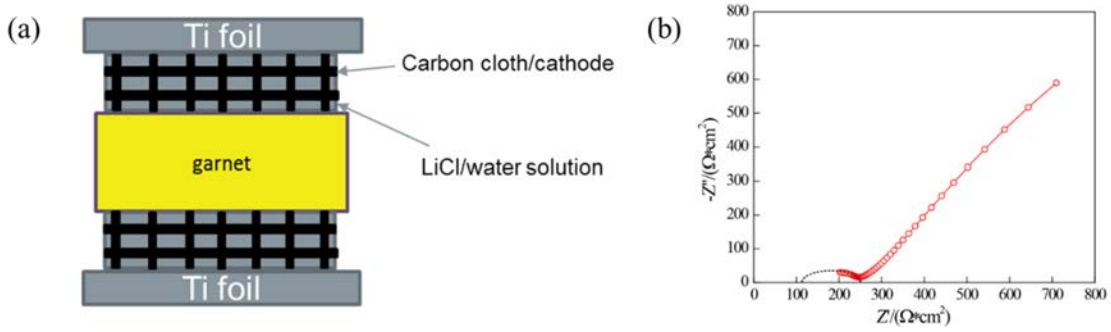

Figure V-212: (a) Schematic of a cathode/garnet/cathode symmetric cell with aqueous interface. (b) Impedance of this cell with aqueous interface

2. Li anode/garnet interface

a. Gel electrolyte interface

Figure V-213a shows that the total resistance of a Li/garnet/Li symmetric cell (formed by melting Li metal on the garnet surfaces) without an interfacial layer is about 3000 Ohm*cm^2. Figure V-213b shows the EIS plot of Li/gel/garnet/gel/Li which has four components. In the high frequency region is an incomplete semi-circle, from the garnet impedance. In the middle frequency region are two semi-circles, due to interfacial charge transfer impedance between garnet and Li metal, which mainly comes from impedance on the gel/garnet and Li/gel interfaces, as the impedance of the gel layer itself is very small. In the low frequency region is a tail, corresponding to diffusion impedance of the interface of gel/stainless steel outside of the lithium metal. Correcting for garnet impedance, the ASR with the gel interlayer is reduced to 200 Ohm*cm^2 for one interface; however, this is done without melting the Li metal as was done for the other cell.

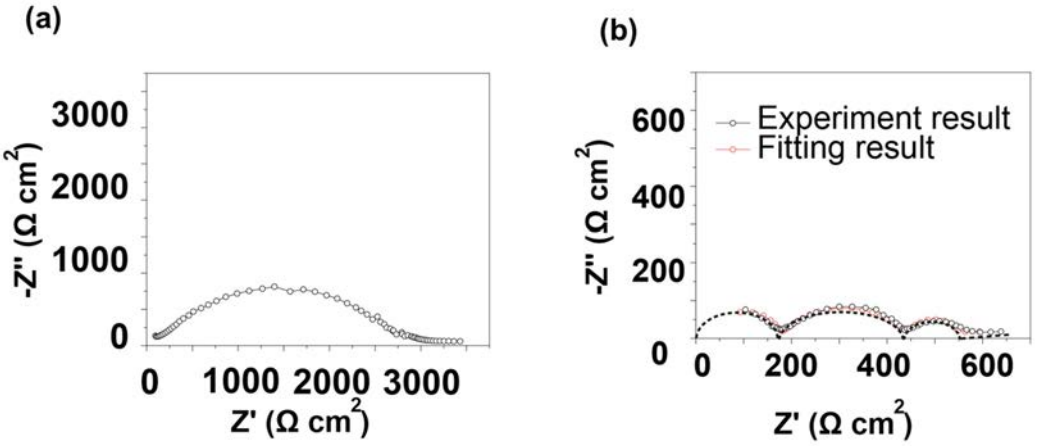

Figure V-213: (a) EIS plot of Li/garnet/Li symmetric cell. (b) EIS plot and equivalent circuit of Li/gel/garnet/gel/Li symmetric cell

b. Si interface

LLZ and Si-coated LLZ was sandwiched by two Li metal electrodes to assemble symmetric cells (Figure V-214a and Figure V-214b). Prior to the electrochemical measurements, all the cells were heated at ~200°C for twenty minutes in a glovebox since thermal treatment promotes superior contact between Li and LLZ. Due to the high reactivity of molten Li, lithiated Si will be formed *in situ* between the Li metal and the Si-coated LLZ. The Nyquist plots of symmetric cells in Figure V-214c exhibit two distinct semi-circles: one at high frequency and another at low frequency. The Li/LLZ/Li symmetric cell delivers a large resistance of 2064 Ohm*cm^2, where the interfacial resistance between Li and LLZ was calculated to be 925 Ohm*cm^2.

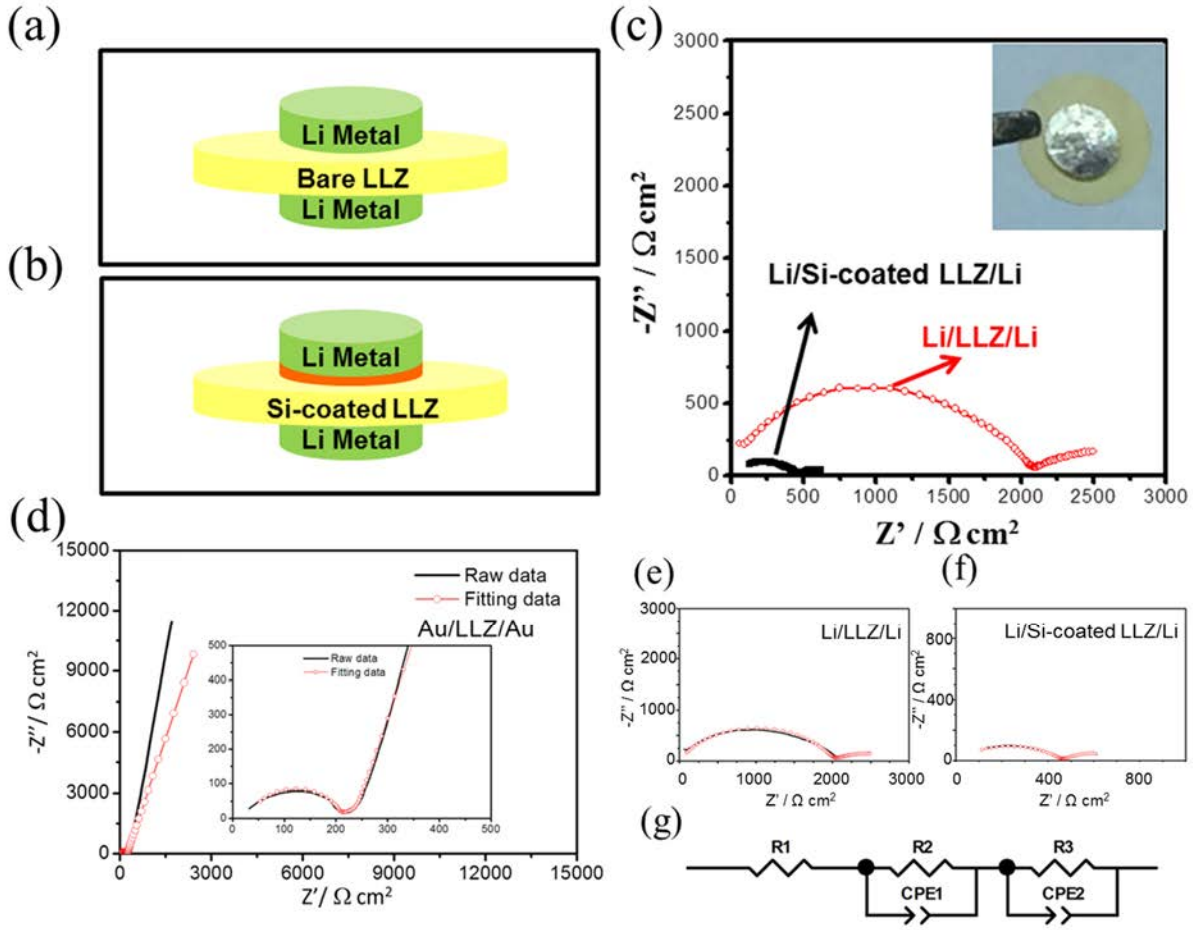

Figure V-214: Schematic illustration showing the structure of symmetric cells with (a) LLZ or (b) Si-coated LLZ SSEs. (c) Electrochemical impedance spectroscopy (EIS) measurements of symmetric cells where the interfacial resistance of the Si-coated garnet cell significantly decreased. Inset of (c) is a digital image of a Li/Si-coated LLZ/Li symmetric cell. (d) Nyquist plots of the Au/LLZ/Au symmetric blocking electrode system at room temperature. The solid black line denotes the experimental data while the red line with hollow spheres represents the fitting data using the equivalent circuit modeling. (e-g) Nyquist plots of (e) Li/LLZ/Li and (f) Li/Si-coated LLZ/Li symmetric cells. (g) The equivalent circuit model used in this study

The first semi-circle at relatively high frequency was used to analyze the interfacial resistance between the Li metal electrode and the LLZ solid electrolyte with/without Si coating. As shown in Figure V-214d, the overall resistance of the LLZ (bulk and grain boundary) measured using Au electrodes is 215 Ohm*cm^2. in Figure V-214e, the first semi-circle of the Li/LLZ/Li cell yields a resistance of 2064 Ohm*cm^2, which can be divided into two parts: one is the resistance of the LLZ (bulk and grain boundary) and the other is the Li metal-LLZ interfacial resistance. Thus, the overall Li metal-LLZ interfacial resistance is 1849 Ohm*cm^2. Since two Li metal-LLZ interfaces are present in the Li/LLZ/Li symmetric cells, the single Li metal-LLZ interfacial resistance is approximately 925 Ohm*cm^2. On the other hand, the Si-coated LLZ cell displays a much smaller resistance of 469 Ohm*cm^2 in the first semi-circle. By subtracting the resistance of the LLZ (215 Ohm*cm^2) and dividing by two, the Li metal/Si-coated LLZ interfacial resistance can be calculated: 127 Ohm*cm^2, which is about 7.3 times lower than bare LLZ.

c. Al interface

Two symmetric cells, Li | Garnet SSE | Li and Li | Al-Garnet SSE-Al | Li, were prepared and tested directly in an argon-filled glovebox. The two cells showed large differences in total resistance, which depend on both the garnet's total resistance and the interface charge transfer resistance, as shown in the Nyquist plots (Figure V-215a and Figure V-215b). The Li | Garnet SSE | Li cell had a total resistance of ~2000 Ohm*cm^2. However, the Li | Al-Garnet SSE-Al | Li cell exhibited a resistance of ~300 Ohm*cm^2, which is almost one order of

magnitude smaller than the uncoated SSE. The small partial semicircle at high frequency can be assigned to the total resistance of the garnet material. The large semicircle at medium frequency and low frequency correspond to the charge transfer resistance, which is the combination of the solid-state electrolyte resistance as well as the Li interfaces within the symmetric cells. The decreased size of the semicircle indicates that the interfacial resistance was significantly reduced using the Al coating. The total garnet resistance was ~150 Ohm*cm^2 and remained unchanged during the Li melting process. By subtracting the garnet ASR, the Li | Garnet SSE | Li cell charge transfer resistance was ~1900 Ohm*cm^2 at 20°C. For the Li | Al-Garnet SSE-Al | Li cell, the charge transfer resistance was decreased to ~150 Ohm*cm^2. Note that the interfacial resistance corresponds to two symmetric interfaces. Therefore, the interfacial resistance is ~950 Ohm*cm^2 and ~75 Ohm*cm^2 for Li | Garnet SSE and Li | Al-Garnet SSE-Al, respectively.

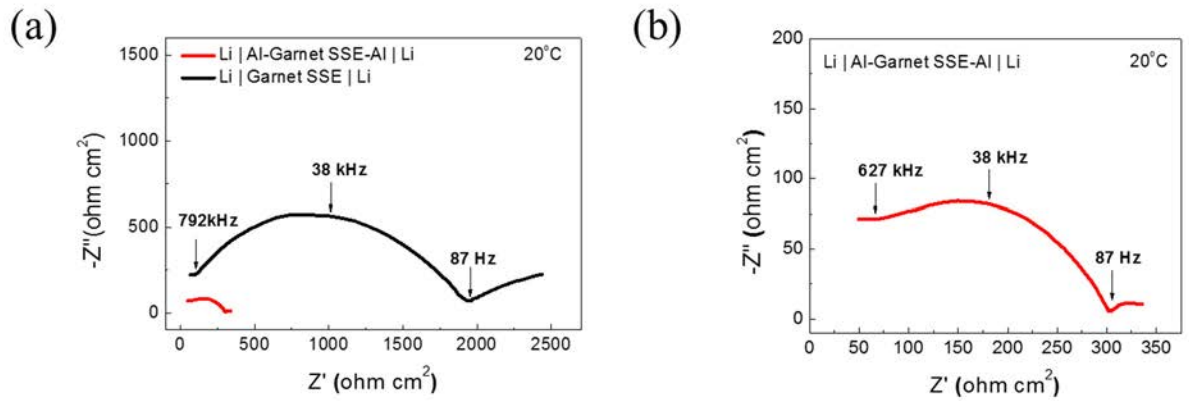

Figure V-215: Nyquist plots of Li | Garnet SSE | Li (a) and Li | Al-Garnet SSE-Al | Li (b) in the frequency of 1 MHz to 100 mHz at 20 ˚C

d. ALD Al_2O_3 interface

To make Li/garnet/Li symmetric cell with ALD Al_2O_3 interface, a ~ 5-6 nm thick ALD-Al_2O_3 coating was applied to the garnet surface. Then a piece of Li metal foil was pressed on the garnet pellets and heated at 250°C for 1 hour under a small pressure. A control sample was made using bare LLCZN pellets in the same way. Figure V-216a shows the schematic of the interface between garnet and Li metal. The SEM images in Figure V-216b clearly demonstrated that the enhancement of interfacial contact by applying ALD Al_2O_3 ultrathin layer on garnet interface. Inset are photo images to show the surface wetting of garnet and the ALD treated garnet. To quantify the effect of ALD on the improvement of garnet/Li interface, symmetric Li/garnet/Li cells were prepared and evaluated by EIS. As shown in Figure V-216c, two distinct arcs were seen in each sample. The bulk garnet ASRs, obtained from the high frequency intercept, are 26 and 28 Ohm*cm^2 for cells with and without ALD coating, respectively (Table V-6). The first arc represents most likely the grain boundary impedance which were 150 Ohm*cm^2 and 4500 Ohm*cm^2 for cells with and without ALD coating, respectively. The second lower frequency arc is characteristic of the interfacial impedance. Interfacial ASR was calculated by dividing this resistance by two before normalizing to the electrode surface area. It can be seen that the ALD treatment decreased the interfacial ASR by EIS from 490 Ohm*cm^2 to 16 Ohm*cm^2. The cells were also tested under DC cycling. As shown in Figure V-216d the symmetric cell with bare garnet had an unstable voltage profile with large voltage overpotential with peak voltage values over 4 volts. In contrast, for the symmetric cell with ALD treated garnet, the stable voltage profile with small voltage range demonstrates that the interfacial resistance between garnet and Li metal was effectively reduced. Inset gives a single cycle of the symmetric ALD treated garnet cell to show the small and flat voltage plateau (~15 mV). From this comparison, the Li/garnet/Li symmetric cell without ALD has an unstable DC resistance, over 260 times (4V/15mV) larger than the DC resistance of the cell treated with ALD. Figure V-216e presents the long-term cycling performance of the symmetric ALD treated garnet cell at a current density of 0.2 mA/cm^2. The cell voltage increased slightly from 15 mV to 20 mV after 30 hours and remained stable for 130 hrs. This cell voltage (20 mV) corresponds to a total cell ASR of 100 Ohm*cm^2 which is the sum of the total electrolyte ASR and both interfaces.

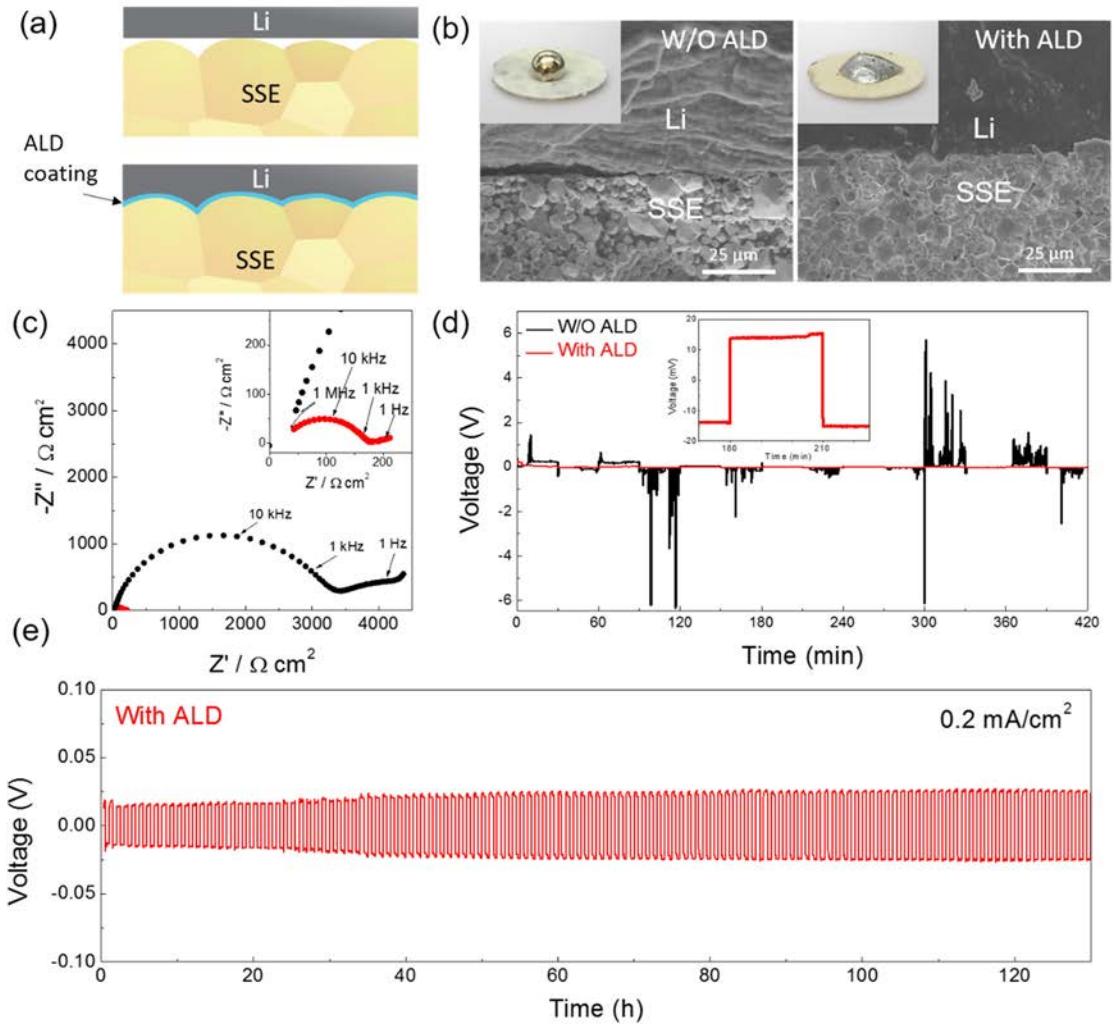

Figure V-216: Characterization of garnet solid state electrolyte/Li metal interface. (a) Schematic of the wetting behavior of garnet surface with molten Li. (b) SEM images of the garnet solid state electrolyte/Li metal interface. Without ALD Al_2O_3 coating, garnet has a poor interfacial contact with Li metal. Inset are photo images of contacts between melted Li metal and garnet surface. (c) Comparison of EIS profiles of the symmetric Li non-blocking garnet cells. Inset shows the enlarged impedance curve of the ALD treated garnet cell. (d) Comparison of Li tripping/plating behavior of the symmetric garnet SSE/Li cells. Inset is the one cycle of stripping/plating for the ALD treated garnet cell, exhibiting a low overall impedance and stable interfacial property. (e) Voltage profile of the ALD treated garnet symmetric cell at a current density of 0.2 mA/cm²

Table V-6: Electrochemical Impedance ASR with Fitting Data for Li/LLCZN/Li Cells with and without ALD Coating on Both Sides of Garnet SSEs

LLCZN SSE	Bulk ASR ($\Omega \cdot cm^2$)	Grain Boundary ASR ($\Omega \cdot cm^2$)	Grain Boundary Capacitance (F)	Interfacial ASR ($\Omega \cdot cm^2$)	Interfacial Capacitance (F)
No ALD	28	4500	2.09×10^{-9}	490	9.9×10^{-4}
ALD	26	150	3.09×10^{-9}	16	2.8×10^{-5}

3. Modeling of interfacial coating layers on garnet-electrode interfaces

We applied first principles calculations to investigate the interface stability between garnet and formed Li-Al alloys. We considered the interface as a pseudo-binary of Li-Al alloy and garnet, then constructed the related phase diagram to identify possible thermodynamically favorable reactions. The compositional phase diagrams were constructed, and the mutual reaction energy of the pseudo-binary calculated using the same approach defined in our previous work (Figure V-217). We found that three kinds of Li-Al alloy showed mutual reactions with garnet because of the slightly thermodynamic "welding" at their interface. Since the calculated reaction enthalpy is only around -60 ~ -40 meV/atom, the small reaction energy indicates that the interfacial reactions are likely to be limited and the formed interface could be relatively thermodynamic stable. Therefore, the interface between Li-Al alloy and garnet may exhibit good chemical stability, which might facilitate Li ion transport through. We apply the computational scheme to investigate interfacial chemical compatibility of these two interfaces with the coating layer with the SSE and LCO, respectively. The previously demonstrated coating layer materials, such as $Li_4Ti_5O_{12}$, $LiTaO_3$, $LiNbO_3$, Li_2SiO_3, and Li_3PO_4, have excellent chemical stability with the LCO and $L_{0.5}CO$ with zero or negligible decomposition energy $\Delta E_{\mathrm{D,min,mutual}}$ (Table V-7). In addition, all coating layer materials show relatively better stability with the sulfide SE comparing to the original sulfide SE-LCO interfaces, which have the interfacial reaction energy $\Delta E_{\mathrm{D,min,mutual}}$ of ~ -500 meV/atom. As a result, the interface with the coating layer has significantly improved stability and suppresses the formation of thick interphase layer. In addition to stabilizing the interface, the coating layer of only a few nanometers is significantly thinner than the decomposition interphase layer of ~10 to 100 nm. The reduced thickness of the coating layer may significantly reduce the high interfacial resistance caused by the thick decomposition interphase layer.

Table V-7: The Mutual Reaction Energy $\Delta E_{\mathrm{D,min,mutual}}$ (in meV/atom) of the Coating Layer Materials with the SSE or LCO Materials

	Li_3PS_4	LLZ	LCO	$L_{0.5}CO$
Li_4TiO_4	-125	0	0	-30
Li_2TiO_3	-75	-5	0	0
$Li_4Ti_5O_{12}$	-80	-75	-1	0
$Li_8Nb_2O_9$	-147	0	0	-20
Li_3NbO_4	-132	-4	0	0
$LiNbO_3$	-155	-76	0	0
$LiNb_3O_8$	-173	-115	-16	0
Li_8SiO_6	-177	0	-3	-50
Li_4SiO_4	-81	-1	0	-12
Li_2SiO_3	-19	-29	0	0
$Li_2Si_2O_5$	-10	-69	-4	0
Li_5TaO_5	-117	0	0	-32
Li_3TaO_4	-64	-3	0	0
$LiTaO_3$	-49	-68	0	0
$LiTa_3O_8$	-64	-105	-22	0
Li_3PO_4	0	0	0	0
$Li_4P_2O_7$	-9	-101	-44	-3
$LiPO_3$	-32	-201	-76	-19

In addition, we also computationally investigated other compounds (listed in Figure V-218 and Table V-7) based on the same cations, such as Ti, Nb, Si, Ta, and P, as potential coating layer materials. All these lithium metal oxide materials have a wide electrochemical window (Figure V-218a). The compounds with higher Li

content generally show lower reduction potential, and the compounds with lower Li content or higher O content show higher oxidation potential. Most of these compounds have excellent chemical stability against LCO and $L_{0.5}CO$ cathode materials with zero or small $\Delta E_{D,min,mutual}$ (Table V-7). All these coating layer materials significantly improve the stability of sulfide SSE-LCO interfaces. The chemical stability between LLZ-coating layer interface varies significantly with the compositions of the coating layer materials. The other Li-rich coating layers, such as Li_4TiO_4, Li_2TiO_3, Li_8SiO_6, Li_4SiO_4, Li_5TaO_5, and Li_3TaO_4 may work better with LLZ than those previously demonstrated for sulfide SEs, such as $Li_4Ti_5O_{12}$, $LiTaO_3$, and Li_2SiO_3.

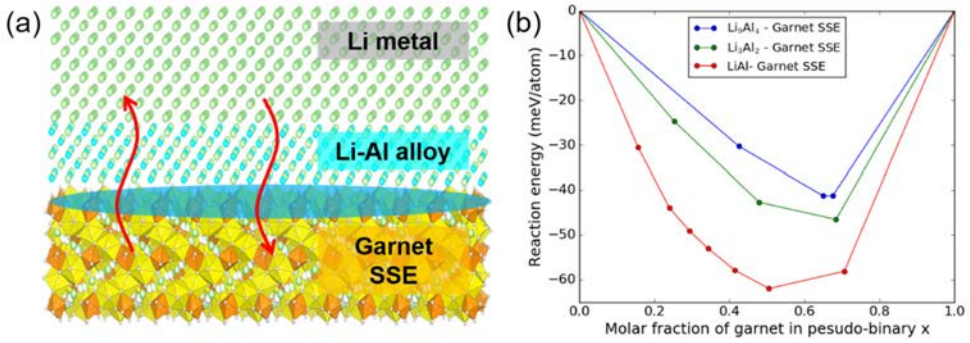

Figure V-217: Calculated mutual reaction energy, ΔED, of garnet and Li-Al alloy interfaces

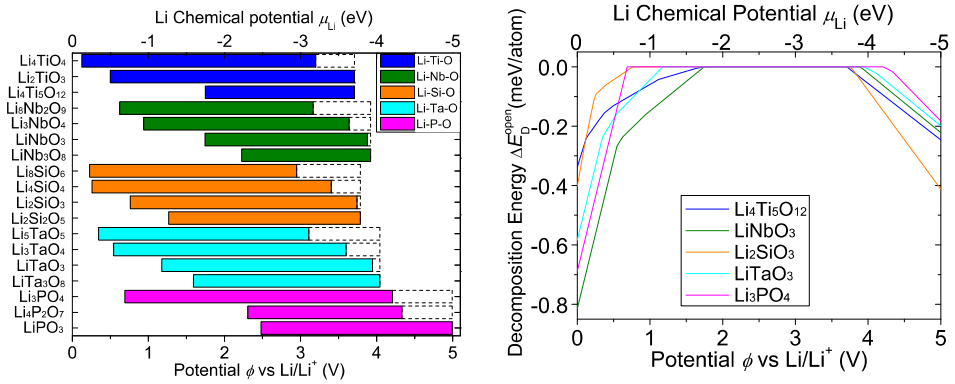

Figure V-218: Electrochemical window (left) and the decomposition energy ΔE_D^{open} (right) of the proposed and previously demonstrated coating layer materials applied between SSE and cathode materials. The dashed line in (a) marks the equilibrium voltage to fully delithiate the materials

Conclusions

For garnet-cathode interface:

- We demonstrated that gel electrolyte can reduce the interfacial resistance by over 4 orders of magnitude achieving an interfacial ASR of ~67 Ohm*cm^2 for planar cathode/garnet interface.
- We demonstrated that increasing surface area can effectively decrease the interface resistance, achieving a 52% decrease in interfacial ASR so far. Further increasing the surface area with 3D printing we expect we can decrease the above gel interface resistance with a planar structure by another 10X achieving an interfacial ASR of ~7 Ohm*cm^2.
- The aqueous interface lead to 7.5 Ohm*cm^2 cathode/garnet interfacial resistance at the planar cathode/garnet interface. Therefore, we have met the ~10 Ohm*cm^2 garnet/cathode milestone without need of modifying interface 3D structure.

For Li-garnet interface:

- We demonstrated gel electrolyte, Si, and Al can reduce interfacial resistance to 200 Ohm*cm^2, 127 Ohm*cm^2, and 75 Ohm*cm^2, respectively for planar Li metal-garnet interface.
- We further demonstrated that ALD-Al_2O_3 can reduce interfacial resistance to 16 Ohm*cm^2 for planar Li metal-garnet interface. Therefore, we have met the ~10 Ohm*cm^2 garnet/anode milestone.
- Similar to what was demonstrated with the cathode/electrolyte structure effect, we expect a 52% reduction (the same as the cathode) by using 3D printed garnet, as demonstrated in the report, this would correspond to only ~8 Ohm*cm^2 anode/garnet ASR. Moreover, increasing the surface area with 3D printing we expect we can decrease the above ALD interface resistance with a planar structure by another 10X.

Products

Presentations/Publications/Patents

1. Eric Wachsman, "All-Solid-State Lithium-ion Batteries for Transformational Energy Storage," June 28, 2016, Stanford University, Stanford, CA.
2. Eric Wachsman, "Ion Conducting Oxides for Electrochemical Energy Conversion and Storage," Nature Conference on Materials for Energy, June 11-14, 2016, Wuhan, China – Keynote.
3. Eric Wachsman, "Ion Conducting Oxides for Electrochemical Energy Conversion and Storage," March 18, 2016, University of South Carolina, Columbia, SC.
4. Eric Wachsman, "All-Solid-State Lithium-ion Batteries for Transformational Energy Storage," Materials Research Society, November 29 - December 4, 2015, Boston, MA.
5. Yizhou Zhu, Xingfeng He, Yifei Mo, "Stability of the Lithium Solid Electrolyte Materials and the Role of Interphases in All-Solid-State Lithium-ion Batteries: Insights from First Principles Calculations", Materials Research Society, Boston, MA (2015).
6. Eric Wachsman, "Overcoming Interfacial Impedance in Solid State Batteries," BMR Program Review, January 20-21, 2016, Berkeley, CA.
7. Yizhou Zhu, Xingfeng He, Yifei Mo*, "First Principles Study on Electrochemical and Chemical Stability of the Solid Electrolyte-Electrode Interfaces in All-Solid-State Lithium-ion Batteries", *Journal of Materials Chemistry A,* **2016,** 4, 3253-3266 (Featured front cover).
8. Yizhou Zhu, Xingfeng He, Yifei Mo*, "Origin of Outstanding Stability in the Lithium Solid Electrolyte Materials: Insights from Thermodynamic Analyses Based on First-Principles Calculations", *ACS Applied Materials & Interfaces,* **2015,** 7, 23685-23693.
9. Kun Fu, Yunhui Gong, Jiaqi Dai, Amy Gong, Xiaogang Han, Yonggang Yao, Chengwei Wang, Yibo Wang, Yanan Chen, Chaoyi Yan, Eric Wachsman, Liangbing Hu, "Flexible, Solid-State Lithium Ion-conducting Membrane with 3D Garnet Nanofiber Networks," *Proceedings of the National Academy of Sciences*, **2016,** 113 (26), 7094-7099.
10. Wei Luo, Yunhui Gong, Yizhou Zhu, Kun Fu, Jiaqi Dai, Steven D. Lacey, Chengwei Wang, Boyang Liu, Xiaogang Han, Yifei Mo, Eric Wachsman, Liangbing Hu, "Transition from Super-lithiophobicity to Super-lithiophilicity of Garnet Solid Electrolyte", *J. Am. Chem. Soc.*, **2016,** 138 (37), 12258–12262.
11. Xiaogang Han, Yunhui Gong, Xingfeng He, Gregory T. Hitz, Jiaqi Dai, Yifei Mo, Venkataraman Thangadurai, Eric Wachsman, Liangbing Hu, "Negating Interfacial Impedance in Garnet-Based Solid-State Li-Metal Batteries", *Nature Materials,* Accepted.
12. Kun Fu, Yunhui Gong, Boyang Liu, Yizhou Zhu, Shaomao Xu, Yonggang Yao, Wei Luo, Chengwei Wang, Steven Lacey, Jiaqi Dai, Yanan Chen, Yifei Mo, Eric Wachsman, Liangbing Hu, "Towards Garnet Electrolyte-based Li metal batteries: An ultrathin, highly effective artificial solid-state electrolyte/Li interface", *Science Advances,* Accepted.

References

1. Thangadurai, V.; Weppner, W., Recent progress in solid oxide and lithium ion conducting electrolytes research. *Ionics* **2006,** 12, 81-92.

2. Robertson, A. D.; West, A. R.; Ritchie, A. G., Review of crystalline lithium-ion conductors suitable for high temperature battery applications. *Solid State Ionics* **1997,** 104, 1-11.
3. Kamaya, N.; Homma, K.; Yamakawa, Y.; Hirayama, M.; Kanno, R.; Yonemura, M.; Kamiyama, T.; Kato, Y.; Hama, S.; Kawamoto, K.; Mitsui, A., A lithium superionic conductor. *Nature Materials* **2011,** 10, 682-686.
4. Thangadurai, V.; Kaack, H.; Weppner, W. J. F., Novel fast lithium ion conduction in garnet-type $Li_5La_3M_2O_{12}$ (M = Nb, Ta). *Journal of the American Ceramic Society* **2003,** 86, 437-440.
5. Thangadurai, V.; Weppner, W., Li(6)ALa(2)Ta(2)O(12) (A=Sr, Ba): Novel garnet-like oxides for fast lithium ion conduction. *Advanced Functional Materials* **2005,** 15, 107-112.
6. Murugan, R.; Thangadurai, V.; Weppner, W., Fast lithium ion conduction in garnet-type Li7La3Zr2O12. *Angewandte Chemie-International Edition* **2007,** 46, 7778-7781.

V.G.5. Nanoscale Interfacial Engineering for Stable Lithium Metal Anodes (Stanford University)

Yi Cui, Principal Investigator
Stanford University
Department of Materials Science and Engineering
Stanford, CA 94305
Phone: 650-723-4613; Fax: 650-736-1984
E-mail: yicui@stanford.edu

Tien Q. Duong, DOE Program Manager
U.S. Department of Energy
Advanced Battery Materials Research (BMR)
Vehicle Technologies Office
1000 Independence Avenue, SW
Washington, DC 20585
Phone: 202-586-7836
E-mail: Tien.Duong@ee.doe.gov

Start Date: October 1, 2015
End Date: September 30, 2016

Abstract

Objectives

This study aims to render lithium (Li) metal anode with high capacity and reliability by developing chemically and mechanically stable interfacial layers between Li metal and electrolytes, which is essential to couple with sulfur cathode for high-energy Li-sulfur batteries. With the nanoscale interfacial engineering approach, various kinds of advanced thin films will be introduced to overcome the issues related to dendritic growth, reactive surface and virtually “infinite” volume expansion of Li metal anode.

Accomplishments

- Achieve minimal volume change of the electrode by designing stable hosts for Li metal.
- Realize stabilized SEI and much more stable cycling.
- Prove highly improved rate capability in full cells.
- Further surface protection was employed to 3D Li.

Future Achievements

- Modified structure design for more efficient composite Li anodes.
- Further surface engineering based on the 3D Li architecture.
- Further improved power output and cycling stability.
- Stable full-cell operation with limited Li amount.

Technical Discussion

Background

The lithium-ion battery has gained great success as a power source for portable electronics, electric vehicles and grid scale energy storage. However, its energy density has achieved a bottleneck which calls for the further innovation of battery technologies especially those beyond lithium-ion. Li metal anode has long been regarded as the “holy grail” for Li battery research, which is not only due to its highest theoretical capacity of 3860 mAh/g and lowest electrochemical potential, but also its key role in Li-S and Li-air battery systems, both of which are the most prominent battery chemistries for the next-generation energy storage technology. However, many challenges have been encountered on its way to commercialization. Among all problems of Li metal, there are two root causes, namely high reactivity of Li and its infinite relative volume change during cycling. On one hand, the high reactivity of Li results in the excess side reactions once is exposed to liquid electrolyte, which further lead to complex interfacial chemistry, blocked ion transport and the consumption of materials. On the other hand, the infinite relative volume change makes the solid electrolyte interphase (SEI) prone to fracture, which not only creates hot spots for uneven lithium-ion flux distribution and thus dendritic deposition, but also exposes fresh Li for further side reactions, leading to low Coulombic efficiency. Under the circumstance, it is necessary to develop surface protection techniques as well as to improve the electrode volume stability in order to solve all the above-mentioned problems.

Introduction

In order to address the issue of infinite relative volume change during cycling, our group, for the first time, introduced stable “host” matrices for metallic Li. By screening a wide variety of possible host materials, suitable ones that have either natural ‘lithiophilicity’ (can be well-wetted by Li metal) or proper surface functionalization have been selected. Li was incorporated into the stable host matrices via thermal molten Li infusion and the electrochemical performance of the resulting three-dimensional (3D) composite Li electrodes were evaluated. The electrolyte interphase of the 3D composite electrodes was further engineered via means of rationally-designed artificial SEI to boost the cell cycling efficiency.

Approach

Carbon-based materials are the ideal hosts for Li due to the reason that they are among the lightest materials available for scaffold construction and can be engineered to have appealingly high surface area with excellent mechanical strength. Moreover, carbon materials are generally stable under the redox environment in Li batteries. Thus, we studied the relative affinity of Li for different carbon materials by contacting them with molten Li. It was found that different from other carbon materials, reduced graphene oxide (rGO) have a remarkably high ‘lithiophilicity’ thanks to the abundancy of polar surface functional groups. Therefore, free-standing GO film was obtained by vacuum filtration, followed by contacting the film with molten Li to obtain layered Li-rGO composite electrode. The morphology of the layered Li-rGO electrodes before and after electrochemical cycling was characterized and the electrochemical performance of the electrodes was evaluated using both symmetric cell configuration and Li-$LiCoO_2$ (LCO) full cell configuration.

For other suitable host materials without natural ‘lithiophilicity’, a universal surface coating method was developed. Specifically, a conformal layer of ZnO can be coated on to the host material by atomic layer deposition (ALD) such that the rapid chemical reaction between ZnO and molten Li can draw extra Li into the host matrix. Highly heat-resistant polyimide (PI) nanofibers were used as an example to demonstrate the effectiveness of ZnO coating on creating ‘lithiophilicity’. The properties of the resulting Li-PI composite electrode were evaluated.

Nanoscale interfacial engineering of the 3D Li metal electrodes is crucial to further improve their cycling efficiency and stability for practical applications. Therefore, an artificial SEI was developed with good mechanical strength, flexibility and lithium-ion conductivity using a composite of lithium-ion conducting inorganic nanoparticles embedded in a polymeric binder matrix. The cycling efficiencies with the protection of the artificial SEI on both Cu current collector and Li-PI composite were studied.

Results

We studied the relative affinity of Li for different carbon materials (Figure V-219). While most of the carbon materials have relatively weak binding with Li, reduced graphene oxide (rGO) exhibits surprisingly high lithiophilicity, which shall be attributed to the synergistic effect of the chemical reactions between Li and its oxygen-containing functional groups and the nano-capillary force from the nanoscale gaps between the rGO flakes.

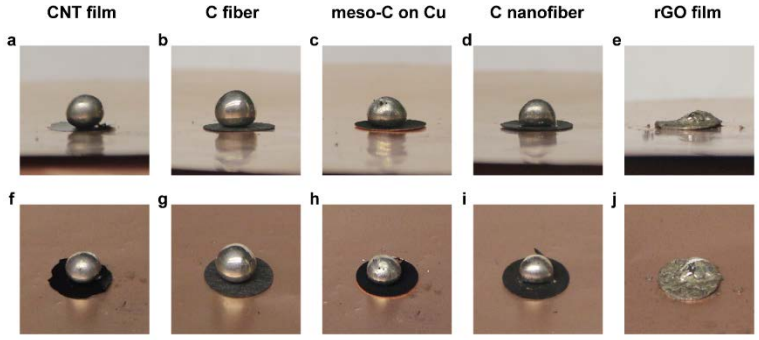

Figure V-219: Surface wetting of molten Li on different carbon materials, including carbon nanotubes (CNT) film (a,f), carbon fiber paper (b,g), mesoporous carbon coated on Cu foil (c,h), electrospun carbon nanofiber (d,i) and GO film
D. Lin, Y. Cui et al. Nature Nanotechnology

The intrinsic lithiophilicity of GO was utilized by directly contacting vacuum-filtrated GO film with molten Li and Li can be drawn rapidly into the matrix without any additional surface modification (Figure V-220). The resulting electrode can be described as a layered structure with Li uniformly infused into the nanogaps between rGO layers. This layered Li-rGO composite electrode can not only realize highly reduced dimension change during electrochemical cycling, effective dendrite suppression due to increased surface area and lithiophilic surface, but also the rGO cap layer can serve as a scaffold for SEI stabilization, improving the cycling Coulombic efficiency.

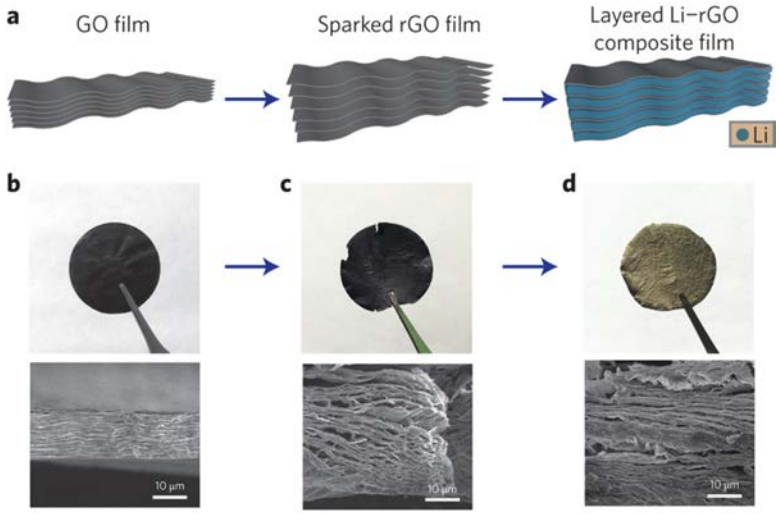

Figure V-220: Schematic of the material design and the consequent synthetic procedures from a GO film (left) to a sparked rGO film (middle) to a layered Li–rGO composite film (right). b–d, Corresponding digital camera images and SEM images of the GO film (b), sparked rGO film (c) and layered Li–rGO composite film (d). The diameters of the films shown in b–d are ~ 47 mm
D. Lin, Y. Cui et al. Nature Nanotechnology

To evaluate the cycling stability of the Li-rGO composite, symmetric cells were assembled and compared. It was found that the Li-rGO symmetric cells exhibits much more stable cycling for prolonged cycles, while the Li foil counterpart encountered soft short circuit within tens of cycles, which is a result of the dendrite propagation. In addition, consistently low overpotential with flat voltage plateaus was attained at various current density from 1-3 mA/cm2, which can be attributed to the increased active surface area and the pre-engineered nucleation sites within the composite. (See Figure V-221.)

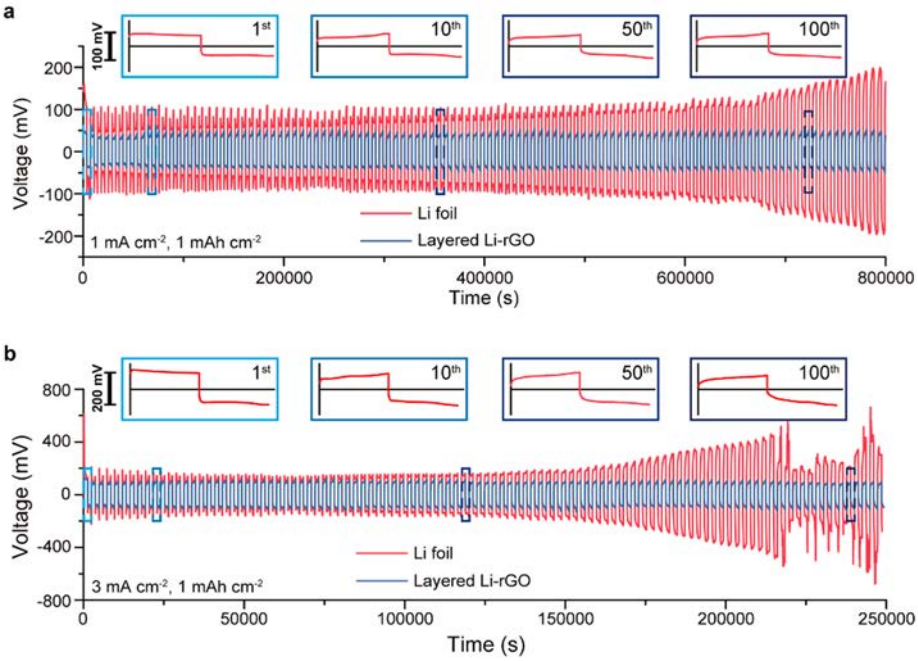

Figure V-221: Comparison of the cycling stability of the layered Li-rGO and the bare Li electrode at a current density of (a) 1 mA/cm² and (b) 3 mA/cm² with a fixed capacity of 1 mAh/cm²
D. Lin, Y. Cui et al. Nature Nanotechnology

When paired with LCO cathode, the layered Li–rGO anodes consistently exhibited a much better rate capability and lower hysteresis compare to Li foil (Figure V-222). With Li–rGO anodes, a much higher LCO capacity can be retained especially at a high rate (~110 mAh g–1 at 4 C and ~70 mAh g–1 at 10 C).

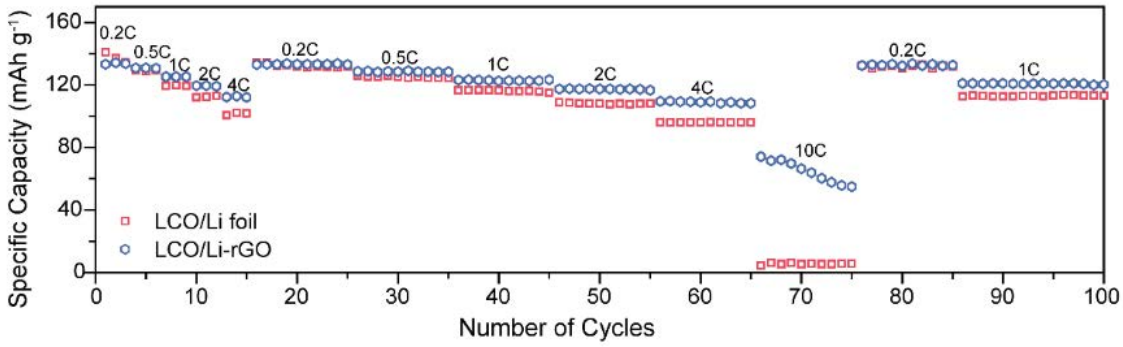

Figure V-222: Rate capability of the LCO/Li–rGO and LCO/Li foil cells at various rates from 0.2 C to 10 C.
D. Lin, Y. Cui et al.

Excellent lithiophilicity of the host materials is required for molten Li infusion. However, unlike rGO, most available materials cannot be well-wetted by molten Li. In this circumstance, we further developed a universal surface functionalization method to afford lithiophilicity via a thin and conformal ALD ZnO coating. This can be explained by the spontaneous reaction between ZnO and molten Li, which afford more lithiophilic species (Li_xZn/Li_2O) on the surface. As a demonstration, electrospun PI nanofibers were treated with ZnO after which molten Li can steadily infuse into the matrix (Figure V-223). The inert PI fiber served as stable host matrix for

Li metal, which achieved minimum volume change during electrochemical cycling and stable voltage profiles in symmetric cell configuration (Figure V-224).

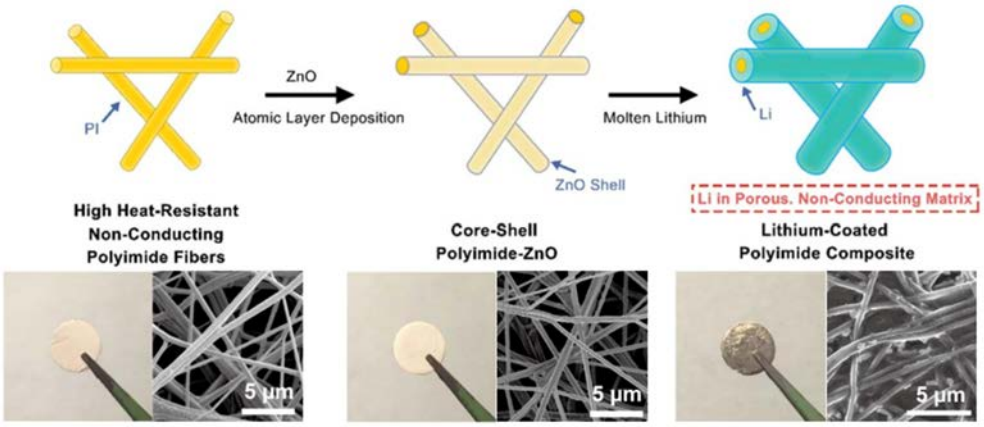

Figure V-223: Schematic of the fabrication of the Li-PI composite electrode. Electrospun PI was coated with a layer of ZnO via ALD to form core-shell PI-ZnO. The existence of ZnO coating renders the matrix "lithiophilic" such that molten Li can steadily infuse into the matrix. The final structure of the electrode is Li coated onto a porous, non-conducting polymeric matrix
Y. Liu, Y. Cui et al. Nature Communications

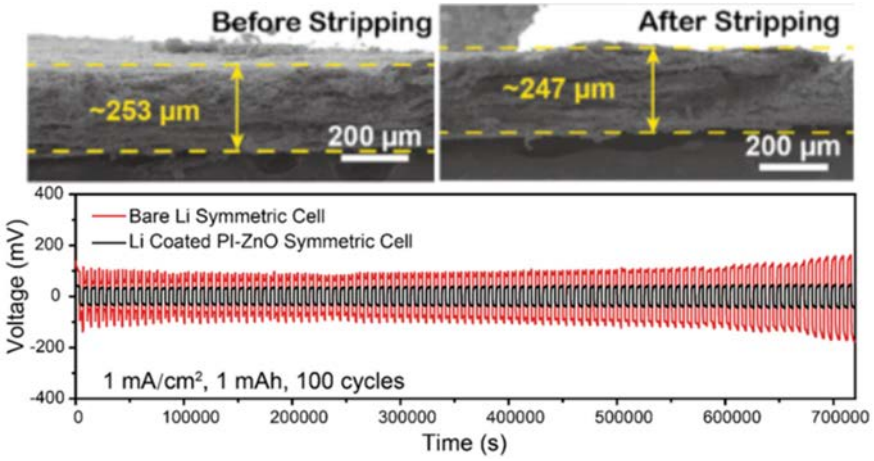

Figure V-224: Electrochemical behaviors of the Li-PI electrodes in EC/DEC electrolyte. (top) Cross-sectional SEM images of nanoporous Li-PI anode before and after complete Li stripping. (bottom) Comparison of the cycling stability of the Li-PI and the bare Li electrode at a current density of 1 mA/cm^2 with fixed capacity of 1 mAh/cm^2
Y. Liu, Y. Cui et al. Nature Communications

We studied the detailed plating/stripping behavior of the electrode and found that Li can be well-confined within the matrix during galvanostatic cycling (Figure V-225). Top fibers were exposed after stripping away 5 mAh/cm^2 Li indicating the top Li layers were dissolved more favorably during stripping. Subsequently, when 3 mAh/cm^2 Li was plated, Li was deposited into the matrix and partially filled the space between the fibers. When all the stripped Li was plated back, the top surface of the matrix was covered again by Li with no discernable dendrites. The well-confined behavior can be rationalized by the electrically insulating polymeric surface such that the metallic Li confined within the matrix served as the only electron conductor for Li deposition. On the contrary, if electrons could be efficiently transported to the electrolyte-facing top surface, undesirable stripping/plating behavior may occur after recurrent cycles. Direct Li nucleation on the top surface might be easier due to the high availability of both electrons and Li ions, which provides favorable sites for dendrite growth while leaving the interior voids empty.

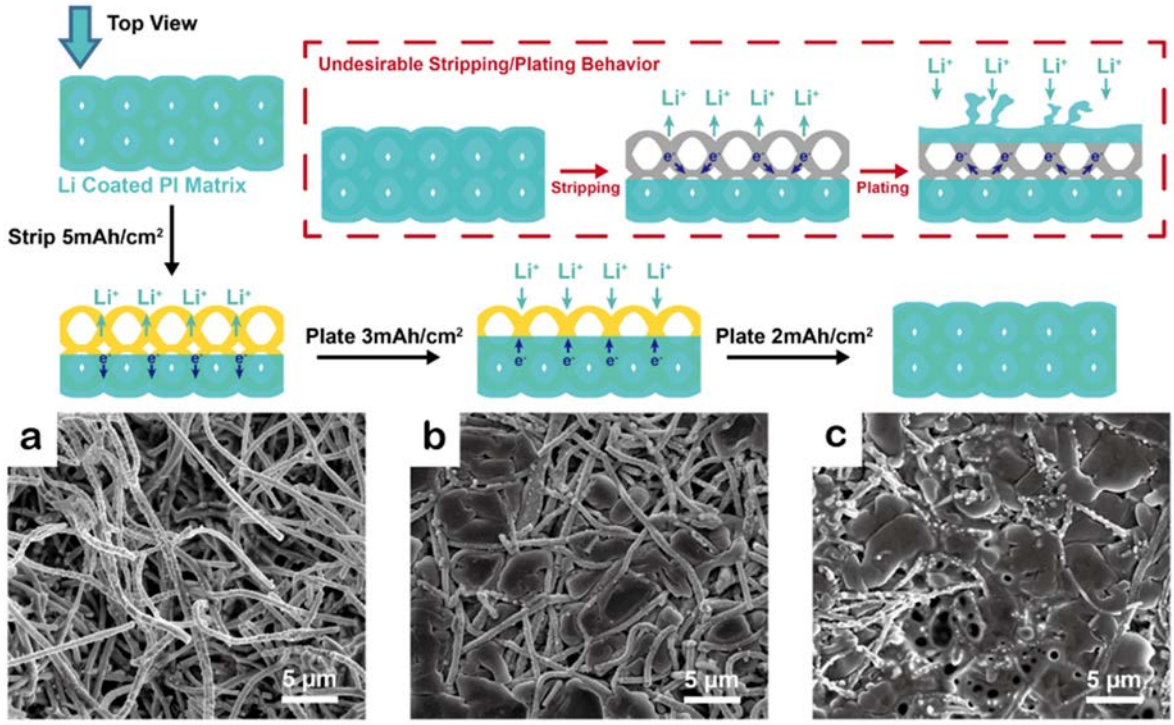

Figure V-225: SEM images and schematics showing the well-confined stripping/plating behavior of the Li-PI electrode. (a) exposed top fibers after stripping away 5 mAh/cm² Li, (b) exposed top fibers partially filled with Li when plating 3 mAh/cm² Li back and (c) completely filled matrix after plating an additional 2 mAh/cm² Li back. The top-right schematic illustrates the alternative undesirable Li stripping/plating where after striping, Li nucleate on the top surface, leading to volume change and dendrites shooting out of the matrix

Y. Liu, Y. Cui et al. Nature Communications

To test the Coulombic efficiency, hereby, the obtained nanoporous Li-PI (10 mAh/cm^2) electrode was paired with lithium titanate (LTO, 3 mAh/cm^2) cathode to study its performance in a full cell configuration (Figure V-226). The slightly oversized nanoporous Li-LTO exhibited outstanding cycling stability of more than 100 cycles compare to bare Li foil (50 μm, ~ 10 mAh/cm^2) or electrodeposited Li, confirming the improved Coulombic efficiency of the Li-PI nanoporous electrode.

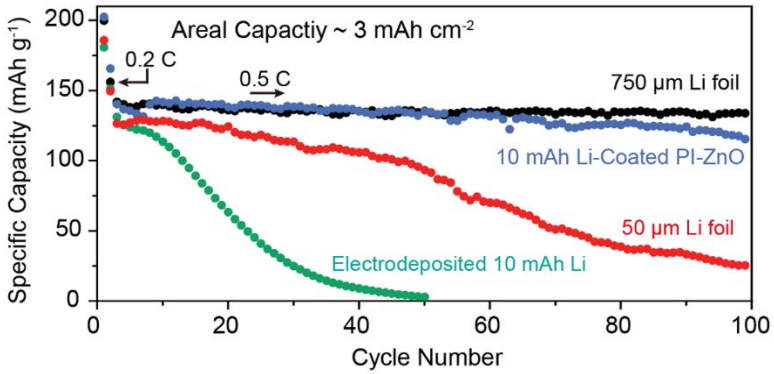

Figure V-226: Discharge capacity of various Li metal anode- LTO cathode full cells for the first 100 galvanostatic cycles in EC/DEC with 1 vol % vinylene carbonate. Rate was set at 0.2 C for the first 2 cycles and 0.5 C for later cycles (1 C = 170 mA/g)

Y. Liu, Y. Cui et al. Nature Communications

The introduction of stable hosts for metallic Li such as layered rGO and nanofibers with lithiophilic coatings has been proven a success in minimizing the volumetric change at the whole electrode level as well as reducing the effective current density and the degree of interface fluctuation during cycling, leading to more

uniform Li deposition with greatly improved cycling stability. Engineering the SEI layer on 3D porous Li electrodes shall be the next step needed to further improve the cycling efficiency. Several requirements need to be satisfied for an ideal SEI layer: (1) High degrees of homogeneity (composition and morphology, etc.) to prevent only limited locations of Li metal nucleation and growth; (2) High elastic modulus and compact structure to mechanically suppress Li dendrite; (3) Sufficient flexibility to accommodate the ineligible interface fluctuation during cycling without repeated breakdown/repair; (4) And importantly, high ionic conductivity to facilitate the uniform transport of lithium ions throughout the whole electrode surface.

We proposed a composite artificial SEI layer design for the stabilization of Li metal anode, which shall be composed of a mechanically robust and lithium-ion conducting inorganic phase connected by a flexible organic binder to maintain structural integrity during cycling. Cu_3N nanoparticles were chosen as the inorganic phase and a common binder material, styrene-butadiene rubber (SBR) as the polymeric phase (Figure V-227). Sub 100-nm Cu_3N nanoparticles can be facilely obtained by a one-step solution reaction and afford a stable dispersion with SBR in solvents such as tetrahydrofuran. Notably, the Cu_3N nanoparticles will be passivated spontaneously when in contact with metallic Li to form Li_3N, which is among one of the fastest lithium-ion conductors with ionic conductivity on the order of ~10-3 - 10-4 S/cm at room temperature.

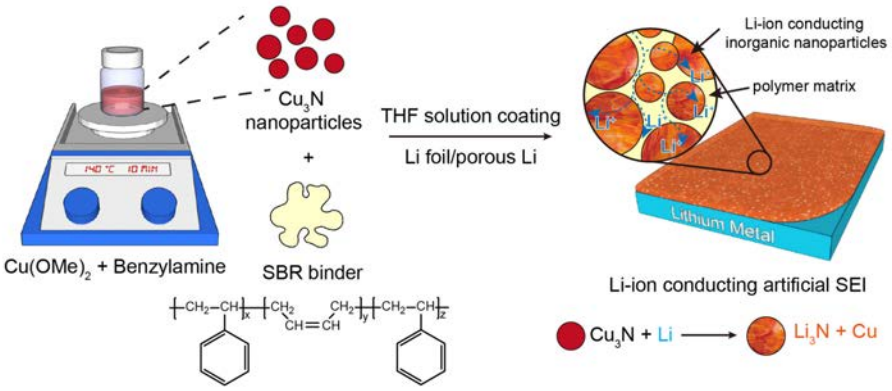

Figure V-227: Schematic illustration of the fabrication of the highly lithium-ion conducting Cu_3N+SBR composite artificial SEI
Y. Liu, Y. Cui et al. Advanced Materials

Though it remains a great challenge to determine the exact Coulombic efficiency of anodes with pre-stored Li, measuring the value on Cu_3N+SBR protected Cu current collectors could serve as a direct evidence of the stabilizing effect our proposed artificial SEI layer when applied on Li metal surface. As can be seen from Figure V-228a, at a current density of 1 mA/cm2 in carbonate electrolyte (1 M lithium hexafluorophosphate in 1:1 ethylene carbonate/diethyl carbonate with 10 wt% fluoroethylene carbonate additive, EC/DEC), the Coulombic efficiency of bare Cu started at around 95% and quickly decayed to merely 70% within 50 stripping/plating cycles due to the growth of Li dendrites and the continuous breakdown/repair of SEI that consumed both Li and the electrolyte. The Cu_3N+SBR protected Cu demonstrated a much improved Coulombic efficiency of ~97.4% averaged between the 20th to 70th cycle and such high efficiency performance was able to sustain for more than 100 cycles. In addition, the overpotential increase due to the existence of the artificial SEI was minimal (Figure V-228a inset), thanks to its relatively high ionic conductivity. Since the effective current density can be significantly reduced on porous Li metal anodes, Coulombic efficiency at a lower current density of 0.25 mA/cm^2 was also studied to better resemble the real working condition of the artificial SEI protected porous Li. With reduced current density, the Coulombic efficiency increased to as high as ~ 98%, which was stable for at least 150 cycles (Figure V-228b). To further investigate the stabilizing effect of the artificial SEI layer, Cu_3N+SBR was doctor bladed on Li foil surface (Figure V-228c), and electrochemical impedance spectroscopy (EIS) measurements in symmetric cell configuration were performed during continuous cycling in EC/DEC electrolyte (Figure V-228d). Noticeably, a continuous increase in the RSEI (impedance of the SEI layer) value was observed for bare Li foil, which indicates the repeating breakdown/repair of the native SEI during cycling. Nevertheless, Li protected by the artificial SEI layer showed nearly constant RSEI throughout 200 cycles. Thus, it is evident that the Cu_3N+SBR coating is beneficial in forming a stable and less resistive SEI layer on Li metal surface during prolonged battery cycling.

Finally, when tested on 3D Li-PI metal anode pairing with LTO, stable cycling was sustained for at least 90 cycles (Coulombic efficiency ~ 97.4%, the actual value shall be even higher considering the low first cycle Coulombic efficiency of LTO) compared to ~ 70 cycles for the unprotected one. The indirect method demonstrates the effectiveness of the artificial SEI coating on further improving the performance of porous Li metal anode towards practical battery applications.

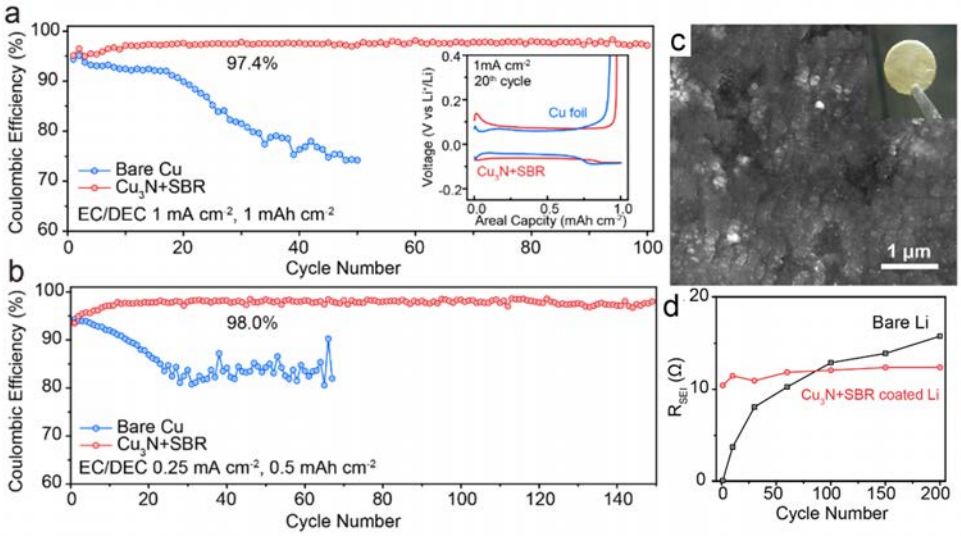

Figure V-228: Coulombic efficiency of Cu_3N+SBR artificial SEI protected Cu foil and bare Cu foil at a current density of (a) 1 mA/cm² (cycling capacity 1 mAh/cm²; inset, the corresponding voltage profiles at the 20th cycle) and (b) 0.25 mA/cm² (cycling capacity 0.5 mAh/cm²). (c) SEM image and digital photography of the Cu_3N+SBR protected Li metal foil. (d) Summary of the RSEI value as a function of cycle number using symmetric cell configuration

Y. Liu, Y. Cui et al. Advanced Materials

Conclusions

In all, in the past one year, we have made exciting progress in designing stable host for Li metal to afford minimal volume change. The new design principle, which emphasizes the importance of minimal volume change on interfacial stability, lithium-ion flux homogeneity and dendrite suppression, is proposed and widely accepted. To fulfill the design, layered Li-rGO composite electrodes were developed. Due to the unique "lithiophilic" nature of rGO, Li can be easily infused into the nanoscale interlayer gaps of rGO to afford a composite. The composite electrodes exhibit highly reduced volume change from infinity to ~20%, offering more stable electrode dimension during cycling. With the rGO as the support, SEI can be stabilized and thus more uniform Li deposition with suppressed dendrite can be observed. Since lithium-ion flux was homogenized with 3D form of Li, more stable cycling at high current density various from 1 to 3 mA/cm^2 was achieved, outperforming the conventional Li foil counterpart. Moreover, full cells with LCO as the cathode were further proven, which exhibits highly improved rate capability especially at high rate of 4-10 C.

To fabricate the 3D form of composite with pre-stored Li in the matrix, it is important to afford "lithiophilic" property for the matrix, which is, however, not observed for most of the materials. As a consequence, it is of great promise to develop surface modification techniques to turn a 'lithiophobic' surface into 'lithiophilic'. In this consideration, we developed a universal surface coating technique to achieve the goal. It was found that these surface coatings can be applied universally to all kinds of materials to afford lithiophilic surface, which largely extend the material choices for constructing the stable host.

Once the stable dimension has been obtained, it is necessary to further protect the Li surface. Due to the 3D form of Li, the exposed surface area is highly increased. As a consequence, passivating the surface is meaningful to reduce the initial SEI formation reactions and build a more stable interface. An artificial SEI layer composed of SBR rubber and embedded Cu_3N nanoparticles was developed for this purpose. The Cu_3N can be spontaneously converted into highly lithium-ion conductive Li_3N, which can help homogenizing the lithium-ion distribution. The SBR rubber can perform as a flexible and robust surface support for the as-formed SEI.

Products

Presentations/Publications/Patents

1. (Plenary) "Nanomaterials Design for Energy Conversion and Storage" 1st International Symposium on Energy Chemistry and Materials", October 29-31, 2015, Fudan University, Shanghai, China.
2. (Plenary) "Electrochemical Nanotechnology: Batteries and Electrocatalysts" International Conference on Innovative Electrochemical Energy Materials and Technologies (EEMT2015), Nanning, China, November 8-11, 2015.
3. (Invited) "Nanomaterials Design of Batteries Guided by *In-Operando* Characterization and Atomistic Simulation", Gordon Research Conference on Batteries, Feb. 21-26, 2016, Ventura, California.

References

1. D. Lin, Y. Liu, Z. Liang, H.-W. Lee, J. Sun, H. Wang, K. Yan, J. Xie, Y. Cui, Nat. Nanotechnol. 2016, 11, 626.
2. Y. Liu, D. Lin, Z. Liang, J. Zhao, K. Yan, Y. Cui, Nat. Commun. 2016, 7, 10992.
3. Z. Liang, D. Lin, J. Zhao, Z. Lu, Y. Liu, C. Liu, Y. Lu, H. Wang, K. Yan, X. Tao, Y. Cui, Proc. Natl. Acad. Sci. U.S.A. 2016, 113, 2862.
4. Y. Liu, D. Lin, P. Y. Yuen, K. Liu, J. Xie, R. H. Dauskardt, Y. Cui, Adv. Mater. in Press.

V.G.6. Lithium Dendrite Suppression for Lithium-Ion Batteries (PNNL)

Wu Xu, Principal Investigator
Pacific Northwest National Laboratory
902 Battelle Boulevard
Richland, WA 99354
Phone: 509-375-6934; Fax: 509-375-2186
E-mail: wu.xu@pnnl.gov

Ji-Guang Zhang, Co-Principal Investigator
Pacific Northwest National Laboratory
902 Battelle Boulevard
Richland, WA 99354
Phone: 509-372-6515; Fax: 509-375-2186
E-mail: jiguang.zhang@pnnl.gov

Tien Q. Duong, DOE Program Manager
U.S. Department of Energy
Advanced Battery Materials Research (BMR)
Vehicle Technologies Office
1000 Independence Avenue, SW
Washington, DC 20585
Phone: 202-586-7836
E-mail: Tien.Duong@ee.doe.gov

Start Date: October 1, 2015
End Date: September 30, 2018

Abstract

Objectives

- Prevent lithium (Li) dendrite formation on Li-metal anodes in Li-metal batteries and on carbon anodes in lithium-ion batteries.
- Enable Li metal to be used as an effective anode in rechargeable Li-metal batteries for long cycle life at a current density suitable for practical applications.
- Explore various factors that affect the morphology of Li deposition, especially under high current density conditions.

Accomplishments

- Optimized the charge/discharge protocol to improve the performance of Li metal batteries. The optimized cycling protocol of slow charge and fast discharge can form a transient high-concentration electrolyte layer on Li surface to protect Li metal anode and to enable sustainable operation of Li metal batteries.
- Developed dual-salt electrolytes to improve charge rate and long-term cycling stability of Li metal batteries
  - Developed LiTFSI-LiBOB and other dual-salt electrolytes with or without additives that can form highly conductive SEI, protect Li metal, and enable long cycle life and fast chargeability of Li metal batteries.
  - Achieved at least 500 stable cycles of Li||NMC cells with 1.75 mAh cm^{-2} loading at charging/discharging current density of 1.75 mA cm^{-2}.
  - Demonstrated Li||NMC cells with 3.0 mAh cm^{-2} loading for stable cycling of more than 100 cycles at 3.0 mA cm^{-2}, 300 cycles at 1.0 mA cm^{-2} and at least 500 cycles at 0.6 mA cm^{-2}.

- Identified the major components in the SEI layers on Li metal anode from dual-salt + additive electrolytes.

Future Achievements

- Verify the formation of a transient high Li^+-concentration electrolyte layer during fast discharging (Li^+ stripping from Li anode).
- Identify the effects of dual-salt electrolytes on Li metal protection during fast charging.
- Identify new electrolytes that are stable with both Li and high voltage cathode.
- Increase CE of Li cycling to be more than 98%.

Technical Discussion

Background

Li dendrite growth and low Coulombic efficiency (CE) during Li deposition/stripping are the two major problems hindering the application of Li metal as an anode material in rechargeable Li metal batteries for their commercial applications.

Introduction

Li-metal batteries are regarded as "Holy Grail" of high-energy-density systems because the Li-metal anode has an ultrahigh theoretical specific capacity (3860 mAh g^{-1}), low density (0.534 g cm^{-3}), and the lowest negative electrochemical potential (-3.040 V vs. standard hydrogen electrode). However, two major problems—Li dendrite growth and low CE of Li deposition/stripping—hinder their commercial applications. The dendritic Li generated at the anode surface can be self-amplified and lead to internal short circuiting of the battery and even more serious safety problems such as thermal runaway, fire, and explosion.[1] Ether-based electrolytes, especially at high salt concentrations have been reported to have high CEs of Li deposition/stripping. However, these ether based electrolytes will be readily oxidized at voltages at about 4 V vs. Li/Li^+ so most of the conventional transition metal oxide cathodes cannot be used, which limits the energy density of the Li-metal batteries.[2,3] On the other hand, the conventional $LiPF_6$/organic carbonate electrolytes used in the state-of-the-art lithium-ion batteries are stable up to at least 4.3 V so conventional cathode materials of ≥4 V can be used in Li-metal batteries to achieve high energy densities.[2] However, the conventional $LiPF_6$/organic carbonate electrolytes have low CEs of about 80%.[4,5] The solid electrolyte interphase (SEI) layer on Li anode surface builds up quickly when Li deposition is conducted at high current densities, causing significant change in the morphologies of Li meal anode. Currently the Li metal anode cannot work well for more than 100 cycles at current densities above 1.0 mA cm^{-2} in conventional carbonate-based electrolytes.[6] The real current density is reduced when a high loading cathode is used in the Li metal battery, which greatly limits their applications in practical Li metal batteries. Therefore, a general solution to form a robust, thin, uniform, and compact SEI layer on a Li-metal anode surface will not only suppress the dendrite growth problem, but also enhance the performance of Li metal batteries in terms of long-term cycling stability, rate capacity, and a wide operating temperature range.

Approach

The following approaches will be used to reach the objectives outlined above. First, the effects of charge/discharge protocol on the stability of Li metal anode and the performances of Li metal batteries will be investigated with a conventional $LiPF_6$/carbonate electrolyte to obtain an optimal charge/discharge protocol. Second, dual-salt electrolytes will be further investigated to form highly conductive SEI, protect Li metal, and enable long cycle life and fast chargeability of Li metal batteries. Finally, the effect of the dual-salt electrolytes on the battery performances of Li metal batteries with 4-V cathode and high areal loading of the cathode active material will be investigated. Various characterization technologies, including high-resolution scanning electron microscopy (SEM), transmission electron microscopy (TEM) and X-ray photoelectron spectroscopy (XPS) will be used to analyze the morphology and composition of the interfacial films on Li-metal surfaces.

The results obtained in these investigations will be combined with density functional theory (DFT) calculations to reveal the mechanism that leads to the enhanced performance in Li-metal batteries.

Results

1. Optimized the charge/discharge protocol for the improved performance of Li metal batteries

The effect of discharging current density on the cycling performance of Li metal cells was studied. Similar to the charge current density, the discharge rate also greatly affects the cycling stability of Li metal batteries (Figure V-229). For Li||$LiNi_{0.4}Mn_{0.4}Co_{0.2}O_2$ (NMC) cells with an areal capacity of 2.0 mAh cm^{-2}, discharge rates at and higher than 1C (i.e. 2.0 mA cm^{-2}) result in stable cycling for at least 150 cycles while the discharge at less than 1C rate leads to fast capacity fading (Figure V-229a). The evolution of charge/discharge voltage profiles at discharge rate of C/10 (Figure V-229b) and 1C (Figure V-229c) corroborates the above finding. When the charge/discharge current density was switched back to C/10 after 150 cycles at C/3 charge and various discharge rates (Figure V-229d), the cells cycled at and above 1C discharge rate can go back to the initial values, demonstrating the good stability; however, the cells previously discharged at low rates cannot, indicating the capacity degradation is irreversible.

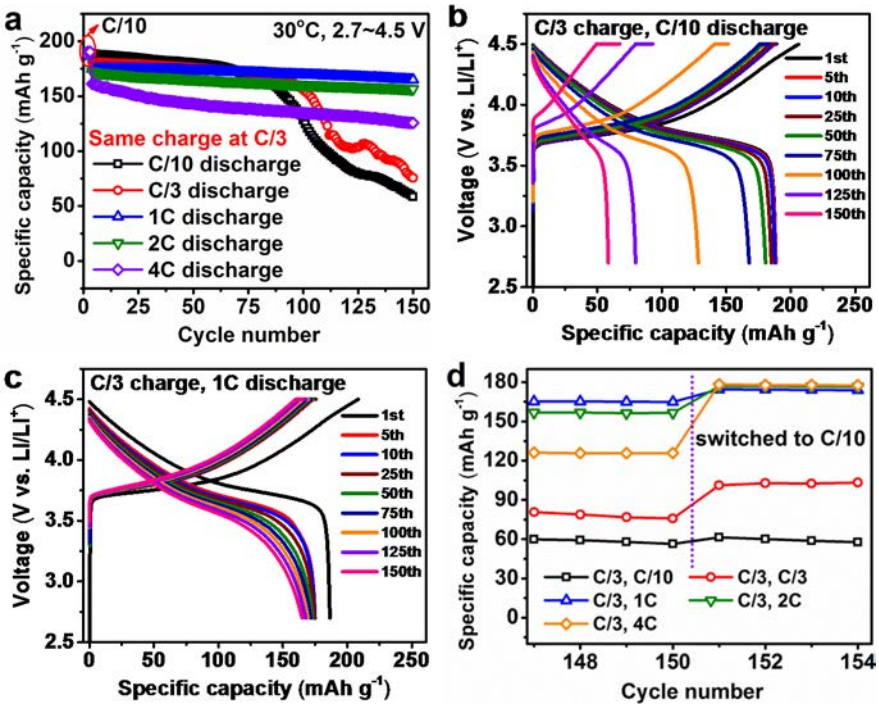

Figure V-229: (a) Cycling stability of Li||NMC cells using $LiPF_6$ electrolyte at different discharge rates. (b, c) Evolution of charge/discharge voltage profiles at C/10 (b) and 1C (c) discharge. (d) Discharge capacities at C/10 after 150 cycles from (a). For all cells, the formation cycles were conducted at C/10 rate, and all other charge processes were performed at C/3 rate

The morphologies of the cycled Li metal anodes were characterized using SEM and are shown in Figure V-230. Striking differences are identified on the Li metal anodes cycled at different discharge rates. At low discharge rates (C/10 to C/3), significant cracking of the surface films (Figure V-230a, b) and severe corrosion to bulk Li anode (Figure V-230e, f) are observed throughout the Li metal anode after cycling. It is indicated that the quality of the SEI layer formed on the Li metal surface is poor and cannot protect bulk Li from electrolyte corrosion when it is cycled at low discharge rates. The continuous reactions between electrolyte and Li metal anode not only consume the Li metal as well as the solvent and lithium salt of the electrolyte, but also generate a large amount of inert byproducts on the Li metal surface. The loose structure of the redeposited Li particles after low discharge rate (C/10) cycling leads to significant volume expansion of Li metal anode (~700 μm) as shown in Figure V-230e. Consequently, the cell impedance (Figure V-230i-k) increases quickly which leads to the early termination of stable cycling of Li metal cells. However, the morphologies of the cycled Li

metal anodes when the discharge rate is increased to 1C or higher are much different. From the top view (Figure V-230c, d) it is surprising to find that the Li surface is covered by a protecting SEI layer without any cracks although some surface variations are observed in the protecting layer. This SEI layer prevents the further penetration of electrolyte and the continuous reactions between Li metal and the electrolyte. As a result, the bulk of the Li metal is well protected as shown in the cross section SEM images shown in Figure V-230g, h. These cross-section images are very close to those of the fresh Li. The well protected Li metal leads to lower electrolyte resistance (R_e), surface film resistance (R_{sf}) and charge transfer resistance (R_{ct}) (Figure V-230k). Therefore, the cycle life of the Li metal batteries operated at relatively higher discharge rates are significantly improved.

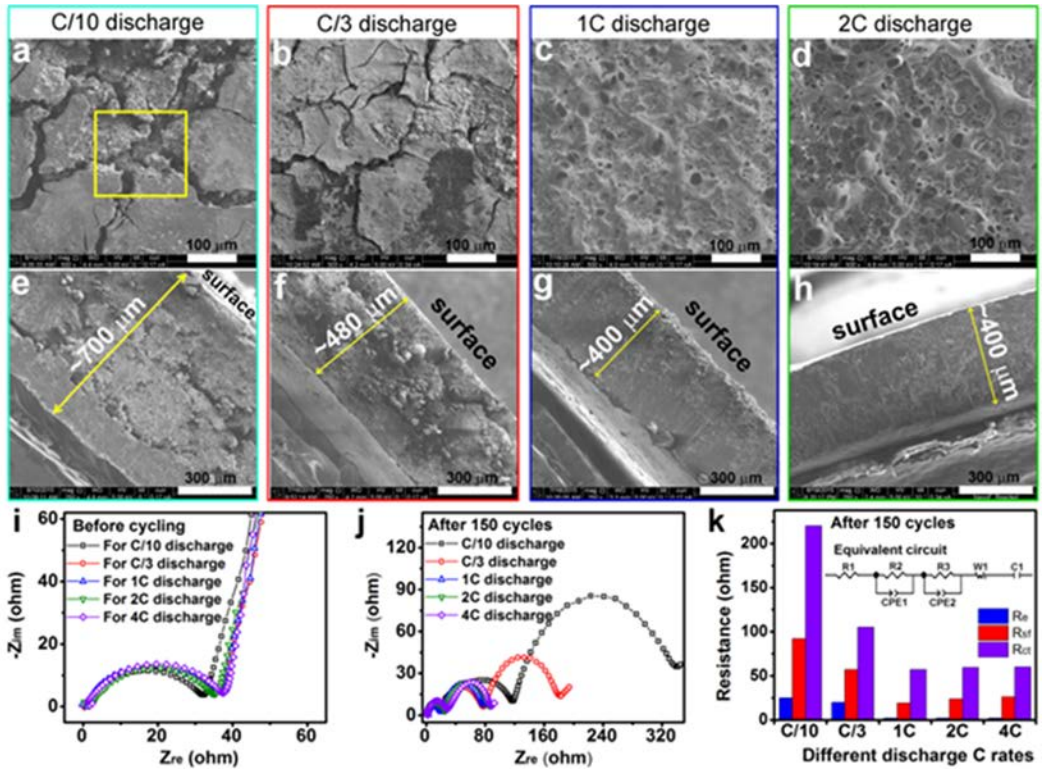

Figure V-230: (a-d) Top view and (e-h) cross-section view of Li metal anodes retrieved from Li||NMC cells after 150 cycles at different discharge rates at 30oC: (a, e) C/10 discharge; (b, f) C/3 discharge; (c, g) 1 C discharge; (d, h) 2 C discharge. (i) and (j) are Nyquist plots of Li||NMC cells cycling at different discharge rates. (k) Fitting results of impedance spectra for cells after 150 cycles at different discharge rates. The inset is the equivalent circuit used for fitting the impedance spectra. All charge processes were performed at C/3 rate

The compositions of the surface layers on cycled Li metal anodes were characterized by XPS. The slow discharge rates result in significant quantity of Li_2O, LiF, as well as some residual lithium salt ($LiPF_x$) in the SEI layer, which cannot effectively protect the metallic Li from continuous reactions with the electrolyte thus leading to the fast degradation of Li metal anode and rapid capacity decay as demonstrated above. However, the fast discharge rates lead to the formation of a lot of poly(ethylene carbonate) constituents integrated with other organic and inorganic lithium salts, which effectively mitigates the parasitic reactions between Li metal and the electrolyte, but still allows fast Li^+ ion conduction and enables the sustainable operation of the Li metal batteries. The mechanisms of the effect of discharge rate on the stability of Li metal anodes are shown in Figure V-231. A transient high concentration electrolyte layer is formed near the surface of Li metal anode during high rate discharge process. At high rate discharge conditions, the Li^+ ions stripping rate is faster than their diffusion rate in the given electrolyte, therefore, a highly concentrated Li^+ ions accumulates in the vicinity of the Li metal anode coordinate with the available organic solvent molecules around the Li metal surface to form more stable solvates which largely suppresses the further corrosion of Li metal anode by free organic solvents and enables stable operation of Li metal batteries. However, at low rate discharge conditions, striped Li^+ ions can easily diffuse away from Li metal surface so they cannot facilitate the formation of stable SEI layer, thus the Li metal anode is seriously corroded by free organic solvents during repeated cycling leading to fast capacity fade and short cycle life.

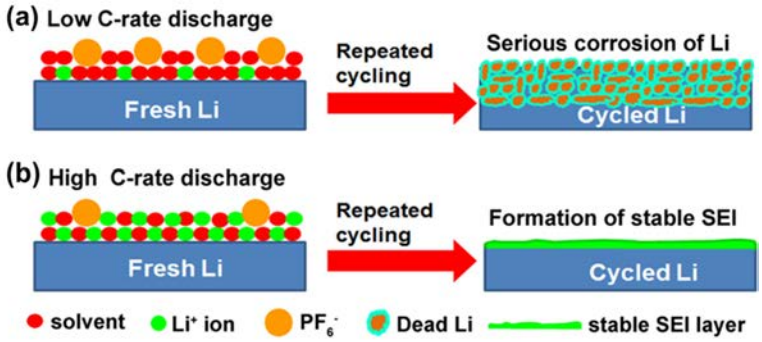

Figure V-231: Schematic illustrations for mechanisms of SEI evolutions on Li metal anodes cycled at (a) low and (b) high discharge C rates

2. Developed dual-salt electrolytes to improve charge rate and long-term cycling stability of Li metal batteries

The effect of a LiTFSI-LiBOB dual-salt electrolyte with EC-EMC solvent mixture on the cycling stability of Li||$LiNi_{0.80}Co_{0.15}Al_{0.05}O_2$ (NCA) coin cells at fast charging was investigated with a comparison to the control electrolyte based on 1.0 M $LiPF_6$/EC-EMC. The NCA cathode had an areal capacity of 1.5 mAh cm^{-2}. The anodic polarization tests at 60°C for one week indicate that both LiTFSI-LiBOB and $LiPF_6$ electrolytes are compatible with Al foil (the substrate for the cathode) at 4.3 and 4.4 V. At 4.5 V both electrolytes exhibit slight corrosion to Al but the LiTFSI-LiBOB electrolyte shows much better stability than the LiPF6 control electrolyte. This LiTFSI-LiBOB electrolyte also enables the Li||NCA cells to exhibit good cycling stability during fast charging (at a relatively high current density of 1.5 mA cm^{-2}) with a cycling efficiency of about 98%, while the cells with the LiPF6 control electrolyte failed quickly at the same cycling condition (Figure V-232). The analyses on the cycled Li anodes indicate that the LiTFSI-LiBOB dual-salt electrolyte had good film-formation ability on Li metal surface and the interface layer enriched with boron and sulfur species is highly conductive.

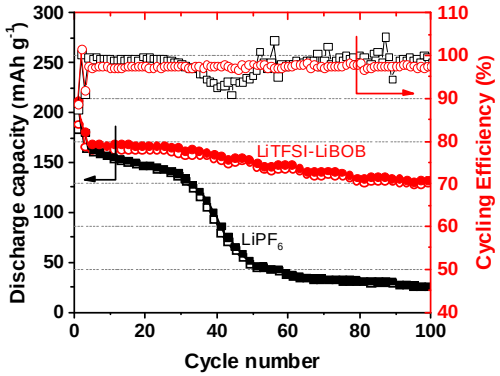

Figure V-232: Room temperature cycling performance of Li||NCA cells using LiTFSI–LiBOB and $LiPF_6$ electrolytes in the voltage range of 3.0 and 4.3 V. The cells were cycled at 1 C (i.e. 1.5 mA cm^{-2}) after two formation cycles at C/10 rate

The effects of the LiTFSI-LiBOB dual-salt electrolytes with and without additive X on battery performances of Li||NMC coin cells were further tested at various charging/discharging current densities and compared with the conventional $LiPF_6$ electrolyte. The NMC cathode had a moderately high areal capacity of ~ 1.75 mAh cm^{-2} (~10.8 mg active material cm^{-2}). The amount of the additive X in the dual-salt electrolytes was optimized to be 0.05 M. As shown in Figure V-233a, the cell using conventional $LiPF_6$ electrolyte shows an abrupt capacity drop after only ca. 60 cycles at the current density of 1.75 mA cm^{-2} for charging and discharging due to the quick formation of a highly resistive SEI layer entangled with Li metal and a continuous growth towards the bulk of Li metal thus leading to the dramatic increase of cell impedance and the electrode over-potential (Figure V-233b). In comparison, the cell using LiTFSI-LiBOB dual-salt electrolyte without additive shows greatly improved cycle life up to 450 cycles (with a capacity retention of 74.5%) prior to the sharp drop of discharge capacity (Figure V-233a), and the cell experiences continuous capacity fade and increased cell over-

potential during cycling (Figure V-233c). The addition of additive X into the dual-salt electrolyte significantly improves the cycling performance of the Li||NMC cells. The capacity loss is only 2.9% in 500 cycles even at a charging current density of 1.75 mA cm^{-2}. More importantly, there is only very limited increase in cell over-potential after 500 cycles (Figure V-233d), indicating that the interphase formed in the additive X-containing LiTFSI-LiBOB electrolyte is highly conductive for Li^+ ion transportation as compared to those formed in the other two electrolytes. With the electrolyte containing optimized amount of additive, the Li||NMC cells can be stably cycled for at least 400 cycles at a charging/discharging current density of 1.75 mA cm^{-2} at 60°C and at least 800 cycles when the cells were cycled at room temperature at the charging current density of 0.58 mA cm^{-2} and the discharging current density of 1.75 mA cm^{-2}. To the best of our knowledge, this fast charging capability and long cycling stability of X-added dual-salt electrolyte is the best performance ever reported for Li metal batteries.

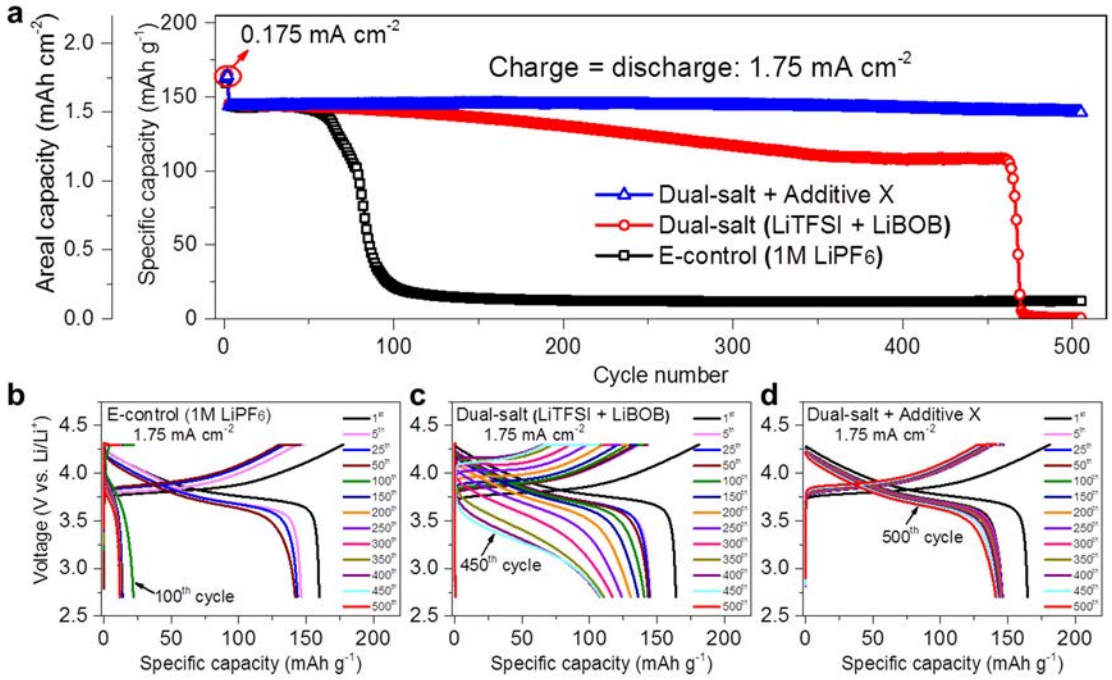

Figure V-233: Electrochemical behaviors of different electrolytes in Li||NMC cells. (a) Long-term cycling performance of the electrolytes with different salts in EC-EMC solvent mixture at the same charge and discharge current density of 1.75 mA cm^{-2} at 30°C. (b-d) Evolutions of charge/discharge voltage profiles of Li||NMC cells using (b) conventional $LiPF_6$ electrolyte, (c) dual-salt (LiTFSI-LiBOB) electrolyte, and (d) additive X-containing dual-salt electrolyte

Detailed analyses were conducted to identify the fundamental mechanism for the significantly improved long-term cycling stability and fast charging capability of Li||NMC cells with the additive X containing LiTFSI-LiBOB dual-salt electrolyte. The SEM images of Li metal anodes after 100 cycles are shown in Figure V-234. The $LiPF_6$-electrolyte caused significant cracking and severe corrosion of bulk Li anode (Figure V-234a) and sporadic needle-like dendritic Li (Figure V-234d) and led to high resistance of the cell. In contrast, when dual-salt electrolytes were used, the bulk Li metal was well reserved with a corrosion depth of about only 30~50 μm (Figure V-234b,c) and the Li surface had a fibrous morphology (Figure V-234e,f). Furthermore, the Li metal cycled in the additive X containing dual-salt electrolyte had more compact and well adhesive surface layer and uniform fibrous Li morphology with a diameter of ~ 1 μm and a length ranging from ~ 10 μm to several tens microns. This electrolyte also gave very small cell impedance. The XPS results show that the SEI layers formed in the dual-salt electrolytes were dominated by polycarbonate species especially when the additive X was added.

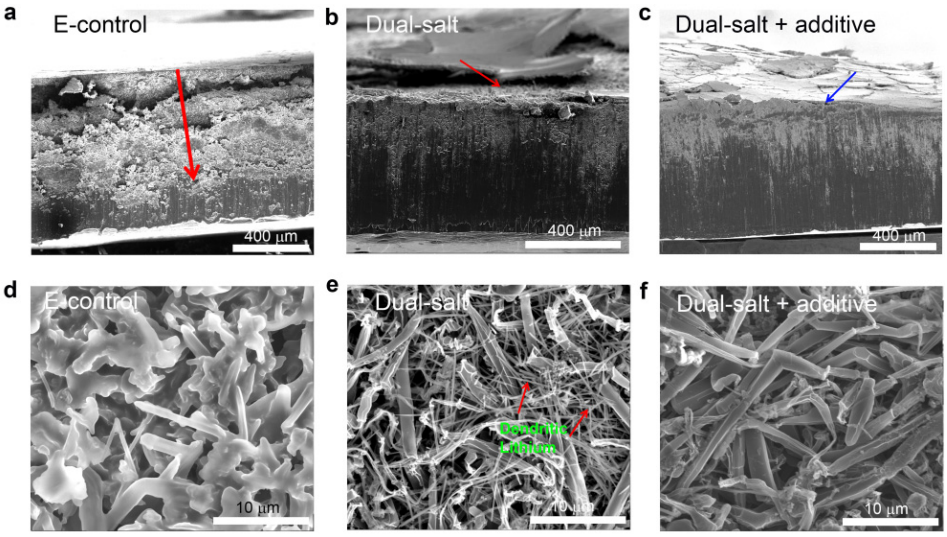

Figure V-234: Morphological images of Li metal anodes. (a-c) Cross-section view and (d-f) top view of Li metal anodes retrieved from Li||NMC cells after 100 cycles using (a, d) conventional $LiPF_6$ electrolyte, (b, e) dual-salt (LiTFSI-LiBOB) electrolyte, and (c, f) 0.05 M additive X-containing dual-salt electrolyte

The Li||NMC cells with high NMC loading (3.0 mAh cm^{-2}) were also tested with an additive-containing dual-salt electrolyte. After formation cycles at 0.3 mA cm^{-2} (i.e. C/10 rate), the cells can be stably cycled for about 100 cycles at 3.0 mA cm^{-2} (i.e. 1C), 300 cycles at 1.0 mA cm^{-2} (i.e. C/3) charging and at least 500 cycles at 0.6 mA cm^{-2} (i.e. 1C) charging (Figure V-235). The increase in charging current density leads to a shorter cycle life of Li||NMC cells. Thus, the additive-containing dual-salt electrolyte can also lead to long-term cycling stability of Li-metal batteries with high areal loading cathode.

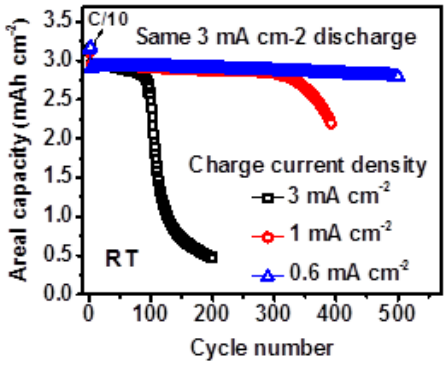

Figure V-235: Cycling performance of Li||NMC cells with 3.0 mAh cm^{-2} NMC loading and using an additive-containing dual-salt electrolyte at 30 °C

Conclusions

It has been demonstrated that the discharging current density or C rate has significant effect on the stability of Li metal anode and the cycling performance of Li metal batteries. During the high C rate discharge (e.g. 1C~2C) process of Li metal batteries, Li^+ ions with a high concentration are accumulated in the vicinity of Li metal anode before they can diffuse to the cathode side, and these highly concentrated Li^+ ions are immediately solvated by the available solvent molecules to form a transient layer of high concentration electrolyte on Li metal surface, which significantly suppresses the interactions among the newly exposed fresh Li metal surface, free organic solvents, and salt anions in the electrolyte. Therefore, this transient layer of highly concentrated electrolyte facilitates the formation of a stable SEI layer composed of a flexible poly(ethylene carbonate) framework integrated with other organic and inorganic components and prevents the corrosion of bulk Li metal anode. Then the cells show remarkably improved cycling performance and CE as compared to those cycled with relatively low discharge C rates. In addition, the short cycling stability and poor

chargeability of conventional $LiPF_6$/carbonate electrolytes can be enhanced by using the LiTFSI-LiBOB dual-salt electrolytes. With the addition of certain additives into the dual-salt electrolytes, the fast charging capability and the long-term cycle life of Li metal batteries can be significantly enhanced. The additives induce the formation of a robust and conductive SEI layer enriched with polycarbonate constituents that can effectively bond the isolated or "dead" Li with the bulk Li metal anode and allow the sustainable operations of Li metal batteries at high charge current densities. The fundamental findings in this work provide new insights for the further development of high performance Li metal batteries through manipulating the salt/solvent/additive chemistry of the electrolytes and optimizing charge/discharge protocols.

Products

Presentations/Publications/Patents

1. W. Xu, J.-G. Zhang, G. L. Graff, X. Chen, F. Ding. "Methods and Energy Storage Devices Utilizing Electrolytes Having Surface-Smoothing Additives". **US Patent No. 9,184,436**, granted date: 11/10//2015.
2. J.-G. Zhang, W. Xu, J. Zheng, B. Adams, S. Jiao. "High Voltage Lithium Metal Batteries with High Coulombic Efficiencies". Provisional Application number 62/337,728, filed date: 5/17/2016.
3. J. Zheng, P. Yan, D. Mei, M. H. Engelhard, S. S. Cartmell, B. J. Polzin, C. Wang, J.-G. Zhang,* and W. Xu,* "Highly stable operation of lithium metal batteries enabled by the formation of a transient high-concentration electrolyte layer," *Adv. Energy Mater.*, 2016, 6, 1502151.
4. H. Xiang, P. Shi, P. Bhattacharya, X. Chen, D. Mei, M. E. Bowden, J. Zheng, J.-G. Zhang, and W. Xu,* "Enhanced Charging Capability of Lithium Metal Batteries Based on Lithium Bis(trifluoromethanesulfonyl)imide-Lithium Bis(oxalato)borate Dual-Salt Electrolytes," *J. Power Sources*, 2016, **318**, 170-177.
5. J. Zheng, P. Yan, R. Cao, H. Xiang, M. H. Engelhard, B. J. Polzin, C. Wang, J.-G., Zhang,* and W. Xu,* "Effects of propylene carbonate content in $CsPF_6$-containing electrolytes on the enhanced performances of graphite electrode for lithium-ion batteries", *ACS Appl. Mater. Interfaces*, 2016, **8**, 5715-5722.
6. W. Xu,* H. Xiang, J. Zheng, D. Mei, P. Yan, R. Cao, M. H. Engelhard, M. E. Bowden, C. Wang, and J.-G. Zhang, "Synergistic Effects of $CsPF_6$ Additive and Propylene Carbonate Content on Enhancing Performances of Graphite Electrode in Lithium-Ion Batteries," in Electronic Proceedings of the 47th Power Sources Conference, Session 24.1, pp. 372-375, June 13-16, 2016, Orlando, Florida.
7. J. Zheng, P. Yan, D. Mei, M. H. Engelhard, S. S. Cartmell, B. J. Polzin, C. Wang, J.-G. Zhang, and W. Xu, "Stable Operation of Lithium Metal Batteries by the Formation of a Transient High Concentration Electrolyte Layer during Fast Discharge", poster presentation at 18th International Meeting on Lithium Batteries, June 19-24, 2016, Chicago, Illinois.
8. W. Xu, H. Xiang, J. Zheng, D. Mei, P. Yan, R. Cao, M. H. Engelhard, M. E. Bowden, C. Wang, and J.-G. Zhang, "Synergistic Effects of $CsPF_6$ Additive and Propylene Carbonate Content on Enhancing Performances of Graphite Electrode in Lithium-Ion Batteries," oral presentation at 47th Power Sources Conference, June 13-16, 2016, Orlando, Florida.
9. W. Xu and J.-G. Zhang, "Lithium Dendrite Prevention for Lithium-Ion Batteries", poster presentation at 2016 DOE AMR Meeting, June 6-10, 2016, Washington DC.
10. H. Xiang, P. Shi, P. Bhattacharya, X. Chen, D. Mei, M. E. Bowden, J. Zheng, J.-G. Zhang, and W. Xu, "LiTFSI-LiBOB Dual-Salt Electrolytes Enhancing the Charging Capacity of Rechargeable Lithium Metal Batteries", poster presentation at 9th Symposium on Energy Storage beyond Lithium-Ion, May 24-26, 2016, Richland, Washington.
11. J. Zheng, P. Yan, D. Mei, M. H. Engelhard, S. S. Cartmell, B. J. Polzin, C.-M. Wang, J.-G. Zhang, and W. Xu, "Stable Operation of Lithium Metal Batteries by the Formation of a Transient High Concentration Electrolyte Layer during Fast Discharge", poster presentation at 9th Symposium on Energy Storage Beyond Lithium-Ion, May 24-26, 2016, Richland, Washington.
12. H. Xiang, D. Mei, P. Yan, P. Bhattacharya, S. D. Burton, A. V. Cresce, R. Cao, M. H. Engelhard, M. E. Bowden, Z. Zhu, B. J. Polzin, C. Wang, K. Xu, J.-G. Zhang, and W. Xu, "Behind the Stability of

Graphite Anode in PC-Containing Electrolytes with a New Additive $CsPF_6$", Presentation at 228th ECS Meeting, Phoenix, AZ, October 11-15, 2015.

References

1. W. Xu, J. Wang, F. Ding, X. Chen, E. Nasybulin, Y. Zhang, J.-G. Zhang, *Energy Environ. Sci.*, 2014, **7**, 513-537.
2. K. Xu, *Chem. Rev.*, 2004, **104**, 4303-4417.
3. J. Qian, W. A. Henderson, W. Xu, P. Bhattacharya, M. Engelhard, O. Borodin, J.-G. Zhang, *Nature Commun.*, 2015, **6**, 6362.
4. F. Ding, W. Xu, X. Chen, J. Zhang, M. H. Engelhard, Y. Zhang, B. R. Johnson, J. V. Crum, T. A. Blake, X. Liu, J.-G. Zhang, *J. Electrochem. Soc.*, 2013, **160**, A1894-A1901.
5. F. Ding, W. Xu, G. L. Graff, J. Zhang, M. L. Sushko, X. Chen, Y. Shao, M. H. Engelhard, Z. Nie, J. Xiao, X. Liu, P. V. Sushko, J. Liu, J.-G. Zhang, *J. Am. Chem. Soc.*, 2013, **135**, 4450-4456.
6. D. Lu, Y. Shao, T. Lozano, W. D. Bennett, G. L. Graff, B. Polzin, J.-G. Zhang, M. H. Engelhard, N. T. Saenz, W. A. Henderson, P. Bhattacharya, J. Liu, J. Xiao, *Adv. Energy Mater.*, 2015, **5**, 1400993.

V.H. Lithium Sulfur Batteries

V.H.1. New Lamination and Doping Concepts for Enhanced Li – S Battery Performance (University of Pittsburgh)

Prashant N. Kumta, Principal Investigator
University of Pittsburgh
Attn: Jennifer Woodward
123 University Place
Pittsburgh, PA 15213-2303
Phone: 412-648-0223; Fax: 412-624-3699
E-mail: pkumta@pitt.edu

Colleen Butcher, DOE Program Manager
U.S. Department of Energy
National Energy Technology Laboratory
626 Cochrans Mill Road
Pittsburgh, PA 15236
Phone: 412-386-7341
E-mail: Colleen.Butcher@netl.doe.gov

Start Date: October 2014
End Date: September 2017

Abstract

Objectives

- To successfully demonstrate generation of novel sulfur cathodes for Li-S batteries meeting the targeted gravimetric energy densities ≥ 350 Wh/kg and ≥750Wh/l with a cost target $125/kWh and cycle life of at least 1000 cycles. The proposed approach will yield sulfur cathodes with specific capacity ≥1400mAh/g, at ≥2.2V generating ~460Wh/kg, energy density higher than the target. Full cells meeting the required deliverables will also be made.
- In order for the mass adoption of EVs and making a significant dent in U.S and global CO_2 production, the key problems of driving range per charge and cost per kWh must be addressed. Barriers addressed:
  - Performance: Low Wh/kg and Wh/L.
  - Life: Poor deep discharge cycles.
  - Cost: High $/kWh.
- Sulfur Cathode Targets: ≥350Wh/kg, ≥750Wh/l, high capacity ≥1400 mAh/g, cyclability (~1000 cycles), loss per cycle ≤0.01% per cycle, CE: ≥99.99%.
- Cell Targets: 350 Wh/kg, 700 Wh/L, <$150/kWh.

Accomplishments

- Demonstrate synthesis of finely dispersed nanoparticles of sulfur (December 2014).
- Developed novel lithium-ion conducting (LIC) membrane systems using ab-initio methods displaying impermeability to sulfur diffusion (December 2014).
- Demonstrate capabilities for generation of novel sulfur 1-D, 2-D and 3-D morphologies exhibiting superior stability and capacity (June 2015).
- Identification and synthesis of LIC materials for use as coatings for sulfur cathodes (June 2015).

- Novel encapsulation and sheathing techniques and exploration of unique architectures and generation of 3-D composites displaying superior lithium-ion conduction, reversible capacity and stability (June 2015).
- Identification of suitable dopants and dopant compositions to improve electronic conductivity of sulfur (October 2015).
- Fundamental electrochemical study to understand the reaction kinetics, mechanism and charge transfer kinetics (October 2015) – Completed.
- Demonstrate synthesis of doped LIC membrane with improved lithium-ion conductivity (December 2015).
- Preparing doped LIC with improved ionic conductivity (January 2016).
- Demonstrated synthesis of doped LIC membrane with improved lithium-ion conductivity (January 2016).
- Identify and develop effective coating methods to form a uniform lamina of LIC membrane over sulfur hetero-structures (March 2016).
- Development of CFN morphology with a stable cycling performance of ~650 mAh/g for over 300 cycles with < 0.02% fade rate (April 2016).
- Demonstration of binding of polysulfide with CFN results in polysulfide retention and hence, improved cycling stability (April 2016).
- Demonstrated the effect of the unique pore size (~2nm) of CFN preventing dissolution of polysulfide from the liquid electrolyte (April 2016).
- Application of TMPM improved the specific capacity of commercial sulfur demonstrating stable capacity of ~550 mAh/g over 100 cycles (April 2016).
- Doping Sulfur with like – sized dopants with enhanced electronic properties (April 2016).
- Developing organic and inorganic Complex Framework materials (CFM) as effective polysulfide traps (July 2016).
- Go/No-Go (October 2015) decision based on the ability to demonstrate improvement in cycling upon use of the LIC coating completed.
- Go/No-Go (July 2016) decision based on the ability to demonstrate improvement in cycling using interface engineering approaches completed.
- Go/No-Go (October 2016) decision based on the ability to generate doped sulfur nanoparticles for improving electronic conductivity completed.

Future Achievements

- Synthesis of VACNT and LIC coated nanosulfur based composite materials.
- Design and engineering of high capacity LIC coated sulfur nanoparticle.
- Generation of integrated doped nanoparticulate sulfur-VACNT-LIC composite electrode
  - Based on insight gained in Phase 1 and Phase 2, design a suitable optimum doped sulfur based VACNT- LIC electrode.
  - Optimize doping composition and thickness to maximize capacity, rate capability and cycling stability.
- Business Value Analysis
  - Further refine and analyze the cost of the electrode materials, electrolytes, separators, binders, and related processes.
  - Develop design criteria and performance testing protocols for final deliverables.
- Fabrication of the desired 4 mAh full cell

- Prismatic pouch cell assembly of the high energy density cathode with optimum thickness and interface engineered materials.
- Formation cycle and cell balancing of the optimized system.
- CCCV test protocol to determine nominal discharge capacity at 100% SOC.

Technical Discussion

Background

Lithium-ion batteries (LIBs) have clearly dominated the area of high energy storage systems for the past decade with significant research and development activity focused on the development of cathode and anode materials to maximize the specific energy storage, stability and cycle life of the batteries. However, with the increasing demand in the EV industry for low cost, low weight and high energy storage batteries, the current focus of research has shifted towards the development of lithium sulfur batteries (LSB) owing to the high theoretical specific capacity exhibited by sulfur compared to other cathode materials currently available. Li–S battery shows a theoretical capacity of 1675 mAh/g corresponding to the formation of Li_2S which makes sulfur a promising electrode to replace the layered transition metal oxides (~150 mAh/g) and $LiFePO_4$ (~170 mAh/g) hitherto deployed in present LIB systems. Moreover, the abundance of sulfur in the earth's crust makes it a more economical and highly attractive proposition compared to currently existing cathode materials.

Despite the potential attributes of sulfur, the existing Li-S battery technology display poor cyclability, low coulombic efficiency (CE) and very low cycle life due to the following fundamental issues: 1. Formation/ dissolution of polysulfides; 2. Sluggish kinetics of subsequent conversion of polysulfides to Li_2S; 3. High diffusivity of polysulfides in the electrolyte; 4. Insulating nature or poor conductivity of sulfur/Li_2S; 5. Volumetric expansion/contraction of sulfur; 6. shuttling of polysulfides along with Li^+. These issues result in the loss of sulfur from the cathode causing mechanical disintegration of the cathode, surface passivation of both anode and cathode in the battery, thereby precipitously decreasing the specific capacity and columbic efficiency (CE). Present generation sulfur cathodes also show low specific storage capacity, very poor charging rates and low loading densities. There is therefore a critical need for research to be conducted to overcome the issues impeding the development of the Li-S battery technology.

Introduction

The increasing demand in the EV industry for low cost, light weight and high energy storage batteries, the current focus of research has shifted towards the development of lithium sulfur (Li–S) batteries owing to the high theoretical specific capacity exhibited by sulfur compared to other cathode materials currently available. Li–S battery shows a theoretical capacity of 1675 mAh/g corresponding to the formation of Li_2S which makes sulfur a promising electrode to replace the layered transition metal oxides (~150 mAh/g, e.g. $LiCoO_2$, $LiMnO_2$) and $LiFePO_4$ (~170 mAh/g) deployed in present LIB systems. Moreover, the abundance of sulfur in the earth's crust, its ubiquitous availability as a byproduct in the extractive mineral and petrochemical industry, combined with ease of processing, makes it a more economical proposition compared to currently existing cathode materials.

Approach

The objectives outlined above will be accomplished by engineering sulfur cathode materials primarily by laminating the electrodes with lithium ion conductor (LIC) coatings to prevent polysulfide dissolution and doping of sulfur to improve the electronic and ionic conductivity. Major technological innovations will be undertaken to accomplish the following objectives in this effort:

Phase – 1 (Year 1): Synthesis, Characterization and Scale up of suitable LIC matrix materials and multilayer composite sulfur cathodes. This phase is completed.

Identify novel LIC coating materials and morphology for composite multilayer sulfur cathode architectures exhibiting: Specific capacity ≥1000 mAh/g (≥8 mAh/cm^2), cyclability (~1000 cycles), loss per cycle ≤0.05% per cycle, Coulombic Efficiency (CE): ≥80%.

Phase – 2 (Year 2): Development of LIC coated sulfur nanoparticles, scale up of high capacity engineered LIC coated multilayer composite electrodes and doping strategies for improving the electronic conductivity of sulfur.

Optimize and scale up of interface engineered multilayer composite LIC coated sulfur cathode architectures exhibiting: Specific capacity ≥1200 mAh/g (≥4 mAh/cm^2), cyclability (~1000 cycles), loss per cycle: ≤0.01% per cycle, CE: ≥80%.

Synthesize and scale up of doped sulfur nanoparticles on gram scale and demonstrate improvement in performance, reflected as an increase in sulfur weight percentage and improvement in rate capability of cycling of the electrodes.

Phase-3 (Year 3): Advanced high energy density, high rate, highly cyclable cell development.

Tie together the three different trees of development i.e. coating development/sulfur particle development/CNT based exploration by identifying suitable configuration integrated electrode (I.E.) with maximum sulfur weight percentage demonstrating high capacity ≥1400 mAh/g, cyclability (~1000 cycles), loss per cycle: ≤0.01% per cycle, CE: ≥80%.

Assemble 4 mAh high energy density Li-S pouch cells and performance testing.

Results

Phase-1 of the current project concluded with the successful identification of effective lithium-ion conducting (LIC) membrane and demonstration of the ability of LIC to shield the polysulfide species from dissolving into the electrolyte. To achieve this target, 4 strategies outlined in the following were employed during Phase-1 of the project: (a) Use of inorganic LICs in the form of pellet coatings (Q1, Q2) (b) fabrication of flexible polymer-sulfur wires (Q2) (c) generation of gel polymer electrolyte (GPE) as an electrolyte medium (Q3) (d) use of complex framework materials (CFM) as trapping agents for sulfur species (Q4). These strategies resulted in improved cycling with scope for further improvement. The aim of Phase-2 studies is to synthesize novel doped LIC materials with high lithium ion conductivity identified in Phase 1, to develop effective coating strategies of these materials and to generate hetero structured composites of sulfur with carbon materials. Towards this end, the following strategies were employed during Phase-2 of the project: (a) Improving ionic conductivity of lithium ion conductors using first-principles driven doping approaches (b) Composite polymer electrolytes demonstrating no capacity loss in commercial sulfur electrodes (c) Sulfur infiltrated framework (SFM) materials with chemical trapping of sulfur (d) Altering the electronic structure of sulfur with size matched dopants. The results of these studies are listed below:

Improving ionic conductivity of lithium ion conductors using first-principles driven doping approaches

In FY14, it was demonstrated using density functional theory (DFT) studies that an improvement in ionic conductivity can be achieved upon the introduction of vacancies in the lattice of Li ion conductor Li_4SiO_4. Li_4SiO_4 is a very wide band gap insulator with strong Si-O hybridization, covalent Si-O bonds and ionic Li-O, large channels for Li-conduction with Li^+ ionic conductivity (~ 10^{-12} S/cm). The effect of doping (dopants-D_1 and D_2) on Li sites and F doping on O sites of Li_4SiO_4 on its ionic conductivity was investigated using first principles calculations in Phase-1. Nudged elastic band method has been used for determining the potential energies and activation barriers E_a for various lithium-ion migration pathways in pure and doped Li_4SiO_4. These calculations suggest a decrease in the activation barrier (Figure V-236) for Li^+ ion conductivity because of doping. The unit cell of Li_4SiO_4 contains two SiO_4^{-4} tetrahedra linked by 8 lithium ions, which are distributed over 18 possible sites. At room temperature, an improvement in ionic conductivity of 3 to 4 orders in magnitude could be obtained by forming simple solid solutions.

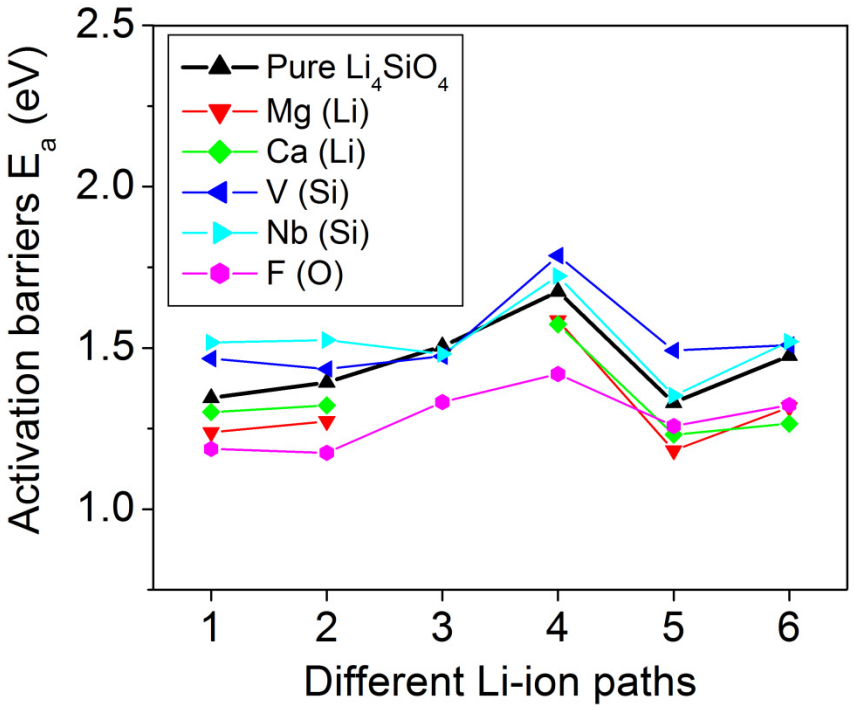

Figure V-236: Activation barriers E_a (eV) for different migration paths of lithium-ions in pure and doped Li_4SiO_4

To validate the theoretical predictions, cation and anion doping of Li_4SiO_4 was performed to obtain final materials of the chemical formula shown by i and ii.

i. $(Li_y[\ ]_xY_x)_4SiO_4$, where Y – D_1, D_2, [ ] – vacancy, x – 0.025 to 0.15

ii. $Li_4Si(O_y[\ ]_xZ)_4$, where Z – D_3, [ ] – vacancy, x – 0.025 to 0.15

Solid state high temperature processing route from suitable precursors was employed to generate doped nanoparticles of LIC. Different precursor ratios were used to tailor the atomic % of lithium vacancies in the LIC and tested for ionic conductivity. Lithium orthosilicate was doped with six different concentrations (2.5 at. %-15 at. %) of each dopant using a high temperature solid state diffusion technique. The X-ray diffraction (XRD) patterns of the various compositions of doped lithium orthosilicate indicate that a maximum of 7.5% lithium sites was successfully doped with the two different cations (D_1 and D_2). Further increase in the dopant concentration results in formation of secondary phases. Similarly, up to 7.5% oxygen sites were replaced with dopant D_3 maintaining phase purity, with secondary phases appearing upon excessive D_3 doping. Figure V-237(a-c) show the results of electrochemical impedance spectroscopy (EIS) analysis of the doped lithium orthosilicate materials and Figure V-237d depicts the ionic conductivity dependence on dopant concentration in the various doped materials. Creation of vacancies in the LIC crystal structure by doping with D_1 (~7.5 at. %) resulted in an increase in ionic conductivity from 1.179×10^{-12} S cm^{-1} to 2.870×10^{-8} S cm^{-1} as seen in Figure V-237d. Doping with D_2 (7.5at. %) and D_3 (10 at. %) results in a 3-order improvement in the ionic conductivity occurring close to the highest doped concentration (Table V-8). A comprehensive study utilizing sputter deposition technique to form uniform ultrathin coatings of LIC onto sulfur heterostructures is currently ongoing. These doped materials are currently being tested as LIC coatings in nano-sulfur based materials.

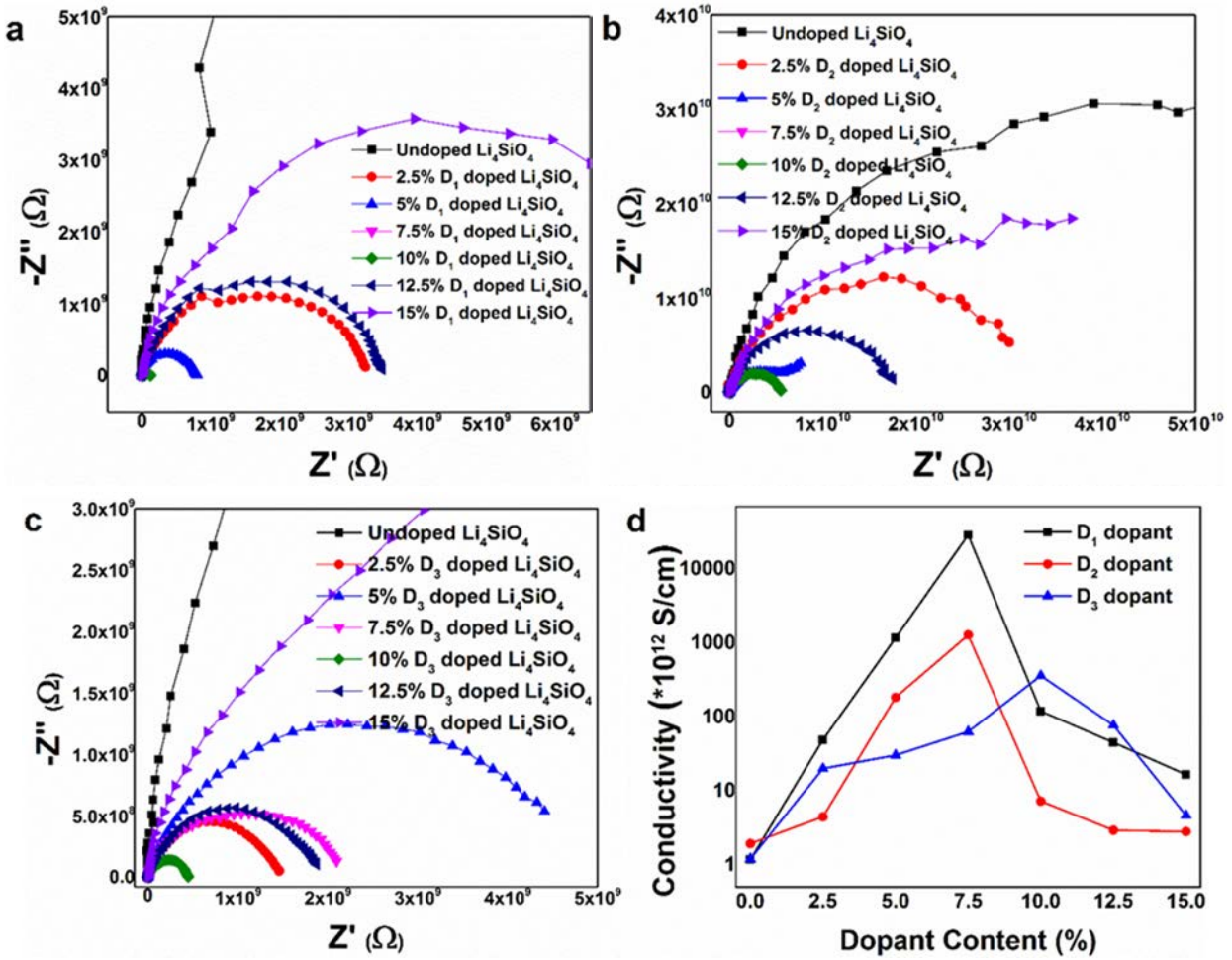

Figure V-237: a) AC impedance based conductivity analysis of D_1 doped Li_4SiO_4; b) AC impedance based conductivity analysis of D_2 doped Li_4SiO_4; c) AC impedance based conductivity analysis of D_3 doped Li4SiO4 and d) Effect of doping D_1, D_2 and D_3 on the conductivity of Li_4SiO_4

Table V-8: Lithium Ionic Conductivities of Li_4SiO_4 upon Doping with Three Different Dopants D_1, D_2 and D_3.

	D_1 doped ($\times 10^{12}$ S/cm)	D_2 doped ($\times 10^{12}$ S/cm)	D_3 doped ($\times 10^{12}$ S/cm)
Li_4SiO_4 – undoped	1.16	1.29	1.19
2.5% doped	49.13	4.44	20.04
5% doped	1169.55	183.51	30.41
7.5% doped	28706.06	1277.59	63.13
10% doped	119.26	7.22	359.62
12.5% doped	45.08	2.93	76.95
15% doped	16.53	2.80	4.66

Composite polymer electrolytes (CPE) demonstrating no capacity loss in commercial sulfur electrodes

Work in Phase-1 of this project involved generation on lithium ion conducting polymeric membranes (LICMs) i.e. gel polymer electrolytes (GPEs) for use as separators in lithium-sulfur batteries. These polymeric LICM materials were used in place of conventional polymeric separator materials and it is expected that they will exhibit superior mechanical properties, flame-resistance and flexibility. To tackle capacity fade associated with the conventional gel-polymer electrolyte materials without fillers, nanoparticulate solid state materials were used as fillers in the GPE matrix. Stability improvement because of using doped solid-state nanoparticles as filler materials in the polymer material resulted in a stable capacity of ~400 mAh/g seen up to 80 cycles. The LICMs with solid state systems acting as tethering sites serve as filters to restrain the polysulfide ensuring improvement in cycling stability. Continuing optimization work into the same undertaken as a part of Phase-2 included engineering of the nature of the LICM materials with regards to polymer composition, filler material composition, particle size and porosity.

As a subtask of Q2, a free standing solid state system incorporated polymer membrane (SSPM) was used as a sieve to restrain the polysulfides from reaching the anode. The SSPM was used in addition to commercial separator to test with commercial sulfur cathode. Incorporation of the SSPM improved the specific capacity of commercial sulfur to ~550 mAh/g for over 100 cycles. This improvement in specific capacity arises from the binding of the polysulfide species onto the solid state functional moieties. Q4 of Phase – 2 involved the development of composite polymer electrolytes (CPE) with solid-state fillers using simple wet-chemical techniques that demonstrated high capacity and prevention of polysulfide dissolution. The CPE demonstrated an electrolyte uptake of ~200 wt% (Figure V-238a) with room temperature ionic conductivities (Table V-9) similar to organic liquid electrolytes. In addition, it can be seen in Figure V-238b and Figure V-238c that the CPE materials possess significantly better mechanical properties (Table V-10) and flame-resistance as compared to commercial separators making them ideal candidates for use in a lithium anode based system on account of improved safety. Testing of these CPEs with commercial sulfur cathodes showed an initial capacity of ~894 mAh/g which remained very stable demonstrating capacity of ~809 mAh/g after 50 cycles (Figure V-238d). Commercial sulfur electrodes normally undergo capacity loss to <100 mAh/g after 10 cycles. Thus, the CPE material demonstrates significant advancement in sulfur electrolytes. The cycling stability of the cathodes tested with CPE is likely due to the physical properties and optimized electrolyte content of these separator – electrolytes.

Table V-9: Lithium Ion Conductivities of Commercial Separator Compared with Composite Polymer Membranes with Three Different Fillers

Sample Composition	Conductivity (S/cm)
Commercial separator with liquid electrolyte	1.283*10-3
CP membrane + LITFSI + Filler 1	1.881*10-3
CP membrane + LITFSI + Filler 2	3.009*10-3
CP membrane + LITFSI + Filler 3	9.4749*10-3

Table V-10: Comparison of the Mechanical Properties of CP Membrane and Commercial Separator

Mechanical properties	CP membrane separator	Commercial separator
Tensile strength (kPa)	1114.8	636.1
Elongation break (%)	107.9	95.2
Young's modulus (GPa)	11.8	10.6

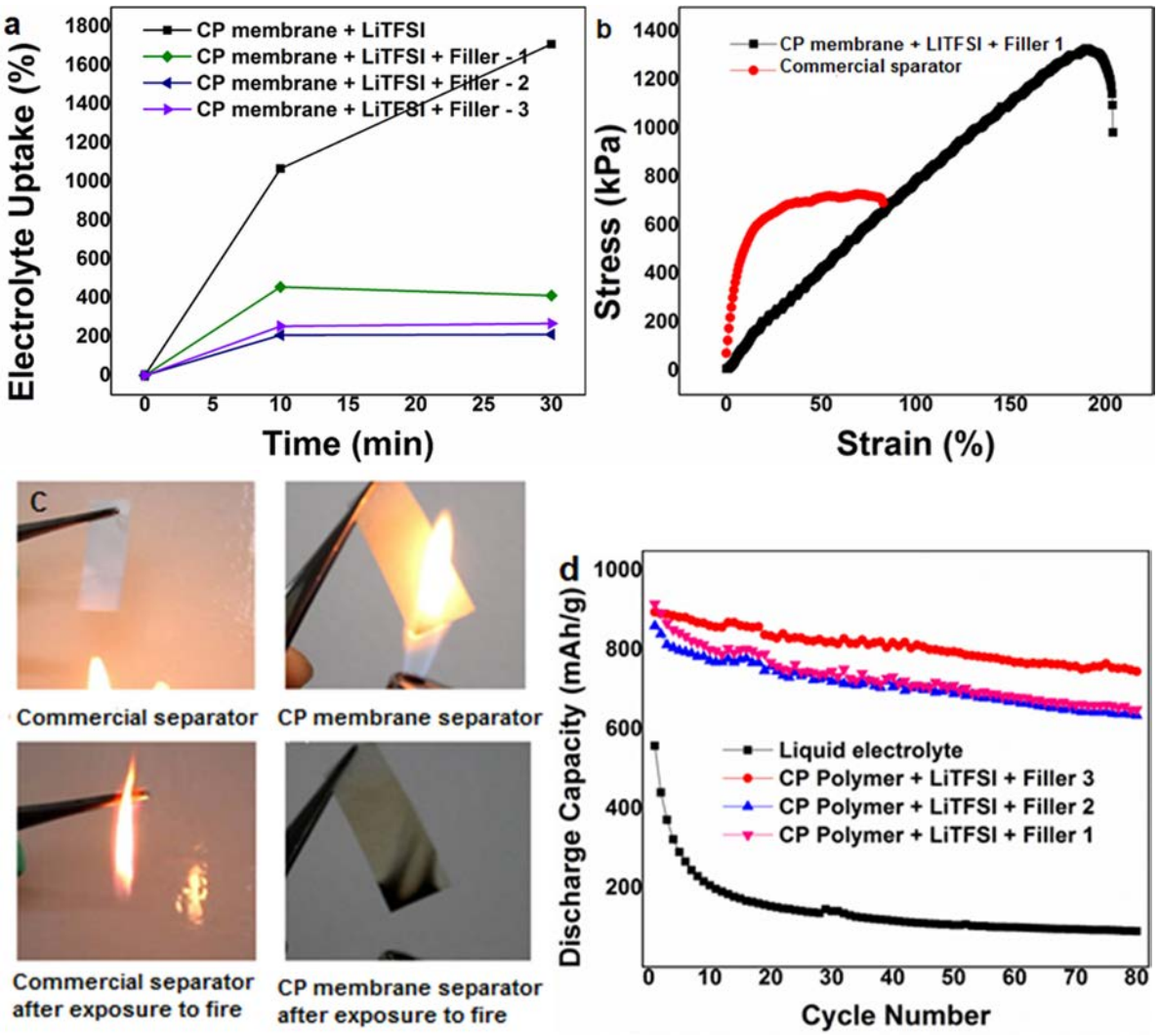

Figure V-238: (a) Electrolyte uptake of CPE membranes (b) Mechanical properties of the CPE membrane (c) Flame-test depicting the superior safety of the CPE materials (d) Cycling behavior of CPE membranes

Altering the electronic structure of sulfur with size matched dopants

Another essential challenge this work aims to undertake is to increase the overall electrode capacity in sulfur cathodes by increasing the inherent electronic conductivity of sulfur. Towards this end, first principles studies were performed in Phase-1 of the study and suitable doping elements were identified to modify the electronic properties of sulfur resulting in its transformation from an insulator material to a semi-conductor/metallic conductor. Q3 of Phase – 2 also involved successfully doping commercially obtained sulfur (S_8) with similar sized dopants (Figure V-239 shows the XRD patterns of doped S) to alter the electronic structure and enhance the electronic conductivity of S. A comprehensive study of the effect of doping of sulfur on rate capability is ongoing.

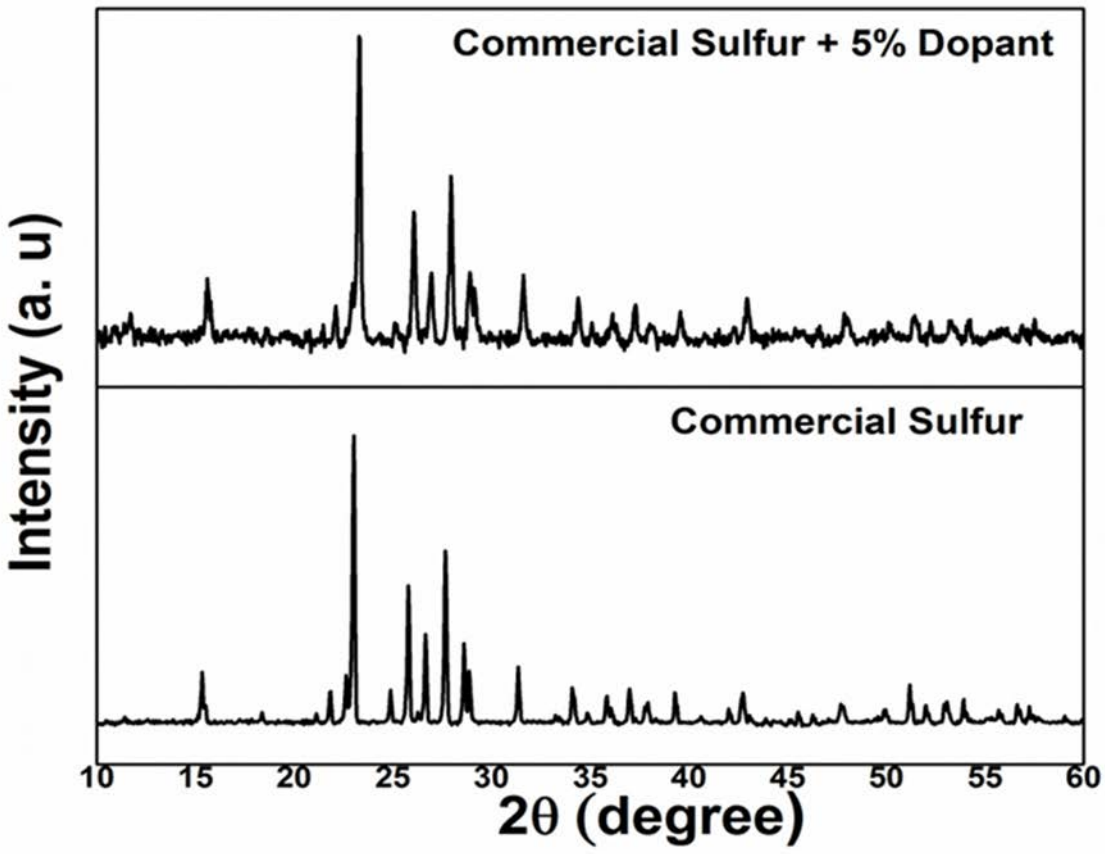

Figure V-239: XRD pattern of synthesized doped sulfur material showing phase-purity and peak shift

Sulfur infiltrated Framework (SFM) materials with chemical trapping of sulfur

A final portion of the study in Phase-2 involved the use of framework materials to host sulfur and entrap polysulfides during cycling, and ensure capacity retention. The strategy with such host-based framework is two-pronged as follows: (a) the host acts as a conductive matrix; and (b) polysulfide species formed during lithiation are trapped inside the host matrix. Work in Phase-1 had identified complex framework materials (CFM) with sulfur infiltrated into the nanopores demonstrating very stable cycling with fade rates <0.01% loss per cycle after a short initial capacity fade. Despite improvements in stability, these structures exhibit an initial capacity loss, the origin of which was explored using X-ray photoelectron spectroscopy studies. Two variants of sulfur infiltrated CFMs, CFM-1 and CFM-2 were synthesized at room temperature and infiltrated with sulfur. The CFMs were used as cathodes for Li – S batteries. CFM-1 shows a very high initial capacity of 1476 mAh g^{-1}, which is the highest capacity value reported in the literature to date[1-3], stabilizing at 609 mAh g^{-1} over 200 cycles. The almost negligible fade rate (0.0014% loss $cycle^{-1}$) and complete prevention of polysulfide dissolution makes these cathode systems most promising candidates for Li-S batteries. However, there is an initial loss in capacity observed and to address this initial capacity loss observed in this system, the mechanism of lithiation and any other associated side reaction (e.g. SEI formation) involved in the electrochemical lithiation process needs to be understood. To rationally design sulfur hosts using complex framework materials (CFM), a basic understanding of the mechanisms involved in trapping polysulfide into the host materials needs to be established. This mechanism would further explain the origin of irreversible capacity loss during the initial cycles. The work uses XPS analysis as a technique to understand the mechanism involved in masking polysulfide dissolution by directly binding the sulfide species onto the CFMs. The proposed concept of using chemical bonding has been reported elsewhere although complete prevention of polysulfide dissolution and retention has not been reported in the open literature to date[4]. The XPS technique was accordingly used to study polysulfide dissolution and to understand S – CFM bonding providing insight into prevention of the polysulfide dissolution in the current work. The mechanistic overview provided by this report could in our opinion lay the foundations and further identify possible pathways for implementing future design strategies to

enhance the capacity and directly aim to resolve polysulfide dissolution problems in the initial cycles plaguing the Li-S battery cathodes.

Table V-11: BET Surface Area Analysis of Two Different Types of CFMs

	BET Surface Area/ m2 g-1	Langmuir Surface Area/m2 g-1	Total Pore Volume/cm3 g-1	Adsorption average pore width/ nm
CFM-1	525.98	829.18	0.324	2.46
CFM-2	684.25	1083.07	0.422	2.47

Table V-11 represents the BET specific surface area and average pore sizes of both the CFM materials. Both materials exhibit a very high surface area of ~ 526 $m^2 g^{-1}$, and ~684.25 $m^2 g^{-1}$, respectively with an average pore size of ~2. 47 nm. The CFMs were found to have high pore volume of ~0.324 $cm^3 g^{-1}$ and ~0.422 $cm^3 g^{-1}$. To prove the nanoporous nature of CFMs and the binding of sulfur to CFM, TEM analysis was employed (Figure V-240). It is noteworthy that these surface areas are greater than those of most carbonaceous host materials that have reportedly been used as sulfur hosts in Li – S batteries[5-8]. The large pore volume of the CFM materials is expected to facilitate in ensuring larger amounts of sulfur encapsulation and thus high sulfur loading in the electrodes. Another unique advantage yielded using CFM materials to encapsulate sulfur is the small average pore diameter of the CFMs (2.46 nm) that aids in minimizing polysulfide dissolution by offering a better mode for trapping and confining the polysulfide species.

The TEM images of CFM-1 at a lower magnification (Figure V-240a) shows the highly porous nature of the CFM. Phase contrast image of S infiltrated CFM-1 (Figure V-240b) clearly shows ~5nm islands of sulfur inside the parent CFM structure indicating sulfur infiltration into the CFM. Figure V-240c demonstrates the local-ordering in the CFM structure. The nature of sulfur inside the CFM structure can be seen in Figure V-240d wherein clear lattice fringes corresponding to sulfur infiltrated within the CFM structure are observed. Two different values of d – spacing, 0.201 nm and 0.277 nm were identified by analyzing the inter-planar distance in the fringes seen in Figure V-240d.

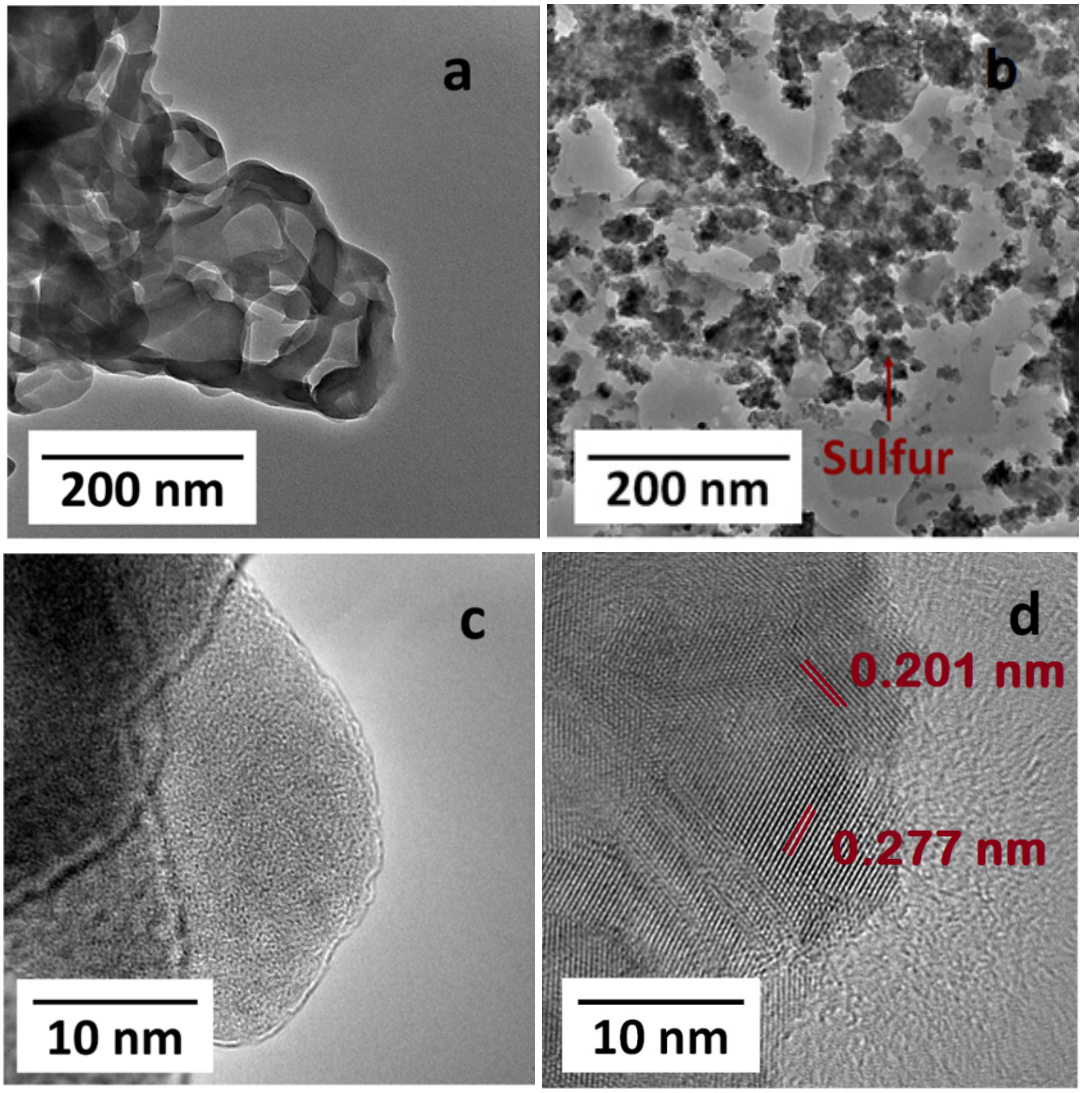

Figure V-240: TEM images of CFM-1 and S –CFM-1 at different magnifications. (5a, 5c) CFM-1; (5b and 5d) S-CFM-1

The nature of sulfur in the S – CFMs was studied using XPS analysis (Figure V-241). XPS analysis was performed on a Thermo ESCALAB 250Xi with suitable background correction. It can be observed that the characteristic S2p3/2 peak is observed for the commercial sulfur powder at 165.21 eV in line with previous reports for orthorhombic sulfur (S8) [9-12]. The XPS spectra of S-CFMs show a shift in the S2p peak as compared to commercial sulfur indicating the absence of free elemental sulfur suggesting binding of sulfur to the CFM structures. The S2p3/2 peak position at 162.45 eV corresponding to the binding of sulfur onto the CFMs is similar to values observed in chemically-bound sulfur studied by Chehimi et al.,[13] further confirming the bound nature of sulfur onto the CFMs. This chemical binding of sulfur along with the nanoporous nature of the CFMs is expected to result in minimal sulfur dissolution into the organic liquid electrolyte[14]. This effect has been observed in sulfur entrapped in single wall carbon nanotubes (SWCNTs) of ~1.5nm diameter by Fujimori et al.[10] wherein sulfur adopts either a linear or a zig-zag orientation as opposed to the conventional cyclic S8 rings of S. Due to an average pore size of 2 nm of CFMs, comparable to the SWCNTs (~2 nm) used, the sulfur strands might experience strain from the CFM pore walls thus yielding a lower S2p binding energy. The complete trapping of the polysulfide in a host matrix however, has not been reported in the literature and it is expected that further optimization of the CFM materials using a mechanistic understanding gained from the rest of this study would help engineer very high capacity cathodes with almost no capacity fade.

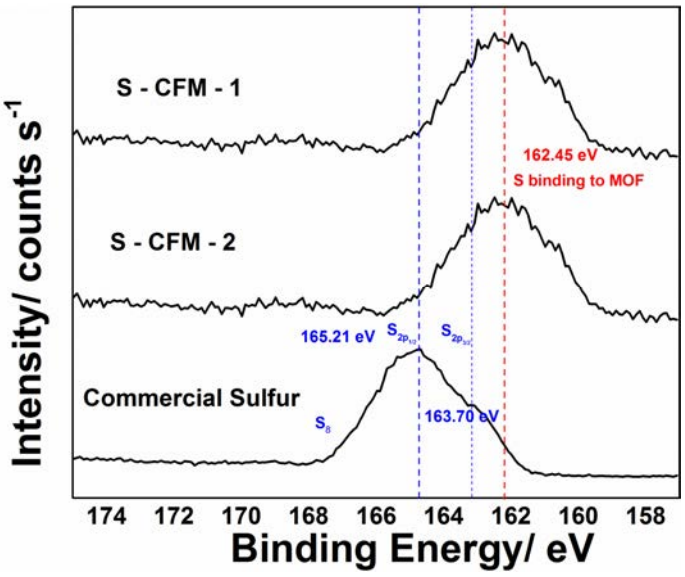

Figure V-241: XPS S2p Binding Energy profile of Commercial Sulfur, S – CFM-1 and S – CFM-2

Though both CFM materials exhibit excellent cycling stability after initial stabilization, a significant portion of the initial observed capacity is lost within the 1st ten cycles. This loss in commercial sulfur is typically attributed to the dissolution of sulfur into the electrolyte and loss of the eventual polysulfide species. However, the stabilization of the capacity following the initial loss appears to draw credence to the possibility of the confinement occurring but the alluding to the possible existence or evidence of other extraneous sacrificial reactions. This result thus implied that the origin of the initial capacity loss in these S – CFMs needs to be better understood warranting better characterization to be conducted to be able to improve the overall performance of the CFM based sulfur electrode system.

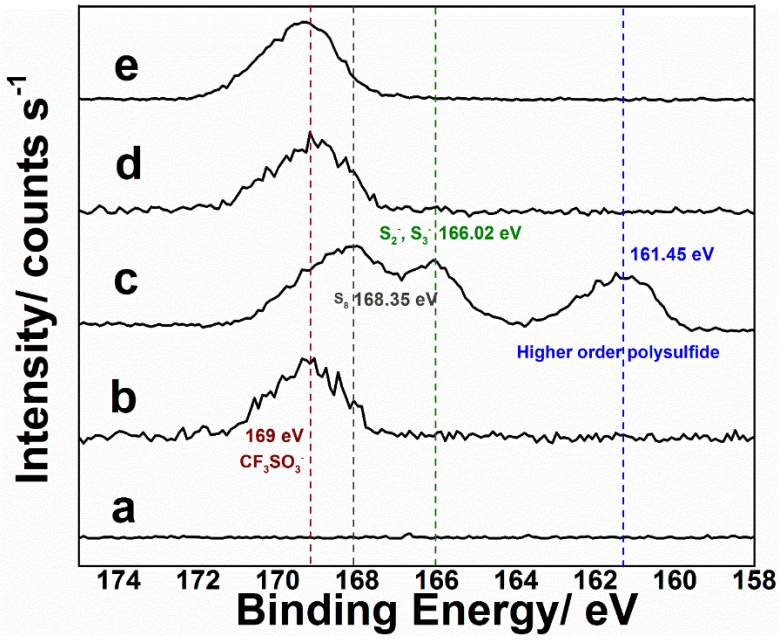

Figure V-242: XPS S2p binding energy profile of a) commercial separator b) commercial separator soaked in electrolyte; separators of c) commercial sulfur electrode; d) S – CFM-1; e) S – CFM-2 electrodes; (after 200 cycles at 0.2 C rate)

The effect of sulfur encapsulation within the CFM structures on the cycling performance of S – CFMs was therefore studied by analyzing the separators retrieved using XPS after 200 charge – discharge cycles. S2p peaks were analyzed to understand the nature of the sulfur/polysulfide species present in the various separators. As control experiments, the commercial separator and commercial separator dipped in the lithium electrolyte were also analyzed and the resultant XPS plots are shown in Figure V-242 (a,b). As expected, the

Celgard separator does not display an S2p peak before cycling while a distinct peak corresponding to the electrolyte species (Trifluoro methyl sulfonate lithium salt) is seen in Figure V-242b [15]. The XPS plot for the post-cycled separator for the commercial sulfur electrode shows S2p peaks at 168.35 eV, 166.02 eV and 161.45 eV. The peak at 168.35 eV corresponds to S2p peak of cyclic S_7, S_8. On the other hand, the peaks at 166.02 eV and 161.45 eV are due to lower and higher order polysulfide, respectively[16-19]. This indicates and validates the well-known phenomenon of the commercial sulfur electrode (Figure V-242c) undergoing rapid loss in capacity due to the rapid dissolution of polysulfide species formed because a lack of any medium or mechanism to retain/constrict the same at the electrode surface. However, the separators corresponding to the S – CFM electrodes (post-cycling, after 200 cycles) (Figure V-242 (d,e)) distinctly display only a single S2p peak at 169 eV which is attributed to the sulfur corresponding to the $LiCF_3SO_3$ from the electrolyte[15] as observed in the case of Figure V-242b for the commercial separator soaked in the electrolyte. The absence of any detectable polysulfide in the post-cycled separators cycled from electrodes generated with the CFM-1 and CFM-2, especially after 200 cycles (Figure V-242 (d, e)) indicates complete constriction of the formed polysulfide within the CFM structures possibly due to chemical-binding of S to the CFM architecture as observed in the TEM images (Figure V-240) and XPS (Figure V-241). In addition, spatial confinement possibly aids in ensuring polysulfide retention at the electrode. Though the porous structures have previously been shown to result in improved cycling behavior, complete masking of polysulfide dissolution using a porous host has seldom or never been reported to the best of our knowledge. The unique cage-like structure of the CFMs along with the chemical binding occurring therein thus results in a very stable cycling performance with a remarkably low fade rate of ~0.0014% $cycle^{-1}$.

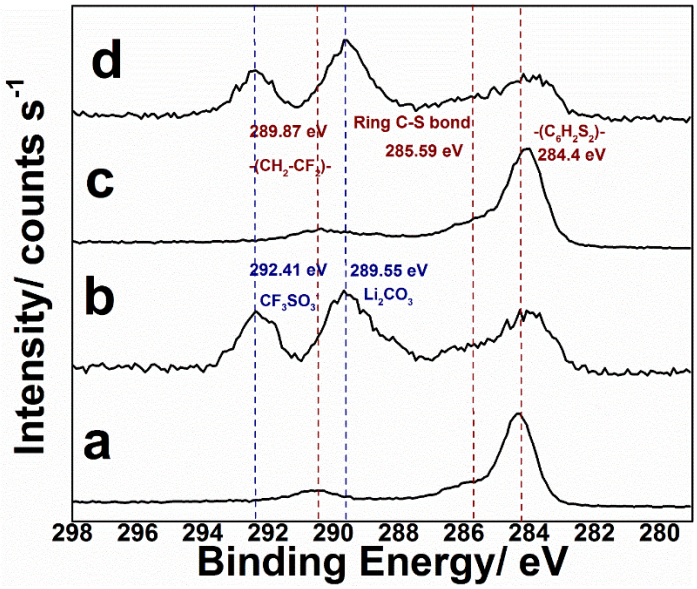

Figure V-243: XPS C1s Binding Energy profile of slurry coated electrodes of a) S – CFM-1 before cycling, b) S –CFM-1 after 200 cycles, c) S – CFM-2 before cycling, and d) S – CFM-2 after 200 cycles at 0.2 C rate

However, both the S-CFM electrodes generated with undergo initial loss in capacity which is typically known to occur and attributed to the polysulfide dissolution. The XPS results discussed above clearly indicate that this loss cannot be related to polysulfide dissolution as evidenced by the lack thereof of any sulfur species detected on the separators [Figure V-242 (d, e)]. To understand the origin of this initial capacity loss observed, XPS was performed on both the S – CFM coated electrodes before and after 200 cycles. Figure V-243 represents the C1s spectrum of slurry cast S – CFM electrodes and the same electrodes post cycling. S – CFM-1 (Figure V-243b) and S–CFM-2 (Figure V-243d) electrode samples have peaks corresponding to – (CF_2 – CF_2) – bonds from PVdF binder (289.87 eV)[20], -C_6H_5S- bond corresponding to ring C – S interactions (285.59 eV)[21] and – $C_6H_4S_2$- (284.4 eV)[22]. The presence of the C-S peaks herein confirms the observations in the S2p spectrum (Figure V-241) and corroborates the hypothesis that sulfur-carbon bonding aids in ensuring superior polysulfide retention within the CFM structure. The S – CFMs post-200 cycles showed two C_{1s} peaks at 292.41 eV and 289.55 eV in addition to the peaks observed before cycling. The peak at 292.41 eV corresponds to the $CF_3SO_3^-$[15] group of the lithium salt $LiCF_3SO_3$ used with the organic electrolyte. The peak at 289.55 eV corresponds to Li_2CO_3[23] resulting from the irreversible reaction of Li^+ ions with the –(CO_3)- groups of the CFM.

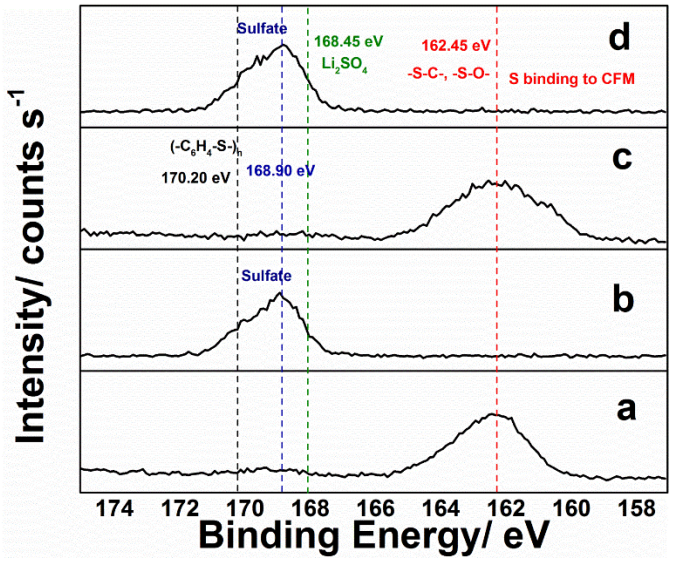

Figure V-244: XPS S2p Binding Energy profile of slurry coated electrodes of a) S – CFM-1-before cycling, b) S – CFM-1 after 200 cycles, c) S – CFM-2-before cycling and d) S – CFM-2 after 200 cycles at 0.2 C rate

Figure V-244 depicts the S2p profiles of the S-CFM electrodes before and after cycling. Both S-CFM-1 and S-CFM-2 electrodes before cycling show S2p peak at 162.45 eV representing the bonding of sulfur to CFMs (as also observed in Figure V-241). Both S – CFM-1 and S –CFM-2 electrodes post-cycling however, show the presence of a satellite peak at 170.20 eV, corresponding to the occurrence of sulfur-carbon bonding [21, 24]. This indicates that sulfur is bound to the carbon before cycling as well as through the various stages of cycling preventing the loss of sulfur through polysulfide run-away to bulk electrolyte during cycling resulting in exceptional cycling stability. In addition to the peaks corresponding to C-S bonding, there are unique peaks observed in the post-cycled electrodes corresponding to the formation of a mixture of sulfate species. The irreversible loss in capacity could thus be attributed to irreversible consumption of sulfur through the formation of lithium, and other sulfates during electrochemical cycling. Thus, deactivation of the active material of sulfur occurs through the formation of sulfate species during the initial cycling resulting in irreversible capacity loss. The results presented herein clearly demonstrate that the embedding of sulfur into the nanoporous CFM frameworks directly in the as-prepared form without any carbonization step ensures minimal polysulfide transport out of the electrode into the separator ensuring minimal capacity loss because: (a) chemical bonding of carbon in the CFM structure with sulfur; and (b) constriction of the lithium polysulfide species within the porous matrix. This is indeed reflected resulting in stable capacity of ~609 mAh g^{-1} with a fade rate of only ~0.0014% cycle $^{-1}$ demonstrating the promise of this novel synthetic strategy. Based on the insight gained from this study sulfur infiltrated framework materials (SFM) with higher ionic conductivities were developed and upon testing showed an initial capacity of 1626 mAh/g with stable performance of 1044 mAh/g for over 100 cycles (Figure V-245). As an additional subtask of Phase-2, an air – stable inorganic framework material (IFM) was explored to trap polysulfides (Figure V-246a shows the XRD patterns of S doped IFM). The IFMs exhibit very high (80%) S infiltration and a low irreversible capacity loss of 15%. Further, the IFMs improved the first cycle specific capacity of S to ~1250 mAh/g stabilizing at ~750 mAh/g (Figure V-246b). The improved specific capacity of the sulfur electrode is attributed to the successful polysulfide trapping by IFMs and work is currently on-going to improve the performance further, the results of which will be reported in future reports.

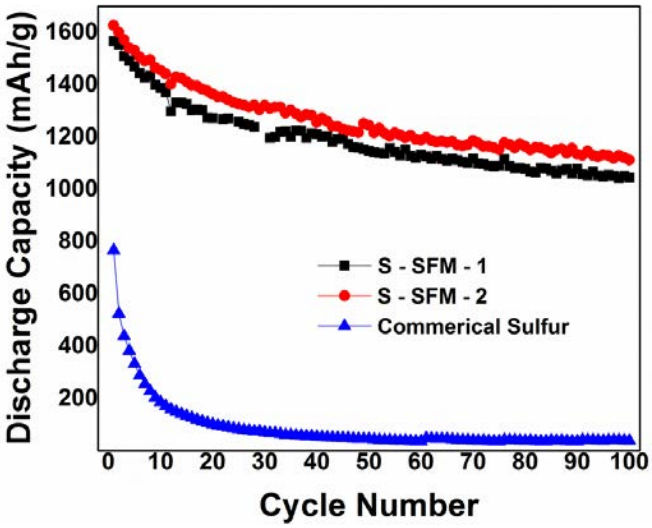

Figure V-245: Cycling performance of Sulfur – infiltrated framework material (SFM)

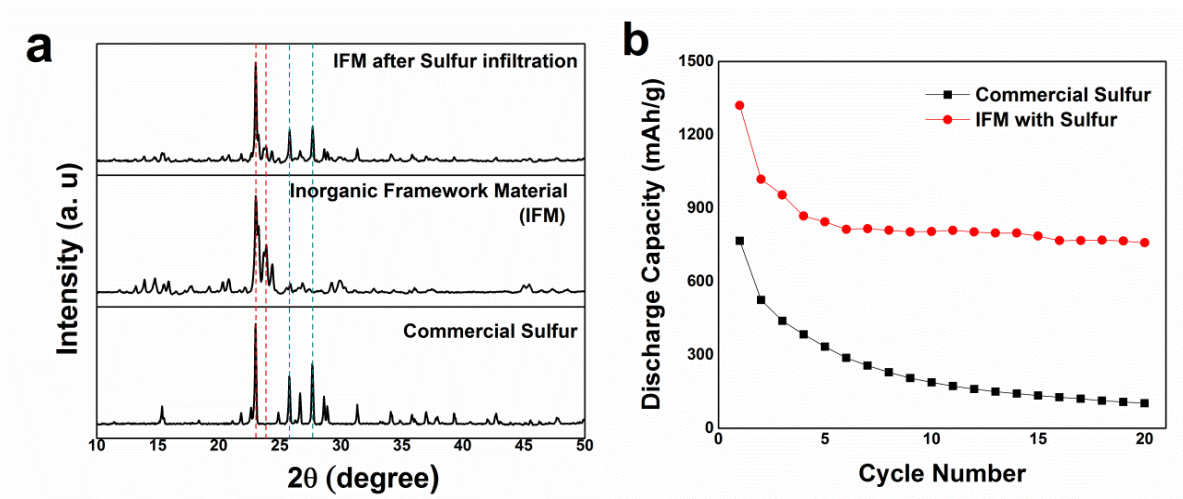

Figure V-246: (a) XRD patterns showing the infiltration of Sulfur into the Inorganic Framework Material (IFM) showing retention of IFM structure. (b) Cycling behavior of Sulfur infiltrated IFM

Conclusions

The aim of Phase-2 was to establish methods to improve sulfur cycling characteristics by employing interface engineering strategies and use of framework structures. In addition, the work was directed at developing doped LIC materials and doped sulfur nanoparticles. By implementing such approaches various materials have been derived with initial capacities in excess of 1400 mAh/g with retention of >1000 mAh/g after 100 cycles. It can also be clearly observed that fade rates have been significantly reduced by using the four approaches in Phase-2 described above. Exceptionally low fade rates of ~0.0014% loss per cycle have been observed and in the case of CFM materials a complete absence of polysulfides at the separator has been shown after 200 cycles. In Phase-3 of the study, emphasis will be laid on optimization of these systems with the goal of achieving more than 1000 mAh/g for 1000 cycles. Results of these studies will be reported in subsequent reports.

Products

Presentations/Publications/Patents

1. P. J. Hanumantha, B. Gattu, et al., Journal of The Electrochemical Society, 2014, 161, A1173-A1180.
2. Jampani, P.H.; Gattu, B.; Shanthi, P.M.; Kumta, P.N. Novel electro-spun sulfur wires for fabricating mattes of lithium-sulfur batteries, International Patent Number: WO 2016/145429 A1 (Awarded: September 15, 2016).
3. Jampani, P.H.; Shanthi, P.M.; Gattu, B.; Kumta, P.N. Novel Flexible Sulfur Wire Fabrics (FSF) for Lithium-Sulfur Batteries, The Electrochemical Society (Spring 2015), Chicago, IL.
4. Shanthi, P.M.; Jampani, P.H.; Gattu, B.; Velikokhatnyi, O.I.; Kumta, P.N. Effect of Coating and Particle Properties on the Cycling Stability of Lithium-ion Conductor (LIC) Coated Sulfur Cathodes, The Electrochemical Society (Spring 2015), Chicago, IL.
5. Shanthi, P.M.; Jampani, P.H.; Gattu, B.; Velikokhatnyi, O.I.; Kumta, P.N. Doped Lithium Orthosilicates - Promising High Rate Lithium-Ion Conductors for Li-S Batteries, The Electrochemical Society (Fall 2016), Honolulu, HI.
6. Shanthi, P.M; Jampani, P.H; Gattu, B; Sweeney, M; Datta, M.K; Kumta, P.N. Nanoporous Non-Carbonized Metal Organic Frameworks (MOFs): Effective Sulfur Hosts for High Performance Li- S Batteries, manuscript submitted (2016).

References

1. Ji, X.; Nazar, L. F., Advances in Li-S batteries. Journal of Materials Chemistry 2010, 20 (44), 9821-9826.
2. Miao, L.-X.; Wang, W.-K.; Wang, A.-B.; Yuan, K.-G.; Yang, Y.-S., A high sulfur content composite with core-shell structure as cathode material for Li-S batteries. Journal of Materials Chemistry A 2013, 1 (38), 11659-11664.
3. Wang, H.; Yang, Y.; Liang, Y.; Robinson, J. T.; Li, Y.; Jackson, A.; Cui, Y.; Dai, H., Graphene-Wrapped Sulfur Particles as a Rechargeable Lithium–Sulfur Battery Cathode Material with High Capacity and Cycling Stability. Nano Letters 2011, 11 (7), 2644-2647.
4. Wang, Z.; Dong, Y.; Li, H.; Zhao, Z.; Bin Wu, H.; Hao, C.; Liu, S.; Qiu, J.; Lou, X. W., Enhancing lithium–sulphur battery performance by strongly binding the discharge products on amino-functionalized reduced graphene oxide. Nat Commun 2014, 5.
5. Chen, R.; Zhao, T.; Tian, T.; Cao, S.; Coxon, P. R.; Xi, K.; Fairen-Jimenez, D.; Vasant Kumar, R.; Cheetham, A. K., Graphene-wrapped sulfur/metal organic framework-derived microporous carbon composite for lithium sulfur batteries. APL Materials 2014, 2 (12), 124109.
6. Chen, S.-R.; Zhai, Y.-P.; Xu, G.-L.; Jiang, Y.-X.; Zhao, D.-Y.; Li, J.-T.; Huang, L.; Sun, S.-G., Ordered mesoporous carbon/sulfur nanocomposite of high performances as cathode for lithium–sulfur battery. Electrochimica Acta 2011, 56 (26), 9549-9555.
7. Jayaprakash, N.; Shen, J.; Moganty, S. S.; Corona, A.; Archer, L. A., Porous Hollow Carbon@Sulfur Composites for High-Power Lithium–Sulfur Batteries. Angewandte Chemie 2011, 123 (26), 6026-6030.
8. Li, X.; Cao, Y.; Qi, W.; Saraf, L. V.; Xiao, J.; Nie, Z.; Mietek, J.; Zhang, J.-G.; Schwenzer, B.; Liu, J., Optimization of mesoporous carbon structures for lithium-sulfur battery applications. Journal of Materials Chemistry 2011, 21 (41), 16603-16610.
9. Yu, X.-R.; Liu, F.; Wang, Z.-Y.; Chen, Y., Auger parameters for sulfur-containing compounds using a mixed aluminum-silver excitation source. Journal of Electron Spectroscopy and Related Phenomena 1990, 50 (2), 159-166.
10. Fujimori, T.; Morelos-Gómez, A.; Zhu, Z.; Muramatsu, H.; Futamura, R.; Urita, K.; Terrones, M.; Hayashi, T.; Endo, M.; Young Hong, S.; Chul Choi, Y.; Tománek, D.; Kaneko, K., Conducting linear chains of sulphur inside carbon nanotubes. Nat Commun 2013, 4.

11. Hollinger, G.; Kumurdjian, P.; Mackowski, J. M.; Pertosa, P.; Porte, L.; Duc, T. M., ESCA study of molecular GeS3-x Tex As2 glasses. Journal of Electron Spectroscopy and Related Phenomena 1974, 5 (1), 237-245.
12. Thomas, J. M.; Adams, I.; Williams, R. H.; Barber, M., Valence band structures and core-electron energy levels in the monochalcogenides of gallium. Photoelectron spectroscopic study. Journal of the Chemical Society, Faraday Transactions 2: Molecular and Chemical Physics 1972, 68 (0), 755-764.
13. Chehimi, M. M.; Delamar, M., X-ray photoelectron spectroscopy of merocyanine dyes. Journal of Electron Spectroscopy and Related Phenomena 1990, 50 (2), C25-C32.
14. Yang, C.-P.; Yin, Y.-X.; Guo, Y.-G.; Wan, L.-J., Electrochemical (De)Lithiation of 1D Sulfur Chains in Li–S Batteries: A Model System Study. Journal of the American Chemical Society 2015, 137 (6), 2215-2218.
15. Lindberg, B. J.; Hamrin, K.; Johansson, G.; Gelius, U.; Fahlman, A.; Nordling, C.; Siegbahn, K., Molecular Spectroscopy by Means of ESCA II. Sulfur compounds. Correlation of electron binding energy with structure. Physica Scripta 1970, 1 (5-6), 286.
16. Liang, X.; Hart, C.; Pang, Q.; Garsuch, A.; Weiss, T.; Nazar, L. F., A highly efficient polysulfide mediator for lithium–sulfur batteries. Nat Commun 2015, 6.
17. Zu, C.; Fu, Y.; Manthiram, A., Highly reversible Li/dissolved polysulfide batteries with binder-free carbon nanofiber electrodes. Journal of Materials Chemistry A 2013, 1 (35), 10362-10367.
18. Su, Y.-S.; Fu, Y.; Cochell, T.; Manthiram, A., A strategic approach to recharging lithium-sulphur batteries for long cycle life. Nat Commun 2013, 4.
19. Zu, C.; Azimi, N.; Zhang, Z.; Manthiram, A., Insight into lithium-metal anodes in lithium-sulfur batteries with a fluorinated ether electrolyte. Journal of Materials Chemistry A 2015, 3 (28), 14864-14870.
20. Dapoz, S.; Betz, N.; Guittet, M.-J.; Le Moël, A., ESCA characterization of heparin-like fluoropolymers obtained by functionalization after grafting induced by swift heavy ion irradiation. Nuclear Instruments and Methods in Physics Research Section B: Beam Interactions with Materials and Atoms 1995, 105 (1–4), 120-125.
21. Riga, J.; Snauwaert, P.; De Pryck, A.; Lazzaroni, R.; Boutique, J. P.; Verbist, J. J.; Brédas, J. L.; André, J. M.; Taliani, C., Electronic structure of sulphur-containing conducting polymers. Synthetic Metals 1987, 21 (1–3), 223-228.
22. Huntley, D. R., The mechanism of the desulfurization of benzenethiol by nickel (110). The Journal of Physical Chemistry 1992, 96 (11), 4550-4558.
23. Cavanagh, A. S.; Lee, Y.; Yoon, B.; George, S., Atomic Layer Deposition of LiOH and Li2CO3 Using Lithium t-Butoxide as the Lithium Source. ECS Transactions 2010, 33 (2), 223-229.
24. Gardella, J. A.; Ferguson, S. A.; Chin, R. L., $\pi^* \leftarrow \pi$ Shakeup Satellites for the Analysis of Structure and Bonding in Aromatic Polymers by X-Ray Photoelectron Spectroscopy. Appl. Spectrosc. 1986, 40 (2), 224-232.

V.H.2. Simulations and X-ray Spectroscopy of Li-S Chemistry (LBNL)

Nitash Balsara, Principal Investigator
University of California
201 C Gilman Hall
Berkeley, CA 94720
Phone: 510-642-8973; Fax: 510-643-5037
E-mail: nbalsara@berkeley.edu

Tien Q. Duong, DOE Program Manager
Advanced Battery Materials Research (BMR)
U.S. Department of Energy
Vehicle Technologies Office
1000 Independence Avenue, SW
Washington, DC 20585
Phone: 202-586-7836
E-mail: Tien.Duong@ee.doe.gov

Start Date: October 2013
End Date: October 2017

Abstract

Objectives

- Develop method of characterizing Li-S battery reaction mechanisms consisting of *in situ* X-ray absorption spectroscopy and molecular simulations.
- Examine Li-S charge/discharge reaction mechanisms.
- Elucidate physical and chemical nature of Li-S battery reaction intermediates in different electrolytes.

Accomplishments

- Established the thermodynamics of differing polysulfide dissolution in two solvents: DMF and diglyme.
- Revealed electrochemical and chemical pathways for conversion of sulfur to intermediate polysulfides in thick cathodes using *in situ* X-ray absorption spectroscopy.
- Provided thermodynamic origins of preferential filling of microporous regions of carbon-based electrodes by liquid sulfur during melt impregnation with validation by X-ray spectroscopy and electron microscopy.

Future Achievements

- Explore and validate the speciation of polysulfide solutions during discharge based on calculated thermodynamic data.
- Examine the role of salt species (anion concentration) in defining electrolyte speciation for Li-S cells.
- Operando X-ray spectroscopic studies of polysulfide speciation and consistent interpretations based on first-principles simulations.

Technical Discussion

Background

Li-S batteries infamously suffer from dissolution of reaction intermediates - lithium polysulfides - formed during charge and discharge. These species can dissolve out of the cathode into the electrolyte reducing the cell capacity, by placing active material out of electrical contact with the cathode, and causing competitive reactions at the anode surface that ultimately result in cell failure. The reaction mechanisms that underlie the formation of polysulfides are still unclear. Uncertainty regarding these reactions has historically stemmed from ambiguity in the interpretation of *in situ* spectro-electrochemical data, especially since pure solutions of individual lithium polysulfide molecules cannot be isolated.

Introduction

Studies of Li-S reaction mechanisms have historically been challenged by the difficulty of differentiating lithium polysulfide reaction intermediates experimentally. The objective of this work is to overcome these issues by leveraging theoretical calculations of polysulfide X-ray absorption spectra. The objectives of this work are: (1) to elucidate the mechanisms by which redox reactions in the sulfur cathode proceed, and (2) to study the physical and chemical nature of lithium polysulfide reaction intermediates.

Approach

Innovative Approach: Molecular dynamic simulations of lithium polysulfide dianions and radical anions in various solvents are used to obtain simulated X-ray absorption spectra (XAS) for isolated polysulfide species. This is done using a first-principles method, dubbed the eXcited electron and Core Hole approach, based on density functional theory, in conjunction with ab initio or classical molecular dynamic simulations of dissolved polysulfide species. Experimental XAS is used to (1) examine Li-S battery reaction mechanisms as they take place in the Li-S cathode, and (2) to probe, *ex situ*, chemically prepared/synthesized mixtures of lithium polysulfide species.

1. Obtain experimental XAS for lithium polysulfide species dissolved in SEO, the polymer electrolyte which will be used for *in situ* battery experiments
2. Perform first-principles calculations to obtain X-ray spectra that can be used to interpret and analyze experimentally obtained data
3. Perform *in situ* studies of Li-S reaction mechanisms by probing cells as they are charging/discharging and cells that have been discharged to various depths of discharge.
4. Analyze resulting experimental spectroscopy using theoretically obtained X-ray spectra for individual polysulfide species.

Results

We have achieved the following progress:

Understanding polysulfide dissolution: While dissolution of lithium polysulfides has been a problem in Li-S batteries for decades, a fundamental understanding of how the polysulfides are dissolved and solvated is still lacking in literature. Our recent work focused on elucidating the thermodynamic origins of the solubility of polysulfides. The solubility of isolated lithium polysulfides is calculated from first-principles molecular dynamics simulations. We explored the associated changes in the dissolution free energy, enthalpy and entropy in two regimes: liquid-phase monodentate solvation in dimethylfomamide (DMF) and polymer-like chelation in bis(2-methoxyethyl) ether (diglyme). Our calculations show that while the dissolution free energy and solubility of the neutral ring molecule, S8, in diglyme is similar to that in DMF, the linear dianionic lithium polysulfides are significantly less soluble in diglyme than in DMF (Figure V-247). Differences in solubility in the different solvents appear to be driven by changes in the balance of enthalpic and entropic forces. For

diglyme, enthalpy of binding is the driving force for solvation, with entropic contributions approximately constant across solutes, and likely driven only by solvent exclusion. However, for diglyme, significant enthalpy gains, due to chelation of solutes, are counterbalanced by associated destabilizing loss of entropy. The decrease in solvent entropy is associated with fixed reorientation of diglyme molecules to coordinate and screen the electrostatic perturbation presented by the polysulfides. The oligoether, diglyme, presents rigid solvate structures with highly chelated lithium ions that greatly restrict the mobility of the associated solvent molecules and the solvate self-diffusion. The entropic losses in the radicals are even larger than in the dianions, due to the more rigid and polar solvate structure of LiSx motifs, resulting in a net unfavorable free energy of dissolution. The monodentate interactions of DMF with solutes and its smaller molecular size place less restrictions on this solvent and enhance solubility overall.

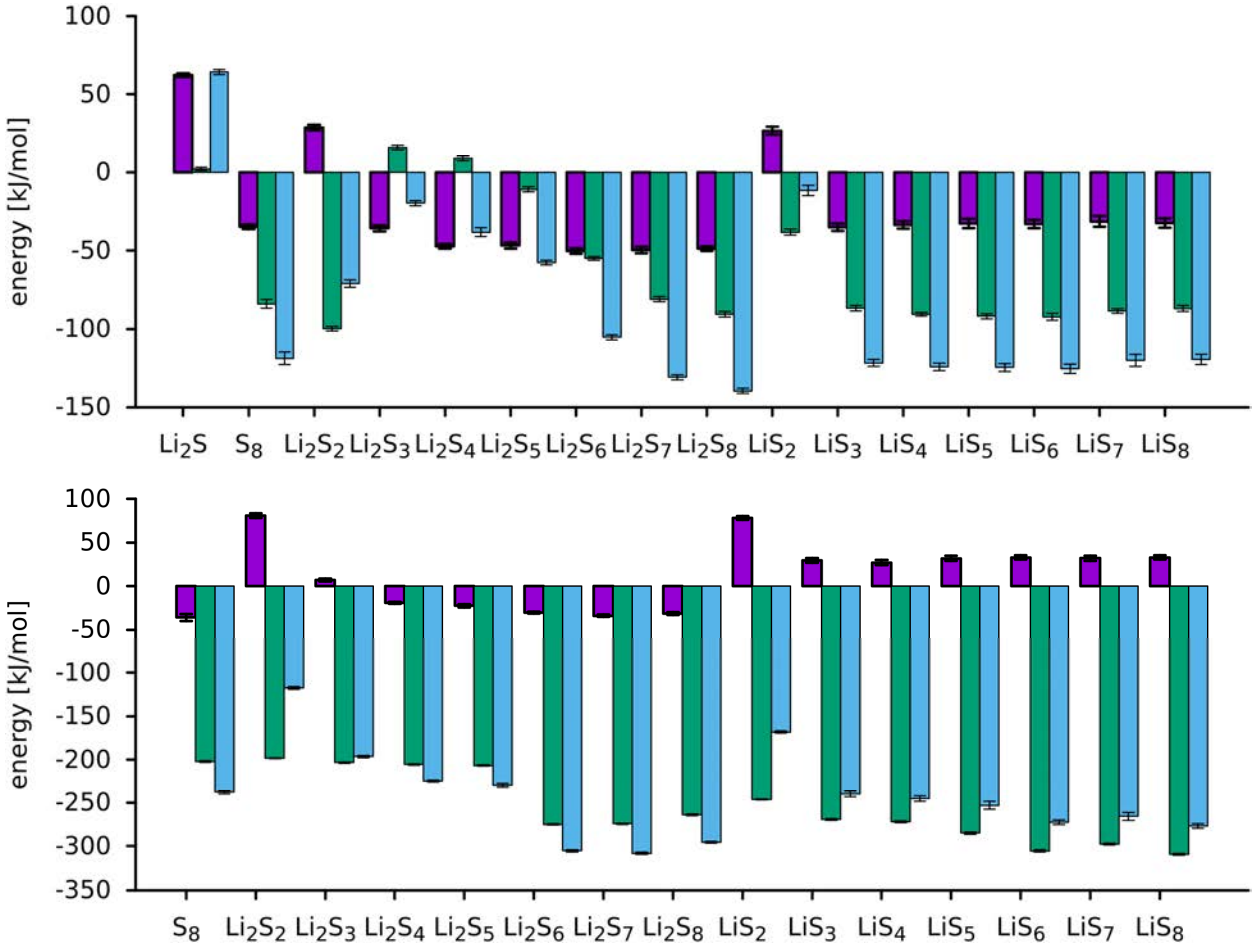

Figure V-247: Thermodynamics of formation of various lithium polysulfides in DMF (top) and diglyme (bottom). The separate total entropy (TΔS - green), enthalpy (ΔH - blue) and Gibbs free energy (ΔG - purple) are indicated. The free energy of solvation of the crystalline solid starting materials (Li2S and S8) is provided for reference

Characterization of polysulfide speciation deep inside thick cathodes: *In situ* X-ray absorption spectroscopy at the sulfur K-edge was used to probe the back of a thick Li-S cathode during discharge. The experimentally obtained spectra were interpreted using theoretical spectral standards previously generated by our group [1]. Analysis of the spectra and the fluorescence intensity measured during each scan showed that polysulfide dianion species produced by electrochemical reactions diffused to the back of the cathode during discharge. To our knowledge, this is the first time this phenomenon has been quantified. We explain this finding as follows: the limited diffusion of lithium ions to the back of a thick Li-S cathode will lead to higher reaction rates in the front of the cathode relative to the back of the cathode. This difference in reaction rate leads to a higher concentration of polysulfide dianions in the front of the cathode, which in turn creates a concentration gradient that leads to the diffusion of polysulfide dianions to the back of the cathode (Figure V-248).

The conversion of sulfur in the back of the cathode occurs in two distinct steps. In the first step, elemental sulfur is consumed by a combination of electrochemical reduction and chemical reactions. In the second step, elemental sulfur is consumed by chemical reactions alone. Going further, our results suggest that intermediate chain polysulfide dianions (Li_2S_x, $4 \leq x \leq 6$) are the dominant species at the back of the cathode. Since elemental sulfur is a crystalline insulating solid, it is likely that chemical (not electrochemical) reactions between elemental sulfur and these intermediate chain-length polysulfide dianions are essential for complete utilization of a sulfur cathode.

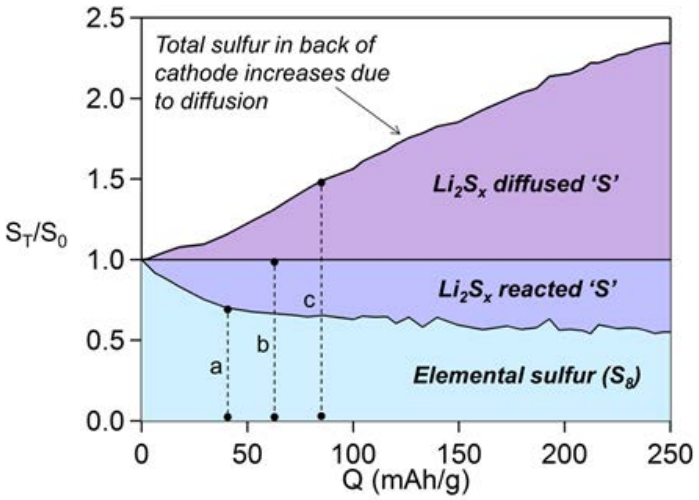

Figure V-248: Ratio of total sulfur (on an atomic basis) in the back of the cathode (ST) to the original amount of sulfur in the back of the cathode (S0)

Taken from Kevin Wujcik, Dunyang Rita Wang, Tod A. Pascal, David Prendergast, Nitash P. Balsara, "In situ X-ray absorption spectroscopy studies of discharge reactions in a thick cathode of a lithium sulfur battery", Journal of the Electrochemical Society (accepted).

Distribution of sulfur in microporous carbon cathodes from melt impregnation: Weakly interacting liquids can impregnate microporous carbon matrices, a fact that has been exploited to fabricate composite carbon/sulfur cathodes for lithium – sulfur batteries by melt impregnation. Through extensive computer simulations, we have isolated the thermodynamic driving forces for the filling of graphitic nanopores with liquid sulfur. We developed a temperature and curvature dependent, scaling model to predict the thermodynamics of filled carbon nanotubes, and proposed a new criterion for nanocapillary action based on the two critical surface tensions of sulfur in this context – viz., liquid-vapor and liquid-solid. Electronic structure calculations reveal that sulfur molecules within 2 nm of a graphene interface experience electronic screening by the semi-metallic carbon surface, as evident by a 0.3 eV red-shift in simulated X-ray absorption spectra (XAS) of interfacial sulfur (Figure V-250). The same red-shift is evident in measured XAS of sulfur cathodes comprising carbon nanospheres at 30 wt% loading (Figure V-249). The nanosphere diameters are ~100 nm, however, BET analysis suggests that the shells of these nanospheres are microporous (pores of diameter less than 2 nm). Our findings indicate that during melt impregnation, liquid sulfur first fills the microporous shells before the inner voids of this carbon electrode. The inner voids are filled at 60 wt% loading with sulfur and provide enough free volume to exhibit evidence for crystalline sulfur (from X-ray diffraction) upon cooling. This hypothesis is validated by high-resolution transition electron microscopy (HRTEM) and associated electron dispersive X-ray spectroscopy (EDS) imaging (Figure V-249). This work highlights how nanoscale cathode morphology can define inhomogeneous distributions of sulfur upon cell fabrication. Open questions remain regarding the accessibility of this nano-confined sulfur to the electrolyte, and the role of nanoconfinement in working cells, which may affect cell performance in terms of accessible capacity and rate-dependent cycling.

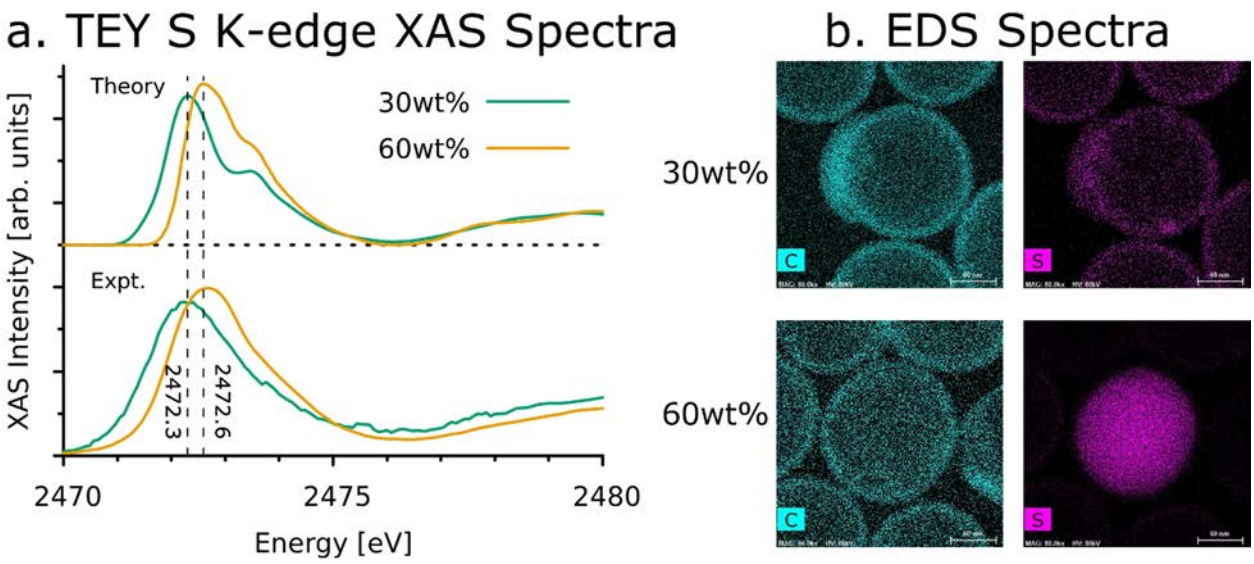

Figure V-249: X-ray spectra of carbon nanoshells at two sulfur loadings. a. Simulated (Theory – top) and measured (Expt. – bottom) X-ray absorption spectra of 30wt% (green) and 60wt% (brown) loaded carbon nanoshells. Dashed vertical lines indicate the positions of the peak maximum. b. Energy dispersive X-ray spectra (EDS) of nanoshells at the carbon and sulfur edges

Taken from Tod A. Pascal, Irune Villaluenga, Kevin Wujcik, Xi Jiang, Didier Devaux, Dunyang Rita Wang, Nitash Balsara and David Prendergast, "Theoretical underpinnings and X-ray spectroscopic validation of inhomogeneous sulfur loading of carbon-based electrodes with bimodal porosity via melt impregnation", Nano Lett. (submitted).

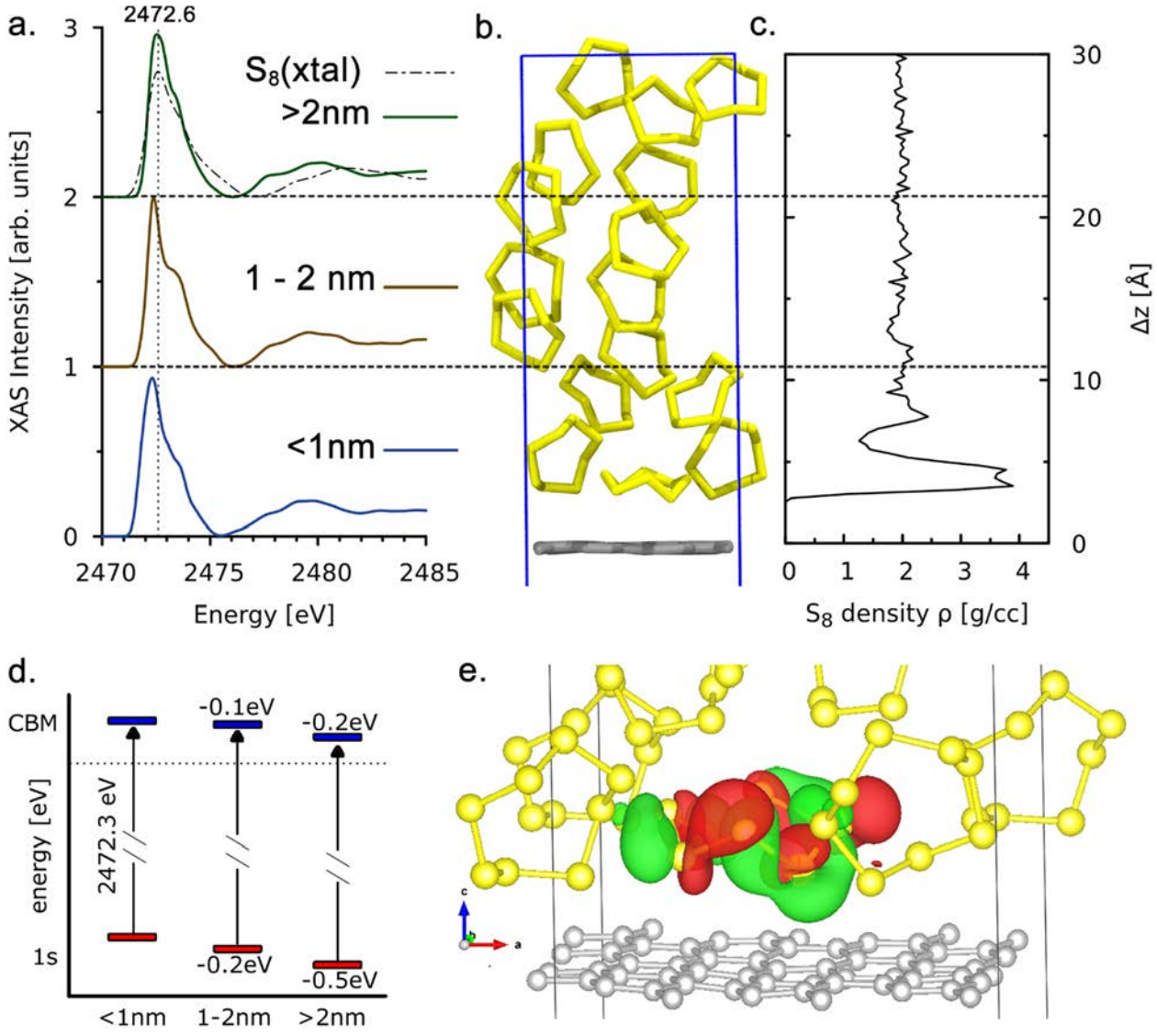

Figure V-250: Electronic structure of sulfur near graphene. a. (from top to bottom) Calculated sulfur K-edge X-ray absorption spectra of sulfur molecules >2nm (green), 1 – 2 nm (brown) and < 1nm (blue) from an interface with graphene. The vertical dashed line is the bulk sulfur "white line" at 2472.6 eV. The XAS of crystalline sulfur at ambient conditions is provided (black dash-dot) as reference. b. Molecular dynamics snapshot of the simulation cell, showing the sulfur atoms (yellow) and the carbon plane. c. Density of sulfur (molecular center of mass) as a function of distance from the graphene sheet from FPMD simulations. d. Energy level diagram showing the energy shifts in the 1s core orbital energy (red) and conduction band minima (CBM – blue) for sulfur molecules at varying distances from the interface. The data (bars) are averaged over all sulfur atoms within that distance range and the width of the bar indicates the standard deviation. e. Electronic component of the core excited state of an interfacial sulfur molecule, with positive (negative) phase indicated in red (green)

Taken from Tod A. Pascal, Irune Villaluenga, Kevin Wujcik, Xi Jiang, Didier Devaux, Dunyang Rita Wang, Nitash Balsara and David Prendergast, "Theoretical underpinnings and X-ray spectroscopic validation of inhomogeneous sulfur loading of carbon-based electrodes with bimodal porosity via melt impregnation", Nano Lett. (submitted).

Conclusions

This program continues to expand our understanding of sulfur and polysulfide behavior in Li-S cells. We have explained significant differences in solubility of polysulfides in polar vs. chelating solvents and the thermodynamic importance of quasi-rigid solvates in polyethers. Using X-ray absorption spectroscopy and previously determined theoretical spectra of pure polysulfides, we have determined the speciation of polysulfides in thick electrodes revealing that conversion of sulfur to intermediate polysulfides is driven by an initial electrochemical process and subsequent chemical equilibrium. Knowing the thermodynamics of

polysulfide solubility, it seems clear that dissolved sulfur would be unstable with respect to polysulfide formation. This will allow us to develop thermodynamic models of the evolving speciation in Li-S cathodes during discharge. Finally, we have revealed the thermodynamics that drives liquid sulfur preferentially inside pores of diameter less than 2 nm in porous carbon cathodes. This has significant consequences for cathodes with mixed porosity and their accessible capacity during discharge and further work remains to establish the role of nanoscale confinement under working conditions.

Products

Presentations/Publications/Patents

1. Kevin H. Wujcik, Dunyang Rita Wang, Aditya Raghunathan, Melanie Drake, Tod A. Pascal, David Prendergast, and Nitash P. Balsara, "Lithium Polysulfide Radical Anions in Ether-Based Solvents", J. Phys. Chem. C 120, 18403 (2016).
2. Kevin Wujcik, Dunyang Rita Wang, Tod A. Pascal, David Prendergast, Nitash P. Balsara, "*In situ* X-ray absorption spectroscopy studies of discharge reactions in a thick cathode of a lithium sulfur battery", Journal of the Electrochemical Society (accepted).
3. Tod A. Pascal, Irune Villaluenga, Kevin Wujcik, Xi Jiang, Didier Devaux, Dunyang Rita Wang, Nitash Balsara and David Prendergast, "Theoretical underpinnings and X-ray spectroscopic validation of inhomogeneous sulfur loading of carbon-based electrodes with bimodal porosity via melt impregnation", Nano Lett. (submitted).
4. Tod A. Pascal, Kevin H. Wujcik, Dunyang Rita Wang, Nitash P. Balsara and David Prendergast, "Thermodynamic Origins of Solvent-Dependent Solubility of Lithium Polysulfides from First Principles", (submitted).
5. David Prendergast, "First-principles exploration beyond Lithium-ion", UK Science and Technology Facilities Council, Batteries Annual Meeting, Abingdon, Oxfordshire, UK, July 14-15, 2016.
6. David Prendergast, "Li-S within BMR and beyond: X-ray spectroscopy and Theory", JCESR Characterization Workshop, PNNL, Richland, WA, May 23, 2016.
7. Tod Pascal, "Probing the solution chemistry of Lithium Sulfur Batteries from First Principles", IUMRS-ICAM 2015 Conference, Jeju Island, South Korea October, 2015.
8. Tod Pascal, "What can X-rays teach us about local atomic structure in energy materials", KAUST Conference on Water and Energy, Jeddah, Saudi Arabia, January 2016.
9. Tod Pascal, "X-ray Absorption Spectroscopy as a probe of the solution phase chemistry of battery materials", MRS Spring Meeting, Phoenix, AZ, March 2016.
10. Tod Pascal, "Seeing is believing: Chemistry, Physics and Materials Science at Lithium Interfaces", EEWS Annual Water/Energy/Environment Nexus, Daejeon, South Korea, August, 2016.
11. Tod Pascal, "Elucidating the Structure of Interfaces with X-Ray Absorption Spectroscopy", Pascal and Prendergast, Advanced Light Source Annual User Meeting, PICKLES Workshop, Berkeley, CA, October, 2016.
12. Tod Pascal, "Sulfo-phobicity and the morphology of Graphitic Materials used in Lithium Sulfur Batteries", Advanced Light Source User Meeting, Berkeley, CA, October, 2016.
13. Nitash Balsara, "Lithium Battery Start-Ups", Session: Contemporary Issues and Case Studies in Electrochemical Innovation, Annual Meeting of the Electrochemical Society, Honolulu, Hawaii, October 3, 2016.
14. Nitash Balsara, "Ion Transport, Lithium Batteries, and the Clean Energy Landscape", Institut Polytechnique, Grenoble, France, September 16, 2016.
15. Nitash Balsara, "Nanostructured Block Copolymers for Lithium Batteries and Biofuels Purification", Plenary Session: Emerging Energy Applications of Nanoscale Science and Engineering, Annual Meeting of the American Institute of Chemical Engineers, San Francisco, California, November 14, 2016.
16. Nitash Balsara, "Lithium Batteries and the Free Energy Landscape", ExxonMobil Research and Engineering Co., Annandale, New Jersey, December 16, 2015.

References

1. Tod A. Pascal , Kevin Hamilton Wujcik , Juan J. Velasco-Velez , Cheng-Hao Wu , Alexander Andrew Teran , Mukes Kapilashrami , Jordi Cabana , Jinghua Guo , Miquel Salmeron , Nitash P. Balsara , and David Prendergast, “The X-ray absorption spectra of dissolved polysulfides in lithium-sulfur batteries from first-principles”, J. Phys. Chem. Lett., 5, 1547 (2014).

V.H.3. Novel Chemistry: Lithium-Selenium and Selenium-Sulfur Couple (ANL)

Khalil Amine, Principal Investigator
Argonne National Laboratory
9700 South Cass Avenue
Argonne, IL 60439-4837
Phone: 630-252-3838; Fax: 630-972-4520
E-mail: amine@anl.gov

Tien Q. Duong, DOE Program Manager
Advanced Battery Materials Research (BMR)
U.S. Department of Energy
Vehicle Technologies Office
1000 Independence Avenue, SW
Washington, DC 20585
Phone: 202-586-7836
E-mail: Tien.Duong@ee.doe.gov

Start Date: October, 2013
Projected End Date: 2017

Abstract

Objectives

The objective of this project is to develop a novel SeS_x cathode material for rechargeable lithium batteries with high energy density, long life along with low cost and high safety.

Accomplishments

- Preparation of space-confined Se and Se-S cathodes .
- The electrochemistry of space-confined Se_2S_5 cathode in carbonate electrolytes was investigated using *in situ* synchrotron X-ray absorption near edge spectroscopy (XANES).
- The electrochemistry of space-confined Se_2S_5 cathode in DOL-DME based electrolytes was investigated using *in situ* synchrotron XANES and *ab* initio calculation.
- A novel electrolyte was proposed for space-confined Se-S cathodes.

Future Achievements

- When this new cathode is optimized, the following electrochemical specifications can be achieved:
  - A cell with nominal voltage of 2 V and energy density of 600 Wh kg^{-1}.
  - A battery capable of operating for 500 cycles with low capacity fade.

Technical Discussion

Background

Lithium-ion batteries (LIBs) have been the main power supply for portable electronics since their commercialization by Sony Corporation in 1990s and are showing great potential for electrical vehicles.[1] However, because of their low energy density, the state-of-the-art LIBs cannot meet the increasing energy demand for the next-generation electric vehicles (500-km drive range). In the search for a transformative new energy storage system, the rechargeable Li/sulfur battery is considered as one of the promising candidates due to its much higher energy density and lower cost than those of state-of-the-art lithium-ion batteries. However,

the insulating nature of sulfur and the dissolution of intermediary polysulfides into the electrolyte significantly hinder its practical application.[2] Very recently, selenium and selenium-sulfur systems have received considerable attention as cathode materials for rechargeable batteries owing to the high electronic conductivity (20 orders of magnitude higher than sulfur) and high volumetric capacity (3254 mAh cm^{-3}) of selenium.

Introduction

In 2012, our group firstly reported that selenium and selenium-sulfur could be cycled versus both lithium and sodium.[3] Selenium-Sulfur mixtures are miscible in a wide concentration range, and many Se-S composites including Se_5S, Se_5S_2, Se_5S_4, SeS, Se_3S_5, SeS_2, and SeS_7 can be prepared, including materials with a small amount of Se such as SeS_{20}. These Se-S materials can offer higher theoretical specific capacities than Se alone, in the range of 675-1550 $mAh \cdot g^{-1}$, with improved conductivity comparing to pure S. However, as a new chemistry, the electrochemistry of Se-S cathodes was not well understood; the lack of such acknowledge significantly hinders the rational design of Li/electrolyte/Se-S chemistries with outstanding electrochemical performance.

Approach

The dissolution of lithium polysulfides in non-aqueous electrolytes has been the major contribution to the low round-trip energy efficiency and insufficient cycle life of Li/S batteries. In addition, the insulating characteristics of both end members during charge/discharge (S and Li_2S) limit such batteries from high rate applications. To overcome this technological barrier, S or Li_2S are generally impregnated in a conducting carbon matrix for a much efficient charge transport into/out of the active materials. However, this approach makes it difficult to increase the loading density of practical electrodes. It is proposed here to solve the above barriers using following approaches: (1) partially replacing S with Se, and (2) nano-confinement of the S_xSe_y in a nanoporous conductive matrix.

Results

Preparation and characterization of space-confined Se-S cathode

Se_2S_5/micro-mesoporous carbon (MPC) composite was prepared through a modified vaporization-condensation method to ensure a good encapsulation of Se_2S_5 into the micro/mesopores of MPC host. The HEXRD patterns of bulk Se_2S_5, MPC and Se_2S_5/MPC composite are compared in Figure V-251a. As shown in Figure V-251a, MPC presents three broad peaks due to its amorphous nature, while the bulk Se_2S_5 exhibits strong diffraction peaks resulting from its good crystallinity. The Se_2S_5/MPC composite shows the same three broad peaks in the same 2-Theta position with MPC, indicating that Se_2S_5 particles may be either small or at an amorphous state. Characteristic Raman peaks of Se_2S_5 (see Figure V-251b) are not observed in the Se_2S_5/MPC composite. Only two broad carbon peaks at 1327 cm^{-1} and 1591 cm^{-1}, representing the disordered graphite (D band) and crystalline graphite (G band), respectively, appear in the Raman spectrum of Se_2S_5/MPC composite (Figure V-251b). This suggests that a negligible amount of Se_2S_5 exists on the surface of Se_2S_5/MPC composites. The intensity ratio (I_D/I_G) of Se_2S_5/MPC between D band and G band has been slightly increased compared to MPC, which should be attributed to the infiltration of Se_2S_5 into the MPC host. The pair distribution function (PDF) of bulk Se_2S_5, MPC and Se_2S_5/MPC in Figure V-251c shows that the short range structure of MPC is similar to graphite: the first three peaks are positioned at real space distances of 1.42, 2.46 and 2.83 Å, matching the in-plane carbon-carbon distances in graphite (1.43Å, 2.46Å and 2.85Å). The bulk Se_2S_5 is pretty crystalline, while the nano Se_2S_5 that formed in the Se_2S_5/MPC composite looks like inorganic glass. The PDF shape of nano Se_2S_5 resembles the PDF for bulk Se_2S_5, indicating that the nano Se_2S_5 has the same local atomic ordering structure of bulk Se_2S_5, not a physical mixture of S and Se. In the HAADF STEM image of Se_2S_5/MPC (Figure V-251d), one can see many small brighter dots with a size of 1-2 nm, especially near the edge of sample due to less overlapping effect at thin areas. These bright dots correspond to high Z elements Se and S since HAADF image is roughly proportional to Z^2. The TEM elemental mapping images in Figure V-251e and Figure V-251f further confirm the uniform distribution of sulfur and selenium in the Se_2S_5/MPC composite. In one word, the above finding indicates that Se_2S_5 is in an amorphous state and well embedded into the micro/mesopores of MPC host materials, which presents similar structures to the previous

reported space-confined Se and S cathodes. The well-prepared composites with encapsulated Se_2S_5 in the MPC host could help us identify the common issue during cycling for Se-based cathodes in different electrolytes.

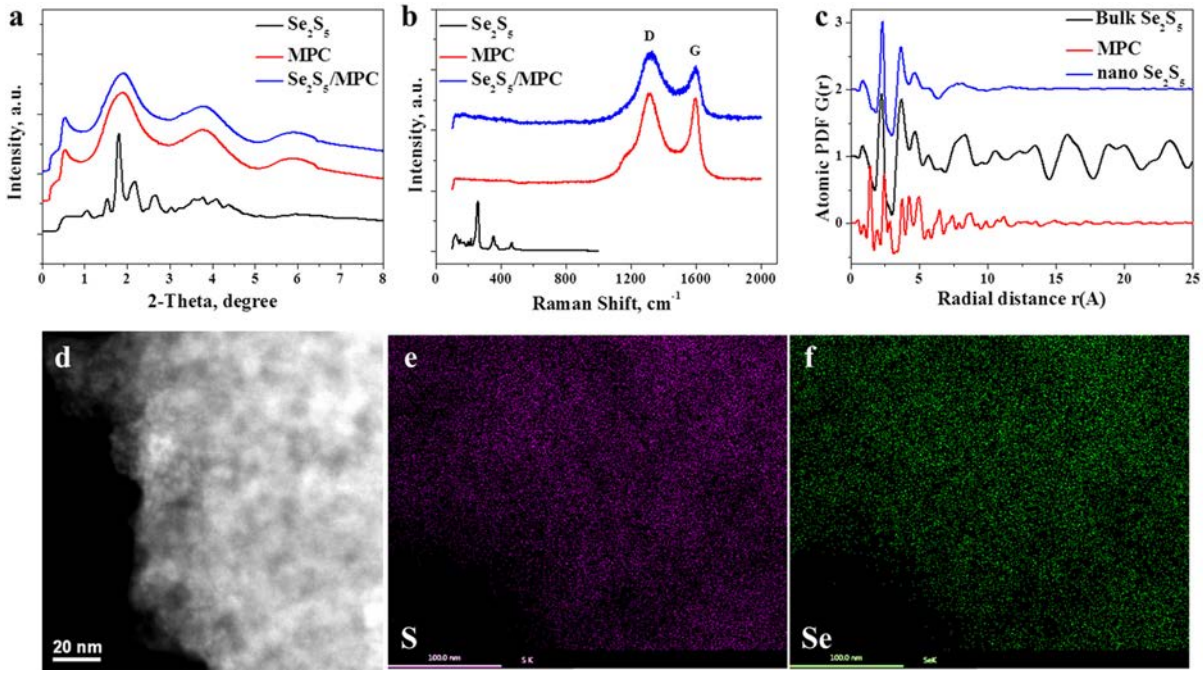

Figure V-251: (a) HEXRD and (b) Raman of MPC, bulk Se2S5 and Se2S5/MPC; (c) PDF of MPC, bulk Se2S5 and nano Se2S5 that formed in the Se2S5/MPC; (d) HAADF STEM image and TEM elemental mapping images of (e) sulfur and (f) selenium in the Se2S5/MPC composite

Electrochemistry of space-confined Se and Se-S cathode in carbonate based electrolytes

Figure V-252a shows the *in situ* XANES Se K-edge measurement of space-confined Se cathode during charge/discharge in carbonate-based electrolytes (see Figure V-252b for the corresponding voltage profile during the *in situ* experiment).[4] The color reflects the normalized absorption intensity, the red color represents high intensity, and the blue color means low intensity. It was found that the absorption intensity of the Se K-edge is weakened when the cell is discharged to 0.8 V and recovered when the cell is charged back to 3.5 V. By selecting XANES spectra of the powder materials Se and Li_2Se as standards, the composition of the Se electrode at different charge-discharge states can be determined by linear combination fitting of the XANES spectra measured during cell cycling with the Athena software package. Most of the spectra can be well fitted, illustrated by extremely small residues with reduced $\chi 2$ from 0.012% to 0.144% as shown in Figure V-252c (black squares). The fitting results suggest that there are no observable soluble polyselenides intermediate phases formed in the carbonate electrolytes. In another word, Se is directly transformed into Li_2Se, bypassing the formation of polyselenides. Therefore, space-confined Se cathode materials could demonstrate excellent electrochemical performance in Li/Se batteries with carbonate electrolytes, which is significantly different from Li/S and Li/O_2 battery. However, in the case of Se_2S_5/MPC (Figure V-252d), it can be obviously found that it presents a complete different electrochemistry from space-confined Se cathode (Figure V-252a). The Se K-edge was shifted to a higher energy position that stands for Li_2Se at the 1st fully discharged state. However, at the end of the 1st charge process, the absorption intensity of Se cannot be recovered, indicating a large amount of irreversible capacity loss. This may be owing to the well-known poor compatibility of polysulfides with the carbonate electrolytes,[5] which may significantly decrease the (de) lithiation reversibility of Se component. Therefore, in order to enable high performance Se-S cathode in carbonate electrolytes, we need to have a smart electrode structure design, especially for interfacial layer between the electrode materials and the carbonate electrolytes.

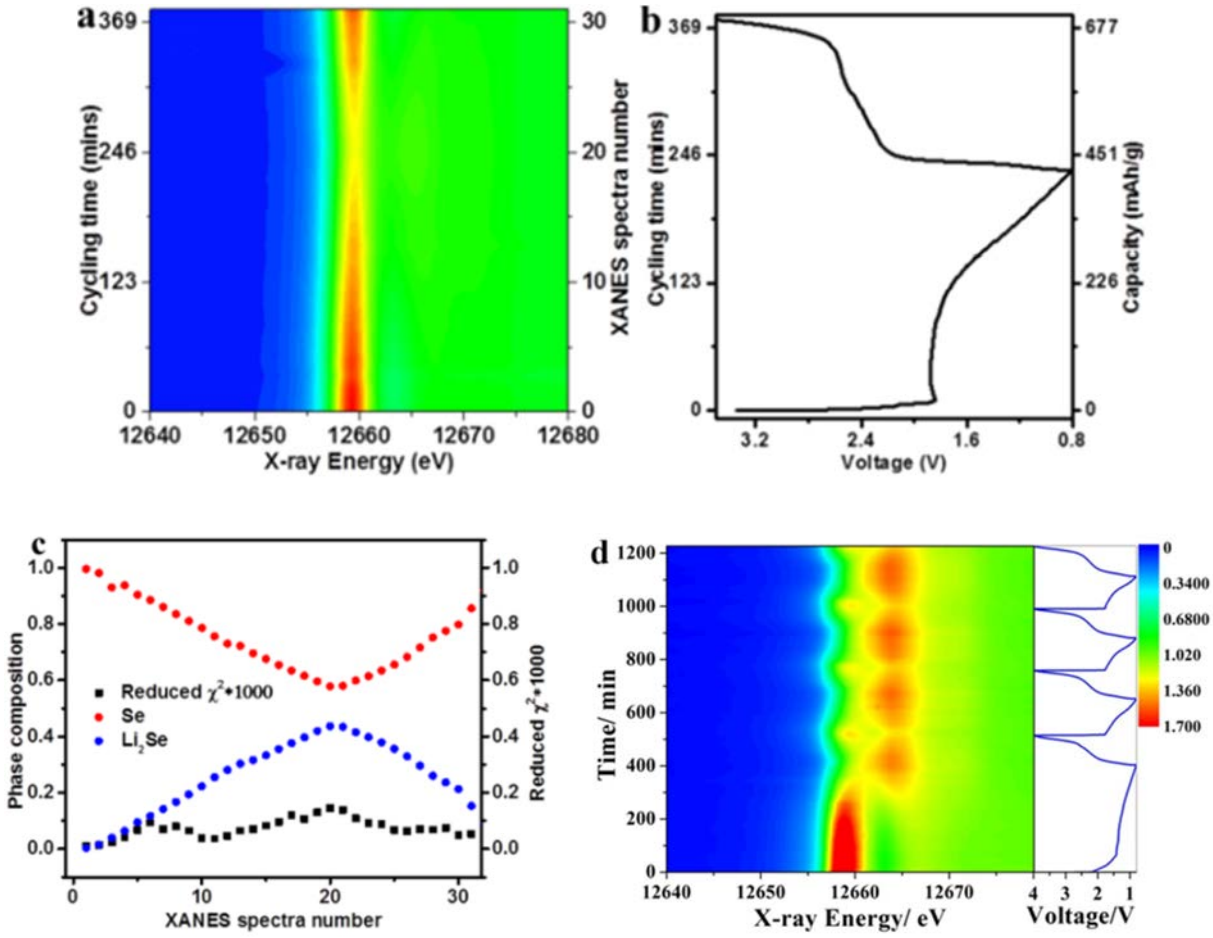

Figure V-252: *In situ* XANES measurement for space-confined Se cathode in GenII electrolyte: (a) normalized XANES spectra of the cycling cell, (b) voltage profile, (c) linear combination fitting of residue values and corresponding phase compositions in different state of charge-discharge. (d) 2D contour plot of *in situ* XANES measurement of space-confined Se2S5 cathode at 0.2 C (1C=1389 mA g^{-1})

Electrochemistry of space-confined Se-S cathode in DOL-DME based electrolytes

We have previously reported that in the commonly used DOL-DME based electrolytes, Se is reduced to the polyselenides, Li_2Se_n ($n \geq 4$), Li_2Se_2, and Li_2Se sequentially during the lithiation process, and Li_2Se is oxidized to Se through Li_2Se_n ($n \geq 4$) during the de-lithiation process in the 1st cycle, which undergoes similar reaction process to the sulfur system.[6] Therefore, it is very important to rationally design Se cathodes with a proper conductive host to constrain the polyselenides on the cathode side and to avoid the shuttle effect using the knowledge learned from Li/S chemistries. Lots of carbonaceous materials with different pore structures, specific surface area and morphologies had been investigated for Se-based cathodes in ether electrolytes. However, it was found that even with a very good encapsulation of Se or S_xSe_y in various carbon host materials, most of the previous reported Se-based cathodes still show a continuous capacity fading and severe shuttle effect even at relatively high charge/discharge rates in DOL-DME based electrolytes.[7-10] This is obviously different from space-confined S cathodes. Figure V-253a shows the cycle performance of Se_2S_5/MPC cathode in the DOL-DME based electrolytes at C/10. It can be seen that even confined in the MPC with a main pore size of only 1.9 nm, the Se_2S_5/MPC cathode presents a rapid capacity fading upon continuous cycling. After 50 cycles of charge/discharge, it can only maintain a discharge capacity of 345.5 mAh g^{-1}. Also, a low coulombic efficiency was observed, indicating a severe shuttle effect. These results were similar to the previous reported space-confined Se-based cathodes. The cycle performance of Se/MPC cathode was shown in Figure V-253b. Its initial discharge/charge capacities were measured to be 481.1 mAh g^{-1} and 509.8 mAh g^{-1}, respectively. However, the capacity was significantly decreased in only 10 cycles and a severe polyselenides shuttle was clearly observed, indicating that the rapid capacity fading and the low coulombic efficiency of the Se_2S_5/MPC composite should come from the Se components.

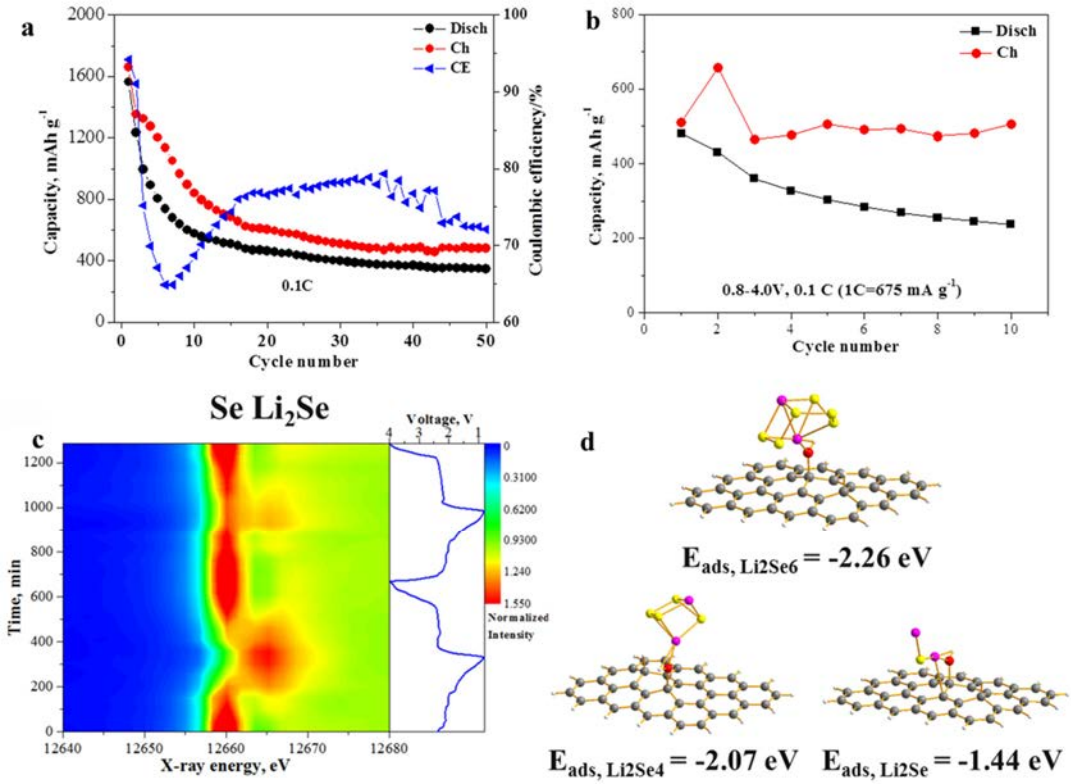

Figure V-253: Cycle performance of (a) space-confined Se2S5 and (b) Se cathode at 0.1 C within 0.8-4.0 V; (c) 2D contour plot of *in situ* XANES data of space-confined Se2S5 cathode at 0.2 C; (d) *ab initio* calculations on the binding energy of different polyselenides with carbon host

In order to gain further insights into the electrochemical behavior of Se_2S_5/MPC cathode in DOL-DME based electrolytes, *in situ* X-ray absorption near edge spectroscopy (XANES) Se K-edge measurement on the Se_2S_5/MPC cathode during cycling was carried out as XANES is useful for determining the average chemical environment of the elements in all phases involves liquid and solid, as well as crystalline and/or amorphous phases. Figure V-253c shows the 2D contour plot of *in situ* XANES data for the discharge and charge process of Se_2S_5/MPC cathode at 0.2 C (1C=1389 mA g^{-1}). In addition, the voltage profile in the first two cycles is also displayed and correlated with the evolution of the XANES data. For example, the inflection point observed in the contour plot of the XANES data coincides well with the critical point in the fully discharge state. The apparent symmetry of the *in situ* XANES dataset for the Se_2S_5/MPC cathode emphasizes that the discharging and charging proceed through a reversible sequence of reactions during the first cycle, which is in agreement with our previous report for space-confined Se cathodes in DOL-DME based electrolytes. However, the 2D contour plot for the 2nd cycle is significantly different from that of the 1st cycle. It can be seen that the reduction of Se component and formation of Li_2Se are not completed. Although Se could be completely recovered at the end of the 2nd charge, the XANES spectrum in the 2nd discharge seems like a mixture of Se, polyselenides and Li_2Se instead of sole Li_2Se. The results clearly show that the Se K-edge shifted from 12656.7 eV to 12660 eV and then shifted back to 12656.7 eV in the first cycle. However, the Se K-edge has little shift in the second cycle, further confirming that the lithiation/de-lithiation reversibility of Se component was decreased.

To elucidate the mechanism of polyselenides dissolution, we performed ab initio calculations to understand the surface interaction of polyselenides with carbon surface. Different polyselenides—Li_2Se_n (n=1, 4, 6) was investigated to compare their bonding strength with carbon host, while the carbon substrate is an H-terminated graphene sheet with hydroxyl functional group as these groups are often present as defect on carbon surface and are likely the active binding sites for polyselenides. The approach may not give an absolute quantification of the binding strength between the polyselenides with the carbon surface, but will provide a good comparison with different polyselenides and hence the interfacial effect on the cycling performance. The most stable geometric configurations of the different polyselenides with H-terminated graphene sheet with hydroxyl

functional group are shown in Figure V-253d with their binding energy values, respectively. As clearly shown, the binding energy of polyselenides with conductive carbon host is as follow Li_2Se_6>Li_2Se_4>Li_2Se, indicating that there is a favorable bonding between long-chain polyselenides with carbon surface. *In situ* XANES study found that the transformation of long-chain polyselenides to short-chain polyselenides was suppressed during cycling, which may be due to the weaker binding energy of short-chain polyselenides with carbon surface than long-chain polyselenides. Therefore, an aggravated formation of long-chain polyselenides could be expected, which will lead to the gradual capacity fading during cycling due to less electron transfer involved. On the contrary, the binding strength of short-chain polysulfides with carbon host was found to be generally stronger than long-chain polysulfides, which may lead to the distinct cycle performance between sulfur cathodes and Se-based cathodes in ether-based electrolytes.[11, 12] Considering *in situ* XANES results and the ab initio calculations together with the related works reported in the current literatures, we concluded that the current DOL-DME based electrolytes may be not a good electrolyte for space-confined Se-based cathodes as the lithiation/de-lithiation reversibility was gradually decreased upon continuous cycling.

Novel electrolyte for space-confined Se-S cathodes with significantly improved electrochemical performance

Based on our understanding of space-confined Se-S cathodes in carbonate based and DOL-DME based electrolytes by *in situ* XANES study, we found that in addition to smarter cathode structures design, electrolytes indeed play a critical role on the electrochemical behaviour of space-confined Se-S cathodes. The optimized electrolyte requires a high stability against the nucleophilic attach of carbonyl groups and suppressed polysulfides/polyselenides dissolution. Figure V-254 shows the cycle performance of space-confined Se_2S_5 cathode in the DOL-DME based electrolyte and a newly developed electrolyte (ANL-1). It clearly shows that both cells had similar charge capacity during the electrochemical test. However, a severe gap between the charge capacity and discharge capacity was observed for the cell using DOL/DME based electrolytes. This gap is primarily caused by the dissolution of lithium polysulfides or lithium polyselenides, which significantly reduces the columbic efficiency. On the other hand, the cell using ANL-1 showed substantially higher columbic efficiency, and good capacity retention. After 50 cycles of charge/discharge at C/20, the space-confined Se_2S_5 cathode could still maintain a reversible capacity above 700 mAh g^{-1}. The function mechanism of this novel electrolyte on the electrochemical performance of space-confined Se-S cathodes is under investigation.

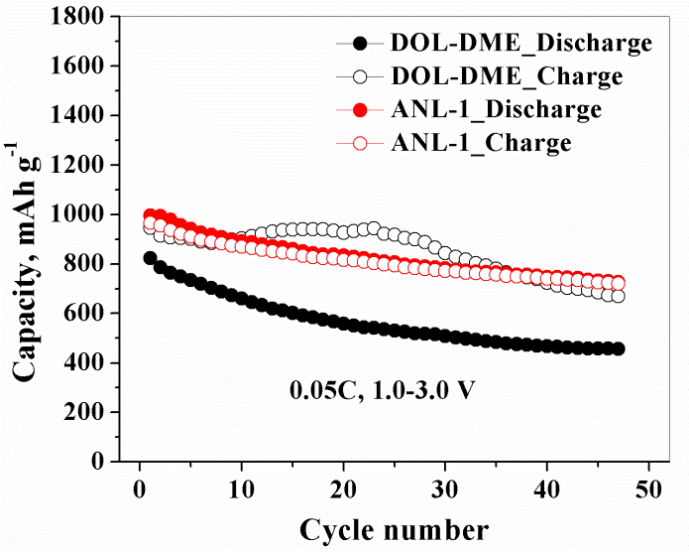

Figure V-254: Cycle performance of space-confined Se2S5 cathode in DOL-DME based and ANL-1 electrolytes at C/20 within a voltage range of 1.0-3.0 V

Conclusions

The interplay of cathode structures, electrolytes and interfaces on the electrochemistry of Se and Se-S cathodes has been well investigated by using *in situ* synchrotron XANES and DFT calculations. It was found that space-

confined Se and Se-S cathodes present distinct electrochemistry compared to space-confined S cathodes in both carbonate based and common DOL-DME based electrolytes, which face more challenged electrode/ electrolyte interfacial problems. We have explored a novel electrolyte for Se and Se-S system, which shows higher stability against polysulfides and suppressed polysulfides/polyselenides dissolution. Preliminary electrochemical result shows significantly suppressed shuttle effect and improved capacity retention using the novel electrolytes. We are going to focus on the understanding of the function mechanism of this novel electrolyte by using *in situ* spectroscopy tools such as nuclear magnetic resonance spectroscopy, Raman spectroscopy and UV-Vis spectroscopy. In addition, smarter cathode structure will be designed to maximize the capacity utilization including optimization on the Se-S phase structures and the pore structure of conductive host materials.

Products

Presentations/Publications/Patents

1. Z. H. Chen and K. Amine, Rechargeable Batteries Using SxSey Cathodes, Fall Meeting of Material Research Society, November, Boston, 2015. (Invited talk)
2. G.L. Xu, T.Y. Ma, C.J. Sun, K. Amine and Z.H. Chen, Unraveling the Capacity Fading of Selenium-based Cathodes in Ether-based Electrolytes by *in situ* X-ray Absorption Near Edge Spectroscopy. IMLB 2016, Chicago.
3. G.L. Xu, T.Y. Ma, C.J. Sun, C. Luo, L. Cheng, Y. Ren, S.M. Heald, C.S. Wang, L. Curtiss, J.G. Wen, D.J. Miller, T. Li, X.B. Zuo, V. Petkov, Z.H. Chen and K. Amine. Nano Letters 2016, 16, 2663-2673.
4. G.L. Xu, T.Y. Ma, C.J. Sun, K. Amine and Z.H. Chen, Unraveling the Capacity Fading of Selenium-based Cathodes in Ether-based Electrolytes by *in situ* X-ray Absorption Near Edge Spectroscopy. 9th International Conference on Advanced Lithium Battery for Automotive Applications (2016), Huzhou, China.
5. G.L. Xu, Z.H. Chen and K. Amine, SELENIUM-DOPED SULFUR CATHODES FOR RECHARGEABLE BATTERIES, US. Patent, No. 15/280,867, filed, 2016.

References

1. Armand, M.; Tarascon, J. M. *Nature* **2008**, 451, 652-657.
2. Ji, X. L.; Lee, K. T.; Nazar, L. F. *Nat. Mater.* **2009**, 8, 500-506.
3. Abouimrane, A.; Dambournet, D.; Chapman, K. W.; Chupas, P. J.; Weng, W.; Amine, K. *J. Am. Chem. Soc.* **2012**, 134, 4505-4508.
4. Cui, Y. J.; Abouimrane, A.; Sun, C. J.; Ren, Y.; Amine, K. *Chem. Commun.* **2014**, 50, 5576-5579.
5. Zhen, L.; Lixia, Y.; Ziqi, Y.; Yongming, S.; Yang, L.; Yan, J.; Yue, S.; Ying, X.; Zhaoliang, Z.; Yunhui, H. *Adv. Energy Mater.* **2014**, 4, 1301473.
6. Cui, Y.; Abouimrane, A.; Lu, J.; Bolin, T.; Ren, Y.; Weng, W.; Sun, C.; Maroni, V. A.; Heald, S. M.; Amine, K. *J. Am. Chem. Soc.* **2013**, 135, 8047-8056.
7. Zhang, Z. A.; Jiang, S. F.; Lai, Y. Q.; Li, J. M.; Song, J. X.; Li, J. *J. Power Sources* **2015**, 284, 95-102.
8. Zhang, Z. A.; Yang, X.; Guo, Z. P.; Qu, Y. H.; Li, J.; Lai, Y. Q. *J. Power Sources* **2015**, 279, 88-93.
9. Jiang, S. F.; Zhang, Z. A.; Lai, Y. Q.; Qu, Y. H.; Wang, X. W.; Li, J. *J. Power Sources* **2014**, 267, 394-404.
10. Qu, Y. H.; Zhang, Z. A.; Jiang, S. F.; Wang, X. W.; Lai, Y. Q.; Liu, Y. X.; Li, J. *J. Mater. Chem. A* **2014**, 2, 12255-12261.
11. Zhang, Q.; Wang, Y.; Seh, Z. W.; Fu, Z.; Zhang, R.; Cui, Y. *Nano Lett.* **2015**, 15, 3780-3786.
12. Liao, K. M.; Mao, P.; Li, N.; Han, M.; Yi, J.; He, P.; Sun, Y.; Zhou, H. S. *J. Mater. Chem. A* **2016**, 4, 5406-5409.

V.H.4. Multi-Functional Cathode Additives (BNL)

Hong Gan, Principal Investigator
Brookhaven National Laboratory
P.O. Box 5000
Upton, NY 11973-5000
Phone: 631-344-4012
E-mail: hgan@bnl.gov

Esther Takeuchi, Co-Principal Investigator
Stony Brook University
Phone: 631-216-7414
E-mail: esther.takeuchi@stonybrook.edu

John Tabacchi, NETL Program Manager
DE-SC0012704 Recipient: BNL
National Energy Technology Laboratory
3610 Collins Ferry Road
Morgantown, WV 26505
Phone: 304-285-4764
E-mail: john.tabacchi@netl.doe.gov

Start Date: October 2014
End Date: September 2017

Abstract

Objectives

Develop a low cost battery technology for PEV application utilizing Li-S electrochemical system by incorporating conductive transition metal sulfides as Multi-Functional Cathode Additives (MFCA) to improve the power performance.

Accomplishments

- Completed the evaluation of commercial and synthesized FeS_2 as cathode additive in Li-S cells.
  - Without $LiNO_3$ electrolyte additive, severe shuttling effect precludes FeS_2 activation.
  - Without activation, synthesized FeS_2 and commercial FeS_2 exhibited no significant effect on Li-S cell performance.
- Completed the evaluation of synthesized Li_2S-TiS_2 composite as cathode additive in Li-S cells. As additive, commercial TiS_2 out performed the synthesized Li_2S-TiS_2 composite.
- Completed the evaluation of commercial TiS_2 as the leading MFCA candidate for Li-S batteries.
  - Completed the TiS_2 particle size/BET surface area studies and demonstrated the importance of TiS_2 high BET surface area and its uniform distribution in sulfur cathode on Li-S cell cycle life.
  - Achieved 500 cycles in the presence of milled TiS_2 with capacity lost less than 0.04% per cycle at 1C discharge rate.
- Identified Cellulose Polymer binder for improved sulfur cathode mechanical integrity. Demonstrated superior adhesion of coated sulfur cathode on Aluminum current collector with Cellulose Polymer binder among four types of polymer binder.
- Identified new carbon additives for high sulfur loading electrodes with good mechanical integrity.
  - Up to 10 mg/cm^2 sulfur loading achieved for slurry coated sulfur electrode with good mechanical integrity and handleability.
  - Achieved up to 12 mAh/cm^2 delivered capacity under low rate discharge.

- Achieved more mechanistic understanding on sulfur-CuS, sulfur-FeS_2 and sulfur-TiS_2 interactions. Developed tube cell vehicle for *in operando* studies of hybrid electrode systems.
  - Cu-ion` dissolution mechanism in sulfur-CuS hybrid electrode cell is elucidated using X-ray Fluorescence Microscopy and X-ray Powder Diffraction in the National Synchrotron Light Source II at BNL.
  - Fe-ion dissolution mechanism in sulfur-FeS_2 hybrid electrode cell is deduced via electrochemical studies and X-ray Photoelectron Spectroscopy in Center for Functional Nanomaterials at BNL.
  - Ability of TiS_2 adsorbing polysulfide and the chemical stability of sulfur-TiS_2 hybrid system demonstrated. *In situ* XRD studies of sulfur-TiS_2 containing cells demonstrated reduction sequence and utilization of TiS_2.

Future Achievements

- Optimize sulfur cathode formulation with TiS_2 additive for improved energy density at the electrode level with ability in making cathode of sulfur loading higher than 6 mAh/cm^2.
- Select the cathode preparation processes and evaluate cell design factors for optimized cell energy density and electrochemical performance.
- Determine the optimized cell activation procedures and characterize the cell electrochemical performance under various testing conditions, especially for high sulfur loading cells.
- Design 4 mAh coin cells for confirmation study and prepare samples for DOE independent verification testing.
- Continue mechanistic studies on the hybrid cell systems to achieve fundamental understanding of the Li-S battery system.
- Cell level interaction studies by developing novel electrolyte for polysulfide dissolution minimization and by anode SEI protection for improved Coulombic efficiency.
- Maximize TiS_2 additive BET surface area for improved cell energy density, high discharge power, and optimized cycle life.

Technical Discussion

Background

The Li-S battery system has gained significant interest due to its low material cost (35% cathode cost reduction over lithium-ion) and its attractive 2.8x (volumetric) to 6.4x (gravimetric) higher theoretical energy density compared to conventional lithium-ion benchmark systems. Sulfur is more abundant on earth crust than many transition metals used in lithium-ion batteries, for example Cobalt, and it is non-toxic and environmentally benign. However, commercialization of this technology requires overcoming several technical challenges. Among them, improving sulfur cathode electronic and ionic conductivities and reducing the polysulfide intermediates dissolution in electrolyte are the major research directions for Li-S battery technology. This project focuses on improving the sulfur cathode energy density, power capability and cycling stability by introducing conductive transition metal sulfides as Multi-Functional Cathode Additives (MFCA).

Introduction

Transition metal sulfides, such as CuS, Cu_2S, FeS_2, TiS_2, CoS_2, etc., are electronically conductive with conductivity comparable to or even higher than that of carbon black. Several of them are also electrochemically active and can be reversibly discharge/charge cycled against Li metal anode. The ability in adsorbing polysulfide also makes transition metal sulfides the ideal candidates as MFCA for sulfur electrode. In this project, we have investigated the interaction between sulfur and CuS, FeS_2 and TiS_2 in more details and elucidated the interaction mechanisms. TiS_2 has been identified as the leading MFCA candidate, which afforded improved sulfur cell power capability and overall electrochemical cycling performance.

Approach

Electronic conductive and electrochemical active transition metal sulfides are evaluated as MFCA in Li-S batteries. In the first year, the team has established the individual baseline sulfur and transition metal sulfide coin cell performances, and demonstrated the strong interactions between sulfur and various MFCA within the hybrid electrode. TiS_2 and FeS_2 were selected as the leading candidates for additional optimization studies, with synthetic method developed. During the second year, we further narrowed down the leading candidate for the cathode optimization studies and completed Phase 1 investigation. Phase 2 studies were initiated with more attention directed towards electrode optimization and cell system optimization for improved electrode integrity, energy density and electrochemical charge/discharge cycling performance. Examples for these effort are electrode binder, carbon additive and electrode formulation optimization. Mechanistic studies were also executed to understand the interaction between sulfur electrode and the MFCA additives.

Results

1) MFCA leading candidate selection

During the 1st year, we have narrowed the MFCA selection to two candidates, FeS_2 and TiS_2. Follow up studies were carried out during this year to further narrow down the selection based on their chemical and electrochemical properties and interaction within the sulfur hybrid electrode.

A. FeS_2 additive evaluation

Iron disulfide was synthesized by dispersing the synthesized nanocrystalline magnetite, sodium thiosulfate and sulfur powder into a tartaric acid – sodium tartrate buffer solution in a Teflon lined autoclave and heated at 220°C. Following the hydrothermal reaction, the pyrite was washed with water, acetone and toluene via centrifugation. The resulting material was dried at 60°C under vacuum overnight.

Both synthesized and commercial FeS_2 were analyzed using XRD. FeS_2 requires to be activated by discharging to ~1.0V in the 1st cycle. The attempt to activate FeS_2 in the sulfur-FeS_2 hybrid electrode was unsuccessful due to the reduction of $LiNO_3$ on cathode at voltage below 1.6V. However, by removing $LiNO_3$ from the electrolyte, severe shuttling effect during the cell charging prevented the cell cycling (Figure V-255). Therefore, evaluation of the sulfur-FeS_2 hybrid cells with either synthesized or commercial FeS_2 was performed between 2.6V and 1.8V at 1C rate cycling in the presence of $LiNO_3$ without the FeS_2 activation. No obvious cycling performance improvement was seen (Figure V-256). Since sulfur-FeS_2 hybrid system is not stable after activation and charging, FeS_2 morphology and particle size effects on sulfur cell performance were not pursued.

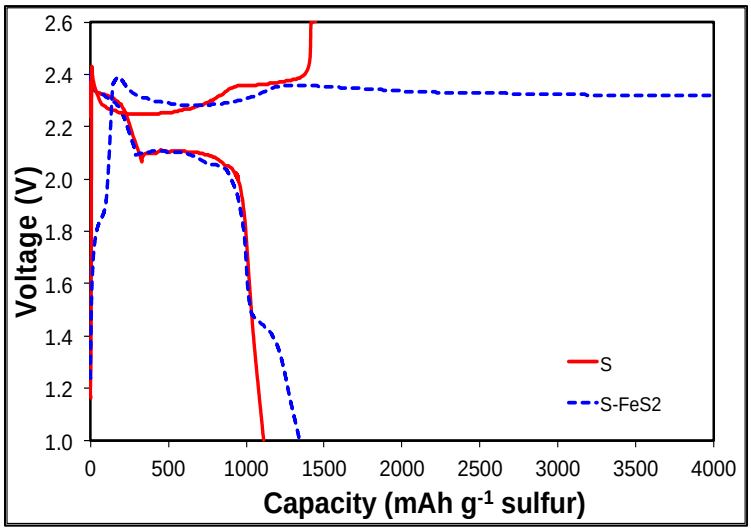

Figure V-255: S-FeS_2 Cathode Activation and Shuttling

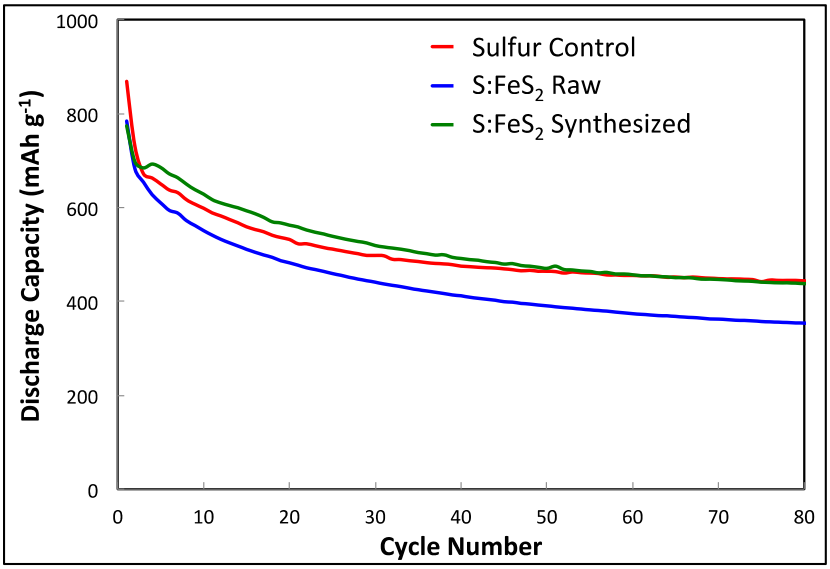

Figure V-256: Synthesized and Commercial

B. TiS_2 additive evaluation

Last year, we demonstrated beneficial effect of TiS_2 additive on sulfur cell cycling. During this Fiscal year, more investigation on TiS_2 additive has been performed and additional material optimization studies were executed.

TiS_2 material power demonstration: TiS_2 is metallic conductive. To demonstrate its power capability, cells with cathode formulation of TiS_2:Carbon:PVDF ratio 85:0:15 were compared along with control cells with ratio of 70:15:15. Figure V-257 shows the cycling capability of these cells at various cycling rate between 3.0V to 1.5V. For cells without carbon, >40% of the theoretical capacity was delivered at 10C rate, indicating the conducting natural of the TiS_2. These results corroborate the earlier finding that TiS_2 can be used as conductive additive to replace part of the carbon in sulfur electrode and still yield improved high power cycling performance.

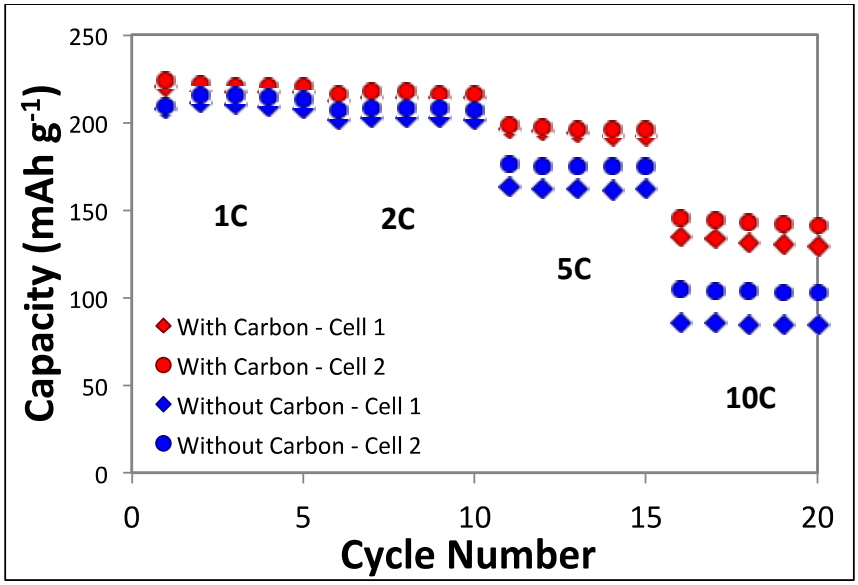

Figure V-257: High Power TiS2 Cell Without Carbon

Synthesized TiS_2 evaluation: Following last year's effort, we have synthesized the TiS_2 samples by reacting Li_2S with $TiCl_4$. The synthesized TiS_2 sample is a composite mixture of 43.4% Li_2S and 56.6% TiS_2 based on the quantitative analysis of Li and Ti via ICP-OES. This material resulted in reasonable cycling performance at

C/2 rate (Figure V-258). Hybrid cathodes with this composite were tested in coin cells in comparison with the sulfur control cells and cells made from hybrid cathode using the commercial TiS_2. Figure V-259 shows the 1st discharge voltage profiles and sulfur utilization of the three cathodes at C/5 rate. Cells containing both types TiS_2 additives exhibited higher initial voltages than the sulfur cells. However, cells with synthesized Li_2S/TiS_2 composite sample exhibited much lower sulfur utilization. This trend is also hold during cell cycling at 1C discharge rate. The poor performance of synthesized TiS_2 composite sample is more likely due to the presence of significant amount of Li_2S, which is non-conductive and introduces more impedance within the hybrid cathode.

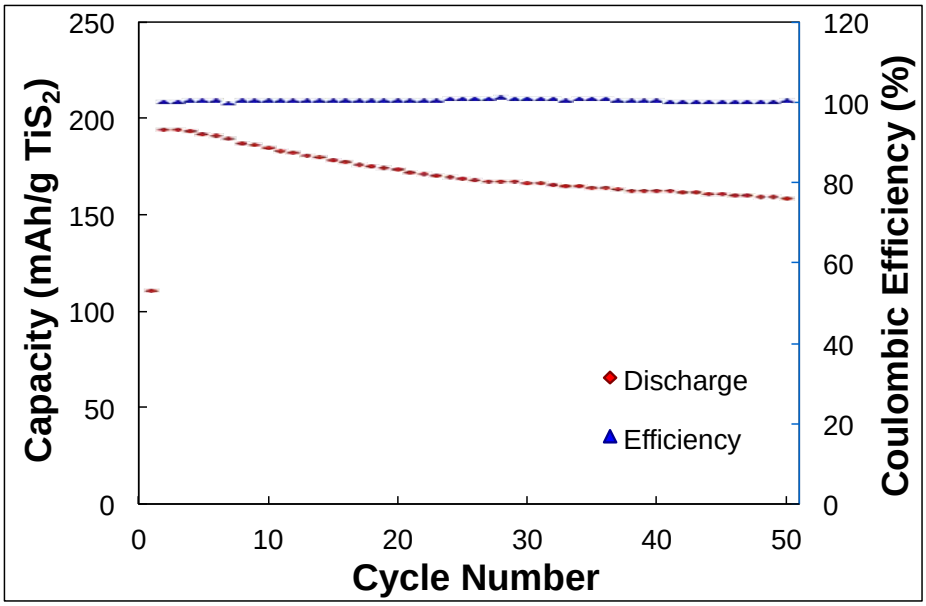

Figure V-258: TiS_2/Li_2S Composite Cell Cycling

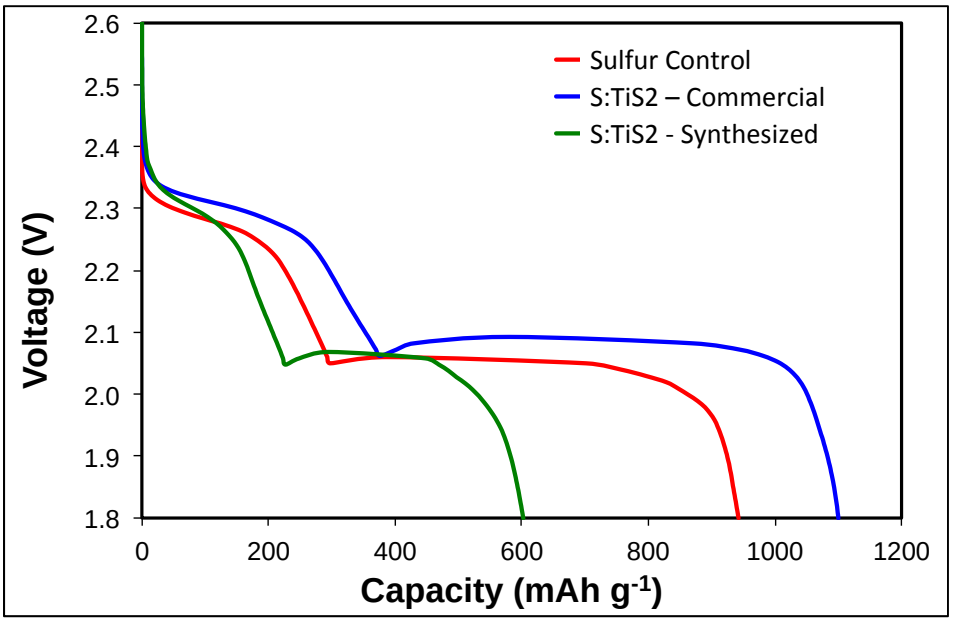

Figure V-259: Sulfur Utilization – 1st Discharge

TiS_2 particle size effect: The commercial raw TiS_2 material with BET surface area of 3.67 m^2/g was milled to produce a sample with BET surface area of 9.37 m^2/g with reduced particle size. By substituting part of the carbon in control electrode (S:C:PVDF = 50:42:8) with either raw or milled TiS_2, hybrid electrodes ($S:TiS_2:C:PVDF$ = 50:17:25:8) were prepared. Electrode with the milled TiS_2 exhibited more uniform Ti distribution than the raw TiS_2 sample (Figure V-260). The cycling performance of the hybrid electrodes using TiS_2 additive and control sulfur electrode under 2C rate discharge are shown in Figure V-261. Clearly, both electrodes containing the TiS_2 additive exhibited higher discharge capacities and lower capacity fade than that of the control cells over 300 cycles, which is consistent with the observation from the previous proof of concept study. In addition, the hybrid electrode with the milled TiS_2 resulted in better overall cycling capacity retention than the cells with raw TiS_2 additive. Figure V-262 shows the cycling test of hybrid sulfur-TiS_2 electrode (with milled TiS_2) at 1C rate with intermittent C/5 rate discharge at every 51st cycles. The hybrid cell exhibited low capacity fade rate over 500 cycles (0.039% per cycle at 1C). The data demonstrate that smaller particle size/larger BET surface area and more uniform distribution of TiS_2 within the sulfur electrode are beneficial for sulfur cell cycle life under 1C rate discharge.

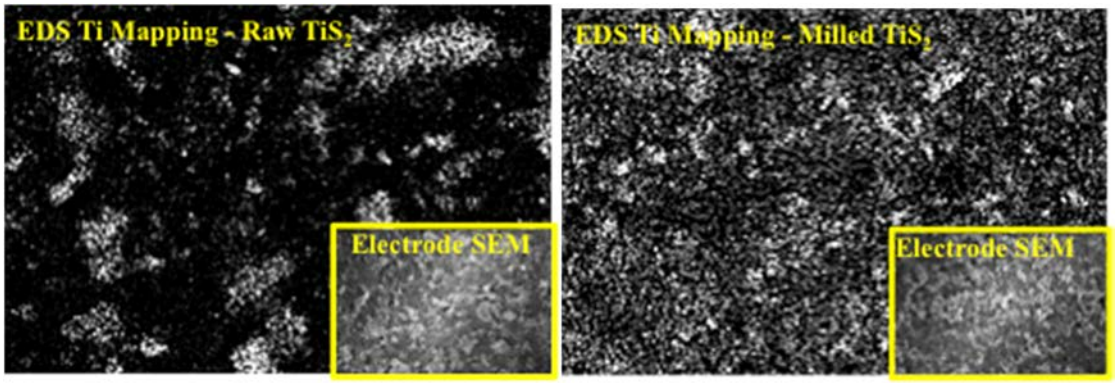

Figure V-260: Ti Mapping by EDS

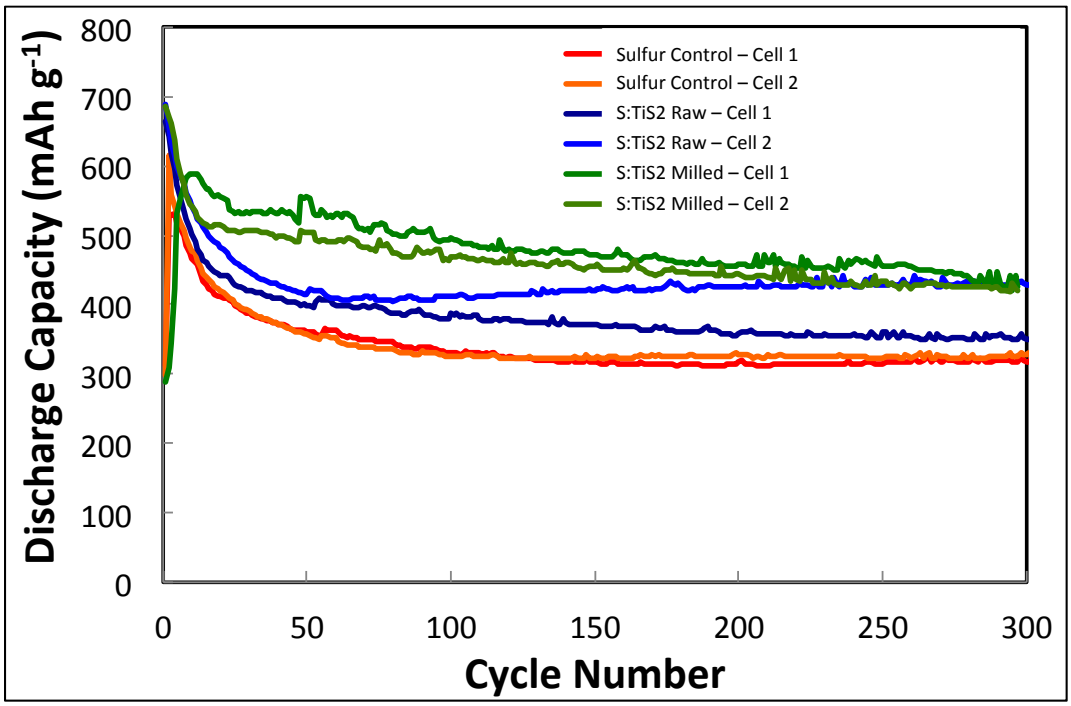

Figure V-261: TiS_2 SA Effect on $S:TiS_2$ Hybrid Cell Cycling – 2 C

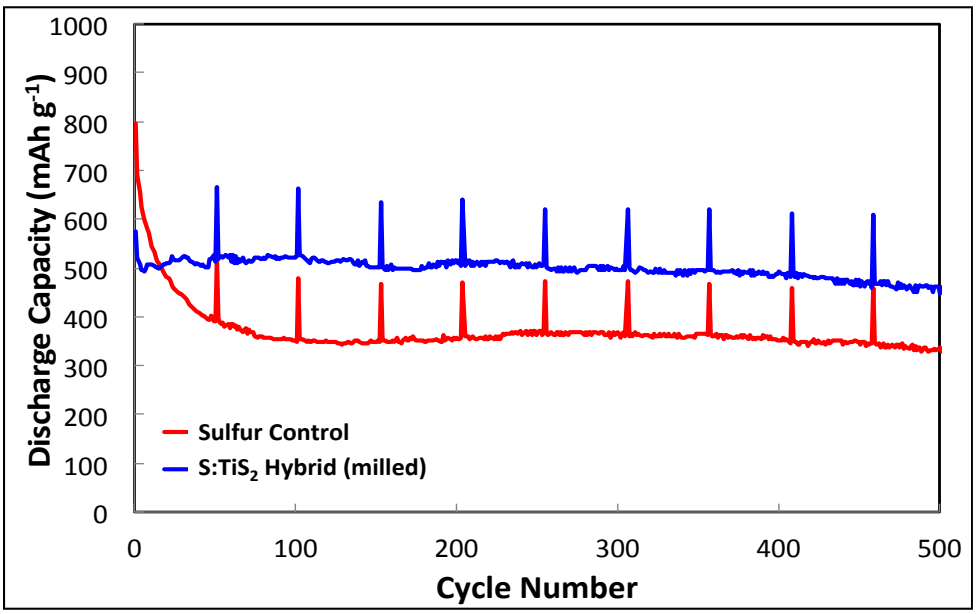

Figure V-262: Hybrid S:TiS_2 Cycle Life Study

We have completed the Phase I studies with multiple MFCA evaluated, including CuS, Cu_2S, FeS, FeS_2, CoS_2 and TiS_2. Milled commercial TiS_2 with smaller particle size and larger BET surface area is identified as the leading MFCA for improved sulfur cell cycle life.

2) Sulfur-TiS_2 hybrid electrode optimization

Phase II studies were initiated and focused on sulfur-TiS_2 hybrid electrode optimization using commercial TiS_2. During this year, we have completed cathode mechanical integrity optimization and sulfur loading studies by selecting and optimizing the binder materials and the conductive carbon additives.

A. Binder Selection

Binder effect investigation: PVDF has been used to process sulfur electrodes in all our previous studies. We have observed poor adhesion of the coated cathode on the Aluminum current collector, especially for the cycled electrodes. While the adhesion to the Aluminum current collector may not be critical for coin cells due to the use of a spring to maintain the cell stack pressure, it will be critical to pouch cell designs in real applications where the stack pressure is typically not maintained via an external force. In our study, five types of binder materials were tested for sulfur electrodes with a standard formulation of Sulfur:Carbon:Binder = 50:42:8 (weight ratio), including PVDF (baseline reference), Polyimide (PI), Cellulose Polymer (CP), Polyvinylpyrrolidone (PVP), and Polyacrylonitrile (PAN). Among these binders, PVP failed the slurry processing due to significant particles segregation. The sulfur electrodes with other four binders were successfully coated with the total material loading ~1.89 mg/cm^2. A Scotch Tape test uncovered a significant effect of binder types on the electrode adhesion. The electrode with PAN exhibited total delamination from Aluminum foil (Figure V-263), while electrode with CP exhibited the lowest weight loss (Figure V-264) and excellent adhesion to the Aluminum current collector. Interestingly, after these electrodes being subjected to 100 discharge/charge cycles in coin cells, good adhesion is maintained for electrodes with CP and PAN binders, while a total delamination from Aluminum current collector is observed for electrode with PVDF binder and severe cracking is observed for electrode with PI binder (Figure V-265). At a C/10 discharge rate, the binder types did not show significant impact on Li-S coin cell cycle life, except that the electrode with PI binder exhibited lower Coulombic efficiency than that of the other three binders. Overall, CP binder resulted in the best mechanical and electrochemical performance.

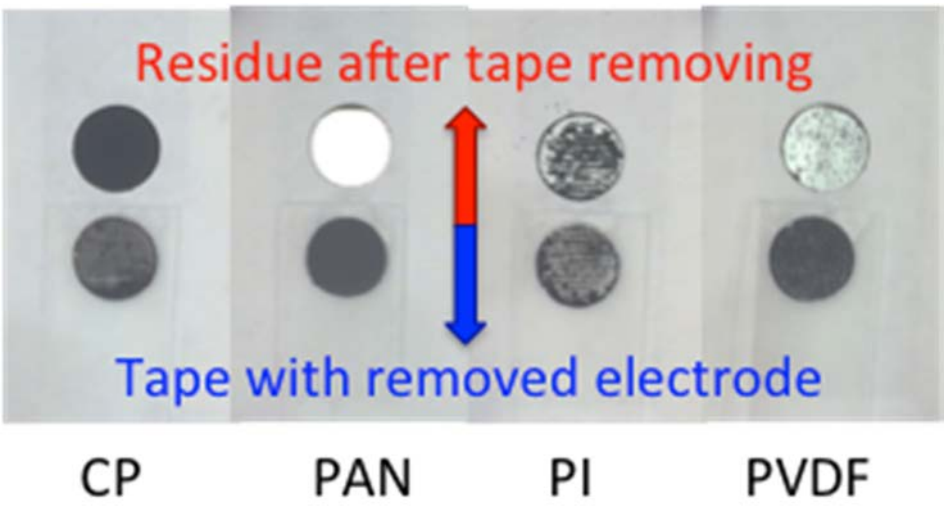

Figure V-263: Tape Testing - Adhesion

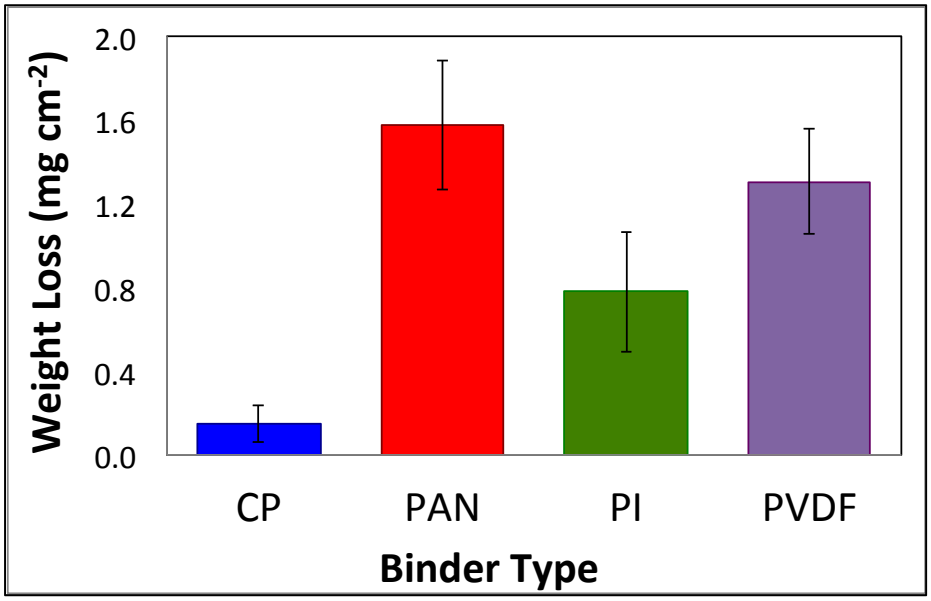

Figure V-264: Tape Test – Areal Weight Loss

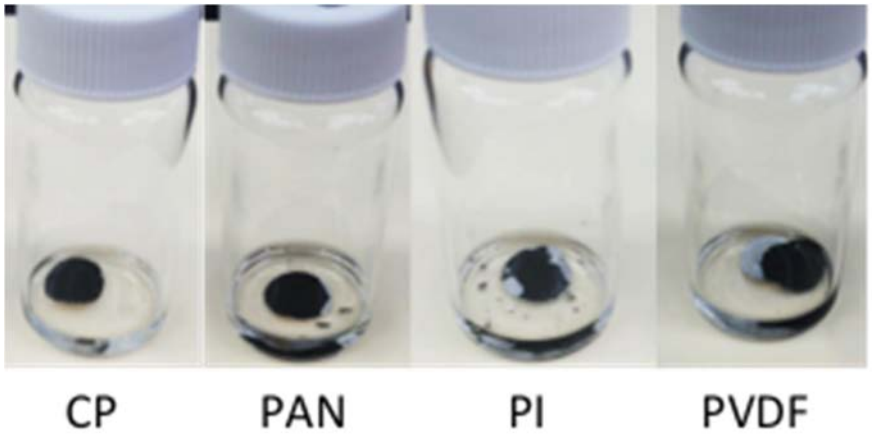

Figure V-265: Cycled Electrode Delamination

Confirmation Study with TiS_2 Additive: To confirm the effectiveness of CP binder for hybrid electrode with commercial TiS_2 as cathode additive, the hybrid sulfur electrode with formulation of Sulfur:TiS_2:Carbon:CP = 50:17:25:8 was prepared against the control of Sulfur:Carbon:CP = 50:42:8. Indeed, the Scotch Tape testing confirmed good adhesion of both electrodes to the Aluminum current collector. Good adhesion also observed after cycling test. Cycling test under 1C discharge rate (with C/5 every 50 cycles) indicates the beneficial effect of TiS_2 additive on the cell capacity retention (Figure V-266) that is still consistent with our previous observation when PVDF was used as binder material. Therefore, CP binder is selected for all future sulfur electrode optimization studies.

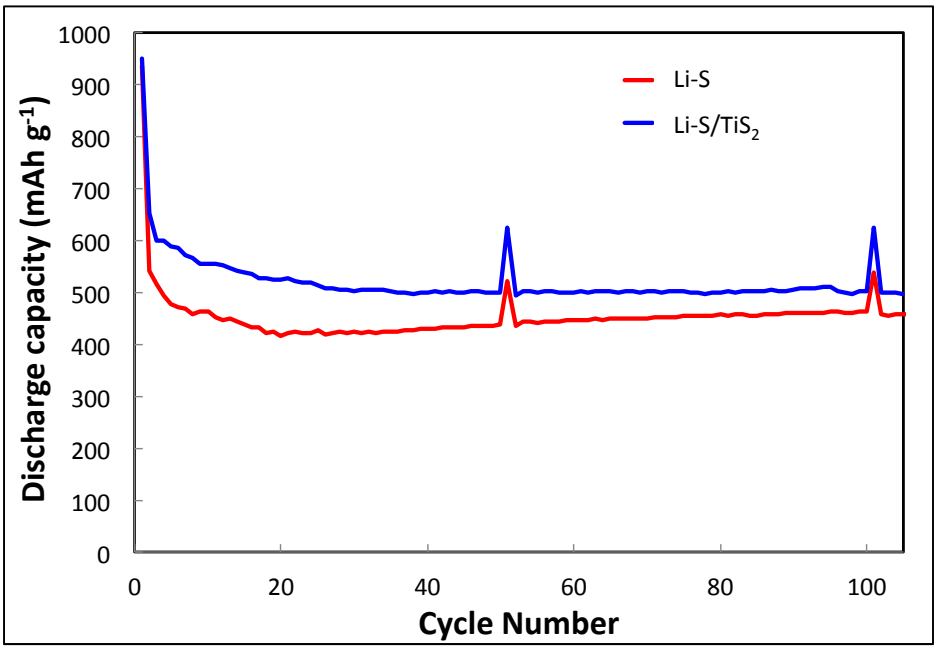

Figure V-266: Hybrid Electrode Cycling at 1 C

B. Conductive Carbon Additive

Our previous studies, including Cellulose Polymer (CP) binder selection, Super C65 was used as the conductive carbon additive with typical sulfur loading of 1.5 mg/cm^2 or less. However, when we attempted to increase sulfur loading to > 4 mg/cm^2, severe electrode cracks and delamination were observed. To achieve > 350 kW/kg energy density at the cell level, targeted by VTO, sulfur loading of > 6 mg/cm^2 is desirable at the practical level. The effect of carbon additive types on sulfur electrode mechanical integrity with high sulfur loading is examined.

Carbon selection to achieve > 6 mg/cm^2 sulfur loading: To maintain low cost, we have evaluated seven commercially available carbons, including Super C65 (control), Ketjen Black, three micro-porous carbons (MP62, MP83 and MP97) and two fibrous carbons (Fiber 150 and Fiber 200). The series of carbon samples were studied to determine their properties. A Raman microscope with a 532 nm laser was used to study the carbon functional groups present in the various carbons. The spectra were collected between 200 and 3200 cm^{-1}. Surface area and pore – size were determined using surface and pore–size analyzer. Then BET and BJH methods were used to quantify the surface of the carbon particles. Thermal data regarding decomposition and water evaporation were collected using TGA/DSC under air and nitrogen. Water content of carbons was measured using the Karl Fischer method. Lastly, particle size was determined using the dynamic light scattering method. These carbons have wide variety of physical properties, such as particle size (30 nm – 40 µm) (Figure V-267), BET surface area (3 – 1200 m^2/g), pore size (0 - 20A) and pore volume (0 - 1.1 cc/g), etc. Sulfur cathode slurries using formulation of S:C:CP = 62:30:8 were tape casted on Aluminum foil with targeted sulfur loading ranging from 1.1 to 10.0 mg/cm^2. Electrodes with sulfur loading of >3.5 mg/cm^2 using carbons of small particle sizes (Super C65 and Ketjen Black) exhibited severe cracks and delamination after

drying with exposed Aluminum foil, while electrodes using micro-porous carbons with large particle sizes exhibited no visible cracks and delamination after drying as shown in Figure V-268. Using MP97, sulfur loading up to 9 mg/cm^2 without electrode cracks was achieved. Electrochemical performance of coin cells using six carbon additives with low sulfur loading (~1.3 mg/cm^2) were examined (Figure V-269). Among them only Ketjen Black and MP97 exhibited equal or better coin cell cycling performance relative to the control cell with Super C65. Since both Super C65 and Ketjen Black did not achieve > 3.5 mg/cm^2 sulfur loading without the mechanical defects, MP97 was selected for additional sulfur electrode development.

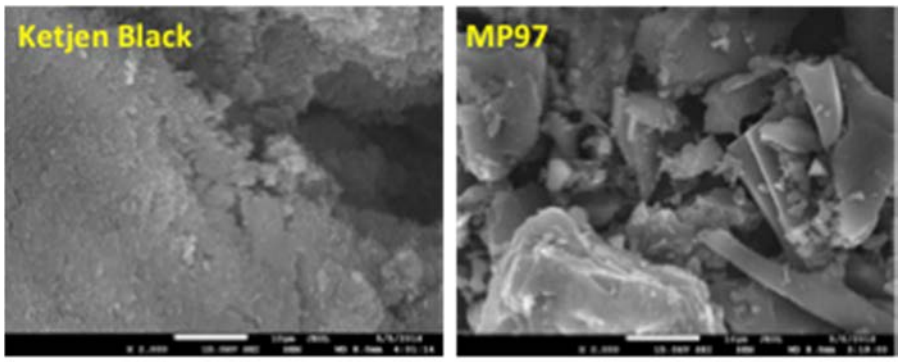

Figure V-267: SEM of Ketjen Black and MP97

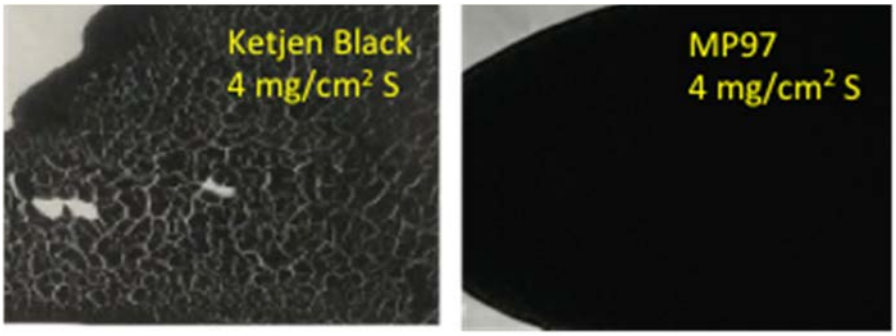

Figure V-268: Sulfur Electrode Cracks After Drying

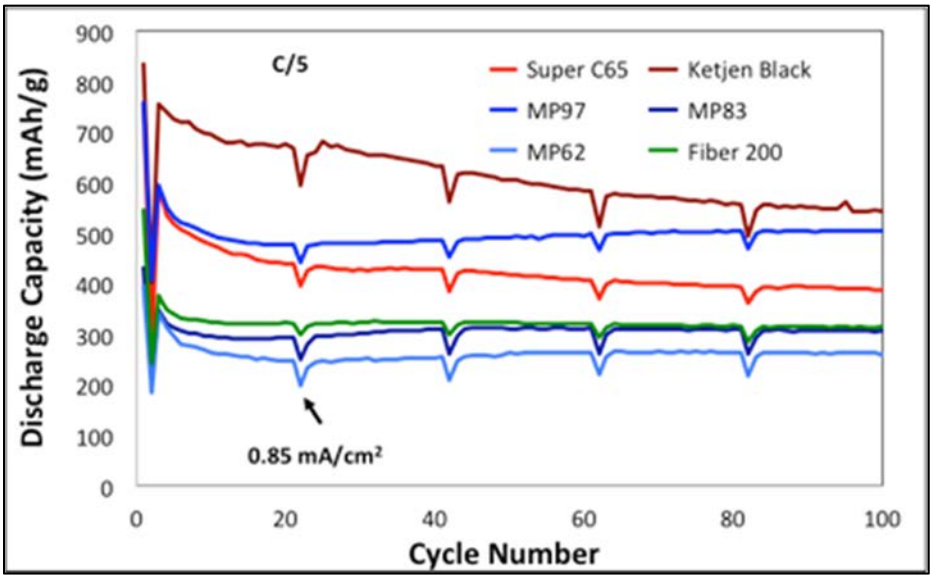

Figure V-269: Carbon Types vs. Coin Cell Cycling

High sulfur loading electrode optimization: Even though the high sulfur loading can be achieved, when CP and MP97 were used as binder and carbon additive, the resulting electrodes were found to be very brittle, especially for the high sulfur loading electrodes, and the electrode surface was very rough. Thus it is not acceptable for practical battery process development and material handling. We found that the electrode brittleness is correlated strongly to the binder type. For electrodes prepared with PVDF binder more flexible and bendable electrodes were obtained. To maintain the good mechanical integrity advantage from CP binder and the flexibility property of the PVDF binder, a composite binder system with CP/PVDF mixture was developed. The electrode surface roughness is correlated to the big particle size of MP97 carbon. The electrode prepared with small particle size carbons (Super C65 and Ketjen Black) exhibit smooth (or less rough) surface (although mechanically not acceptable for high sulfur loading). Composite carbon additives containing the mixture of MP97 and Super C65 were adopted in our sulfur cathode formulation. By introducing the above improvement, electrodes with sulfur loading up to 10 mg/cm^2 were obtained, which exhibited good mechanical integrity and handleability. Under low current density, linear relationship between sulfur loading and the delivered areal capacity is observed in coin cell test, with up to 12 mAh/cm^2 delivered for the 10 mg/cm^2 sulfur loading sample (Figure V-270).

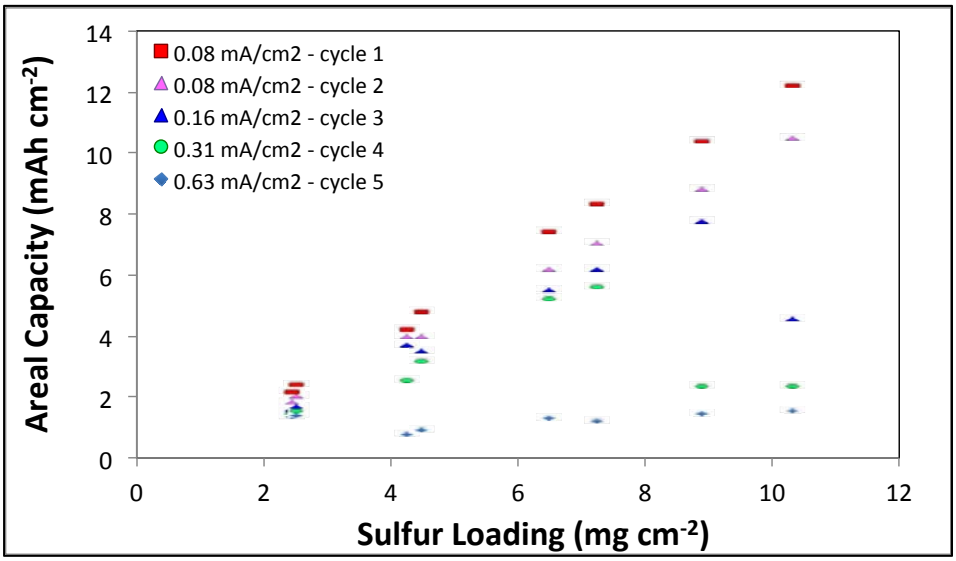

Figure V-270: Sulfur Loading Effect on Discharge

3) Mechanism of sulfur-MFCA interaction

Unique behaviors were observed for different types of MFCA. During past two years, we have evaluated CuS, FeS_2 and TiS_2 as cathode additives in sulfur battery system. Both CuS and FeS_2 were found to have strong interaction with sulfur during cell cycling, leading to metal-ion dissolution into electrolyte and poor cell cycle life with fast capacity fade. In contrast TiS_2 has very different behavior, which results in improved sulfur cell capacity retention and longer cycle life. Fundamental studies have been carried out throughout the year to understand the mechanisms involved with these systems.

A. Sulfur-CuS interaction

Dissolution mechanism has been identified for sulfur-CuS hybrid system. However, the exact detailed mechanisms were unclear, such as the precursor materials or phases for the dissolution, the timing of this dissolution, the rate of the dissolution, and the magnitude of the dissolution. We have developed *in operando* experiments to answer these questions using airtight tube cell vehicle. *In operando* studies on the sulfur-CuS hybrid cathode system were successfully carried out in elucidating the Cu-ion dissolution mechanism by using Sub-micron Resolution X-ray Spectroscopy (SRX) Beamline, and X-ray Powder Diffraction (XPD) Beamline at NSLS II. By applying XRF, we can monitor the Cu fluorescence from cathode and anode surfaces simultaneously along with electrochemical cell discharge/charge cycling (Figure V-271). The onset point for Cu-ion dissolution from cathode and Cu species deposition on anode is clearly identified. By using XRD, the material phase changes along with cell discharge are also pinpointed (Figure V-272), which are used to

elucidate the reaction/dissolution mechanism by correlating the chemical/structural transformation with the Cu-ion dissolution. The data indicate that the Cu-ion dissolution is originated from CuS (instead of Cu_2S) that interacts with low ordered polysulfide, either S_3^{2-} species or super saturated S^{2-}, at the beginning of the 2.1V voltage plateau.

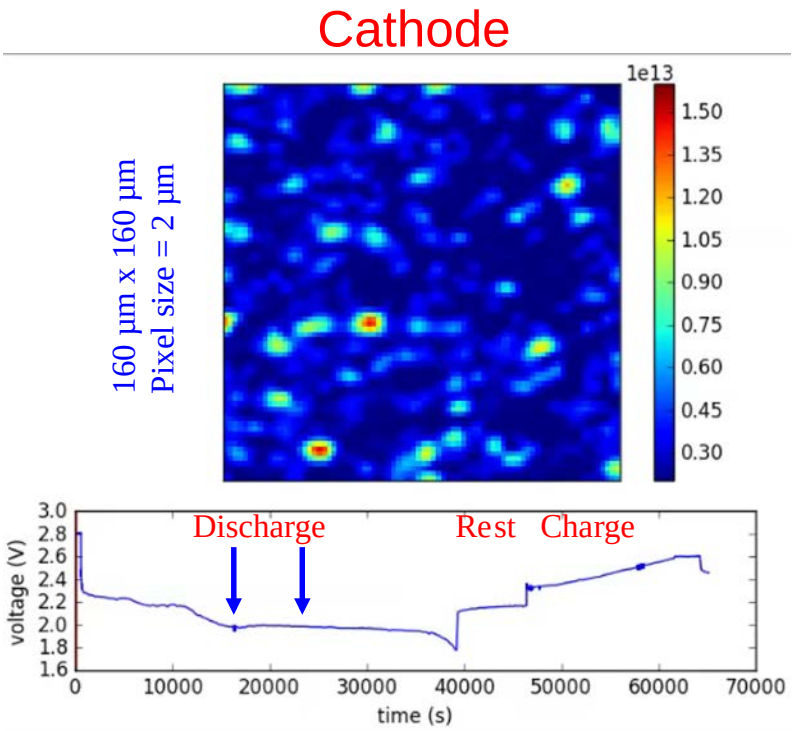

Figure V-271: XRF *Operando* Study

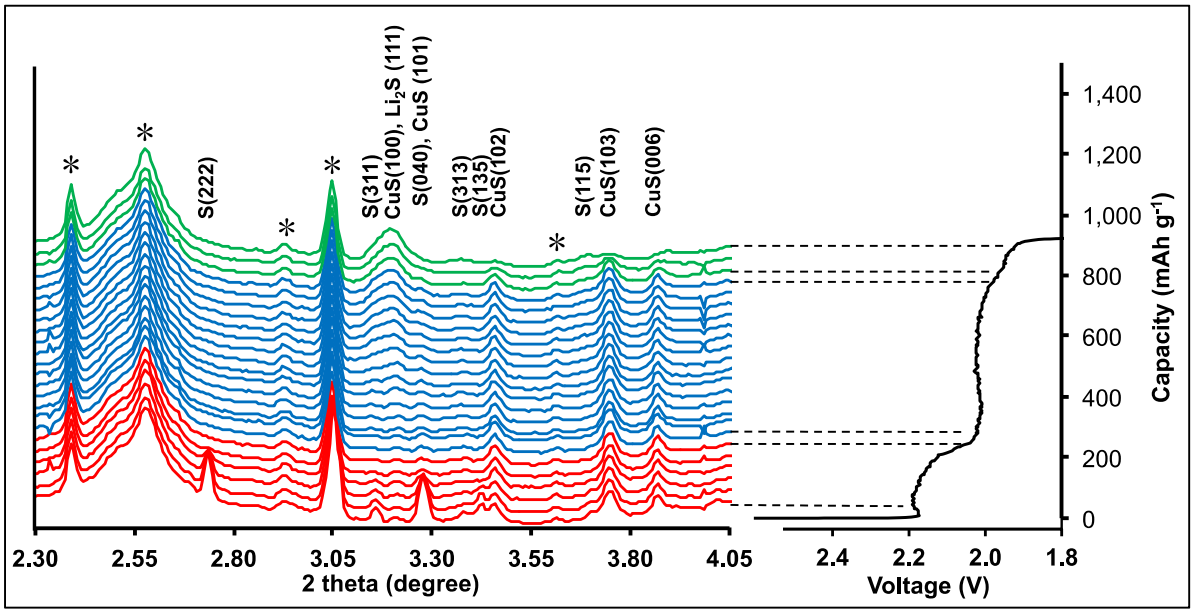

Figure V-272: Operando Study – XPD vs. Cell Discharge Capacity

B. Sulfur-FeS_2 interaction

As a MFCA additive, FeS_2 does not work well in sulfur cell system. FeS_2 electrochemical activation requires the cell to be discharged to 1.0V. Under such a condition, $LiNO_3$ electrolyte additive cannot be used due to its reduction on the cathode surface at voltage below 1.6V. However, without $LiNO_3$, the FeS_2 can be activated,

but cannot be cycled due to the severe shuttling effect (Figure V-255). We found that this severe shuttling effect was linked to the dissolution of Fe species. Fe dissolution happened for the hybrid cell with FeS_2 activation (discharge to 1.0V), as evidenced by the anode discoloration (Figure V-273), which was recovered from the cycled cells. The sulfur control cell exhibited clean anode surface and smooth surface morphology. In contrast, the hybrid cell anode was dark colored with granular rough morphology. EDS and XPS proved the existence of Fe species on the anode recovered from discharged sulfur-FeS_2 hybrid cathode cell in the form of FeS and FeO (Figure V-274). Additional studies indicate that the Fe species dissolution only happens during the 1st recharging of the activated sulfur-FeS_2 hybrid electrode. EDS detected no Fe on anode surface if FeS_2 was not activated or FeS_2 was activated only without cell recharging. The presence of electronic conductive FeS on anode SEI contributes to the reduced anode charge transfer impedance – leading to fast charge transfer between lithium anode and polysulfide.

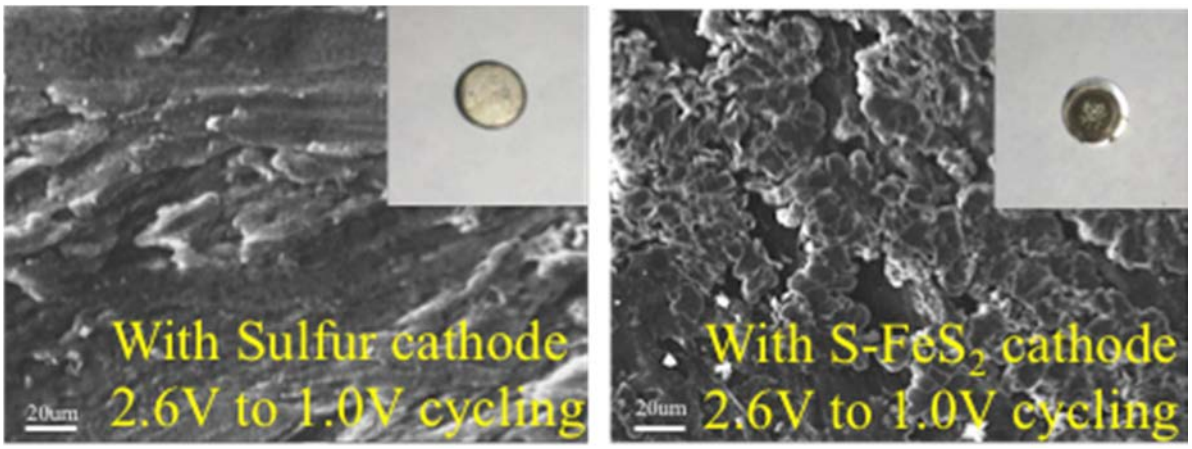

Figure V-273: Anode SEI Morphology and Discoloration

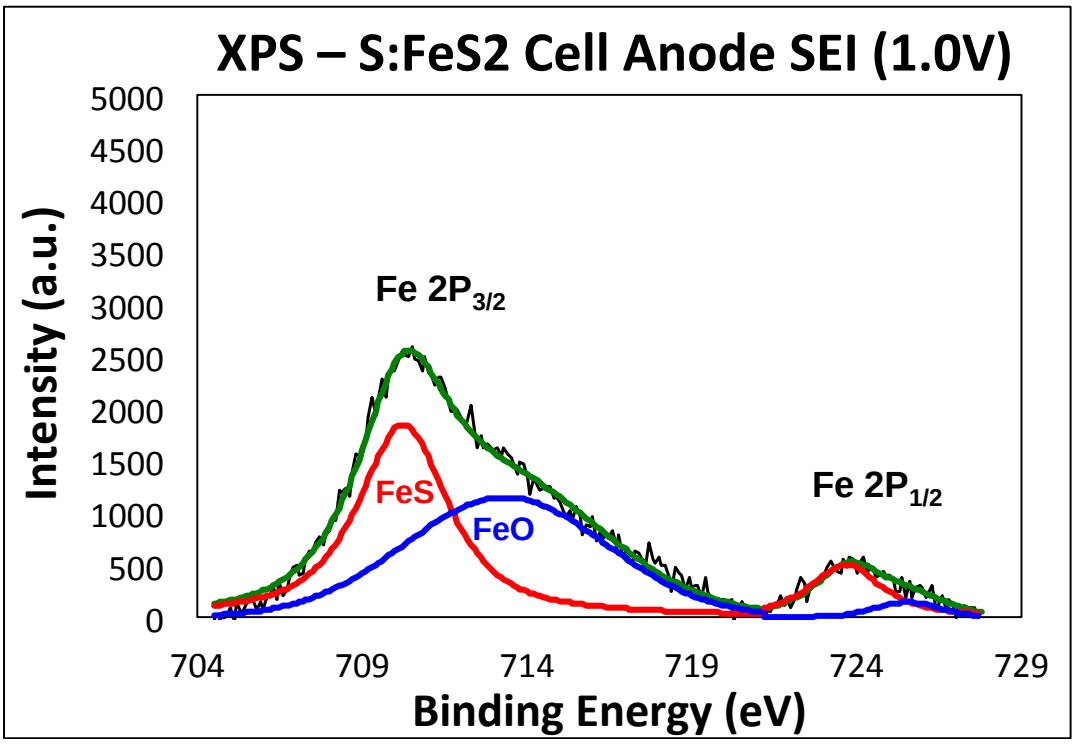

Figure V-274: XPS – S:FeS_2 Cell Anode SEI After Cycling

C. Sulfur-TiS_2 interaction

Unlike CuS and FeS_2, sulfur hybrid electrode with TiS_2 as MFCA additive exhibits improved cycling performance (Figure V-261, Figure V-262, and Figure V-266). The metal ion dissolution issue uncovered for the CuS and FeS_2 systems was not observed for the TiS_2 system. The recovered anode from cycled sulfur-TiS_2 hybrid cell displayed very clean appearance on its surface similar to that from the sulfur control cell (Figure V-275). In addition, EDS detected no Ti on the anode surface by (Figure V-276). These observations clearly indicate the stability of TiS_2 within the Li-S cell system. No Ti species dissolution occurs throughout the cell discharge/change cycles. To have a better understanding of why TiS_2 help Li-S cell performance, we also looked into the possible interaction between TiS_2 and the polysulfide. Li_2S_8 solution in electrolyte solvent was made with dark brown color. After adding TiS_2 powder into this solution, the color became light yellow (Figure V-277). This observation clearly indicates the strong interaction between TiS_2 and polysulfide and possible adsorbing polysulfide on the surface of TiS_2. The reduced polysulfide concentration within the Li-S battery will minimize the capacity lost and improve the sulfur utilization and cycling efficiency, which is consistent with what we observed in sulfur-TiS_2 hybrid cell testing.

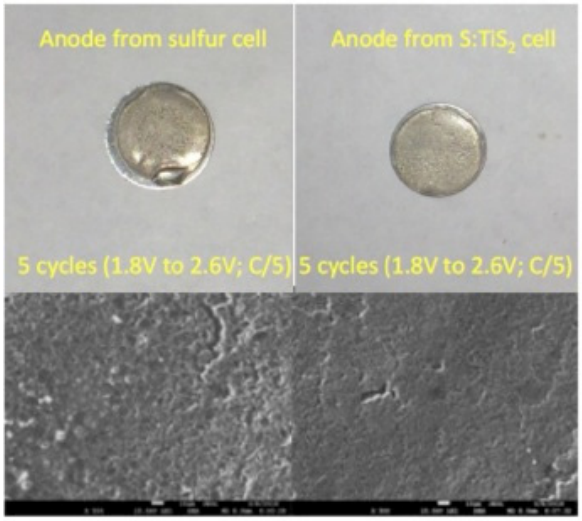

Figure V-275: Anode From Cycled Cells

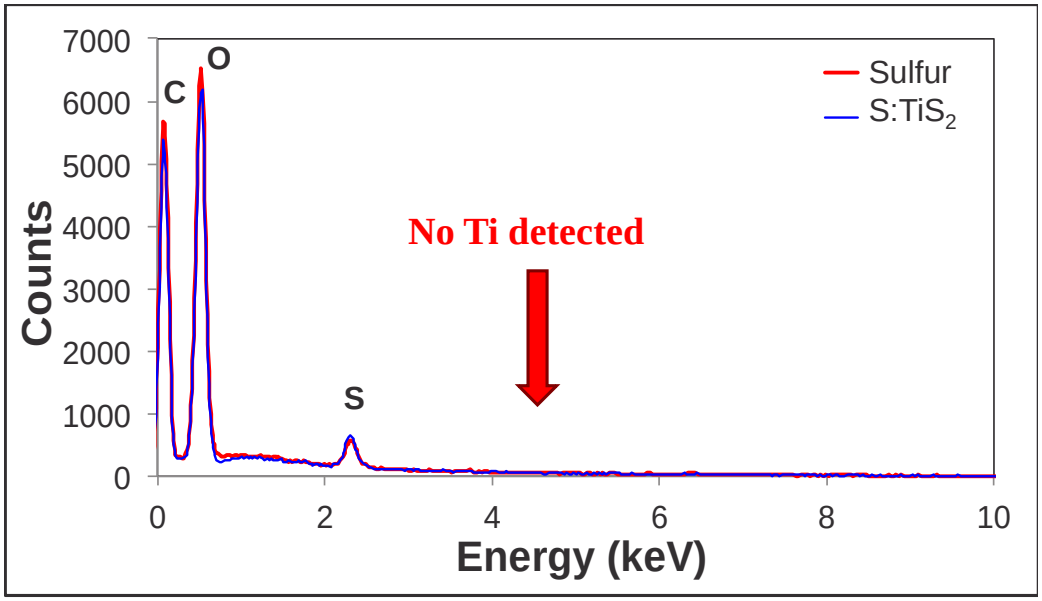

Figure V-276: EDS – Anode From Cycled Cells

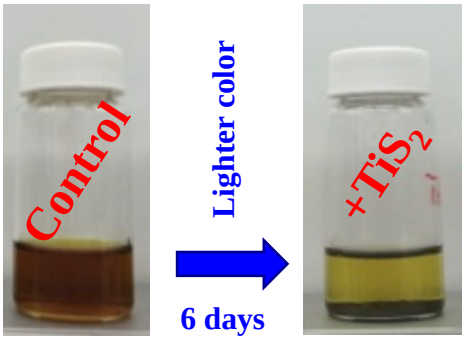

Figure V-277: Polysulfide – TiS_2 Interaction

Using *in situ* XRD method, our study focused on the structural evolution of TiS_2 and sulfur in TiS_2-sulfur composite electrodes with different TiS_2 to sulfur ratios. The discharge profiles of all five *in situ* cells are shown in Figure V-278. While sulfur demonstrated the highest overall discharge capacity, the $3TiS_2$/S showed the highest utilization of sulfur. The discharge of TiS_2 did not show any plateaus, and the S-containing samples showed discharge plateau at 2.4 V and 2.0 V, which are consistent with the discharge process of sulfur.

XRD spectra of TiS_2, $3TiS_2$/S, TiS_2/S, TiS_2/3S and S showed that all the peaks in the three mixture sample can be indexed to TiS_2 phase or sulfur phase, indicating no existence of other phases. During discharge and charge, the shifting of major peaks at each lithiation stage can be clearly seen, Figure V-279. The (001) and (004) peaks of TiS_2 moved toward lower degree during discharge, implying expansion of layer spacing upon lithiation. From the d spacing plots in Figure V-280, sulfur started to discharge simultaneously with TiS_2, and with the presence of sulfur, TiS_2 could be lithiated to the same extent as TiS_2 only indicating high electrochemical utilization of the TiS_2.

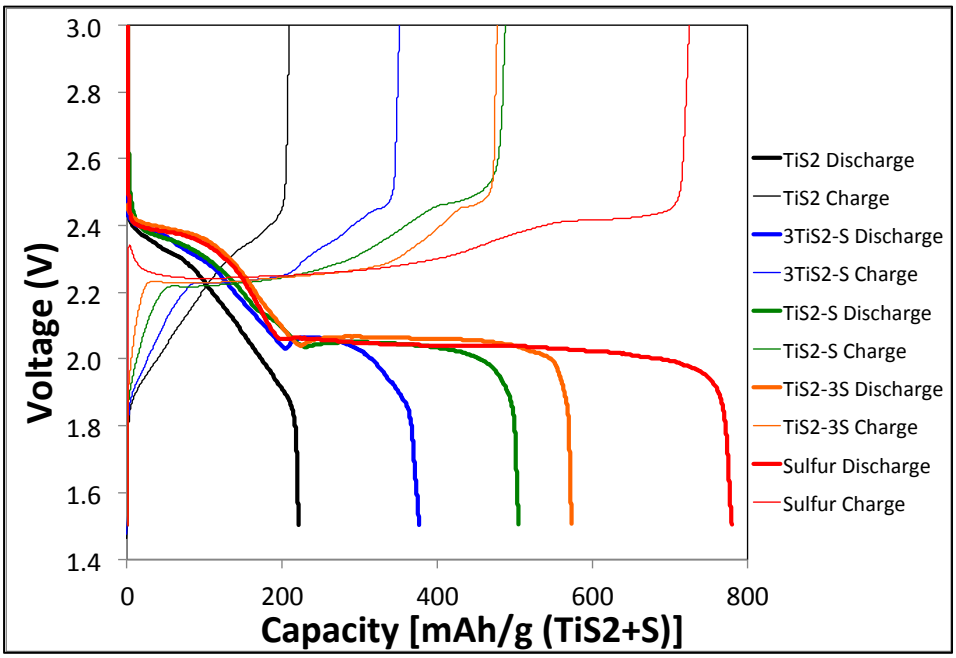

Figure V-278: Voltage vs. Capacity (mAh/g TiS_2+S) Plots of the *in situ* XRD Cells

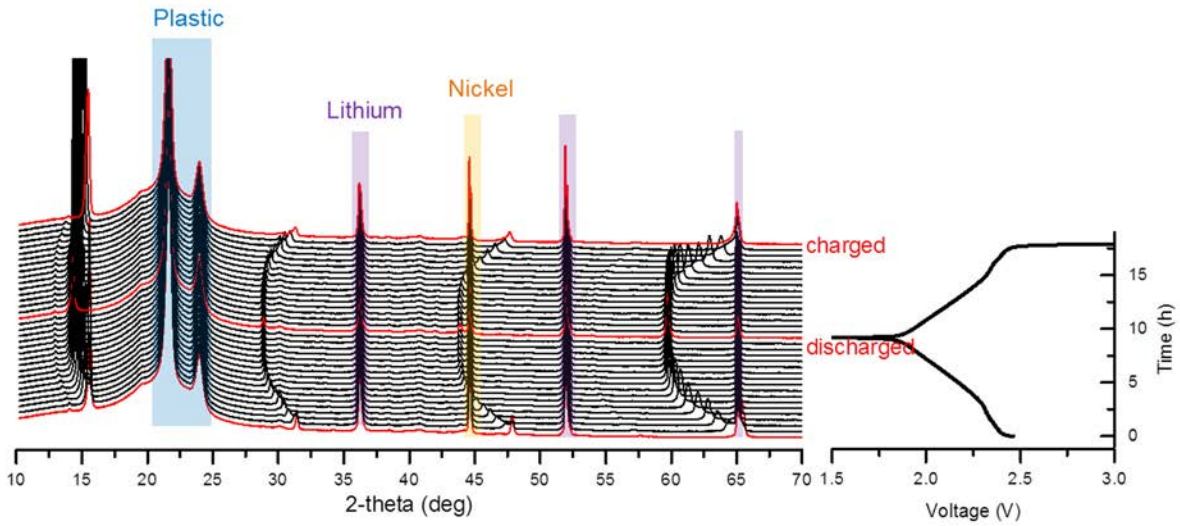

Figure V-279: *In situ* XRD Full Scan of TiS_2 Discharge/Charge

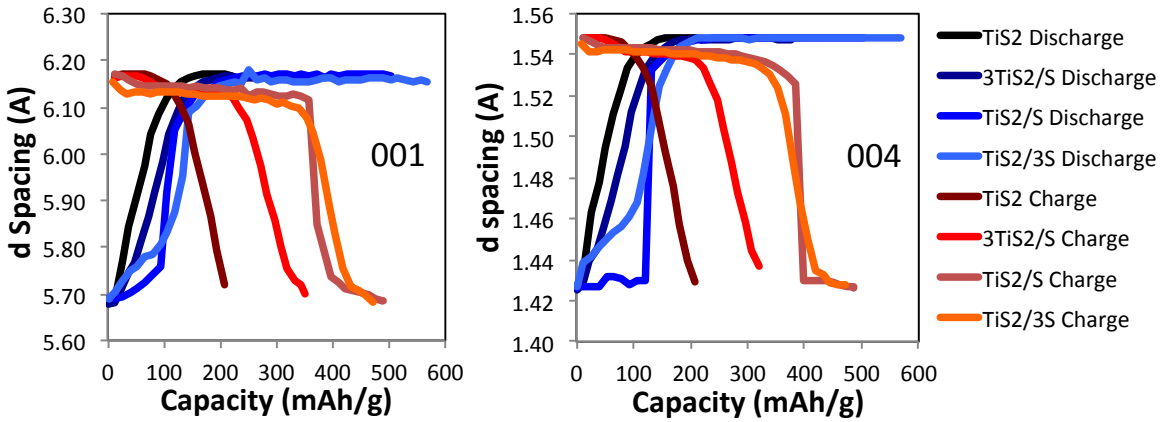

Figure V-280: Lest, d Spacing vs. Capacity Plot of TiS2 (001) Plane; Right, d Spacing vs. Capacity Plot of TiS2 (004) Plane

Conclusions

Phase I investigation on MFCA for Li-S batteries was completed this year. We further narrowed down TiS_2 as the best MFCA for Li-S battery among all the metal sulfides studied in this project with FeS_2 eliminated from the leading candidate list. TiS_2 additive improves the power capability of the sulfur electrode and helps maintaining higher sulfur utilization during coin cell cycling. The beneficial effect is correlated to its high electronic and ionic conductivities, high stability without Ti-ion dissolution under Li-S battery chemical and electrochemical environments, and its ability in adsorbing polysulfide. Additional Li-S cell cycling performance improvement was achieved by introducing milled TiS_2 additive with smaller particle size and higher BET surface area. Uniform TiS_2 particle distribution within the sulfur cathode was also proved to be critical to achieve long cycle life and high sulfur utilization. These results provide guidance for future direction of MFCA research.

Beyond the cathode active materials (sulfur and MFCA), we have studied other electrode components in Phase II investigation to further optimize the sulfur electrode at the system level for improved electrochemical performance. Binder study and carbon additive study were completed this year. Binder type has significant effect on sulfur electrode mechanical integrity. Among the 5 binder candidates, Cellulose Polymer binder was demonstrated to be the best for achieving good sulfur electrode mechanical integrity with excellent adhesion to Aluminum current collector, even after cell cycling. To achieve sulfur loading at the level higher than 6 mg/cm^2, seven low cost commercially available carbons were evaluated as host material for sulfur electrode. We demonstrate that the carbon particle size plays a major role in obtaining the electrode with sulfur loading

higher than 6 mg/cm^2 and simultaneous yields acceptable mechanical integrity. A microporous carbon (MP97) was chosen as the leading conductive carbon additive for our future sulfur cell technology development, which provides a balance between mechanical properties and the electrochemical performance. The interaction between binder and carbon additive and their effect on sulfur electrode brittleness and surface roughness was also investigated. Composite binder (CP/PVDF) and composite carbon additive (MP97/Super C65) were selected for our cathode formulation, resulting in good mechanical integrity and relatively easy handling.

Fundamental studies were also carried out throughout the year. The dissolution mechanism of sulfur-CuS hybrid system has been studied in details with the aid of multiple *in operando* techniques at the NSLS II. The electrochemical behavior of sulfur-FeS_2 hybrid cell system was also investigated. The dissolution of Fe-ion into the electrolyte was correlated to the FeS_2-activated-cell charging step. In both CuS and FeS_2 cases, the metal ion dissolution leads to the deposition of conductive metal sulfides (Cu_2S and FeS) on the anode surface that causes the lowered charge transfer impedance on the anode SEI. As a result, faster charge transfer reaction between polysulfide and lithium metal became uncontrollable, leading to severe shuttling effect and high capacity fade rate. The benefit of TiS_2 additive in Li-S battery is correlated to its chemical stability with no Ti-ion dissolution under Li-S cell cycling conditions. In addition, polysulfide adsorbing by TiS_2 was demonstrated that correlates well with the observation that sulfur-TiS_2 hybrid electrodes with higher TiS_2 BET and more uniform TiS_2 distribution results in better cell cycle life and higher sulfur utilization.

Presentations/Publications/Patents

1. Helen Liu, Ke Sun, Hong Gan, "The effects of carbon type and cathode loading on Li-S battery performance", Poster at 2015 American Institute of Chemical Engineers (AIChE) Annual Meeting, Nov. 8-13, 2015.
2. Hong Gan, Ke Sun, Helen Liu, "Li-S battery – Sulfur utilization and cell design", Presentation at *Long Island Forum for Technology (LIFT)*, Farmingdale State College's Renewable Energy and Sustainability Center, Dec. 4th, 2015.
3. Ke Sun, Dong Su, Qing Zhang, David Bock, Yu-chen Karen Chen-Wiegart, Amy Marschilok, Kenneth Takeuchi, Esther Takeuchi, Hong Gan, "Conductive CuS Cathode Additive for Li-S Battery", Poster Presentation at JCESR/PNNL Li-S workshop on May 23, 2016.
4. Ke Sun, Dong Su, Qing Zhang, David Bock, Amy Marschilok, Kenneth Takeuchi, Esther Takeuchi, Hong Gan, "Transition Metal Sulfides As Conductive Additives for Sulfur Electrode in Li-S Battery", Oral Presentation (# A02-0247) at 229th ECS Spring Meeting (May 29-June 2, 2016), San Diego, CA.
5. K. Sun, Q. Zhang, C. Cama, D. C. Bock, D. Su, Y-C. K. Chen-Wiegart, Xiao Tong, H. Liu, J. Jou, J. P. Huang, A. C. Marschilok, K. J. Takeuchi, E. S. Takeuchi, H. Gan, "Multi-functional Cathode Additives for Li-S Battery Technology", DOE VTO 2016 Annual Merit Review and Peer Evaluation Meeting (June 6-10, 2016), Washington, DC.
6. K. Sun, D. Su, X. Tong, D. C. Bock, C. Cama, R. A. DeMayo, J. P. Huang, Q. Zhang, A. C. Marschilok, K. J. Takeuchi, E. S. Takeuchi, H. Gan, "Capacity Contributing Conductive Cathode Additive for Sulfur Batteries", Poster presentation (#P1-1132) at 18th International Meeting on Lithium Batteries (June 19-24, 2016), Chicago IL.
7. Hong Gan and Esther Takeuchi, presentation at the 2016 BMR Li-S Meeting at Lawrence Berkeley National Laboratory on Aug. 9, 2016, "Multi-Functional Cathode Additives (MFCA) for Li-S Battery Technology".
8. Ke Sun, Dong Su, Qing Zhang, David C. Bock, Amy C. Marschilok, Kenneth J. Takeuchi, Esther S. Takeuchi, and Hong Gan, "Interaction of CuS and Sulfur in Li-S battery system", *J. Electrochem. Soc.* 162 (14), A2834-A2839 (2015).
9. Ke Sun, Christina A. Cama, Rachel A. DeMayo, David C. Bock, Xiao Tong, Dong Su, Amy C. Marschilok, Kenneth J. Takeuchi, Esther S. Takeuchi and Hong Gan, "Interaction of FeS_2 and Sulfur in Li-S Battery System", *J. Electrochem. Soc*., 164 (1), A6039-A6046 (2017).
10. Hong Gan, Ken Sun, "Hybrid Cathodes for Lithium-ion Battery Cells" – Patent Application S.N. 15/138,470 filed on 4/26/16.

V.H.5. Development of High Energy Lithium Sulfur Batteries (PNNL)

Jun Liu, Principal Investigator
Pacific Northwest National Laboratory
Energy and Environment Directorate
902 Battelle Boulevard
Richland, WA 99354
Phone: 509-375-4443; Fax: 509-371-6242
E-mail: jun.liu@pnnl.gov

Dongping Lu, Co-Principal Investigator
Pacific Northwest National Laboratory
Energy and Environment Directorate
902 Battelle Boulevard
Richland, WA 99354
Phone: 509-372-4483; Fax: 509-375-2186
E-mail: dongping.lu@pnnl.gov

Tien Q. Duong, DOE Program Manager
Advanced Battery Materials Research (BMR)
U.S. Department of Energy
Vehicle Technologies Office
1000 Independence Avenue, SW
Washington, DC 20585
Phone: 202-586-7836
E-mail: Tien.Duong@ee.doe.gov

Start Date: October 1, 2015
End Date: September 30, 2018

Abstract

Objectives

- Investigate the fundamental reaction mechanism of polysulfides in thick sulfur electrodes using advanced characterization tools.
- Develop new approaches to retain high capacity in high loading sulfur electrode and enable stable operation of high energy lithium-sulfur (Li-S) batteries.

Accomplishments

- Developed effective electrode additives to improve sulfur utilization (>1000 mAh/g) for thick cathodes with sulfur loading up to 8 mg/cm^2.
- Discovered electric field induced reversible shielding mechanism for graphite in concentrated electrolytes.
- Adopted ALD coating of Al_2O_3 to suppress the lithium polysulfide induced shuttle and self-discharge reactions.
- Demonstrated prototypes of lithium-ion sulfur and Li-S pouch cells leveraging the new findings/knowledge achieved in our research.

Future Achievements

- Improve volumetric energy density and cycling stability of high loading sulfur cathodes.
- Understand electrolyte and additive degradation mechanism in high loading sulfur electrodes.

- Identify effective approaches to minimize quick capacity drop and efficiency fluctuation in high loading sulfur electrodes during initial 5-10 cycles.
- Develop effective approach to reduce electrolyte/sulfur ratio while maintain high sulfur utilization.

Technical Discussion

Background

Lithium-sulfur (Li-S) battery represents an attractive alternative to the state-of-the-art lithium-ion batteries to meet the increasing demand of high-efficient and cost-effective energy storage technologies. This is owing to the overwhelming superiorities of Li-S batteries such as high theoretical energy density, low cost and natural abundance of sulfur. For example, the theoretical specific energy of Li-S batteries is ~2300 Wh/kg, which is almost three times that of state-of-the-art lithium-ion batteries.[1] However, the market penetration of Li-S batteries is limited because of their low practically accessible energy density and poor long-term cycle life. More work need to be done to advance Li-S battery technology and accelerate market acceptance of long-range electrical vehicles (EVs).

Introduction

To achieve reasonable system energy density for practical applications, both high fraction of sulfur in carbon-sulfur composites and high overall sulfur loading are required.[2] Unfortunately, it is quite challenging to increase sulfur mass loading while maintain high material utilization rate and cycling stability as those demonstrated in the thin film counterpart. This is because the intrinsically low electronic and ionic conductivities of sulfur and Li_2S/Li_2S_2 severely limit the electrochemical reaction kinetics, which is exaggerated remarkably with the increase of sulfur loading. Thus, there is an urgent need for a facile approach to prepare sulfur electrodes with high mass loading and practically usable energy density. Based on our sulfur cathode material synthesis and electrode preparation method (U.S. Patent Application No. 14/177,954), sulfur electrodes with adjustable loadings of 2-8 mg/cm^2 can be successfully prepared at large scale. However, challenges remain as to how to address electrode wetting issue and improve sulfur utilization rate for high loading electrodes. In addition, our previous study indicates that Li corrosion is one of the greatest obstacles for stable cycling of Li batteries due to unavoidable reactions between Li and electrolyte.[3] This problem becomes more severe with the increase of sulfur loading and/or for the extended cycle time. The anode corrosion also significantly affects understanding of sulfur cathodes through electrochemical test of Li-S batteries. To decouple the lithium metal problem for cathode studies, intercalation based anodes such as graphite was used to replace Li metal anode and construct a novel prototypical lithium-ion sulfur battery, because graphite exhibits limited volume expansion during cycling and the continuous accumulation of SEI on the anode surface can be avoided. To clearly understand interfacial behaviors of graphite anode in ether based electrolyte and address possible issues that influence battery performance, systematic study on electrode interface was conducted using advanced *in situ*/*ex situ* techniques.

Approach

Our efforts in FY16 were mainly concentrated on (1) addressing electrode wetting issues in high loading sulfur cathodes using electrode additive, (2) using *in situ* AFM and other *ex situ* techniques to advance the fundamental understanding of interfacial behaviors of graphite in ether based concentrated electrolytes, (3) adopting ALD coating of Al_2O_3 to suppress shuttle and interfacial reactions of polysulfide, and (4) demonstrating of Li-S and lithium-ion sulfur pouch cells by leveraging the findings achieved during the project execution.

Results

1. Develop electrode additives to enhance sulfur utilization for high mass loading electrode

Sulfur electrode wetting is a bottleneck inhabiting realization of high energy in thick electrodes. To address this problem, novel electrode additives were adopted in FY16 and significant enhancement in cell performance

(including sulfur utilization, rate capability and cycling stability) has been demonstrated. These findings enable utilization of high loading sulfur cathodes for high energy Li-S batteries.

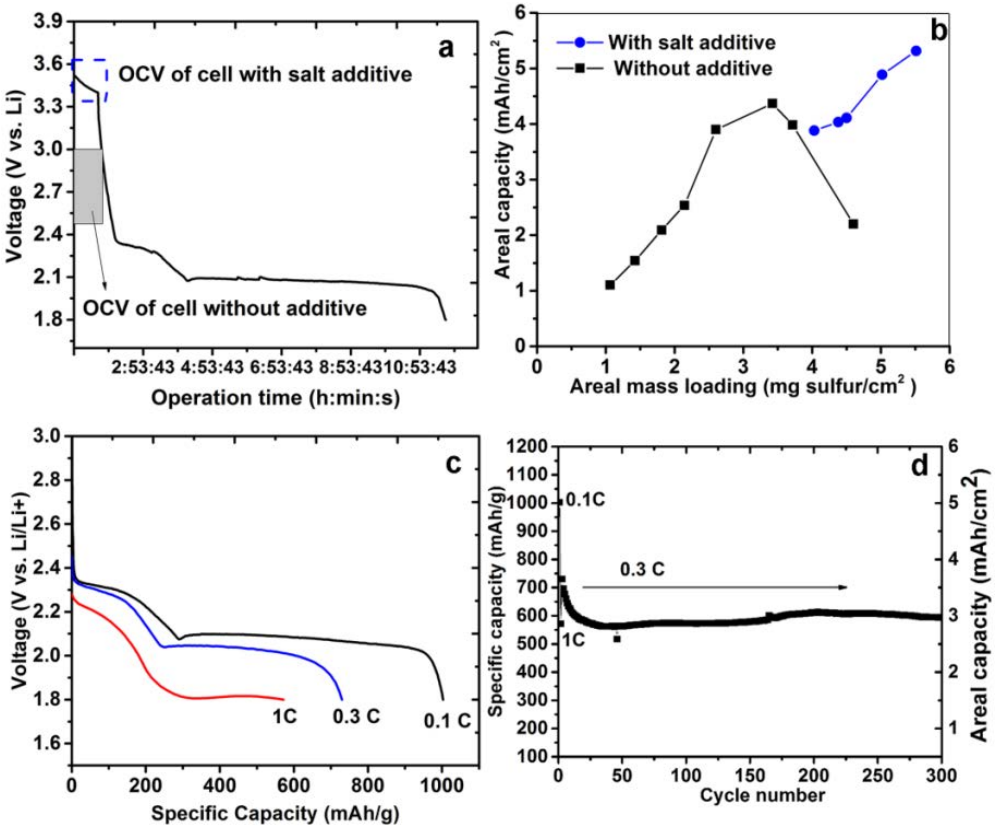

Figure V-281: Electrochemical performance of high loading sulfur cathodes containing 5 wt.% LiTFSI additive: (a) open circuit voltage (OCV) and first discharging profile, (b) dependence of areal capacities of sulfur cathodes on the sulfur mass loading (blue) and its comparison with that of electrodes without additives (black), (c) discharging profiles of Li-S cell at different C rates, and (d) cycling performance

Figure V-281 shows improved electrochemical performance of Li-S batteries with a sulfur cathode containing 5 wt% LiTFSI, an example of electrode additive. It is identified that the enhanced wettability of sulfur electrodes containing additives has a profound effect on the cell's open circuit voltage (OCV) and sulfur utilization rate. Figure V-281a shows representative OCV evolution and the first discharging curves of a Li-S cell. The sulfur mass loading of the electrode is more than 5 mg/cm^2. Interestingly, the OCV of the representative thick electrode containing the LiTFSI additive was 3.5 V, which is more than 10% higher than that of a cell that does not contain an additive. This result indicates that electrolyte penetration is efficient in the thick sulfur electrodes with the LiTFSI additive as compared to electrodes without such an additive. It is believed that when the cathode is infiltrated by the electrolyte, the pre-cycling salt additive can dissolve and generates capillary channels for quick electrolyte infiltration. Smooth electrolyte penetration into electrodes, particularly thick electrodes, ensures adequate ionic transport, reduces cell internal resistance, and hence improves cell OCV. In addition, quick and adequate electrolyte penetration with the additive can effectively improve sulfur utilization rate and/or discharge voltage plateaus. As shown in Figure V-281a, the first discharge capacity of Li-S cells is above 1000 mAh/g with two typical discharge plateaus at 2.3 V and 2.1 V, respectively. For the Li-S cells without electrode additives, the electrode areal capacity linearly increases upon increasing sulfur loading from 1 to 3.5 mg/cm^2 and then decreases with loading above 4 mg/cm^2, resulting in a peak value of 4.5 mAh/cm^2 at loading of ca. 3.5 mg/cm^2. However, in the representative electrodes having the additives, the electrode areal capacity is greatly improved and no decline in electrode areal capacity is observed for sulfur loading from 4 mg/cm^2 to 5.5 mg/cm^2. Similarly, with 5% solvent additive such as TEGDME, a linear increase of areal capacity is achieved with sulfur loading up to 7.5 mg/cm^2. These results indicate that sulfur utilization rate does not change significantly despite increasing sulfur mass loading, which further demonstrates the effectiveness of additives in improving electrode wetting. In addition to electroactive

material utilization, the rate capability of Li-S cells also depends on the electrode wettability and electrolyte uptake. For example, as shown in Figure V-281c, a representative electrode containing the salt additive exhibits discharge capacities of 1000 and 750 mAh/g at 0.1 C and 0.3 C rates, respectively. Even when the C rate is increased to 1 C, a discharge capacity of 600 mAh/g can be achieved. These results indicate that the salt and solvent additives disclosed here can improve power output of Li-S cells with high mass loading sulfur cathodes. Moreover, the cell cycling stability can also be improved by using the salt additive. Capacities around 600 mAh/g with areal capacity 3 mAh/cm^2 are obtained after 300 cycles. We hypothesize that the salt additive, which is easily dissolved in electrolyte solvents, are distributed uniformly within and/or on the electrode to form an interconnected network, which improves affinity of the electrode with electrolyte and hence facilitates electrolyte infiltration.

2. Electric field induced reversible shielding mechanism of concentrated electrolyte

In FY15, the highly concentrated 5 Ṁ LiTFSI-DOL (Ṁ: mol salt/liter solvent) electrolyte was discovered by our group to enable stable operation of lithium-ion sulfur cells with graphite as the anode (US patent: No. US20160126589). In addition, it was found that concentrated electrolyte can function well for graphite anode regardless of the solvent type. To explore the function mechanism behind this phenomenon, electrochemical *in situ* AFM and other advanced *Ex situ* techniques were employed to investigate electrode interfacial behaviors and properties in this concentrated electrolyte with/without an electric field.

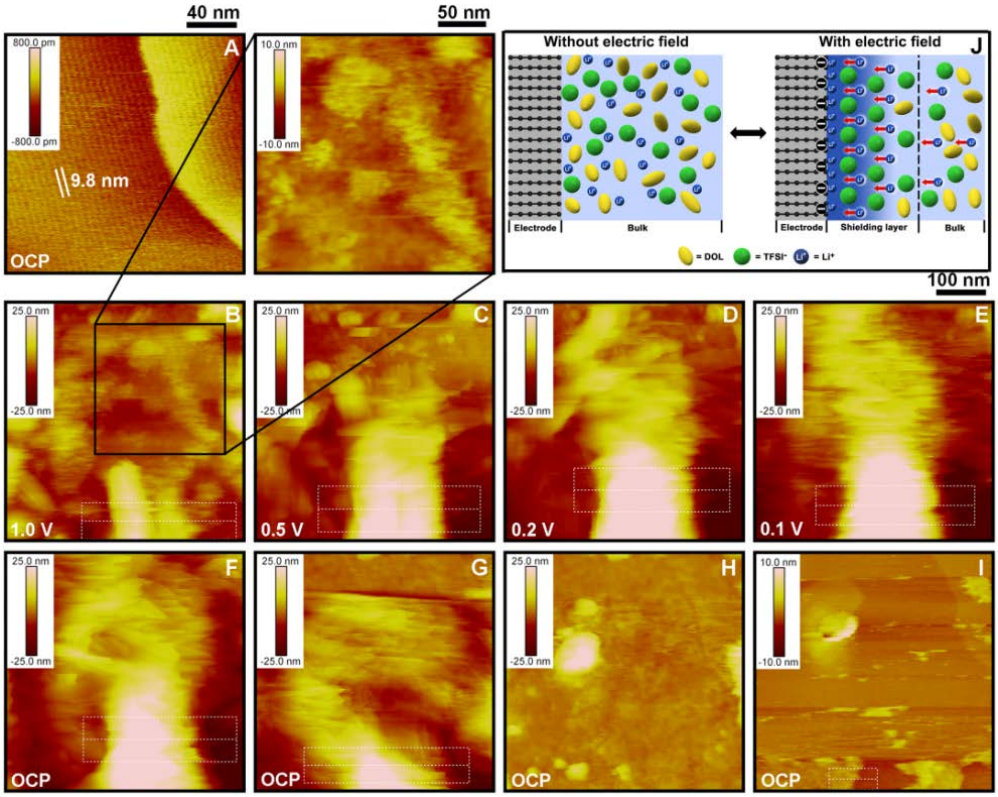

Figure V-282: AFM topographic images of an HOPG electrode immersed in an 5 Ṁ LiTFSI-DOL electrolyte with and without electrode polarization. (A) Before polarization (at open circuit potential). Polarized at: (B) 1.0 V, (C) 0.5 V, (D) 0.2 V, (E) 0.1 V. Time after removal of polarization: (F) 10.4 min, (G) 17.2 min, (H) 20.5 min. Time after addition of free DOL in (H): (I) 24.2 min. (J) Schematic diagram of electrode-concentrated electrolyte interface with and without electrode polarization

In the absence of the field, highly ordered surface structures covering the surface of the HOPG were clearly observed (Figure V-282A). The application of the polarization (electric field) to the HOPG electrode (working electrode) led to profound changes at the electrode surface. Immediately upon polarization of the electrode to 1.0 V (vs. Li$^+$/Li) from the open circuit potential (OCP) at 2.85 V, the HOPG surface transformed from the ordered structure (Figure V-282A) into a compact surface coating (Figure V-282B), denoting the fast response of the surface structuring to an electric field. Shortly after, another nonuniform coating of crystal-like aggregates began to grow above the compact coating. Polarization to more negative potentials and for longer

periods of time resulted in the continuous growth of this second coating (Figure V-282C - Figure V-282E). Upon removal of the field, i.e., at OCP, the height of the second layer coating decreased and almost completely disappeared after a 20 min rest (Figure V-282F - Figure V-282H). The formation of these coatings at low potential was largely reversible, indicating that the nature differed markedly from that of a traditional insoluble SEI layer. Notably, a significant restructuring of the surface was evident at 1.0 V (Figure V-282B), a potential at which there was a negligible current (From CV data, not shown here), confirming that solvent/anion reduction reactions were not the origin of the transformation. Instead, a completely new SEI formation and function mechanism has been discovered, in which the electrolyte components reversibly form a protective surface coating on the graphite electrode during the Li^+ intercalation/deintercalation upon changing the potential (Figure V-282J).

To explain the observed behaviors of graphite electrode in the highly concentrated electrolyte, the effect of electric polarization on the electrode/electrolyte interface must be considered. The application of the electric field generates an electric double-layer restructuring of the electrolyte constituents next to the electrode surface (Figure V-282J). For dilute electrolytes, MD simulations indicate that much of this double-layer consists of polarized uncoordinated solvent molecules, dominated by the more polarizable solvent in the solvent mixtures. These solvent molecules are highly susceptible to reduction by the electrons on the polarized surface. Highly concentrated electrolytes, however, have few solvent molecules (relative to the number of ions) and the majority of these are coordinated to the Li^+ cations. Such mixtures resemble—to some extent—ionic liquids composed of the same anions and organic cations. The negative polarization of a graphite surface exposed to an ionic liquid results in a very different surface structure than for dilute electrolytes containing organic solvents. Polarization in the concentrated electrolytes is expected to result in further exclusion of the solvent from the surface (relative to the bulk concentration) due to preferential adsorption of the Li^+ cations as the potential is decreased (Figure V-282J). The exclusion of the solvent molecules from the electrode surface in the restructured double-layer explains the largely reduced solvent decomposition in the concentrated electrolytes. The surface layer on the HOPG noted upon initial negative polarization during the *in situ* AFM measurements (Figure V-282B) therefore likely consists of the precipitation of solvated LiTFSI. The formation of the surface layer is critical for the protection of graphite during the Li^+ intercalation/deintercalation processes. Within the layer, the solvent molecules near the surface will be predominantly coordinated to Li^+ cations and thus charge transfer (reduction) may preferentially occur to the readily available cations rather than the solvent molecules. This further concentration of the already highly concentrated electrolyte via negative polarization of the electrode leads to the growth of “crystalline solid” on the electrode surface (Figure V-282B - Figure V-282E) which further protects electrode from solvent co-intercalation. The 5 Ṁ LiTFSI-DOL electrolyte has a DOL:LiTFSI molar ratio of 2.86:1. Once the concentration exceeds 7 Ṁ, white solids crystalize which are identified to be (DOL)1:LiTFSI crystalline solvate by single-crystal XRD analysis. At these extreme conditions, the activity of the free DOL molecules is very limited thus solvent co-intercalation was greatly suppressed. Upon depolarization of the anode (removal of the negative charge), these layers dissolve back into the electrolyte, i.e., the electrolyte regains its uniform composition.

3. Electrochemical performance of Lithium-ion sulfur battery and interface of graphite anode

Based on the electrolyte and sulfur cathode developed at PNNL, lithium-ion sulfur battery (LG/S full cell) coupling the integrated Ketjen Black (IKB)/S cathode and lithiated graphite anode were assembled and evaluated electrochemically. Promising electrochemical properties are demonstrated from the full cell data in terms of reversible capacity, Coulombic efficiency (CE) and cycling stability. At a low rate of 0.1 C, the LG/S cell exhibits a high capacity of 980 mAh/g (2 mAh/cm^2) with two flat discharge plateaus at 2.2 and 2.0 V, respectively (Figure V-283a). In the first charging process, a capacity around 1080 mAh/g is obtained, delivering a high CE of 90.7% without $LiNO_3$ additive in the electrolyte. When the rate is elevated to 0.5 C after 5 cycles at 0.1C, a capacity as high as 815 mAh/g is delivered. After 100 cycles, a capacity retention of 81.3% can be achieved at 0.5 C with a high Coulombic efficiency .The high performance of LG/S cell is attributed to both bulk and interfacial stability of graphite anode in the concentrated electrolyte. Figure V-283c shows smooth surface and well maintained graphite particle after 5 cycles with the electrolyte in Li-graphite half-cell. In addition, the interfacial properties of graphite are studied after being cycled in LG/S full cell. Figure V-283d exhibits a cross-sectional image of a single graphite particle by focused ion beam (FIB)-SEM after 100 cycles in sulfur battery. The particle shows a solid dark core with a thin layer of coating outside (ca. 100-200 nm). The EDS analysis (Figure V-283e and Figure V-283f) was performed at the very surface and core area of the selected particle. It is clear that the core of graphite is dominated by carbon with a trace

amount of oxygen. The surface layer is the byproducts from polysulfide deposition. This means graphite interface is stable enough to endure the attack from polysulfides and maintains its structure integrity. Therefore, the irreversible loss of polysulfides and SEI accumulation on the anode side are both mitigated, which greatly improves the cycling stability of the lithium-ion sulfur cell. The lithiated graphite is reductive and may react with high order Li polysulfide to produce low order Li sulfide like Li_2S_2/Li_2S if there is no sufficient surface passivation layer to block the graphite from contacting ploysulfide or electron transfer.

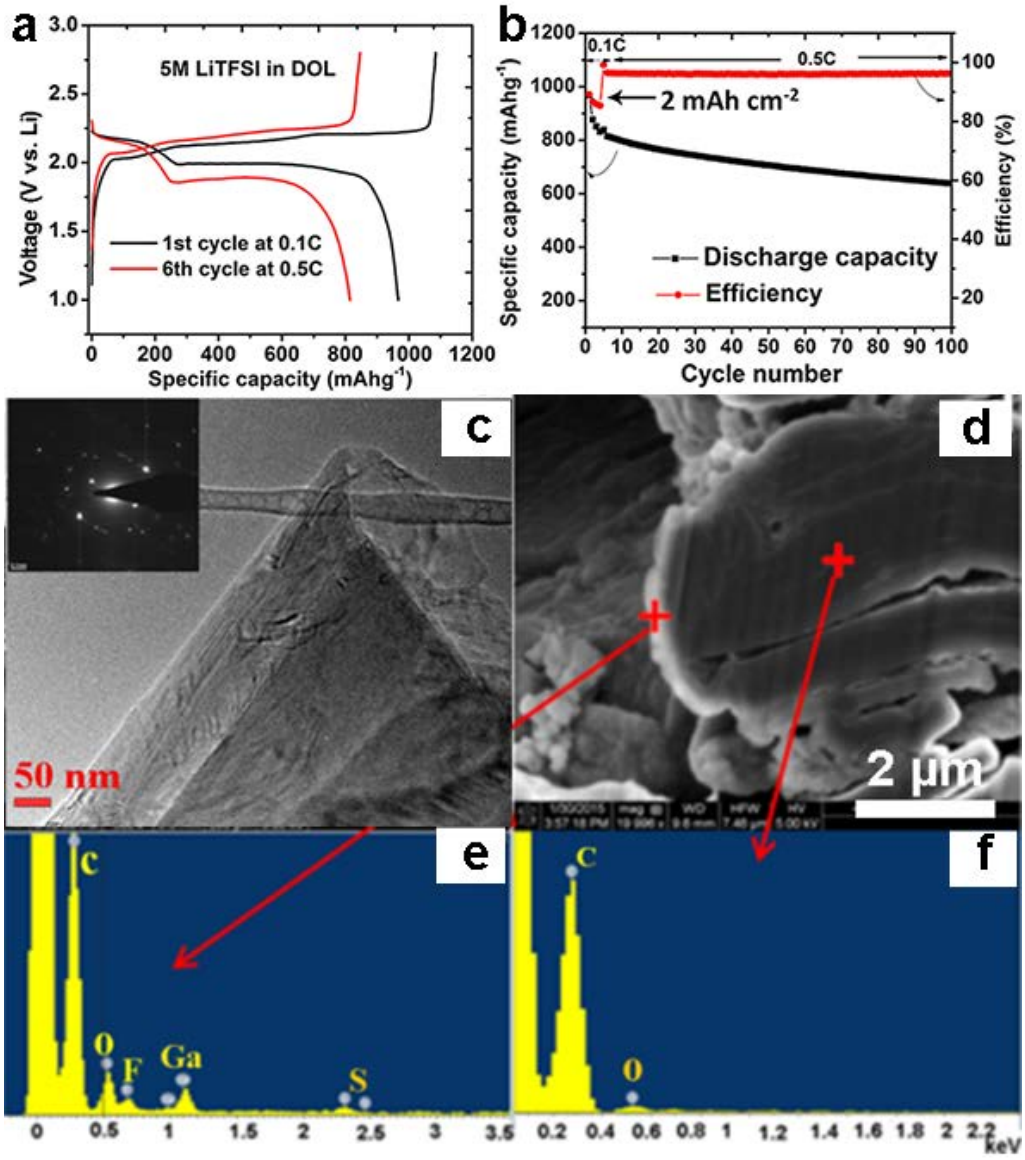

Figure V-283: (a) Charge/discharge curves of LG/S full cell in 5 Ṁ LiTFSI/DOL electrolyte without $LiNO_3$ and (b) corresponding cycling stability and Coulombic efficiency. (c) TEM image of the graphite after five cycles with 5 Ṁ LiTFSI/DOL electrolyte in Li-Graphite half-cell and corresponding ED pattern (insert). (d) FIB-SEM cross-sectional image of a single graphite particle after 100 cycles with sulfur cathode. (e) and (f) Point EDS at the very edge and core area of the graphite particle in (d), respectively

4. Tackle polysulfide shuttle effect in Lithium-ion sulfur batteries by anode surface passivation

Lithium-ion sulfur batteries with graphite as anode was successfully demonstrated,[4] but polysulfide shuttle effect still occurs on the graphite and results in low coulombic efficiency (CE) and limited cycle life. This is due to the lack of effective passivation layer to protect graphite anode. To address this problem, we developed an anode surface passivation strategy to suppress the polysulfide shuttle reactions and therefore improve the

performance of graphite-sulfur batteries (Figure V-284a). Non-conductive Al_2O_3 passivation layers with different thicknesses (1 nm, 2 nm, and 4 nm) were coated on the graphite anode by using an atomic layer deposition (ALD) method. Figure V-284b compares the coulombic efficiency of the sulfur cathodes with pristine graphite and graphite coated with 1 nm, 2 nm and 4 nm Al_2O_3 passivation layers (named as 1 nm, 2 nm and 4 nm Al_2O_3/graphite, respectively).

The 1st cycle CE is only 84%, and the average CE is about 94% from 2nd to 100th cycle, for the sulfur cathode with pristine graphite (Figure V-284b). When the graphite anode is coated with 1 nm Al_2O_3 passivation layer, the sulfur cathode exhibits slightly higher capacities, but much enhanced CE (90% in the 1st cycle and ~ 96% afterward), compared to the baseline. The optimal performance of the sulfur cathode is achieved in the case of 2 nm Al_2O_3/graphite. For example, the sulfur cathode maintains an average CE of 96% from the very 1st cycle to 100th cycle (Figure V-284b). If a thicker Al_2O_3 passivation layer (4 nm) is applied on the graphite anode, the CE of sulfur cathode is kept at the similar level as 2 nm Al_2O_3/graphite, but the discharge capacity drops dramatically. The reduced capacity can be attributed to the thick insulating Al_2O_3 layer, which greatly impedes the diffusion of lithium ions and electrons across the SEI layer. Profound effects of Al_2O_3 coating on the interfacial properties of electrodes were also proved by EIS test. Figure V-284c - Figure V-284f compares the morphology of SEI layers on graphite and 2 nm Al_2O_3/graphite anodes after 100 cycles. Compared to the graphite before cycling, the one after cycling is totally covered with a thick and rough SEI layer, as seen in Figure V-284c and Figure V-284d. Flake-like structures can be easily found at the particle surface (insert of Figure V-284d), and is identified as polysulfide deposition by EDS analysis. In contrast, the 2 nm Al_2O_3/graphite anode after cycling possesses a smooth and thin SEI layer, with no obvious flake-like structure observed (Figure V-284e and Figure V-284f). These results indicate that the Al_2O_3 passivation layer reduce the insoluble polysulfide deposition on the graphite anode.

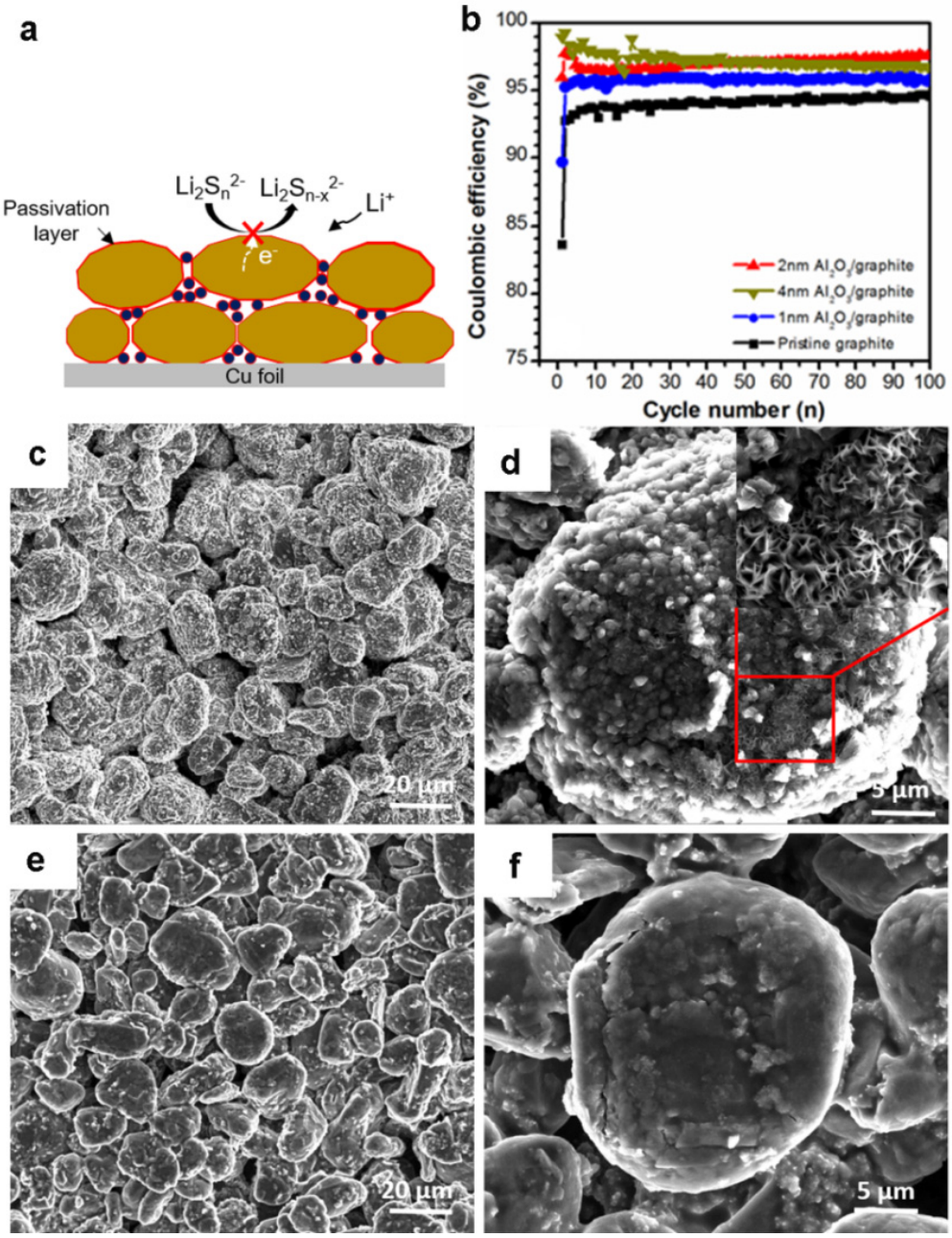

Figure V-284: (a) Schematic diagram of surface passivation layer on the graphite anode blocking the diffusion pathway of electrons, therefore suppressing polysulfide reduction reaction. (b) Coulombic efficiency of graphite-sulfur batteries using pristine graphite, 1 nm, 2 nm, and 4 nm Al_2O_3/graphite as the anode. SEM images of (c, d) graphite and (e, f) 2 nm Al_2O_3/graphite anodes after cycling

5. Demonstration of Li-S pouch cell

To verify the feasibility of the achieved findings/approaches for applications in practical cells, we assembled pouch cells using thick sulfur electrode for electrochemical evaluation. In addition to use the electrode additive approach to enhance the sulfur utilization rate in thick electrode, we also modified the synthesis IKB by introducing nitrogen functional groups into material. Significant enhancement in electrode wetting for thick sulfur electrode has been demonstrated and related mechanism understanding is in progress. Accordingly, the nitrogen doped IKB was synthesized at relevant scales and used for pouch cell preparation. The large area sulfur electrodes (shown in Figure V-285a) with mass loadings about 4.5 mg/cm^2 were coated and processed at Advanced Battery Facility at PNNL. The designed pouch cell has a dimension of 72 mm×41mm×4mm (Figure V-285b) and a total mass of 14 g including 1.72 g sulfur active material and 5 g electrolyte, with an

electrolyte/sulfur ratio of 2.9/1. The capacity achieved from the cell is 1.68 Ah at a current of 100 mA and room temperature. Figure V-285c shows the first discharge curves of the pouch cell plotted in forms of both specific capacity and energy density. The actual specific capacity of sulfur is ca. 1000 mAh/ g (Figure V-285c, blue curve), indicating a comparable sulfur utilization with those obtained in coin cells. Based on the output energy and total mass of the cell, the measured energy density of the pouch cell is 247 Wh/ kg (Figure V-285c, black curve), which can be further improved to 300 Wh/ kg by simply optimizing the inactive components of the pouch cell (e.g. electrode current collectors and pouch). More improvement is needed for improved energy density and cycling stability. Our continued efforts on pouch cell preparation and optimization will be focused on (1) employing sulfur electrode with higher mass loading, (2) introducing electrode additives into electrode to further improve sulfur utilization rate, and (3) optimization of electrolyte for long term cycling stability after solving the gassing problem.

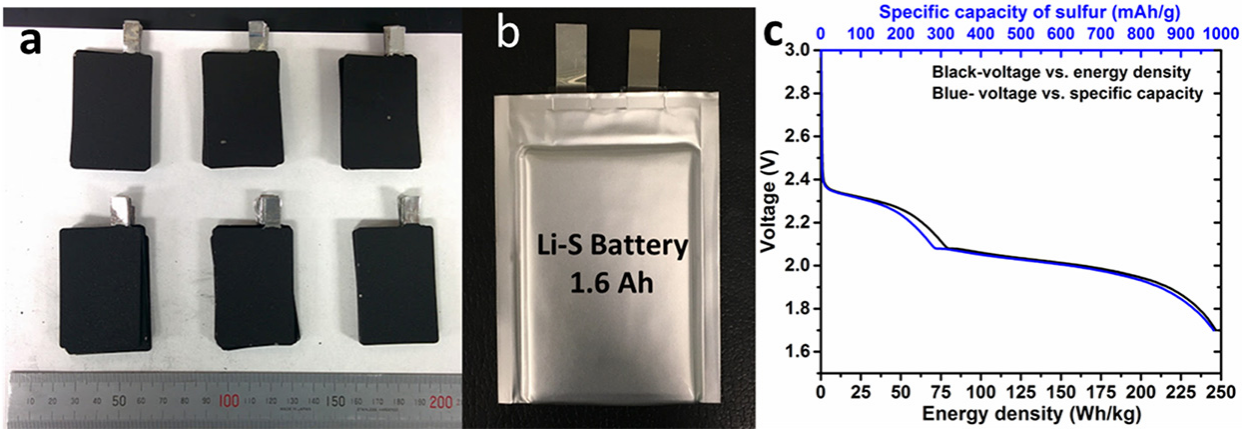

Figure V-285: (a) photo image of the prepared sulfur cathode with mass loading 4.5 mg cm^{-2}, (b) photo image of 1.6 Ah Li-S pouch cell and (c) first discharge profiles (black-energy density and blue-specific capacity)

Conclusions

Utilization of electrode additives is a facile and effective approach to enhance electrode wettability and rate capability performance of high loading sulfur cathodes. High sulfur utilization (>1000 mAh/g) can be achieved for thick electrodes with sulfur loading up to 8 mg/cm^2. Lithium-ion sulfur batteries employing graphite as the anode has been successfully demonstrated. Without using any additive such as $LiNO_3$, the LG/S full-cell with sulfur loading of > 2 mg/cm^2 delivers a high reversible capacity of 980 mAh/g and a capacity retention of 81.3% after 100 cycles. A fundamentally new surface protection mechanism is reported for graphite anode with concentrated electrolytes. Upon the negative polarization of the anode, the anions and partially solvated cations precipitate into a Li^+ cation conducting layer near the electrode surface, which effectively prevents the co-intercalation of solvent molecules into graphite. An anode surface passivation approach of ALD coating of Al_2O_3 was employed to address the polysulfide shuttle issue in graphite-sulfur batteries. The coulombic efficiency and capacity of sulfur cathodes were greatly improved by depositing a thin Al_2O_3 passivation layer (2 nm) on the graphite anode. Using sulfur cathodes with mass loading at 4.5 mg/cm^2, Li-S pouch cells with a capacity of 1.6 Ah was built and tested. Preliminary electrochemical test indicates an energy density of ca. 250 Wh/kg at the cell level with sulfur utilization ca. 1000 mAh/g and electrolyte/sulfur ratio of 2.9:1. More efforts are needed for further improvement of energy density and long term cycling stability of these Li-S and lithium-ion sulfur cells.

Products

Presentations/Publications/Patents

1. Lu D., Li. Q. Liu J., Xiao J., Zhang J. Liu J. and Graff G.L., Additives to Enhance Electrode Wetting and Performance and Methods of Making Electrodes Comprising the Same. Patent Application: #30459 CIP.
2. Lu D., Tao J., Yan P., Henderson W. A., Li Q., Shao Y., Graff G. L., Polzin B., Zhang J., Yoreo J.D., Liu J., and Xiao J., Reversible Shielding of Electrodes, submitted for publications.
3. Lu D., Xiao J., Liu J., Li Q.,Ferrara S., Graff G. L., Zhang J. and Liu J., Non-lithium Metal Anode for Lithium-Sulfur Batteries, The 9th Symposium on Energy Storage Beyond Lithium-ion (BLI-IX), Richland, WA, May 24-26, 2016.
4. Liu J. and Lu D. Development of high energy lithium sulfur battery, 2016 Annual Merit Review and Peer Evaluation Meeting, Washington D.C, June 6–10, 2016.
5. Lu D., Xiao J., Liu J., Li Q.,Ferrara S., Graff G. L., Zhang J. and Liu J., Lithium-Sulfur Batteries: High Loading Cathode, New Electrolyte and Non-lithium Metal Anode, 18th International Meeting on Lithium Batteries, Chicago, IL, June 19-24, 2016.
6. Liu J., Lu D., and Zhang J., Development of high energy lithium sulfur battery, Li-sulfur Battery Workshop, Berkeley, CA. August 9, 2016.

References

1. Bruce P. G., Freunberger S. A., Hardwick L. J.,Tarascon J.-M., Nat. Mater. 2012, 11, 19-29.
2. Lu D., Zheng J., Li Q., Xie X., Ferrara S., Nie Z., Mehdi L. B., Browning N. D., Zhang J. G.,Graff G. L., Adv. Energy Mater. 2015, 5, 1402290.
3. Lu D., Shao Y., Lozano T., Bennett W. D., Graff G. L., Polzin B., Zhang J., Engelhard M. H., Saenz N. T., Henderson W. A., Bhattacharya P., Liu J., Xiao J., Adv. Energy Mater. 2015, 5, 1400993.
4. Lu D., Yan P., Shao Y., Li Q., Ferrara S., Pan H., Graff G. L., Polzin B., Wang C., Zhang J.-g., Liu J., Xiao J., Chem. Commun. (Cambridge, U. K.) 2015, 51, 13454-13457.

V.H.6. Nanostructured Design of Sulfur Cathodes for High Energy Lithium-Sulfur Batteries (Stanford University)

Yi Cui, Principal Investigator
Stanford University
Department of Materials Science and Engineering
Stanford, CA 94305
Phone: 650-723-4613; Fax: 650-736-1984
E-mail: yicui@stanford.edu

Tien Q. Duong, DOE Program Manager
Advanced Battery Materials Research (BMR)
U.S. Department of Energy
Vehicle Technologies Office
1000 Independence Avenue, SW
Washington, DC 20585
Phone: 202-586-7836
E-mail: Tien.Duong@ee.doe.gov

Start Date: October 1, 2015
End Date: September 30, 2016

Abstract

Objectives

The charge capacity limitations of conventional transition metal oxide cathodes are overcame by designing optimized nano-architectured sulphur cathodes. This study aims to enable sulphur cathodes with high capacity and long cycle life by developing sulphur cathodes from the perspective of nanostructured materials design, which will be used to combine with lithium metal anodes to generate high-energy lithium-sulphur batteries. Novel sulphur nanostructures will be designed and adsorption/diffusion/catalytic mechanism will be proposed to overcome the issues related to sulphur volume expansion, polysulphide dissolution and insulating nature of sulphur/Li_2S.

Accomplishments

- Designed non-conductive oxide coated porous carbon flakes for sulphur and polysulphides confinement.
- Demonstrate the balance of surface adsorption and diffusion of Li_2S_x species on nonconductive metal oxides.
- The selection criterion of metal oxide is proposed to guide the rational design of cathode materials for advanced Li-S batteries.
- Investigated the lithium ion diffusion mechanism in different types of metal sulphides.

Future Achievements

- Increasing the mass and the percentage of sulphur loading in the electrode.
- Identify the adsorption mechanism between sulphur species and different types of metal sulphides.
- Build cell for testing diffusion coefficient of Li_2S_x species on various types of metal sulphides.
- Demonstrate the catalytic effect of Li_2S_x species on metal sulphides, enabling good performance of Li-S batteries.

Technical Discussion

Background

Lithium-sulphur batteries can bring about significant improvements to the current state-of-the-art battery technologies due to its high specific energy density and cost saving. The capacity decay of lithium-sulphur battery during cycling is a multifaceted problem. There exist multiple materials challenges that prevent it from reaching the cycling performance suitable for portable electronics and electrical vehicles. The rapid capacity decay of sulphur cathode can be attributed to several reasons: 1) significant volumetric expansion (~80% change) when sulphur is reduced to lithium sulphide (Li_2S); 2) dissolution of intermediate lithium polysulphides (Li_2S_x, $4 \leq x \leq 8$) in the electrolyte; 3) low ionic and electronic conductivity of both sulphur and Li_2S.

Introduction

Introducing anchoring materials, which can induce strong binding interaction with Li_2S_n species, has been demonstrated as an effective way to overcome this problem and achieve long-term cycling stability and high-rate performance. The interaction between Li_2S_n species and anchoring materials should be studied at the atomic level in order to understand the mechanism behind the anchoring effect and to identify ideal anchoring materials to further improve the performance of Li-S batteries. The importance of balancing sulphide species adsorption and diffusion on non-conductive metal oxides with better surface diffusion will lead to higher Li_2S deposition efficiency. In the reverse reaction process, catalysis of the decomposition of Li_2S and oxidization of Li_2S to Li_2S_x and finally to sulphur near the surface of the substrate are crucial steps to realizing high capacity and Columbic efficiency, yet have been relatively neglected in the Li-S chemistry. In this respect, a systematic consideration of the substrates that are capable of catalyzing Li_2S decomposition is also critical to the development of advanced Li-S batteries.

Approach

Using first-principles approach with van der Waals interaction included, we systematically investigate the adsorption of Li_2S_n species on various oxides and sulphides, and study the detailed interaction and electronic structure, including binding strength, diffusion energy barrier and catalytic effect. We gain insight into how van der Waals interaction and chemical binding contribute to the adsorption of Li_2S_n species for anchoring materials with strong, medium, and weak interactions. Combining theoretical calculations and experimental design, we select a series of metal oxides/sulphides as model systems to identify the key parameters in determining the energy barrier for Li_2S oxidation and polysulphide adsorption.

Results

The diffusion of lithium on the surface of various metal oxides has been investigated by DFT calculation (Figure V-286). Because the most favorable binding site of sulphides is two Li bonding with metal oxide, the calculated Li ion diffusion can also indicates the diffusivity of sulphides on the surface of the oxide. On MgO(100), CaO(100) and La_2O_3(001) surfaces, the diffusions of Li in different dimensional can be realized on three equivalent adsorption sites (Figure V-286). Among the three kinds of surfaces, the diffusion barrier of Li on CaO(100) is largest. The space group of MgO is same with CaO, however, the diffusion barrier of Li on MgO(100) is about 0.45 eV lower than that on CaO(100). The suitable adsorption energies of lithium sulphur species and small diffusion barriers of Li on MgO will lead to the formation of abundant lithium sulphide particles on MgO/C surfaces, which are responsible for the best cycling performance of MgO/C cathodes. On CeO_2(111) surfaces, the large diffusion barrier is 0.66 eV, which is similar with that on La_2O_3(001) surfaces. This may explain why CeO_2/C and La_2O_3/C cathodes show similar cycling performance. Among the five kinds of metal oxides surfaces, the largest diffusion barrier (1.22 eV) of Li is found to be on Al_2O_3(110), which is about three times of that on MgO(100). It is seen that lithium sulphide species can strongly adsorb, however, difficult to diffuse on Al_2O_3. Although Al_2O_3 has the best Li_2S_8 adsorption performance, the slow diffusion of Li_2S_x indicated that Al_2O_3 may not be a good additive for sulphur cathode. Our results indicate an optimized balance between lithium polysulphides adsorption and surface diffusion is favorable for the lithium sulphide

species deposition on the surface of oxide/carbon matrix, keeping materials active during the cycling and ensuring the final good cycling performance of batteries.

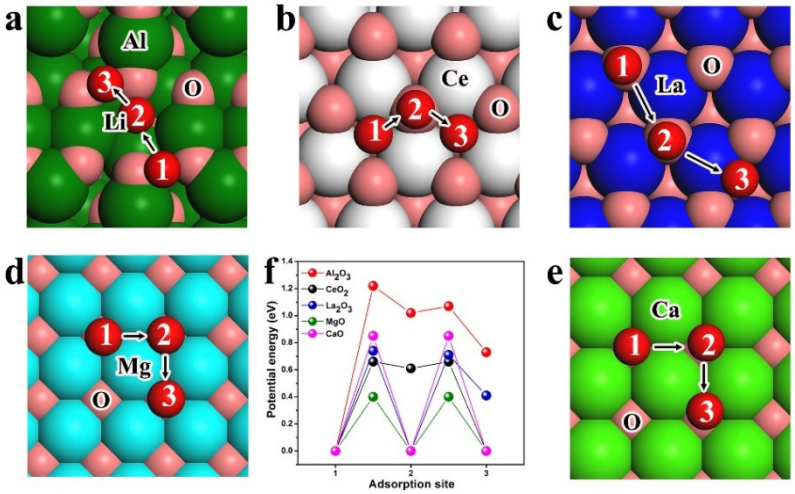

Figure V-286: Lithium diffusion mechanism on the surface of various metal oxides. (a-e) Minimum energy path for lithium ion diffusion on Al_2O_3(110), CeO_2(111), La_2O_3(001), MgO(100) and CaO(100) surfaces, respectively. (f) Potential energy profiles for Li^+ diffusion along different adsorption sites on the oxide surface

Based on our experimental results, we clarify three functions of these oxides (Figure V-287). The first basic function of these metal oxides is the polysulphide adsorption. Our DFT calculation and temperature swing adsorption experiments confirm that the monolayer chemisorption is dominant during the polysulphide capture. The second role of these metal oxides especially some nonconductive oxides is the Li_2S_x transfer station, which transport the Li_2S_x from the poorly conductive oxide surface to high conductive carbon matrix to ensure the full electrochemical conversion. The third role is to induce the controlled growth of Li_2S_x species on the surface instead of random deposition. Based on these functions of nonconductive metals oxides, we can propose an oxide selection criterion for in Li-S batteries. Because the first role of oxides is adsorption, the binding between the sulphides species and the matrix should be strong, which can both suppress the shuttle effect and enable the full utilization of active materials. Considering that the polysulphide capture is the monolayer chemisorption and the adsorption amount will depend on the surface area of oxides, uniformly distributed oxides nanostructures with high surface area are essential. Although strong binding and high surface area are preconditions, the surface diffusion properties of oxides are also very important, which affect the distribution and structure of lithium sulphides. An optimized balance between lithium polysulphides adsorption and surface diffusion is favorable for the lithium sulphide species to deposit on the surface of oxide/carbon matrix, keep active during the cycling and ensure the final good cycling performance of batteries. In addition, some other factors such as electric conductivities, chemical stability, and lithiation/delithiation of the oxides also need to be considered.

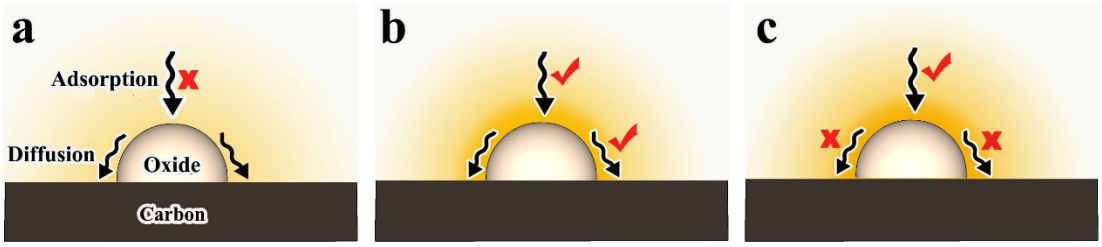

Figure V-287: Schematic of the polysulphide adsorption and diffusion on the surface of various nonconductive metal oxides. (a) the metal oxide with weak polysulphide adsorption capability, only few polysulphides can be captured by the oxide; (b) The metal oxide with both strong adsorption and good diffusion, which is favorable for the electrochemical reaction and the controllable deposition of sulphur species; (c) The metal oxide with strong bonding but without good diffusion, the growth of lithium sulphide and the electrochemical reaction on the oxide/C surface will be impeded

We further explore the interaction mechanism between sulphur species and different types of metal sulphides, and identify the optimal material to improve the capacity and cycling stability of sulphur cathode. In order to

study the interaction between lithium polysulphide and the metal sulphides, first-principle simulations are applied. Figure V-288a-f show the adsorption conformations for Li_2S_6 on various sulphides (VS_2, CoS_2, TiS_2, FeS, SnS_2 and Ni_2S_3 are selected here). It can be clearly seen that the chemical interaction is dominantly contributed by the bond formed between Li ion in Li_2S_6 and sulphur ion in sulphide. The binding energy, E_b, is computed to measure the binding strength between Li_2S_6 species and the anchoring materials (AM). It is defined as the energy difference between the Li_2S_6−AM adsorbed system (ELi_2S_6+AM) and the summation of pure Li_2S_6 (ELi_2S_6) and pure AM (EAM), which can be expressed as $E_b = ELi_2S_6 + EAM - ELi_2S_6$+AM (the positive binding energy indicates that the binding interaction is favored, and the larger value the stronger anchoring effect). According to the simulation, the binding strength between Li_2S_6 and Ni_3S_2, SnS_2, FeS, CoS_2, VS_2 and TiS_2 are 0.72 eV, 0.80 eV, 0.87 eV, 1.01 eV, 1.04 eV and 1.02 eV, respectively. The magnitudes of E_b also indicate that the stronger interaction can induce better anchoring effect, which can improve the performance of Li-S battery. Furthermore, all the sulphide materials in our study can induce larger binding strength than that by graphene (0.67 eV), which exhibits very weak chemical binding to Li_2S_6 and the adsorption is dominated by physical vdW interaction. This is the reason why these sulphides can mitigate polysulphide dissolution and suppress shuttle effect, leading to better performance in Li-S battery than that of commonly adopted sp2 carbon materials.

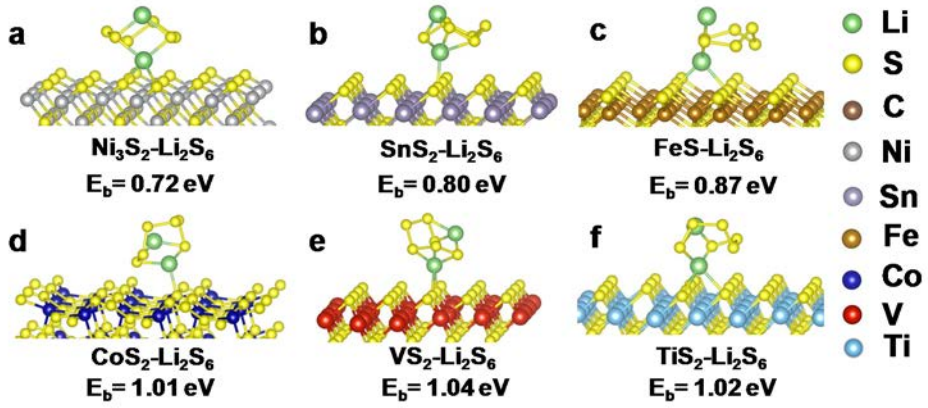

Figure V-288: Atomic conformations and binding energy for Li_2S_6 species adsorption on (a) Ni_3S_2, (b) SnS_2, (c) FeS, (d) CoS_2, (e) VS_2 and (f) TiS_2. Here, green, yellow, grey, purple, brown, blue, red and cyan balls represent lithium, sulphur, nickel, tin, iron, cobalt, vanadium and titanium atoms, respectively

The lithium ion diffusion coefficient can serve as a good descriptor to verify whether metal sulphides (M_xS_y) can propel the polysulphide redox reaction process as fast lithium ion diffusion facilitates the sulphur transformation chemistry at the M_xS_y interface. Cyclic voltammetry (CV) was used to investigate electrode kinetics with respect to the lithium ion diffusion coefficient. Taking the S-VS_2@G/CNT electrode as a representative example, Figure V-289a shows the CV curves of the electrode measured under different scanning rates ranging from 0.2 to 0.5 mV s^{-1} between 1.5 and 2.8 V (vs. Li/Li^+). At all scan rates, there are two cathodic peaks at around 2.30 V (IC1) and 1.95 V (IC2), corresponding to the reduction of elemental sulphur (S8) to long-chain lithium polysulphides and the subsequent formation of short-chain Li_2S_2/Li_2S. The anodic peak at around 2.50 V in the anodic sweep results from the transition of Li_2S_2/Li_2S to polysulphides and elemental sulphur (IA). The cathodic and anodic current peaks (IC1, IC2, IA) of all the M_xS_y containing electrodes have a linear relationship with the square root of scanning rates (Figure V-289b-d), indicative of the diffusion-limited process. Therefore, the classical Randles Sevcik equation can be applied to describe the lithium diffusion process: Ip = (2.69 × 105) n1.5 S DLi+0.5 CLi ν0.5, where IP is the peak current, n is the charge-transfer number, S is the geometric area of the active electrode, DLi+ is the lithium ion diffusion coefficient, CLi is the concentration of lithium ions in the cathode, and ν is the potential scan rate. The slope of the curve (Ip/ν0.5) represents the lithium ion diffusion rate as n, S, and CLi are unchanged. It can be clearly seen that the S@G/CNT electrode exhibits the lowest lithium ion diffusivity, which mainly arises from the weak lithium polysulphides adsorption and Li2S conversion capability, induced high polysulphides viscosity in the electrolyte or deposition of a thick insulating layer on the electrode. In contrast, the S-VS2@G/CNT, S-CoS2@G/CNT, and S-TiS2@G/CNT electrodes demonstrate much faster diffusion compared to the S@G/CNT electrode and better reaction kinetics than the S-Ni3S2@G/CNT, S-SnS2@G/CNT, and S-

FeS@G/CNT electrodes, indicating that the introduction of M_xS_y hosts enables highly efficient conversion of sulphur redox.

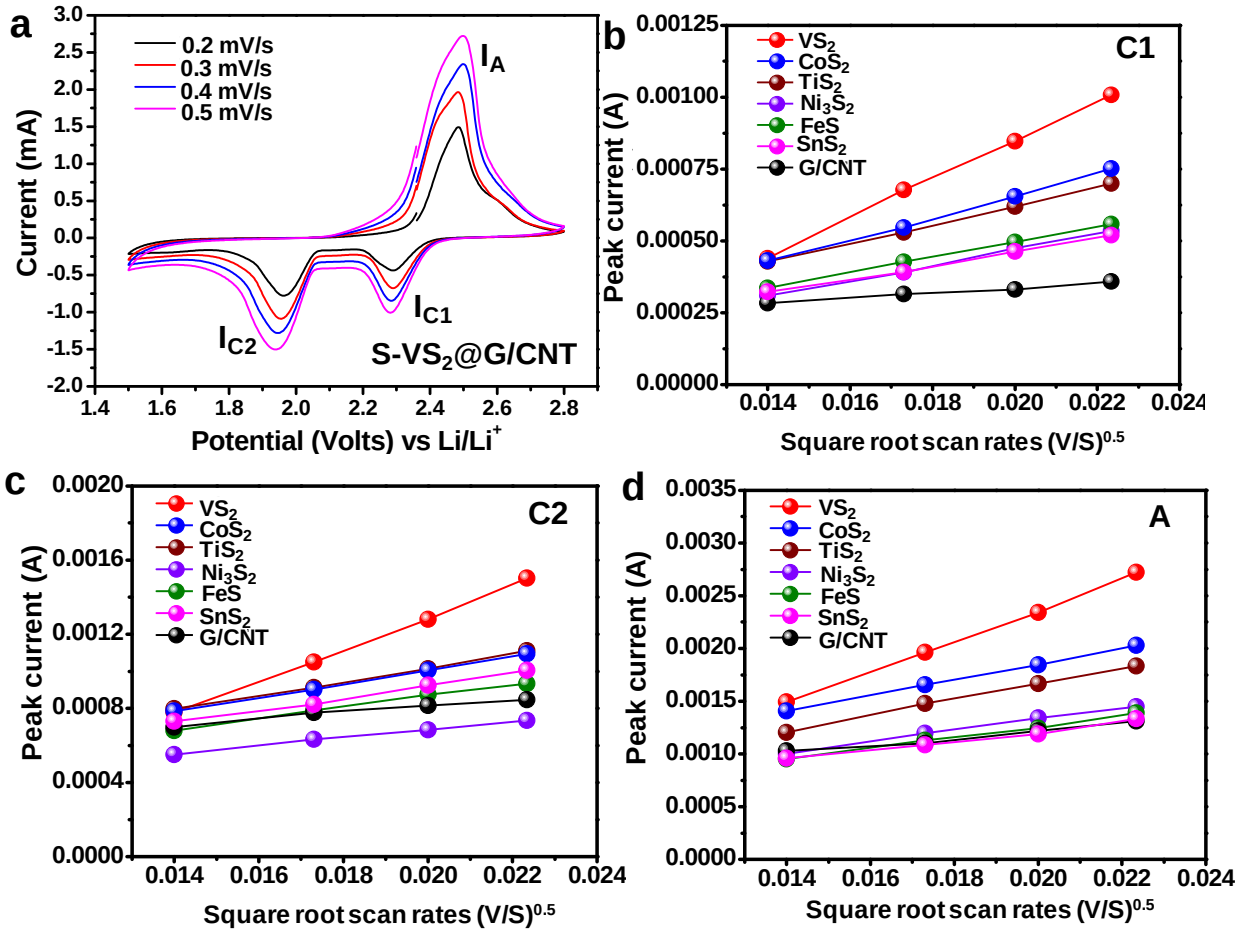

Figure V-289: (a) CV curves of the S-VS_2@G/CNT electrode at various scan rates. Plots of CV peak current for the (b) first cathodic reduction process (IC1: S8→Li_2S_x), (c) second cathodic reduction process (Li_2S_x→Li_2S_2/Li_2S), and (d) anodic oxidation process (Li_2S_2/Li_2S→S8) versus the square root of the scan rates.

Conclusions

In all, in the past one year, we have made great progress in understanding the mechanism of surface adsorption and diffusion of Li_2S_x species on anchoring materials. Adsorption test, microstructure analysis and electrochemical performance evaluation combined with density functional theory (DFT) calculations reveal that better surface diffusion leads to higher deposition efficiency of sulfide species. A comprehensive oxide-selection criteria referring to the strong binding, high surface area and good surface diffusion properties is proposed. Based on our experimental results, our DFT calculation and temperature swing adsorption experiments confirm that the monolayer chemisorption is dominant during the polysulphide capture. The second role of these metal oxides especially some nonconductive oxides is the Li_2S_x transfer station, which transport the Li_2S_x from the poorly conductive oxide surface to high conductive carbon matrix to ensure the full electrochemical conversion. The third role is to induce the controlled growth of Li_2S_x species on the surface instead of random deposition. Because the first role of oxides is adsorption, the binding between the sulphides species and the matrix should be strong, which can both suppress the shuttle effect and enable the full utilization of active materials. Considering that the polysulphide capture is the monolayer chemisorption and the adsorption amount will depend on the surface area of oxides, uniformly distributed oxides nanostructures with high surface area are essential. Although strong binding and high surface area are preconditions, the surface diffusion properties of oxides are also very important, which affect the distribution and structure of lithium sulphides. An optimized balance between lithium polysulphides adsorption and surface

diffusion is favorable for the lithium sulphide species to deposit on the surface of oxides/sulphides and carbon matrix, keep active during the cycling and ensure the final good cycling performance of batteries.

Products

Presentations/Publications/Patents

1. (Plenary) "Nanomaterials Design for Energy Conversion and Storage" 1st International Symposium on Energy Chemistry and Materials", October 29-31, 2015, Fudan University, Shanghai, China.
2. (Plenary) "Electrochemical Nanotechnology: Batteries and Electrocatalysts" International Conference on Innovative Electrochemical Energy Materials and Technologies (EEMT2015), Nanning, China, November 8-11, 2015.
3. (Invited) "Nanomaterials Design of Batteries Guided by *In-Operando* Characterization and Atomistic Simulation", Gordon Research Conference on Batteries, Feb. 21-26, 2016, Ventura, California.

References

1. X. Tao, J. Wang, C. Liu, H. Wang, H. Yao, G. Zheng, Z. W. Seh, Q. Cai, W. Li, G. Zhou, C. Zu, and Y. Cui, "Balancing surface adsorption and diffusion of lithium-polysulfides on nonconductive oxides for lithium-sulfur battery design", Nature Communications , 2016, 7, 11203.
2. G.M. Zhou, H. Tian, Y. Jin, X. Tao, B. Liu, R. Zhang, Z. W. Seh, D. Zhuo, Y. Liu, J. Sun, J. Zhao, C. Zu, D. Wu, Q. Zhang, Y. Cui, " Catalytic oxidation of Li2S on the surface of metal sulphides for Li-S batteries", PNAS, 2016, under revision.

V.H.7. Addressing Internal "Shuttle" Effect: Electrolyte Design and Cathode Morphology Evolution in Li-S Batteries (TAMU)

Perla B. Balbuena, Principal Investigator
Texas A&M University
3122 TAMU
College Station, TX 77843
Phone: 979-845-3375; Fax: 979-845-6446
E-mail: balbuena@tamu.edu

Tien Q. Duong, DOE Program Manager
Advanced Battery Materials Research (BMR)
U.S. Department of Energy
Vehicle Technologies Office
1000 Independence Avenue, SW
Washington, DC 20585
Phone: 202-586-7836
E-mail: Tien.Duong@ee.doe.gov

Start Date: October 1, 2014
End Date: September 30, 2017

Abstract

Objectives

- Elucidate effects of electrolyte chemistry and polysulfide shuttle on the formation of interfacial films at the anode surface.
- Evaluate the effects of the cathode microstructure on overall cell performance and develop strategies for polysulfide retention at the cathode.
- Build and test a cell operating for 500 cycles at efficiency greater than 80%.

Accomplishments

- A joint publication of the team summarized the various efforts in cathode synthesis, electrochemical cell testing, effects of cathode microstructure porosity and loading during discharge on macroscopic transport and electrochemical properties and atomistic characterization and identification of products of discharge reactions. The paper was published in the J. of the Electrochemical Society[1].
- Several new materials were examined computationally to characterize their ability for retention of polysulfides (PS) at the cathode side thus avoiding their migration to the anode side. It was concluded that one of their most important properties is the extent to which the PS species react with the new surfaces. Excessive reactivity was found to be not favorable. Two papers were published in the *Journal of Physical Chemistry C*[2] and *J. of Coordination Chemistry*[3].
- A thorough investigation was done to evaluate the effect of PS migration on the reactivity at the anode side. The most common solvents (ethylene carbonate (EC), dimethyl ether (DME), 1,3 dioxolane (DOL), 1,1,2,2-tetrafluoro-3-(1,1,2,2-tetrafluoroethoxy)-propane (D2) were tested in 1M solutions of LiTFSI and in presence of long-chain polysulfide (PS) species to evaluate their reactivity on the anode surface. Two papers were published in the *J. of Phys. Chem. C*[4] and ACS Applied Materials and Interfaces[5]. More recent work focused on the effects of high salt concentration (4M) and the nature and chemical structure of the salt on their reactivity at the Li metal anode. One paper has been submitted to the *J. of Phys. Chem. C*.
- In collaboration with researchers at PNNL, we have examined and identified the solid-electrolyte interphase (SEI) formed at the anode in presence of long chain PS species. The PNNL experiments

consisted on building a model Li-S cell and using a series of analytical techniques (the main one X-Ray Photolectron Spectroscopy, XPS) to characterize the products of electrolyte decomposition during cycling of the model Li-S cell. AIMD simulation results were used to characterize and identify the XPS peaks. A manuscript is in preparation.

- Sulfur lithiation leads to 80% volume expansion. Therefore, if the cathode porosity is not enough, this may lead to partial pore blockage and increased electrolyte phase transport resistance and cell shut down. A mesoscopic model is used to understand sulfur loading and cathode porosity effects on pore blockage and cell inefficiency. Also it was theoretically predicted that LiCl salt as an electrolyte additive may improve the Li-S cathode performance.

Future Achievements

- Solvation effects play a crucial role on the chemistry of Li/S batteries. We are quantifying these effects in the bulk electrolyte, and at the interfaces. The study includes the effects of solvation on redox couples in solution, effects of lower amounts of solvent on discharge reactions and on parasitic reactions, and on solubility of long-chain PS species.
- It was recently theoretically predicted that LiCl salt as an electrolyte additive may improve the Li-S cathode performance. A mesoscopic model was used in conjunction with first principles calculations to evaluate these effects. Current experimental efforts are conducted to test the predictions.
- Additional experimental efforts demonstrated that a novel autogenic process to synthesize carbon-sulfur composites allows pressurized and vaporized sulfur to homogeneously penetrate the microstructure of the surrounding C substrate allowing greater electrochemical contact of S and C due to homogeneous deposition of vaporized S during the cooling process. Current electrochemical tests are being performed on this new material.

Technical Discussion

Background

This work addresses the chemistry of the Li-sulfur battery investigating interfacial and bulk reactions at both electrode surfaces and at the bulk electrolyte, as well as discerning the effects of structure and chemistry of the cathode on its performance. The team has expertise on developing and applying atomistic modeling methods to investigate the nucleation and growth of the SEI layer on surfaces in contact with an electrolyte solution, as well as on developing and applying mesoscopic models to characterize the effects of electrode microstructural evolution on electrochemical and physical properties. A recently demonstrated ultrasound-mediated1 aqueous synthetic route to produce porous carbon-sulfur electrode in one pot synthesis was initially employed for the synthesis of the C/S composite material. Under ultrasonic irradiation, dil. HCl solution reacted with aqueous sulfur precursor, $Na_2S_2O_3$ in presence of commercially available mesoporous carbon forming water soluble NaCl byproduct yielding nanosized pure S/carbon composite. This process avoids the widely used, less energy efficient ‘melt-down’ approach, which requires sulfur heating that melts on the walls of porous carbon in liquid phase. The novel C/S cathode architecture yielded stable cycling performance and high cycling efficiency with fluorine-based electrolyte.1 For the C/S composite vs Li cell, the coulombic efficiency in the DOL/D2 electrolyte was shown to be greater than 96% for 100 cycles, which is superior to numerous known electrolyte formulations and existing reports.

Introduction

This project provides new information about the chemistry of the composite C/S cathode as a function of its morphology, as well as about the interfacial reactions taking place at the surface of the Li anode in presence of PS species, and the chemical, interfacial, and structural effects on the cell performance and cell life. All of this new information results from a synergetic study involving atomistic and mesoscopic modeling and synthesis and characterization of C/S composites and complete cell and is expected to result in new electrolyte formulations and development of alternative strategies for PS retention at the cathode. Moreover, the final outcome of the project will be the delivery a cell operating for 500 cycles at efficiency greater than 80 %.

Approach

This study focuses on the rational design of the electrolyte chemistry and improved cathode architecture design based on the development of new understanding of the main challenges obtained from first-principles atomistic (Balbuena, TAMU) and mesoscopic modeling (Mukherjee, TAMU) and state of the art synthesis and characterization (Pol, Purdue). Using atomistic methods, we evaluate the role that the insoluble PS species adsorbed on the Li anode have on electrolyte decomposition leading to the formation of a SEI layer at the anode surface. Also, we investigate the reactions at the cathode side and the type of interactions and/or reactions that may be occurring in the bulk electrolyte. Focusing initially in the electrolyte chemistry based on partially fluorinated co-solvents, our analyses will be oriented to determine the reasons for the success or failures of specific chemistries. In addition, a mesoscale modeling approach is employed to study the effect of microstructure evolution due to non-conducting product precipitation in typical cathode carbon mesoporous structures and concomitant impact on electrochemical properties (e.g. electronic/ionic conductivity, lithium transport, impedance response) and performance. The key implications of the mesoscale approach are: discerning the role of cathode morphological changes and elucidating the mechanisms of the relative role that an improved electrolyte design plays on the performance. The combined first-principles and mesoscopic computational approach allows physics-based exploration toward tackling the overall internal shuttle effect. This is complemented with electrolyte synthesis, based on guidelines from computation, and experimental investigations of cell performance. The idea is to identify the reasons behind the current successes and failures of current technologies and develop a better understanding of the microscopic processes in order to design alternative materials and/or processes for the various Li/S battery components.

Results

Overall Summary: Initially carbon microstructures were fabricated from a starch precursor using a novel inexpensive process based on a one-step, reproducible, solid state route. Once the microstructured porous carbon was synthesized, a sonication process was employed to insert nanosize sulfur, thus creating the C/S composite. Ultrasonic microjets were able to *in situ* form nanosize sulfur embedded into the micro and mesoporous carbon structures. The composite material was characterized with SEM and EDS elemental analysis. EDS images showed segregated carbon and sulfur regions (Figure V-290, center). Thermogravimetric (TGA) and X-Ray diffraction further revealed the presence of orthorhombic S. Various DFT analyses showed no evidence of C-S chemical bonding, assuming that crystalline sulfur is contained in porous carbon, and no sulfur rupture was detected even in the presence of surface defects in carbon. On the other hand, AIMD simulations of discharge of model cathodes represented by S_8 rings contained inside C pores in presence of Li ions in the liquid electrolyte indicated the rapid reduction of the S_8 rings and the formation of various anionic S species and lithiated PS (Figure V-290, bottom). Low-coordinated C atoms at the edge of carbon pores played an active role on the reduction of sulfur rings, offering sites for adsorption of S and formation of S-C bonds. An electrochemical cell was built with the newly synthesized C/S material and tested in presence of an electrolyte constituted by 50%DOL, 50%D2 and 1M LiTFSI. At the first cycle the capacity was 780 mAh/g that was reduced to 600 mAh/g at the cycle 20. Overall, there was a 44% capacity loss during the first 100 charge-discharge cycles at a high coulombic efficiency of 97%. A mesoscale model revealed that the microstructural evolution was affected by porosity, pore size distribution, specific surface area, and sulfur loading of the carbon framework.

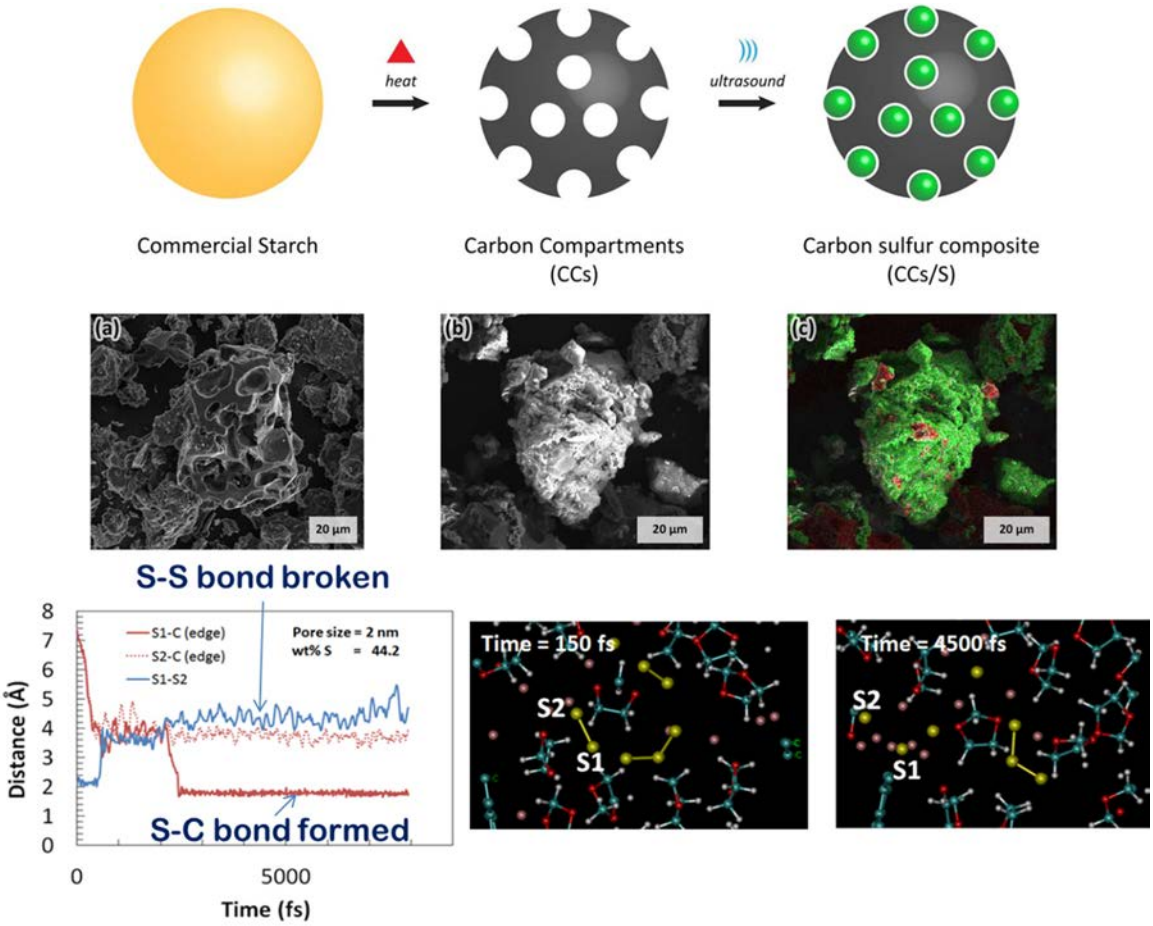

Figure V-290: Schematic describing the ultrasonic synthesis of the CCs/S composite. Top: Graphical representation of the CCs synthesis process and the sonochemical sulfur loading technique. Center: (a) SEM micrograph of a porous CC particle without sulfur. (b) SEM micrograph of the carbon-sulfur composite produced via the sonochemical sulfur deposition process. (c) Elemental mapping of the carbon-sulfur composite by EDS color pixel-mapping. Sulfur is highlighted in green, while carbon is highlighted in red. Bottom: AIMD simulations showing S_8 decomposition in a carbon pore of 2 nm in contact with the electrolyte solution. Total reduction of C and formation of SC bonds are observed. From J. Electrochem. Soc. 163 (5) A730-A741 (2016)

The deposition of insoluble PS species caused an increase of the surface area initially; however, further deposition clogged the pores (Figure V-291). The calculated evolution of impedance as a function of the state of discharge indicated that tortuosity increases dramatically with the increase of the insoluble surface films of Li_2S and possibly Li_2S_2, which was determined as one of the major contributors to capacity limiting effects (Figure V-291).

Given the need of retention of the soluble long chain PS species at the cathode, we examined the possibility of the carbon porosity to trap some of these species. It was found that only the small nanopores (0.75 to 1 nm) would be able to strongly adsorb long chain PS (Figure V-292, left). A pore size distribution (PSD) of the synthesized carbon showed the presence of nanopores (< 2nm). However, once sulfur is added, the PSD changed yielding a broader range of porosities between 4 and 10 nm. Thus, this material did not show good promise with respect to adsorption of PS. The next step towards keeping the small porosity was to sonochemically synthesize nanosulfur encapsulated in graphene sheets. The new material had a higher capacity and a lower 34% capacity loss after 100 cycles. This was attributed to the presence of smaller pores facilitating long PS retention (Figure V-292, right). Additional materials were then tested as possible PS retention agents, including some that are well-known to have good affinity with S, such as MnO_2, Mn-doped graphene, Fe_2O_3 and MnO_2 films exposing their most stable facets (Figure V-293, left).

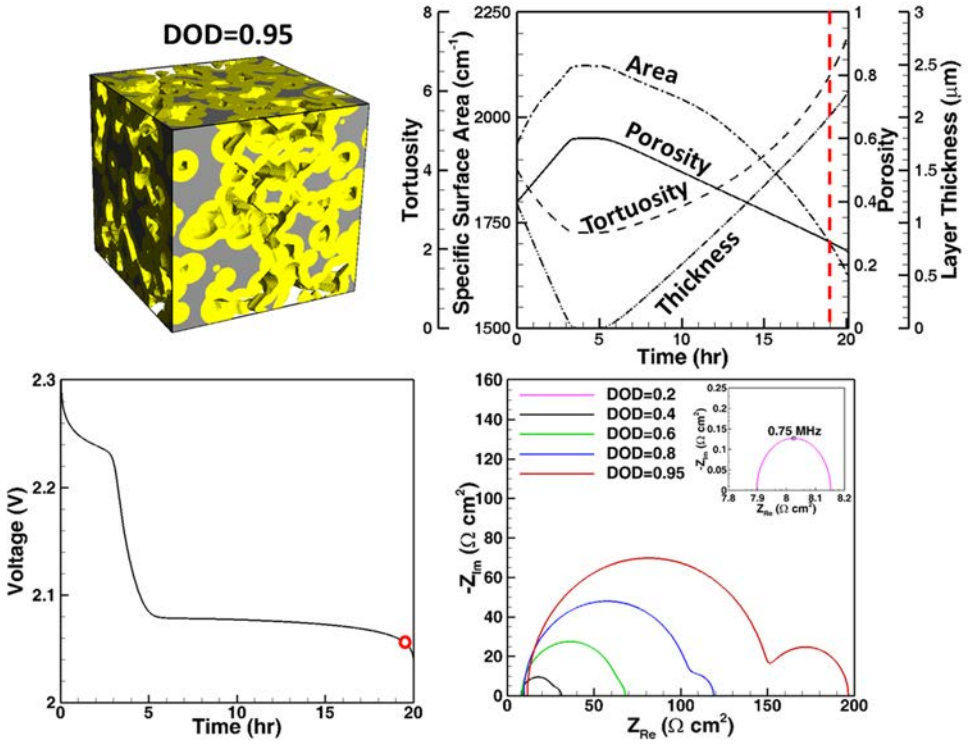

Figure V-291: Top left: Reconstructed microstructure of the composite cathode showing the deposition of Li_2S on the carbon pores during discharge. Top right: Calculated evolution of surface area, porosity, tortuosity, and film thickness. Bottom left: Red circle shows the calculated discharge curve. Bottom right shows the calculated impedance for the different discharge levels

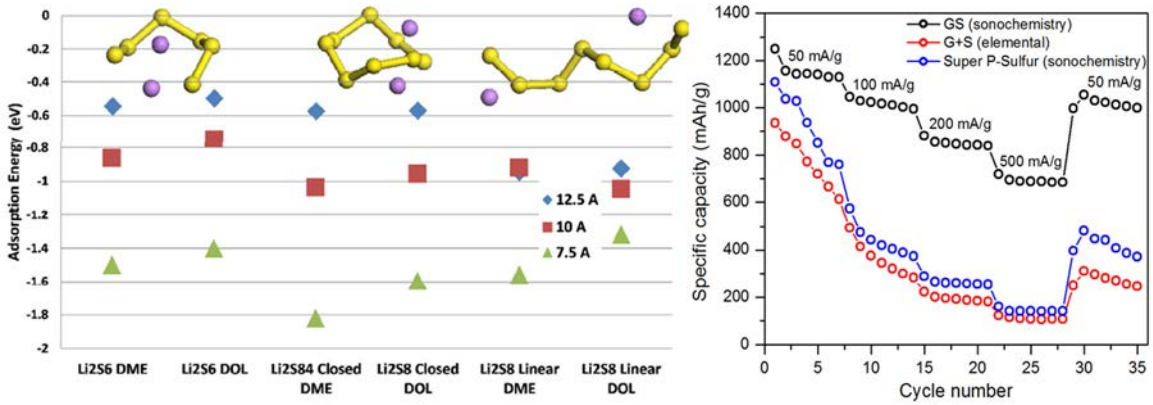

Figure V-292: Left: Adsorption energies of PS species Li_{2S8} (closed and linear) and Li_{2S6} to graphene slit pores of 7.5, 10, and 12.5 Å, respectively, calculated by the DFT-D3 approach. The PS species are dissolved in DME or DOL respectively at their bulk densities at 298 K. From J. Phys. Chem. C, 2016, 120, 4296-4305. Right: High capacity observed in graphene/sulfur composite when prepared sonochemically (black circles). red and blue symbols are other forms of carbon and other synthesis methods for graphene sulfur composites respectively

It is important to realize that both S and Li could be attracted to a substrate; however, if S is attracted preferentially, then the Li ions will be solvated by the solvent molecules and the problem of insolubility will be solved. But the degree of S affinity with the substrate needs to be controlled, because if S is excessively reduced, insoluble PS species are irreversibly adsorbed again leading to capacity failure. Following these ideas, a thin film of Al_2O_3 was deposited using atomic layer deposition techniques over the graphene encapsulated S and tested electrochemically. Interestingly, a much better performance was obtained with only 15% capacity loss after 100 cycles (Figure V-293, right).

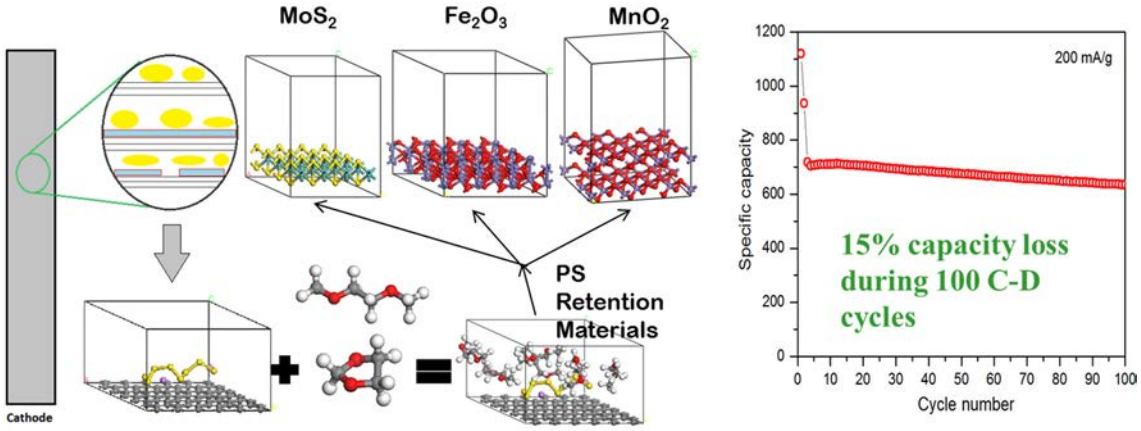

Figure V-293: Left: Schematic of the materials tested computationally as potential retention agents. It was concluded that a moderate surface reactivity is the key for good retention without excessive formation of insoluble short chain PS species. Right: Long-cycle stable cycling capability is observed when thin (1nm) Al_2O_3 coating is implemented using ALD technique

One further issue was detected with our mesoscopic models: the nucleation of insoluble Li_2S and its effect on the overall capacity. The nucleation modes could be heterogeneous (island formation) or homogeneous, depending on the temperature and concentration of anions in solution, the first one is the preferred mode since the second could lead to an insulator film (Figure V-294). A Kinetic Monte Carlo (KMC) model was developed to study the film growth. It was found that the desorption rate depends on the Li_2S/substrate interaction energy and on the diffusion rate of the adsorbate on the substrate. These properties could be engineered with appropriate substrates. For example, silicene although it has a favorable affinity for retention of long chain PS, it forms a homogeneous Li_2S film which is an important factor that limits the cathode capacity.

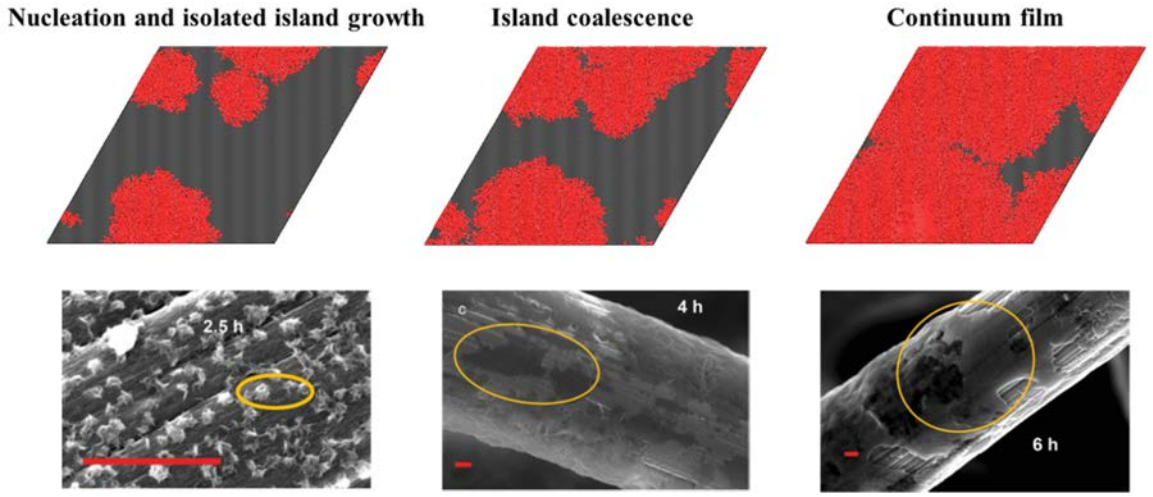

Figure V-294: Top: Prediction of a multiscale Li_2S growth model on a substrate showing the time evolution of the growth. Bottom: Experimental observations taken from Fan et al. Advanced Materials, 27 (2015) 5203

Finally, significant efforts were dedicated to understand the complex decomposition reactions at the anode, the effects of PS migration on the SEI layer formed on the Li metal surface, and the mechanisms of decomposition of additive oxidants such as $LiNO_3$. It was found that the decomposition of the long chain PS species precedes that of $LiNO_3$. Thus Li_2S is formed on the surface first (Figure V-295) and then $LiNO_3$ decomposes; however the oxidation of Li_2S to Li_2SO_3 or Li_2SO_4 that has been suggested by experimental studies is not observed in the AIMD simulations, presumably due to a much slower kinetics for the oxidation stage. However, new simulations were carried out assuming the formation of a Li_2SO_4 film to determine its passivation role. It was found that thicknesses greater than 2 nm are needed to avoid PS decomposition.

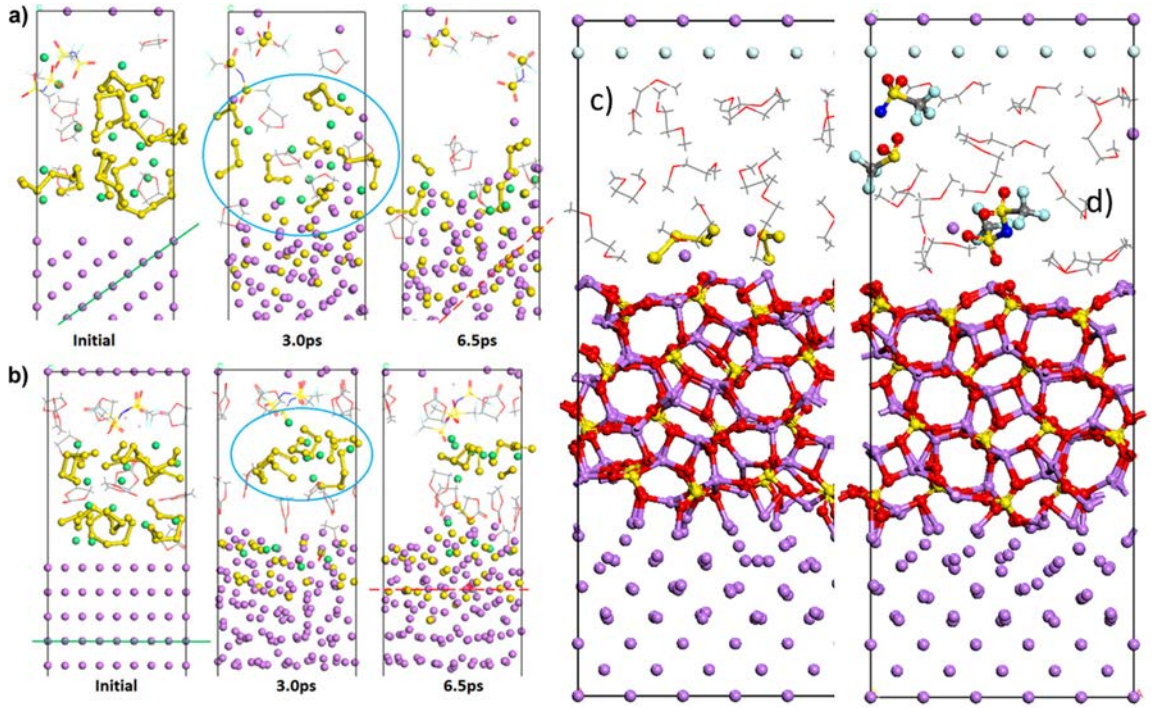

Figure V-295: Snapshots of the dynamic evolution PS decomposition in contact with Li(111) surface slab (a) and Li(110) surface slab (b). Here, purple, green, and yellow spheres represent Li from anode, Li from electrolyte, and S atoms, respectively. The DOL solvent is represented in a line display style where O (red) and C (gray) atoms are shown. Green lines indicate the respective crystallography plane; red dashed lines show the orientation where S atoms tend to accommodate; the blue circle shows where the cluster is localized. From ACS Appl. Mater. Interfaces, 2016, 8, 4700, 4708. c) and d): Effect of a 1.5 nm film of Li_2SO_4 on top of the Li metal anode on the PS and salt decomposition that slow down significantly

Current work focuses on solvation of species at both interfaces: electrolyte/cathode and electrolyte/anode. For the electrolyte/cathode we are investigating the solvation of Li cations and PS anions by different solvents and the effects of the salt anions and cations on such solvation. DFT and AIMD simulations were conducted to characterize the behavior of the electrolyte mixtures, ion association and transport, and reduction of the species as a function of the number of electrons in the system, representing applied voltage. We are interested in examining the case of the limit of very low solvent and the effects on discharge reactions. On the anode side, we have examined the effects of the nature of the salt by analyzing the differences between LiTFSI and LIFSI at 1M and 4M concentrations. The differences in the initial SEI products were established in each case, as well as the solvation and networking effects in the bulk electrolyte and near the surface (Figure V-296).

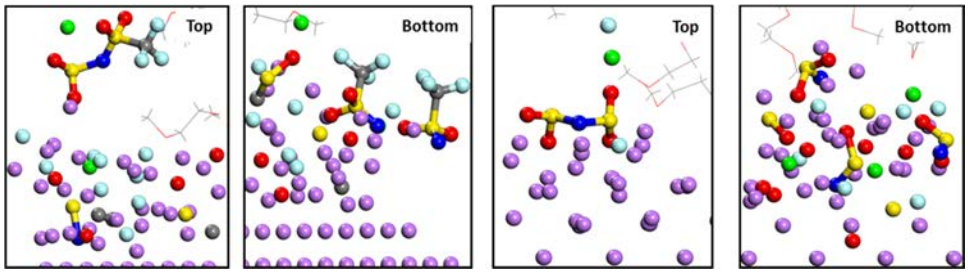

Figure V-296: Snapshots of the dynamic evolution of 4M salt decomposition in contact with a Li(100) surface slab. Purple, green, yellow, light blue, dark blue and red spheres represent Li from the anode, Li from the electrolyte, S, F, N. and O atoms, respectively. The DME solvent is represented in a line display style where O (red) and C (gray) atoms are shown. Left two images correspond to LiTFSI, and the right two images are from LiFSI. The images labeled "top" have initial configurations at the middle of the simulation cell, and in the ones labeled "bottom" the salts were initially in contact with the bottom Li metal surface

It was found that for the case of LiTFSI, large fragments may be found as initial SEI products (such as CF_3SO_2N and $CF_3SO_2NSO_2$ radical anions), as well as CF_3 groups, in addition to LiF, the SEI is dominated by C-containing species. Various solvents (with variable solvation power) and salts were investigated. A manuscript has been submitted for publication. In addition, new simulations are being conducted to characterize the discharge reactions in a larger system containing solid S and C in contact with the electrolyte phase. These simulations have already shown formation of long chain PS species and now the focus is on the first plateau of the discharge curve, where the long chain PS are reduced to shorter chain and on the analysis of the deposition of the insoluble products on the C surfaces. On the other hand the products from LiFSI decomposition contain LiF as a major component, and other short fragments such as NSO_x as additional constituents.

In addition, in collaboration with PNNL researchers, we have completed a novel integrated experimental-computational investigation of the SEI products on a model Li/S battery built at PNNL where *in situ* modern X-Ray Photoelectron Spectroscopy (XPS) and other analytical techniques were used to obtain the spectra corresponding to the F and S species. Such spectra have been fully identified by a combination of experimental XPS and AIMD simulation techniques and reveal the complex nature of the SEI due to the PS decomposition on the metal surface. A manuscript is ready to be submitted.

Further efforts were focused on understanding the effect of sulfur loading and LiCl salt in the Li-S Cathode. Sulfur lithiation leads to 80% volume expansion. Therefore, if the cathode porosity is not enough, this may lead to partial pore blockage and increased electrolyte phase transport resistance and cell shut down. A mesoscopic model was used to understand sulfur loading and cathode porosity effects on pore blockage and cell inefficiency. Also it was theoretically predicted that LiCl salt as an electrolyte additive may improve the Li-S cathode performance. First-principles simulations demonstrated that the negatively charged Li vacancy is the major charge carrier in solid Li_2S precipitation. The Cl^- ion can be incorporated into Li_2S during discharge, which can increase the concentration of negatively charged Li vacancies, which leads to a significant decrease in electrical resistivity. The density of states of Cl^--incorporated Li_2S illustrates that the valence bands of the Cl^--incorporated are not completely occupied. Hence, the hole polaron can also serve as a charge carrier when the negatively charged Li vacancies are exhausted out. Currently these effects are tested experimentally (Figure V-297).

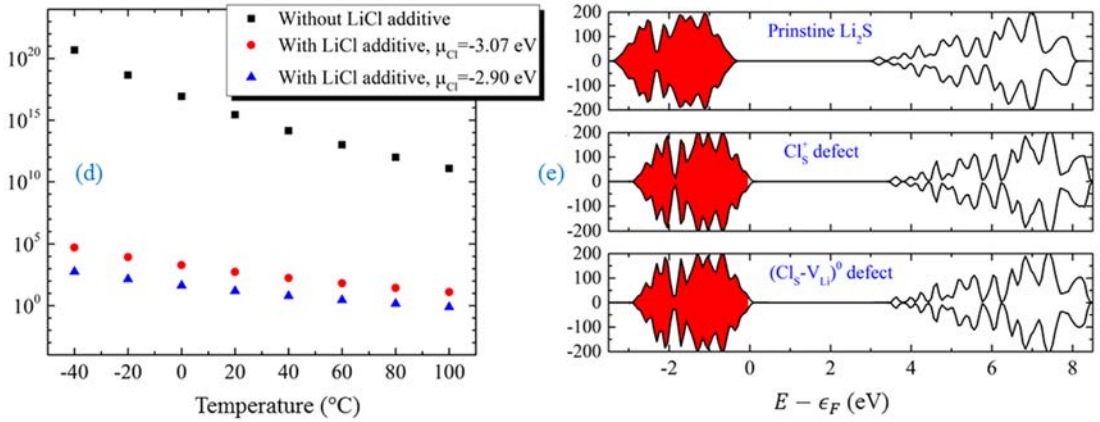

Figure V-297: Left: Cl^- incorporated into Li_2S has much smaller electrical resistivity than pristine Li_2S. Right: Density of states of pristine Li_2S and Cl^--incorporated Li_2S

A novel autogenic process to synthesize carbon-sulfur composites was demonstrated which allows pressurized and vaporized sulfur to homogeneously penetrate the microstructure of the surrounding C substrate allowing greater electrochemical contact of S and C due to homogeneous deposition of vaporized S during the cooling process. The autogenic loading of S is sensitive to the heating profile, that is, the time allowed for phase transformation between melting, vaporization, and deposition. Two heating profiles were used: (1) melting-focused, and (2) vaporizing focused. The difference in the two profiles was carried out to determine the effect of vaporization vs. melting time for sulfur penetration of the carbon matrix. Electrochemical experiments are being carried out to test the new composites.

Conclusions

An integrated theoretical-experimental approach has led to a successful evolution of new cathode materials with improved capacities evaluated after 100 cycles. DFT analysis determined that the carbon nanoporosity may be an important factor for PS retention. Therefore the initial porous carbon/S composite was replaced by a graphene encapsulated sulfur that when prepared sonochemically led to a better capacity retention. In addition, to mitigate the PS shuttle effect, various alternative materials were tested computationally. It was found that materials with moderate reactivities that do not yield significant amounts of insoluble PS species are the most promising for long chain PS retention at the cathode. Among them MnO_2 was found to meet those requirements. However, another important aspect is the deposition of the new material on the cathode surface. To achieve a uniform deposition, a thin film of Al_2O_3 was coated on the graphene encapsulated sulfur prepared sonochemically. This new composite improved further the capacity to a 15% of capacity loss after 100 cycles. Other issues such as the deposition of Li_2S were carefully investigated with multiscale modeling. It was found that the mode of deposition is another important variable which depends on the adhesion properties of the new material to the substrate. More work is needed in this aspect. Also, first-principles simulations demonstrated that the negatively charged Li vacancy is the major charge carrier in solid Li_2S precipitation. The addition of LiCl salt as an electrolyte additive was shown to improve the Li-S cathode performance, and is currently tested experimentally. Finally, better interactions between C and S are expected from a new synthesis method due to homogeneous deposition of vaporized S in a carbon matrix during the cooling process.

Products

Presentations/Publications/Patents

1. Z. Liu, D. Hubble, P. B. Balbuena, and P. P. Mukherjee, "Adsorption of Insoluble Polysulfides Li_2Sx (x = 1, 2) on Li_2S Surfaces," Phys. Chem. Chem. Phys., 17, 9032-9039, (2015).
2. Luis E. Camacho-Forero, Taylor W. Smith, Samuel Bertolini, and Perla B. Balbuena, "Reactivity at the Lithium-Metal Anode Surface of Lithium-Sulfur Batteries," J. Phys. Chem. C, 119 (48) 26828-26839 (2015).
3. C. S.J. Tsai, A. D. Dysart, J. H. Beltz, V. G. Pol, "Identification and Mitigation of Generated Solid By-Products during Advanced Electrode Materials Processing,", Environm. Sci. Technol., 50 (5), 2627-2634, (2016).
4. Arthur A. Dysart, Juan C. Burgos, Aashutosh Mistry, Chien-Fan Chen, Zhixiao Liu, Perla B. Balbuena, Partha P. Mukherjee, Vilas G. Pol, "Towards Next Generation Lithium-Sulfur Batteries: Non-Conventional Carbon Compartments/Sulfur Electrodes and Multi-scale Analysis," J. Electrochem. Soc., 163, 5, A730-741, (2016).
5. Zhixiao Liu, Samuel Bertolini, Partha Mukherjee, and Perla B. Balbuena, "Li_2S Film Formation on Lithium Anode Surface of Li-S batteries," ACS Appl. Mat. & Interfaces, 8, (7), 4700-4708, (2016).
6. Ethan Kamphaus and Perla B. Balbuena, "Long-Chain Polysulfide Retention at the Cathode of Li-S Batteries," J. Phys. Chem. C, 120 (8), 4296-4305, (2016).
7. Zhixiao Liu, Perla B. Balbuena, and Partha P. Mukherjee, "Evaluating Silicene as a Potential Cathode Host to Immobilize Polysulfides in Lithium-Sulfur Batteries," J. Coord. Chem., 69, (11-13), 2090-2105, (2016).
8. P. Barai, A. Mistry, and P. P. Mukherjee, "Poromechanical Effect in the Lithium-Sulfur Battery Cathode," Extreme Mechanics Letters, doi:10.1016/j.eml.2016.05.007 (2016).
9. S-M. Hong, E. Jang, A. D. Dysart, V. G. Pol, K. B. Lee, "CO_2 Capture in the Sustainable Wheat-Derived Activated Microporous Carbon Compartments", Scientific Reports, 2016, 6, 34590.

References

1. Dysart, A. D.; Burgos, J. C.; Mistry, A.; Chen, C. F.; Liu, Z. X.; Hong, C. N.; Balbuena, P. B.; Mukherjee, P. P.; Pol, V. G. Towards Next Generation Lithium-Sulfur Batteries: Non-Conventional Carbon Compartments/Sulfur Electrodes and Multi-Scale Analysis. Journal of the Electrochemical Society 2016, 163, A730-A741.

2. Kamphaus, E. P.; Balbuena, P. B. Long-Chain Polysulfide Retention at the Cathode of Li-S Batteries. J. Phys. Chem. C 2016, 120, 4296-4305.
3. Liu, Z. X.; Balbuena, P. B.; Mukherjee, P. P. Evaluating silicene as a potential cathode host to immobilize polysulfides in lithium-sulfur batteries. J. Coord. Chem. 2016, 69, 2090-2105.
4. Camacho-Forero, L. E.; Smith, T. W.; Bertolini, S.; Balbuena, P. B. Reactivity at the Lithium-Metal Anode Surface of Lithium-Sulfur Batteries. J. Phys. Chem. C 2015, 119, 26828-26839.
5. Liu, Z.; Bertolini, S.; Mukherjee, P. P.; Balbuena, P. B. Li_2S Film Formation on Lithium Anode Surface of Li-S batteries. ACS Appl. Mater. & Interfaces 2016, 8, 4700-4708.

V.H.8. Mechanistic Investigation for the Rechargeable Li-Sulfur Batteries (U of Wisconsin)

Deyang Qu, Principal Investigator
University of Wisconsin Milwaukee
3200 N Cramer Street
Milwaukee, WI, 53211
Phone: 414-229-3716; Fax: 414-229-5191
E-mail: qud@uwm.edu

Xiao-Qing Yang, Co-Principal Investigator
Brookhaven National Laboratory
Chemistry Department
Bldg. 555
Upton, NY 11973
Phone: 631-344-3663; Fax: 631-344-5815
E-mail: xyang@bnl.gov

Tien Q. Duong, DOE Program Manager
Advanced Battery Materials Research (BMR)
U.S. Department of Energy
Vehicle Technologies Office
1000 Independence Avenue, SW
Washington, DC 20585
Phone: 202-586-7836
E-mail: Tien.Duong@ee.doe.gov

Start Date: September 1, 2015
End Date: August 30, 2016

Abstract

Objectives

- Development of a reliable analytical method for the quantitative and qualitative determination of dissolved elemental sulfur and polysulfide ions in non-aqueous electrolyte, based on High Performance Liquid Chromatography (HPLC)/Mass Spectroscopy (MS).
- Fundamental research on the mechanism of sulfur cathode redox reaction in Li-S batteries.
  - To establish *in situ* and *ex situ* electrochemical-HPLC/MS/UV methods.
  - To investigate the distribution of dissolved polysulfide ions during the discharge and recharge of a Li-S battery.
  - To investigate the relationship between the diffusivity of the polysulfide ions and the physical / chemical structure of the porous sulfur cathode.
- Investigation of the chemical reaction and equilibrium of dissolved elemental sulfur and polysulfide ions.
  - To search for the electrolyte which is adequate for Li-S batteries.
  - To search for the additives which can form a stable SEI layer on Li anode which can prevent chemical reaction between dissolved sulfur compounds.

Accomplishments

- Several HPLC/MS/UV essays have been developed and tested for the reliable and accurate analysis of dissolved elemental sulfur and polysulfide ions in the Li-S electrolyte. We believe it is the first (maybe only) method for the accurate determination of polysulfide ions in Li-S electrolytes. It was

also proven that the polysulfide itself CANNOT be separated by HPLC and detected by MS, they much be derivatized first.

- The solubility of sulfur in various non-aqueous electrolytes has been determined. The solubility of sulfur was found not only related to the solvent, but also related to the concentration of salt.
- An *in situ* electrochemical-HPLC experiment provided firm evidence that the polysulfide ions formed during the very initial electron transfer were shorter chain polysulfide ions, not S_8^{2-} as reported in the literature.

Future Achievements

- Understanding the mechanism of the sulfur redox reaction especially chemical equilibriums among dissolved polysulfide ions during the courses of discharge and recharge of Li-S batteries
- Development of *in situ* electrochemical-microscopic cell to investigate the impact of polysulfide ions on Li anode.
- Mitigation of the "shuttle effect"

Technical Discussion

Background

Great excitement has arisen in the field of lithium-sulfur (Li-S) batteries recently. Li-S is considered to be one of the most promising battery chemistries beyond state-of-art lithium-ion batteries. This can be attributed to its high energy density of 2600 Wh/Kg, the natural abundance of sulfur, and its nature of being environmentally benign [1]. However, the redox reaction of sulfur is considered to be one of the most complex electrochemical reactions, involving the formation of multiple polysulfide ions from multi-step, electron-transfer, homogenous and heterogeneous chemical reactions. The polysulfide ions are generally soluble in the electrolyte. When the octasulfur gains electrons during the reduction, the resulting linear polysulfide ions become soluble and diffuse away from the positive electrode. The soluble long-chain polysulfide ions could react with short-chain lithium polysulfide producing medium-chain polysulfide ions, causing the so-called "shuttle effect", or react with the metallic Li anode forming insoluble Li_2S_2 or Li_2S, resulting in premature passivation of the Li anode, this effect can greatly accelerate the self-discharge and loss of cyclability. [2,3]. Detailed mechanisms for the sulfur redox reaction in non-aqueous electrolytes are still not well understood, partially due to the lack of a reliable analytical method to qualitatively separate and analyze the various soluble polysulfide species formed during the reduction and oxidation processes even with decades of genuine efforts. The quantitative analysis of the soluble polysulfide ions at various stages of the electrochemical charge and discharge of a sulfur cathode play a critical role in understanding the fundamental mechanism of the sulfur redox reaction and the improvement in the performance of a Li-S battery.

Initially, UV-Visible spectroscopy was used as the major instrument to investigate the soluble polysulfide ions in aprotic solvents, since polysulfide solutions are generally colored. It was believed that the polysulfides of different types give different color [4-6]. Electro-analytical methods, specifically cyclic voltammetry, were also used in an attempt to identify the polysulfide ions [7]. The mechanisms for the sulfur redox reactions as well as the chemical equilibriums among the polysulfide ions were also studied by means of spectro-electrochemical methods [8-10]. However the results from UV-Vis spectrometry and cyclic voltammetry provided limited information about the polysulfide species due to the overlap of absorbance and redox peaks for different polysulfide species, respectively. For example, broad and overlap absorption bands were demonstrated in UV-Vis spectra, first derivative of the UV-Vis spectra was used to identify the number and position of the bands. Therefore, isolation of a population of single polysulfide chain lengths was proven to be a challenge using UV-Vis [11].

Most recently, *in situ* Raman spectroscopy was used to investigate the polysulfides formed during the operation of a Li-S cell [12]. However, most of the Raman data for polysulfide were obtained from crystalline solids, which is not helpful to interpret the Raman spectra of solvated polysulfide ions. Therefore, theoretically calculated Raman spectra have to be used to assign the polysulfide ions to the experimental peaks. Abruna et al

reported on the use of X-ray absorption near edge spectroscopy (XANES) to probe the polysulfide, however only the average oxidation state of sulfur could be estimated [13].

The main issue for the instrumental analysis of polysulfides is that it is almost impossible to prepare polysulfide anions with a precisely defined chain length in solution for reference measurements, since disproportionation and redox reactions result in distribution of polysulfide anions with various chain length. Due to the different chain length and molar mass of different polysulfide species, the powerful and widely used analytical method, chromatography tandem with mass spectroscopy (MS), could be potentially used to analyze the polysulfide species, because no reference of pure polysulfides are needed for the quantitative and qualitative measurement.

Introduction

Genuine efforts were made to develop an analytical method for the reliable qualitative analysis of polysulfide ions in non-aqueous electrolyte during the charge and discharge of a Li-S battery using reverse phase high performance liquid chromatography (RP-HPLC) and electrospray ionization mass spectroscopy (ESI/MS) [14]. However, the analysis of polysulfide species by RP-HPLC/ESI-MS without a specially developed assay is questionable. Reverse phase (RP) chromatography is a typical partition chromatography, in which the stationary phase is nonpolar and mobile phase is relatively polar. The C_{18} column used in reference 4 was a highly nonpolar, bonded-phase column, in which silica coated with siloxane and n-octyldecyl groups was used as the stationary phase; methanol was used as the mobile phase. The retention mechanism for partition chromatography is based on the intermolecular interaction among the mobile phase, analytes and stationary phase of the column. Most of the applications for RP chromatography are for the separation nonionic, polar compounds of low to moderate molecular weight [15]. Special methods, e.g. derivatization and ion paring, need to be developed for the separation of small inorganic ionic analytes. Polysulfide anions are particularly difficult to be separated, even with electrophoretic and ion paring chromatography [16,17].

In conclusion, caution has to be taken to qualitatively analyze sulfur and polysulfide ions in non-aqueous electrolytes. Without special treatments, polysulfide ions cannot be separated in a RP column due to the lack of a retention mechanism with the non-polar stationary phase in a RP column. Neither S_8 nor polysulfide ions can be ionized by ESI, and therefore cannot be analyzed by ESI/MS. The eluents around 2 min and 6 min retention time were DME and S_8, respectively. Polysulfide ions can be neither separated nor analyzed by RP-HPLC ESI/MS. Further work is clearly needed in order to develop a feasible assay for the analysis of polysulfide ions produced during the operation of a Li-S battery.

Approach

The research was to understand the fundamental mechanism of the sulfur redox reaction. Through the development of unique HPLC-MS essay, we developed a tool for the qualitative and quantitative determination of both dissolved sulfur and polysulfide ions. A combination of High Performance Liquid Chromatography (HPLC)/Mass Spectroscopy (MS) together with *in situ* electrochemical measurements in a specially designed cell. The electrochemically formed dissolved polysulfide ions can be separated (by HPLC) and determined (by MS).

Results

1. Quantitative and Qualitative Determination of the Dissolved Elemental Sulfur

A fast and reliable analytical method was developed for the quantitative determination of dissolved elemental sulfur in non-aqueous electrolytes for Li-S batteries. By using HPLC with a UV detector, the solubility of S in 12 different pure solvents and in 22 different electrolytes was determined. It was found that the solubility of elemental sulfur is dependent on the Lewis basicity, the polarity of solvents and the salt concentration in the electrolytes. In addition, the S content in the electrolyte recovered from a discharged Li-S battery was successfully determined by the proposed HPLC/UV method. Thus, the feasibility of the method to the online analysis for a Li-S battery is demonstrated.

HPLC separation can be used for elemental sulfur in electrolyte of a Li-S battery. A systematic quantification of elemental S in the common organic solvents and electrolytes of interest to Li-S batteries. Figure V-298 demonstrates that the elemental sulfur can be effectively separated and detected using commercial HPLC columns. The elemental sulfur had the retention time of 4.2 min (for Zorbax 300SB) and 4.8 min (for Xterra MS). The wide linear range of the results indicated the reliability and sensitivity of the method.

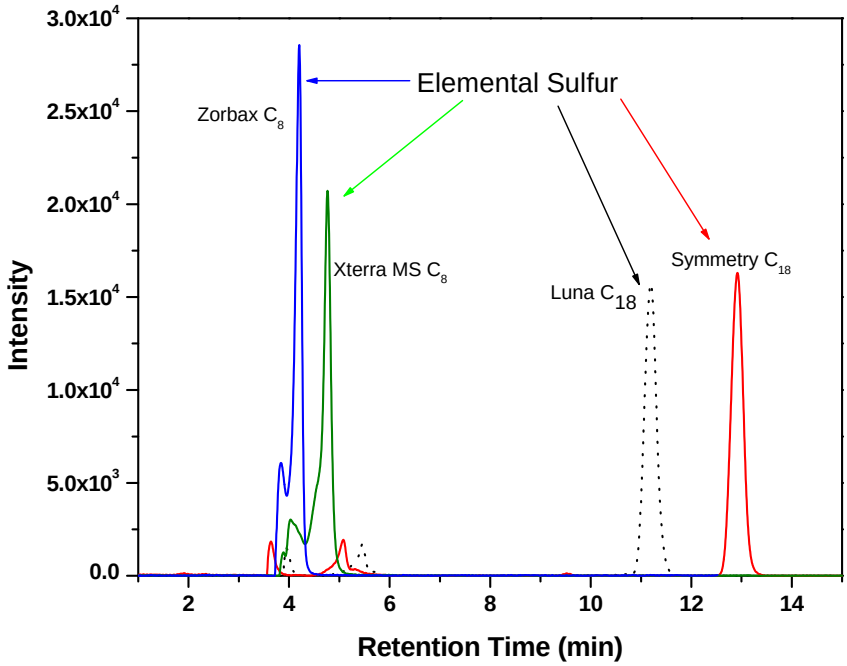

Figure V-298: The chromatograms of elemental sulfur on different reversed phase HPLC columns
D. Zheng, X.R. Zhang, C. Li, M. E. McKinnon, R.G. Sadok, Deyu Qu, X.Q. Yang, D.Y. Qu, J. Electrochem. Soc. 162(2015)A203-206.

The solubility of elemental sulfur in different organic and inorganic media reported in the literature e.g. in reference 19, had limited usefulness for Li-S batteries since most of the solvents were inadequate for Li-S electrolyte. The solubility was mainly determined by sequentially adding a solvent until the visual disappearance of solid S in the corresponding solution. Large error would be introduced.

The solubility of S in various solvents and the corresponding electrolytes with 0.1 M and 1 M LiTFSi determined by the HPLC method is summarized in Table V-12, while the solubility of S in DMSO with 1 M of different salts is tabulated in Table V-13. Based on the results tabulated in Table V-12 and Table V-13, two observations can be found. First, in a pure organic solvent, the solubility of S is dependent on the polarity and the Lewis basicity of the solvent. The solubility of a non-polar S molecule should be higher in a non-polar solvent than that in a polar solvent, for example, the solubility of S in hexane is an order of magnitude higher than that in acetonitrile. The relative polarities of hexane and AN are 0.009 and 0.460, respectively [20]. The S is also more soluble in a solvent with high Lewis basicity, for example, the solubility of S in pyridine is about 5 times over that in DME. This is in agreement with the Lewis basicity ($SbCl_5$ affinity) of pyridine (142.3kJ mol^{-1}) and DME (83.68 mol^{-1}) [21], despite the similar relative polarity of the two solvents (0.231 for DME, and 0.302 for pyridine). Secondly, in an electrolyte solution, the solubility of S is greatly influenced by the existence of supporting salts. As the concentration of the salt in an electrolyte increases, the solubility of S decreases compared to the solubility in pure solvent. As demonstrated in Table V-12, the solubility of S decreases on average 12.5% and 53.4% in the 0.1 M and 1.0 M LiTFSi electrolytes from their corresponding solvents, respectively. Table V-13 demonstrated that the solubility of S is also influenced with the type of the salt. Noticeable differences in the solubility of S in DMSO with different salts at the same molar concentration can be observed in Table V-14.

Table V-12: Solubility of Elemental S in Pure Solvents and in Corresponding Electrolytes with Different LiTFSi Concentrations Obtained through HPLC/UV Method

Solvent	Solubility mM, pure solvent	Solubility (mM), 0.1M electrolyte	Solubility (mM), in 1.0M electrolyte
AN	0.610	0.596	0.390
PY	48.046	28.005	15.909
DMF	5.944	5.895	2.603
PC	1.318	1.255	0.633
GBL	3.888	3.366	1.606
DGME	10.259	9.511	3.875
DME	9.957	8.963	3.994
DMSO	3.936	3.845	1.933
BMPTFSi	0.349	0.245	0.216

Table V-13: Solubility of Elemental S in DMSO with 1M of Different Salts Obtained through HPLC/UV Method

Salt	Solubility (mM)
LiTFSi	1.933
$LiClO_4$	2.416
$LiBF_4$	1.768
$LiCF_3SO_3$	2.161
$TEABF_4$	2.170

2. Qualitative, Qualitative and Complete Determination of the All Dissolved Polysulfide Ions

Polysulfide species in an aprotic solution can be analyzed by directly introducing into the ESI/MS. However, analysis of the polysulfide species in the electrolyte of Li-S batteries by direct injection (-) ESI/MS is hindered by the high concentration of the supporting salt LiTFSi. The major limitation for ESI/MS is that the ionization process is susceptible to ion suppression, which mainly results from the competition between matrix components and the analytes. In order to detect polysulfides in the electrolyte of a Li-S battery with ESI/MS, they have to be separated from the high concentration of TFSi anions. However, ionic polysulfide species cannot be simply separated by RP-HPLC system due to the lack of retention mechanism.

The derivatization reaction of polysulfide ions was developed and an example is shown in the following equation. By bonding with two 4-(dimethylamino) benzoyl groups, the polysulfide ions were derivatized into covalent compounds which have retention in a RP-HPLC column. Figure V-299 clearly demonstrates that the effective separation of polysulfide species derivatized by 4-(dimethylamino) benzoyl chloride was successfully achieved.

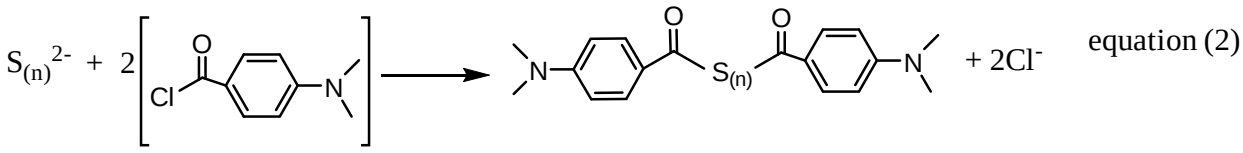

equation (2)

4-(dimethylamino) benzoyl chloride

As shown in the above equation, the derivatization of polysulfide species introduces the 4-(dimethylamino) benzoyl functional group. The basic tertiary amine is a good proton acceptor and thus the derivatized polysulfide species can be efficiently ionized during ESI process. The left bottom graph in Figure V-299 shows the (+)ESI/MS spectra of $[RS_3R+H]+$ as an example, in which not only the expected m/z ratio but also the unique isotopic distribution from ^{32}S and ^{34}S were observed.

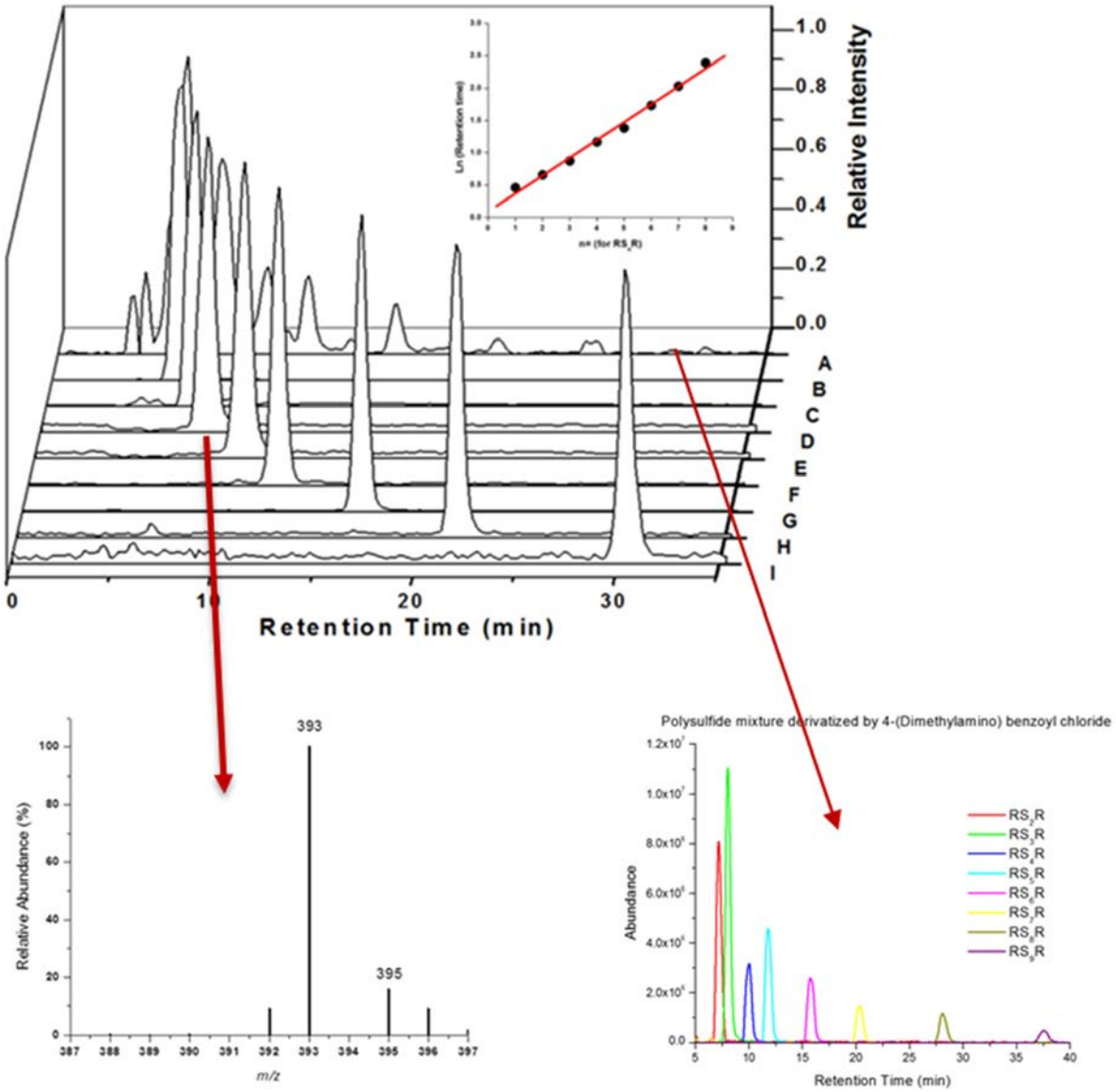

Figure V-299: The chromatograms of derivatized solution A (Na_2S and S_8 in acetonitrile, molar ratio of Na_2S:S is 1:3). A=total ion current chromatogram; B= ion chromatogram for m/z 329; C= ion chromatogram for m/z 361; D= ion chromatogram for m/z 393; E= ion chromatogram for m/z 425; F= ion chromatogram for m/z 457; G= ion chromatogram for m/z 489; H= ion chromatogram for m/z 521; I= ion chromatogram for m/z 553. Inset: The dependencies of the retention time on polysulfide chain length for the derivatized RS_nR (top graph); The ESI/MS spectrum of protonated derivatized polysulfide $[RS_3R+H]+$ (left bottom); Enlargement of curve A (full spectrum) in the top graph (right bottom)

D. Zheng, Deyu Qu, X.Q. Yang, X. Q. Yu, H.S. Lee, D.Y. Qu,Adv. Energy Mater.5(2015)1401888

Figure V-300 shows The RP-HPLC ESI/MS analysis for the electrolyte recovered from the discharged Li-S cell. The derivatized polysulfides in the electrolyte with high concentration LiTFSi were clearly separated in the RP HPLC column and effectively detected by ESI/MS. It's also noticeable in Figure V-300 that there are some doublet peaks in chromatograms for the derivatized polysulfide species with long sulfur chain length. This phenomenon is due to the so-called "injection solvent effect", which occurs when an analyte is more soluble in the solvent in the injected sample than the mobile phase, the chromatographic peak could be distorted resulting peak splitting or broadening.

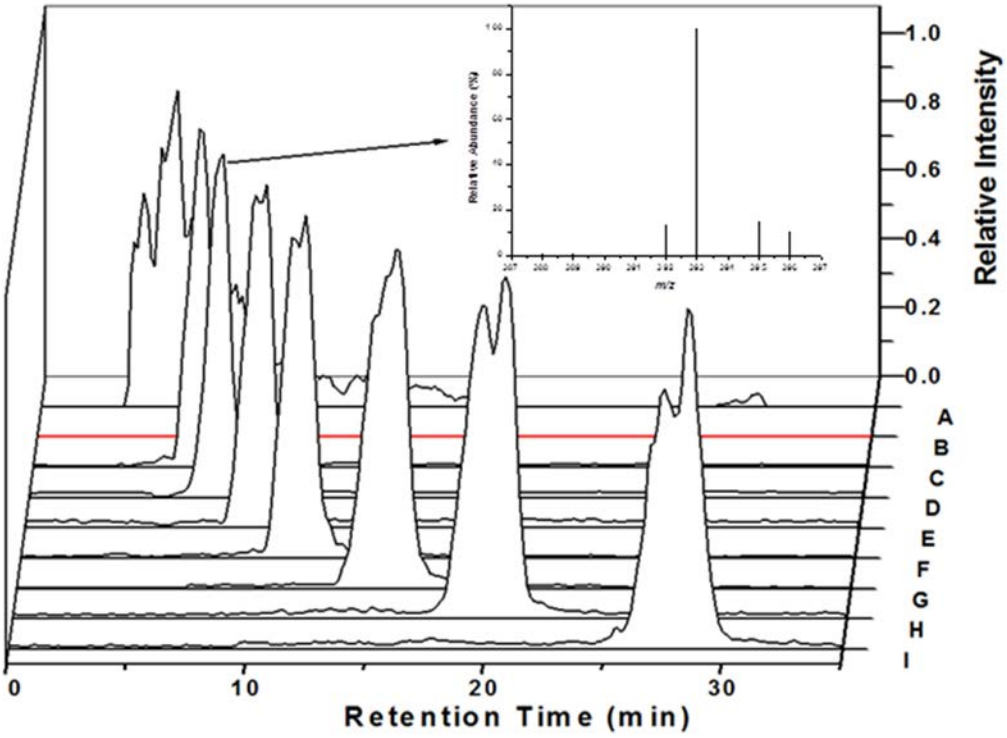

Figure V-300: The chromatograms of derivatized recovered electrolyte from discharged Li-S battery. A=total ion current chromatogram; B= ion chromatogram for m/z 329(not observed); C= ion chromatogram for m/z 361; D= ion chromatogram for m/z 393; E= ion chromatogram for m/z 425; F= ion chromatogram for m/z 457; G= ion chromatogram for m/z 489; H= ion chromatogram for m/z 521; I= ion chromatogram for m/z 553. Inset: The ESI/MS spectra of protonated derivatized polysulfide $[RS_3R+H]^+$

In conclusion, by using a novel derivatization reagent with polar and basic functional groups, the polysulfide species in an organic electrolyte containing high concentration of salt can be successfully separated and analyzed by the RP-HPLC ESI/MS. For the first time, the relative distribution of polysulfide species in such electrolyte was quantitatively and reliably determined. The HPLC ESI/MS assay will provide a reliable tool for the analysis of polysulfide species in the Li-S battery, which is critical for the investigation of the sulfur redox mechanism.

3. The First Electrochemically Formed Polysulfide Ions - *in situ* and *ex situ* Electrochemcial HPLC/MS Experiment

The polysulfide ions formed during the first reduction wave of sulfur in Li-S battery were determined through both *in situ* and *ex situ* derivatization of polysulfides. By comparing the cyclic voltammetric results with and without the derivatization reagent (methyl triflate) as well as the *in situ* and *ex situ* derivatization results under potentiostatic condition, it was found that the major polysulfide ions formed at the first reduction wave of elemental sulfur were the S_4^{2-} and S_5^{2-} species, while the widely accepted reduction products of S_8^{2-} and S_6^{2-} for the first reduction wave were in low abundance.

The fast kinetics of the subsequent complicated disproportionation and chemical reactions of polysulfides in the electrolyte could be the limitation to the studies of the electrochemical reduction mechanism of sulfur, since the electrochemically generated polysulfide ions could become disproportionated during discharge and during the sampling process of *ex situ* derivatization. Therefore, the *ex situ* derivatization method may not be able to differentiate the polysulfide ions formed electrochemically from those formed from the subsequent chemical processes.

We developed a unique *in situ* derivatization method to alleviate the influence of the subsequent rapid chemical reactions of the electrochemically produced polysulfide species. The polysulfides were derivatized as soon as they formed on the electrode, before having a chance to disproportionate or become reacted. The derivatization reactions were faster than the potential disproportionation reactions and the chemical reactions between the polysulfide ions themselves and with elemental sulfur.

As shown in Figure V-301, Curve 1 shows the cyclic voltammogram of 20 mM methyl triflate in LiTFSi/DME solution. No redox peaks can be observed in curve 1. Methyl triflate is electrochemically stable within the potential range. Curves 2 and 3 show cyclic voltammograms of catholyte A, which contained polysulfide ions, after derivatization with methyl triflate and catholyte A alone, respectively. The redox peaks in curve 3 demonstrate that the polysulfide ions in catholyte A before derivatization can either be reduced or oxidized. After all the polysulfide ions in catholyte A have been derivatized by methyl triflate, there are no signs of redox reactions (curve 2). The disappearance of redox peaks of the polysulfide ions reveals that the derivatized polysulfide ions were inert to electrochemical redox reactions. Any polysulfides produced electrochemically can be captured by methyl triflate and the derivatized polysulfide ions are immune to both chemical and electrochemical reactions.

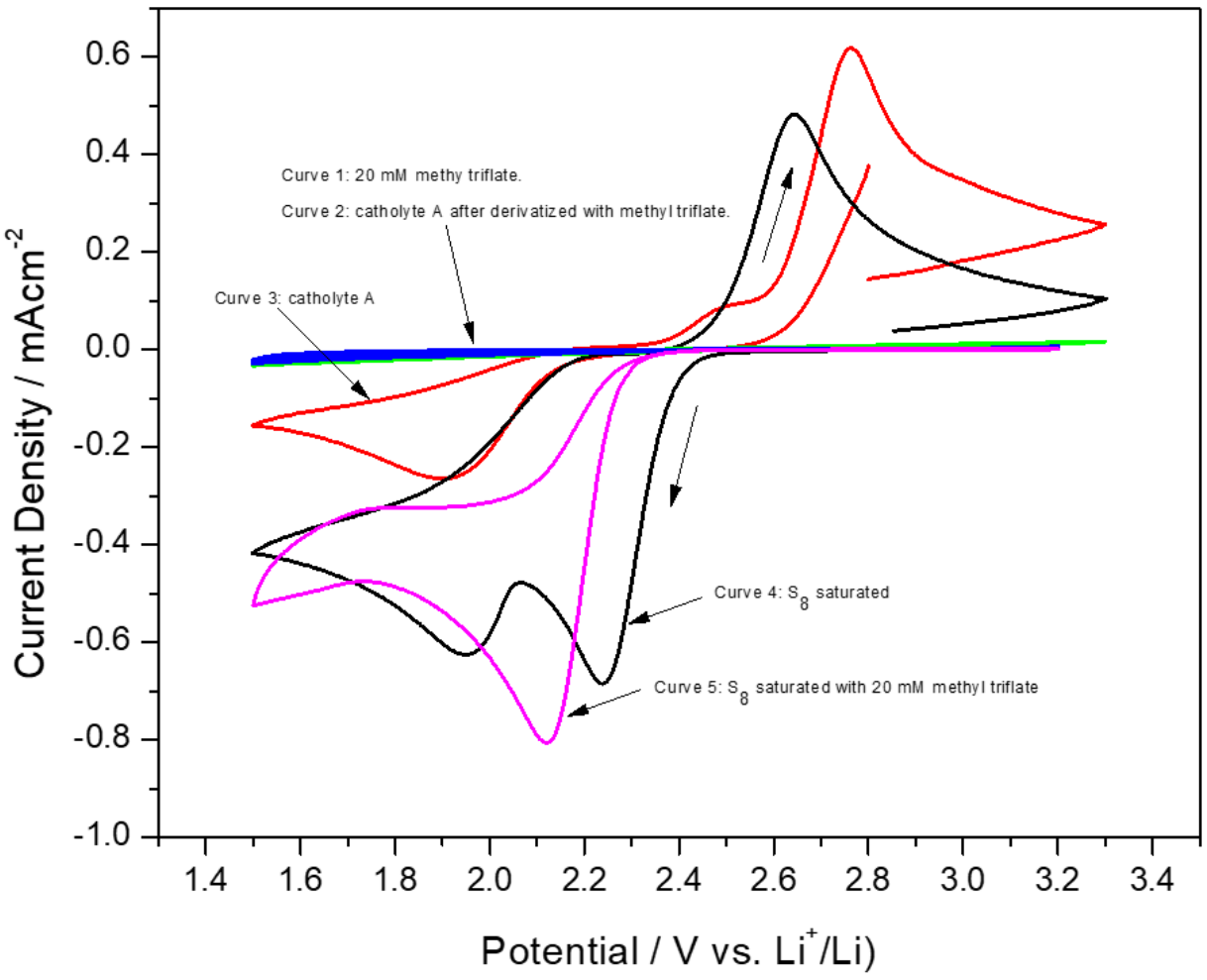

Figure V-301: Cyclic voltammograms of different electrolytes with 1M LiTFSi/DME on glassy carbon electrode. Scan rate of 30mV/s. Black line = S_8 saturated electrolyte; red line = simulated electrolyte A; blue line = 20 mM methyl triflate; green line = simulated electrolyte A after derivatization by methyl triflate; magenta line = S_8 saturated electrolyte with 20 mM methyl triflate

Dong Zheng, Xuran Zhang, Jiankun Wang, Deyu Qu, Xiaoqing Yang, Deyang Qu, J. of Power Sources 301(2016)312-316.

Figure V-302 shows the chromatograms of the electrolytes from Li-S batteries polarized at 2.3 V and derivatized by the *in situ* and *ex situ* methods. Interestingly, Me_2S_8 was hardly present in the catholyte in which methyl triflate was added, and neither were Me_2S_7 nor Me_2S_6 the most abundant species in that catholyte either. In other words, the immediate product of the electrochemical reduction of sulfur was not S_8^{2-}. In almost all the reported mechanisms, S_8^{2-} was believed to be the major initial product of the sulfur reduction. The direct experimental evidence in Figure V-302 clearly shows otherwise.

However, significantly more long chain polysulfide ions were found in the *ex situ* derivatized catholyte. Even though both Li-S cells were discharged to similar capacity, more S_8 was consumed in the catholyte without the addition of methyl triflate. Table V-14 tabulates the comparison of the actual remaining sulfur in the catholyte after discharge with that of the theoretical amount (the initial amount of sulfur minus the amount consumed electrochemically). Obviously, the electrochemical reduction cannot account for all the sulfur consumption in the *ex situ* derivatization. The additional consumption of sulfur can be attributed to the chemical reactions between the polysulfide and elemental sulfur. When methyl triflate was added to the catholyte, the polysulfide ions were immediately derivatized and subsequent chemical reactions with sulfur were avoided.

Table V-14: Summary of Discharge Capacities and Elemental Sulfur Remained in the Li-S Catholyte after *Ex Situ* and *In Situ* Derivatization

Derivatization method	Discharge capacity from polarization at 2.3V (mAh)	Percentage of elemental sulfur left from theoretical calculation based on 2-electron transfer	Percentage of elemental sulfur left from HPLC/UV measurement
in situ	1.42	34.0%	37.9%
ex situ	1.43	33.3%	24.9%

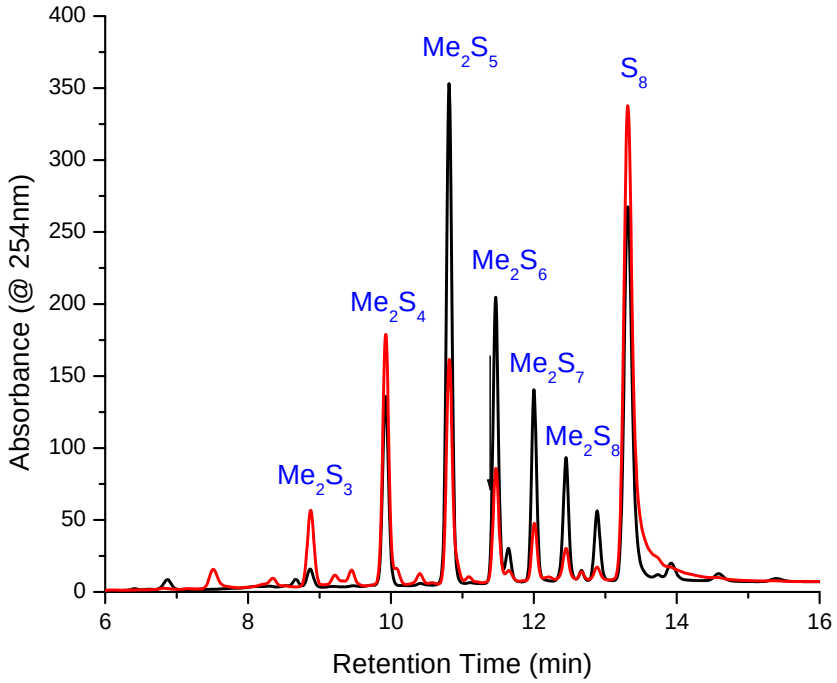

Figure V-302: HPLC chromatogram for the derivatized electrolytes from Li-S batteries polarized at 2.3 V (vs Li/Li^+). Black line = *ex situ* derivatization method; red line = *in situ* derivatization method

4. Stability of Li Anode in the Electrolyte Containing Sulfur and Polysulfide

Various commonly used electrolytes for Li-S batteries were studied using HPLC/MS with a derivatization method. Unfortunately, none of them were found very suitable for Li-S batteries. Because either the dissolve S destroyed the SEI layer and reacted with the Li, such as in LiTFS/DME, LiTFSi/DME, LiTFSi/DME/DOL; or the salts reacts with polysulfide ions, e.g. LiDFOB/DME and LiBOB/DME. As an example, the S dissolved in the most commonly used electrolyte (LiTFSi/DME/DOL) in Li-S batteries was exposed to Li for 8 days, the solution was then derivatized and analyzed by chromatogram, the elemental sulfur was found reduced to polysulfide ions of various lengths. In another example, LiBOB/DME electrolyte was found reacting with polysulfide ions, even though it remained stable with elemental sulfur and Li metal.

The reaction between polysulfides and a lithium anode in a Li-S battery was also examined by the HPLC method. The results demonstrated that the polysulfide species with six sulfur atoms or more were reactive with lithium metal. Although the reaction can be greatly inhibited by the addition of $LiNO_3$ in the electrolyte, $LiNO_3$ cannot form a stable protection layer on Li anode to prevent the reaction during storage. The results show that $LiNO_3$ can significantly slow down the interaction between the polysulfides with Li metal, but cannot stop the reaction.

Conclusions

A simple and effective HPLC/UV method was successfully introduced into the quantification of sulfur's solubilities in pure organic solvents, in pure organic electrolytes, and in electrolyte of Li-S battery. It's found that the solubility of elemental sulfur is influenced by the Lewis basicity and the polarity of the solvents.

By using a novel derivatization reagent with polar and basic functional groups, the polysulfide species in an organic electrolyte containing high concentration of salt can be successfully separated and analyzed by the RP-HPLC ESI/MS. For the first time, the relative distribution of polysulfide species in such electrolyte was quantitatively and reliably determined. By the means of the analytical tool, it was found that the major polysulfide species formed at the first reduction wave of elemental sulfur were the S_4^{2-} and S_5^{2-} species instead of the widely accepted S_8^{2-} and S_6^{2-} species, which were found to be the result of subsequent chemical reactions with elemental sulfur. The HPLC ESI/MS assay will provide a reliable tool for the analysis of polysulfide species in the Li-S battery, which is critical for the investigation of the sulfur redox mechanism.

Various commonly used electrolytes for Li-S batteries were studied using HPLC with a derivatization method. Unfortunately, none of them were found very suitable for Li-S batteries. Because either the dissolve S destroyed the SEI layer and reacted with the Li or the salts reacts with polysulfide ions. Although the reaction can be greatly inhibited by the addition of $LiNO_3$ in the electrolyte, $LiNO_3$ cannot form a stable protection layer on Li anode to prevent the reaction during storage.

Products

Presentations/Publications/Patents

1. Dong Zheng, Xiao-Qing Yang, Deyang Qu, "Reaction between Lithium Anode and Polysulfide Ions in a Lithium-Sulphur Battery", ChemSusChem. 9(2016) 2348-2350.
2. Dong Zheng, Xiaoqing Yang, and Deyang Qu, "Stability of the solid electrolyte interface on the Li electrode in Li-S batteries", ACS Appl. Mater. & Interface, 8(2016)10360-10366.
3. Dong Zheng, Xuran Zhang, Jiankun Wang, Deyu Qu, Xiaoqing Yang, Deyang Qu, Reduction Mechanism of Sulfur in Lithium-Sulfur Battery: from elemental sulfur to polysulfide, J. of Power Sources 301(2016)312-316.
4. Dong Zheng, Xiaoqing Yang, Deyang Qu, Preferential Solvation of Lithium Cations and the Impacts on the Oxygen Reduction in Li-Air Batteries, ACS Appl. Mater. & Interface 7(2015)19923-19929.
5. "Quantitative and qualitative analysis of dissolved polysulfide ions formed during the charge and discharge of Li-S batteries" China International Conference on the Frontier Technology of Advanced Batteries, CIBF2016", May 24-26, Shenzhen China.
6. "Rechargeable Lithium Sulfur Batteries – the Mechanism of Sulfur Redox Reaction" ECS Midwest charpter, 04/05/2016.
7. "Quantitative and qualitative analysis of dissolved polysulfide ions formed during the charge and discharge of Li-S batteries", 10th International Forum on Lithium-ion Battery Technology & Industrial Development, Beijing, China 10/15 – 10/15/2015.
8. "Rechargeable Lithium Sulfur Batteries – the Mechanism of Sulfur Redox Reaction" University of Washington Seattle, Department of Material Engineering. 11/2/2015.

References

1. P.G. Bruce, S.A. Freunberger, L.J. hardwick, J-M. Tarascon, Nature Materials, 11, 19, (2012).
2. L.F. Xiao, Y.L. Cao, J. Xiao, B. Schwenzer, M.H. Englhard, L.V. Saraf, Z. Nie, G. J. Exarhos, J. Liu, J. Mater. Chem. A, 1, 9517, (2013).
3. X.L. Ji, L.F. Nazar, J. Mater. Chem. 20, 9821, (2010).
4. R. Bonnaterre, G. Cauquis, J. Chem.Soc., Chem.Commun. 1972, 1, 293.
5. F. Seel, H.J. Guttler, G. Simon, A. Wieckowski, Pure and Appl. Chem. 1977, 49, 45.

6. M.U.M. Patel, R. Demir-Cakan, M. Morcrette, J-M. Tarascon, M. Gaberscek, R. Dominko, ChemSusChem. 2013, 6, 1177.
7. G.L. Guillanton, Q.T. Do, D. Elothmaini, J. Electrochem. Soc. 1996, 143, L223.
8. J. Badoz-Lambling, R. Bonnaterre, Electrochim. Acta 1978, 21, 119.
9. B.S. Kim, S.M. Park, J. Electrochem. Soc. 1993, 140. 115.
10. J. Paris, V. Plichon, Electrochim. Acta 1981, 26, 1823.
11. C. Barchasz, F. Molton, C. Duboc, J-C Lepretre, S. Patoux, F. Alloin, Anal. Chem. 2012, 84, 3973.
12. M. Hagen, P. Schiffels, M. Hammer, S. Dorfler, J. Tubke, M.J. Hoffmann, H. Althues, S. Kaskel, J. Electrochem. Soc. 2013, 160, A1205.
13. M.A. Lowe, J. Gao, H.D. Abruna, RSC Advances 2013, 3, 1957.
14. Y. Diao, K. Xie, S.H. Xiong, X.B. Hong, J. Electrochem. Soc., 159, A421, (2012).
15. D.A. Skoog, F. J. Holler, T.A. Nieman, Principles of Instrumental Analysis, 5th ed. P739, Thomason Learning, New York 1998.
16. Z. Uddin, R. Markuszewski, D. C. Johnson, Analytica Chimca Acta, 200, 115, (1987).
17. R. Steudel, G. Holdt, Thomas Göbel, J. Chromatography A, 475, 442, (1989).
18. D.R. Lauren, J.H.Watkinson, J. Chromatogr. 348, 317(1985).
19. B. Meyer, Chem. Rev. 76, 367 (1976).
20. C. Reichardt, “Solvents and Solvent Effects in Organic Chemistry”, Wiley-VCH, 2003.
21. J.H. Karchmer, “Analytical Chemistry of Sulfur and its Compounds, Part 1”, Wiley-Interscience, 1970.

V.H.9. Statically and Dynamically Stable Lithium-Sulfur Batteries (UTA)

Arumugam Manthiram, Principal Investigator
University of Texas at Austin
204 E. Dean Keeton Street, Stop C2200
Austin, TX 78712
Phone: 512-471-1791
E-mail: manth@austin.utexas.edu

Tien Q. Duong, DOE Program Manager
Advanced Battery Materials Research (BMR)
U.S. Department of Energy
Vehicle Technologies Office
1000 Independence Avenue, SW
Washington, DC 20585
Phone: 202-586-7836
E-mail: Tien.Duong@ee.doe.gov

Start Date: October 1, 2015
End Date: September 30, 2018

Abstract

Objectives

The objective of this project is to develop statically and dynamically stable lithium-sulfur (Li-S) batteries by integrating polysulfide (PS)-filter-coated separators with a protected lithium-metal anode through additives or a modified Li_2S cathode with little or no charge barrier during first charge. The project includes a demonstration of electrochemically stable cells with sulfur capacities of >1,000 mAh g^{-1} and cycle life in excess of 500 cycles (dynamic stability) along with positive storage properties (static stability) at >70 wt. % sulfur content and ~5 mg cm^{-2} loading.

Accomplishments

- Establishment of (i) a materials chemistry database investigating the physical/chemical characteristics of 12 coating materials with four different morphologies, and (ii) the corresponding fabrication methods for preparing lightweight, flexible PS-filter-coated separators, including binder-supporting, CNT-supporting, and layer-by-layer (LBL) methods
- Significant improvement in dynamic cell performances (cycling stability) on applying the (PS)-filter-coated separators with, for example, the activated charcoal coating, demonstrating a high discharge capacity of 1,088 mAh g^{-1} and a low capacity-fade rate of 0.12% per cycle after 500 cycles
- Significant improvement in static cell performances on applying, for example, the LBL CNF-coated separators, demonstrating a retention of 850 mA h g^{-1} after resting the cell for 120 days

Future Achievements

- Improvements in dynamic electrochemical performances to attain (i) high electrochemical utilization (80 – 90 %), (ii) low capacity fade rate (< 0.05% per cycle), and (iii) long cycle life (> 500 cycles)
- Improvements in static electrochemical performances to achieve (i) low self-discharge rate (< 0.5% day^{-1}), and (ii) reversible cycle stability
- Optimization of cathode configuration to realize a high sulfur content of 70 wt. % along with a sulfur loading of 5 mg cm^{-2} and good electrochemical stability

Technical Discussion

Background

Li-S batteries are receiving great attention as a most promising next generation power source for electric vehicles at an affordable cost with minimal environmental impacts. This is because sulfur is abundant, is environmentally benign, and offers an order of magnitude higher charge-storage capacity with a two-electron transfer reaction compared to the insertion-compound electrodes used in current lithium-ion technology.

However, the commercialization of Li-S batteries is hampered by several scientific and technological challenges: low electronic conductivity of sulfur and the dissolution and migration of PSs from the cathode to the Li-metal anode through the separator. The poor electronic conductivity often necessitates a high content of carbon, resulting in a decrease in volumetric energy density. The PS migration causes static and dynamic instability with high self-discharge, poisoning of Li-metal surface, and poor cycling efficiency, hindering the practical utility of Li-S cells.

Introduction

The goal of this project is to overcome the above-listed persistent problems and demonstrate statically and dynamically stable Li-S cells with reasonable sulfur loading and content for electric vehicles. The strategy aims at improving the electrochemical utilization and suppressing the PS diffusion by employing a customized separator coated with a PS filter. The coated PS filter faces toward the cathode for intercepting and stabilizing the migrating PSs before they diffuse out from the cathode region. The PS-filter coating, consisting of a thin-film carbon/polymer, possesses both physical and chemical PS-trapping capabilities. As a result, the fabricated Li-S cells with coated separators show both static and dynamic stability with low self-discharge and long lifespan. In addition, our PS-filter coatings have light weight, high flexibility, and good mechanical strength.

Approach

The electrochemical stability of the Li-S cells is improved by three approaches that are complementary to each other.

- The first approach focuses on the establishment of an electrochemically stable cathode environment by employing PS-filter-coated separators. The PS-filter coatings aim to suppress the severe polysulfide diffusion and improve the redox capability of the Li-S cells with high-sulfur loadings. The study includes an understanding of the materials characteristics, fabrication parameters, electrochemical properties, and battery performance of the PS-filter-coated separators.
- The second approach focuses on electrode engineering from two aspects. First, the investigation of a Li-metal anode with coating- and additive-supporting approaches is aimed at improving the safety of Li-S cells. Second, the research on an activated-Li2S cathode with little or no charge-barrier will promote the performance and safety of the cell with Li2S cathode and graphite anode.
- The integration of approaches (i) and (ii) would create statically and dynamically stable Li-S batteries for electric vehicles.

Results

We have investigated the physical/chemical characteristics of the coating materials for creating a materials chemistry database in Year 1. We have selected four major carbon materials categorized by their different morphologies: (i) spherical carbons, (ii) carbon nanofibers (CNFs), (iii) graphene, and (iv) carbon nanotubes (CNTs). The materials chemistry database allows for the establishment of lightweight, flexible PS-filter-coated separators and the enhancement of the electrochemical performances of the corresponding Li-S cells. Thus, in terms of battery electrochemistry, we have demonstrated the enhanced dynamic and static electrochemical performances of Li-S batteries by assessing the cells fabricated with various PS-filter-coated separators.

Specifically, we have developed various PS-filter-coated separators with different functional coatings consisting of 12 carbon materials that can be categorized into four main groups based on their unique morphologies: spherical, fibrous, tubular, and flaky carbon materials. The PS-filter coatings are effective in reducing the capacity fade during dynamic cell cycling and suppressing the severe self-discharge behavior during static cell resting. Thus, in Year 1, we have successfully passed Technical and Go/No-Go Milestones by attaining and even demonstrating battery characteristics better than the targeted cell performances.

1. Materials chemistry database

We have selected 12 carbon materials and categorized them into four main groups by their unique morphologies: spherical, fibrous, tubular, and flaky carbon materials. The first group includes spherical carbons with nonporous and porous structures (micro-/meso-/macro-porous structures). The second group includes carbon materials with different morphologies: carbon nanofibers (CNFs), carbon nanotubes (CNTs), and graphene (G). Table V-15 summarizes their materials chemistry, porosity, and the coating-method study. The most interesting results are that we have developed three modified coating methods for preparing smooth and robust carbon coatings onto a polypropylene membrane (Celgard 2500): (i) tape-casting method coupled with binders, (ii) vacuum-filtration process coupled with carbon nanotube (CNT), and (iii) layer-by-layer (LBL) coating configuration. These approaches provide the coatings with strong adhesion in between the carbon materials and with the polypropylene membranes.

Table V-15: Materials Chemistry Database

(Coating material): coating methods	Carbon sample	Surface area [m^2 g^{-1}]	Pore volume [cm^3 g^{-1}]	Pore size [nm]	Microporosity	
					Surface area [m^2 g^{-1}]	Pore volume [cm^3 g^{-1}]
(i-a): T&B, V*	Acetylene Black	82	0.29	14	0	0
(i-a): T&B, V*	Super P Carbon	89	0.44	19	0	0
(i-a): T&B, V*	Carbon Black (Lampblack)	30	0.22	29	0	0
(i-b): T&B, V*	Carbon Black (Vulcan)	298	1.03	14	85	0.04
(i-b): T&B, V*	Activated Carbon	732	0.53	3	585	0.31
(i-b): T&B, V*	Activated Charcoal	1,002	0.70	3	754	0.40
(i-b): T&B, V*	Microporous Carbon	1,321	3.62	10	753	0.41
(i-b): T&B, V*	Ketjen Black	950	2.92	12	58	0.02
(ii): LBL-V	CNF	26	0.09	14	0	0
(iii): LBL-V	CNT	40	0.20	36	0	0
(iv): T, B, V	R-GO	272	0.57	2	0	0
(iv): T, B, V	EO-GO	251	0.43	7	36	0.017

Coating materials: (i) spherical carbons: (i-a) nonporous carbon and (i-b) porous carbon, (ii) carbon nanofibers (CNF), (iii) carbon nanotubes (CNT), and (iv) graphene: reduced graphene oxide (R-GO) and edge-oxidized graphene oxide (EO-GO)

Coating methods: (T) tape-casting, (B) binder-supporting, (V*) vacuum-filtration process with carbon nanotube (CNT) as the framework, and (LBL-V) layer-by-layer vacuum-filtration process

2. Static and dynamic electrochemical stability: Group (i) – PS-filter-coated separators with spherical carbon coating

In group (i), eight types of spherical carbons were coated onto a polypropylene membrane through two different processes: tape-casting and vacuum-filtration methods. The tape-casting samples were prepared by coating the spherical-carbon-polyvinylidene difluoride (PVDF) mixtures onto polypropylene membranes. The vacuum-filtration samples were obtained by directly vacuum-filtering the spherical-carbon-single wall carbon nanotube (SWCNT) mixtures onto polypropylene membranes. All carbon coatings had the same light-weight mass of 0.1 mg cm^{-2}. Pure sulfur cathodes that had sulfur loading of 3.6 mg cm^{-2} and sulfur content of 70 wt.% were used in investigating the electrochemistry.

The dynamic electrochemical performances of the Li-S cells utilizing the spherical-carbon-coated separators through two coating methods are summarized in Figure V-303a. At a C/10 rate, the cells employing the spherical-carbon-coated separators that were fabricated by the tape-casting method exhibit lower electrochemical utilization and poorer cycling stability as compared to those fabricated with the vacuum-filtration method. The relatively poor performances originating from the tape-casting methods are ascribed to the insulating nature of the PVDF binder. Although PVDF binders provide good adhesion among spherical carbon powders and between the carbon coating and polypropylene membrane, they increase the internal resistance of the corresponding cells and thereby lower their electrochemical utilization and redox-reaction capability. Also, PVDF binders might block the porous spaces of spherical carbons, reducing the polysulfide-trapping capability contributed by nanopores.

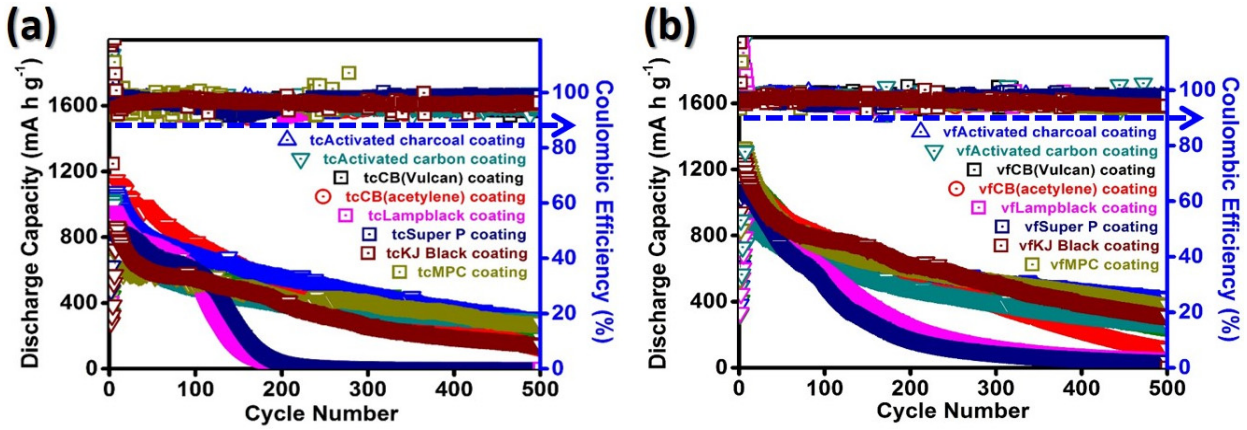

Figure V-303: Cycling performance at C/10 rate of the cells fabricated with various spherical-carbon-coated separators prepared by (a) tape-casting (tc) and (b) vacuum-filtration (vf) methods

In order to eliminate the drawbacks of PVDF binders, SWCNTs were employed as the conductive binder to replace the PVDF binder in the vacuum-filtration method. In Figure V-303b, the cells fabricated with the vacuum-filtered separators exhibit high discharge capacities and reasonable cyclability, resulting mainly from the "SWCNT conductive binders." The SWCNT binders offer extra electron transport pathways and do not block the nanopores of spherical carbons. As a result, the cells fabricated with the porous spherical-carbon-coated separators that were prepared by the vacuum-filtration method demonstrate superior electrochemical performance. Among them, the carbon coatings using microporous carbon (MPC), Ketjen (KJ) Black, activated charcoal, and activated carbon show long-term cyclability for 500 cycles. Specifically, the cells using the activated charcoal-coated separators exhibit a high discharge capacity of 1,088 mA h g^{-1}, approaching 65% of the electrochemical utilization of sulfur. The corresponding areal capacity approaches 4.3 mAh cm^{-2}, which surpasses the targeted capacity of 4 mAh cm^{-2}. The cell also exhibits a reversible discharge capacity of 423 mAh g^{-1} with a low capacity fade rate of 0.12% per cycle after 500 cycles. The outstanding cycling performance is due to the fact that the coating layer forms polysulfide traps and functions as an additional current collector to reutilize/reactivate the trapped active material during long-term cell cycling.

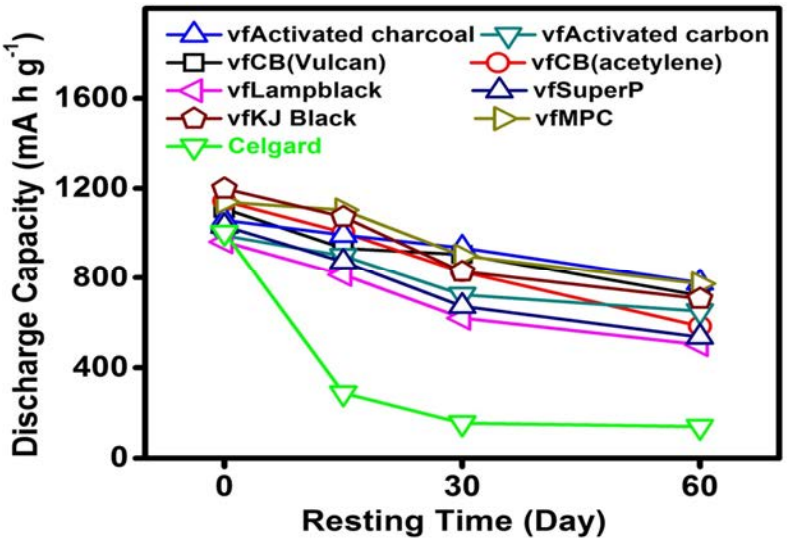

Figure V-304: Self-discharge analysis of cells with and without spherical-carbon-coated separators

Static electrochemical stability was assessed by analyzing the self-discharge behavior as shown in Figure V-304. The static battery performances were investigated for the cells employing the vacuum-filtered separators. This is because the dynamic electrochemical stability of the vacuum-filtered separators compares advantageously with the tape-casted separators. The retained capacities of the cells fabricated with different kinds of spherical-carbon-coated separators were monitored after resting for 0, 15, 30, and 60 days. The cells employing the spherical-carbon-coated separators retain high capacities after resting for 60 days. In the case of the cells using porous activated charcoal-coated separators, the capacity-retention and capacity-fade rates are, respectively, 73% and 0.4% day^{-1}. These favorable features demonstrate that the targeted low self-discharge rate of 0.5% day^{-1} is attained by employing the spherical-carbon-coated separator fabricated by the vacuum-filtration method.

3. Static and dynamic electrochemical stability: Group (ii) – PS-filter-coated separators with carbon nanofiber (CNF) coating

In group (ii), nonporous CNFs were used for studying the effect of a layered coating on improving the dynamic and static electrochemical performances of Li-S cells. The CNFs were coated onto a polypropylene membrane by the layer-by-layer (LBL), vacuum-filtration technique with polyethylene glycol (PEG) as the binder. The light-weight CNF#1, CNF#2, and CNF#3 coatings had coating masses of 0.1, 0.2, and 0.4 mg cm^2.

The CNF coating provides a conductive thin film in between the cathode and the separator, which functions as an upper current collector for reducing the cell resistance and increasing the electrochemical-reaction capability. As a result of the high utilization of sulfur, besides showing a high peak discharge capacity of > 1,200 mA h g^{-1} and a high areal capacity of 4.0 mA h cm^{-2}, the cells employing various CNF-coated separators show stable cycling performances for 500 cycles (Figure V-305a and Figure V-305b). The cells employing the CNF#3 coating retain high reversible capacities of 529 and 542 mA h g^{-1} at, respectively, C/5 and C/10 rates. The capacity-fade rates are 0.11% per cycle, a result of the CNF coating functioning as the PS filter for suppressing the polysulfide migration. After trapping the polysulfides, the conductive CNF coatings support the high electrochemical activity of the trapped active materials so as to retain the high reversibility. The static electrochemical stability was examined by analyzing the self-discharge effect (Figure V-305c). We monitored the remaining capacities of the cells after resting for 120 days, presenting one of the longest analytical data reported so far in the literature. The experimental cells employing the LBL CNF-coated separators show stable and high remaining charge-storage capacities of up to 850 mA h g^{-1} (with CNF#3 coating) after resting for 120 days. The capacity-retention and capacity-fade rates attain, respectively, 63% and 0.3% day^{-1}. The stable and reversible capacities and the low self-discharge constants demonstrate that the dissolution of active material and the diffusion of polysulfides are greatly reduced during long-term cell-storage period.

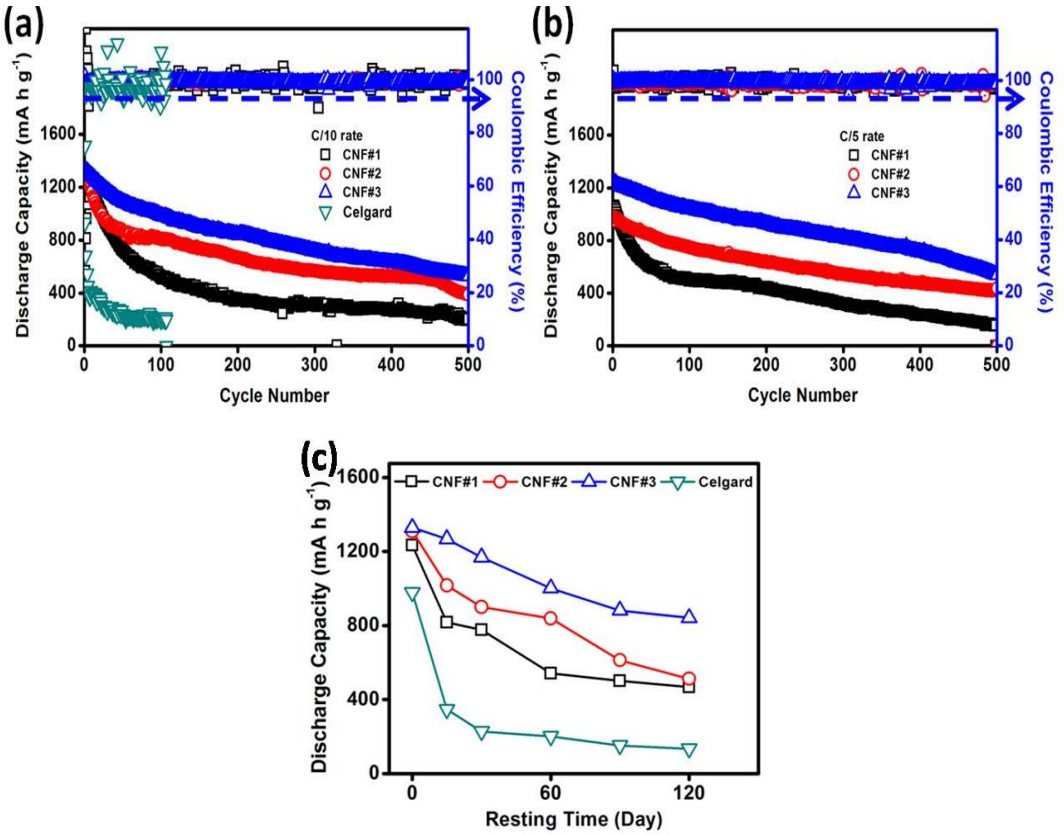

Figure V-305: Cycling performance of the cells employing various LBL CNF-coated separators at (a) C/10 and (b) C/5 rates. (c) The corresponding self-discharge analysis

4. Static and dynamic electrochemical stability: Group (iii) – PS-filter-coated separators with carbon nanotube (CNT) coating

In group (iii), we prepared the CNT-coated separators *via* the LBL vacuum-filtration method. The CNT/PEG mixtures that consisted of conductive CNTs with PEG polymers were attached onto polypropylene membranes. The weights of CNT#1, CNT#2, and CNT#3 coatings are, respectively, 0.04, 0.08, and 0.12 mg cm^{-2}. Such optimized CNT-coated separators reduce the weight of added components and simplify the assembly process of the cells as compared to other novel cell configurations with additional free-standing architectures.

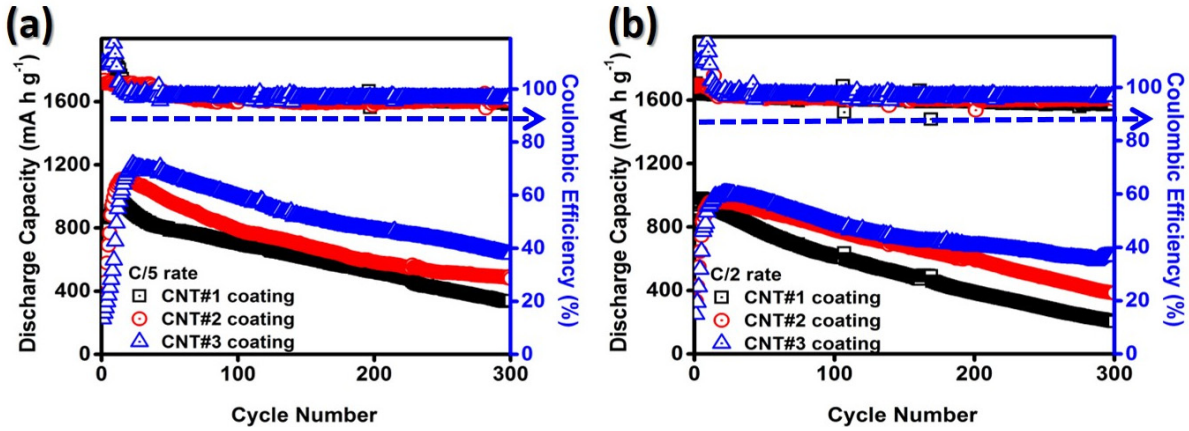

Figure V-306: Cycling performance of the cells employing the various LBL CNT-coated separators at (a) C/5 and (b) C/2 rates

The dynamic electrochemical performances of the cells utilizing the CNT#1-, CNT#2-, and CNT#3-coated separators at C/5 and C/2 rates are summarized in Figure V-306. The LBL CNT coatings associated with PEG functional binders were employed to immobilize the migrating polysulfides within the cathode region of the cell, effectively suppress the severe capacity fade of Li-S cells, and enhance further the rate capability. Therefore, the pure sulfur cathodes exhibit a peak discharge capacity of above 1,200 mA h g^{-1} at C/5 rate, presenting a better cell performance than the targeted capacity of 1,000 mA h g^{-1}. The cells using the CNT#2- and CNT#3-coated separators achieve the targeted high areal capacity of 4.0 mA h cm^{-2}. In terms of dynamic battery chemistry, the cells utilizing the various CNT-coated separators display stable cyclability for 300 cycles. The cells employing the CNT#3-coated separator retain high reversible capacities of 630 and 615 mA h g^{-1} at, respectively, C/5 and C/2 rates after 300 cycles. The calculated capacity-retention rates are 53% and 60% at, respectively, C/5 and C/2 rates. The capacity-fade rates are as low as 0.15% and 0.13% per cycle. In addition, with the light-weight LBL thin-film coating technique, the total sulfur content that includes everything in the cathode region approaches 68 wt. %.

5. Static and dynamic electrochemical stability: Group (iv) – PS-filter-coated separators with graphene coating

In Group (iv), the edge-oxidized graphene oxide (EO-GO) that provides functional groups for trapping polysulfides and the reduced graphene oxide (R-GO) that offers high conductivity for enhancing the redox-reaction accessibility were used as the separator-coating material (coating mass: 0.4 mg cm^{-2}). The cell resistance (Figure V-307a) indicates that the R-GO coating optimizes a better cell conductivity than that provided by the EO-GO coatings.

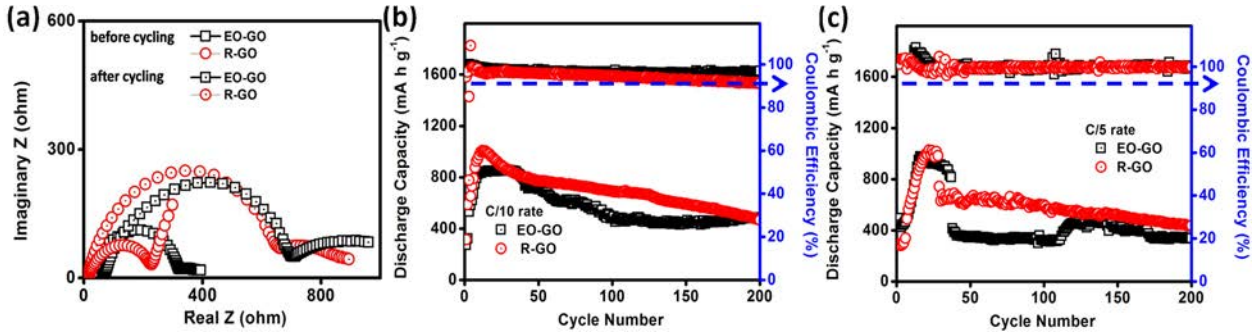

Figure V-307: (a) Impedance spectroscopy of the cells fabricated with the EO-GO and R-GO coated separators before and after cycling. Cycling performance of the cells employing the EO-GO and R-GO coated separators at (a) C/10 and (b) C/5 rate

Figure V-307b and Figure V-307c show the dynamic performances at C/10 and C/5 rates of the cells employing the EO-GO and the R-GO coated separators. With the R-GO coated separators, the targeted discharge capacity and areal capacity are achieved. On the other hand, while the peak discharge capacity obtained with the EO-GO coated separator is lower than that achieved with the R-GO coated separators, its capacity retention rate is 60% with a reversible capacity approaching 500 mA h g^{-1} after 200 cycles. Specifically, the graphene coating is expected to provide a conductive layer between the cathode and the separator and act as a trap for polysulfides. The superior conductivity of R-GO over EO-GO leads to higher discharge capacities. On the other hand, the functional groups present on EO-GO are expected to bind to polysulfide groups and aid their entrapment. This might explain the relatively better capacity retention observed with EO-GO coated separators. In order to investigate the mechanisms underlying the electrochemical performance of the coated separators, impedance spectroscopy was also carried out to analyze the changes in cell resistance after cycling. After 50 cycles, the impedance values seen with both materials are similar, suggesting that EO-GOs keep good cycle stability mainly due to their strong polysulfide-trapping capability. This may also help explain the convergence observed with capacities at higher cycle numbers for the cells with R-GO and EO-GO.

The static stabilities of the cells fabricated with the EO-GO- and the R-GO-coated separators were tested by a series of self-discharge experiments. The OCV and peak discharge capacities were measured for the cells with rest periods of 0 – 90 days, as shown in Figure V-308. The OCV measured with bare separators quickly decreases to less than 2.1 V, while the OCV values observed with the coated separators remain stable around

2.3 V. Both the EO-GO- and R-GO-coated separators demonstrate excellent static stability with a low capacity-fade rate of 0.4% day^{-1}. This demonstrates the excellent capability of the graphene-coated separators to entrap polysulfide species and reduce the loss of electrochemically active material during cell resting.

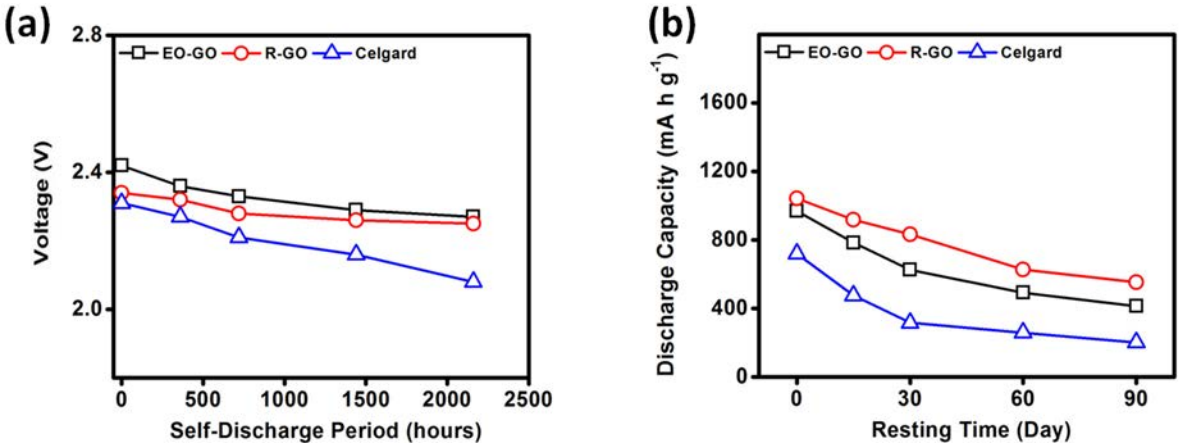

Figure V-308: Self-discharge analysis of the cells with and without the R-GO- and EO-GO-coated separators: (a) OCVs and (b) cell capacity

Conclusions

In general, the analytical Table V-15 summarized the materials chemistry of the coating materials and their corresponding coating methods for fabricating PS-filter-coated separators. In group (i), we made the spherical carbon study comprehensive from nonporous to micro-/meso-/macro-porous carbons. In groups (ii) – (iv), we made the study of the carbon materials with various morphologies. For all these carbon materials in groups (i) – (iv), we made corresponding optimal coating methods to fabricate smooth carbon coatings onto a polypropylene membrane. As a result, these optimal PS-filter-coated separators were able to be applied to Li-S cells for optimizing the static and dynamic cell performances.

The static and dynamic electrochemical stabilities of the cells demonstrate that the developed PS-filter-coated separators were able to attain the targeted battery performances with pure sulfur cathode in the cells. The excellent dynamic and static electrochemical stability demonstrated in Year 1 might pave the way for further progress that would be completed in Year 2. As a result, these optimal PS-filter-coated separators were able to be applied to Li-S cells for optimizing the static and dynamic cell performances.

Products

Presentations/Publications/Patents

Publications

1. S.-H. Chung, C.-H. Chang, and A. Manthiram, "A Core–Shell Electrode for Dynamically and Statically Stable Li–S Battery Chemistry," *Energy & Environmental Science* **9**, 3188–3200 (2016).
2. S.-H. Chung, C.-H. Chang, and A. Manthiram, "Hierarchical Sulfur Electrodes as a Testing Platform for Understanding the High–loading Capability of Li–S Batteries," *Journal of Power Sources* **334**, 179–190 (2016).
3. L. Luo, S.-H. Chung, and A. Manthiram, "Trifunctional Multi–Walled Carbon Nanotubes/ Polyethylene Glycol (MWCNT/PEG) –Coated Separator through a Layer–by–Layer Coating Strategy for High–Energy Li–S Batteries," *Journal of Materials Chemistry A*, **4**, 16805–16811 (2016).
4. S.-H. Chung, C.-H. Chang, and A. Manthiram, "A Carbon-Cotton Cathode with Ultrahigh-Loading Capability for Statically and Dynamically Stable Lithium–Sulfur Batteries," *ACS Nano*, DOI: 10.1021/acsnano.6b06369 (2016).

5. C.-H. Chang, S.-H. Chung, and A. Manthiram, "Highly Flexible, Freestanding Tandem Sulfur Cathodes for Foldable Li–S Batteries with High Areal Capacity," *Materials Horizons* (in review).

Presentations

1. A. Manthiram, "Nanomaterials for Electrical Energy Storage," *International Symposium on Clusters and Nanomaterials*, Richmond, VA, October 26 – 29, 2015 (invited).
2. A. Manthiram, "Electrical Energy Storage: Next Generation Battery Chemistries," *2015 International Conference on Innovative Electrochemical Energy Materials and Technologies (EEMT2015)*, Nanning, China, November 8 – 11, 2015 (invited plenary talk).
3. A. Manthiram, "Electrical Energy Storage: Materials Challenges and Prospects," *2015 Fall Meeting of the Materials Research Society*, Boston, MA, November 29 – December 4, 2015 (invited talk at Symposium X: Frontiers of Materials Research).
4. C.-H. Chang, S.-H. Chung, and A. Manthiram, "Tandem Pure Sulfur Cathodes for Li-S Batteries with High Areal Capacities," *2016 Graduate and Industry Networking*, Austin, TX, January 28 – February 2, 2016.
5. C.-H. Chang, S.-H. Chung, and A. Manthiram, "From Trash to Treasure: Transforming Waste Newspapers into an Interlayer of Lithium-Sulfur Battery for Improving Electrochemical Performance," *2016 Energy Week*, Austin, TX, February 16 – 19, 2016.
6. A. Manthiram, "Tutorial on Electrode Materials and Electrolytes for Next Generation Rechargeable Batteries," *2016 Spring Meeting of the Materials Research Society*, Phoenix, AZ, March 28, 2016.
7. A. Manthiram, "Next Generation Battery Chemistries: Materials Challenges and Prospects," *Materials Challenges in Alternative and Renewable Energy (MCARE) Meeting*, Clearwater, FL, April 17 – 21, 2016 (invited plenary talk).
8. A. Manthiram, "High-energy-density, Long-life Lithium-sulfur Batteries," *229th Electrochemical Society Meeting*, San Diego, CA, May 29 – June 3, 2016 (invited).
9. A. Manthiram, "Statically and Dynamically Stable Lithium-sulfur Batteries," *2016 Annual Merit Review Meeting of the Office of Vehicle Technologies*, U.S. Department of Energy, Washington, D.C, June 6 – 10, 2016.
10. A. Manthiram, "Conversion-reaction Cathodes for Electrical Energy Storage: Challenges and Prospects," *China Conference on Energy Materials and Energy Chemistry 2016*, Hunan University, Changsha, China, June 15 – 16, 2016 (invited plenary talk).
11. C.-H. Chang, S.-H. Chung, and A. Manthiram, "Tandem Sulfur Cathodes with High Areal Capacity for Li-S Batteries," *18th International Meeting on Lithium Batteries*, Chicago, IL, June 18 – June 24, 2016.
12. S.-H. Chung, C.-H. Chang, and A. Manthiram, "Development of High-Performance, High-Loading Sulfur Cathodes," *18th International Meeting on Lithium Batteries*, Chicago, IL, June 18 – June 24, 2016.
13. A. Manthiram, "Metal-Sulfur Batteries with High Sulfur Loading," *18th International Meeting on Lithium Batteries*, Chicago, IL, June 18 – June 24, 2016 (invited).
14. A. Manthiram, "Materials for Electrochemical Energy Conversion and Storage Technologies," Indian Institute of Technology Madras, Chennai, India, August 16, 2016 (invited).
15. A. Manthiram, "Electrical Energy Storage: Next Generation Battery Chemistries," *4th International Workshop on Nanotechnology, Renewable Energy, and Sustainability*, Xi'an Jiaotong University, Xi'an, China, September 19, 2016 (invited keynote talk).
16. A. Manthiram, "New Battery Chemistries Enabled by Solid-electrolyte Separators," Hanyang University, Seoul, South Korea, September 21, 2016 (invited).

V.I. Lithium Air Batteries

V.I.1. Rechargeable Lithium-Air Batteries (PNNL)

Ji-Guang Zhang, Principal Investigator
Pacific Northwest National Laboratory
902 Battelle Boulevard
Richland, WA 99354
Phone: 509-372-6515; Fax: 509-375-2186
E-mail: jiguang.zhang@pnnl.gov

Wu Xu, Co-Principal Investigator
Pacific Northwest National Laboratory
902 Battelle Boulevard
Richland, WA 99354
Phone: 509-375-6934; Fax: 509-375-2186
E-mail: wu.xu@pnnl.gov

Tien Q. Duong, DOE Program Manager
Advanced Battery Materials Research (BMR)
U.S. Department of Energy
Vehicle Technologies Office
1000 Independence Avenue, SW
Washington, DC 20585
Phone: 202-586-7836
E-mail: Tien.Duong@ee.doe.gov

Start Date: October 2015
End Date: September 2018

Abstract

Objectives

- To develop stable electrolytes and air electrodes and reduce the charging overvoltage of Li-O_2 batteries.
- To improve the cycling stability of rechargeable Li-O_2 batteries.

Accomplishments

- Developed highly concentrated electrolytes based on dimethyl sulfoxide (DMSO) to protect Li metal anodes and to enhance electrolyte stability against reduced oxygen species, achieving greatly improved cycle life for Li-O_2 batteries.
- Demonstrated B_4C as a stable air-electrode material to improve the cycle life of Li-O_2 batteries.
- Developed a simple method to *in situ* generate ultrathin protection layers on both Li anode and carbon nanotube (CNT)-based air-electrode surfaces, leading to greatly enhanced cycle life.
- Discovered the mechanism behind the good cycle life of binder-free air electrodes based on $NiCo_2O_4$ nanowire catalyst on carbon fabric and prelithiation treatment.

Future Achievements

- Investigate temperature effect on oxygen reduction reaction (ORR) and oxygen evolution reaction (OER) of Li-O_2 batteries.

- Identify the factors that affect the stability of Li metal anodes in Li-O_2 batteries.
- Develop surface coating or electrolyte additives to stabilize Li metal anodes and improve the cycle life of Li-O_2 batteries.

Technical Discussion

Background

During the discharging process of Li-O_2 batteries, the reduced oxygen species attack all components in a Li-O_2 battery and significantly limit the reversibility of the batteries. In addition, the overvoltage (typically over 1 V) during the charging process of Li-O_2 batteries needs to be reduced to improve the energy efficiency of Li-O_2 batteries.

Introduction

Li-air or Li-O_2 batteries have an ultrahigh theoretical specific energy (~5,200 Wh kg^{-1} when the weights of Li and O_2 are included), and are expected to have a practical specific energy of over 800 Wh kg^{-1}, which is about four times of that of state-of-the-art lithium-ion batteries (approximately 200 Wh kg^{-1}).[1,2] However, development of rechargeable Li-O_2 batteries faces significant challenges including decomposition of electrolytes, large overvoltage that occurs during charging, design of cathode materials with high capacity and stability, and protection of Li metal anodes.[3,4] More importantly, highly reactive reduced oxygen species ($O_2^{-\bullet}$, LiO_2, O_2^{2-}, LiO_2^-, and Li_2O_2) are generated on the air-electrode surface via the ORR during the discharge of a Li-O_2 battery, and these species attack every component in Li-O_2 batteries and significantly limit the reversibility of the rechargeable Li-O_2 batteries. Therefore, the chemical and electrochemical stability of all Li-O_2 battery components, including the electrolyte solvent, electrolyte salt, cathode material (typically carbon based), and binder, needs to be reevaluated in an O_2-rich environment. Also, good catalysts need to be developed to reduce the overvoltage during oxygen reduction and evolution reactions so the cycling stability of Li-O_2 batteries can be improved.

Approach

Several approaches have been employed to improve the performance of Li-O_2 batteries. New electrolytes and non-carbon-based air electrodes that are stable against the reactive reduced-oxygen species are developed. The stability of carbon-based air electrodes are improved with selected OER catalysts to encapsulate the carbon surface so as to avoid carbon oxidation and improve the cycling stability of these electrodes. The stability of the electrolytes and coated air electrodes during discharge and charge processes of Li-O_2 batteries are systematically investigated to improve the performance of Li-O_2 batteries.

Results

1. Development of binder-free air electrodes based on transition metal oxide nanowires on carbon fabric composites with prelithiation treatment for Li-O_2 batteries

The binder-free air electrode based on nanowire (NW) nickel cobalt oxide ($NiCo_2O_4$, NCO) catalyst on carbon fabric (CF) composite has been investigated systematically. The morphology and crystal characterizations of the NCO/CF composite are shown in Figure V-309. When the binder-free NCO/CF electrode was assembled into the Li cells and after prelithiation to a certain voltage in argon atmosphere, the NCO nanowire was transformed to ultra-nanosized (about 2 nm) Ni and Co particles well dispersed in a Li_2O moiety (Figure V-310) according to the conversion reaction of $NiCo_2O_4 + 8Li^+ + 8e^- \rightarrow Ni + 2Co + 4Li_2O$. When the prelithiated NCO (PL-NCO) electrode was assembled into Li-O_2 cells with 1 M lithium trifluoromethanesulfonate (LiTf)-tetraglyme electrolyte and cycled in the range of 2.0~4.5 V, nanosized Ni and Co particles were the catalysts for oxygen reduction during the first discharge process. During the first charge process, the nanosized Ni and Co would be oxidized to NiO and CoO nanoparticles by chemical reactions via oxygen oxidation and/or electrochemical reactions of $Ni + Li_2O \rightarrow NiO + 2Li^+ + 2e^-$ and $Co + Li_2O \rightarrow CoO +$

$2Li^+ + 2\ e^-$. Since the reversible reactions of NiO (or CoO) to Ni (or Co) with Li_2O occur at a voltage of about 1.2 V—below the discharge voltage (2.0 V) set for the cycling protocol—the NiO and CoO nanoparticles were the catalysts starting from the second discharge/charge cycle. That is one of the reasons why the capacity of the first cycle is much higher than that of the subsequent cycles as shown in Figure V-311. The prelithiation of NCO was performed at several cutoff voltages. The optimal prelithiation cutoff voltage was found to be 0.5 V, which allows the Li-O_2 cells with the prelithiated NCO/CF electrode to show stable cycling at a capacity above 1200 mAh g^{-1} for 120 cycles and 1000 mAh g^{-1} for 140 cycles (Figure V-312). At higher prelithiation cutoff voltages, the lithiation of NCO is limited; but at too low a lithiation cutoff voltage, the NCO nanowires experience inevitable damage and the electrode surface is covered with thick discharge products

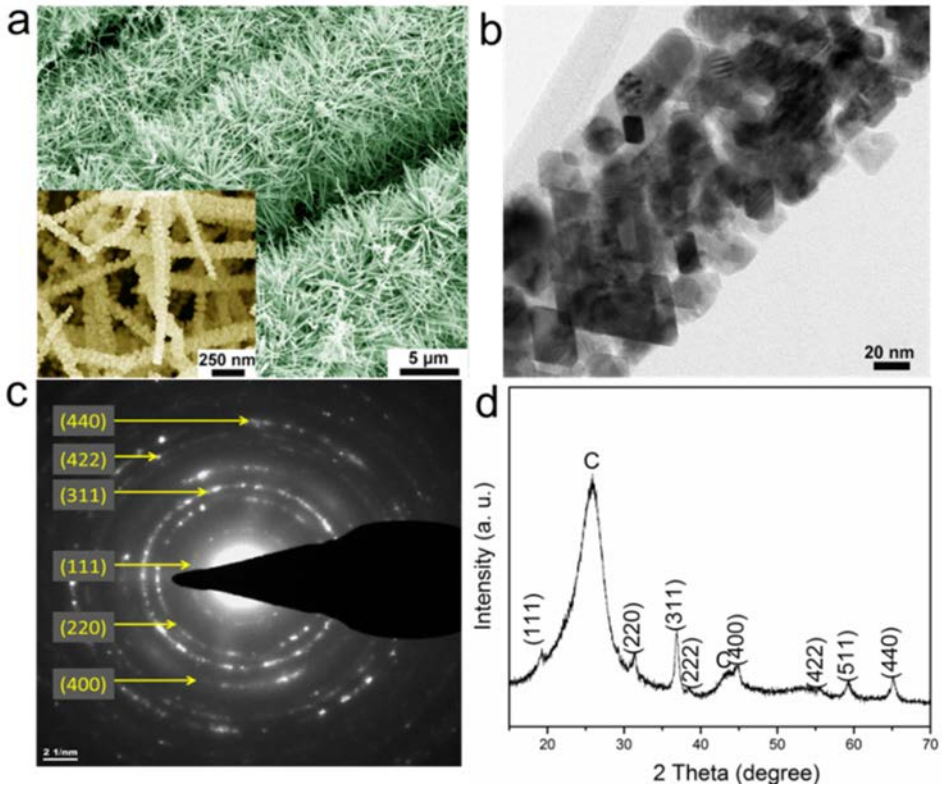

Figure V-309: Morphology and crystal structure characterizations of NCO/CF. (a) Scanning electron microscope (SEM) image of NCO NWs grown on CF; the inset is a high-magnification SEM image of NCO NWs. (b) Transmission electron microscope (TEM) image of a single NCO NW. (c) Selected area electron diffraction (SAED) pattern of NCO from its single NW. (d) X-ray diffraction (XRD) pattern of the resulting NCO/CF composite

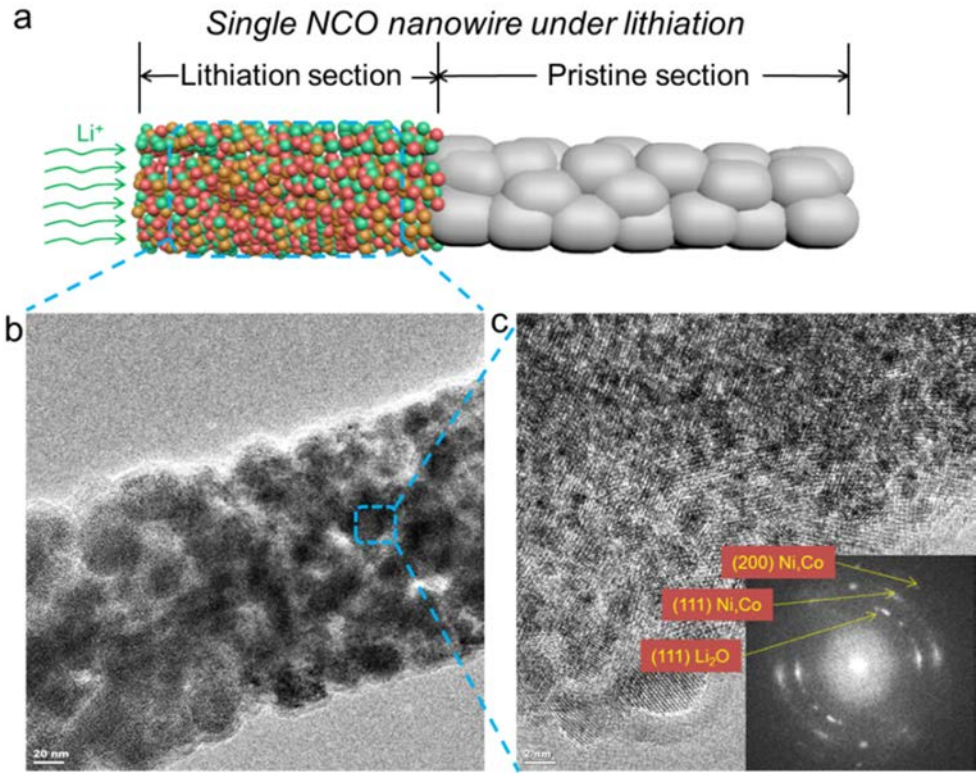

Figure V-310: Characterization of lithiated NCO NW. (a) Schematic illustration of NCO nanowire under lithiation. (b) TEM and (c) high-magnification TEM images of a selected lithiation area of NCO nanowire. Inset: SAED pattern of lithiated NCO

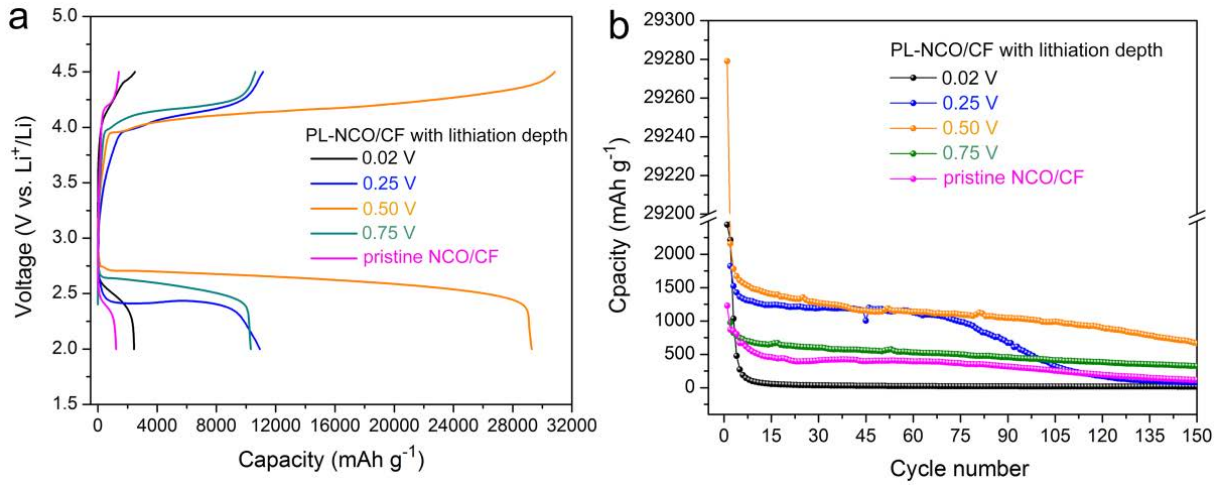

Figure V-311: Electrochemical characterizations of PL-NCO/CF air electrodes in Li–O_2 cells cycled at 0.1 mA cm^{-2}. (a) First-cycle discharge/charge profiles of as-prepared PL-NCO/CF air electrodes with different lithiation depths (0.02, 0.25, 0.50, and 0.75 V) and the pristine NCO/CF air electrode. (b) Cyclic stability of four PL-NCO/CF electrodes and the pristine NCO/CF electrode

2. Development of highly concentrated LiTFSI-DMSO electrolytes to improve stability of Li metal anodes and air electrodes for long-term cycling stability of Li-O_2 batteries

The effects of concentration of LiTFSI-DMSO electrolytes on the cycling performance of Li-O_2 batteries with CNTs/polyvinylidene fluoride/carbon-paper air electrodes were investigated. Three LiTFSI/DMSO electrolytes with mole ratios of 1:12 (1.0 M), 1:4, and 1:3 were studied. The capacity of Li-O_2 batteries was limitied to 600 mAh g^{-1} during cycling tests. As shown in Figure V-312, the LiTFSI-3DMSO electrolyte produced stable cycling for at least 90 cycles with minimal change in voltage profiles of the Li-O_2 battery. This good result can be attributed to the absence of free DMSO solvent molecules in this highly concentrated electrolyte. With a decrease in salt concentration, the cycling stability of the Li-O_2 cells degraded. Computational calculations show that the Gibbs activation energy barriers for C–H bond scission in DMSO, Li^+-$(DMSO)_4$, and $TFSI^-$-Li^+-$(DMSO)_3$ by the attack of $O_2^{\bullet-}$ are 192, 210, and 216 kJ mol^{-1}, respectively, indicating that the free DMSO solvent is not stable against $O_2^{\bullet-}$ but the DMSO in solvates or complexes is greatly stabilized. The air electrodes and Li metal anodes from cycled cells were analyzed after cleaning. Figure V-313 shows that the LiTFSI-3DMSO supports a well-protected CNT electrode and Li metal anode, while the other two electrolytes result in thick deposits on the air electrode and more serious corrosion of the Li anode, which are due to the decomposition of free DMSO by the attack of $O_2^{\bullet-}$ and the reaction of free DMSO with Li metal, respectively.

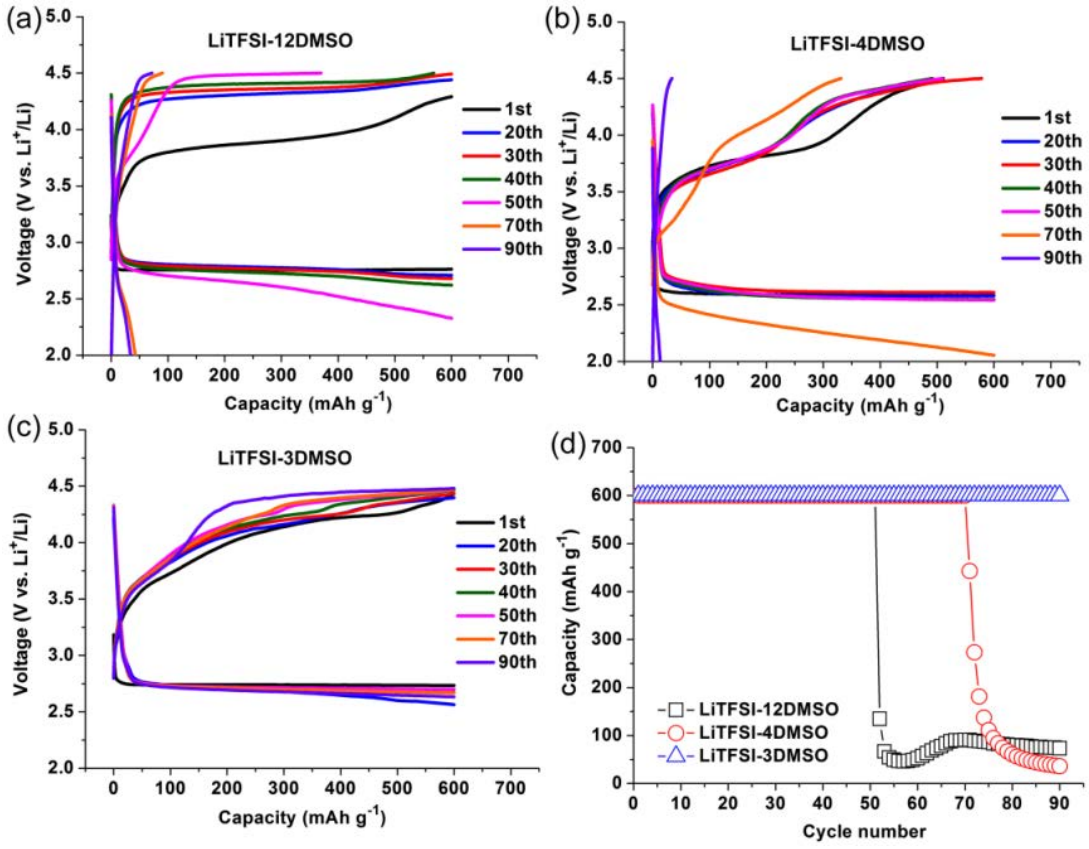

Figure V-312: Electrochemical performance of Li-O_2 batteries with three LiTFSI-DMSO electrolytes cycled under capacity-limited protocol (600 mAh g^{-1}) in the voltage range of 2.0 to 4.5 V at 0.1 mA cm^{-2}. a-c) Voltage profiles for a) LiTFSI-3DMSO electrolyte, b) LiTFSI-4DMSO electrolyte, and c) LiTFSI-12DMSO electrolyte. d) The corresponding cycling stability of the three electrolytes

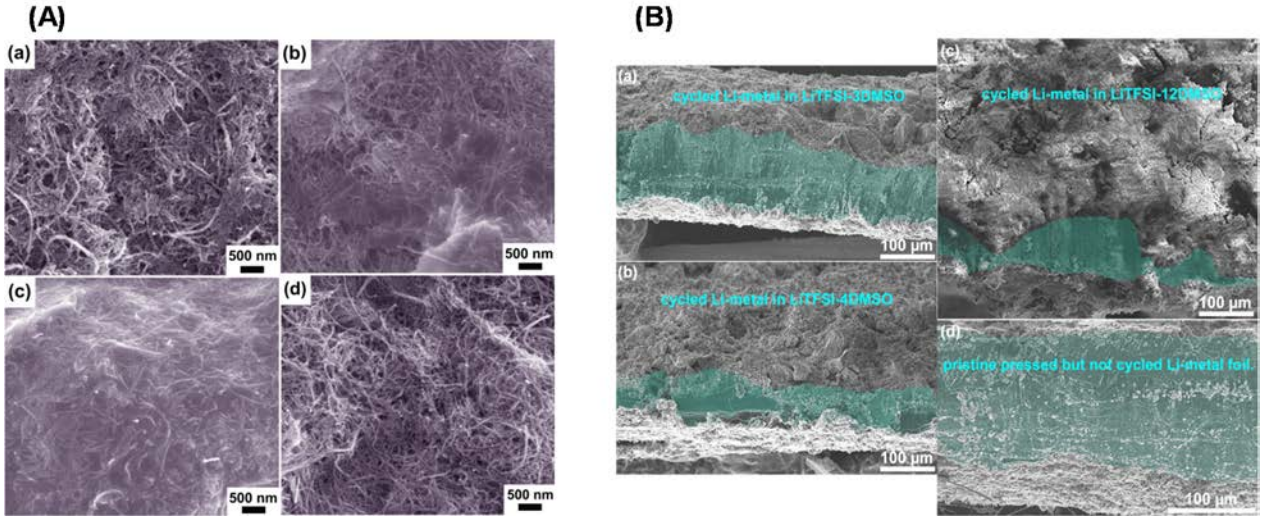

Figure V-313: SEM images of (A) CNT-based electrodes in top surface view and (B) Li metal anodes in cross-section view in charged state after 90 discharge/charge cycles with LiTFSI-3DMSO (a), LiTFSI-4DMSO (b), and LiTFSI-12DMSO (c), as well as the pristine CNT electrode without cycling (d)

3. Development of non-carbon air electrodes for long-term cycling Li-O_2 batteries

The electrochemical activity and chemical stability of boron carbide (B_4C) as a non-carbon-based oxygen electrode material for aprotic Li-O_2 batteries has been systematically investigated. XRD results indicate that B_4C nanoparticles are stable against Li_2O_2 and KO_2. Due to the relatively low electronic conductivity (~1 S cm^{-1}) and specific surface area (~12.5 m^2 g^{-1}) of B_4C powders, the content of nonconductive polytetrafluoroethylene (PTFE) binder was found to play an important role in the electrode performance, and the optimal PTFE content is 7 wt% in the B_4C/PTFE air electrode. Li-O_2 cells using the optimized B_4C-based air electrodes exhibit much better cycling stability than those using TiC- and CNT-based air electrodes in 1 M $LiCF_3SO_3$-tetraglyme electrolyte (Figure V-314). The performance degradation of the B_4C-based electrode is mainly due to the loss of active sites on the B_4C electrode during cycles, as identified by the structure and composition characterizations. The XRD results show that B_4C nanoparticles are stable after 250 cycles and almost no residues of Li_2O_2 and Li_2CO_3 are left on the electrode surface. The SEM image of the B_4C air electrode after 250 cycles shows a clean surface and nearly the same porous structure as those of the pristine electrode, indicating the good stability of the optimized B_4C/PTFE air electrodes. The x-ray photoelectron spectroscopy analysis of the cycled B_4C air electrode also shows no generation of B-O species. These results clearly demonstrate that B_4C is a very promising alternative oxygen electrode material for aprotic Li-O_2 batteries. It can also be used as a standard electrode to investigate the stability of electrolytes.

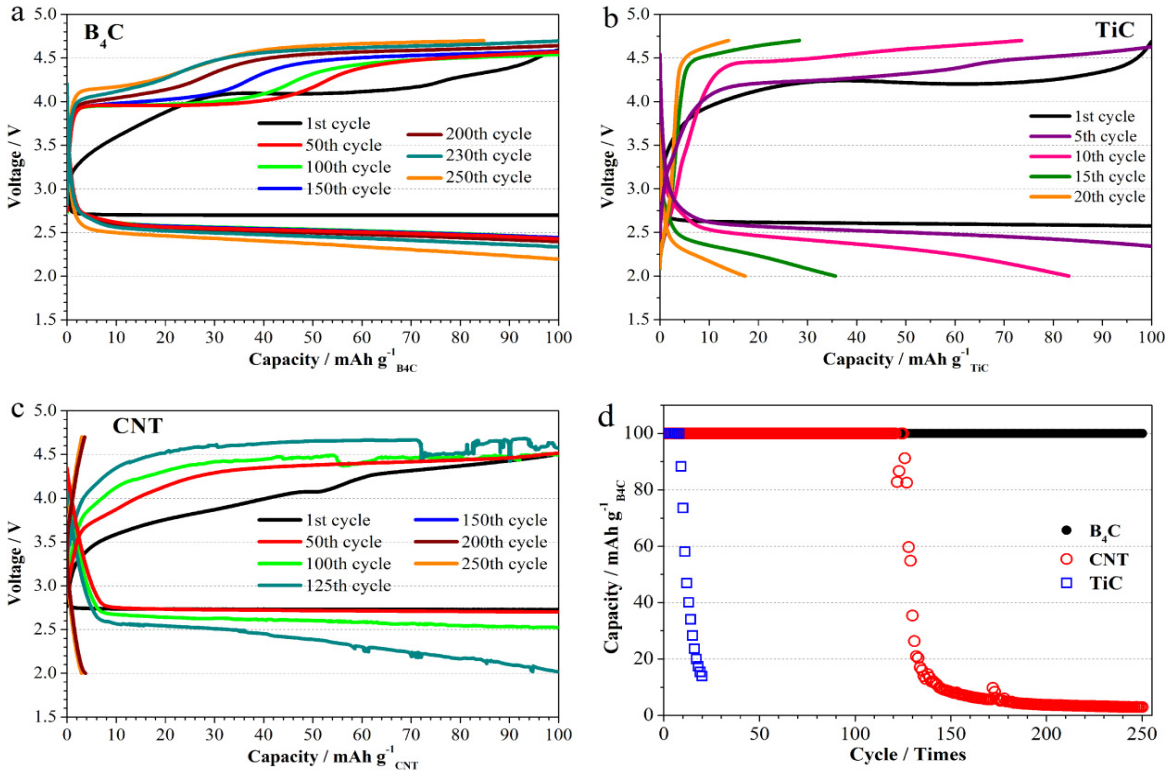

Figure V-314: (a-c) Discharge/charge profiles of Li-O_2 cells with different electrodes: (a) B_4C, (b) TiC, (c) CNT. (d) Discharge capacity with cycles for the three cells. The cells were tested under 100 mAh g^{-1} capacity limit at a current density of 0.1 mA cm^{-2} within the voltage range of 2.0~4.7 V

4. Protection of carbon air electrodes via simple *in situ* pretreatment for enhanced long-term cycling stability of Li-O_2 batteries

A lithiation method has been developed to treat the CNT-based air electrodes prior to cell assembly and to generate an ultrathin artificial layer on the air electrode surface. The pretreated CNT air electrodes (samples A, B, C, and D) show improved cycle life in Li-O_2 cells with the conventional 1.0 M LiTf-tetraglyme electrolyte under the 1000 mAh g capacity-limited test protocol (Figure V-315). The optimized pretreatment (sample C) can increase the stable cycle life of Li-O_2 cells to 110 cycles as compared to ~40 cycles for cells using pristine CNT electrodes.

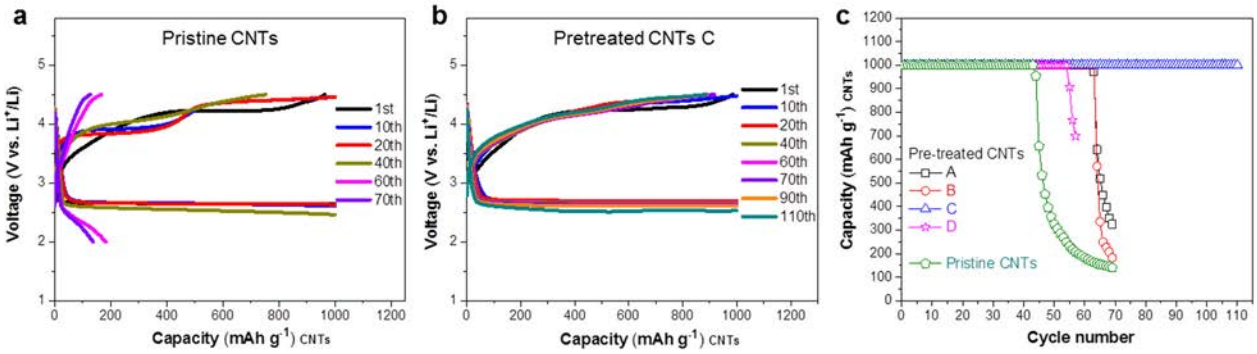

Figure V-315: Cycling performance of Li-O_2 cells with CNT-based air electrodes before and after pretreatment under 1000 mAh g^{-1} capacity limit at a current density of 0.1 mA cm^{-2} within the voltage range of 2.0~4.5 V. (a, b) discharge and charge profiles of pristine CNT electrode (a) and pretreated CNT electrode C. (c) Capacity with cycling of pristine CNT electrode and four pretreated CNT electrodes

Conclusions

We found that a highly concentrated LiTFSI-DMSO (mole ratio 1:3) electrolyte can greatly improve the stability of the electrolyte with Li metal anodes and reactive reduced oxygen species at the air electrode, so the Li-O_2 cells using this electrolyte have significantly improved cycling stability. We also developed binder-free air electrodes based on transition metal oxide nanowires/carbon-fiber composites after prelithiation treatment. The pre-lithiated NCO electrode can exhibit an ultrahigh capacity of up to 29,000 mAh g^{-1} in the first discharge/charge cycle and stable cycling at a capacity of 1000 mAh g^{-1} for 140 cycles. We also developed a simple *in situ* pretreatment method to protect CNT-based air electrodes, which results in greatly improved cycle life of the Li-O_2 cells based on the CNT air electrode. Furthermore, we showed that B_4C-based non-carbon air electrodes can significantly enhance the cycling stability of Li-O_2 cells as compared to TiC- and CNT-based air electrodes. These findings open new avenues for further development of aprotic Li-O_2 batteries with long cycle life.

Products

Presentations/Publications/Patents

1. B. Liu, P. Yan, W. Xu, J. Zheng, Y. He, L. Luo, M. E. Bowden, C.-M. Wang, and J.-G. Zhang, "Electrochemically formed ultrafine metal oxide nanocatalysts for high-performance lithium-oxygen batteries", *Nano Lett.*, 2016, **16**, 4932-4939.
2. B. Liu, W. Xu, P. Yan, X. Sun, M. E. Bowden, J. Read, J. Qian, D. Mei, C.-M. Wang, J.-G. Zhang, "Enhanced Cycling Stability of Rechargeable Li-O_2 Batteries Using High-Concentration Electrolytes", *Adv. Funct. Mater.*, 2016, **26**, 605-613.
3. S. Song, W. Xu, R. Cao, L. Luo, M. H. Engelhard, M. E. Bowden, B. Liu, L. Estevez, C.-M. Wang, and J.-G. Zhang, "B_4C as a stable and non-carbon based oxygen electrode material for aprotic lithium-oxygen batteries," poster presentation at *18th International Meeting on Lithium Batteries*, June 19-24, 2016, Chicago, Illinois.
4. S. Song, W. Xu, R. Cao, L. Luo, M. H. Engelhard, M. E. Bowden, B. Liu, L. Estevez, C.-M. Wang, and J.-G. Zhang, "B_4C as a stable and non-carbon based oxygen electrode material for aprotic lithium-oxygen batteries," poster presentation at *9th Symposium on Energy Storage beyond Lithium-Ion*, May 24-26, 2016, Richland, Washington.
5. B. Liu, W. Xu, P. Yan, M. H. Engelhard, X. Sun, D. Mei, S. T. Kim, J. Cho, C.-M. Wang, and J.-G. Zhang, "Optimization of concentrated DMSO-based electrolytes for stable cycling of Li-O_2 batteries," poster presentation at *9th Symposium on Energy Storage beyond Lithium-Ion*, May 24-26, 2016, Richland, Washington.
6. B. Liu, W. Xu, P. Yan, X. Sun, M. E. Bowden, J. Read, J. Qian, D. Mei, C.-M. Wang, J.-G. Zhang, "Enhanced Cycling Stability of Rechargeable Li-O_2 Batteries Using High Concentration Electrolytes," Poster presentation at *2015 MRS Fall Meeting & Exhibit*, Boston, MA, November 29 – December 4, 2015.

References

1. A. C. Luntz, B. D. McCloskey, *Chem. Rev*., 2014, **114**, 11721.
2. N. Feng, P. He, H. Zhou, *Adv. Energy Mater*. 2016, **6**, 1502303.
3. Y. Shao, F. Ding, J. Xiao, J. Zhang, W. Xu, S. Park, J. G. Zhang, Y. Wang, J. Liu, *Adv. Funct. Mater*., 2013, **23**, 987.
4. D. G. Kwabi, V. S. Bryantsev, T. P. Batcho, D. M. Itkis, C. V. Thompson, Y. Shao-Horn, *Angew. Chem. Int. Ed*., 2016, **55**, 1.

V.I.2. Efficient Rechargeable Li/O_2 Batteries Utilizing Stable Inorganic Molten Salt Electrolytes (Liox Power)

Vincent Giordani, Principal Investigator
Liox Power, Inc.
129 N Hill Avenue 107
Pasadena, CA 91106
Phone: 626-389-6311
E-mail: vincent@liox.com

Tien Q. Duong, DOE Program Manager
Advanced Battery Materials Research (BMR)
U.S. Department of Energy
Vehicle Technologies Office
1000 Independence Avenue, SW
Washington, DC 20585
Phone: 202-586-7836
E-mail: Tien.Duong@ee.doe.gov

Start Date: October 1, 2014
End Date: September 30, 2017

Abstract

Objectives

- The objective of this project is to develop high specific energy, rechargeable Li-air batteries having lower over-potential and improved robustness under ambient air compared to current Li-air batteries.
- The technical approach involves replacing traditional organic and aqueous electrolytes with a nonvolatile, inorganic molten salt comprising nitrate anions and operating the cell at elevated temperature (>80°C).
- The research methodology includes powerful *in situ* spectroscopic techniques coupled to electrochemical measurements (e.g. operando electrochemical mass spectrometry) designed to provide quantitative information about the nature of chemical and electrochemical reactions occurring in the air electrode.

Accomplishments

- We demonstrated a reversible Li/O_2 cell with a new morphology for lithium peroxide (publication in JACS, 2016).
- We screened numerous alternative O_2 cathode materials in replacement of unstable amorphous carbons. These include metal alloys, conducting ceramics and cermets, metal oxides.
- We introduced Iridium Oxide IrO_2 nanoparticles as the O_2 electrode material and demonstrated promising electrochemical performance.
- We showed that nickel nanoparticles catalyze the formation of lithium oxide discharge product and promote reversible nitrate reduction which provides new rechargeable battery chemistry based on the reaction between lithium and the nitrate anion (i.e., $2Li + NO_3^- = Li_2O + NO_2^-$ with E^0=2.45 V).

Future Achievements

- Demonstrate discharge specific energy and energy density ≥500 Wh/kg and ≥800 Wh/L, respectively, based on air electrode mass and volume.

- Study the Li/electrolyte interface and develop solid electrolyte membranes stable to Li to ensure chemical integrity and long cycle life for lithium metal.
- Demonstrate 10+ cycles at ≥90% round-trip energy efficiency in laboratory-scale Li-O_2 cells comprising a molten nitrate electrolyte and a protected Li anode.
- Fabricate and test 4 and 10 mAh cells.

Technical Discussion

Background

The rechargeable lithium-oxygen battery has attracted attention due to its large theoretical energy density compared to modern lithium-ion batteries. This large energy density is attributed to the reaction of lithium with molecular oxygen to form lithium peroxide, which grows on the surface of the cathode. While this is a promising chemistry, there are many practical challenges that remain to be solved, such as the decomposition of organic electrolyte in the presence of superoxide anions and large overpotentials on charge.

Introduction

We propose a system which inherently avoids many of the issues associated with organic electrolyte decomposition, while also forming lithium peroxide with a unique morphology. By using a $LiNO_3/KNO_3$ eutectic molten salt in place of a conventional solvent/salt electrolyte, solvent decomposition is obviated. In addition, the elevated temperature operation as well as the large concentration of Li^+ ions encourage faster diffusion and kinetics. This project aims at solving particularly intractable problems relating to air electrode efficiency, stability and tolerance to the ambient environment. Furthermore, these solutions may translate into reduced complexity in the design of a Li-air stack and system, which in turn may improve prospects for use of Li-air batteries in EVs. Additionally, the project provides materials and technical concepts relevant for the development of other medium temperature molten salt Li battery systems of high specific energy, which may also have attractive features for EVs.

Approach

Replace volatile, unstable and air-intolerant organic electrolytes common to prior research with inert molten nitrate electrolytes and operate cell above liquidus temperature (> 80°C). Improve reversibility and rate capability since discharge products (Li_2O_2, Li_2O, LiOH and Li_2CO_3) are stable and sparingly soluble in molten nitrate electrolytes. Combine quantitative gas analysis (pressure monitoring, mass spectrometry) with precise coulometry, as well as *in situ* spectroscopic techniques such as Raman to analyze air electrode processes.

Results

Identify non-carbonaceous stable air electrode materials

We have previously reported that the amorphous carbon air electrode was unstable in the molten salt Li/O_2 cell (lithium carbonate Li_2CO_3 gradually passivates the carbon surface and inhibit O_2 electroreduction) and was responsible for limited cycle life (~30 cycles). One of the key objectives within this project is to identify non-carbonaceous air electrode materials. We investigated the electrochemical behavior of commercially available metal nanopowders, namely, Fe, Ni, Co and Pt, as well as nanoporous Au, in molten salt Li/O_2 cells. Although some of these materials might not be practical because of their cost (Pt, Co and Au), fundamental understanding of the chemical interactions between the cathode material and the ORR products (O_2^-, LiO_2, and Li_2O_2) is necessary to develop suitable air electrodes. Nanoporous gold electrodes (A= 1 cm^2) were obtained from white gold leaf with Ag etched away in HNO_3 at 80°C. Nanoporous Au was presoaked in aqueous solution of nitrate eutectic mixture before careful drying at 200°C overnight. *in situ* pressure analysis coupled to mass spectrometry during battery 1st cycle (0.25 mA/cm^2) in $LiNO_3$-KNO_3 eutectic was used to determine e^-/O_2 and OER/ORR molar ratios. Preliminary results indicate $e^-/O_2 \neq 2$, for both discharge and charge, and OER/ORR equals to 0.77, suggesting gold tends to decompose during cycling. Results obtained using

transition metal nanopowder cathodes (Ni, Fe and Co) showed somewhat limited O_2 activity. We performed cyclic voltammetry measurements to quickly evaluate cathode material electrochemical behavior with and without O_2 gas in the head-space. (See Figure V-316.)

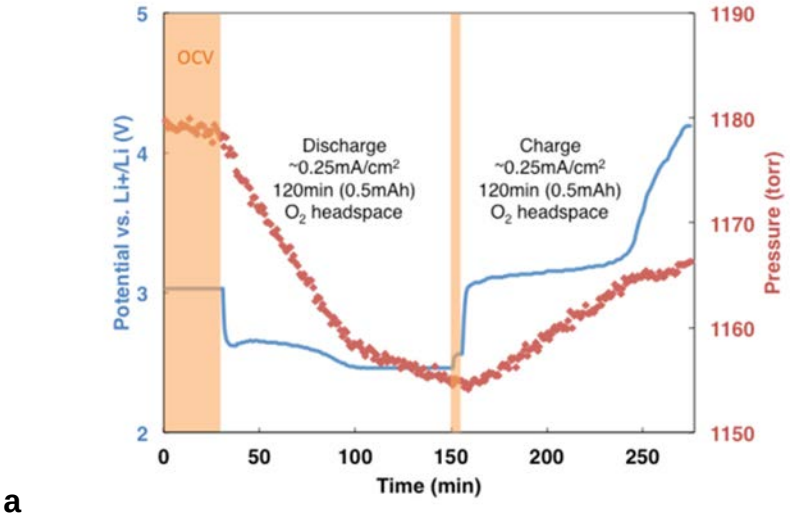

a

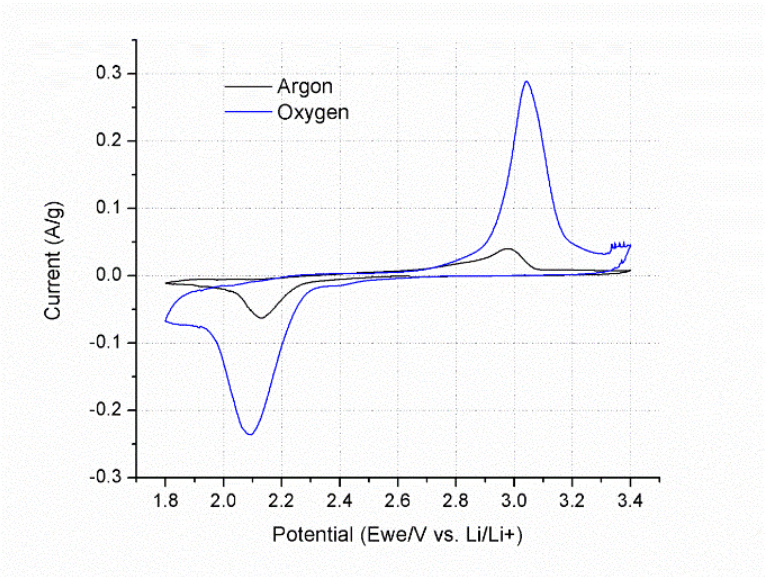

b

Figure V-316: a. Li/O_2 cell galvanostatic cycling (0.25 mA/cm²) in (Li-K)NO_3 eutectic at 150°C using nanoporous Au cathode. b. CV (0.1 mV/s) both under Ar and under O_2 for cells containing iron nanopowder cathode in (Li-K)NO_3 eutectic at 150 °C

Table V-16 summarizes e-/O_2 and OER/ORR molar ratios for electronically conductive ceramics and cermets-based cathode in Li/O_2 cells. Additional materials such as NbC, C_3N_4, SiN, TiN, LSM-YSZ, YSZ, SiB were also investigated, as the O_2 cathode material. Typically the cathode material powder was directly pressed onto a 10 mm OD stainless steel 316 mesh. Figures of Merit for this chemistry are e^-/O_2= 2.0 both on discharge and on charge (based on the cell discharge reaction: $2Li^+ + 2e^- + O_2 \rightarrow Li_2O_2$), and OER/ORR= 1 (overall cell cycling efficiency). Most reported materials showed $e^-/O_2 \neq 2.0$ and OER/ORR< 1, indicating existence of parasitic reactions during electrochemical cycling (e.g. cathode material chemical oxidation).

Table V-16: Molten Nitrate Li-O_2 Cell Characteristics: e^-/O_2 and OER/ORR Ratios.

O_2 electrode	$(e^-/O_2)_{discharge}$	$(e^-/O_2)_{charge}$	OER/ORR
Desired	**2.0**	**2.0**	**1.00**
Super P Carbon	2.0	2.1	0.73
Boron-doped Carbon Nanotubes	2.0	2.3	0.49
Reduced Graphene Oxide	1.8	8.8	0.07
Nickel	2.2	8.0	0.28
Gold	3.8	5.7	0.77
Palladium	2.5	No OER	N/A
IrO_2	2.2	2.2	0.95
RuO_2	3.0	10.0	0.30
LSM-Ni	1.2	No OER	N/A
TiC	No ORR	No OER	N/A

Air electrode based on IrO_2 nanopowders

IrO_2 nanopowder (~40 m^2/g BET surface area) was used as received from commercial source. Composite electrodes were prepared using a 78:2:20 wt.% of IrO_2, PTFE binder, and $LiNO_3$-KNO_3 eutectic, respectively. The mixture was coated on a stainless steel mesh and dried at 200°C for 1 day prior to battery electrochemical testing. The results demonstrate reversible electrode behavior under O_2, for a carbon-free cathode. The desired cell reaction: $2Li + O_{2(g)} = Li_2O_2$ has an equilibrium potential of 2.82 V at 150°C based on the Gibbs free energy of formation for lithium peroxide, which agrees with the median potential (*E* at i=0 on the anodic sweep) based on the CV curve. Typical voltage profile for molten nitrate Li/O_2 cell is observed (very small overpotentials, i.e. <100 mV) with pressure analysis showing O_2 consumption during discharge and O_2 release during charge. The Go/No-Go decision point consisted in demonstrating e^-/O_2=2 and OER/ORR ratio=1, +/- 5% and correcting for the effect of Li_2O_2 crossover. Precise O_2 quantification on the 1st cycle using pressure data and mass spectrometry revealed e^-/O_2 ratios of 2.2 for both the discharge and the charge half-cycle, and OER/ORR ratio equals 0.95. (See Figure V-317.)

Attempts to characterize the discharge product by XRD showed no crystalline Li_2O_2 on the surface of IrO_2, while SEM images recorded before (at OCV) and after a 2 mAh discharge under O_2 (to 2.6 V cutoff) showed formation of a nano-textured material referred as “platelets” on the IrO_2 particle surface. Additional characterization is needed to confirm whether amorphous Li_2O_2 or a mixed-valence oxide/peroxide (Li_xO_2) material is formed during ORR. Extended cycling data show stable peak-to-peak O_2 pressure, which cannot be achieved when Super P carbon is used as the air cathode. *In situ* mass spectrometry study during electrochemical cycling is currently ongoing to confirm O_2 is the only evolved gas during cell charging. (See Figure V-318.)

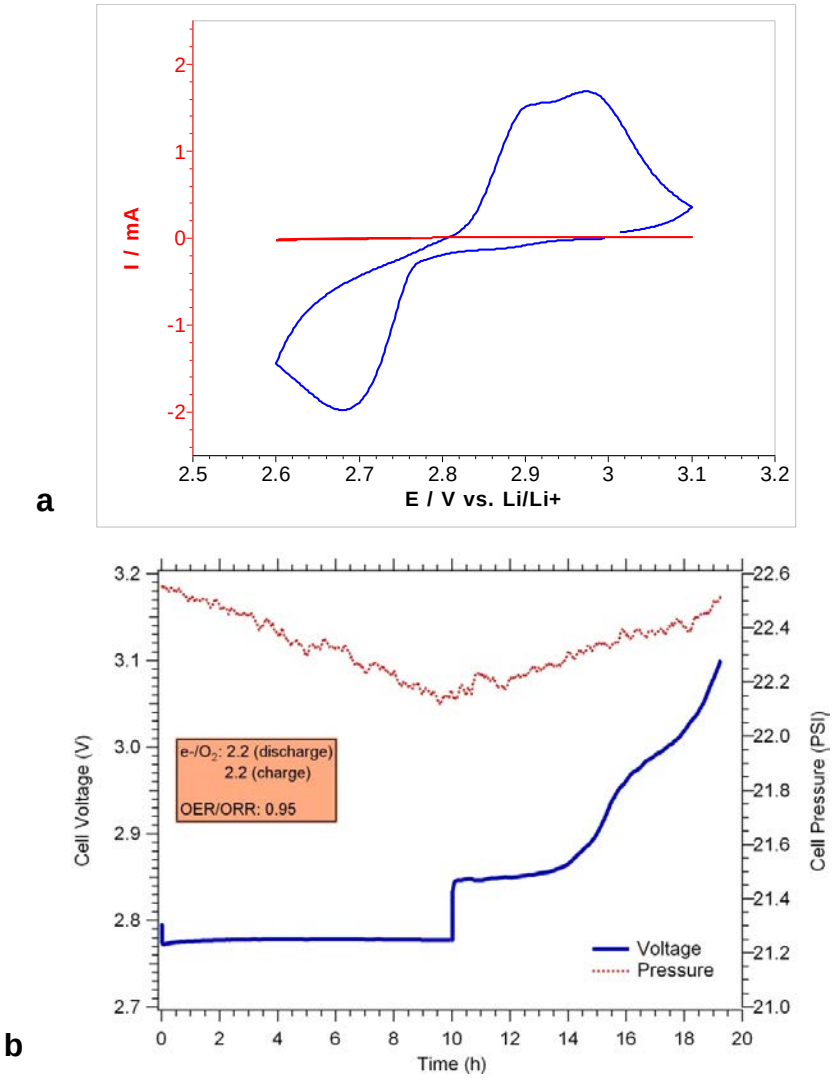

Figure V-317: a. Cyclic voltammetry curves for Li/O_2 cells (0.05 mV/s) in $(Li\text{-}K)NO_3$ eutectic at 150°C using IrO_2 cathode (red under Ar, blue under O_2). b. Li/O_2 cell voltage profile with *in situ* pressure monitoring (0.1 mA/cm^2) using IrO_2 nanopowder cathode in $(Li\text{-}K)NO_3$ eutectic at 150°C

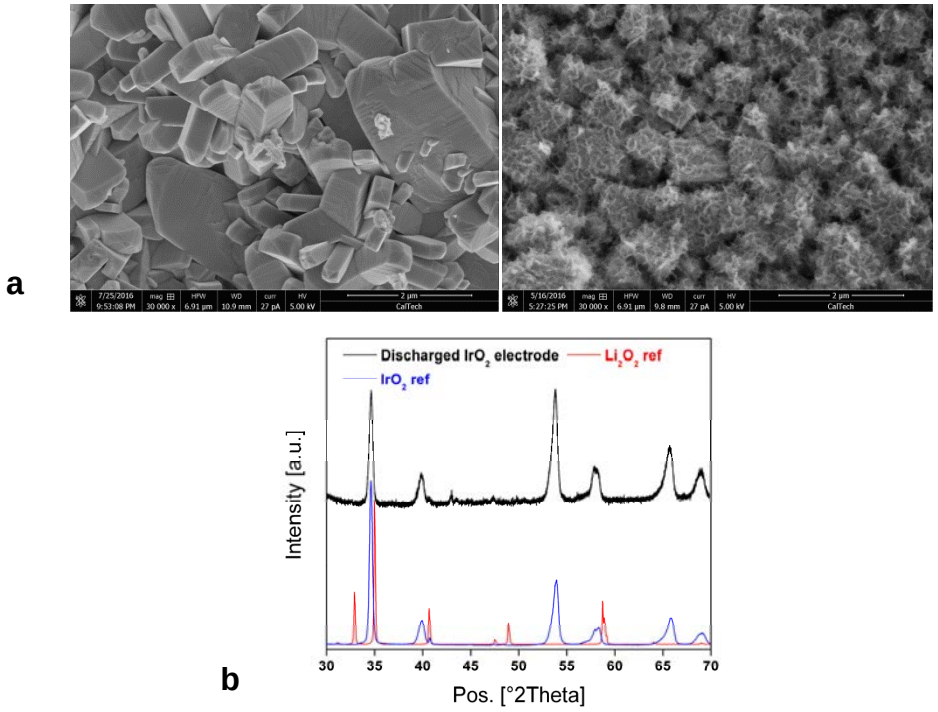

Figure V-318: a. IrO_2 air cathode SEM analysis: a) before discharge and b) following a discharge under O_2 to a 2.6 V cutoff. b. PXRD of IrO_2 nanopowder cathode following discharge under O_2

Optimizing electrode design for high rate capabilities

Power capability was assessed in Li/O_2 cells comprising a lithium anode, a molten nitrate electrolyte, and a Super P carbon:PTFE air cathode (pressed on a stainless steel mesh). Typical air electrode mass and volume was 4 mg (carbon + binder) and 7.8 mm^3 (1 cm diameter electrode, 100 microns thick), respectively. Potential step experiments were performed to measure the maximum attainable current (and associated peak power) for both the discharge and the charge process. Figure V-319 shows cell discharge and charge current variation with time, using a 2.72 V constant discharge voltage and a 2.92 V constant charge voltage, respectively (± 100 mV overpotential based on $E_{eq.(Li2O2)}$ = 2.82 V). Power (W) is given by the product of applied voltage and the electric current. Discharge specific power was found to be ca. 2500 W/kg while discharge power density being ca. 1280 W/L, respectively, based on air electrode mass and volume.

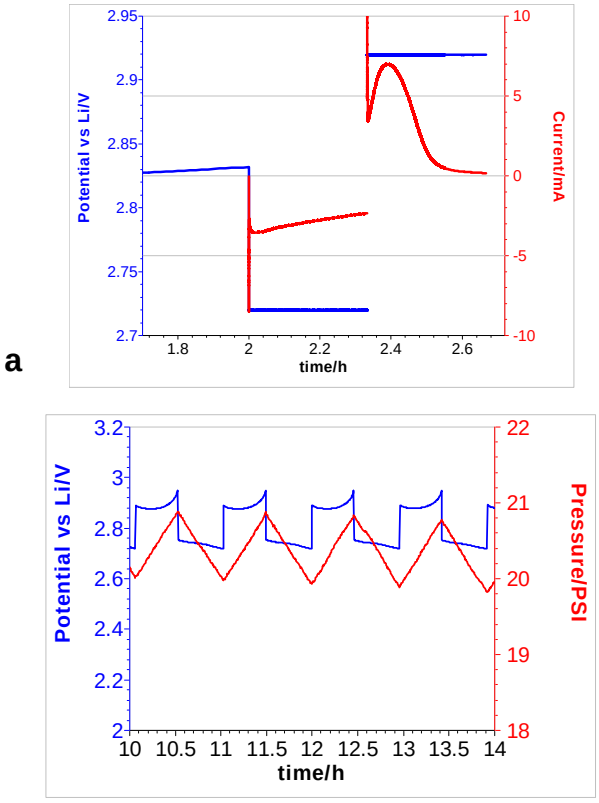

Figure V-319: a. Cell discharge/charge current variation with time (2.72 V constant discharge voltage/2.92 V constant charge voltage), under O_2 gas, at 150°C. b. Li/O_2 cell galvanostatic cycling in $LiNO_3$-KNO_3 at 150 °C under O_2 at 2 mA constant current (500 mA/g_{carbon} or 2.5 mA/cm^2 current density)

Of note, fairly high peak currents can be achieved during charge, consistent with fast kinetics for Li_2O_2 oxidation in the molten nitrate electrolyte. Cycling behavior at high rate is presently being investigated. Li/O_2 cells using the $LiNO_3$-KNO_3 molten salt electrolyte are cycled at 2 mA constant current. The typical pressure profile is observed with pressure loss during discharge due to oxygen consumption and pressure increase during charge due to oxygen evolution from lithium peroxide oxidation (Li_2O_2 = 2 Li + O_2).

Separately, nano-architectured nickel truss electrodes were prepared. The 3D electrodes, capable of accommodating battery discharge products, mitigate issues related to lithium peroxide solubility, and improve battery Coulombic efficiency. Architected cathode fabrication begins with writing a polymer template using 3D direct laser writing - the rastering of a two-photon photopolymerization process in 3D space. The resulting polymer template can then be coated in a material of choice (here sputtered nickel) or pyrolyzed into a conductive carbon. The Ni truss is directly written onto a nickel foil current collector. The goal for full sized cathode is a square of size 5x5 mm and about 100 microns tall with surface area increased by a factor of 4 compared to a foil (actual surface area is tunable, and depends on coating roughness). The key is to control pore volume to allow product growth, and mitigate Coulombic inefficiencies due to discharge product (i.e., Li_2O_2) electrical disconnection. (See Figure V-320.)

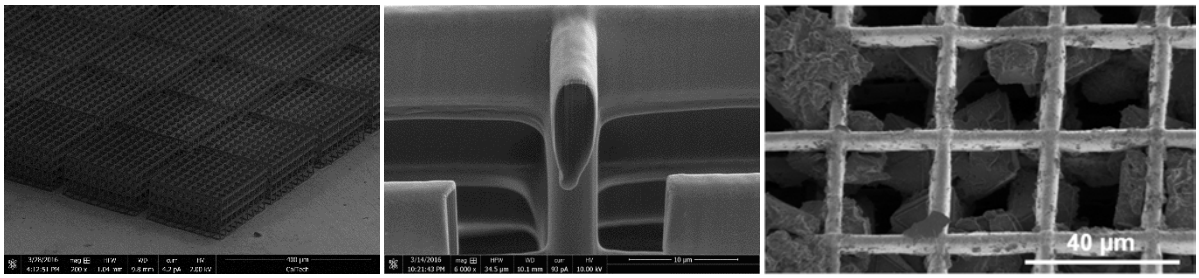

Figure V-320: SEM images of the as-prepared Ni truss nano-architectured electrode, cross-section of Ni-coated truss, and electrochemically discharged truss electrode showing ORR products growth

Li metal cycling and effect of Cs^+ cations

We investigated the electrochemical behavior of Li anodes in several different melt compositions. The anode SEI reaction can be written as follows: $2Li + NO_3^- = Li_2O + NO_2^-$. Li_2O passivates lithium metal while NO_2^- anion dissolves in the melt solution. Buildups of nitrite anion in solution can cause undesirable side reactions with lithium metal accompanied by gas evolution (e.g. NO). We found that ternary mixtures of alkali metal nitrate salts including $CsNO_3$ improve the Li/electrolyte interface. (See Figure V-321.)

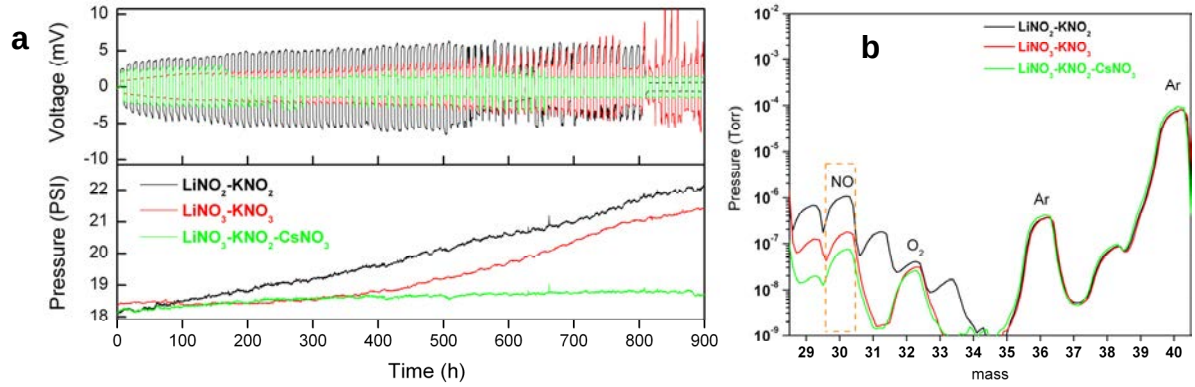

Figure V-321: a. Li/Li symmetric cell cycling at 150°C under Ar with *in situ* pressure analysis as a function of molten nitrate electrolyte. b. *Ex situ* gas analysis of cell head space (carrier gas: Ar) following cycling experiment (~ 1000 hours). Black: $LiNO_2$-KNO_2 eutectic. Red: $LiNO_3$-KNO_3 eutectic. Green: $LiNO_3$-KNO_2-$CsNO_3$ eutectic

Addition of $CsNO_3$ salt to the melt slows down electrolyte decomposition onto Li, as confirmed by mass spec showing a decrease in NO gas signal. Both cycling and pressure profiles demonstrate fairly stable Li/electrolyte interface when Li-K-Cs ternary mixture is used. Other research groups have reported the beneficial effect of cesium cations onto lithium metal cycling. Further investigation is currently ongoing.

Solid electrolytes for lithium anode protection

The chemical stability of ceramic electrolytes towards molten nitrate salts at 150°C for extended period of time (1-6 months) was investigated. Protected anodes are of potential interest in order to mitigate side reaction between the electrolyte and Li metal, leading to battery self-discharge. Different solid electrolyte samples were kept in contact with 1 g of melt at 150°C in a Swagelok cell and XRD was recorded once a month to monitor any change in the crystal structure, indicative of chemical reaction(s) with molten $LiNO_3$-KNO_3. Figure V-322 displays XRD patterns of solid electrolyte material at different aging times. One can clearly observe a peak shift which indicates possible cation swapping and change in the crystal lattice parameters. Additional materials are currently being prepared and more testing is underway to fully evaluate their stability in the molten salt electrolyte.

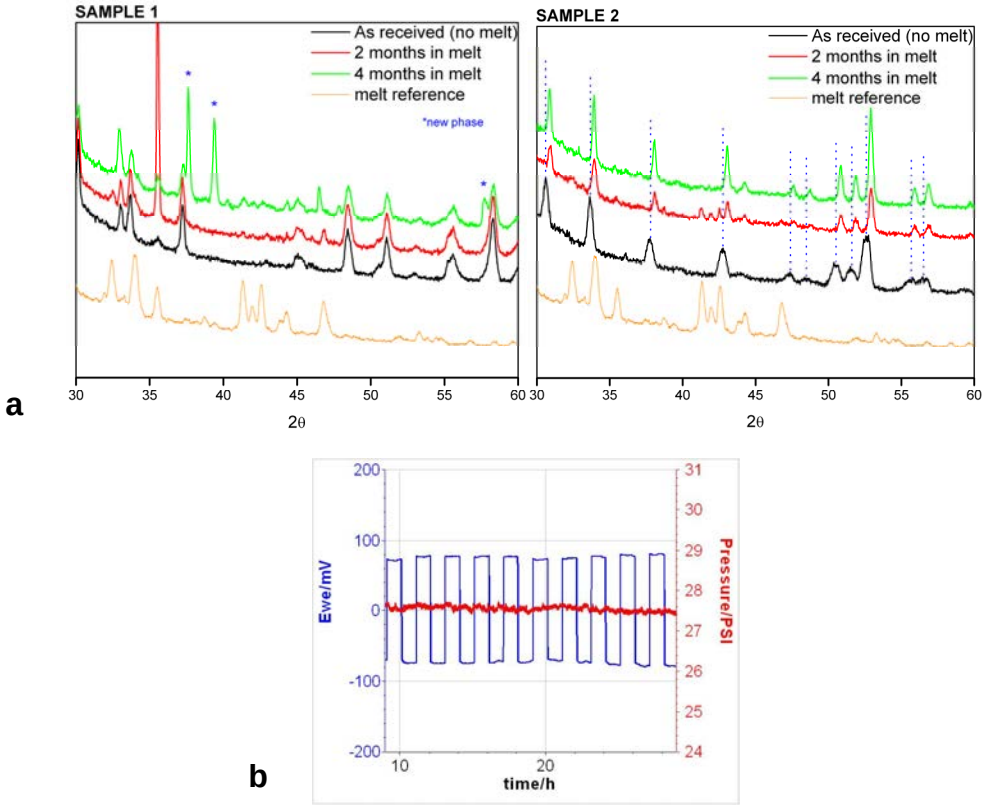

Figure V-322: a. XRD analysis of ceramic electrolytes (Sample 1: LATP, Sample 2: Garnet material) aged in $LiNO_3$-KNO_3 eutectic melt at 150° b. Li/Garnet Electrolyte/Li symmetric cell cycling at 150 °C (0.2 mA/cm^2), under Ar gas, with *in situ* pressure monitoring (Electrolyte thickness ~500 microns)

Conclusions

We investigated the oxygen electrochemistry in several different classes of material including oxidatively stable carbons, noble metals, metal oxides, conducting cermets and ceramics. Figures of merit e^-/O_2 and OER/ORR molar ratios were determined in order to identify suitable materials for the air electrode, compatible with the molten nitrate salts and chemically stable towards ORR products. Iridium oxide nanopowders were successfully implemented in Li-O_2 cells and demonstrated promising electrochemical performance. We designed new 3D nano-architectured cathodes (Ni and C nanotrusses) for discharge product accommodation and enhanced rate capability. Ceramic electrolytes including LATP type and Garnet type have been tested for lithium metal anode protection.

The pursuit of this project will include demonstrating high discharge specific energy and energy density (500 Wh/kg and 800 Wh/L, respectively), evaluating protected Li electrodes for elevated temperature operation, characterizing dendrite growth as a function of temperature and current density, scaling-up downselected cell components for 4 mAh and 10 mAh Li-oxygen cells.

Products

Presentations/Publications/Patents

Presentations

1. Cathode design for high energy molten salt lithium-oxygen batteries. ECS Prime Meeting, Honolulu, USA (2016).
2. Intermediate temperature molten salt lithium batteries, new chemistries and beyond. 18th IMLB, Chicago, USA (2016).
3. A catalytic molten salt electrode for lithium batteries. Gordon Research Conference - Batteries, Ventura, USA (2016).

Publications

1. A Molten Salt Lithium-Oxygen Battery. JACS **138** 2656-2663 (2016).

Patents

1. Intermediate temperature alkali metal/oxygen batteries employing molten nitrate electrolytes. J Uddin, D Addison, V Giordani, US Patent 2016/0049707 (2016).

V.I.3. Li-Air Batteries (ANL)

Khalil Amine, Principal Investigator
Argonne National Laboratory
9700 South Cass Avenue
Argonne, IL 60439-4837
Phone: 630-252-3838; Fax: 630-972-4520
E-mail: amine@anl.gov, and junlu@anl.gov

Larry Curtiss
Argonne National Laboratory
Material Science Division
9700 South Cass Avenue
Argonne, IL 60439-4837
Phone: 630-252-7380
E-mail: curtiss@anl.gov

Tien Q. Duong, DOE Program Manager
Advanced Battery Materials Research (BMR)
U.S. Department of Energy
Vehicle Technologies Office
1000 Independence Avenue, SW
Washington, DC 20585
Phone: 202-586-7836
E-mail: Tien.Duong@ee.doe.gov

Start Date: 2014
Projected End Date: 2018

Abstract

Objectives

- Develop stable electrolytes and new cathode architectures for lithium air batteries to lower the charge overpotential, improve the cell efficiency, and increase cycle life.
  - Gradual electrolyte decomposition (in particular in ether-based electrolytes) occurs in the presence of the reduced oxygen species, especially superoxide anion (O^{2-}).
  - Commonly used carbons and cathode catalysts do not access the full capacity of the oxygen electrode and cause significant charge overpotentials. This lowers efficiency and limits cycle life.
- Understand the oxygen crossover effect at the anode on the electrochemical performance of Li-air battery. Lithium electrode degradation due to oxygen crossover and reaction with the electrolyte destroys the integrity and functioning of the cell. This lowers cycle life.

Accomplishments

- Developed new cathode materials with improved transition metal-based catalysts for Li_2O_2 formation and decomposition with low charge potentials and increased cycle life.
- Our previous investigations of discharge product compositions with various catalyst has led to a new cathode material based on a Ir catalyst that can stabilize LiO_2 in the discharge product for the first time, which provides a new way to reduce charge overpotential.
- The evidence for the presence of lithium superoxide comes from an array of characterization techniques including Raman, EPR and DEMS. NMR, Raman, and FTIR are used to establish the stability of the ether based electrolyte.

- Computational studies have shown that an Ir_3Li intermetallic provides a lattice that promotes growth of the lithium superoxide and that the electrolyte can suppress the disproportionation reaction of crystalline lithium superoxide to lithium peroxide and oxygen.

Future Achievements

- New cathode materials with improved transition metal-based catalysts for low charge potentials and increased cycle life.
- Electrolytes with enhanced stability.
- Lithium anode protection strategies.
- New characterization techniques.

Technical Discussion

Background

Lithium-air batteries can be considered the 'holy grail' of lithium batteries because they offer, in principle, at least ten times the energy density of conventional lithium-ion systems.[1-4] The lithium-ion cell chemistry, the best to date, would provide a theoretical specific energy of ~900 Wh/kg if the calculation is based on the masses of the anode and cathode materials alone; in practice, 150-200 Wh/kg has been accomplished at the cell level.[5, 6] In contrast, a lithium-air cell, when discharged to Li_2O_2 at an average 3.1 V would provide a theoretical specific energy of 3623 Wh/kg, or when discharged to Li_2O at the same voltage, 5204 Wh/kg.[7] Note that gasoline (octane) offers a theoretical energy of ~13,000 Wh/kg if the mass of the injected oxygen is not considered in the calculation because it is supplied externally and combusted within, and exhausted from, the engine. By the same token, a lithium-air cell would offer a specific energy of ~11,000 Wh/kg if the 'free' oxygen supplied during discharge and released during charge is ignored in the calculation.

While the inherent energy potential of lithium metal approaches that of gasoline, today's battery manufacturers have not yet been able to unlock this potential. While today's lithium-ion batteries may provide acceptable power for hybrid electric vehicles (HEVs) and all-electric vehicles (EVs), they do not provide sufficient energy for an acceptable driving distance. This range limitation and the absence of a battery charging infrastructure have limited public interest in electric vehicles. A breakthrough in Li-air battery technology would significantly increase the possibility of extending the electric range of these vehicles with the added advantages of reducing battery cost and weight.

Introduction

This promising Li-air battery technology has many challenges and requires significant research efforts to meet these challenges and to unlock its full potential. The successful implementation of non-aqueous Li-air cells has been hampered because of severe materials problems that have limited electrochemical performance. These include (1) the non-aqueous electrolytes can be unstable under both the charge and discharge conditions, thereby seriously limiting cycle life; (2) during discharge, the solid and insoluble Li_2O_2 and/or other Li_2O products are deposited on the surface or within the pores of the carbon cathode, thereby passivating the surface as well as clogging the pores and restricting oxygen flow; (3) degradation of the lithium anode due to oxygen crossover destroys the integrity and functioning of the cell; and (4) commonly used transition metal cathode catalysts, do not access the full capacity of the oxygen electrode or enable sufficiently high rates.[8]

The team led by Dr. Khalil Amine and Dr. Larry Curtiss at Argonne National Laboratory (ANL) is working on problems that limit the electrochemical performance of the Li-air battery, including the stability of the organic electrolytes, cathode catalysts, and stability of the lithium anode under oxygen-crossover conditions. This effort will lead to the development of a reversible lithium air battery that provides much higher energy density than state-of-the-art lithium-ion battery for powering electric vehicles. The technology, if successful, can also benefit many military applications that require very high energy density such as satellite, military vehicles for silent watch and operation.

Approach

Issues that limit the performance of the Li-air battery include (1) electrolytes decomposition; (2) inefficient cathode materials; and (3) lithium electrode degradation. During the previous years of this project we made progress in finding cathode materials that result in lithium peroxide formation, which can reduce the charge overpotential that leads to the large inefficiencies in the performance of the Li-O_2 battery. Although the lower charge potential reduces sources of electrolyte instability, the cycle life remained poor. The possible reasons for this include other sources of electrolyte instabilities and cathode degradation leading to increased charge potentials with cycling.

This project addresses the cycle life problem of Li-air batteries through experimental and theoretical investigation of (a) the discharge formation mechanism and relationship to electrolytes, (b) investigation of the morphology and composition of the discharge product, and (c) investigation of electrolyte decomposition mechanisms. This understanding is being used to (1) develop new cathode materials to promote formation of discharge morphologies such as those involving superoxides with better conductivity to decrease charge overpotentials, (2) cathode and electrolyte materials that do not degrade with cycling and (c) electrolyte modification to protect the lithium anode.

The experimental work to create advanced electrolytes, carbons, catalysts, cathodes, and anodes is guided by theory and modeling. The experimental results will be thoroughly analyzed with very sophisticated analytical techniques and used to fine-tune the computational studies. Fundamental understanding of the underlying principles will be provided to greatly facilitate the next steps in the development cycle.

Results

New cathode materials with improved transition metal-based catalysts for Li_2O_2 formation

Uniformly dispersed Pd nanoparticles on ZnO-passivated porous carbon were synthesized via an atomic layer deposition (ALD) technique. The Pd and ZnO ALD process was carried out in a commercial bench top ALD reactor. Graphitized carbon black was used as the substrate. The ZnO was used to passivate carbon defect sites on the carbon surface to prevent electrolyte decomposition during cycling. Various numbers of ALD cycles of ZnO deposition was used in the synthesis. This was used to assess the dependence of the battery performance on the thickness of the passivation layer on the carbon. Transmission electron microscopy (TEM) was used to characterize the Pd/ZnO/C cathode materials as shown in Figure V-323. It showed discrete crystalline Pd nanoparticles decorating the surface of the ZnO-passivated porous carbon support in which the size of the nanoparticles ranged from 3-6 nm, depending on the number of Pd ALD cycles performed. X-ray absorption spectroscopy (XAS) at the Pd K edge revealed that the carbon-supported Pd existed in a mixed phase of metallic palladium and palladium oxide. The TEM images also showed a uniform dispersion of the Pd nanoparticles over the carbon substrate. It should also be pointed out that the porous structure of carbon is well preserved during the process of synthesizing Pd nanoparticles on the ZnO-passivated carbon samples by ALD. A well preserved porous structure with the appropriate pore size is needed for good electrochemical performance, since it is considered one of the factors that have significant impact on cell capacity and cycle life in Li-O_2 cells.

The Pd/ZnO/C cathode material was tested in a rechargeable Li-O_2 battery and it showed a highly active catalytic effect toward the electrochemical reaction—in particular, the oxygen evolution reaction. The electrochemical performance of these cathode architectures was evaluated in a Swagelok-type cell under one atm O_2 atmosphere with a MACCOR cycler. The cell consisted of a Li-foil anode, an as-prepared Pd/ZnO/C cathode and a TEGDME-LiCF_3SO_3. As shown in Figure V-324 the performance of the Li-O_2 cell is significantly improved when Pd nanoparticles on ZnO-passivated carbon is used as the electrocatalyst. The Pd based cathode not only contributes to a higher capacity by providing more active sites for the ORR reaction, but also leads to a different morphology of the discharge products. The results also showed that the ALD Pd/ZnO tandem bilayer on carbon is an effective cathode architecture for significantly decreasing the charge potential of Li-O2 batteries, which leads to a high round-trip efficiency of the cell. Finally, it should also be pointed out that the cells with a Pd/ZnO/C-based cathode started to fade with relatively short discharge/charge cycles, even under the capacity-controlled mode. The reason for this is the accumulation of LiOH on the lithium anode due to the oxygen-crossover. A large number of microscopic ‘tunnels’ exist within the LiOH

layer, which provide a pathway for sustained ion transport by enabling the connection of lithium with the electrolyte. This results in the complete degradation of the Li anode by the corrosion of the oxygen.

Ir catalyst that stabilizes lithium superoxide

Two cathode materials were studied: one based on reduced graphene oxide (rGO) and the other based on rGO with added Ir nanoparticles. SEM images of the pristine rGO and Ir-rGO composite reveal porous 3-dimensional (3D) networks of rGO composed of wrinkled 2D rGO sheets. TEM images of the Ir nanoparticles on rGO are shown in Figure V-325 and indicate that the well-dispersed Ir nanoparticles decorated on rGO are very small (<2 nm) with evidence for the presence of some small Ir clusters. A backscattering image shows some scattered larger Ir particles of about 500 nm in size, which may be due to agglomeration of the smaller nanoparticles, and Fast Fourier Transform analysis of HR-TEM images show that the nanoparticles are Ir. An XPS analysis indicates the Ir surface is only partially oxidized.

The performance of the rGO and Ir-rGO cathodes was examined using a lithium metal anode, electrolyte (1M $LiCF_3SO_3$ in tetraethylene glycol dimethyl ether (TEGDME), and a porous cathode. Figure V-326a and Figure V-326b show voltage profiles for the Ir-rGO and rGO cathode architectures, respectively. The Ir-rGO discharge product shows a very low charge potential of ~3.2 V that rises to 3.5 V over 40 cycles leading to over 85% efficiency in this system. The voltage profile of the rGO cathode shows a much larger charge potential of ~4.2 V with lower efficiency of ~67%.

The HE-XRD pattern for the discharge product on the Ir-rGO cathode (1000 mAh/g capacity) during the first cycle shows peaks corresponding to crystalline LiO_2 [(101), (111), (120)], and no evidence for peaks corresponding to Li_2O_2. The identification of the LiO_2 peaks is based on a theoretical XRD pattern derived from our DFT predicted crystalline LiO_2 structure since no experimental XRD pattern has been reported. The LiO_2 structure is orthorhombic. The standard Li_2O_2 XRD pattern was used to determine the absence of Li_2O_2.

This is the first time that crystalline LiO_2 was stabilized in a Li-O_2 battery, with no evidence for the presence of Li_2O_2 from various characterization techniques. A novel templating growth mechanism involving the use of Ir nanoparticles on the cathode surface may be responsible for the crystalline LiO_2 growth. Our results demonstrate that the LiO_2 formed in the Li-O_2 battery is stable enough that it can be repeatedly charged and discharged with a very low charge potential. We anticipate that this discovery will lead to future research into methods to synthesize and stabilize LiO_2. This can open the avenue for high-energy density lithium superoxide-based batteries as well as other potential uses such as a source of oxygen storage.

Characterization of lithium superoxide and electrolyte stability in the Ir-rGO Li-O_2 cell

Further evidence for the presence of LiO_2 was obtained from Raman, EPR and differential electrochemical mass spectrometry (DEMS) measurements. The stability of the lithium superoxide in the tetraglyme/LiTFSI electrolyte used in the cell was investigated using Raman spectroscopy. The Raman spectra of the discharge product of the Ir-rGO cathode in Figure V-327 shows the presence of a 1123 cm^{-1} peak, consistent with the range of values that have been observed for superoxide stretching frequencies.

We have also carried out EPR measurements and find a signal that is consistent with the presence of LiO_2 shown in Figure V-328 in the initial discharge product of the cell using the Ir-rGO cathode Figure V-328 reveals a new peak at 3193 G due to LiO_2 that is not present in the cathode without the discharge product. There is no EPR experimental data for orthorhombic LiO_2 so we have calculated EPR parameters and they are qualitatively consistent with the experimental position.

This stability of the TEGDME electrolyte in the presence of superoxide was confirmed by experimental investigations of the electrolyte performance in this cell. In this work we used various techniques to detect potential decomposition products after various amounts of cycling. The Li-O_2 cell based on Ir-rGO cathode material can cycle for 40 or more cycles before failure, similar to what has been found for Li_2O_2 based Li-O_2 cells. The failure is likely due to lithium anode degradation. There is little evidence of any side reactions in the Raman data for the first discharge cycle, from Raman and FTIR data after charging for up to 30 cycles, or from NMR data up to 20 cycles, although there could be a decomposition products not detected. The stability confirms our computational studies that predict the decomposition of the TEGDME electrolyte is unlikely under these conditions. The FTIR and Raman results also confirm that the discharge product is gone after

charging. Issues with electrolyte stability and decomposition most likely still remain, similar to the electrolytes used for other Li-O_2 systems, but they do not seem any worse.

We have also derived a possible mechanism for the formation of the lithium superoxide. Based on density functional calculations we have found that there is a good lattice match of crystalline LiO_2 with an Ir_3Li intermetallic component of the cathode can act as a template for electrochemical nucleation/growth of crystalline LiO_2. The Ir_3Li intermetallic is found in electron diffraction patterns in TEM studies. In addition, the computational studies show the stabilization of the LiO_2 is aided by the formation of crystalline LiO_2 and the presence of an electrolyte at the interface, which suppress disproportionation.

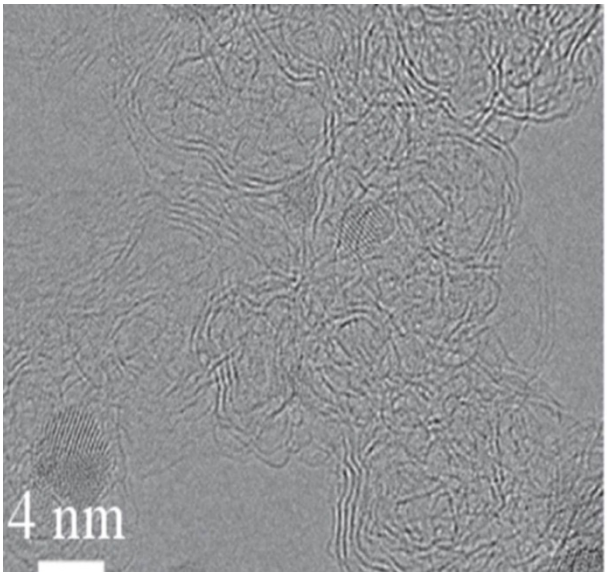

Figure V-323: SEM image of 3c-Pd/2c-ZnO/C sample (c refers to number of ALD cycles)

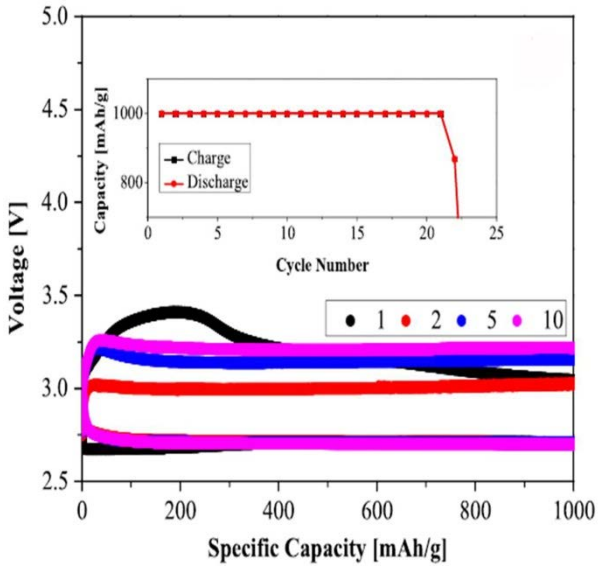

Figure V-324: Voltage profile for 13c-Pd/2c-ZnO/C sample (c refers to number of ALD cycles)

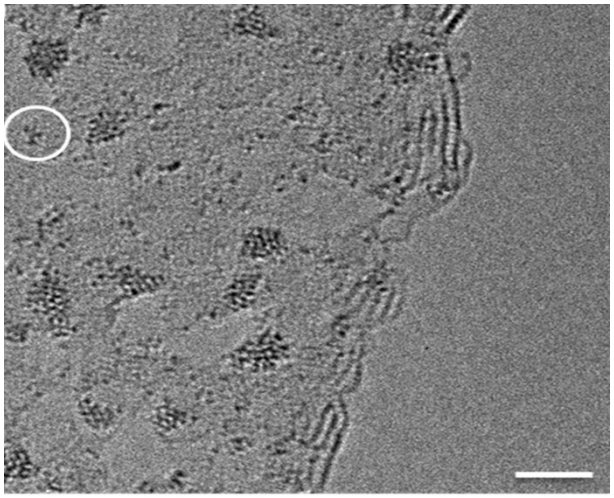

Figure V-325: TEM Image of Ir nanoparticles on an rGO surface. Scale bar is 2 nm

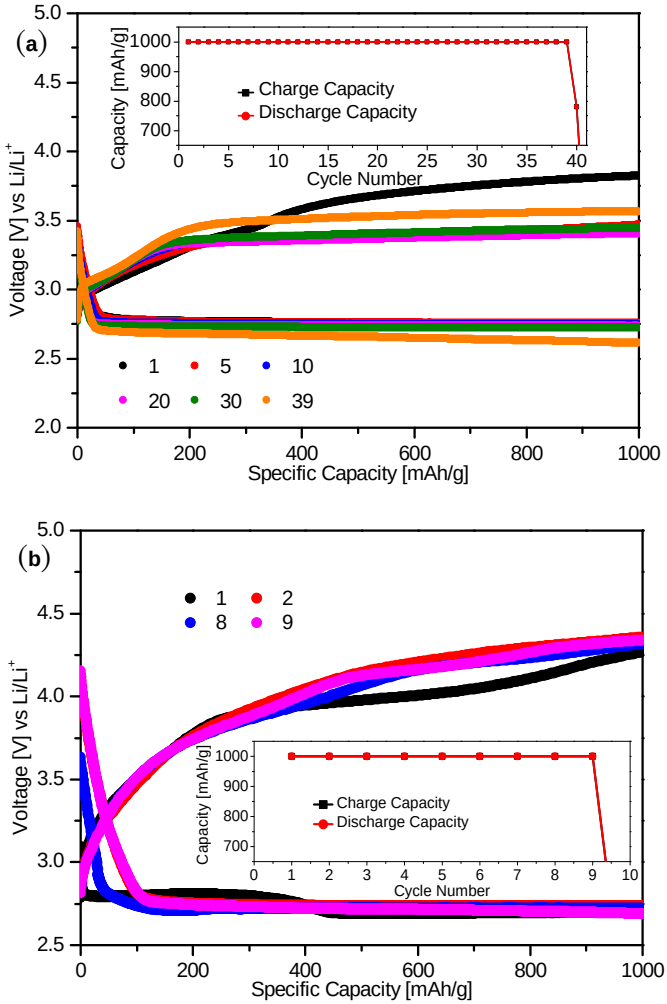

Figure V-326: Voltage profiles for (a) Ir-rGO and (b) rGO

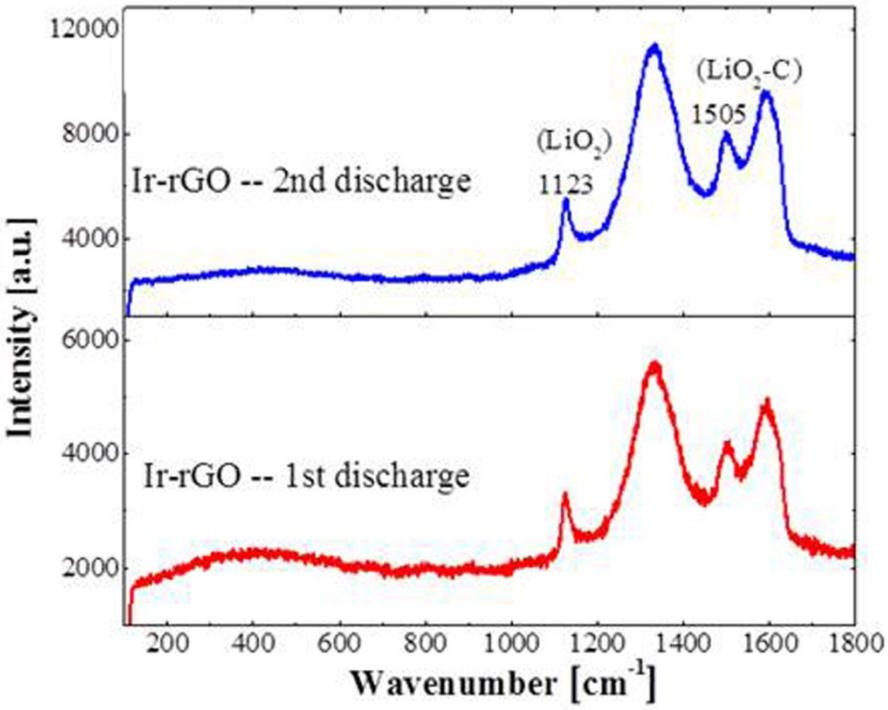

Figure V-327: Raman spectra of the Ir-rGO cathode after 1st and 2nd discharge in the Li-O2 cell

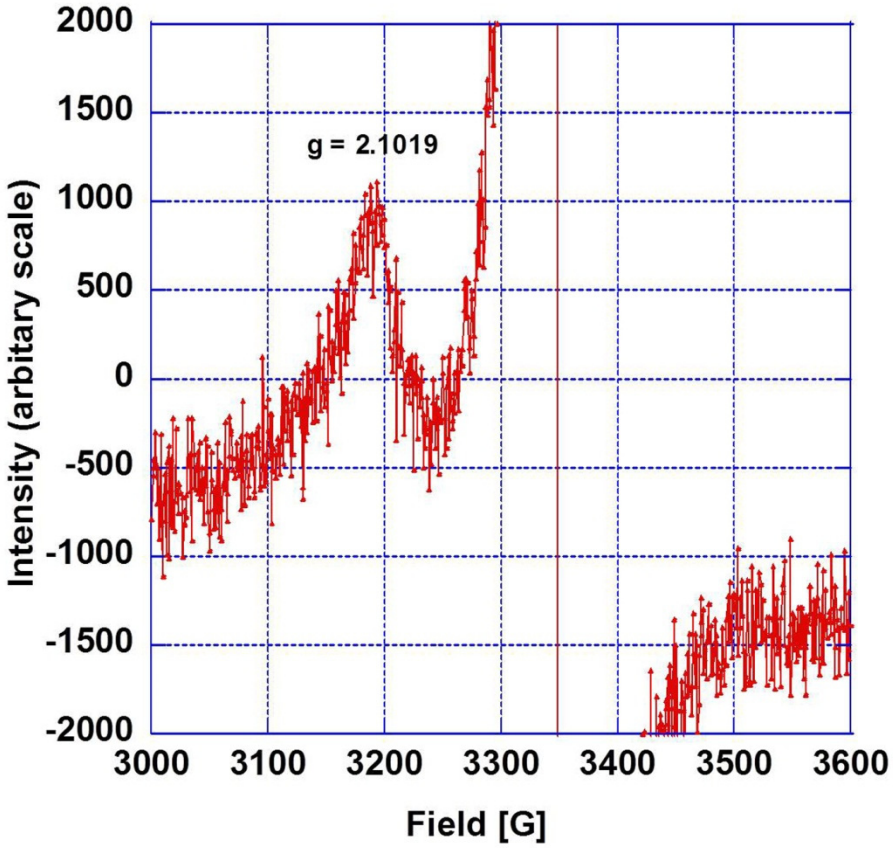

Figure V-328: EPR spectra of the discharge product on the Ir-rGO cathode in the Li-O_2 cell

Conclusions

In this project, an integrated experimental and theoretical approach was used to address the technical barriers for non-aqueous Li-air battery. This project addresses the cycle life and energy density of Li-air batteries through investigation of (a) the discharge formation mechanism and relationship to electrolytes, (b) investigation of the morphology and composition of the discharge product, and (c) investigation of electrolyte decomposition mechanisms.

Accomplishments during the past year include:

- Developed new cathode materials with improved transition metal-based catalysts for Li_2O_2 formation and decomposition with low charge potentials and increased cycle life.
- Our previous investigations of discharge product compositions with various catalyst has led to a new cathode material based on a Ir catalyst that can stabilize LiO_2 in the discharge product for the first time, which provides a new way to reduce charge overpotential.
- The evidence for the presence of lithium superoxide comes from an array of characterization techniques including Raman, EPR and DEMS. NMR, Raman, and FTIR are used to establish the stability of the ether based electrolyte.
- Computational studies have shown that an Ir_3Li intermetallic provides a lattice that promotes growth of the lithium superoxide and that the electrolyte can suppress the disproportionation reaction of crystalline lithium superoxide to lithium peroxide and oxygen.

Future research will focus on an integrated effort on finding cathode and electrolyte materials that will increase the cycle life and energy density of the Li-O_2 battery.

Products

Presentations/Publications/Patents

Publications/Patents

1. A Lithium-Oxygen Battery Based on Lithium Superoxide J. Lu, Y. J. Lee, X. Luo, K. C. Lau, M. Asadi, H.-H. Wang, S. Brombosz, J. G. Wen, D. Zhai, Z. Chen, D. J. Miller, Y. S. Jeong, J.-B. Park, Z. Z. Fang, B. Kumar, A. Salehi-Khojin, Y.-K. Sun, L. A. Curtiss, K. Amine, Nature 529, 377 (2016).
2. "Insight into the Catalytic Mechanism of Bimetallic Platinum-Copper Core-Shell Nanostructures for Nonaqueous Oxygen Evolution Reactions," L. Ma, X. Luo, A. J. Kropf, J. Wen, X. Wang, S. Lee, D. J. Myers, Dean Miller, T. Wu, J Lu, and K. Amine, Nano Lett. 16 (1), 781-785 (2016).
3. "Uniformly dispersed FeOx atomic clusters by pulsed arc plasma deposition: An efficient electrocatalyst for improving the performance of Li-O2 battery," X. Luo, J. Lu, E. Sohm, L. Ma, T. Wu, J. G. Wen, D. Qiu, Y. Xu, Y. Ren, D. J. Miller, K. Amine, Nano Res. 9, 1913 (2016).
4. Concentrated Electrolyte for the Sodium-Oxygen Battery: Solvation Structure and Improved Cycle Life, M. He, K. C. Lau, X. Ren, N. Xiao, W. D McCulloch, L. A. Curtiss, Y. W, Angew. Chem. Int. Ed. 128, 15536 (2016).
5. Lithium-air batteries having ether based electrolytes, K. Amine, L. A. Curtiss, J. Lu, K. C. Lau, Y.-K Sun, Patent No. 8,968,941.

Invited Talks

1. L. A. Curtiss, "Computational Studies of Catalytic Materials for Li-O2 Batteries," Pacifichem, Dec. 15-20, 2015, Honolulu, HA.
2. L. A. Curtiss, "Computational Insight and Design of Cathodes Materials and Electrolytes for Li-O2 Batteries, ECS Meeting, October 11-15, 2015 Phoenix AZ.
3. L. A. Curtiss, "Subnanometer metal clusters as catalysts in Li-O2 batteries", International Symposium on Clusters and Nanomaterials (ISCAN), October 26-29, 2015, Richmond, VA.

4. L. A. Curtiss, “The Role of Lithium Superoxide in Li-O2 Batteries,” International Meeting on Lithium Batteries, June 19-24, 2016, Chicago, IL.
5. “Subnanometer metal clusters as electrocatalysts in Li-O2 batteries,” L. A. Curtiss, Cluster Surface Interactions Workshop, June 1-3, 2016, Argonne National Lab, Argonne, IL.
6. “Insight into the Role of Lithium Superoxide in Li-O2 Electrochemistry from Spectroscopic Studies,” L. A. Curtiss, 24th Austin Symposium on Molecular Structure and Dynamics at Dallas, March 5-7, 2016, Dallas, TX.

References

1. Peng, Z.; Freunberger, S. A.; Chen, Y.; Bruce, P. G. *Science* **2012**, 337, 563-566.
2. Jung, H. G.; Hassoun, J.; Park, J. B.; Sun, Y. K.; Scrosati, B. *Nat. Chem.* **2012**, 4, 579-585.
3. Oh, S. H.; Black, R.; Pomerantseva, E.; Lee, J. H.; Nazar, L. F. *Nat. Chem.* **2012**, 4, 1004-1010.
4. Thotiyl, M. M. O.; Freunberger, S. A.; Peng, Z. Q.; Chen, Y. H.; Liu, Z.; Bruce, P. G. *Nat. Mater.* **2013**, 12, 1049-1055.
5. Girishkumar, G.; McCloskey, B.; Luntz, A. C.; Swanson, S.; Wilcke, W. J. *Phys. Chem. Lett.* **2010**, 12193 2203.
6. Armand, M.; Tarascon, J. M. *Nature* **2008**, 451, 652-657.
7. Lu, J.; Li, L.; Park, J.-B.; Sun, Y.-K.; Wu, F.; Amine, K. *Chem. Rev.* **2014**, 140411104032007.
8. Bruce, P. G.; Freunberger, S. A.; Hardwick, L. J.; Tarascon, J. M. *Nat. Mater.* **2012**, 11, 19-29.

V.J. Sodium-Ion Batteries

V.J.1. Exploratory Studies of Novel Sodium-ion Battery Systems (BNL)

Xiao-Qing Yang, Principal Investigator
Brookhaven National Laboratory
Chemistry Division
Bldg. 555
Upton, NY 11973
Phone: 631-344-3663; Fax: 631-344-5815
E-mail: xyang@bnl.gov

Xiqian Yu, Co-Principal Investigator
Brookhaven National Laboratory
Chemistry Division
Bldg. 555
Upton, NY 11973
Phone: 631-344-4142; Fax: 631-344-5815
E-mail: xyu@bnl.gov

Tien Q. Duong, DOE Program Manager
Advanced Battery Materials Research (BMR)
U.S. Department of Energy
Vehicle Technologies Office
1000 Independence Avenue, SW
Washington, DC 20585
Phone: 202-586-7836
E-mail: Tien.Duong@ee.doe.gov

Start Date: October 1, 2015
End Date: September 30, 2016

Abstract

Objectives

- To establish and investigate the structural changes of new tunnel structured $Na_{0.44}[Mn_{0.44}Ti_{0.56}]O_2$ as anode material for Na-ion batteries during charge-discharge cycling.
- To evaluate and study the electrochemical performance of anew O3-type layer-structured metal oxide cathode $Na(NiCoFeTi)_{1/4}O_2$ for sodium ion batteries.
- To provide valuable information about how to design thermally stable cathode materials for Na batteries for HEV and PHEV applications.
- To develop new *in situ* diagnostic techniques with surface and bulk sensitivity for studying the structural changes of various anode and cathode materials for Na batteries.
- To develop *in situ* diagnostic techniques with surface and bulk sensitivity to improve the calendar and cycle life of batteries by studying the mechanism of capacity and power fading of Na-ion and Na metal batteries.

Accomplishments

- Through collaboration with Prof. Yongsheng Hu at Institute of Physics, Chinese Academy of Sciences, the structural changes in a new cathode materials $Na_{0.44}[Mn_{0.44}Ti_{0.56}]O_2$ during Na insertion and extraction were studied using *in situ* XRD experiment. The results show continuous peak shift

during Na insertion/extraction but no new phase formation upon Na insertion/extraction into/from $Na_{0.44}[Mn_{0.44}Ti_{0.56}]O_2$ in a wide Na content range was observed. Although a significant amount of Mn3+ was reserved in $Na_{0.44}[Mn_{0.44}Ti_{0.56}]O_2$ structure for the entire range of electrochemical cycles, the main crystal structure was maintained during the entire charge/discharge process without any obvious structure transformation. This is further supported by *ex situ* STEM results. The results of this study were published on *Nature communications*.

- Through collaboration with Prof. Yuguo Guo at Institute of chemistry, Chinese Academy of Sciences, Structure evolution of sodium iron ferrocyanide (Prussian Blue Analogous) as cathode materials for Na-ion batteries has been studied using *ex situ* X-ray absorption near edge spectroscopy (XANES) and Extended X-ray absorption find structure spectroscopy (EXAFS) at different charge or discharge states at the Fe k-edge. The energy of the absorption maximum (7,131 eV) for the fully charged electrode (4.4 V) is similar to that of the $K_3Fe(CN)_6$, which confirms that most of Fe in the charged states are in the Fe^{3+} state. The results of this study was published on *Nano Research*.
- Through collaboration with prof. Zhengwen Fu at Fudan University, O3-type layered transition metal oxide $Na(NiCoFeTi)_{1/4}O_2$ as a high rate and long cycle life cathode material for sodium ion batteries has been studied using synchrotron based XRD and XAS, the results was published on *J. Mater. Chem. A.*

Future Achievements

- The Synchrotron based XRD and XAS, as well as pair distribution function (PDF) techniques will be applied to study the new $NaMnCuO_2$ cathode materials for Na-ion batteries.
- The full field transmission x-ray microscopy (TXM) technique as well as micro- and nano- probe scanning TXM techniques will be developed and applied for Na battery research to study the element distribution of new NASICON based solid electrolyte materials for Na batteries.
- The collaborative research with US academic research institutions and industrial partners will be further expanded and strengthened.

Technical Discussion

Background

In order to meet the challenges of powering PHEVs, the next generation of rechargeable battery systems with higher energy and power density, lower cost, better safety characteristics, and longer calendar and cycle life beyond lithium-ion batteries, which is today's state-of-the-art technology, need to be developed. Recently, Na-ion battery systems have attracted more and more attention due to the more abundant and less expensive nature of Na resources. The issue is not insufficient lithium on a global scale, but what fraction can be used and still be economically effective. Most untapped lithium reserves occur in remote or politically sensitive areas. Scale-up will require a long lead time, involve heavy capital investment in mining, and may require the extraction and processing of lower quality resources, which could drive extraction costs higher. Currently, high costs remain a critical barrier to the widespread scale-up of battery energy storage. Recent computational studies on voltage, stability and diffusion barrier of Na-ion and lithium-ion materials indicate that Na-ion systems can be competitive with lithium-ion systems. But building a sodium battery requires redesigning battery technology to accommodate the chemical reactivity and larger size of sodium atoms. Lithium batteries pack more of an electrical punch than sodium batteries because lithium atoms naturally release more energy when losing an electron than sodium does. So, for sodium batteries to reach energy densities similar to lithium ones, the positive electrode in the sodium battery needs to hold more ions. And ideally, the ion-sized spaces in the electrode do not change size during the electron exchange, so that sodium ions can easily squeeze in and out as the battery charges and discharges. Since Na-ion batteries are an emerging technology, new materials to enable Na electrochemistry and the discovery of new redox couples and the diagnostic studies of these new materials and redox couples are quite important. In sodium electrochemical systems, the greatest technical hurdles to overcome are the lack of high-performance electrode and electrolyte materials that are easy to synthesize, safe, non-toxic, with long calendar and cycling life and low cost. Furthermore, fundamental scientific questions need to be further elucidated, including (1) the difference in transport and kinetic behaviors between Na and Li in analogous electrodes; (2) Na insertion/extraction mechanism; (3) solid electrolyte interphase (SEI) layer on

the electrodes from different electrolyte systems; and (4) charge transfer in the electrolyte–electrode interface and Na+ ion transport through the SEI layer. This project will use the synchrotron based *in situ* x-ray diagnostic tools developed at BNL to evaluate the new materials and redox couples, to explore in fundamental understanding of the mechanisms governing the performance of these materials and provide guidance for new material developments. This project will also focus on developing advanced diagnostic characterization techniques to investigate these issues, providing solutions and guidance to solve the problems. The synchrotron based *in situ* X-ray techniques (x-ray diffraction and hard and soft x-ray absorption) will be combined with other imaging and spectroscopic tools such as high resolution transmission electron microscopy (HRTEM), mass spectroscopy (MS). The BNL team has built a good working relationship with several beamlines at the newly built National Synchrotron Light Source II (NSLSII) with assigned beamtime at Beamline 3-ID and Beamline 28-ID for FY2016. By collaborating with Dr. Dong Su and Dr Huoling Xin, this team also has sufficient time using the HRTEM. The BNL team has been closely working with top scientists on new material synthesis at ANL, LBNL, and PNNL, with U.S. industrial collaborators at General Motors and Johnson Controls, and international collaborators in Japan and South Korea. These collaborations will be strengthened and expanded to give this project a vision on both today's state-of-the-art technology and tomorrow's technology under development, with feedback from upstream material designers and synthesizers and downstream industrial end users.

Introduction

Among various Na insertion electrode materials, tunnel-type $Na_{0.44}MnO_2$ has been widely investigated as a positive electrode for aqueous sodium-ion batteries. However, the low achievable capacity hinders its practical applications. Our collaborators at Institute of Physics (IOP), Chinese Academy of Sciences (CAS) in China designed and synthesized a novel sodium rich tunnel-type positive material with a nominal composition of $Na_{0.66}[Mn_{0.66}Ti_{0.34}]O_2$. The tunnel-type structure of $Na_{0.44}MnO_2$ obtained for this compound was confirmed by XRD and atomic-scale STEM/EELS. When cycled as positive electrode in full cells using $NaTi_2(PO_4)_3$/C as negative electrode in 1M Na_2SO_4 aqueous electrolyte, this material shows the highest capacity of 76 mAh g^{-1} among the Na insertion oxides with an average operating voltage of 1.2 V at a current rate of 2C. These results demonstrate that $Na_{0.66}[Mn_{0.66}Ti_{0.34}]O_2$ is a promising positive electrode material for rechargeable aqueous sodium-ion batteries The structural changes of this material during cycling were studied by BNL team using synchrotron based *in situ* XRD and XAS.

High rate capability and long cycle life are challenging goals for the development of room temperature sodium-ion batteries. Our collaborators at Fudan University in China designed and synthesized a novel single phase quaternary O3-type layer-structured transition metal oxide $Na(NiCoFeTi)_{1/4}O_2$ as a new cathode material for sodium-ion batteries. It can deliver a reversible capacity of 90.6 mAh g^{-1} at a rate as high as 20C. At 5C, 75.0% of the initial specific capacity can be maintained after 400 cycles with a capacity-decay rate of 0.07% per cycle, demonstrating a superior long-term cyclability at high current density. X-ray diffraction and absorption characterizations performed at BNL revealed reversible phase transformations and electronic structural changes during the Na^+ deintercalation/intercalation process. Ni, Co and Fe ions contribute to the charge compensations during charge and discharge. Although Ti ions do not contribute to the charge transfer, it plays a very important role to stabilize the structure during charge and discharge by suppressing the Fe migration. In addition, Ti substitution can also smooth the charge-discharge plateaus effectively, which provides a potential advantage for the commercialization of this material for room temperature sodium-ion batteries

Approach

- The A combination of time resolved X-ray diffraction (TR-XRD) and mass spectroscopy (MS), together with *in situ* soft and hard X-ray absorption (XAS) during heating and transmission electron microscopy (TEM) to study the thermal stability of the Na battery electrode materials.
- Synchrotron based X-ray diffraction (XRD), X-ray absorption spectroscopy (XAS), to elucidate and differentiate the contribution from each component and element to the capacity and structural changes of various cathode and anode materials for Na-ion batteries.
- Extended collaboration with other US and international academic institutions and US industrial partners.

Results

1. The Structure evolution upon Na extraction/insertion of $Na_{0.66}[Mn_{0.66}Ti_{0.34}]O_2$ during charge-discharge

In FY2016, BNL has been focused on the studies of a new novel sodium rich tunnel-type positive material with a nominal composition of $Na_{0.66}[Mn_{0.66}Ti_{0.34}]O_2$. When cycled as positive electrode in full cells using $NaTi_2(PO_4)_3$/C as negative electrode in 1M Na_2SO_4 aqueous electrolyte, this material shows the highest capacity of 76 mAh g^{-1} among the Na insertion oxides with an average operating voltage of 1.2 V at a current rate of 2C. These results demonstrate that $Na_{0.66}[Mn_{0.66}Ti_{0.34}]O_2$ is a promising positive electrode material for rechargeable aqueous sodium-ion batteries. In order to further understand the structural changes in $Na_{0.66}[Mn_{0.66}Ti_{0.34}]O_2$ during Na extraction and insertion, *in situ* XRD experiment was performed on a $Na_{0.66}[Mn_{0.66}Ti_{0.34}]O_2$|Na half-cell in a wide voltage range of 1.5-3.9 V and the results are presented in Figure V-329. Most of the XRD reflections (e.g.,(040), (210), (140), (201)) display continuous peak shift during Na extraction/insertion. There is no evident appearance of a new phase formation upon Na extraction/insertion in a wide Na content range. The main tunnel structure of the $Na_{0.66}[Mn_{0.66}Ti_{0.34}]O_2$ was maintained during the entire charge/discharge process. In particular, the phase evolution exhibits a symmetric behavior between the charge and discharge processes in the voltage range of 2.7-3.9 V, showing that the phase evolution proceeds through a solid solution reaction upon the initial charge process. It indicates a high structure stability of $Na_{0.66}[Mn_{0.66}Ti_{0.34}]O_2$ during Na extraction and insertion, which can explain the excellent cycle performance in both non-aqueous and aqueous electrolyte. Furthermore, the solid solution phase transition behavior_ENREF_54, which is induced by Ti-substitution, is also expected to enhance the high-rate capability and cycling stability of the $Na_{0.66}[Mn_{0.66}Ti_{0.34}]O_2$ material.

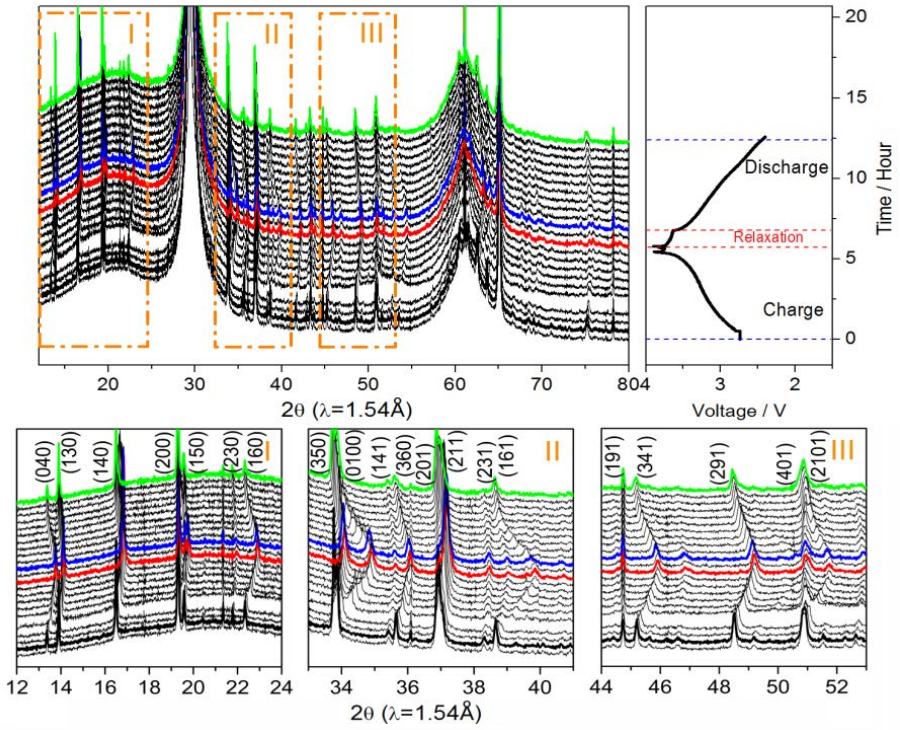

Figure V-329: Structure evolution upon Na extraction/insertion. *In situ* XRD patterns collected during the first discharge/charge of the $Na_{0.66}[Mn_{0.66}Ti_{0.34}]O_2$|Na half-cell under a current rate of C/10 at a voltage range between 1.5 and 3.9 V. For comparison, the 2θ angle has been converted to values corresponding to the more common laboratory Cu Ka radiation (χ = 1.54 Å)

X.-Q. Yang el. Al., Adv. Energy Mater., Volume 5, Issue 22, November, 2015, DOI: 10.1002/aenm.201501005.

2. The Structure evolution upon Na extraction/insertion of $Na(NiCoFeTi)_{1/4}O_2$ (O3-NCFT) during charge-discharge cycling

In FY2016, BNL also carried out the studies of a novel single phase quaternary O3-type layer-structured transition metal oxide $Na(NiCoFeTi)_{1/4}O_2$ (O3-NCFT) synthesized by a simple solid-state reaction as a new cathode material for sodium-ion batteries. It can deliver a reversible capacity of 90.6 mAh g^{-1} at a rate as high as 20C. At 5C, 75.0% of the initial specific capacity can be maintained after 400 cycles with a capacity-decay rate of 0.07% per cycle, demonstrating a superior long-term cyclability at high current density. Synchrotron based X-ray diffraction characterizations revealed reversible phase transformations during the Na+ deintercalation/intercalation process. XRD patterns were collected at a series depths of charge and discharge states, as shown in Figure V-330. The (003) and (006) peaks reflect the change of lattice parameter c, while (101) and (012) peaks mainly depend on the change of lattice parameter a and b. At the beginning of the charge, the (003) peak continuously shifted to the lower two-theta angles, indicating that a solid solution reaction was involved with c-axis expansion. As the Na ions were extracted, when x=0.85, a new (003) peak emerges, as we know, the (003) peak is a single-fold peak. Thus, every new (003) peak is a fingerprint for the formation of a new phase. Combining with other diffraction peaks, the new formed phase is resolved as a P3 stacking ordering. In the range of 0.85>x>0.75, two-phase coexistence could be observed. During the discharge process 0.5<x<1, the phase transition behaviour follows an inversed way of the charge process. This reversible phase transition behaviour in the range of 0.5<x<1 are responsible for the excellent capacity retention.

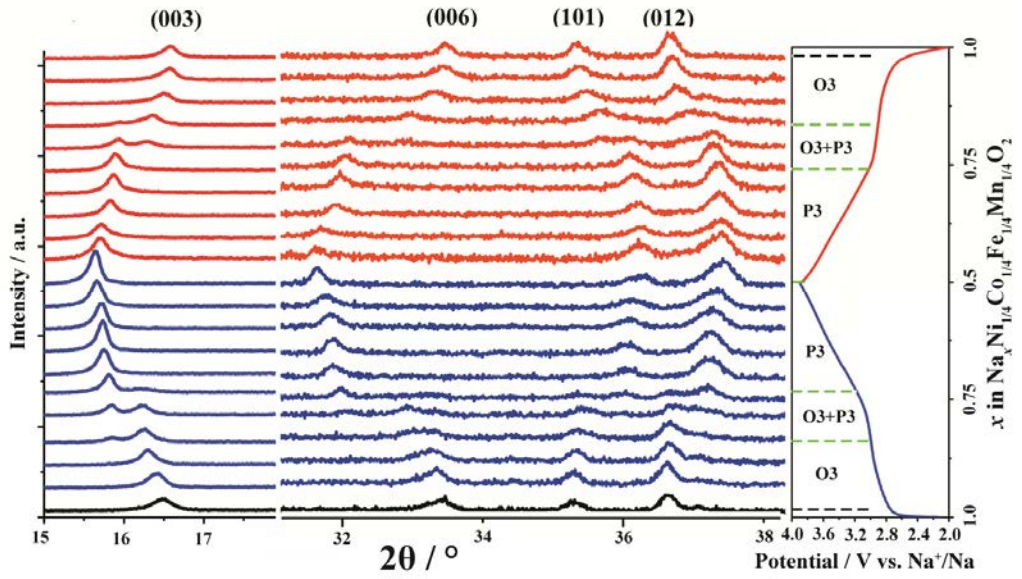

Figure V-330: Structure evolution of O3-NCFT during the electrochemical cycle. *Ex situ* X-ray diffraction patterns collected during the first charge/discharge of the Na/O3-NCFT cells under a current rate of C/10 at potential range between 2.0 and 3.9 V. The corresponding charge-discharge profile is given on the right side of XRD patterns.
X.-Q. Yang el. Al., J. Mater. Chem. A, 2015, 3, 23261-23267 (October 2015); DOI: 10.1039/C5TA05769H.

3. The oxidation state changes upon Na extraction/insertion of $Na(NiCoFeTi)_{1/4}O_2$ (O3-NCFT) during charge-discharge cycling studied by XAS

In FY2016, BNL also carried out the x-ray absorption studies of a novel single phase quaternary O3-type layer-structured transition metal oxide $Na(NiCoFeTi)_{1/4}O_2$ (O3-NCFT) synthesized by a simple solid-state reaction as a new cathode material for sodium-ion batteries. The local structures and valence state changes of Ni, Co, Fe and Ti of the O3-NCFT during charge and discharge were studied using *ex* situ X-ray absorption spectroscopy at the Ni, Co, Fe and Ti K-edge. Figure V-331 (a), (c) show the Ni and Co K-edge X-ray absorption near edge structure (XANES) spectra during the charge process respectively. Figure V-332(e) and (g) show the Fe and Ti K-edge X-ray absorption near edge structure (XANES) spectra during the charge process respectively. For the Ni K-edge (a), A rigid shift of the white line to high energy is observed, indicating the oxidation of Ni ions during Na extraction. The absorption edge at the end of the charged state is quite similar to the reference compound $LiNiO_2$, indicating the valance state of Ni in NCFT after 0.5 Na extracted is Ni^{3+}. For Co and Fe (c and e), small shifts of the edge position to higher energy are observed. Compared with the metal oxide reference spectrum, it can be estimated that the valence states of Co and Fe after charge are between $^{3+}$ and $^{4+}$. For Ti (Figure V-332(g)), the energy position of K-edge does not shift, but with little shape change. It is reasonable because the valance state of Ti is $^{4+}$ in the pristine NCFT. During the discharge process (Figure V-331 (b); (d) and Figure V-332(f) and (h), all of the XANES spectrum for Ni, Co, Fe and Ti undergo opposite evolutions., as shown in Figure V-331 and Figure V-332.

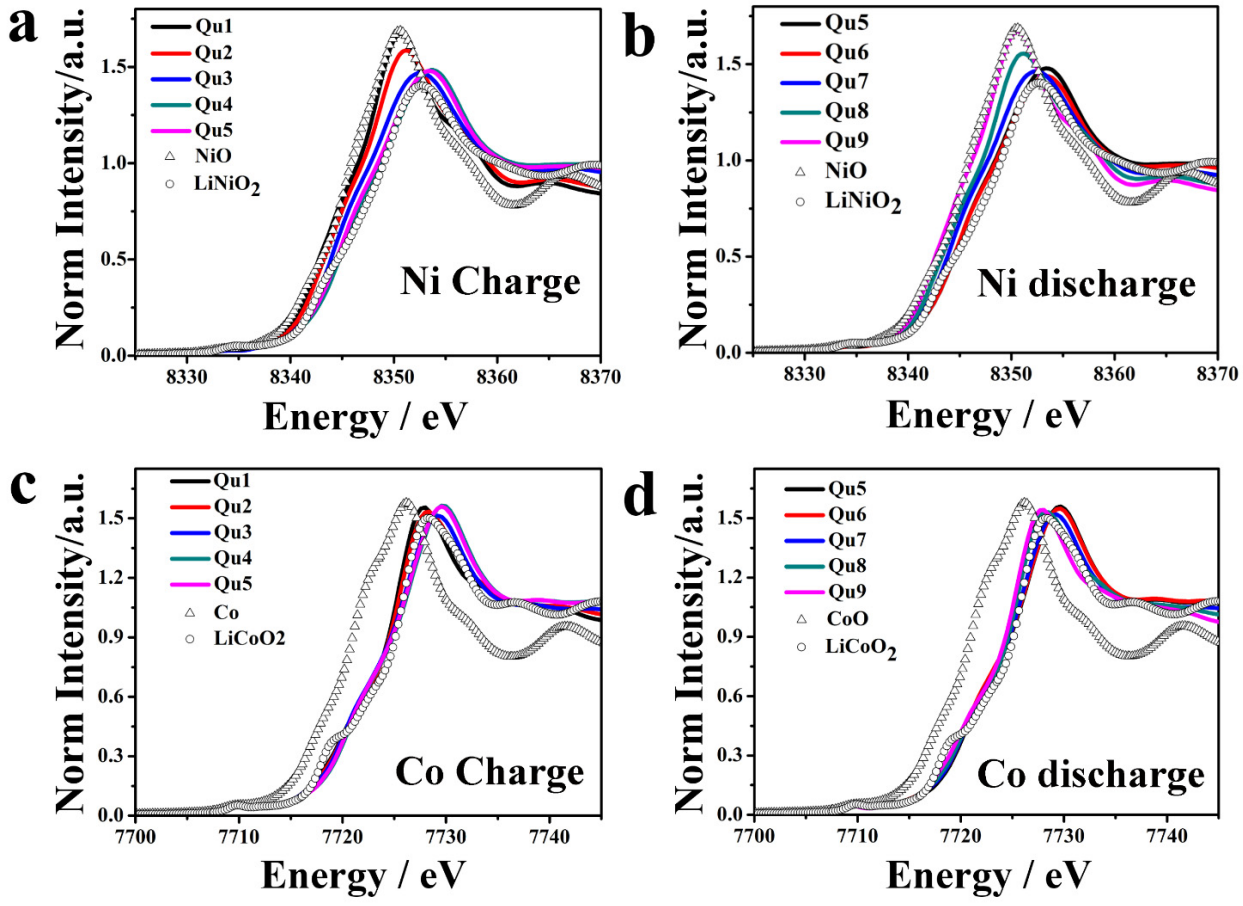

Figure V-331: (a) and (c) Normalized XANES of O3-NCFT at various stages during the first charge at Ni and Co K-edges, respectively, (b) and (d), Normalized XANES at various stages during the first discharge at Ni and Co K-edges respectively. Qu1-Qu5 refer to the different states of charge process and Qu5-Qu9 refer to the different state of discharge process

X.-Q. Yang el. Al., J. Mater. Chem. A, 2015, 3, 23261-23267 (October 2015); DOI: 10.1039/C5TA05769H.

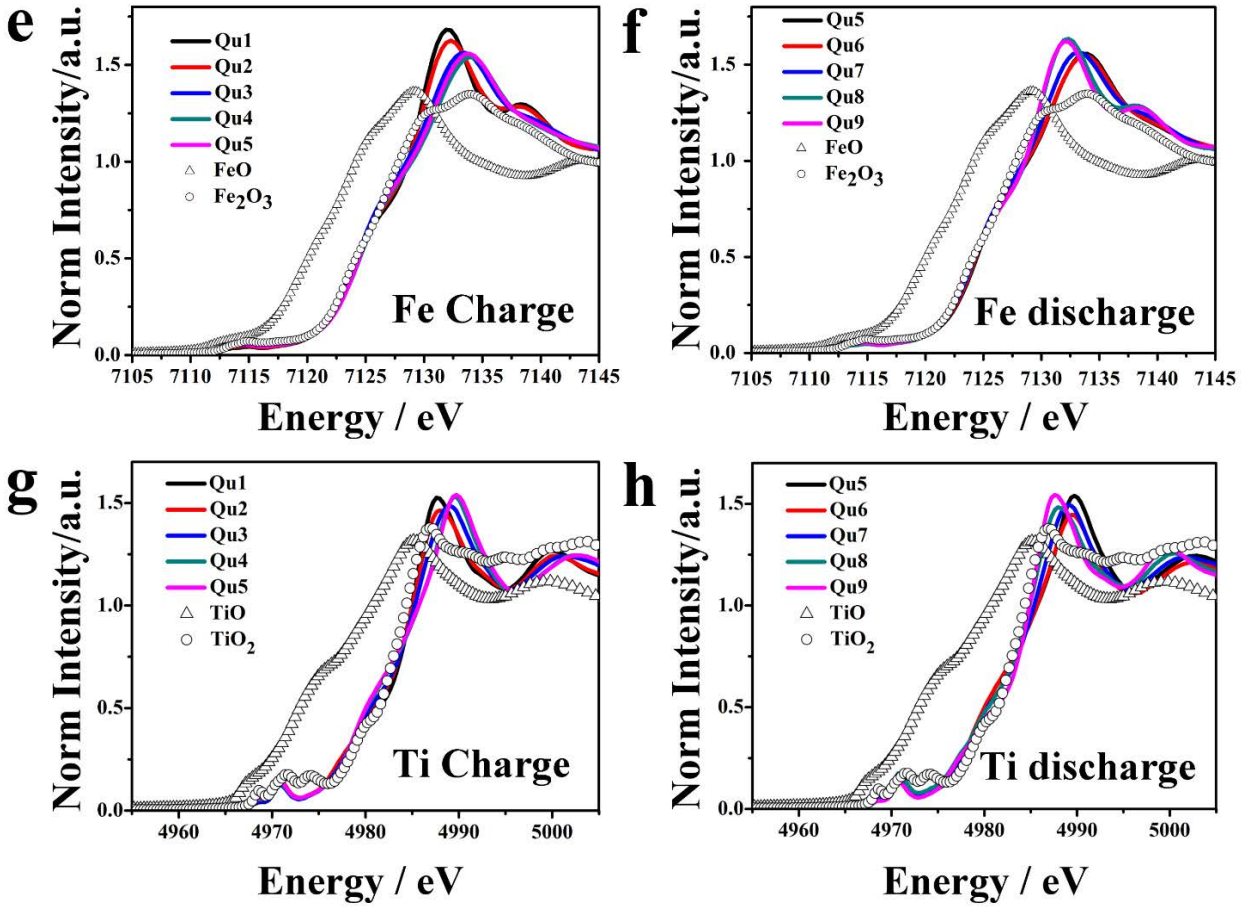

Figure V-332: (e) and (g) Normalized XANES of O3-NCFT at various stages during the first charge at Fe and Ti K-edges, respectively, (f) and (h), Normalized XANES at various stages during the first discharge at Fe and Ti K-edges respectively. Qu1-Qu5 refer to the different states of charge process and Qu5-Qu9 refer to the different state of discharge process

X.-Q. Yang el. Al., J. Mater. Chem. A, 2015, 3, 23261-23267 (October 2015); DOI: 10.1039/C5TA05769H.

Conclusions

$Na_{0.66}[Mn_{0.66}Ti_{0.34}]O_2$ was successfully designed and synthesized by a simple solid-state method and its structure was systematically studied using synchrotron powder XRD, atomic-scale STEM and EELS. It retains the orthorhombic structure (space group: *Pbam*), which is similar to the structure of tunnel-type $Na_{0.44}MnO_2$ and distinguished from P2-$Na_{0.66}MnO_2$ with layered structure (space group: P63/mmc). It has been found that $Na_{0.66}[Mn_{0.66}Ti_{0.34}]O_2$ can be used as a positive electrode material for aqueous sodium-ion batteries. In particular, it shows the highest reversible capacity of ca. 76 mAh g^{-1} at a current rate of 2C among all the oxide electrode materials, with an average operating voltage of 1.2 V when coupled with $NaTi_2(PO_4)_3$/C negative electrode in aqueous sodium-ion batteries. Another appealing feature is that the material retains tunnel structure without phase transformation during Na extraction and insertion, which ensures the prolonged cycle stability. The $Na_{0.66}[Mn_{0.66}Ti_{0.34}]O_2$|$NaTi_2(PO_4)_3$/C aqueous sodium ion full cell demonstrates excellent cycle performance with very small capacity decay after 300 cycles. We believe that $Na_{0.66}[Mn_{0.66}Ti_{0.34}]O_2$ with outstanding performance represents a novel and attractive positive electrode material that would open a new approach for the development of low cost and non-toxic aqueous sodium-ion batteries for large-scale electrical energy storage systems.

A new O3-type layer-structured metal oxide cathode $Na(NiCoFeTi)_{1/4}O_2$ for sodium ion batteries was successfully synthesized . It delivers a reversible capacity of 116 mAh g^{-1} in first cycle and has 93.03% capacity retention after 100 cycles at 1C rate. At a rate as high as 20C, a reversible capacity of 90.6 mAh g^{-1} can still be achieved. During 5C cycling, 75.0% of the initial specific capacity can be maintained after 400 cycles with a capacity-decay rate of 0.07% per cycle, indicating a superior long-term cyclability at high current

density. The Ti substitution could smooth the charge/discharge plateaus effectively, and may contribute to the suppression of Fe migration. On the other hand, the synthesis method of this material is very facile and cost effective. Combining its high rate capability and long cycle life, NCFT could be a very promising cathode material for room temperature high power sodium-ion batteries. The structural evolution and oxidation state changes of this novel $Na(NiCoFeTi)_{1/4}O_2$ cathode material for Na-ion batteries was systematically studied using synchrotron based *in situ* XRD and XAS at BNL.

Products

Presentations/Publications/Patents

1. Ji-Li Yue, Yong-Ning Zhou, Xiqian Yu, Seong-Min Bak, Xiao-Qing Yang, and Zheng-Wen Fu, "O3-type layered transition metal oxide $Na(NiCoFeTi)_{1/4}O_2$ as a high rate and long cycle life cathode material for sodium ion batteries", J. Mater. Chem. A, 2015, 3, 23261-23267 (October 2015); DOI: 10.1039/C5TA05769H.
2. Yuesheng Wang, Linqin Mu, Jue Liu, Zhenzhong Yang, Xiqian Yu, Lin Gu, Yong-Sheng Hu, Hong Li, Xiao-Qing Yang, Liquan Chen, Xuejie Huang, "A Novel High Capacity Positive Electrode Material with Tunnel-Type Structure for Aqueous Sodium-Ion Batteries", *Advanced Energy Materials*, Volume 5, Issue 22, November, 2015, DOI: 10.1002/aenm.201501005.
3. Jue Liu, Liang Yin, Lijun Wu, Jianming Bai, Seong-Min Bak, Xiqian Yu, Yimei Zhu, Xiao-Qing Yang, and Peter G. Khalifah, "Quantification of Honeycomb Number-Type Stacking Faults: Application to Na3Ni2BiO6 Cathodes for Na-Ion Batteries", Inorg. Chem., 2016, 55 (17), pp 8478–8492, DOI: 10.1021/acs.inorgchem.6b01078, Publication Date (Web): August 17, 2016.
4. Seongmin Bak, Xiqian Yu, Enyuan Hu, Jue Liu, Hung Sui Lee, Xiao-Qing Yang*, Yong-Sheng Hu, Lin Gu, Hong Li, Xuejie Huang, and Liquan Chen, "*In situ* characterization of advanced electrode materials for Na-ion batteries by using synchrotron based techniques", presented at 2016 MRS Spring Meeting, March 28 to April1, 2016, Phoenix, Arizona, USA., **Invited**.
5. Xiqian Yu, Enyuan Hu, Jue Liu, Seongmin Bak, Hung Sui Lee, Xiao-Qing Yang*, Zhizhen Zhang, Lin Gu, Yong-Sheng Hu, Hong Li, Xuejie Huang, and Liquan Chen "Structural characterization studies of advanced electrode and solid electrolyte materials for Lithium-ion and sodium batteries using synchrotron based x-ray techniques and TEM", presented at the Conference of International Battery Frontier 2016 (CIBF2016), May 24-26, 2016, Shenzhen, China. **Invited.**
6. Enyuan Hu, Xiao-Qing Yang*, Xiqian Yu, Yongning Zhou, Seong-Min Bak, Hung-sui Lee, Zhaoxiang Wang2 and Yijin Liu, "Using Synchrotron Based *in situ* X-ray Diffraction and Absorption and TXM Techniques to Study the New Electrode Materials for Next Generation of Batteries", presented at the Seminar at Energy Sciences Institute, Yale University New Haven, September 14, 2016, **Invited.**

VI. Battery500 Innovation Center

VI.A.1. Battery500 Consortium

Jun Liu, Director and Principal Investigator
Pacific Northwest National Laboratory
Energy and Environment Directorate
902 Battelle Boulevard
Richland, WA 99354
Phone: 509-375-4443; Fax: 509-371-6242
E-mail: jun.liu@pnnl.gov

Participating Institutes
PNNL, BNL, INL, SLAC/Stanford University,
University of Washington, UC San Diego,
UT Austin, Binghamton University

Tien Q. Duong, DOE Program Manager
Advanced Battery Materials Research (BMR)
U.S. Department of Energy
Vehicle Technologies Office
1000 Independence Avenue, SW
Washington, DC 20585
Phone: 202-586-7836
E-mail: Tien.Duong@ee.doe.gov

Start Date: September 15, 2016
End Date: September 30, 2021

Abstract

Objectives

- The Battery500 Consortium will develop commercially viable lithium battery technologies with a cell level specific energy of 500Wh/kg through innovative electrode and cell designs that enable us to extract the maximum capacity of advanced electrode materials.
- The consortium will utilize a lithium anode combined with a compatible electrolyte system, and two cathodes, a nickel-rich NMC ($LiNi_xM_{1-x}O_2$, M = Mn or Co and x > 0.7) and sulfur both of which can attain a theoretical energy density of around 1000 Wh/kg. The focus is to design novel electrode and cell architectures that will decouple the cathode and anode SEI reactions and will allow 50% of the capacity to be attained at the cell level, compared with around 25% today in order to meet the 500 Wh/kg goal.
- The consortium will focus on three keystone projects: (1) Materials and Interfaces -High utilization of high-energy cathodes and high-capacity Li metal anode by developing interface doping/coating on cathode materials and novel electrolyte for stable operation of Li metal anode, (2) Electrode Architecture - New electrode architectures to increase electrode thickness and maximize active materials utilization, and 3D Li architectures to stable the metal anode, and (3) Cell Design and Integration - A new battery design to decouple cathode and anode interfacial reactions to achieve more than 500 Wh/kg energy density, and standard methodology to perform diagnostic evaluation and performance validation of the battery.
- The consortium will integrate the multi-institute capabilities in battery materials and chemistry, electrode architecture, cell design and fabrication, and advanced diagnosis to optimize the materials performance in realistic cell architectures to achieve the DOE goal.

Accomplishments

- The following projects have been defined in alignment with the three keystone projects and are ready to launch:
  Cathode materials; Cathode modification; Cathode architecture; Li metal deposition; Li metal surface protection and polymer membrane; Li architecture; Electrolytes; Solid state electrolytes and separators; Ni-NMC cell fabrication; Li-S cells; Characterization; Methods and standards; Performance and diagnosis; Characterization of cathode and anode/electrolyte interfaces; Modeling of thick electrodes and Li-metal morphology.
- Roles and responsibilities of each PIs defined.
- Quarterly milestones and review criteria established.

Future Achievements

The main expected outcome for FY2017 is to identify specific key challenges and demonstrate pathways to go beyond the current state-of-the-art lithium-ion batteries with transition metal oxide cathodes and graphite/Si anode by utilizing Li metal anodes. Specifically, the following outcome will be expected:

- First, the consortium will establish baseline cathode materials, anode materials, electrolytes and cell architecture, and will establish and implement project plans for each PIs and institutions.
- In first phase, the consortium will complete the first synthesis of NMC 622 material, with a specific capacity of 200 mAh/kg and 3.8V, and bench mark with NMC 622 materials from other groups.
- In 2017, the consortium will develop electrolyte formulation for Li deposition with over 3.8 V and 99.0% coulomb efficiency
- In FY2017, the consortium will demonstrate 1 Ah pouch cell with 300 Wh/kg energy density, and over 50 cycles and continuing, and will complete the preliminary testing protocols and demonstrate utilization of these protocols.

Appendix A: Acronyms

Acronym	Expansion
3M	Minnesota Mining and Manufacturing Company
AABC	Advanced Automotive Batteries Conference
AAM	Acrylamide
AB	Acetylene black
ABF	Annular bright field (image)
ABMR	Advanced Battery Materials Research
ABR	Applied Battery research
AC	Alternating Current
ACS	American Chemical Society
ADF-STEM	Annular dark-field - scanning transmission electron microscope
ADP	Advanced drying process
AEY	Auger electron yield
AFM	Atomic force microscopy
AGE	glycidyl ether
AIBN	azobisisobutyronitrile
AIMD	Ab initio molecular dynamics
ALD	Atomic layer deposition
ALS	Advanced Light Source
ALSS	Advanced Light Source Synchrotron
AMO	Advanced Manufacturing Office (at DOE)
AMR	Annual Merit Review
ANL	Argonne National Laboratory
ANOVA	Analysis of variance
AOP	(VTO) Annual operating plan
APS	Advanced Photon Source
APT	Atom probe tomography
ARC	Accelerated rate calorimetry
ARL	Army Research Laboratory
ARPA-E	Advanced Research Projects Agency - Energy
ARRA	American Recovery & Reinvestment Act
ASI	Area-specific impedance
ASR	Area specific resistance
ATMC	Automatic Tuning Matching Cycler

Acronym	Expansion
ATR-FTIR	Attenuated total reflection-Fourier transform infrared spectroscopy
AVS	American Vacuum Society
BATT	Batteries for Advanced Transportation Technologies
BES	Basic Energy Sciences (DOE Office)
BET	Brunauer, Emmett, and Teller (surface area analysis)
BEV	Battery electric vehicle
BF-TEM	Bright field - transmission electron microscopy
BLAST	Battery Lifetime Analysis Simulation Tool
BMF	Battery manufacturing facility
BMR	(Advanced) Battery Materials Research (Program)
BMS	Battery management system
BNL	Brookhaven National Laboratory
BOL	Beginning of life
BP	Budget period
BPR	Ball to powder ratio
BSE	Backscattered electron (microscopy)
BSF	Battery scaling factor
BTC	Battery Technology Center
BYU	Brigham Young university
CABS	Consortium for Advanced Battery Simulation
CAD	Computer-aided Design
CAE	Computer-aided engineering
CAEBAT	Computer-aided engineering of batteries
CAFE	Corporate Average Fuel Economy (Standards)
CAMP	Cell analysis, modeling, and prototyping (facility)
CAS	Chinese Academy of Sciences
CBC	Carbon Black from Cabot
CBF	Critical Barrier Focus
CBM	Conduction band minimum
CC	Constant-concentration
CCCV	Constant current constant voltage
CCD	Charge-coupled device
CE	Coulombic efficiency
CEC	California Energu Commision

Acronym	Expansion
CEF	Cathode Energy Factor
CEI	Cathode electrolyte interfaces
CF	Carbon fabric
CFM	Complex framework materials
CG	Concentration gradient
CMC	Carboxymethyl cellulose
CMD	Classical molecular dynamics
CNT	Carbon nano-tubes
CNT/PEG	Carbon Nanotubes/ Polyethylene Glycol
COTS	Commercial-Off-The-Shelf
CP	Cross-polarization
CPE	Constant phase element
CPI	Compact Power Inc.
CRADA	Cooperative Research and Development Agreement
CS	Charge-sustaining
CSTR	Continuous stirred tank reactor
CSWG	Crash Safety Work Group
CU	Colorado University
CV	Cyclic voltammetry
DEMS	Differential electrochemical mass spectrometry
DES	Deep eutectic solvent
DETMSA	N, N-Diethyltrimethylsilylamine
DFEC	(4R,5S)-4,5-Difluoro-1,3-dioxolan-2-one
DFT	Density function theory
DLD	Delay-line detector
DMA	Dopamine methacrylamide
DMAPA	N-[3-(Dimethylamino)propyl] acrylamide
DMC	Dimethyl carbonate
DMDS	Dimethyl disulfide
DME	Dimethyl ether
DMF	Dimethylformamide
DMSO	Dimethylsulfoxide
DOD	Depth-of-discharge
DOE	Department of Energy

Acronym	Expansion
DOL	Dioxolane
DOPA	3,4-Dihydroxyphenyl-L-alanine
DOT/NHTSA	Department of Transportation/National Highway Traffic Safety Administration
DP	Dry process
DPA	Destructive physical analysis
DPP	Dynamic particle-packing (model)
DSC	Differential scanning calorimetry
DST	Dynamic stress test
EADL	Electrochemical Analysis and Diagnostic Laboratory (at ANL)
EB	Electron beam
EBG	Engine Benchmarking Group
EC	Ethylene carbonate
ECP	EC Power
ECS	Electrochemical Society
ED	Electrode domain
EDL	Electrolyte deposition layer
EDS	Energy dispersive spectroscopy
EDV	Electric Drive Vehicle
EDX	Energy-dispersive x-ray (spectroscopy)
EELS	Electron energy loss spectroscopy
EERE	Energy Efficiency and Renewable Energy (DOE Office)
EG	Ethylene glycol
EIS	Electrochemical Impedance Spectroscopy
EMC	Electron Microscopy Center
EMSL	Environmental Molecular Sciences Laboratory
EPA	Environmental Protection agency
EPMA	Electron probe micro-analysis
EPR	Electron paramagnetic resonance
EQCM	Electrochemical quartz crystal microbalance
ESI	Electrospray ionization
EUCAR	European Council for Automotive Research and Development
EV	Electric vehicle
EVI	Electric Vehicle Initiative
EVSE	Electric vehicle supply equipment

Acronym	Expansion
EW	Electrochemical window
EXAFS	Extended X-ray absorption fine structure
FC	Fast-charge
FCE	First cycle efficiency
FCG	Full concentration gradient
FCTO	Fuel Cell Technologies Office (at DOE)
FE	Finite element
FEA	Finite element analysis
FEC	Fluoro ethylene carbonate
FEM	Finite element method
FEMC	Trifluoroethylmethyl carbonate
FE-SEM	Field Emission Scanning Electron Microscope
FFT	Fast Fourier Transforms
FIB	Focused Ion Beam
FIR	First cycle irreversible loss
FOA	Federal Opportunity Anouncement
FP	First principles
FPMD	First-Principles Molecular Dynamics
FSP	Flame Spray Pyrolysis
FTIR	Fourier Transform InfraRed spectroscopy
FTIR-ATR	Fourier Transform infrared attenuated total reflection
FWHM	Full width at half maximum
FY	Fiscal year
GCMC	Glycerol carbonate methyl carbonate
GC-MS	Gas chromatography - mass spectroscopy
HD	High dielectric
HEHV	High energy high voltage
HEM	High energy material
HEMM	High energy mechanical milling
HEMR	High-energy mechanochemical reduction
HEV	Hybrid electric vehicle
HEXRD	High-energy X−ray diffraction
HF	Hydrofluoric acid
HOMO	Highest occupied molecular orbital

Acronym	Expansion
HOPG	Highly oriented pyrolytic graphite
HP	High power
HPLC	High-performance liquid chromatography
HPPC	Hybrid pulse power characterization
HQ	Hydro-Québec
HR	High resolution
HRTEM	High-resolution transmission electron microscopy
HR-XRD	High-resolution X-ray diffraction
HSE	Heyd-Scuseria-Ernzerhof (exchange-correlation functional)
HT	High temperature
HV	High voltage
HXN	Hard x-ray nano-probe
IA	(IEA) Implementing Agreement
IAPG	Interagency Advanced Power Group
IBA	International Battery Materials Association
ICP	Inductively coupled plasma
ID	Intensity of the carbon D-band
IEA	International Energy Agency
IEC	International Electrotechnical Commission
IFM	Inorganic framework material
IKB	Integrated Ketjen black
IMRC	International Materials Research Congress
INL	Idaho National Laboratory
IOP	Institute of Physics
IP	Intellectual property
IPA	Isopropyl alcohol
IR	Infra-red
IRCL	Irreversible capacity loss
ISC	Internal short circuit
ISCAN	International Symposium on Clusters and Nanomaterials
JCESR	Joint center for energy storage research
JT	Jahn Teller (distortion)
LAMMPS	Large-scale Atomic/Molecular Massively Parallel Simulator
LATP	Lithium aluminum titanium phosphate

Acronym	Expansion
LBDC	Lithium butylene dicarbonate
LBNL	Lawrence Berkeley National Laboratory
LCA	Life cycle analysis
LCO	Lithium cobalt oxide
LCP	Lower cut-off potential
LCV	Lower cutoff voltage
LEC	Lithium ethyl carbonate
LEDC	Lithium ethylene dicarbonate
LFO	Li_5FeO_4
LFP	Li iron phosphate
LIB	Lithium-ion battery
LIBS	Laser induced breakdown spectroscopy
LIC	Lithium-ion conducting
LICM	Lithium-ion conducting membrane
LIFSI	Lithium bis(fluorosulfonyl)imide
LL	Layered-layered
LLR	Low lithium-rich (cathode)
LLS	Layered-layered spinel
LLTO	$(Li,La)TiO_3$
LLZ	$Li_7La_3Zr_2O_{12}$
LLZO	Lithium lanthanum zirconate
LLZT	$Li_{6.5}La_3Zr_{1.5}Ta_{0.5}O_{12}$
LMC	Lithium methyl carbonate
LMNO	Lithium manganese nickel oxide
LMO	Lithium manganese oxide
LMR	Lithium Manganese-rich (layered cathode material)
LMR-NMC	$0.5Li_2MnO{\cdot}0.5LiNi_{0.44}Co_{0.25}Mn_{0.31}O_2$
LMW	Low molecular weight (binder)
LNCA	$Li(Ni_{0.80}Co_{0.15}Al_{0.05})O_2$
LNMC	(Layered structure) $LiNi_{1/3}Mn_{1/3}Co_{1/3}O_2$
LNMFO	$LiNi_{0.5-x}Mn_{1.5-x}Fe_{2x}O_4$
LNMO	$LiNi_{0.5}Mn_{0.5}O_2$
LPS	β-Li_3PS_4
LS	Low spin

Acronym	Expansion
LSB	Lithium sulfur batteries
LSTC	Livermore Software Technology Corporation
LSV	Linear scanning voltammetry
LT	Low temperature
LTO	Lithium titanate, $Li_4Ti_5O_{12}$
LUMO	Lowest unoccupied molecular orbital
LV	Low viscosity
LZP	Phosphate polyanion zirconate
MAA	Methacrylate-co-methacrylic acid
MAS	Magic angle spinning
MCMB	Mesocarbon micro beads
MCT	Multi cycle test
MD	Molecular dynamics
MECT	Mechanical-electrical-chemical-thermal (model)
MERF	Materials Engineering Research Facility
MFCA	Multifunctional cathode additive
MIT	Massachusetts Institute of Technology
MLD	Molecular layer deposition
MPC	Micro-mesoporous carbon
MPNC	Nitrogen-doped mesoporous carbon
MRI	Magnetic resonance imaging
MRS	Materials Research Society
MS	Mass spectroscopy
MSMD	Multi-scale, multi-domain
MW	Molecular weight
NASA	National Aeronautics and Space Administration
NCA	$LiNi_{0.8}Co_{0.15}Al_{0.05}O_2$
NCM	$Li_{1+w}[Ni_xCo_yMn_z]_{1-w}O_2$
NCO	Nickel cobalt oxide
NDE	Non-destructive evaluation
NEBD	Nano-size probe electron diffraction
NERSC	National Energy Research scientific Computing Center
NETL	National Energy Technology Laboratory
NG	Nitrogen-doped graphene

Acronym	Expansion
NHTSA	National Highway Transportation Safety Administration
NMC	$LiNi_{1/3}Co_{1/3}Mn_{1/3}O_2$
NMP	N-methylpyrrolidone
NMR	Nuclear magnetic resonance
NPD	Neutron powder diffraction
NR	Neutron reflectometry
NRE	Non-recurring engineering (cost)
NREL	National Renewable Energy Laboratory
NSLS	National Synchrotron Light Source
NSLSII	National Synchrotron Light Source II
NSOM	Near-field scanning optical microscopy
NTG	Newman-Tiedemann-Gu (electrochemistry model)
OCP	Open-circuit potential
OCV	Open circuit voltage
OD	Outside diameter
OEM	Original equipment manufacturer
OER	Oxygen evolution reaction
ORNL	Oak Ridge National Laboratory
ORR	Oxygen reduction reaction
OS	Orgnic solvent
OSSE	Octahedral site stabilization energy
PAN	Polyacrylonitrile
PARC	Palo Alto Research Center
PC	Propylene carbonate
PCB	Printed circuit board
PDF	Pair density function
PDI	Polydispersity index
PE	Polyethylene
PEFM	Poly(2,7-9,9-dioctylfluorene-co-2,7-9,9-(di(oxy-2,5,8-trioxadecane)) fluorine-co-2,7-fluorenone-co-2,5-1-methylbenzoic ester)
PEG	Polyethylene glycol
PEO	Polyethyleneoxide
PEV	Plug-in electric vehicle
PFG	Pulse field gradient
PFM	Poly(9,9-dioctylfluorene-co-fluorenone-co-methylbenzoic ester)

Acronym	Expansion
PFPE	Perfluoropolyether
PHEV	Plug-in hybrid electric vehicle
PHEV40	PHEV with 40-mile range
PMHS	Polymethylhydrosiloxane
PNNL	Pacific Northwest National Laboratory
POC	Proof of concept
PP	Polypropylene
PPY	Polypyrene (polymer)
PS	Polystyrene
PSD	Pore size distribution
PSU	Pennsylvania State University
PTF	Post Test Facility
PTFE	Poly(tetrafluoroethylene) (cathode)
PU	Polyurethane
PVD	Physical vapor deposition
PVDF	Poly(vinylidenefluoride)
PVP	Polyvinylpyrrolidone
PXRD	Powder X-Ray Diffraction
R&D	Research and Development
R2R	Roll-to-roll
RAFT	Reversible Addition–Fragmentation chain Transfer (polymerization)
RAL	Rutherford Appleton Laboratory
RD&D	Research, Development, and Design
RE	Reference electrode
RH	Relative humidity
ROE	Return on Equity
RP	Reverse phase
RPM	Revolutions per minute
RPT	Reference performance test
RT	Room temperature
RUS	Resonant ultrasound spectroscopy
SAE	Society of Automotive Engineers
SAED	Selected area electrode diffraction
SAH	Succinic anhydride

Acronym	Expansion
SBIR	Small Business Innovation Research
SBIR/STTR	Small Business Innovation Research/Small Business Technology Transfer
SBR	Styrene-butadiene rubber (binder)
SDS	Safety data sheet
SEET	Structural, electrical, electrochemical and thermal
SEI	Solid electrolyte interphase
SEM	Scanning electron microscopy
SEO	Poly(styrene)-b-poly(ethylene oxide)
SEP	Separator evaluation platform
SFG	Sum Frequency Generation
SFM	Sulfur infiltrated framework
SG	Sulfur-doped graphene
SIMS	Secondary ion mass spectrometry
SINS	Synchrotron infrared nano-spectroscopy
SLAC	Stanford acceleration laboratory
SLD	Scattering length density
SLMP	Stabilized lithium metal powder
SLP	Single layer pouch (cells)
SNL	Sandia National Laboratories
SNS	Spallation Neutron Source
SOA	State of the art
SOC	State of charge
SOFC	Solid oxide fuel cell
SPH	Smooth particle hydrodynamics
SQS	Special quasi-random structures
SRL	Surface reconstruction layer
SRX	Sub-micron Resolution X-ray Spectroscopy
SS	Solid-state
SSE	Solid-state electrolyte
SSL	Surface segregation layers
SSPM	Solid state system incorporated polymer membrane
SSRL	Stanford Synchroton Radiation Lightsource
STEM	Scanning transmission electron microscopy
STTR	Small Business Technology Transfer Program

Acronym	Expansion
SWCNT	Single-walled carbon nanotube
SXRD	Synchrotron X-ray diffraction
TAC	Technical Advisory Committee
TAMU	Texas A&M University
TAP	Technology assessment program
TCO	Total cost of ownership (model)
TCP	Technology collaboration program
TEGDME	Tetraethyleneglycoldimethyl
TEM	Transmission electron microscopy
TEP	Trisethlyl phosphite
TES	Tender-Energy X-ray Absorption Spectroscopy
TEY	Total electron yield
TFEEC	Trifluoroethyl ethyl carbonate
TFPC	Trifluoropropylene carbonate
TGA	Thermal gravimetric analysis
THF	Tetrahydrofuran
THFIPB	Tris(hexafluoroisopropyl) ester
TM	Transition metal
TMA	Tri-methyl aluminum
TMPM	2,2,6,6-tetramethylpiperidin-4-yl methacrylate
TMSB	Tris(trimethylsilyl) borate
TMSP	Tris(trimethylsilyl) phosphate
TRL	Technology readiness level
TR-XAS	TR-XRD and absorption
TR-XRD	Time-resolved X-ray diffraction
TTFP	Tris(2,2,2,-trifluoroethyl)phosphite
TVR	Taylor Vortex Reactor
TWG	Transmission benchmark workgroup
TXM	Transmission X-ray Microscopy
TXM-XANES	Transmission X-ray microscopy with X-ray near edge absorption spectroscopy
UC	University of California
UCAP	Ultracapacitor
UCP	Upper cutoff potential
UCV	Upper cut-off voltage

Acronym	Expansion
UDDS	Urban Dynamometer Driving Schedule
UHMWPE	Ultra High Molecular Weight Polyethylene
USABC	United States Advanced Battery Consortium
USCAR	United States Council for Automotive Research
USDRIVE	Driving Research and Innovation for Vehicle efficiency and Energy sustainability
UTA	University of Texas, Austin
UV	Ultraviolet
UV-VIS	Ultraviolet–visible spectroscopy
UW	University of Washington
VASP	Vienna Ab-initio Simulation Package
VBM	Valence band maximum
VC	Vinylene carbonate
VFM	Variable frequency microwave
VIBE	Virtual Integrated Battery Environment
VTF	Vogel-Tammann-Fulcher (function)
VTO	Vehicle Technologies Office
WAXS	Wide angle X-ray scattering
WOT	Wide open throttle
WPI	Worcester Polytechnic Institute
XAFS	X-ray absorption fine structure
XANES	X-ray absorption near edge structure
XAS	X-ray absorption spectroscopy
XEDS	X-ray energy dispersive spectroscopy
XFC	Extreme fast charging
XPD	X-ray powder diffraction
XPS	X-ray photoelectron spectroscopy
XRD	X-ray diffraction
XRF	X-ray fluorescence (microscopy)

Appendix B: Contributors/Collaborators

Contributor/Collaborator (Organization)	Section(s) in Annual Progress Report, FY 2016
Abraham, Daniel P. (Argonne National Laboratory)	IV.C.3, IV.F.10
Ahmad, Iftikhar (Lambda Technologies)	IV.F.8
Ahmed, Shabbir (Argonne National Laboratory)	III.A.1
Alamgir, Mohamed (LG Chem Power, Inc.)	II.A.2, II.A.5
Amine, Khalil (Argonne National Laboratory)	IV.D.2, V.H.3, V.I.3
Arnold, John (Miltec UV International)	IV.F.12, IV.F.7
Arsenault, Renata (Ford Motor Company)	II.A.10
Aurora, Peter (Navitas Advanced Solutions Group, LLC.)	IV.F.2
Bae, Chulheung (Ford Motor Company)	II.A.2
Bai, Jianming (Brookhaven National Laboratory)	V.D.4
Balbuena, Perla B. (Texas A&M University)	V.H.7, V.F.4
Balsara, Nitash (University of California at Berkeley)	V.H.2
Bareño, Javier (Argonne National Laboratory)	IV.B.3
Basco, John (Argonne National Laboratory)	III.B.1
Battaglia, Vincent (Lawrence Berkeley National Laboratory)	V.B.1
Bloom, Ira (Argonne National Laboratory)	III.B.1, IV.B.3
Butcher, Colleen (National Energy Technology Laboratory)	IV.F.12, IV.F.7, IV.F.8, V.H.1
Ceder, Gerbrand (Lawrence Berkeley National Laboratory)	V.F.3
Chen, Guoying (Lawrence Berkeley National Laboratory)	V.E.1
Cheng, Yang-Tse (University of Kentucky)	V.F.5
Chiang, Yet-Ming (Massachusetts Institute of Technology)	V.B.3
Cobb, Corie L. (PARC, a Xerox Company)	IV.F.10
Costantino, Henry R. (Group14 Technologies Inc.)	IV.F.1
Croy, Jason R. (Argonne National Laboratory)	V.D.5, V.D.9, V.E.8
Cui, Yi (Stanford University)	V.C.2, V.G.5, V.H.6
Cunningham, Brian (U.S. Department of Energy)	II, II.C, III, III.C.1
Curtiss, Larry (Argonne National Laboratory)	V.I.3
D'Anna, Tom (FEV North America, Inc.)	II.A.11
Dees, Dennis W. (Argonne National Laboratory)	III.A.1, IV.C.4, IV.C.5
Denlinger, Matthew (Ford Motor Company)	II.A.3
Deppe, Jack (Deppe Consulting)	I, IV
Doeff, Marca M. (Lawrence Berkeley National Laboratory)	V.D.7

Contributor/Collaborator (Organization)	Section(s) in Annual Progress Report, FY 2016
Du, Peng (Silatronix)	IV.F.5
Dudney, Nancy (Oak Ridge National Laboratory)	V.G.1, V.G.3
Dunn, Jennifer (Argonne National Laboratory)	III.A.2
Duong, Tien (U.S. Department of Energy)	IV.F.13, V
Gaines, Linda (Argonne National Laboratory)	III.A.2
Gallagher, Kevin G. (Argonne National Laboratory)	III.A.1
Gan, Hong (Brookhaven National Laboratory)	V.H.4
Gao, Huajian (Brown University)	V.F.5
Gillard, Samuel (U.S. Department of Energy)	III.B.4, III.B.1, III.B.2, III.B.3
Giordani, Vincent (Liox Power, Inc.)	V.I.2
Goodenough, John B. (University of Texas at Austin)	V.D.8
Grey, Clare (University of Cambridge)	V.E.4
Hayner, Cary (SiNode Systems)	II.A.8
Hellring, Stuart (PPG Industries, Inc.)	IV.F.11
Howell, David (U.S. Department of Energy)	All
Iddir, Hakim (Argonne National Laboratory)	IV.C.1
Jacobs, Alex (Sila Nanotechnologies, Inc.)	IV.F.4
Jansen, Andrew N. (Argonne National Laboratory)	IV.B.1
Jorgensen, Scott (General Motors)	II.A.4, II.A.5
Kaczmarek, Susan (Energetics, Incorporated)	All
Kelly, Kenneth (National Renewable Energy Laboratory)	III.A.3
Kepler, Keith (Farasis Energy, Inc.)	IV.D.4
Kercher, Andrew (Oak Ridge National Laboratory)	V.D.6
Keyser, Matthew (National Renewable Energy Laboratory)	III.B.4
Kiggans, Jim (Oak Ridge National Laboratory)	V.D.6
Kornish, Brian (PPG Industries, Inc.)	IV.F.11
Kostecki, Robert (Lawrence Berkeley National Laboratory)	IV.C.5, V.E.2
Krumdick, Gregory K. (Argonne National Laboratory)	IV.E.1, IV.E.2
Kumar, B. J. (Energetics, Incorporated)	All
Kumta, Prashant N. (University of Pittsburgh)	V.C.1, V.H.1
Li, Jianlin (Oak Ridge National Laboratory)	IV.E.5
Liu, Gao (Lawrence Berkeley National Laboratory)	IV.F.9, V.B.4
Liu, Jun (Pacific Northwest National Laboratory)	V.C.1, V.H.5, VI.A.1
Lopez, Herman (Envia Systems)	II.A.1

Contributor/Collaborator (Organization)	Section(s) in Annual Progress Report, FY 2016
Lu, Dongping (Pacific Northwest National Laboratory)	V.H.5
Lu, Wenquan (Argonne National Laboratory)	IV.B.2, IV.F.2
Lynds, Shaw (Maxwell Technologies, Inc.)	II.A.4
Makila, Tommi (Energetics, Incorporated)	All
Manthiram, Arumugam (University of Texas at Austin)	V.H.9
Marcicki, James (Ford Motor Company)	III.C.3
Mazzeo, Brian (Brigham Young University)	V.F.6
Meng, Ying Shirley (University of California at San Diego)	V.E.5
Michelbacher, Christopher (Idaho National Laboratory)	II.A.11
Moganty, Surya (NOHMs Technologies, Inc)	II.A.9
Monroe, Charles (Oxford University)	V.G.2
Nanda, Jagjit (Oak Ridge National Laboratory)	IV.F.9, V.D.1, V.G.2
Nelson, Paul (Argonne National Laboratory)	III.A.1
Nuhfer, Kimberly (National Energy Technology Laboratory)	IV.D.6, V.G.2
O'Connor, Ian (Saft America, Inc.)	II.A.6
Parker, Walter G. (National Energy Technology Laboratory)	IV.F.1, IV.F.3, V.C.3, IV.F.2
Persson, Kristin (Lawrence Berkeley National Laboratory)	V.F.2
Pesaran, Ahmad (National Renewable Energy Laboratory)	I, III.C.1, IV
Pintauro, Peter (Vanderbilt University)	IV.F.9
Polzin, Bryant (Argonne National Laboratory)	IV.F.10
Prezas, Panos (Argonne National Laboratory)	III.B.1
Qi, Yue (Michigan State University)	V.F.5
Qu, Deyang (University of Wisconsin at Milwaukee)	V.H.8
Rago, Nancy Dietz (Argonne National Laboratory)	IV.B.3
Rempel, Jane (TIAX LLC)	IV.D.6
Riggi, Adrienne (National Energy Technology Laboratory)	III.C.3, IV.D.5
Robertson, David (Argonne National Laboratory)	III.B.1
Ross, Philip N. (Lawrence Berkeley National Laboratory)	V.E.6
Sakamoto, Jeff (University of Michigan)	V.G.2
Seabaugh, Matthew (Nexceris, LLC)	IV.F.2
Sheldon, Brian W. (Brown University)	V.F.5
Shirk, Matthew (Idaho National Laboratory)	III.B.2
Siegel, Donald (University of Michigan)	V.G.2
Singh, Jagat D. (3M)	IV.D.1

Contributor/Collaborator (Organization)	Section(s) in Annual Progress Report, FY 2016
Smith, Patricia (U.S. Navy)	V
Snyder, Kent (Ford Motor Company)	IV.F.10
Somorjai, Gabor A. (University of California at Berkeley)	V.E.6
Srinivasan, Venkat (Lawrence Berkeley National Laboratory)	V.F.1
Steele, Leigh Anna M (Sandia National Laboratories)	III.B.3
Stefan, Ionel (Amprius, Inc.)	II.A.3, IV.F.6
Strand, Dee (Wildcat Discovery Technologies)	V.C.3
Susarla, Naresh (Argonne National Laboratory)	III.A.1
Tabacchi, John (National Energy Technology Laboratory)	IV.D.1, IV.F.6, V.H.4
Takeuchi, Esther (Stony Brook University)	V.H.4
Tataria, Harshad (General Motors)	II.A.6
Tenent, Robert (National Renewable Energy Laboratory)	IV.E.6
Thackeray, Michael M. (Argonne National Laboratory)	V.D.5, V.D.9, V.E.8
Tong, Wei (Lawrence Berkeley National Laboratory)	V.D.10
Turner, John A. (Oak Ridge National Laboratory)	III.C.2
Vaughey, John T. (Argonne National Laboratory)	IV.C.2
Venkatachalam, Subramanian (Envia Systems)	IV.D.3
Voelker, Gary E. (Miltec UV International)	IV.F.7, IV.F.12
Wachsman, Eric (University of Maryland)	V.G.4
Wang, Chong-Min (Pacific Northwest National Laboratory)	V.E.7
Wang, Donghai (Pennsylvania State University)	II.B.1, IV.D.5
Wang, Feng (Brookhaven National Laboratory)	V.D.4
Wang, Francis (SiNode Systems)	II.A.8
Wang, Yan (Worcester Polytechnic Institute)	II.A.10
Waterhouse, Robert (AMTEK Research LLC)	II.A.7
Wheeler, Dean (Brigham Young University)	V.F.6
Whittingham, M. Stanley (Binghamton University)	V.D.2
Wixom, Michael (Navitas Systems)	IV.F.10
Wolfenstine, Jeffrey (Army Research Laboratory)	V.G.2
Wood III, David L. (Oak Ridge National Laboratory)	IV.E.4, IV.E.3, IV.F.10
Wood, Weston (AMTEK Research LLC)	II.A.7
Woodford, William (24M Technologies, Inc.)	IV.F.13
Xiao, Xingcheng (General Motors)	V.F.5
Xing, Yangchuan (University of Missouri)	IV.F.3

Contributor/Collaborator (Organization)	Section(s) in Annual Progress Report, FY 2016
Xu, Wu (Pacific Northwest National Laboratory)	V.G.6, V.I.1
Yang, Xiao Guang (Ford Motor Company)	II.A.11
Yang, Xiao-Qing (Brookhaven National Laboratory)	V.E.3, V.H.8, V.J.1
Yu, Xiqian (Brookhaven National Laboratory)	V.E.3
Zaghib, Karim (Hydro-Quebec/IREQ)	V.B.2
Zhang, Ji-Guang (Pacific Northwest National Laboratory)	V.C.1, V.D.3, V.G.6, V.I.1
Zheng, Jianming (Pacific Northwest National Laboratory)	V.D.3
Zhou, Zoe (Ford Motor Company)	II.A.9

U.S. DEPARTMENT OF ENERGY
Energy Efficiency & Renewable Energy

For more information, visit: energy.gov/eere/vehicles

DOE/EE-1531 • August 2017